PHYS

VOLUME

Published by the American [illegible]
for the
AMERICAN PHYSICAL

Officers

President

J. H. Van Vleck
Harvard University
Cambridge, Mass.

Vice-President

Enrico Fermi
Institute for Nuclear
University of Chicago
Chicago 37, Illinois

Secretary

K. K. Darrow
Bell Telephone Labs.
Office
Columbia University
New York 27, New

Treasurer

G. B. Pegram
Columbia University
New York 27, New

Local Secretary
for the Pacific

J. Kaplan
University of Calif.
Angeles
Los Angeles, California

Managing

S. A. Goudsmit
Brookhaven National
Upton, Long Island
New York

THE PHYSICAL REVIEW

A Journal of Experimental and Theoretical Physics established by E. L. Nichols in 1893

BOARD OF EDITORS

Editor

S. A. Goudsmit

Associate Editors

Harvey Brooks	M. Goldhaber	W. F. [illegible]
C. P. Cheves	E. Hoffstadter	P. G. [illegible]
C. L. Critchfield	A. W. Lawson	W. E. [illegible]
N. Dearborn	A. Pais	Cornelius [illegible]
C. E. Johnson	E. Segrè	W. [illegible]
Ernest Ruhl	C. H. Townes	Associate [illegible]

Manuscripts for publication should be submitted to S. A. Goudsmit, Brookhaven National Laboratory, Upton, Long Island, New York. Authors [illegible] are requested to pay a publication charge [illegible], which includes these as 100 free reprints. [illegible] of more than eight pages.

Proof and all correspondence concerning papers in the process [illegible] should be addressed to the Publication Manager, American Physical Society, 175 Fifth Avenue, New York 10, New York.

Subscription Price

Foreign Postage and Exchange [illegible]

Single Numbers*

Twenty-five complete yearly volumes complete your set available.

Prior to 1920: $25.00
Thereafter: $50.00

Single numbers: $2.00 each, prior to July, 1929;
$1.00 each, July, 1929–December, 1941;
$2.00 each, January, 1942–December, 1945;
$3.00 each, thereafter.

General Index, 1913–1929: $4.00.

Subscriptions, remittances, and orders for back numbers should be addressed to the American Institute of Physics, 57 East 55 Street, New York 22, New York.

Changes of address in the case of members of the American Physical Society should be addressed to the Treasurer; in the case of other subscribers, to the American Institute of Physics.

* This issue is [illegible] Physics Department, Cornell University, Ithaca, New York.

The Physical Review is published each month by Lancaster Press, Inc., Lancaster, Pennsylvania.

Entered as second-class matter [illegible], 1926, at the Post Office at Lancaster, Pennsylvania, under the Act of March 3, 1879.

Acceptance for mailing at special rate of postage provided for in paragraph (d-2), section 34.40, P. L. & R., of 1948, authorized [illegible]

THE
PHYSICAL REVIEW

A journal of experimental and theoretical physics established by E. L. Nichols in 1893

SECOND SERIES, VOL. 88, No. 3 NOVEMBER 1, 1952

Elastic Scattering of 10-Mev Deuterons by H^3 and He^3*

J. C. ALLRED, A. H. ARMSTRONG, A. M. HUDSON, R. M. POTTER, E. S. ROBINSON, LOUIS ROSEN, AND E. J. STOVALL, JR.
University of California, Los Alamos Scientific Laboratory, Los Alamos, New Mexico

(Received July 16, 1952)

The d-t and d-He^3 differential elastic scattering cross sections have been measured for the 10-Mev deuteron bombarding energy of the external beam of the Los Alamos cyclotron. Nuclear plates detected the charged particles in the angular region 30° to 140° in the c.m. coordinate system. Although the cross section as a function of angle shows marked asymmetries, indicative of scattering contributions from partial waves of high angular momentum, the two curves are identical above 45° in the c.m. system.

I. INTRODUCTION

THE scattering of light nuclei is, in itself, an important method for studying the nature of nuclear forces. However, aside from the general interest in interactions between light nuclei, there is additional importance attached to the pair of interactions d-t and d-He^3 because the respective compound nuclei differ only by one unit of charge. It was therefore anticipated that an accurate determination of the differential elastic scattering cross sections for the above reactions would provide information concerning the equality of n-n and p-p forces.

There already exists an imposing amount of evidence which points to the equality of n-n, p-p, and n-p forces. This evidence may be briefly summarized as follows:

(a) It is possible to calculate the mass differences of mirror nuclei which undergo radioactive transitions from a knowledge of the electrostatic energies of the nuclei and the n-p mass difference.[1–5] This suggests that the strictly nuclear forces among a group of nucleons are not influenced, if neutrons are replaced by protons and vice versa.

(b) Further evidence for the equality of n-n and p-p forces is to be found in the almost linear variation of nuclear binding energies as a function of atomic weight.[6]

(c) Finally, the equivalence of n-n and p-p forces has been inferred from experiments on n-d and p-d scattering.[7] Also, analysis of p-p scattering has shown the ^1S wave interactions between neutron-proton and proton-proton to be approximately equal if ranges and potential shapes are assumed identical except for a small difference in potential depth.[8] This, however, can be accounted for by the magnetic interaction between nucleons, if a Yukawa potential is postulated.[9,10] Although, until recently, it appeared that interpretation of the results of the high energy scattering experiments required postulating inequality of p-p and n-p forces,[11] these data can now be explained by introduction of a spin orbit interaction which is velocity dependent,[12] or by a very short-range repulsive force.[13]

The interactions $d+t \rightarrow He^4+n$ and $d+He^3 \rightarrow He^4+H^1$ have been investigated at this laboratory for 10-Mev deuterons[14,15] with the result that, within experimental error, the differential cross sections are found to be identical. It is, however, questionable whether these results can be cited as evidence for the equality of n-n and p-p forces since it may be that these results can be satisfactorily explained by a stripping theory.[16,17] However,

* Work performed under the auspices of the AEC.

[1] Fowler, Delsasso, and Lauritsen, Phys. Rev. **49**, 561 (1936).
[2] White, Delsasso, Fox, and Creutz Phys. Rev. **56**, 512 (1939).
[3] White, Creutz, Delsasso, and Wilson, Phys. Rev. **59**, 63 (1941).
[4] L. D. P. King and D. R. Eliot, Phys. Rev. **58**, 846 (1940) and **59**, 403 (1941).
[5] Brown, Snyder, Fowler, and Lauritsen, Phys. Rev. **82**, 159 (1951).
[6] L. A. Young, Phys. Rev. **48**, 913 (1935).
[7] Gregory Breit, Phys. Rev. **80**, 1110 (1950).
[8] Breit, Condon, and Present, Phys. Rev. **50**, 825 (1936).
[9] Breit, Hoisington, Shore, and Thaxton, Phys. Rev. **55**, 1103 (1939).
[10] J. Schwinger, Phys. Rev. **78**, 135 (1950).
[11] R. S. Christian and E. W. Hart. Phys. Rev. **77**, 441 (1950).
[12] K. M. Case and A. Pais, Phys. Rev. **80**, 203 (1950).
[13] R. Jastrow, Phys. Rev. **79**, 389 (1950).
[14] Brolley, Fowler, and Stovall, Phys. Rev. **82**, 502 (1951).
[15] J. C. Allred, Phys. Rev. **84**, 695 (1951).
[16] S. T. Butler, Proc. Roy. Soc. (London) **A208**, 559 (1951).
[17] S. T. Butler and J. L. Symonds, Phys. Rev. **83**, 858 (1951).

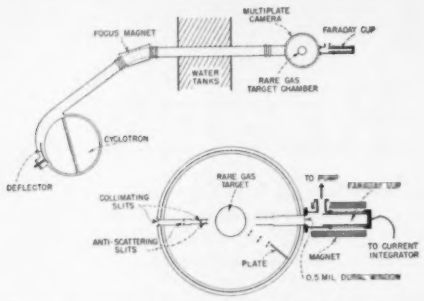

FIG. 1. Experimental geometry, showing details of mounting Faraday cup at rear of multiplate camera.

the similarity (or dissimilarity) of the differential d-t and d-He^3 elastic scattering cross section may well be more amenable to interpretation on the basis of the charge independence of nuclear forces.

II. EXPERIMENTAL ARRANGEMENT

The Los Alamos cyclotron and focusing magnet provided a well-collimated beam of 10-Mev deuterons at a distance of 15 feet from the cyclotron tank and 4 feet from the water walls. A nuclear multiple plate camera was aligned with its axis coincident with the axis of the deuteron beam. At the center of the camera was placed a thin-walled target chamber which served to confine the He^3 and tritium gases. The nuclear plate detectors were arranged behind slit systems and around the periphery of the camera in such a way that each plate could "see" an accurately defined section of the reaction volume. The angular resolution of the slit systems through which the reaction particles passed was $\pm 0.8°$. The angular divergence of the incident deuteron beam was 0.85° in the vertical direction and 1.2° in the horizontal direction. After traversing the 0.5-mil Duraluminum window of the nuclear plate camera, those deuterons scattered through large angles by the window were removed by an additional collimating system built into the camera. This collimating system permitted a maximum angular divergence of $\pm 2°$. Data on the range and intensity distributions of the reaction products were taken over the laboratory angular interval 15° to 115°.

A detailed description of the method for utilizing the cyclotron beam and of the design and construction of the camera are given elsewhere.[18,19]

In an experiment where small amounts of rare gases are used, as in the case in the present experiment, the advantages of nuclear emulsions as detectors are significant. In the first place, they make possible the rapid acquisition of data over a large angular region. Since these data are obtained simultaneously at angular intervals of 2.5°, one can derive accurate relative cross-sectional values from a single run and for the same set of cyclotron conditions. The second significant advantage is to be found in the ability to discriminate between real and spurious counts by means of the orientation and range of the tracks in the detectors. This is quite important when one is obliged to use a target chamber to confine the scattering gas, since the chamber itself becomes a scatterer and one must discriminate against particles which suffer such scattering.

The experimental details and procedure for making cross-sectional measurements with our nuclear multiplate camera were altered somewhat for the present experiment from that previously described.[20] The changes in the experimental arrangement are illustrated in Figs. 1 and 2. The target gases were contained in a hollow cylinder with a 0.5-mil Duraluminum window around its periphery. This target chamber was made by slotting a hollow Duraluminum cylinder over a region encompassing 300° and then covering the slotted section with 0.5-mil Duraluminum foil. The foil was sandwiched between the above cylinder and a second cylindrical shell, which was slotted and machined to fit snugly around the main cylinder in such a way that the two slotted sections overlapped. The outer shell and foil were then arc-welded to the inner cylinder, the welding being done in a argon atmosphere. A target chamber prepared in the above manner can hold a positive pressure of approximately one atmosphere. In case of window failure during a run, the gas would have been confined by the camera and could have been recovered. However, no target window failures occurred while He^3 or tritium were contained.

The charge measurement was carried out as previously described[20] with the exception that the Faraday cup was attached to the camera proper so as to obviate the necessity for placing the camera and Faraday cup in another vacuum system. The Faraday cup had its own pumping system and was evacuated to a pressure less than 10^{-5} mm Hg before each run.

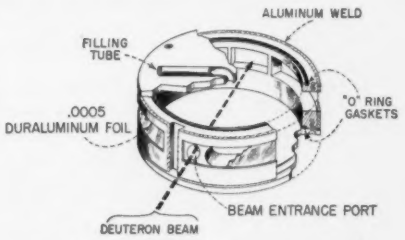

FIG. 2. Cutaway drawing of rare gas target chamber.

[18] Curtis, Fowler, and Rosen, Rev. Sci. Instr. **20**, 388 (1949).
[19] Allred, Rosen, Tallmadge, and Williams, Rev. Sci. Instr. **22**, 191 (1951).
[20] L. Rosen and J. C. Allred, Phys. Rev. **82**, 777 (1951).

III. PURIFICATION AND HANDLING OF GASES

The beta-decay of tritium permits the preparation of an isotopically pure He^3 sample. A sample of tritium (in this case 95 percent H^3, 5 percent H^1) reacted with finely divided and out-gassed uranium to form UH_3. The decay rate of the tritum is about 0.5 atomic percent per month. Since He^3 has a monatomic molecule, the volume growth of He^3 is about one percent per month. The He^3 gas used in the present experiment was obtained in this manner. Additional purification of the He^3 is done by passing the gas sample over activated charcoal at liquid air temperature.

The physical properties of UH_3 make the purification of the tritium sample quite convenient. At room temperature the pressure of tritium over UH_3 with an excess of uranium is $\sim 10^{-6}$ mm Hg. Thus one can remove any gaseous contaminant by pumping on the UH_3 at room temperature with a mercury diffusion pump. Moderate heating evolves the hydrogen isotopes, which are admitted to the target chamber at the desired pressure. Finely divided uranium is an excellent getter; hence, traces of water vapor or oxygen are readily removed by the heated uranium.

Since the rate of evolution of the tritium-hydrogen mixture is somewhat variable, an auxiliary expansion volume, V_1 of Fig. 3, is used in the initial stage of target filling. The volume of the system comprising the uranium furnace, V_1, and the manometer leads was arranged so as to be approximately that of the Dural gas target chamber inside the camera. Gas is initially evolved to about twice the desired pressure in the filling system. The uranium furnace is then closed off from the system, and the gas is admitted tc the target chamber. This procedure eliminates the possibility of target window breakage by gas surges from the uranium furnace.

After the target gas has come to temperature equilibrium with the target chamber and filling system, the bombardment is begun. At the conclusion of the run. the tritium-hydrogen mixture is recovered in the uranium furnace. When the furnace is reconnected to the target chamber, the tritium-hydrogen pressure drops rapidly to a value of the order of 10^{-5} mm Hg at room temperature.

He^3 gas is stored in the container V_2. A sufficient quantity is used to fill the target chamber to the desired pressure by expansion. The gas is recovered in V_2 by means of the Toepler pump shown in Fig. 3. A two-way stopcock is provided at the top of the Toepler pump for use in the He^3 fillings.

The pressure is measured by reading the manometer with a good cathetometer. The temperature is taken as room temperature, which is the same as the temperature of the body of the nuclear plate camera. The temperature and pressure readings are taken after the gas has come to temperature equilibrium in the target, as evidenced by the stability of the pressure reading. The

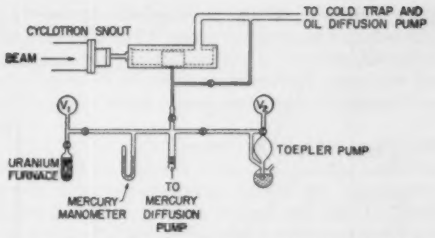

FIG. 3. Gas system for filling the rare gas target with H^3 and He^3 and recovering the samples after running.

atomic density, n_0, in atoms/cm³, is calculated from

$$n_0 = nPAT_0 d/P_0(T_0+t)V_0,$$

where n = number of atoms per molecule of target gas; P = pressure of gas in target; A = Avogadro's number = 6.025×10^{23} molecules/mole; T_0 = standard temperature = 273°K; P_0 = standard pressure = 76.0 cm Hg; t = room temperature in °C; V_0 = molar volume at STP = 2.24×10^4 cm³; d = (density of Hg at temperature t)/(density of Hg at 0°C).

IV. EXPERIMENTAL PROCEDURE

The procedure for making a run is as follows:

The multi-plate camera is loaded with nuclear plates (Ilford C-2), the emulsion thickness chosen being such that the highest range particles to be observed will be stopped within the emulsion. The camera and target chamber are then pumped down by means of an oil diffusion pump to a pressure less than 10^{-4} mm Hg. Simultaneously, the Faraday cup is pumped down by its own oil diffusion system to a pressure less than 10^{-5} mm Hg. At this time the current integrator is calibrated,[20] after which the target chamber is disconnected from the camera and both are closed off from the pumping system. Tests are now made with He^4 to determine whether the target chamber is completely tight at a pressure significantly higher than the pressure to be used in the run. If the chamber does not leak, the scattering gas is introduced into it in the manner described in Sec. III. The pressure of the gas is now observed until temperature equilibrium is attained with the target chamber and camera, as evidenced by the constancy of the pressure. During this time the cyclotron is warmed up and an internal beam obtained. After the final pressure measurement the deflector is energized, and a beam of 0.05 to 0.3 μa is passed through the target for a time ranging from 3 to 15 minutes. This accomplished, the pressure in the target is remeasured and the gas reclaimed. If H^3 is used as the target gas, the camera is pumped down by means of a fore pump vented to an outdoor stack as a precaution against traces of H^3 gas which might have found their way into the camera. The last step involves opening the camera to the air for removal of plates.

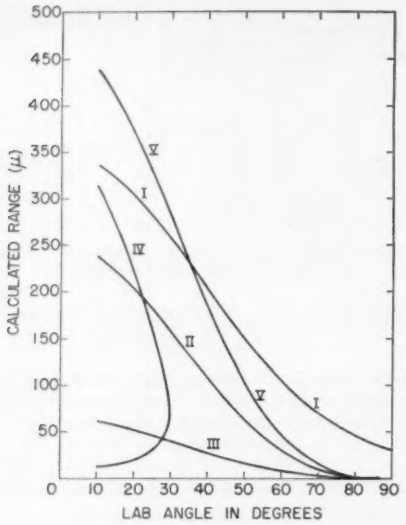

FIG. 4. Range *versus* angle for the scattering interactions of 10-Mev deuterons with protons, tritons, and He^3 nuclei. I. deuterons scattered by H^3 or Hd^3; II. recoil tritons; III. recoil He^4 nuclei; IV. deuterons scattered by H^1; V. recoil protons.

In order to make an over-all check on the accuracy with which we might expect to make absolute cross-sectional measurements under the new conditions of containing the target gas and mounting the Faraday cup, we ran experiments on *d-p* and *d-d* scattering. Both of these reactions have been investigated with high accuracy[20-22] and under more favorable conditions than could now be employed. The gases were introduced in precisely the same manner as was to be used for the H^3 and He^3. The results of these runs show that, although the target walls are responsible for a considerable number of background tracks, the error introduced by background at angles above 20° in the laboratory system is quite small. Above this angle, the cross sections obtained for *d-p* and *d-d* elastic scattering agree to within 3 percent with previous measurements. This result gave us confidence that we were measuring current correctly, and that the 0.5-mil Duraluminum target window was not producing spurious effects by way of multiple small angle scattering of the reaction particles.

V. ANALYSIS OF PLATES

The precedure for analyzing the plates is the same as has been previously described.[20] The analysis of each plate starts with a determination of the distribution in range of the charged particles recorded in one or more swaths of the plate. Each swath is approximately 100 microns wide and 3 cm long. Since elastic scattering processes yield monoergic groups of particles, it is immediately possible from energy considerations to identify each group of tracks with the corresponding reaction product. Having made this identification, one counts the tracks falling within the desired range groupings over a sufficient number of swaths to give the statistical accuracy desired. The range analysis makes possible discrimination against all tracks not due to elastic scattering and, in the case of tritium, those due to deuterons scattered by hydrogen contamination in the tritium as well as hydrogen nuclei projected by the deuterons. Protons from the $d+He^3 \rightarrow He^4+p$ reaction are of sufficiently high energy as to cause no confusion. He^4 particles from the $d+t \rightarrow He^4+n$ reaction are of sufficiently low energy so that they also cause no difficulty. Neither of the above reactions has a sufficiently high cross section to add significantly to the track density on the plates.

The range distribution of the various reaction particles recorded can be anticipated on the basis of energy and momentum considerations and the appropriate range-energy relationships for the nuclear emulsion used. Let E_D = incident deuteron energy; E_1 = energy of deuteron scattered by a mass 3 particle; E_2 = energy of projected mass 3 particle; E_3 = energy of deuteron scattered by a proton; E_4 = energy of projected proton; E_5 = maximum energy of proton for reaction disintegration of the deuteron upon collision with either a triton of a He^3; Q = binding enregy of deuteron = −2.2 Mev; θ = angle which scattered deuteron makes with incident deuteron direction: ϕ = angle which projected particle (He^3, H^3, or H^1) makes with incident deuteron direction. Then

$$E_1=(4/25)E_D\{\cos\theta+[(9/4)-\sin^2\theta]^{\frac{1}{2}}\}^2; \quad (1)$$

$$E_2=(24/25)E_D\cos^2\phi; \quad (2)$$

$$E_3=(4/9)E_D\{\cos\theta\pm[(1/4)-\sin^2\theta]^{\frac{1}{2}}\}^2; \quad (3)$$

$$E_4=(8/9)E_D\cos^2\phi; \quad (4)$$

$$E_5=(2/25)E_D\{\cos\phi+[6+10(Q/E_D)-\sin^2\phi]^{\frac{1}{2}}\}^2. \quad (5)$$

Each energy may now be converted into a range in Ilford C-2 nuclear emulsions by use of the appropriate range-energy relationship.[24] Figure 4 gives the variation of range in Ilford C-2 emulsions with angle for the various reaction particles from the processes with which we are concerned and for an incident deuteron energy of 10 Mev.

The energy of the incident deuteron beam was determined from the ranges in Ilford C-2 emulsions of the elastically scattered deuterons on either side of the incident beam direction, and the above-mentioned range-energy curves. Account was taken of energy losses by the scattered deuterons in the target gas and in the

[21] Mather, Karr, and Bondelid, Phys. Rev. **78**, 292 (1950).
[22] Rodgers, Leiter, and Kruger, Phys. Rev. **78**, 656 (1950).
[23] Allred, Erickson, Fowler, and Stovall, Phys. Rev. **76**, 1430 (1949).
[24] J. Rotblat, Nature **167**, 550 (1951).

target chamber window. The incident beam energy for the present experiments was determined to be 10.3 ±0.2 Mev.

It is apparent from the range-energy curves that, at least in principle, it is possible to resolve the various groups of particles present in each reaction over most of the angular region in which measurements can be made. The greatest difficulty arises from H^1 contamination in the H^3. However, since the cross section for d-p scattering is accurately known at the energy in question, it is possible to determine the amount of H^1 contamination in the tritium. This is done by counting tracks in the proton peak from *d-p* scattering at angles where this peak is well resolved from the deuteron and triton peaks. By this means we determined that our H^3 sample contained 5.5 atomic percent H^1 impurity. It was then possible to correct for the H^1 contamination at angles where we did not have adequate resolution to separate the reaction products from *d-p* scattering from those arising from *d-t* scattering by using the derived value of H^1 impurity and the known cross section for *d-p* scattering.

Figure 5 shows the range distribution of the charged particles at various angles for *d-t* and *d*-He^3 interactions. The identity of the particles responsible for the various groups is inferred from Fig. 4. The reaction products enter the surface of the plate at a grazing angle of 11.8° and the plotted ranges of Fig. 5 are projected ranges, rather than absolute ranges.

From an inspection of the range distributions in Fig. 5, it is apparent that a good deal of "background" is present. This background introduces considerable inaccuracy in making absolute cross-sectional measurements on the elastic processes, since it is difficult to determine precisely just how much background is included within the range limits of a given group of particles. The background correction was made by drawing in the background on the basis of its magnitude on either side of the particle group in question in such a way that the peak went to zero on both sides. The widths of the resultant peaks were required to be consistent with the widths calculated from homogeneity of the beam, angular resolution, and range straggling.

VI. CORRECTIONS AND EVALUATION OF ERRORS

As indicated above, it is necessary to make corrections for background and hydrogen contamination in the H^3. The correction for H^1 contamination amounts to as much as 20 percent in some cases, due to the relatively large *d-p* cross section as compared to *d-t*. However, in most cases, this correction is no more than 10 percent and can be made quite precisely. The correction for other background, including protons from deuteron disintegration, is also as much as 20 percent in the worst cases and this produces considerable inaccuracy in the final results.

The errors involved in the absolute elastic scattering cross sections were evaluated as follows: geometry, ±1 percent; background, ±0–20 percent; charge measurement, ±1.5 percent; microscope calibration, ±0.5 percent; personal errors, ±1 percent; statistics, ±2–3 percent. Errors were evaluated separately for each angle at which a cross-sectional measurement was made.

Runs were made at pressures of 0.7 to 9.2 cm Hg and with integrated currents of 2.9 to 69.6 μcoulombs. The results were self-consistent within the inaccuracies imposed by statistics and background. The fact that widely different gas pressures and currents yielded the same cross-sectional values is convincing evidence that serious errors do not arise due to background from multiple scattering in the target gas, or from scattering by the slits and target windows. It is also evidence that our current measurement was not influenced by the target gas and that our pressure measurements were self-consistent.

VII. RESULTS AND DISCUSSION

Table I and Fig. 6 give the data obtained for the elastic scattering cross section as a function of angle in the c.m. system.

There is unmistakable evidence (see Fig. 5) for deuteron disintegration in both the *d-t* and *d*-He^3 interactions. It is also apparent that deuterons on He^3 produce more disintegrations than deuterons on H^3.

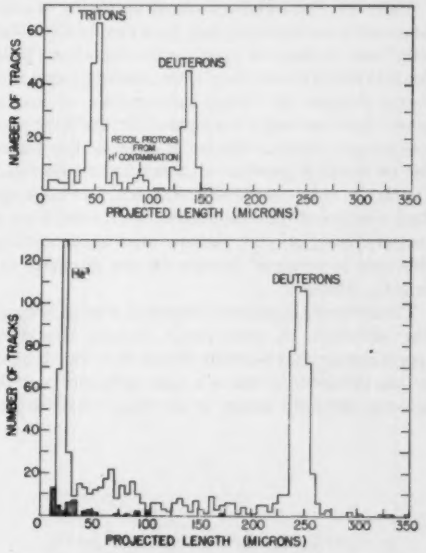

FIG. 5. Range distributions observed for the interaction of 10.2-Mev deuterons with tritium (above) and He^3 (below). The laboratory angles of observation are 50° and 30°, respectively. The shaded area in the lower histogram indicates the result of a background run made without gas in the target. The results are normalized to integrated beam current and plate area analyzed.

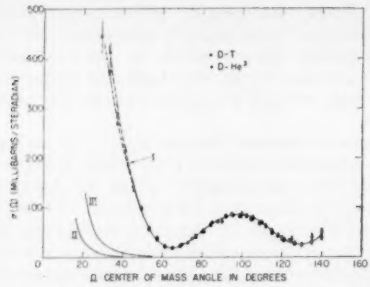

FIG. 6. Differential cross section *versus* center-of-mass angle for d-t and d-He^3 elastic scattering; II. calculated Coulomb scattering for d-t; III. calculated Coulomb scattering for d-He^3. $E_D = 10.2$ Mev.

A least squares analysis of the variation with angle of the differential elastic cross section for d-t and d-He^3 scattering gives the following result:

$$\sigma(\Omega) = 0.0790 - 0.1013\cos\Omega - 0.3776\cos^2\Omega + 0.3111\cos^3\Omega + 0.7601\cos^4\Omega + 0.0929\cos^5\Omega + 0.0800\cos^6\Omega.$$

This indicates that at least D waves, and possibly F waves, are effective in the scattering processes.

Above 45° c.m., where Coulomb scattering is small compared to nuclear scattering, the d-t and d-He^3 differential cross sections for elastic scattering appear to be identical within the accuracy of the present experiments. If one assumes the charge independence of nuclear forces, then one might anticipate that, for large scattering angles, the two differential cross sections should also be identical provided all other factors are equal. The factors to be considered are the difference in electrostatic energies of the compound nuclei, the difference in magnetic energies, and, perhaps most important, the difference in potential barriers for the incoming and outgoing deuteron.

The difference in magnetic energies is negligibly small. The difference in electrostatic energies should be approximately that between H^3 and He^3. This is given by the difference of the n-p mass difference and the beta-ray end-point energy in the decay of H^3 to He^3.

TABLE I. Differential cross sections as a function of center-of-mass angle for d-t and d-He^3 scattering at 10.2-Mev bombarding energy

Ω degrees	d-t $\sigma(\Omega)$ barns	d-He^3 $\sigma(\Omega)$ barns
29.1	0.444 ±0.028	
33.2	0.374 ±0.017	0.418 ±0.019
37.3	0.268 ±0.012	0.290 ±0.013
41.4	0.216 ±0.010	0.215 ±0.011
45.4		0.142 ±0.007
49.5	0.0968±0.0045	0.100 ±0.005
53.5	0.0559±0.0031	0.0597±0.0029
57.5	0.0362±0.0023	0.0391±0.0021
61.4	0.0221±0.0013	0.0240±0.0016
65.4	0.0200±0.0015	0.0183±0.0013
69.3	0.0252±0.0013	0.0235±0.0012
70.0	0.0258±0.0015	
73.1	0.0298±0.0016	0.0295±0.0014
75.0	0.0383±0.0022	
76.9	0.0456±0.0022	0.0404±0.0019
80.0	0.0503±0.0025	
80.7	0.0567±0.0028	0.0515±0.0024
84.4	0.0662±0.0036	0.0639±0.0031
85.0	0.0705±0.0033	
88.1	0.0732±0.0038	0.0721±0.0033
90.0	0.0724±0.0035	
91.7	0.0838±0.0041	0.0804±0.0039
95.0	0.0870±0.0043	
95.3	0.0852±0.0040	0.0861±0.0040
98.8	0.0834±0.0042	0.0837±0.0039
100.0	0.0861±0.0040	
102.2	0.0818±0.0040	0.0843±0.0040
105.0	0.0763±0.0036	0.0768±0.0038
105.5	0.0780±0.0039	0.0814±0.0043
108.8	0.0682±0.0032	0.0696±0.0033
110.0	0.0705±0.0034	0.0695±0.0033
112.0	0.0609±0.0033	0.0642±0.0031
115.0	0.0529±0.0026	0.0478±0.0032
115.1	0.0546±0.0027	0.0532±0.0045
118.1	0.0433±0.0023	0.0452±0.0026
120.0	0.0403±0.0020	0.0356±0.0020
121.0	0.0348±0.0016	0.0364±0.0029
123.9		0.0347±0.0054
125.0		0.0362±0.0051
126.6	0.0268±0.0013	0.0300±0.0034
130.0		0.0246±0.0021
135.0	0.0300±0.0033	0.0409±0.0050
140.0	0.0392±0.0044	0.0538±0.0076

Its value is 764 kev,[25] which is quite small compared to the excitation energy.

The difference in Coulomb barriers in the two cases is approximately 0.25 Mev. In the center-of-mass system, the energy available is about 6 Mev, which is large compared to the highest Coulomb barrier (~0.5 Mev for d-He^3).

[25] Taschek, Jarvis, Argo, and Hemmendinger, Phys. Rev. **75**, 1268 (1949).

d-d Elastic Scattering at 10.5 Mev*

LOUIS ROSEN AND J. C. ALLRED
University of California, Los Alamos Scientific Laboratory, Los Alamos, New Mexico

(Received July 16, 1952)

Deuterons from the 42-inch cyclotron were scattered by a thin deuterium gas target. Scattered particles were detected by photographic emulsions in a nuclear multiplate camera. The differential cross section for elastic scattering was measured at 5° intervals in the center-of-mass system, from 25° to 145°, the estimated absolute rms standard error of the measured cross sections being ±3.1 percent. The measurements extend the angular range of the previous measurements of Allred, Erickson, Fowler, and Stovall at 10.8 Mev, and are in very good agreement with their values when the difference in bombarding energy is taken into account.

I. INTRODUCTION

THE *d-d* interaction has long been a subject of experimental and theoretical study, since the small number of nucleons involved and the identity of the particles simplify somewhat the possible modes of interaction and make the mathematical treatment of this problem feasible. In the energy region of the present measurements, the differential cross section for *d-d* elastic scattering has been measured previously at this laboratory by a thechnique in which a proportional counter detected deuterons scattered by a thin deuterium gas target, the incident deuteron energy being 10.8 Mev.[1] Exploratory measurements were also made[2] in which the proportional counter was replaced by a small camera containing a single nuclear emulsion plate. In this paper, the results of measurements made with a nuclear multiplate camera[3] are reported. These results extend the angular range of the previous measurements and are in essential agreement with them, when the difference in energy is taken into account.

Initially, the purpose of this experiment was to serve as a check on the properties of the rare gas target of the previous paper,[4] as well as on the newer mounting of the Faraday cup at the back of the camera. In the course of that investigation, runs were made in which deuterium gas was contained within a rare gas target chamber which was centrally located in the evacuated camera. Another set of data was taken with the gas target chamber absent and the whole camera filled with gas. Preliminary analysis of these data indicated that the data taken without the rare gas target in position could extend the angular range of the previous differential cross section measurements on *d-d* scattering. The following investigation was conducted without the gas target chamber.

II. EXPERIMENTAL PROCEDURE

The instrumentation of the cyclotron,[5] the use of the nuclear multiplate camera, and the analysis of the plates were the same as in the previous paper.[4] Similar techniques have been fully described elsewhere.[6]

Runs were made at pressures from 0.8 to 10.1 cm Hg, at accurately measured temperatures in the range 20° to 25°C, with integrated deuteron currents in the range 3.0 to 20.5 μcoulomb. The target gas contained 99.5 percent deuterium and 0.5 percent hydrogen, according to the manufacturer's specifications. This analysis was confirmed by the observed number of proton tracks in the distributions of range *versus* number for the scattered particles. Reference 2 indicates the method which we used for analysis of gas impurities from the scattering data.

A total of 124,000 tracks were counted, about 2200 tracks per plate analyzed. The incident beam energy was 10.5±0.15 Mev as determined by the method of reference 2.

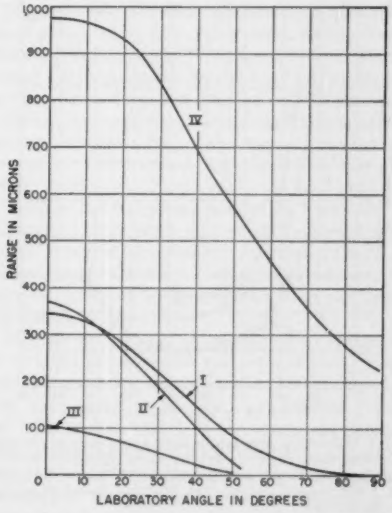

FIG. 1. Variation of range with angle for the products of the *d-d* interaction: I. elastically scattered deuterons; II. tritons from $D(d,p)T$; III. He^3 from $D(d,n)He^3$; IV. protons from $D(d,p)T$.

* Work performed under the auspices of the AEC.

[1] Allred, Erickson, Fowler, and Stovall, Phys. Rev. **76**, 1430 (1949).

[2] Rosen, Tallmadge, and Williams, Phys. Rev. **76**, 1283 (1949).

[3] Allred, Rosen, Tallmadge, and Williams, Rev. Sci. Instr. **22**, 191 (1951).

[4] Allred, Armstrong, Hudson, Potter, Robinson, Rosen, and Stovall, Jr., Phys. Rev. **88**, 425 (1952).

[5] Curtis, Fowler, and Rosen, Rev. Sci. Instr. **20**, 388 (1949).

[6] L. Rosen and J. C. Allred, Phys. Rev. **82**, 777 (1951).

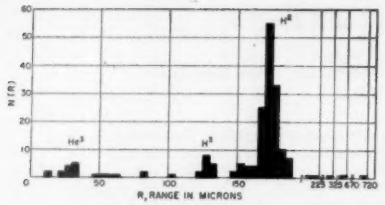

FIG. 2. Range distribution of d-d interaction products at 37.5° in the laboratory system, 181 tracks.

III. ANALYSIS OF DATA; RESULTS

Figure 1 shows the distribution in range of the scattered deuterons as a function of laboratory angle, together with the ranges of the protons, tritons, and He^3 particles from the reactions $D(d,p)T$ and $D(d,n)He^3$. It is seen that in the angular range from 5° to 25° in the laboratory system, the tritons may add counts to the deuteron peak since, in our experiment, it was not possible to observe the differences in specific ionization. In this region, where the two peaks overlap, the triton contribution was subtracted on the basis of the previously measured $D(d,p)T$ differential cross section at this bombarding energy.[7]

Figure 2 shows a typical range distribution for the scattered and reaction particles. These particles were observed at 37.5°, an angle at which the triton peak is resolved. The deuteron peak, between 150 and 200 μ, determines the number of deuterons scattered within the solid angle defined by the slit system geometry and the total width of the swaths read on each plate.

Figure 3 and Table I give the measured differential cross section as a function of center-of-mass angle. As is to be expected from the identity of the particles, the differential cross section is symmetrical about 90°. Figure 3 also shows the previous data at 10.8 Mev of Allred *et al.*[1] and a portion of the lower energy angular distributions measured by Blair *et al.*[8] The measurements at 10.8 and 10.5 Mev are in good agreement with the results of Burrows, Gibson, and Rotblat[9] at 8 Mev.

The estimated absolute rms standard error of the cross sections of Table I is ±3.1 percent, apportioned as follows: counting statistics, ±2.2 percent; current integration, ±1.7 percent; measurement of gas pressure and temperature, ±0.5 percent; geometrical factors, ±1.0 percent; and errors due to microscope calibration and personal factors, ±1.0 percent. Among the cross sections measured in six runs, the mean deviation was calculated at angles which were duplicated in two or more runs. The standard error derived from this calculation was 2.3 percent, a measure of the internal consistency of the data.

TABLE I. Measured differential cross sections, $\sigma(\Omega)$, in 10^{-24} cm²/steradian as a function of center-of-mass angle, Ω, in degrees.

Ω	$\sigma(\Omega)$	Ω	$\sigma(\Omega)$
25	0.389±0.012	90	0.100±0.003
30	0.354±0.011	95	0.097±0.003
35	0.295±0.009	100	0.104±0.003
40	0.263±0.008	105	0.109±0.003
45	0.213±0.007	110	0.123±0.004
50	0.197±0.006	115	0.124±0.004
55	0.152±0.005	120	0.140±0.004
60	0.143±0.004	125	0.162±0.005
65	0.128±0.004	130	0.185±0.005
70	0.122±0.004	135	0.221±0.007
75	0.107±0.003	140	0.253±0.008
80	0.102±0.003	145	0.287±0.009
85	0.101±0.003		

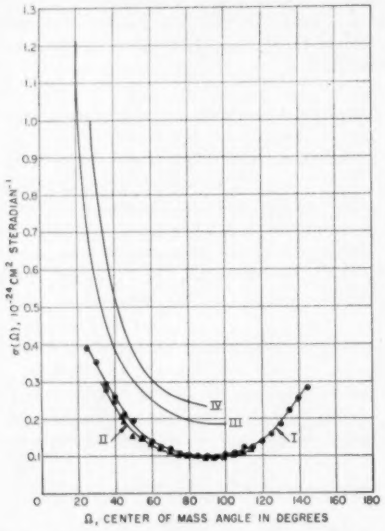

FIG. 3. Differential cross section for d-d scattering as a function of center-of-mass angle: I. Present data, E_D=10.5 Mev; II. Allred, Erickson, Fowler, and Stovall, E_D=10.8 Mev; III and IV. Blair, Freier, Lampi, Sleator, and Williams, E_D=3.50 and 2.01 Mev, respectively.

The authors wish to thank Dr. J. L. Fowler and members of the cyclotron group for their valuable aid in the experiments of this and the previous paper. For the analysis of the plates, we are indebted to the staff of the nuclear plate group.

[7] Allred, Phillips, and Rosen, Phys. Rev. **82**, 782 (1951).
[8] Blair, Freier, Lampi, Sleator, and Williams, Phys. Rev. **74**, 1594 (1948).
[9] Burrows, Gibson, and Rotblat, Proc. Roy. Soc. (London) **A209**, 489 (1951).

Elastic Scattering of 9.7-Mev Protons by Deuterium and by Hydrogen*

J. C. Allred, A. H. Armstrong, R. O. Bondelid,† and Louis Rosen
University of California, Los Alamos Scientific Laboratory, Los Alamos, New Mexico

(Received July 16, 1952)

The proton-deuteron and proton-proton differential scattering cross sections have been measured with a 9.7-Mev cyclotron external proton beam and with photographic plates as detectors of the scattered particles. In both interactions the angular distributions are similar to those observed at lower energies, and the total cross sections are in good agreement with reasonable extrapolations of the low energy data. The p-d data show some evidence for deuteron disintegration. Neglecting spin-orbit coupling, the p-p data are consistent with pure S wave scattering with a phase shift of $57.8°\pm1.2°$.

I. INTRODUCTION

THE investigation of p-d scattering was undertaken for the purpose of extending to 10 Mev the series of precise cross-section measurements made at Los Alamos and elsewhere in the energy region below 5.2-Mev incident proton energy.[1–4] It was hoped that accurate p-d scattering data up to 10 Mev would permit a check on existing theories[5–7] of the p-d interaction and aid in the development of new theories where existing theories appear inadequate.

The investigation of p-p scattering was originally performed to check the background determination in the p-d experiment. Because of the lack of data in this energy range, it seemed desirable to report our results in detail, although the accuracy attained was no better than about 4.5 percent.

II. EXPERIMENTAL PROCEDURE

Thin gas targets, spectroscopically pure, of deuterium for one experiment and hydrogen for the other, were bombarded with 9.7-Mev protons from the external beam of the Berkeley 60-inch cyclotron. The scattered and recoil nuclei were detected simultaneously over 2.5° intervals on photographic plates in a multiplate camera which has been previously described in detail.[8] In the p-d scattering investigation the range covered extended from laboratory angles of 10° to 170° with respect to the direction of the incident proton beam; in the p-p scattering experiment an upper limit of 60° in the laboratory system was imposed by the energetics of the interaction.

The direction and energy of the incident proton beam were determined for each run by a method previously described.[9] The energy averaged over all six p-d runs was 9.7 ± 0.15 Mev. The calculated energy for the last run of the p-p scattering experiment was consistently higher than that for the first two. Hence the cross-section values are listed separately instead of being averaged with the others. The average energy for runs *PP*-4 and *PP*-5 was 9.7 ± 0.15 Mev; that for *PP*-6 was $9.8_6\pm0.15$ Mev.

From examination of range distributions, the width at half-maximum of the incident proton beam was determined to be less than 0.15 Mev. The maximum divergence of the incident proton beam due to geometry of the system was 1.2° in the horizontal direction and 0.85° in the vertical direction. Protons scattered by more than 3.5° were prevented from entering the scattering chamber by a collimating system built into the camera. The angular resolution of the detection slit system was ±0.8°.

Magnetic shielding was required to prevent the external proton beam from being deflected into one side of the magnetic yoke by the fringing field of the cyclotron. A 5-ft long channel of soft iron of rectangular cross section with the large face perpendicular to the magnetic field of the cyclotron provided shielding sufficient to reduce the fringing field of the magnet near the cyclotron tank to 10^3 oersted. Additional shielding of the camera itself by a soft iron case ½-inch thick reduced the field inside the scattering chamber to 7 oersted.[10] The collimated proton beam entered the camera through a 0.5-mil Duraluminum window over the entrance port, passed through another 0.5-mil Dural window over the exit port, and was finally collected in an electrostatically shielded Faraday cup.

With the exception of the measurement of integrated current, the procedure for making a run was identical with that previously described.[4,8] A number of such runs were made with both H_2 and D_2 at different pressures and with various values of the integrated current in order to provide suitable track densities at all scattering angles and in order to check the purity and temperature constancy of the gas, the accuracy of the current inte-

* Work performed under the auspices of the AEC.
† Now at the Naval Research Laboratory, Washington, D. C.
[1] Sherr, Blair, Kratz, Bailey, and Taschek, Phys. Rev. **72**, 662 (1947).
[2] Rodgers, Leiter, and Kruger, Phys. Rev. **78**, 656 (1950).
[3] Karr, Bondelid, and Mather, Phys. Rev. **81**, 37 (1951).
[4] Louis Rosen and J. C. Allred, Phys. Rev. **82**, 777 (1951).
[5] R. A. Buckingham and H. S. W. Massey, Proc. Roy. Soc. (London) **A179**, 123 (1941).
[6] Buckingham, Hubbard, and Massey, Proc. Roy. Soc. (London) **A211**, 183 (1952).
[7] J. L. Gammel, Phys. Rev. **78**, 321 (1950).
[8] Allred, Rosen, Tallmadge, and Williams, Rev. Sci. Instr. **22**, 191 (1951).
[9] Rosen, Tallmadge, and Williams, Phys. Rev. **76**, 1283 (1949).
[10] Details of this arrangement are given in a paper by T. M. Putnam to be published in a forthcoming issue of the *Review of Scientific Instruments*.

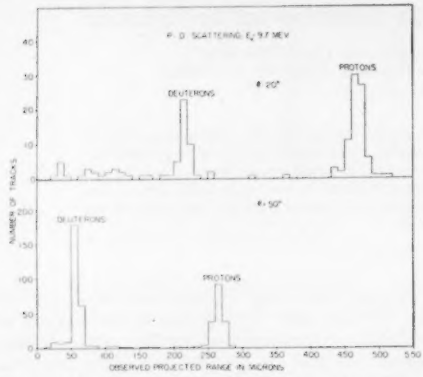

FIG. 1. Observed range distributions of scattered protons and recoil deuterons at laboratory angles of 20° (above) and 50° (below).

grator, and the multiple small angle scattering in the target gas. Six satisfactory runs were obtained with deuterium and three with hydrogen as the target. In those with deuterium the pressure ranged from a minimum of 5-cm Hg to a maximum of 21-cm Hg, and integrated current from a corresponding minimum of 2 microcoulombs to a maximum of 22 microcoulombs. For all three runs with the hydrogen target, the pressure was 5-cm Hg, while integrated current varied from 2 to 10 microcoulombs.

Several background runs without gas in the camera were made for the purpose of determining the background corrections for multiple scattering by the slits collimating the beam and defining the scattering angle, and for scattering by water vapor liberated from the emulsion.

The number of protons which passed through the scattering chamber during an exposure was determined by measuring the total charge accumulated on the faraday cup, the interior of which was at a pressure of 5×10^{-7}-mm Hg. In order to suppress secondary electrons from the aluminum foil which isolated the Faraday cup from the scattering chamber, a negative potential

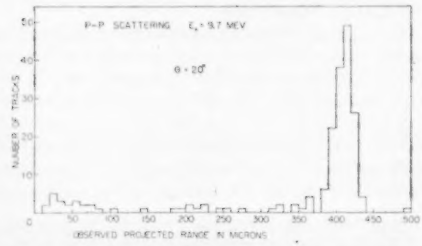

FIG. 2. Observed range distribution of protons scattered by protons.

TABLE I. Differential cross-section values in the center-of-mass system as a function of angle for p-d scattering at 9.7-Mev proton bombarding energy.

Center-of-mass angle (Degrees)	$\sigma(\Omega)$ (Barns)	Center-of-mass angle (Degrees)	$\sigma(\Omega)$ (Barns)
18.7	0.152 ±0.007	114.9	0.0231±0.0009
22.4	0.147 ±0.006	117.4	0.0208±0.0010
26.2	0.150 ±0.006	120.0	0.0206±0.0008
29.8	0.145 ±0.006	120.0	*0.0217±0.0010
33.6	0.145 ±0.006	122.4	0.0205±0.0009
37.2	0.127 ±0.005	124.9	0.0221±0.0009
44.5	0.122 ±0.005	127.2	0.0230±0.0010
50.0	*0.106 ±0.004	129.5	0.0246±0.0010
51.7	0.114 ±0.004	130.0	*0.0268±0.0011
55.2	0.104 ±0.004	131.7	0.0287±0.0012
58.8	0.0932±0.0035	133.9	0.0318±0.0013
60.0	*0.0967±0.0036	135.0	*0.0367±0.0015
65.0	*0.0920±0.0035	136.0	0.0350±0.0014
65.7	0.0835±0.0034	138.0	0.0392±0.0016
69.1	0.0826±0.0032	140.0	*0.0454±0.0017
70.0	*0.0817±0.0030	141.9	0.0510±0.0020
72.5	0.0699±0.0027	145.0	*0.0633±0.0027
79.2	0.0610±0.0024	145.6	0.0647±0.0027
80.0	*0.0645±0.0024	149.2	0.0780±0.0031
82.4	0.0592±0.0025	150.0	*0.0817±0.0029
85.0	*0.0557±0.0022	152.5	0.0882±0.0036
85.6	0.0521±0.0020	155.0	*0.103 ±0.005
90.0	*0.0484±0.0020	155.7	0.106 ±0.004
91.9	0.0451±0.0018	158.8	0.132 ±0.005
98.0	0.0372±0.0015	161.7	0.146 ±0.006
100.0	*0.0364±0.0014	164.5	0.162 ±0.006
103.9	0.0304±0.0012	167.2	0.180 ±0.007
105.0	*0.0301±0.0012	169.8	0.184 ±0.010
106.7	0.0278±0.0013	171.2	0.190 ±0.010
109.5	0.0247±0.0010	172.4	0.193 ±0.012
110.0	*0.0268±0.0010	173.7	0.180 ±0.012
112.2	0.0233±0.0010	175.0	0.190 ±0.015
		176.2	0.195 ±0.015

* Values obtained from recoil deuterons.

of 135 volts with respect to ground was placed on the current collector. An excessive leakage current between the outside of the current collector and ground was

TABLE II. Differential cross-section values in the center-of-mass system as a function of angle for p-p scattering at 9.7- and 9.85-Mev proton bombarding energies.

Center-of-mass angle (Degrees)	$\sigma(\Omega)$ at 9.7±0.15 Mev (Barns)	$\sigma(\Omega)$ at 9.85±0.15 Mev (Barns)
24		0.0592±0.0026
26		0.0555±0.0026
29	0.0517±0.0023	0.0536±0.0025
31		0.0509±0.0023
34	0.0528±0.0021	0.0496±0.0023
41	0.0543±0.0021	0.0548±0.0025
44	0.0528±0.0026	0.0568±0.0029
51	0.0543±0.0021	
54	0.0554±0.0023	
61	0.0554±0.0023	0.0541±0.0025
64	0.0567±0.0025	
71	0.0588±0.0024	
74	0.0599±0.0029	
81	0.0582±0.0023	
84	0.0578±0.0023	
91	0.0585±0.0024	
94	0.0584±0.0024	
101	0.0567±0.0022	
104	0.0599±0.0025	
111	0.0582±0.0024	
114	0.0578±0.0027	
121	0.0564±0.0024	

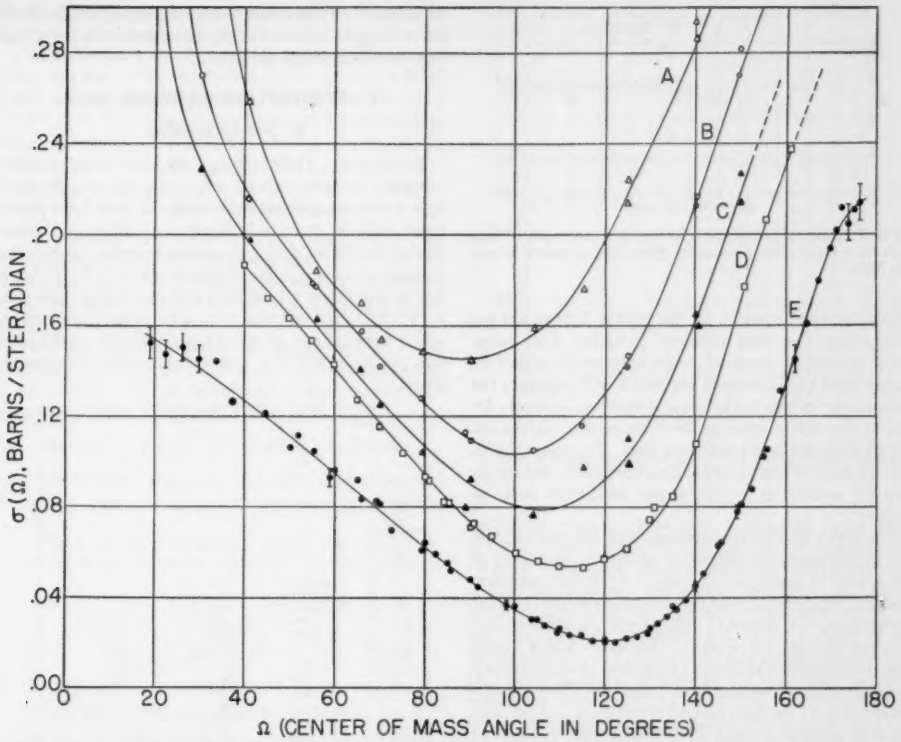

FIG. 3. Measured differential cross sections *versus* center-of-mass angle for *p-d* scattering, for protons of bombarding energy 1.5 to 9.7 Mev. A, B, C, Sherr *et al.* (reference 1), $E_p = 1.51$, 2.53, 3.49 Mev, respectively; *D*, Rosen and Allred (reference 4), $E_p = 5.18$ Mev; *E*, present data, $E_p = 9.7$ Mev.

observed and found to be due to ionization of the air by the intense gamma-ray background of the cyclotron. This leakage current was eliminated by an electrostatic shield placed around the Faraday cup and maintained at its potential.

The current integrator used was made available to us by the Crocker Radiation Laboratory and has been described by Cork, Johnston, and Richman.[11] It is essentially a bridge device in which the Faraday cup is connected to one plate of a standard condenser, and the potential applied by a slide-rack voltmeter. The capacitance of the condenser (1.075 ± 0.005 μf) was determined by the Bureau of Standards and was checked against a secondary standard before and after the experiment. No corrections to the current integration data were made.

III. ANALYSIS OF DATA AND EVALUATION OF ERRORS

The photographic plates were analyzed in the same manner as in the *d-p* scattering experiment of Rosen and Allred.[4] After making certain corrections which are described below, the differential cross sections are obtained directly from the number of tracks of proper range per unit swath width observed on the plates. Figure 1 shows typical range distributions of the scattered protons and recoil deuterons for the *p-d* interaction; and Fig. 2 shows a characteristic distribution of proton ranges resulting from the *p-p* interaction.

In both experiments a considerable amount of low energy background is apparent at the smaller angles. This is due partly to interaction particles whose energy has been degraded by penetration of the slit edges, and partly to protons from the incident beam which have penetrated or been scattered by the beam-collimating slits. Comparison of the *p-d* with the *p-p* data shows that a part of the "background" in the *p-d* interaction can be attributed to the disintegration of the deuteron. The correction for background tracks originating from all these sources was based on the shape of the range distribution in the neighborhood of the peak. In the *p-p* interaction it never exceeded 3 percent. No such

[11] Cork, Johnston, and Richman, Phys. Rev. **79**, 71 (1950).

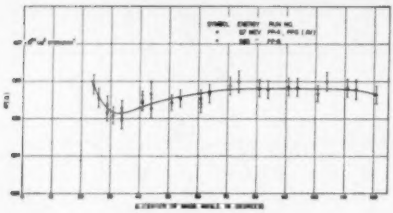

FIG. 4. Measured differential cross section *versus* center-of-mass angle for p-p scattering, for protons of bombarding energy 9.7 and 9.85 Mev.

correction was necessary for the proton data of the p-d interaction. The data obtained from the short range recoil deuterons, however, were in general subject to background corrections of the order of 7 percent; the uncertainty in this background correction accounts for almost the entire error in the cross-section values obtained from the recoil deuteron data. The range distributions showed that above 20° no correction was necessary for scattering by heavy gas impurities such as oxygen.

The errors which were common to all the runs of these two experiments are estimated as follows: geometry of slit system of multiplate camera, 1.0 percent; measurements of temperature and pressure, 0.5 percent; current integration, 2.5 percent; microscope calibration and personal factors, 1.0 percent. The errors which varied with angle are the statistical error and the uncertainty in assignment of background correction. The average uncertainty in the background corrections is 2 percent. Since in general at least 2500 tracks were counted at each angle, the statistical error is 2 percent or less. Thus, the absolute error varies from a minimum of 3.5 percent, at angles where background correction is unnecessary, to an average of 5 percent, at the angles where the correction is needed. In both experiments the greatest errors occur in the values for the smallest and the largest angles where large background corrections introduce the greatest uncertainties.

The final results for the differential elastic scattering cross sections as a function of angle are given in Tables I and II for the p-d and p-p interactions, respectively.

In Fig. 3 are shown our measured differential cross-section values for p-d scattering at 9.7 and 5.2 Mev, together with the measurements of Sherr *et al.* (reference 1) from 1.5 to 3.5 Mev. The errors in the values of our 9.7-Mev data are indicated at the extreme ends of the curve, where the uncertainties are largest, as well as for representative points at other parts of the curve. The values calculated from the recoil deuterons are in general slightly higher than those obtained from the scattered protons. The difference is probably due to errors in applying the background corrections.

The angular distributions of cross section for p-p scattering at 9.7 and 9.85 Mev are shown in Fig. 4. Although the values obtained at the higher energy were not averaged with the others, a single smooth curve has been drawn through the points.

IV. INTERPRETATIONS OF THE DATA

A. p-d Interaction

Buckingham, Hubbard, and Massey[6] have recently extended the prevous work of Buckingham and Massey[5] on n-d scattering to p-d scattering. In their later paper these authors have calculated the differential cross section for p-d scattering at various energies, taking into account relative angular momenta up to $l=2$. We have interpolated their phase shifts for our energy ($k=4.38\times10^{12}$ cm^{-1}) and calculated the differential cross section which Buckingham, Hubbard, and Massey would predict on their MHWB model (symmetrical exchange force).

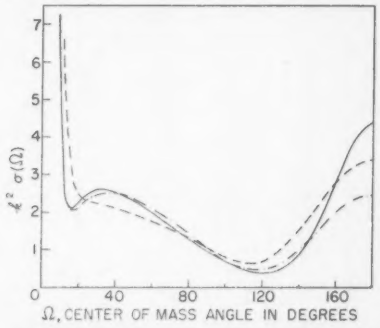

FIG. 5. $k^2\sigma(\Omega)$ *versus* Ω, center-of-mass angle. The solid line is the calculation of Christian and Gammel (see text) and is in essential agreement with the measured values in the angular region over which measurements were made. The dashed line is the curve of Buckingham, Hubbard, and Massey, derived from our interpolation of their phase shifts. The dash-dot line is the calculation of Christian and Gammel using only partial waves for $l=2$.

Recently Christian and Gammel[12] have made similar calculations using a Yukawa potential with a $\frac{1}{2}(1+P_x)$ exchange dependence. They have taken into account partial waves of order higher than $l=2$. The results of the two calculations are shown in Fig. 5. The solid line is the calculated cross section of Christian and Gammel which includes waves of higher order. This curve fits the experimental data, in the region in which measurements were made, with the rms deviation of 2 percent and a maximum deviation of 4 percent. The dashed line is the cross section of Buckingham, Hubbard, and Massey calculated from our interpolation of their phase shifts. It is seen that while there is agreement with the data in a general way, the fit is not nearly so good as that of Christian and Gammel. In the figure, the dash-dot line shows the result of a calculation by Christian and Gammel using only partial waves for $l=2$. Evi-

[12] R. S. Christian and J. L. Gammel, private communication.

dently there is an important contribution to the scattering by waves of higher order.

The phase shifts for $l=2$, for the quartet and doublet scattering are, in the order $\delta_0{}^q$, $\delta_0{}^d$, $\delta_1{}^q$, $\delta_1{}^d$, $\delta_2{}^q$, $\delta_2{}^d$, for Christian and Gammel: 68.6°; 90.0°; 33.4°; −2.9°; −8.0°; 6.9°. The interpolated phase shifts of Buckingham, Hubbard, and Massey are, similarly; 86.7°; −79.7°; 24.6°; −14.7°; −10.3°; 5.2°.

B. The p-p Interaction

The p-p scattering data have been analyzed by the procedures developed by Jackson and Blatt[13] for the determination of the S wave phase shift, possible contributions from P and D waves, and the shape of the potential well.

From the angular distribution shown in Fig. 4 and assuming no scattering other than S wave, an apparent S wave phase shift is calculated at each angle. The apparent S wave phase shift (δ_a) is given by

$$2\delta_a=\sin^{-1}\{\sin\omega-q[(\sigma(\theta)/\sigma_M(\theta))-1]\}-\omega,$$

where $\sigma(\theta)/\sigma_M(\theta)$ represents the ratio of the observed scattering cross section to the calculated cross section

TABLE III. Calculated values of δ_a for p-p scattering.

θ	$\sigma(\Omega)\times10^{26}$ (cm²)	δ_a (Apparent S wave phase shift)	Absolute error in δ_a (energy uncertainty included)	Relative error in δ_a
25°	0.0590	57° 54′	±1.5°	0.96°
30°	0.0522	57° 30′	±1.5°	0.96°
35°	0.0516	56° 33′	±1.6°	1.0°
40°	0.0524	56° 50′	±1.7°	1.0°
50°	0.0546	57° 27′	±1.7°	1.0°
60°	0.0564	58° 00′	±1.7°	1.0°
70°	0.0579	58° 37′	±1.7°	1.1°
80°	0.0580	58° 28′	±1.8°	1.1°
85°	0.0580	58° 23′	±1.8°	1.1°
90°	0.0580	58° 23′	±1.8°	1.1°

for Mott scattering in the c.m. system at angle θ, and ω and q are functions of the incident proton energy.

The values calculated from the smooth curve of Fig. 5 at 10 angles are listed in Table III, together with the absolute and relative errors.

The difference between the apparent and true S wave phase shifts depends, of course, on the phase shift of the higher partial waves. According to Jackson and Blatt, it may be approximated as

$$\delta_a-\delta_0=p_1\delta_1+p_2\delta_2,$$

where p_n are functions of the angle, energy, and S wave phase shift.

Neglecting D and higher shifts and assuming no tensor forces, the intercept of a plot of δ_a *vs* p_1 should give the S wave phase shift and the slope the value of the P wave phase shift. This plot is shown in Fig. 6, from

[13] J. D. Jackson and J. M. Blatt, Revs. Modern Phys. **22**, 77 (1950).

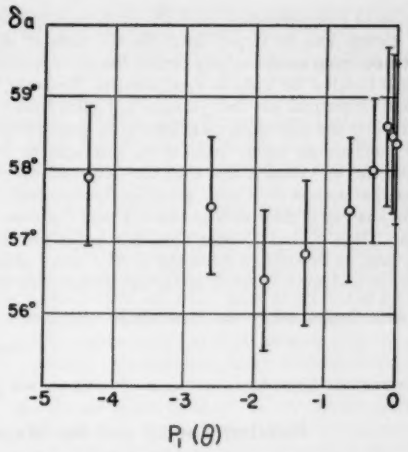

FIG. 6. δ_a *versus* $p_1(E,\theta)$ for the p-p scattering measurements (see text).

which the S wave phase shift is deduced to be 58.1° ±1.2°. Figure 6 also indicates a small attraction in the ^3P state. It appears, however, that, within the accuracy of our measurements, the nuclear scattering can be said to occur only in the ^1S state, and, under this condition, the S wave shift is simply the average value of δ_a, which is 57.8°±1.2°. The large error arises from the fact that since the data at all angles are taken simultaneously, systematic errors such as those due to uncertainty in beam energy and charge measurement enter into the cross-section value at each angle in the same way. The error in δ_0 due to such systematic errors is thus not lessened by averaging over all angles.

It should be noted that, for a central force, the repulsive P wave would tend to increase the cross section over pure S wave for small scattering angles, while an attractive P wave would be evidenced by a decrease in the cross section over pure S wave for small scattering angles. Either contribution would go to zero at 90° c.m. Our calculated apparent S wave phase shift from all of our cross sections is only 0.5° less than the S wave phase shift calculated from the data in the region around 90°. (Since the S wave phase shift is a slowly varying function of energy, the phase shifts obtained from the 9.85-Mev data were averaged with those obtained from the 9.7-Mev data.)

Following Jackson and Blatt, we observe that information as to the shape of the interaction potential can be obtained from a plot of energy *versus* the quantity K of the effective range theory. This quantity is determined from the average value of δ_a to be 7.68±0.20 and from δ_0, as determined from Fig. 6, to be 7.60±0.20. Jackson and Blatt have plotted this quantity as a function of energy for the square and Yukawa wells in such a

way as to give equivalent good fits to the very precise low energy Van de Graaff data. On the basis of this plot, and again assuming only central forces, our results appear to favor the Yukawa type potential. However, it should be pointed out that Jackson and Blatt have investigated the allowable uncertainties in cross-section and bombarding energy required to discriminate between the two shapes, and that our uncertainties are somewhat greater than those given by these authors.

An analysis of these data in terms of the f function of Breit, Condon, and Present[14] yields a value for this function, as determined from the 57.8° S wave phase shift, of 15.7 ± 0.5, which is in fair agreement with the value 16.5 ± 0.17 predicted by Yovits, Smith, Hull, Bengston, and Breit[15] for the Yukawa well.

The authors are indebted to Dr. J. G. Hamilton, Dr. T. M. Putnam, Dr. R. L. Thornton, and the operating crew of the Berkeley 60-inch cyclotron for their aid in performing these experiments. Thanks are also due Dr. R. G. Thomas for his helpful criticism during the preparation of this paper and to the nuclear plate group for their analysis of the plates.

Note added in proof:—The points at angles from 169.8° to 176.2°, inclusive, on Fig. 3E are plotted incorrectly. They should be lowered 5 to 10 percent to conform with the values given in Table I.

[14] Breit, Condon, and Present, Phys. Rev. **50**, 825 (1936).

[15] Yovits, Smith, Hull, Bengston, and Breit, Phys. Rev. **85**, 540 (1952).

PHYSICAL REVIEW VOLUME 88, NUMBER 3 NOVEMBER 1, 1952

Number Theory and the Magnetic Properties of an Electron Gas

M. F. M. OSBORNE
Naval Research Laboratory, Washington, D. C.
(Received June 5, 1952)

Theorems involving the correction terms of lattice point problems in the theory of numbers are interpreted to derive the orders of magnitude of the oscillatory (de Haas-van Alphen effect) and non-oscillatory (Landau and surface diamagnetism) terms in the magnetic moment of a Fermi gas in a finite cylindrical container. The results are valid for systems from atomic dimensions up, and all values of the magnetic field. The different types of moment are different from strong and weak fields, and may depend, for small particles, on the nature of the surface potential at the walls of the container. The applicability of the method to physical problems, and the difficulties associated with statistical mechanical problems involving magnetic fields are discussed.

I. INTRODUCTION

THE problem of the diamagnetism of an electron gas was first examined from a fundamental standpoint by Bohr[1] and Van Leeuwen,[2] who showed for a rather general class of conditions that no magnetic properties whatever were to be found on the basis of classical statistics. Bohr, in particular, showed that this conclusion was a consequence of exact cancellation between the large diamagnetic properties of electrons whose orbits did not collide with the wall and the paramagnetic properties of those orbits which did collide with the walls. Landau[3] re-examined the problem on the basis of quantum statistics and showed that a small diamagnetism was to be expected when the levels were quantized on the basis of either Boltzmann or Fermi-Dirac statistics. However, it was not at all clear how the conclusions of Bohr were related to those of Landau via the correspondence principle. The reason for this was that Landau assumed a very strong magnetic field (orbit radius very much less than dimensions of the container) and did not attempt to satisfy the boundary conditions at the walls of the container, but merely counted those quantum states which had the center of gravity of their probability distribution inside the container. If one attempts to follow the details of the Landau derivation, it appears that the results obtained are quite sensitive to such apparently trivial details as the order of integration over the different quantum numbers and of differentiation with respect to H to obtain the moment, the choice of origin for the energy level, and the choice of several possible forms for the Euler-McLaurin formula for replacing a sum by an integral.

Moreover, there is the added embarrassment that, if higher terms in the Euler-McLaurin formula are included, one may find infinite contributions to the moment because certain derivatives are infinite at the ends of the range of integration. Thus one can obtain the Landau result but one can also obtain quite different results which one has no *a priori* reason for rejecting.

The discrepancies can be roughly divided into two classes. First, a large difference in the moment per unit volume is computed by

$$M/V=kT(\partial/\partial H)\Sigma_i \log[1+\exp(E_0-E_i)/kT)]$$

as opposed to

$$M/V=-kT\,\Sigma_i(\partial E_i/\partial H)1/\{\exp[(E_i-E_0)/kT]+1\};$$

[1] N. Bohr, unpublished dissertation, Copenhagen, 1911. For an account of this work, see reference 5, p. 97.
[2] J. H. Van Leeuwen, J. phys. et radium **2**, 361 (1921).
[3] L. Landau, Z. Physik **64**, 629 (1930).

that is, different order for summing and differentiating the partition function, the sum having been replaced by an integral over the density of states.

The second type of discrepancy arises as follows. One must remember that the sought-for Landau moment/cc is small, of order 10^{-6} H. If one does not take the limit volume→infinity for the specimen, then small terms which are size-dependent arise, and contribute to the moment for macroscopic specimens (of order centimeter dimensions) amounts of the same order of magnitude as the Landau contribution. Moreover, these terms are different for different choices of all the apparently trivial details of calculations mentioned above.

Teller[4] and Van Vleck[5] attempted to clarify the first type of inconsistency which arises between differentiating with respect to the field before or after carrying out the sum over states. For example, Van Vleck, using a cylindrical container, attempted to show that the large contribution to the moment of electrons which do not encircle the origin nor collide with the walls just canceled, except for the Landau diamagnetism, the contribution of the electrons which do collide with the wall. However, if one includes the states of positive quantum number l (orbits which do encircle the origin which he, following Landau and Teller, excluded quite arbitrarily), the cancellation is completely destroyed for a container of finite macroscopic dimensions. One then finds a huge diamagnetic moment. It was this observation which led this writer[6] to conclude (also erroneously, as will be apparent from the subsequent discussion) that a gas of electrons in a finite container has a large diamagnetic moment.

The above discussion refers primarily to the strong fields (by definition orbit radius < specimen size) where the contradictory results associated with the small quantities involving dimensions (which did not give contributions to the moment small compared to the expected Landau result) were simply ignored or evaded by passing to the limit of infinitely large containers. In most statistical-mechanical problems such "surface terms" are indeed negligible.

For the case of weak fields (orbit radius > specimen size) or small containers, there is an equally great variety of conclusions. Van Vleck[7] suspected, on the basis of the principle of spectroscopic stability, that the susceptibility would be the same as for strong fields, an inference not borne out by the conclusions of this paper. Papaetrou[8] made a perturbation calculation of plane waves taking into account degeneracy and concluded to a strong diamagnetism for weak fields, and moreover concluded that the diamagnetism for very weak fields was different depending upon whether the ratio of the edge length for rectangular containers was rational or not. He offered only a tentative explanation for this strange result. Slater[9] concluded to a strong diamagnetism for weak fields, whereas Welker[10] concluded there was none, but this method of calculation led Papapetrou[11] to interpret Welker's calculations as indicating a strong diamagnetism for adiabatic magnetization. Dingle[12] also concluded that for finite containers and weak fields a diamagnetism larger than the Landau value was to be expected.

In the low temperature region Shoenberg,[13] (quoting unpublished results of Landau), Blackman,[14] and Peierls[15] derived expressions giving an oscillating moment (the de Haas-van Alphen effect) but they also used Landau-type wave functions which do not satisfy the boundary conditions at the walls of the container. Here also extreme care has to be taken in carrying out the necessary calculations in order to avoid, or rather, ignore inconsistencies of the type mentioned above.

This situation led Besden[16] to attack numerically the problem of a container of a specified volume containing a specified number ($\sim 10^8$) of particles in order to solve exactly the problem of fitting the wave functions properly inside the container. He found a diamagnetic behavior suggestive of the de Haas-van Alphen effect, and possibly also of superconductivity.

The origin of these differences may be expressed most simply in the following way. Consider a finite Fermi-Dirac system in a magnetic field with discrete energy levels $E_i = E_i(H, d, p)$, where by d and p we refer explicitly to the dependence on dimensions of the container and physical constants. The total energy of this system is:

$$U = \Sigma_i E_i / \{\exp[(E_i - E_0)/kT] + 1\}, \qquad (1)$$

where E_0 is defined by the expression

$$N = \Sigma_i 1 / \{\exp[(E_i - E_0)/kT] + 1\}. \qquad (2)$$

N is the number of particles in the finite container, and N is finite and constant. The rate of change of the energy of the system with varying magnetic field is $-M$, the moment. For constant number of particles in the system it is:

$$\begin{aligned} -M &= (\partial U/\partial H)_N = (\partial U/\partial H)_{E_0} + (\partial U/\partial E_0)_H (dE_0/dH) \\ &= (\partial U/\partial H)_{E_0} - (\partial U/\partial E_0)_H (\partial N/\partial H)_{E_0} / \\ &\qquad (\partial N/\partial E_0)_H. \end{aligned} \qquad (3)$$

Remembering that H appears explicitly only in E_i, then on differentiating there is considerable cancellation and

[4] E. Teller, Z. Physik **67**, 311 (1931).
[5] J. H. Van Vleck, *The Theory of Electric and Magnetic Susceptibilities* (Oxford University Press, London, 1932), p. 356.
[6] M. F. M. Osborne, Phys. Rev. **81**, 147 (1951).
[7] See reference 5, p. 354.
[8] A. Papapetrou, Z. Physik **112**, 587 (1939).
[9] J. C. Slater, Phys. Rev. **52**, 214 (1937).
[10] H. Welker, Sitzber. bayer. Akad. **14**, 115 (1938).
[11] Reference 8, p. 601.
[12] R. B. Dingle, Phys. Rev. **82**, 966 (1951).
[13] D. Shoenberg, Proc. Roy. Soc. (London) **A170**, 341 (1939).
[14] M. Blackman, Proc. Roy. Soc. (London) **A166**, 1 (1938).
[15] R. Peierls, Z. Physik **81**, 186 (1933).
[16] D. J. Besden, Phys. Rev. **79**, 417 (1950); unpublished thesis, Rice Institute (1950).

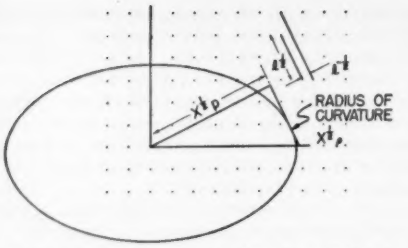

FIG. 1. Geometrical determination of Fourier coefficient $a_{l,\lambda}$.

one finally obtains* exactly

$$M=-\sum_i(\partial E_i/\partial H)/\{\exp[(E_i-E_0)/kT]+1\}. \quad (4)$$

In this form, especially when one considers Fermi-Dirac statistics, it can be made evident why inconsistencies appear. If one takes as usually the case that the energy states whose classical orbits do not intersect the wall are as given by the energy states in free space, then all the contributions of these states to the sum in Eq. (4) are positive. This contribution alone leads naturally to a huge moment. If, nevertheless, the net result for the moment is to be small (see Bohr and Landau) this huge contribution must be almost exactly canceled by a contribution of equal magnitude but opposite sign by those states which do intersect the wall. If we ask: what are the orders of magnitude of the numbers of these two classes of states, those which do intersect the wall and those which do not?, and remember the very small (Landau) order of magnitude to which the two contributions to the moment must be equal, we see that the accuracy of the counting and the energy evaluation must be as good for the surface states as those in the interior, or the cancellation will be imperfect and a too-large absolute value for the moment is to be expected.

The average value of the energy is of order $\frac{3}{5}$ the maximum energy E_0, i.e., most of the states have orbits whose dimensions are comparable to those at the top of the Fermi sea. It can be easily shown by considering the cross-sectional areas where the centers of orbits of different classes lie that the orders of magnitude of (1) the numbers of interior states, (2) the numbers of states which encircle the origin without intersecting the wall, and (3) the numbers of states which intersect the wall are like (1) $\pi R^2L_z k_0^3$, (2) $\pi r_0^2L_z k_0^3$, and (3) $2\pi Rr_0L_z k_0^2$ or relatively like (1), 1, (2) r_0^2/R^2, and (3) r_0/R. Here r_0 is the radius of the orbit for $E=E_0$, R, L_z are the dimensions of the container, $k_0=(2mE_0)^{\frac{1}{2}}/\hbar$, and E_0 is the Fermi energy.

If E_0 is in volts, R, L_z in cms, H in gauss (along z), the relative numbers of states are approximately like 1, $E_0^{\frac{1}{2}}/(HR)$, E_0/H^2R^2. The contributions to the moment of the first and second classes of state are approximately where $\mu=e\hbar/2mc$:

(1) For interior states not encircling the origin:

$$M_i\sim-\mu\pi R^2L_z k_0^3\sim\pi R^2L_z 10^3.$$

(2) For interior states encircling the origin: ($l>0$)

$$M_{l>0}\sim-\mu\pi r_0^2L_z k_0^3\sim-\pi R^2L_z 10^3\cdot E_0(\text{volts})/R^2H^2.$$

Hence for the surface states, whose orbits do intersect the walls, the contribution M_S must be equal and opposite to the sum of the above to the order of magnitude of the Landau diamagnetism, $M_L\sim10^{-6}HR^2L_z$. Thus we see that for strong fields and macroscopic specimens, the contributions of the second and third classes of states are by no means negligible when one is looking for moments as small as the Landau moment. It is just the details of the delicate ways in which they *are* neglected which are responsible for the various inconsistencies mentioned previously.

Let us rewrite Eq. (4) as follows: Let $1(x)$ be the unit function

$$1(x)=0,\ x<0$$
$$=\tfrac{1}{2},\ x=0$$
$$=1,\ x>0$$

in such a way that

$$\int_{x<0}^{\infty}(d1/dx)dx=1.$$

Then we can write Eq. (4) as:

$$M=-(\partial U/\partial H)_N=(\partial/\partial H)\int_0^{\infty}\Sigma_i 1(E-E_i)$$
$$\times(1/\{\exp[(E-E_0)/kT]+1\})dE, \quad (5)$$

where the differentiation with respect to H is to be taken only where H appears explicitly, that is, in $E_i=E_i(H, d, \hat{p})$ only. Now consider the expression $\Sigma_i 1(E-E_i)$. This is the number of states of energy E_i less than any chosen energy E, plus states of energy $E_i=E$ counted as $\frac{1}{2}$. It is expressions of just this type which are given by solutions of lattice point problems in the theory of numbers, to which we now turn. It will be found that just the refinements of number theory give the information necessary to compute the magnetic moment.

II. LATTICE POINT PROBLEMS OF NUMBER THEORY

Kendall's[17] lattice point problem for the plane (we shall indicate the necessary generalizations for a three-dimensional problem) consists of the following. Given a closed curve, everywhere convex, and with specified continuity conditions on its derivatives, how many points whose coordinates are integers lie inside or on the closed curve? The answer by definition is $G(E)$ where by E we may here understand one or more parameters specifying the size and shape of the curve, such as the axes of an ellipse. $G(E)$ is given by the area

* *Correction added in proof:* This procedure gives the adiabatic moment. Equation (4) is the correct expression for the isothermal moment obtained from the free energy.

[17] D. G. Kendall, Quart. J. Math. (Oxford) **19**, 1 (1948).

plus a series of periodic correction terms. The area plus the correction terms can be shown to converge to the exact number of points inside the closed curve, plus those on the curve counted as $\frac{1}{2}$, i.e., to:

$$[G(E+0)+G(E-0)]/2.$$

Kendall gives (his notation) the following asymptotic expression for the number of lattice points inside or on a closed centrally-symmetric oval, everywhere convex, with a finite second derivative of the curvature, and with no points of zero or infinite curvature: O denotes order of magnitude.

$$G(E)=\text{area}+\sum_{n,m}a_{nm},$$
$$a_{nm}=(x^{\frac{1}{2}}\rho^{\frac{1}{2}}/\pi l^{\frac{1}{2}})\cos(2\pi(lx)^{\frac{1}{2}}\rho-3\pi/4)+O(x^{1/6}/l^{5/6}). \quad (6)$$

$x^{\frac{1}{2}}$ is a parameter determining the size of the oval (Fig. 1). If we imagine n, m to specify a direction in the plane, then $x^{\frac{1}{2}}\rho$ is the distance from the origin of a line perpendicular to the direction n, m and tangent to the oval. $x^{\frac{1}{2}}\rho$ is the radius of curvature at the point of tangency and $l^{\frac{1}{2}}=(m^2+n^2)^{\frac{1}{2}}$ is the spacing of lattice points on the line through lattice points at right angles to the direction n, m, and $1/l^{\frac{1}{2}}$ is the separation of successive lattice "lines" normal to the direction n, m. Unity, the spacing of the integers, is the unit of length.

Kendall shows that the error $\sigma=(\Sigma_{n,m}|a_{nm}|^2)^{\frac{1}{2}}$ in taking the area of the oval as the number of lattice points is of order of the square root of the maximum radius of curvature. This has a geometrical interpretation as the maximum number of points just caught or just missed by an arc of unit sagitta, and ρ_{max} as radius of curvature. For a circle, (chord)$^2=8\cdot$(radius curvature $\cdot$sagitta), or

$$c=2(2\rho s)^{\frac{1}{2}}\sim\rho^{\frac{1}{2}} \text{ for } s=1. \quad (7)$$

We wish to show that this geometrical interpretation of the total error as described by number theory can be extended to each one of the terms a_{nm}. Consider the oval (Fig. 1) as growing (increasing $x^{\frac{1}{2}}$) and consider the number of points just caught or missed by the arc tangent to the lattice line, m, n, that is, perpendicular to the direction m, n. The increment will be periodic in the lattice spacing $1/l^{\frac{1}{2}}$ for this lattice line, that is, of order $A\sin[2\pi\rho x^{\frac{1}{2}}/(1/l^{\frac{1}{2}})-\varphi]$. The amplitude A will be the number of points on an arc of sagitta $s=1/l^{\frac{1}{2}}$ and radius of curvature $x^{\frac{1}{2}}\rho$, and these points are $l^{\frac{1}{2}}$ apart. Hence, chord length is approximately

$$(x^{\frac{1}{2}}\rho\cdot s)^{\frac{1}{2}}=[x^{\frac{1}{2}}\rho\cdot(1/l^{\frac{1}{2}})]^{\frac{1}{2}},$$

and the number of points on this length is $(x^{\frac{1}{2}}\rho)^{\frac{1}{2}}/l^{\frac{1}{2}}=A$. Hence, the fluctuation with growth of $G(E)$ owing to the curve cutting this particular lattice line is

$$a_{nm}=O(x^{\frac{1}{2}}\rho^{\frac{1}{2}}/l^{\frac{1}{2}})\sin[2\pi\rho(lx)^{\frac{1}{2}}-\varphi], \quad (8)$$

which is just the form of the coefficient a_{nm}. This geometrical analysis is insufficient to give the exact amplitude $x^{\frac{1}{2}}\rho^{\frac{1}{2}}/\pi l^{\frac{1}{2}}$ and the phase $\varphi=3\pi/4$, nor does it give the residual $O(x^{1/6}/l^{5/6})$. It does give correctly the behavior of all the oscillatory terms required by number theory, even though the above heuristic derivation is applicable only when m and n have no common factor.

For nonsymmetric ovals, Kendall shows that the coefficients a_{nm} are of the form Eq. (6) with imaginary exponentials instead of sines. However, on summation only the real part contributes to the real number of points within the oval.

One can also apply the above geometrical argument to curves with points of infinite radius of curvature. Kendall examines the oval $u^2x+v^4\leq x^2$ which has infinite radius of curvature at $u=\pm x^{\frac{1}{2}}$, $v=0$. He shows for this oval that

$$a_{m,0}=2\Gamma(5/4)J_{3/4}(2mx^{\frac{1}{2}})x^{3/8}/\pi^{\frac{1}{2}}m^{\frac{1}{2}}$$
$$=O[x^{3/8}\sin(2\pi mx^{\frac{1}{2}}-\varphi)], \quad x\gg1, \quad (9)$$

from which he infers that the error $\sigma=O(x^{3/8})$. But this is just the order of magnitude of points just caught or missed by an arc (not approximable by a circle) of unit sagitta around the points $(u,v)=\pm x^{\frac{1}{2}}$, 0. At $u=x^{\frac{1}{2}}-1$, $v\sim x^{3/8}$ and by the above geometrical interpretation of $a_{m,0}$

$$a_{1,0}=O[x^{3/8}\sin(2\pi x^{\frac{1}{2}}-\varphi)]. \quad (10)$$

This is just the lowest and predominant frequency of the fluctuation in the number of points as the curve grows (increasing $x^{\frac{1}{2}}$) in the direction 1, 0.

In the case of a right angle triangle, taken as the area between $(u/a)+(v/b)=1$ and $u=-\frac{1}{2}$, $v=-\frac{1}{2}$, Fig. 2, the interpretation of the real part of the coefficient a_{nm} as the oscillating number of points just caught or missed as the figure changes its dimensions is also valid. We understand a, b both$\gg1$. It can be easily verified, by evaluating the coefficient

$$a_{nm}=(-1)^{m+n}\int_{u=-\frac{1}{2}}^{a+a/2b}\int_{-\frac{1}{2}}^{b-ub/a}\times\exp[2\pi i(mu+nv)]dudv, \quad (11)$$

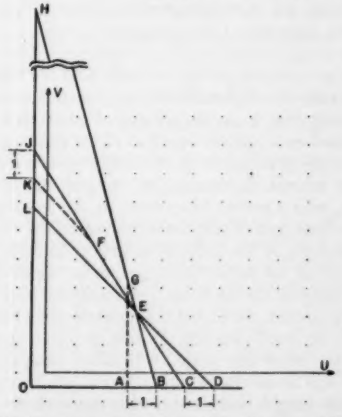

FIG. 2. Number theory analysis for a triangular area. *ODL* for the case $a=b$; *OCJ* for the case $a-b=\epsilon$; *OBH* for the case $b\gg a$.

that a_{11} is for $b=a$

$$a_{11}=[\exp(2\pi i a)a/2\pi i]+O(1). \quad (12)$$

Here $R(a_{11})$ in order of magnitude represents the fluctuating number of points along the hypotenuse, LD (Fig. 2). For $a-b=\epsilon \ll a$, $\epsilon \gg 1$,

$$a_{11}=\frac{-[a\exp(2\pi i(b+b/2_a))-b\exp(2\pi i(a+a/2b))]}{4\pi^2(a-b)}+O(1). \quad (13)$$

$R(a_{11})$ is here a fluctuation of the order of the number of points along the segments $DE\sim CE$ and $FJ\sim FK$ of Fig. 2.

For the case $b\gg a$ of Fig. 2, it can be shown that a_{10} is

$$a_{10}=[(b+\tfrac{1}{8})/2\pi i]+(b/4a\pi i)\exp[2\pi i(a+a/2b)]-[b/a(2\pi i)^2]+b/(4a\pi i). \quad (14)$$

Here $R(a_{10})$ is a fluctuation of the order of the number of points along $GB\sim GA$. In all cases the periodicity and amplitude are correctly given in order of magnitude and the geometrical interpretation is valid.

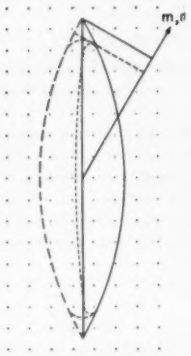

FIG. 3. Modifications of a flat-sided oval in order to fulfill Kendall's criteria. The coefficient a_{mn} corresponding to the direction m, n indicated would be very small.

For closed curves which are concave and have either cusps or inflection points, we make also the reasonable conjecture that the coefficient a_{mn} has this same interpretation, that is, as the number of points just caught or missed as a periodic function of the displacement of the periphery of the curve. We assume that it is periodic in the normal distance of the tangent line from the origin, with a period determined by the spacing of the lattice lines, and of amplitude determined by the radius of curvature at the point of tangency, and the spacing (sagitta) of the lattice lines, just as for Kendall's oval. If no tangent can be drawn perpendicular to the direction of interest, we expect the corresponding coefficient a_{mn} to be small (see Fig. 3) and, if this tangent falls near an influection point, a detailed analysis of the curve will be necessary to determine how many points are just caught or missed over a range of the normal distance corresponding to the spacing of the lattice lines, just as in the case of the oval $u^2x+v^4\leq x^2$.

There is another sort of conclusion which can be inferred from Kendall's arguments. Consider a closed curve one side of which is straight, of length c, and lies somewhere in the space between two principal lattice lines. Kendall's formula applied uncritically for the error σ of order $\rho_{\max}^{\frac{1}{3}}$ would indicate an infinite error, but if we replace the straight portion by an arc slightly rounded at the ends to provide a closed continuous convex curve, this arc being at most of unit sagitta, then the modified oval fulfills the criteria which Kendall requires and contains exactly the same set of lattice points as the original curve. We now apply Kendall's argument to the modified oval, for which $\rho_{\max}^{\frac{1}{3}}\sim c$, that is, the length of the flat portion. Thus, for such flat-sided curves the maximum error is approximately the length of the flat side. This fits quite satisfactorily the interpretation of the error as the number of points just caught or missed. It is also the amplitude of the largest periodic coefficient a_{10} of the modified oval.

There is a particular circumstance for such flat-sided ovals, however, for which this oscillatory term and the corresponding contribution to the error can be removed. Let us suppose we are considering a particular class of flat-sided ovals where the flat side always bisects the space between two principal lattice lines. Then the number of points inside this curve is exactly one-half the number contained in the completely convex figure obtained by reflecting the given curve in its flat side. To this figure, we can then apply Kendall's arguments for the closed continuous convex curve, rounding off corners without loss of lattice points where necessary, and the large term previously given by the flat side will not appear. These different possibilities are illustrated in Fig. 3 by dotted lines.

There is yet another inference which can be drawn from Kendall's conclusions which we use in our discussion of the electron gas. Kendall shows that the error in using the area as an estimate of the number of lattice points inside a curve is of order $\rho_{\max}^{\frac{1}{3}}$ and also of the order of the square root of the perimeter. From this we infer that, given a number of different closed curves, each enclosing exactly the same set of lattice points, the one whose perimeter and maximum radius of curvature is least has an area which is the best estimate of the number of points inside. This argument will be useful in deriving the order of magnitude of the Landau and other non-oscillatory terms in the diamagnetism.

Based on the above geometrical interpretation of the results of number theory for closed curves lying in a plane, one can easily give the generalization for a three-dimensional figure. The volume of a slab or segment of unit thickness is of order $(\rho_1\rho_2)^{\frac{1}{2}}$ where ρ_1, ρ_2 are the principal radii of curvature. Then the number of points just caught or just missed as the solid grows is of order $(\rho_1\rho_2)^{\frac{1}{2}}$. If the surface is developable, that is, one of the principal radii of curvature is infinite, the other ρ finite, the error is of order $\rho^{\frac{1}{2}}c$. This simply

means the number of points in a slab of unit thickness and dimensions corresponding to the finite radius of curvature ρ and the length of the longest straight line c which can be drawn in the surface. This expression can be generalized for different directions exactly as in the case of the mnth coefficient in the plane. Similarly, when the enclosed surface is bounded by a plane (both radii of curvature infinite) we can take the number of points in this plane as the amplitude and the normal to the plane will determine the coefficient to which it applies and the periodicity, which is the spacing of lattice planes parallel to this plane face. Also, if it should happen that for a particular class of closed surfaces with flat sides, the flat side bisects the space between two principal lattice planes, we may close off the surface symmetrically with respect to this flat side and apply our arguments to the resulting volume and then take one-half the result, exactly as we did for the closed curve in two dimensions.

If we admit the conclusion (generalizing Kendall's conclusion for a plane curve) that the error is least when $(\rho_1\rho_2)_{\max}$ or the area is least for different surfaces containing the same set of points, we may bevel off any edges which do not contain lattice points in order to improve the accuracy of using the enclosed volume as a measure of the number of points inside. It is important in this case that in beveling off we do not remove any lattice points in the process. It should also be noted that beveling only removes an appreciable volume for acute angle edges. For obtuse angles the requirement that ρ be finite and continuous means that not much volume can be removed. The beveling only occurs over unit distance at most.

A few remarks should be made here concerning the sense in which the correction to the area as a measure of the number of points inside is to be taken. The first sense is that in which the closed curve lies at random in the plane of the lattice points. The second is that to be taken when the closed curve is one in a family of different sizes and of fixed position and orientation in the lattice plane. The error is then taken in the sense of the average error as the parameters specifying the size and shape of the different members of the family are varied. It is in this second sense of the error that we are primarily interested. General conclusions, such as have been drawn above concerning the error and the periodicity, usually apply to both conceptions, at least this seems plausible.

It may be mentioned that the exact meaning of the order of magnitude from the number theory standpoint is a question of considerable subtlety and complexity. We shall use it in what follows in the conventional sense, since it seems to apply well to the "average" order of magnitude of the error when the number of points inside is very large. For a more precise discussion we refer to the literature,[17] as the problem, although it has received much attention, has not yet been solved. There is reason for believing that the square root of the radius of curvature as a correction may be exceeded for a denumerably infinite set of closed curves in the family. This may imply that the fluctuations in the magnetic moment in the derivation which follows are, from a number theory standpoint, upper limits of the order of magnitude of the moment which may not be exceeded except at discrete values of the Fermi energy E_0 and magnetic field H.[18] It is difficult to ascribe physical significance to such isolated values.

III. THE ENERGY LEVEL DISTRIBUTION FOR A FINITE CONTAINER

We now have the problem of using the above considerations to determine the number of energy levels less than any arbitrary energy E_a for a charged particle in a finite cylindrical box in a uniform magnetic field. This number is essential to determining the thermodynamic properties, in particular the magnetic moment, of a gas of such particles according to Fermi statistics. The Schrödinger equation for this problem is [19]

$$-(\hbar^2/2m)(\partial^2\psi/\partial r^2+\partial\psi/r\partial r+\partial^2\psi/r^2\partial\theta^2+\partial^2\psi/\partial z^2) -(i\hbar eH/2mc)\partial\psi/\partial\theta+V(r,z) +(mr^2/2)(eH/2mc)^2\psi=E\psi, \quad (15)$$

where $V(r, z)$ is the scalar potential of the box. For the present we shall take

$$V(r,z)=V_r(r)+V_z(z),$$

where $V_z(z)=V_z(-z)$, and introduce the notation

$$V_z(L_z(E_a))=E_a, \quad \text{or} \quad L_z(E_a)=V_z^{-1}(E_a),$$

and, similarly,

$$R(E_a)=V_r^{-1}(E_a)$$

to denote turning points determined by the scalar potential where the kinetic energy vanishes for some arbitrary energy E_a. Under the assumption

$$\psi=\rho(r)\exp(il\theta)\zeta(z),$$

the Schrödinger equation separates and we have

$$-(\hbar^2/2m)(\rho''/\rho+\rho'/r\rho-l^2/r^2)+\hbar eHl/2mc +V_r(r)+(mr^2/2)(eH/2mc)^2=E_r, \quad (16)$$
$$-(\hbar^2/2m)\zeta''/\zeta+V_z(z)=E_z.$$

By definition the eigenvalue for the energy is

$$E=E_r(l,n)+E_z(n_z)=E(l,n,n_z).$$

We will use the WKB approximation in solving these equations where the radial quantum number is n, taking on values $0, +1, +2, \cdots$, and the n_z quantum number is $n_z=0, +1, +2\cdots$. The orbital quantum number l ranges through all permissible integral (+, − and 0) values for which $E=E(l,n,n_z)\leq E_a$, and satisfies the requirement that the radial WKB integrand be real, and with real limits of integration. If we introduce the

[18] There is a discussion of a class of these discrete values by M. C. Steele, following paper [Phys. Rev. 88, 451 (1952)], Eq. (52).

[19] C. G. Darwin, Proc. Cambridge Phil. Soc. 27, 86 (1931).

notation $2mE(l, n, n_z)/\hbar^2=k^2$, $2mE_a/\hbar^2=k_a^2$, $2mE_0/\hbar^2=k_0^2$, $2mE_z(n_z)/\hbar^2=k_z^2(n_z)$, $L=(\hbar c/eH)^{\frac{1}{2}}$ (approximately the radius of the smallest quantized orbit in field H), and the radial equation can be written, substituting $E_r=E(l, n, n_z)-E_z$, and $\rho(r)=u(r)/r^{\frac{1}{2}}$,

$$d^2u/dr^2+(k^2-2mV_r(r)/\hbar^2-k_z^2(n_z)-l^2/r^2 -r^2/4L^4-(l/L^2)+1/4r^2)u=0, \quad (17)$$

and the z equation is

$$d^2\zeta/dz^2=-(k_z^2(n_z)-(\hbar^2/2m)V_z)\zeta. \quad (18)$$

In accordance with the arguments of Kemble[20] and Kramers[21] in applying the WKB method in polar coordinates, one drops the $1/4r^2$ term in Eq. (17) so that the radial quantum number is given by

$$n=(1/\pi)\int_{r_l}^{r_u}(k^2-2mV_r(r)/\hbar^2-k_z^2(n_z) -(l^2/r^2)-(r^2/4L^4)-l/L^2)^{\frac{1}{2}}dr-\tfrac{1}{2}, \quad (19)$$

and the z quantum number by [this determines $k_z(n_z)$]

$$n_z=(1/\pi)\int_{z_l}^{z_u}(k_z^2(n_z)-\hbar^2V_z(z)/2m)^{\frac{1}{2}}dz-\tfrac{1}{2}, \quad (20)$$

where the subscripts u, l indicate the coordinates where the integrands of (19) or (20) vanish. We can solve for them explicitly when we know $V_r(r)$ and $V_z(z)$.

We now have the problem of counting all the possible eigenvalues of $E=E(l, n, n_z)$ (determined by combined solutions for E and E_z from Eqs. (19) and (20) less than some arbitrary E_a). Since the quantum numbers n, l, n_z are integers, an estimate of this number of states according to number theory, is the volume in quantum number space (n, l, n_z considered as *continuous* variables) enclosed by the surface $E(l, n, n_z)\leq E_a$ and the planes $n_z=-\frac{1}{2}$ and $n=-\frac{1}{2}$. On these planes the upper and lower limits of coordinate integration in Eqs. (19) and (20) come together. According to our previous discussion, this is just one-quarter of the volume and encloses one-quarter of the points of a figure closed symmetrically about these planes. Let us call this (quarter) volume in quantum number space $V(E_a)$. We may subsequently improve it as an estimate of $G(E_a)$, the number of *integer* coordinates n, l, n_z inside, by beveling off its sharp edges and subtracting the volume so removed from $V(E_a)$, and by adding periodic terms based on the dimensions and curvatures of the surface $E(l, n, n_z)=E_a$. So we have for $V(E_a)$,

$$V(E_a)=\int_{n_z=-\frac{1}{2}}^{n_{zu}}\int_{l_l}^{l_u}\int_{n=-\frac{1}{2}}^{n_u}dn_z dl dn, \quad (21)$$

where subscripts u, l refer to upper and lower limits. The question now is what are the limits of integration, which are *not* required to be integers. Being a volume integral, these limits will depend on the order of integration; however, if we integrate on n first, the upper limit on n is just Eq. (19) with k replaced by k_a. So integrating on dn in Eq. (21), we have, as the $\frac{1}{2}$ terms cancel,

$$V(E_a)=\int_{n_z=-\frac{1}{2}}^{n_{zu}}\int_{l_l}^{l_u}\frac{1}{\pi}\int_{r_l}^{r_u}(-l^2/r^2-r^2/4L^4+k_a^2 -2mV_r(r)/\hbar^2-k_z^2(n_z)-l/L^2)^{\frac{1}{2}}dr. \quad (22)$$

To integrate further, as we still have a triple integral, we refer to Fig. 4, where the WKB integrand is plotted as a function of r^2 and l. In the form given by Eq. (22) above, it is seen that $V(E_a)$ is just the integral of the radial WKB integrand over all regions of r, l, n_z space where this integrand is real. The value of $n+\frac{1}{2}$ corresponds to the integration on r along paths such as DB, FM, or HK in Fig. 4. The lower and the upper points of the curve correspond to r_l, and r_u of Eq. (19).

If we actually carry out the r integration, and compute $n+\frac{1}{2}$ before proceeding with the n_z, l integrals, it will be necessary to divide the region of Fig. 4 into two parts, to the left and right of GL, corresponding to whether the upper limit of r is determined by the wall of the box [scalar potential $V_r(r)$] or the vector potential of H. However, since the total expression Eq. (22) is still just a multiple intergal on r, l, and n_z, we may integrate in any order we like so long as we cover the same region, and we may write it as follows:

$$V(E_a)=\int_{n_z=-\frac{1}{2}}^{n_{zu}}dn_z\int_{r=0}^{V_r^{-1}[E_a-E_z(n_z)]}dr\,\frac{1}{\pi} \times\int_{l=-(r^2/2L^2)+r[k_a^2-(2mV_r(r)/\hbar^2)-k_z^2(n_z)]^{\frac{1}{2}}}^{-(r^2/2L^2)-r[k_a^2-(2mV_r(r)/\hbar^2)-k_z^2(n_z)]^{\frac{1}{2}}}Y\,dl, \quad (23)$$

$$Y=(-(l^2/r^2)-(r^2/4L^4) +k_a^2-(2mV_r(r)/\hbar^2)-k_z^2(n_z)-(l/L^2))^{\frac{1}{2}}.$$

These lower and upper limits on l correspond in Fig. 4 to JLA and ACG, respectively, $l=-r^2/2L^2$ corresponds

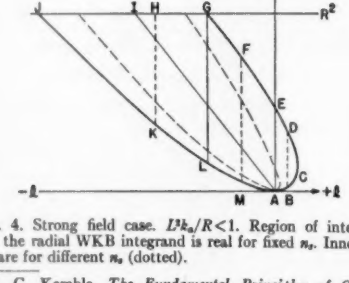

FIG. 4. Strong field case. $L^3k_a/R<1$. Region of integration where the radial WKB integrand is real for fixed n_z. Inner parabolas are for different n_z (dotted).

[20] E. C. Kemble, *The Fundamental Principles of Quantum Mechanics* (McGraw-Hill Book Company, Inc., New York, 1937), p. 107.

[21] H. A. Kramers, Z. Physik **39**, 828 (1926).

to IA. Or, with $l'=l+(r^2/2L^2)$:

$$V(E_a)=\int_{n_z=-\frac{1}{2}}^{n_{zm}} dn_z \int_{r=0}^{V_r^{-1}[E_a-E_z(n_z)]} dr \times \int_{l'=-r[k_a^2-(2mV_z(z)/\hbar^2)-k_z^2(n_z)]^{\frac{1}{2}}}^{+r[k_a^2-(2mV_z(z)/\hbar^2)-k_z^2(n_z)]^{\frac{1}{2}}} Y'dl', \quad (24)$$

$$Y'=[k_a^2-(2mV_r(r)/\hbar^2)-k_z^2(n_z)-l'^2]^{\frac{1}{2}}/r.$$

With this order of integration, n_{zm} is given by the largest value it can obtain, for $E_r=0$.

$$n_{zm}=\frac{1}{\pi}\int_{z=-V_z^{-1}(E_a)}^{+V_z^{-1}(E_a)}[k_a^2-(2mV_z(z)/\hbar^2)]^{\frac{1}{2}}dz-\tfrac{1}{2}. \quad (25)$$

Integrating on n_z corresponds to adding the contributions of successively smaller parabolas (dotted) of Fig. 4.

All of this is independent of whether the field is strong or weak and whether the box is large or small, so long as the box potential is separable in r and z. Note, and this is the important point, that this $V(E_a)$, Eq. (24) or (26), is actually independent of the magnetic field. Hence, if used by itself as an estimate for $G(E_a)$, it will give no contribution to the magnetic moment (which involves a differentiation with respect to H) whatever. The only terms which can contribute to the moment will be oscillatory terms, depending on the curvatures of the energy surface or small corrections which may arise if we find we can snip off small edges of the "Fermi volume" without loss of quantum numbers, these oscillatory and subtractive terms being essentially the improvements on $V(E_a)$ as an estimate of $G(E_a)$. It can be shown that this conclusion also holds using the higher corrections to the WKB approximation given by Dunham,[22] as the field dependent terms disappear with the same substitution $l\to l'$ which removed them above.

From Eq. (24) we have

$$V(E_a)=\int_{n_z=-\frac{1}{2}}^{n_{zm}} dn_z \int_{r=0}^{V_r^{-1}[E_a-E_z(n_z)]} \times[k_a^2-k_z^2(n_z)-2mV_r(r)/\hbar^2]rdr. \quad (26)$$

We cannot proceed with our integral without definite assumptions concerning the potentials $V_r(r)$, $V_z(z)$ since k_z depends on n_z through Eq. (20). However, if we assume the simplest of all potentials, a simple well in r and z, so that

$$V_r(r)=0, \quad r<R,$$
$$=M>E_a, \quad r>R;$$
$$V_z(z)=0, \quad -L_z/2<z<+L_z/2,$$
$$=M>E_a, \quad |z|>L_z/2;$$

then, for all $E_a<M$, the turning points, when they occur at the walls, are constants, and we have[23]

$$k_z(n_z)=(n_z+\tfrac{1}{2})\pi/L_z,$$

$$V(E_a)=\int_{n_z=-\frac{1}{2}}^{k_aL_z/\pi-\frac{1}{2}}(R^2/4)[k_a^2-(n_z+\tfrac{1}{2})^2\pi^2/L_z^2]dn_z \quad (27)$$
$$=(4\pi/3)(\pi R^2L_z)(2mE_a)^{\frac{1}{2}}/\hbar^3.$$

This is just the formula for the number of levels less than E_a in the absence of a magnetic field.

The disadvantage of integrating first on r and thus computing n directly is that it can be done exactly for paths BD or FM, but a series expansion which will depend on H is necessary to get it in a tractable form for subsequent integrations on l and n_z for paths such as HK. The paths DB, FM, HK correspond respectively to orbits which encircle the origin, interior orbits which do not encircle the origin, and surface states, or orbits which touch the wall. Hence, any errors committed by dropping terms in the expansion for the surface states will just appear as an H dependence of $V(E_a)$ in the final result, which could be carried out exactly by integrating first on l and then on r.

It will be seen that it is essential to include the states of positive l to get a total $V(E_a)$ independent of H, so that the calculations of Van Vleck,[5] who computed surface states but neglected the states of positive l, must have been in error by just an amount sufficient to compensate for the omission of positive l states. Similarly, this writer's calculations[6] were also in error.

In order to apply the corrections, both periodic and those due to edges and cusps in the surface, let us plot the energy surface in quantum number space. To do this it will only be necessary to represent specific regions of the surface accurately, since we know its overall volume, Eq. (27). This energy surface plot is given in Fig. 5. The portion of the surface $MHDCB$, which corresponds to integrating on r to compute n in

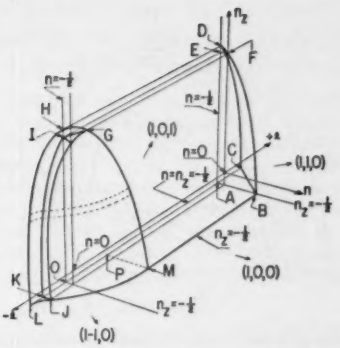

FIG. 5. Energy surface in quantum number space for strong fields.

[22] J. L. Dunham, Phys. Rev. 41, 713, 721 (1932).

[23] The use of the WKB relation between n_z and E_z instead of an exact relation which could here be obtained will not alter any of the conclusions which follow.

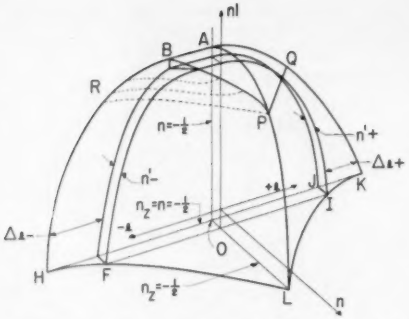

FIG. 6. Energy surface in quantum number space for weak fields.

the region $GLMACF$ of Fig. 4, can be expressed exactly and is

$$n=(1/\pi)\{(L^2k_a^2/2)-\pi^2L^2[(n_z+\tfrac{1}{2})^2/2L_z^2]-l-|l|\}-\tfrac{1}{2}. \quad (28)$$

This is valid for all l greater than the l coordinate of the line GM of Fig. 5, which is

$$l=-R^2/2L^2+R[k_a^2-(n_z+\tfrac{1}{2})^2\pi^2/L_z^2]^{\frac{1}{2}}.$$

$-R^2/2L^2$ is the "length" of DH,

$$\pm R[k_a^2-(n_z+\tfrac{1}{2})^2\pi^2/L_z^2]^{\frac{1}{2}}$$

corresponds to MHL measured from a plane through OH perpendicular to the l axis. The cusp-shaped region MLH which corresponds to the region GLJ of Fig. 4, or surface states, is given approximately by

$$n\simeq\{L^2[k_a^2-(n_z+\tfrac{1}{2})^2\pi^2/L_z^2]/2\pi\}\times[x(1-x^2)^{\frac{1}{2}}-\sin^{-1}x+\pi/2]+O(a)-\tfrac{1}{2}. \quad (29)$$

Here $a=L^2[k_a^2-(n_z+\tfrac{1}{2})^2\pi^2/L_z^2]/R<1$ for validity of approximations $x=(l''-a)/(1-2al''+a^2)^{\frac{1}{2}}$, where

$$l''=(l+R^2/2L^2)/R[k_a^2-(n_z+\tfrac{1}{2})^2\pi^2/L_z^2]^{\frac{1}{2}},$$
$$x\simeq(l-R^2/2L^2)/R[k_a^2-(n_z+\tfrac{1}{2})^2\pi^2/L_z^2]^{\frac{1}{2}}<1.$$

These are obtained by integrating Eq. (19) with $r_u=R$, and using the transformations of Eq. (29).

If we like, in order to justify applying our arguments to number theory, we may imagine Fig. 5 to be extended by reflection in the $n=-\frac{1}{2}$ and $n_z=-\frac{1}{2}$ plane. We can then expect that the largest periodic corrections arise from the ruled surfaces $BMHD$ and BDC and that there will be nonperiodic corrections based on rounding off the edges DH and $HLDC$. There is no edge at all at $CBML$ when reflection occurs at $n_z=-\frac{1}{2}$, and we cannot smooth off the edge BD without losing lattice points as the quantum states at $l=0$ are good quantum states.

Let us consider these various corrections. We shall compute them in order of magnitude only, although in most cases exact evaluation of the integrals gives a quite good estimate of the numerical coefficients required. Exact evaluation is best carried out by the number theory development of the correction terms as performed by Steele using the method of critical points.[24] In fact, the quantitative evaluations which follow can be regarded just as geometrical interpretations of the critical point method.

Consider first the edge DH. At this edge we may approximately subtract from the total volume without loss of lattice points a triangular prism of length $DH=R^2/2L^2$, of base $EF=\frac{1}{2}$, and of height

$$(dn_z/dn)_{n=0}\cdot(\Delta n=\tfrac{1}{2}).$$

We say "approximately subtract" since the remaining figure must have a surface of continuous curvature, by our previous number theory discussion. Figure 5 for strong fields has $(dn_z/dn)_{n=0}\gg1$, so that this approximation is valid. As the field gets weaker the edge DH is less acute, and this approximation is less valid. When this edge approaches 90°, it may fail completely (Fig. 6). In so doing we improve the estimate of the volume as a measure of the total number of lattice points, since we reduce the total surface area and also the region removed is one of large radius of curvature (it increases with n_z on the Fermi surface). Thus the net volume removed is

$$\delta V_{-L}\sim-\tfrac{1}{2}(L_z/L^2k_a)(R^2/2L^2)(\tfrac{1}{2}). \quad (30)$$

The corresponding contribution to the moment at $T=0°$ is, for $E_0=$ Fermi energy,

$$M_L=(\partial/\partial H)\int_0^{E_0}\delta V_{-L}(E_a)dE_a\simeq-\pi R^2L_zE_0/L^4k_0H$$
$$=O[-\pi R^2L_zc^2HE_0^{\frac{1}{2}}/\hbar cm^{\frac{1}{2}}]. \quad (31)$$

This is the order of magnitude of the Landau moment and is diamagnetic.

Consider next the contribution of the surface states to the moment, which we may obtain by removing without loss of lattice points a thin strip of thickness $\Delta n=\frac{1}{2}$ (from $n=-\frac{1}{2}$ to $n=0$) along the edge HL. In order to find its dimensions Δl, as a function of l and n_z (Fig. 5), we must find an expression for the quantum number n, valid for small ranges of n, that is $(n+\frac{1}{2})<\frac{1}{2}$ (near J of Fig. 4). This we may obtain from Eq. (19) (with $r=R$) as follows:

Let Δl be the distance in l from the line HL of Fig. 5, so that

$$l=(-R^2/2L^2)-R[k_a^2-(n_z+\tfrac{1}{2})^2\pi^2/L_z^2]^{\frac{1}{2}}+\Delta l. \quad (32)$$

If we substitute this expression for l in Eq. (19) and expand in terms of Δl keeping only the smallest powers, we find after considerable manipulation, and writing $(n_z+\frac{1}{2})^2\pi^2/L_z^2=k_z^2(n_z)$, as for Eq. (27)

$$n=(1/\pi R^{\frac{1}{2}})\{L^2[k_a^2-k_z^2(n_z)](2\Delta l)^{\frac{1}{2}}\}[1+O(a)]-\tfrac{1}{2}. \quad (33)$$

This reaches the value $n=0$ at

$$\Delta l=O\{R/L^{4/3}[k_a^2-k_z^2(n_z)]^{1/6}\}. \quad (34)$$

The length of the strip HL is $\sim L_zk_a/\pi$ (largest n_z

[24] J. G. van der Corput, Amsterdam Roy. Acad. Sci. **51**, 650 (1948).

value) so that the volume removed is of order

$$\delta V(E_a)_{\text{surf}} = -\int_{n_z=-\frac{1}{2}}^{L_z k_a/\pi-\frac{1}{2}} dn_z \int_{\Delta l=0}^{\Delta l=\text{Eq. (34)}} d(\Delta l) \times \int_{n=-\frac{1}{2}}^{n=\text{Eq. (33)}} dn \quad (35)$$
$$= -O(RL_z k_a^{2/3}/L^{4/3}),$$

and the contribution to the moment at $T=0°$ is of order

$$M = (\partial/\partial H)\int_0^{E_0} \delta V(E_a)_{\text{surf}} dE_a$$
$$= O(RL_z k_0^{2/3}/L^{4/3})(E_0/H)$$
$$= -O(\pi R^2 L_z \cdot m^{1/3} e^{2/3} E_0^{4/3}/R\hbar^{4/3} c^{2/3} H^{1/3}), \quad (36)$$

valid for $k_0 L^2/R<1$. This is the order of magnitude of the surface diamagnetism previously reported,[25] and found by Steele using the method of critical points. Here again a numerical evaluation of the exact volume between $n=-\frac{1}{2}$ and 0 and the limits on Δl in this edge would give a fair value of the numerical coefficient required in Eq. (36). It is considerably less than unity, as the edge HL is quite "thin," varying as $(\Delta l)^{\frac{1}{2}}$.

Finally we have the edge CD, which is actually a right angle in Fig. 5, completed by reflection in the plane $n=-\frac{1}{2}$. The maximum volume that could be removed along this edge without loss of lattice points is of order $(\frac{1}{2})(L_z k_a/\pi)(\frac{1}{2})$. This is independent of the magnetic field and hence can make no contribution to the moment, considered as a correction to $V(E_a)$.

We now have to consider periodic terms [see Eq. (6)] corresponding to the direction (1, 0, 0) in Fig. 5. Consider first a slab of unit sagitta as having a radius of curvature of order $1/(d^2n/dn_z^2)_{n_z=0}$, of length $BM=AO-OP=R^2/2L^2-Rk_a$. The distance of the tangent plane from the origin is $AB=L^2k_a^2/2$, so that

$$\delta V(E_a)_{1,0,0} \simeq (d^2n/dn_z^2)_{n_z=0}^{-\frac{1}{2}}(R^2/2L^2-Rk_a) \times \cos 2\pi(k_a^2L^2/2-\varphi).$$

Using $(d^2n/dn_z^2)_{n_z=0}^{-1}=L_z/\pi L$, and calculating the moments from $\delta V(E_a)_{1,0,0}$ as in Eqs. (31), (35) we find at $T=0$

$$M_{1,0,0} \simeq (L_z/\pi L)(R^2/2L^2-Rk_0) \cdot\{[\partial(k_a^2L^2/2)/\partial H]_{E_a=E_0}/[\partial(k_a^2L^2/2)/\partial E_a]_{E_a=E_0}\} \cdot\cos 2\pi(k_0^2L^2/2-\varphi). \quad (37)$$

The expression in brackets implies the approximation that the last oscillation of the sinusoid determines its integral, and that the sinusoid contributes the major part of $\partial/\partial H$. In other words, this contribution to the moment is the effect of the Fermi surface just catching or missing a lattice plane in quantum number space. In terms of physical constants, Eq. (37) becomes

$$M_{1,0,0} = O(\pi R^2 L_z e^{\frac{1}{2}} H^{\frac{1}{2}}/c^{\frac{1}{2}}\hbar^{\frac{1}{2}}) \cos(2\pi m E_0 c/\hbar eH-\varphi) - O(L_z R e^{\frac{1}{2}} m^{\frac{1}{2}} E_0^{\frac{1}{2}}/\hbar c^{\frac{1}{2}} H^{\frac{1}{2}}) \cos(2\pi m E_0 c/\hbar eH-\varphi). \quad (38)$$

This is just the order of magnitude of the leading term in the de Haas-van Alphen effect (1st term) and the surface correction (2nd term) thereto found by Steele.

In the direction (1, 1, 0), Fig. 5, the lattice planes are $1/\sqrt{2}$ apart. The distance of the tangent plane (to ruled surface BCD) is $BA/2^{\frac{1}{2}}=(\frac{1}{2}L^2k_a^2/\sqrt{2})$. The radius of curvature in the section perpendicular to BC is $\sim(d^2n/dn_z^2)_{n_z=0}^{-1}$ as before. $BC=L^2k_z^2/\sqrt{2}$ so that the fluctuating correction to the volume $V(E_a)$ is

$$\delta V(E_a)_{1,1,0} \sim (L_z/\pi L)(k_a^2L^2/2^{\frac{1}{2}}) \times\cos[2\pi(km^2L^2/2)(\sqrt{2}/\sqrt{2})-\varphi],$$

and the contribution to the moment at $T=0°$,

$$M_{1,1,0} = O(L_z m E_0^2 c^{\frac{1}{2}}/e^{\frac{1}{2}}\hbar^{\frac{1}{2}}H^{\frac{1}{2}}) \cos(2\pi m E_0 c/\hbar eH-\phi). \quad (39)$$

It will be seen that the terms contributing to the moment in Eqs. (38) and (39) are in relative order of magnitude like unity, L^2k_0/R, $L^4k_0^2/R^2$. Thus, as the field gets weaker ($L^2k_0/R \sim 5/HR$) they approach the same order of magnitude, and are equal just when this description of the quantum states fails and we consider the field to be weak instead of strong.

Note that if we pick directions such as (1, 0, 1) in Fig. 5, where the slope $dn_z/dn=1$ of the tangent plane is less than $(dn_z/dn)_{n=0} \sim L_z/L^2k_a \sim L_zH/5$, there is no tangent plane which can be drawn except at the artificially-rounded edge DH which contributed the Landau diamagnetism. This is to say the periodic correction terms corresponding to these directions are small in agreement with Steele's findings.[18]

In the direction (1, −1, 0) where the curve is both concave and convex, a detailed analysis of the region of the inflection points will be required. However, since MJL is a curve, it does not seem possible for the number of points just caught or missed to be as large as those on the straight edges BM or CB, evaluated above, hence the correction $\delta V_{1,-1,0}(E_a)$ and the moment will be correspondingly smaller.

If we consider the shape which the Fermi surface obtains as the magnetic field weakens, it can be seen that the developable portion $MBDH$ gets smaller while the region of surface states and those of positive l get larger until the turning points for orbits of energy E_0 (at the top of the Fermi sea) are no longer determined

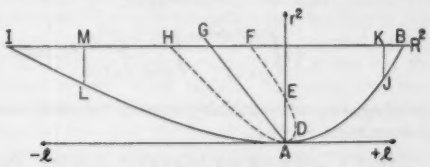

FIG. 7. Region for integration of the WKB radial integrand for weak fields. $L^2k_a/R>1$.

[25] M. F. M. Osborne and M. C. Steele, Phys. Rev. 86, 247 (1952).

by the vector potential but by the wall. The Fermi surface ultimately approaches that of Fig. 6. The diagram for the WKB integration corresponding to Fig. 6 is given in Fig. 7. There are two points to be noted, however. For small values of $k_a^2-k_z^2(n_z)$, region $QPRBA$ of Fig. 6 (see the dotted parabola of Fig. 7), the figure still preserves the character of the strong field surface. Second, surfaces interior to the given surface of Fig. 6 approach the shape of Fig. 5. This simply means that as the orbital component of energy and hence radius of orbit is small compared to the container dimensions, Fig. 5 still applies.

If we examine the Fermi surface shown in Fig. 6, we see along the edges KQ and HB volume may be removed without loss of lattice points. We can evaluate $n+\frac{1}{2}<\frac{1}{2}$ for small powers of Δl using

$$l=-R^2/2L^2\pm R[k_a^2-k_z^2(n_z)]^{\frac{1}{2}}\mp\Delta l,$$

where Δl is the distance in l from the edges KA and AH. As before, to do this we write Eq. (19) in the form

$$n+\tfrac{1}{2}=(1/\pi)\int_{r_l}^{R}(1/r)[(r^2-r_l^2)(r_u^2-r^2)/4L^4]^{\frac{1}{2}}dr, \quad (40)$$

and denote by $r_{u+}, r_{l+}, r_{-u}, r_{l-}$ the roots of the integrand for positive and negative values of l, corresponding to paths JK and LM of Fig. 7 for small quantum numbers n. These are given in Eq. (41) in terms of

$$1/a=R/L^2[k_a^2-k_z^2(n_z)]^{\frac{1}{2}}<1.$$

n_+ and n_- indicate the values of n for these paths. In Eq. (42), as before, we have $k_z(n_z)=(n_z+\frac{1}{2})\pi/L_z$ and also define ξ as $k_a^2-k_z^2(n_z)$.

$$\begin{aligned} r_{u\,l\pm}^2&=4L^4\xi(1+1/4a^2\pm 1/a\cdots),\\ r_{l\,l\pm}^2&=R^2[1-(2\Delta l/\xi^{\frac{1}{2}}R)(1\pm 1/a+1/a^2\cdots)]. \end{aligned} \quad (41)$$

Ultimately, we find for n in the neighborhood of the edges KQ and RH

$$(n+\tfrac{1}{2})_\pm=n_\pm'=R^{-\frac{1}{2}}\xi^{-\frac{1}{4}}(\Delta l)^{\frac{1}{2}}(1\mp 1/a+1/a^2)/3\pi. \quad (42)$$

If we integrate $dnd(\Delta l)dn_z$ over values of n for which $0<n+\frac{1}{2}<\frac{1}{2}$ and the corresponding values of Δl and n_z given by Eq. (42), we can find the net volumes $\delta V(E_a)_\pm$ of the two edges. We indicate by $\Delta l_{\pm 1}$ the values of Δl for which $n_\pm'=\frac{1}{2}$, from Eq. (42).

$$\begin{aligned} -\delta V(E_a)_\pm=&\int_{n_z=-\frac{1}{2}}^{n_z\le L_z k_a/\pi-\frac{1}{2}}\int_{\Delta l=0}^{\Delta l_{+1}}\int_{n_+'=0}^{n_+'}dn_z d\Delta l dn_+'\\ &+\int_{n_z=-\frac{1}{2}}^{n_z\le L_z k_a/\pi-\frac{1}{2}}\int_{\Delta l=0}^{\Delta l_{-1}}\int_{n_-'=0}^{n_-'}dn_z d\Delta l dn_-'. \end{aligned}$$

On integrating and combining terms of the same order of magnitude, we find

$$-\delta V(E_a)_\pm=O(R^{1/3}R_a^{4/3}L_z)+O(R^{7/3}L_z/L^4k_a^{2/3}). \quad (43)$$

Note that the second term of Eq. (43) which is the contribution of the term in $1/a^2$ in Eq. (42) is the only term containing the magnetic field and hence the only part of the volume which can contribute to the moment; the terms in $1/a$ of Eq. (42) canceled out. If we evaluate the contribution to the moment at $T=0°$, we have

$$\begin{aligned} \delta M_\pm&=(\partial/\partial H)\int_0^{E_0}\delta V(E_a)_\pm dE_a\\ &=O(e^2R^{1/3}E_0^{2/3}H/h^{4/3}c^2n^{1/3})\cdot\pi R^2L_z, \end{aligned} \quad (44)$$

valid for $k_0L^2/R>1$. This is the order of magnitude of the Dingle diamagnetism.[12]

The derivation is valid to the extent that the energy surfaces (E_a) over which we integrated, Eq. (44), are represented by Fig. 6. Since interior surfaces approach Fig. 5, these would contribute a different moment corresponding to Eq. (36) with smaller effective E_0. If, for example, $k_0L^2/R=2$, $\frac{3}{4}$ of the volume is represented by energy surfaces like Fig. 6, $\frac{1}{4}$ by Fig. 5, and Eq. (44) is valid to, say, 12 percent. For this reason the volume integral of Eq. (43) is carried out in order of magnitude only.

Exact evaluation will show that the numerical coefficient required in (44) is considerably less than 1, as the "edges" BH and QK are rather "thin" in the n direction, varying like $(\Delta l)^{\frac{1}{2}}$, as was also the case for the surface diamagnetism in the case of strong fields. As was previously reported,[25] the two types of moment go into each other as the field changes from strong to weak, as is indeed evident when we consider the regions of their origin in the Fermi volume. As before, in the case of strong fields, the edge AL at $l=0$ cannot be removed without loss of lattice points.

Although the analytic expression for surface in the region of the Landau edge AB is exactly the same as it was for the strong field case, we can no longer with certainty bevel off and conclude that there is also a term giving the Landau diamagnetism. The reason for this is that the Landau edge is now no longer an acute angle but a rather obtuse one, so that if we remember that we must bevel off to a surface which has a continuous radius of curvature not larger than the largest already present, not much volume can be removed. Surfaces considerably interior to that of Fig. 6, since they approach Fig. 5, would have an acute Landau edge, and these would contribute to a Landau-like term in the integral over dE_a giving the moment. In any event, the Landau diamagnetism is considerably smaller than that given by Eq. (44), and for some conditions[24] may be smaller than the surface diamagnetism of Eq. (36).

We would now like to estimate the order of magnitude of periodic terms corresponding to the directions $(1,-1,0)$ and $(1,1,0)$, Fig. 6. Although the surface is saddle-shaped in these two directions, we still take, as was mentioned seemed plausible, the product of the square root of the two radii of curvature as an estimate of the number of points just caught or missed in these

directions. Since the dimensions of the figure along the lines OH and OK are

$$Rk_a[1\pm O(R/L^2k_a)], \quad R/L^2k_a<1 \ (l, \text{ at } n-\tfrac{1}{4}),$$

whereas the distance OL is

$$Rk_a(1-O(R/L^2k_a)^2). \quad (n+\tfrac{1}{4}, \text{ at } l=0),$$

we can expect that the distance to the tangential plane in the direction 1, 1, 0, or 1, −1, 0 is in order of magnitude

$$(Rk_a/2^{\frac{1}{2}})[1\pm O(R/L^2k_a)].$$

The radii of curvature (one positive, one negative) are in order of magnitude $(d^2n/dl^2)_{n_z=0}^{-1}$ and either $(d^2l/dn_z^2)_{n_z=0}^{-1}$ or $(d^2n/dn_z^2)_{n_z=0}^{-1}$ which are, respectively, $O(Rk_a)$ and $O(L_z^2k_a/R)$.

Hence, the periodic correction to $V(E)$ is of the order of magnitude

$$\delta V(E_a)\sim(Rk_a)^{\frac{1}{2}}(L_z^2k_a/R)^{\frac{1}{2}} \times[\cos\{2\pi Rk_a(1\pm R/L^2k_a)-\varphi\}]. \quad (45)$$

This contributes to the moment, for $T=0°$,

$$M=O(E_0e/Rhc)\cos\{2\pi[R(2mE_0)^{\frac{1}{2}}/\hbar] \times[1\pm ReH/c(2mE_0)^{\frac{1}{2}}]-\varphi\}\cdot\pi R^2L_z. \quad (46)$$

This is in agreement with the form and order of magnitude of periodic terms found by Dingle.[18] All the physical parameters appear correctly, but the period given by Dingle's leading term is three times as great. However, our analysis could not be expected to give this degree of accuracy. Note that in Eq. (46) if R is small, say 10^{-6} cm, this term fluctuates so slowly with magnetic field that it might almost be interpreted as a constant moment of most uncertain sign.

We may also apply the above analysis to the parabolic potential given by Darwin.[19] The Fermi surface in Darwin's notation is shown in Fig. 8. If we identify as the "volume" of Darwin's parabolic well $\pi R_0^2L_z$, where R_0 is the radius at which the scalar potential of the wall is equal to the Fermi energy E_0, then it can easily be shown that the edge DK contributes a moment of the order of the Landau moment M_L. The nose KLM, which lies entirely between the planes $n+\frac{1}{2}=0$ and $n+\frac{1}{2}=\frac{1}{2}$, contributes $M_L\cdot 1/Lk_0=M_L(eH/\hbar c)^{\frac{1}{2}}\cdot\hbar/(2mE_0)^{\frac{1}{2}}$, i.e., considerably smaller, except for very large fields (in striking contrast to the contribution of the surface states for the cylindrical box.) The oscillatory terms corresponding to the directions 1, 1, 0 and 1, 0, 0 can easily be evaluated (see Fig. 2) and are smaller than their counterparts for the cylindrical box potential.

These differences between the box and parabolic well are not surprising, as all the states in a parabolic well potential are in a sense surface states to some degree, whereas for the box a significant distinction can be made between those states which do and those which do not touch the wall. A $1/r$ or $\exp(-kr)$ potential box (atomic system) might give still different results.

[18] R. B. Dingle, Proc. Roy. Soc. (London) **A211**, 500 (1952); **212**, 38 (1952).

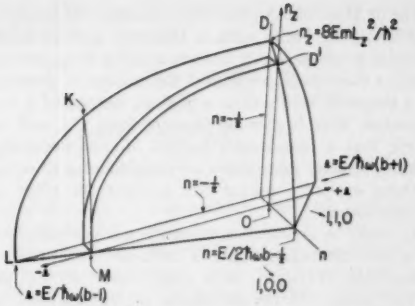

FIG. 8. Energy surface for the Darwin potential.

IV. DISCUSSION

If we consider the application of these ideas to a real metal of shape other than a cylinder, it seems plausible to believe that expressions for the Landau diamagnetism, the de Haas-vanAlphen effect, and certainly the surface diamagnetism for strong fields will still apply. The surface diamagnetism is essentially a consequence of the quantization of orbits which intersect the wall, and if the radius of curvature of this orbit is small compared to the radius of curvature of the surface, it can be considered as plane, and Steele's result for the cubical box and the results of this paper for a cylindrical box are in agreement, so that one can expect that for any surface whose radius of curvature is large compared to that of the quantized orbits considered, the same result will apply.

Moreover, we can also expect that the introduction of a finite surface potential spread over a finite distance will not essentially alter these results, so long as the thickness of the surface layer is small compared to the radius of the orbit or the dimensions of the box. Since the thickness of the surface layer has been estimated at from 10^{-6} to 10^{-3} cm, one can expect that for most magnetic fields and particles not too small this can be regarded as a surface of zero thickness and the above results for a rectangular well potential will still apply.

It is evident from all of the foregoing discussion that the observed fluctuations in the magnetic moment according to the de Haas-van Alphen effect can always be interpreted as a Fermi surface just catching or just missing the lattice points or quantum states of a plane as the magnetic field changes the shape but not the volume of the Fermi surface. Moreover, the nonperiodic contributions to the magnetic moment follow from the fact that the Fermi surface can be shrunk, without loss of lattice points, into a figure of smaller surface area and smaller radius of curvature.

It should be possible to conclude from observation

of the de Haas-van Alphen effect considerable information about the Fermi surface. However, such an interpetation would probably have to await a discussion by number theoretical methods of the problem of particles in a magnetic field and in a periodic instead of a box potential. Here it may be expected from the work of Steele that a considerable portion of the phenomena can be correctly represented by using Landau counting without explicitly taking into account the effect of surface states.

It might be appropriate to mentioned here the effect of a finite temperature and of collisions. If, instead of integrating $\delta V(E_a)dE_a$ to a sharp cutoff at E_0, the Fermi energy, in the expression for the moment as given by Eqs. (31), (35) or (38), where $\delta V(E_a)$ is one of the correction terms, we use the Fermi distribution for a finite temperature, this will have the general effect of "blurring" the cutoff. This has a negligible effect on the nonperiodic contributions to the moment, reducing them by a factor $[1-O(kT/E_0)^2]$. The oscillatory terms are not much affected so long as $kT \ll e\hbar H/2mc = \mu H$, since then the cutoff occurs over an energy range (kT) small compared to the spacing of the levels μH. On the other hand for $kT > \mu H$ the oscillatory moment is damped out by a factor $O(kT/\mu H) \times (e^{-2\pi kT/\mu H})$ with respect to its $T=0$ value.

If the energy levels are blurred by collisions by an amount ϵ, the above expressions with kT replaced by ϵ will apply approximately, in order to estimate the collision damping. However, the damping of the oscillatory terms will depend to a considerable extent on the actual shape of the blurred level. The effect of collisions has been considered by Dingle in detail.[26] Kendall discusses the problem of lattice spots of finite size, but his development does not seem immediately applicable to the problem of collision damping.

The results of this paper apply for boxes ranging from atomic to astronomical dimensions, the definition of "strong" and "weak" fields being adjusted accordingly. The only restriction is that the number of electrons in the box be sufficiently greater than one (say ten or more) so that $V(E_a)$ is a fair estimate of $G(E_a)$. If we try to find combinations of moment, field strength, and dimensions such that the moment per unit volume is $>H$, the applied field, we find that only for very small fields or small dimensions, $HR<10^{-8}$ gauss cm for the oscillatory moments, [Eq. (46)], or very large specimens[12] ($R \sim km$) and very small fields ($H<10^{-9}$) for non-oscillatory moments [Eqs. (44) or (36)] is this possible. Adjusting the effective mass or the Fermi energy can modify these conclusions a little.[27]

These conclusions are in striking contradiction to those of Papapetrou and Slater, who concluded by perturbation arguments for weak fields or "small" boxes (Slater) that a strong diamagnetism was to be expected. If our conclusions from number theory are correct, it means that one must examine with great care any perturbation calculation in a magnetic field for statistical mechanical problems.[28] The conclusions of Welker, who found (neglecting H^2 terms in the Hamiltonian) two huge susceptibilities which just canceled each other, are more in keeping with the results of this paper [see Eq. (27) for $V(E_a)$].

There is a second point to be remembered in applying the conclusions of this paper to a physical problem. The perfect balance [Eq. (27)] insofar as magnetic properties are concerned, between interior and surface states, which is only altered by a consideration of number theory corrections, is only valid for the state of thermodynamic equilibrium. Be the departure from equilibrium ever so slight, this balance may be completely upset. This consideration is important in discussing the magnetic properties of the ionosphere, and may be significant in theories of superconductivity when it is recalled that multiply-connected bodies may not be in their lowest state of thermodynamic equilibrium when a magnetic field is present.

V. GENERALIZATION

It is interesting to consider the problem of generalizing to other quantum-mechanical problems the number theory point of view in computing the density of states. This aspect of a quantum-mechanical problem was first considered by Bohr and Kalckar.[29] Auluck and Kothari[30] have also considered an assembly of oscillators from this viewpoint.

It has been known for a long time that in the correspondence principle limit

$$V(E_a) = \int_{H(p,\,q) \leqslant E_a} dp_1 \cdots dq_s / h^s \qquad (47)$$

is an estimate of the number of states (i.e., quantum cells) less than E_a. When this is applied to a Hamiltonian containing a vector potential where $H = H(p + eA/c, q)$, it is immediately plausible why the result of Eq. (27) was obtained. A canonical transformation[1] of $p + eA/c \rightarrow p'$, $q \rightarrow q'$, with unit Jacobian can always transform the six-dimensional volume integral of Eq. (47) to a form where the magnetic field does not appear either in the integrand or in the limits of integration, hence $V(E_a)$ is independent of H.

The question now is: can we generalize the method of Eq. (47) to compute number theory correction terms to $V(E_a)$ in order to calculate $G(E_a)$? The number theory analog to Eq. (47) which agrees with it exactly is

$$V(E_a) = \int_{E(n_1,\,n_2,\,n_3) \leqslant E_a} dn_1 dn_2 dn_3. \qquad (48)$$

$E(n_1, n_2, n_3)$ are the eigenvalues of $H(p, q)\psi = E\psi$. The

[27] J. Bardeen, Phys. Rev. **80**, 567 (1950).

[28] See reference 5, p. 277 ff.

[29] N. Bohr and F. Kalckar, Kgl. Danske. Videnskab. Selskab Mat.-fys. Medd. **14**, No. 10 (1937).

[30] F. C. Auluck and D. S. Kothari, Proc. Cambridge Phil. Soc. **42**, 272 (1946).

number theory correction terms for Eq. (48) are

$$\delta V(E_a)_{lmn}=R(a_{lmn})$$

$$=R\Big(\int_{E(n_1,\,n_2,\,n_3)\leqq E_a}\exp[2\pi i(ln_1+mn_2+nn_3)]\times dn_1dn_2dn_3\Big), \quad (49)$$

where the number of states less than E_a is $G(E_a)=V(E_a)+\Sigma_{l,m,n}a_{lmn}$. It would appear that to compute Eq. (49) by analogy to Eq. (47) one might proceed as follows. In Eq. (49) dn_i is replaced by dp_idq_i/h and n_i is replaced by

$$n_i=\int_{H(p,\,q)\leqq E_a}dp_idq_i/h=n_i(E_a,\,[p,\,q]_i'), \quad (50)$$

i.e., by the area of the p_iq_i cross section of the surface $H(pq)=E_a$ in phase space. ($[p,\,q]_i'$ means the set of p's and q's except p_i, q_i.) Since this is subsequently to be integrated over all phase space by Eq. (49), in Eq. (50) when substituted into Eq. (49), E_a is again replaced by $H(pq)$. Thus Eq. (49) becomes, computed in analogy to Eq. (47),

$$a_{lmn}=\int_{H(p,\,q)<E_a}\exp\{2\pi i(ln_1(H(p,q)[p,q]_1')+mn_2(H(p,q)[p,q]_2')+nn_3(H(p,q)[p,q]_3'))\}\cdot dp_1\cdots dq_3/h^3, \quad (51)$$

where the n_i in the exponent are the cross sections as given by Eq. (50).

This scheme has been applied to give exact results for the simple problem of the particle in a box and the harmonic oscillator. Its success, or some modification of it, when applied to problems where the variables are not separable or there are several particles with interaction remains to be determined. One may expect that the critical point method, and the methods of combinatorial analysis will find application in such problems.

It is a pleasure to acknowledge the benefit of numerous discussions in the course of this work with M. C. Steele.

PHYSICAL REVIEW VOLUME 88, NUMBER 3 NOVEMBER 1, 1952

Application of the Theory of Numbers to the Magnetic Properties of a Free Electron Gas*

M. C. Steele
Naval Research Laboratory, Washington, D. C.

(Received June 5, 1952)

The methods of number theory are used to find the magnetic properties of a free electron gas. The mathematical procedure which connects number theory to quantum mechanics is given in detail since the same or a similar method may be useful in other problems of solid state and nuclear physics.

The magnetic moment calculation is given in three parts. For the case in which surface states are not considered the results obtained are in agreement with those of previous workers. But when the use of a finite container (rectangular box) to hold the electrons is considered, it is no longer possible to neglect surface states. Through the use of the WKB approximation it is found that the surface states give rise to new size-dependent terms in both the oscillatory and nonoscillatory parts of the magnetic moment. The oscillatory corrections are generally negligible compared to the usual de Haas-van Alphen effect. However, the nonoscillatory correction, which is diamagnetic in character, can be larger than the Landau diamagnetism for properly chosen magnetic field strengths and containter sizes.

The calculation is concluded with a consideration of the effect of the electron spin. It is found, in agreement with other workers, that the only effect of spin on the oscillatory part of the magnetic moment is to introduce a phase change of $\pm\pi$ in alternate terms. The "surface" diamagnetic correction due to a finite container is found to be independent of electron spin.

Details on the use of the method of critical points for evaluating integrals asymptotically are given in the appendix.

I. INTRODUCTION

THE extension of Landau's[1] original work on the diamagnetism of free electrons has already been undertaken by several different methods. Landau[2] himself showed that in addition to the nonperiodic diamagnetic susceptibility the electron gas should exhibit the de Haas-van Alphen[3] effect. Sondheimer and Wilson[4] have recently confirmed this result by an elegant use of the density matrix. However, neither of the above-mentioned papers attempted to find the effect brought about by using a finite container to hold the electrons. It is well known[5] that the absence of diamagnetism of free electrons in classical theory is dependent upon the behavior of the electrons on the surface of the container. The preceding paper in this

* Based on a thesis presented for the degree of Doctor of Philosophy at the University of Maryland, June, 1952.

[1] L. Landau, Z. Physik. **64**, 629 (1930).

[2] D. Shoenberg, Proc. Roy. Soc. (London) **A170**, 341 (1939), (quoting L. Landau).

[3] W. J. de Haas and P. H. van Alphen, Proc. Acad. Sci. Amsterdam **33**, 1106 (1930).

[4] E. H. Sondheimer and A. H. Wilson, Proc. Roy. Soc. (London) **A208**, 173 (1951).

[5] See, for example, J. H. Van Vleck, *Theory of Electric and Magnetic Susceptibilities* (Oxford University Press, London, 1932), p. 100.

issue by M. F. M. Osborne deals at great length with the relation between the classical and quantum theoretical results for a cylindrical container. In the present paper, we shall deal with a rectangular box as the container. Although this choice of geometry has the drawback of not allowing the boundary conditions to be satisfied on all the surfaces, it has the advantage of permitting an analytical solution for the surface effects. On the other hand, Osborne's geometry only allowed an order of magnitude calculation. At first we shall neglect the surface effects and show how number theoretical methods can be used to obtain a result which is in complete agreement with other workers.[2,4] Following this we shall extend the problem to take into account the finite size of the box. This calculation will use both the WKB approximation and number theory. Finally we shall indicate how the electron spin affects the result.

II. PRELIMINARY FORMULAS AND THEIR RELATION TO NUMBER THEORY

A. Free Energy

The free energy of a system of N noninteracting electrons is

$$F=NE_0-kT\sum_i \log(1+e^{(E_0-E_i)/kT}), \tag{1}$$

where E_0 is the Fermi energy, k is Boltzmann's constant, T is the absolute temperature, and E_i are the energy levels for any one of the electrons. E_0 and N are related through the normalizing condition

$$N=\sum_i 1/(1+e^{(E_i-E_0)/kT}). \tag{2}$$

Both Eqs. (1) and (2) are derived on the assumption that there are only electrons of one value of spin present in the system. When both values of spin are allowed, all sums are multiplied by two if N still refers to the total number of electrons.[6] We now assume the existence of an energy distribution function $\rho(E)$, where

$$G(E)=\int_0^E \rho(E)dE \tag{3}$$

represents the number of states having energies equal to or less than E. Then the sums in Eqs. (1) and (2) can be replaced by integrals. The free energy can then be written

$$F=NE_0-kT\int_{E_L}^{\infty} \rho(E)\log(1+e^{(E_0-E)/kT})dE, \tag{4}$$

where E_L is the lowest energy level of the electron. Integrating by parts gives

$$F=NE_0-\left[-kTG(E_L)\log(1+e^{(E_0-E_L)/kT})+\int_{E_L}^{\infty} G(E)f(E)dE\right], \tag{5}$$

where $f(E)$ is the Fermi function

$$f(E)=1/(1+e^{(E-E_0)/kT}). \tag{6}$$

B. Magnetic Moment

In all the work that follows, the magnetic moment will be obtained from the formula[7]

$$M=-(\partial F/\partial H)_{T,V}, \tag{7}$$

where M is the magnetic moment, H is the magnetic field intensity, and V is the volume. We shall only consider systems in which N is held constant so that $E_0(N, H)$ and H can be considered as the variables that determine M. Then Eq. (7) can be written as

$$M=-(\partial F/\partial H)_{E_0}-(\partial F/\partial E_0)_H(dE_0/dH). \tag{8}$$

But from Eqs. (1) and (2) we have

$$(\partial F/\partial E_0)_H=N-\sum_i 1/(1+e^{(E_i-E_0)/kT})=0 \tag{9}$$

so that

$$M=-(\partial F/\partial H)_{E_0}=-(\partial(F-NE_0)/\partial H)_{E_0}. \tag{10}$$

C. Relations to the Theory of Numbers

From Eq. (10) it is clear that we must find F before computing M. But Eq. (5) which is the desired expression for F shows that our immediate aim is to evaluate the function $G(E)$. For the particular problem of the diamagnetism of free electrons, Landau[1] used the Euler-Maclaurin formula for getting $G(E)$. In the course of repeating Landau's calculations, the present author found that the results obtained by using the Euler-Maclaurin formula depended not only on the order of summation over quantum numbers but also on the particular form of the formula. Since it was believed that the theory of physical phenomena should be independent of order of summation, a detailed study was undertaken to resolve the difficulty. It was at this stage that the concepts of number theory were first employed.

Let us suppose that for a particular problem the solution of Schrödinger's equation gives rise to an eigenvalue relation in which the energy levels are expressed as explicit functions of quantum numbers.[8] Then by fixing the energy parameter at E the eigenvalue relation will describe some surface in quantum number space. Now the computation of $G(E)$ resolves itself into the problem of counting the number of quantum states within or on the particular energy surface. This counting is completely analogous to the number theory problem of finding the number of lattice points within a closed surface located in a grid of discrete unit cells. (A lattice point is defined as a point having integers for

[6] This is true when the spin interaction with applied fields is not accounted for. When spin energy is included, one has two independent sums to consider.

[7] This formulation of the magnetic moment follows the development given in Mott and Jones, *Properties of Metals and Alloys* (Oxford University Press, London, 1936).

[8] It will be shown later that the use of the WKB approximation will allow the computation of $G(E)$ even when the eigenvalues are not known as explicit functions of the quantum numbers.

coordinates.) The discreteness of the quantum numbers is sufficient to indicate that there will be corrections to the result obtained by merely computing the volume enclosed by the energy surface.

Lattice point problems have been considered in great detail by mathematicians. The problem of the lattice points of a circle has received particular attention since it is considered the most fundamental as well as the most interesting. Generally the mathematician is more concerned about finding the order of magnitude of the corrections to the number of lattice points than actually getting an explicit relation for the desired total number. Although order of magnitude relations are of value in solid state problems, it was felt more desirable to strive for explicit relations in all cases. Unfortunately we shall see that even in relatively simple quantum-mechanical problems the task of getting an explicit representation for $G(E)$ becomes quite formidable. Number theorists have used a variety of methods in solving lattice point problems. The particular procedure to be used throughout this paper follows closely the work of Kendall[9] on the number of lattice points inside a random oval. Details of the method as applied to quantum mechanics will be given in the text that follows.

III. NO SURFACE EFFECTS (SPINLESS ELECTRONS)

We first consider the magnetic properties of a spinless electron gas enclosed in a box of dimensions L_x, L_y, L_z. This calculation will be restricted to such magnetic field strengths and dimensions of the container as to avoid (seemingly) the need for considering the effect of surface states.

A. Schrödinger Equation

If the applied magnetic field H is along the z axis, the Schrödinger equation for an electron in the box can be written as

$$\frac{1}{2m}\left[-\hbar^2\nabla^2+\frac{e^2A_y^2}{c^2}-\frac{2e\hbar}{ci}A_y\frac{\partial}{\partial y}\right]\psi=E\psi, \tag{11}$$

where $\mathbf{H}=\nabla\times\mathbf{A}$ and we choose $\mathbf{A}=(0, Hx, 0)$. This equation can be separated into two ordinary differential equations if we assume a solution of the form

$$\psi=\phi(x)\zeta(z)e^{2\pi i n_y y/L_y}. \tag{12}$$

Substituting Eq. (12) into Eq. (11) and introducing separation constants gives

$$\frac{-\hbar^2}{2m}\frac{d^2\phi}{dx^2}+\left[\frac{1}{2m}\left(\frac{hn_y}{L_y}-\frac{e}{c}A_y\right)^2-E_1\right]\phi=0, \tag{13}$$

and

$$\frac{-\hbar^2}{2m}\frac{d^2\zeta}{dz^2}-E_2\zeta=0, \tag{14}$$

where $E=E_1+E_2$. The motion in the direction of the field is clearly that of a free particle so that we can immediately write the eigenvalues as

$$E_2=h^2n_z^2/2mL_z^2, \tag{15}$$

if we assume periodic boundary conditions in the z dimension. With this assumption, the quantum number n_z takes on all positive and negative integer values (including zero).

We will now use the WKB approximation to solve for the eigenvalue E_1, since this is the method which will be subsequently applied to estimate the effect of surface states. Equation (13) is the Schrödinger equation of a one-dimensional system with a classical Hamiltonian of the form

$$\mathcal{H}=p^2/2m+U=E_1, \tag{16}$$

where

$$U=\frac{1}{2m}\left(\frac{hn_y}{L_y}-\frac{e}{c}A_y\right)^2. \tag{17}$$

Inserting the value $A_y=Hx$, the classical turning points of the motion become

$$x=\frac{chn_y}{eHL_y}\pm\frac{c}{eH}(2mE_1)^{\frac{1}{2}}. \tag{18}$$

(For symmetry it is convenient to set the origin of coordinates such that the walls are at $\pm L_x/2$.) Using these turning points in the WKB quantum condition

$$\oint p_x dx=(n+\tfrac{1}{2})h \tag{19}$$

leads to the eigenvalue relation

$$E_1=2\beta H(n+\tfrac{1}{2}), \tag{20}$$

where $\beta=eh/2mc$, the Bohr magneton. These levels are recognized as the energy values of a simple harmonic oscillator having a frequency of $eH/2\pi mc$. From Eq. (18) we see that the equilibrium position of the oscillator (center of the orbit) is chn_y/eHL_y and the "orbit radius" is $(c/eH)(2mE_1)^{\frac{1}{2}}$. The eigenvalues given by Eq. (20) are highly degenerate because of the multitude of n_y values that can be assigned (n_y takes on the same range of values as n_x) in the orbit center. In fact, the degeneracy will be fixed by the maximum value that can be assigned to n_y and still have the parabolic potential determine the turning points. For $|n_y|$ greater than this critical value, Eq. (20) will no longer be applicable, since one turning point will then be fixed at $\pm L_x/2$, where the potential is assumed to be infinite. We will now obtain an explicit expression for this degeneracy since this will clarify the approximations to be made. If we fix the value of E_1, the harmonic oscillator solution, Eq. (20), will fail when the condition $U=E_1$ is satisfied simultaneously with the condition that one of the turning points is at $\pm L_x/2$. This leads

[9] D. G. Kendall, Quart. J. Math. (Oxford) 19, 1 (1948).

to the restriction

$$|n_y| \leq |eHL_xL_y/2ch-(L_y/h)(2mE_1)^{\frac{1}{2}}|$$

on n_y. The total degeneracy of the level E_1 is therefore

$$(eHL_xL_y/ch)-(2L_y/h)(2mE_1)^{\frac{1}{2}}. \tag{21}$$

If n_y is allowed to take on values outside of the above range, we would have to obtain a new expression for the eigenvalues.[10] The states resulting from this extension in n_y are our so-called surface states. At this point, we follow Landau[1] in specifying that for sufficiently strong magnetic fields and/or large enough L_x we can neglect the second term in Eq. (21) and designate the degeneracy, D, of the oscillator levels by

$$D=eHL_xL_y/ch. \tag{22}$$

This specification is equivalent to saying that the orbit radius corresponding to energies of the order of the Fermi energy is small compared to the dimension L_x. When E_1 is of order 1 electron volt, this requires

$$HL_x \gg 2c(2mE_1)^{\frac{1}{2}}/e \sim 10. \tag{23}$$

This condition is satisfied even for relatively low fields if we use macroscopic dimensions.

Before proceeding with the calculation of the free energy it should be noted that, in treating the magnetic susceptibility with a classical model, omission of the surface states under any circumstances would lead to a huge diamagnetism.[5] The question therefore arises as to the legitimacy of our neglecting the surface states in the quantum-mechanical case. At this stage, we merely indicate that some compensation was made for omitting the surface states when we increased the degeneracy of the interior states from Eq. (21) to Eq. (22). If this compensation happens to restore the effects of the neglected states, then we have justified the use of the increased degeneracy. Detailed calculations given later in this paper will show that the compensation is fortuitously exact, but without such calculations it is not at all obvious that Landau's argument for neglecting the surface states is valid. An elaboration of this point was believed to be in place since there has appeared in the literature[11] a somewhat misleading qualitative physical explanation to justify Landau's approximation.

Calculation of $G(E)$ and the Free Energy

combining of Eqs. (20) and (15) gives

$$E=h^2n_z^2/2mL_z^2+2\beta H(n+\tfrac{1}{2}). \tag{24}$$

This level is degenerate in the quantum number n_y to the extent D given in Eq. (22). Equations (24) and (22) describe a parabolic cylinder in quantum number space. Our calculation of $G(E)$ is therefore equivalent to the problem of finding the number of lattice points within such a cylinder bounded by the $n=0$ plane. Since the degeneracy is independent of E we need only consider the two-dimensional lattice point problem in the n, n_z plane. In that plane Eq. (24) describes a parabola which is cut off by the line $n=0$. The particular number theory problem of computing the lattice points under such a curve had not been considered at the time this work was initiated. But following the work of Kendall[9] it is possible to obtain here an explicit representation for the number of lattice points. A detailed account of this calculation is given below, since the method employed may be of value in other problems.

Let us allow the parabola in the n, n_z plane to be randomly located but with its axis parallel to the n axis. Then we can write the equation of the parabola as

$$E=A(n_z-\alpha_2)^2+B(n+\tfrac{1}{2}-\alpha_1), \tag{25}$$

where

$$A=h^2/2mL_z^2, \quad B=2\beta H.$$

Now the number of lattice points under this parabola (cut off by the line $n=\alpha_1$) will be periodic in α_1 and α_2 with a periodicity of a single lattice spacing (unity) along either the n or n_z axes. We can therefore represent $G(E)$ as a doubly periodic function in a Fourier series,

$$G(E)=D\sum_{\kappa=-\infty}^{\infty}\sum_{\lambda=-\infty}^{\infty}a_{\kappa\lambda}e^{2\pi i(\kappa\alpha_1+\lambda\alpha_2)}. \tag{26}$$

The Fourier coefficients $a_{\kappa\lambda}$ depend upon the parameter E as well as the factors A and B. Before proceeding with the determination of $a_{\kappa\lambda}$ we must examine the question of where the parabola should be cut off. In the final analysis we must set $\alpha_1=\alpha_2=0$, in order that the parabola given by Eq. (25) be correctly oriented in accordance with the quantum-mechanical requirement specified by Eq. (24). Further, the lowest value of n is supposed to be zero. However, by setting $\alpha_1=0$ and leaving the cutoff of the parabola at $n=0$, the Fourier series will only count one-half of the states along the $n=0$ line. This would be due to the large discontinuity experienced by the number of lattice points as one slides the parabola (along the n axis) so that the cutoff passes through an integer value of n. The Fourier series would then give the average of the two values on either side of the discontinuity. Since the discontinuity would correspond to the number of states along $n=0$, we would be undercounting the states by one-half the amount along that line. In order to avoid this difficulty and still maintain the requirement $\alpha_1=\alpha_2=0$, it is convenient to move the cutoff from $n=0$ to $n=-\frac{1}{2}$. This shift of the cutoff increases the area enclosed by our closed curve but it does not change the number of lattice points. The particular choice of $n=-\frac{1}{2}$ for the cutoff may appear to be arbitrary at this stage, since we could have chosen any value in the range

$$-1<n<0$$

[10] The quantum number n_y can actually take on all integer values in the range $|n_y| \leq |eHL_xL_y/2ch+(L_y/h)(2mE_1)^{\frac{1}{2}}|$. We will deal with the complete range further on in this paper.

[11] See, for example, F. Seitz, *Modern Theory of Solids* (McGraw-Hill Book Company, Inc., New York, 1940), p. 585.

without changing the number of lattice points. We shall see that the value $n=-\frac{1}{2}$ simplifies the problem considerably.

Let $G(E)$ also be represented by the sum

$$G(E)=D\sum_{n,n_2} c(n_2-\alpha_2, n+\tfrac{1}{2}-\alpha_1), \tag{27}$$

where $c(u, v)$ = unity or zero according as (u, v) does or does not fall in the range

$$Av^2+Bu\leqq E, \quad u\geqq 0. \tag{28}$$

The summation in Eq. (27) is extended over all lattice points but only a finite number of these contribute non-zero terms. From Eq. (26) and the periodicities in α_1 and α_2, it follows that

$$a_{\kappa,\lambda}=\int_0^1\int_0^1 \frac{G(E)}{D}e^{-2\pi i(\kappa\alpha_1+\lambda\alpha_2)}d\alpha_1 d\alpha_2. \tag{29}$$

If we now make the transformation

$$u=n+\tfrac{1}{2}-\alpha_1, \quad v=n_2-\alpha_2, \tag{30}$$

and use Eq. (27), we get

$$a_{\kappa,\lambda}=(-1)^\kappa \iint\limits_{Av^2+Bu\leq E} e^{2\pi i(\kappa u+\lambda v)}dudv. \tag{31}$$

Since α_1 and α_2 will both be set to zero and the cutoff will be at $n=-\frac{1}{2}$, it follows from Eq. (30) that the limits of integration in the u, v plane will be

u: from 0 to E/B;

v: from $-(E/A)^{\frac{1}{2}}$ to $(E/A)^{\frac{1}{2}}$.

From Eq. (31) we have

$$a_{\kappa,\lambda}=(a_{-\kappa,-\lambda})^*; \quad a_{\kappa,-\lambda}=(a_{-\kappa,\lambda})^*, \quad \text{and} \quad a_{\kappa,\lambda}=a_{\kappa,-\lambda},$$

so that $G(E)$ can be written as

$$G(E)=D\sum_{\kappa,\lambda=-\infty}^{\infty} a_{\kappa,\lambda}=D[a_{0,0}+2\sum_{\kappa=1}^{\infty}R(a_{\kappa,0})+2\sum_{\lambda=1}^{\infty}R(a_{0,\lambda})+4\sum_{\kappa,\lambda=1}^{\infty}R(a_{\kappa,\lambda})] \tag{32}$$

(where R denotes "the real part of"). Utilizing the symmetry of our boundary curve with respect to v, it follows from Eq. (31) that

$$R(a_{\kappa,\lambda})=(-1)^\kappa \iint\limits_{Av^2+Bu\leq E}\cos(2\pi\kappa u)\cos(2\pi\lambda v)dudv. \tag{33}$$

The coefficient $a_{0,0}$ which corresponds to the area of the closed curve is found to be simply

$$a_{0,0}=4E^{\frac{1}{2}}/3BA^{\frac{1}{2}}. \tag{34}$$

(This is the first advantage of having chosen $n=-\frac{1}{2}$ as the cutoff.) For $\kappa\neq 0$, the general coefficient $R(a_{\kappa,\lambda})$ can be expressed as

$$R(a_{\kappa,\lambda})=(-1)^\kappa B^{\frac{1}{2}}U_{\frac{1}{2}}(w, y)/A^{\frac{1}{2}}\pi(2\kappa)^{\frac{1}{2}}, \tag{35}$$

where

$$w=4\pi E/B, \quad y=2\pi\lambda(E/A)^{\frac{1}{2}}, \tag{36}$$

and $U_{\frac{1}{2}}(w, y)$ is the $\frac{3}{2}$ order Lommel function of two variables discussed by Watson[12] in his Bessel function treatise. For $\kappa=0$, we have

$$R(a_{0,\lambda})=E^{\frac{1}{2}}A^{\frac{1}{2}}J_{\frac{1}{2}}(y)/\pi B\lambda^{\frac{1}{2}}, \tag{37}$$

where $J_{\frac{1}{2}}$ is the $\frac{3}{2}$ order Bessel function of the first kind. From the results given above, $G(E)$ can be explicitly expressed as

$$G(E)=\frac{4DE^{\frac{1}{2}}}{3BA^{\frac{1}{2}}}+2D\sum_{\lambda=1}^{\infty}\frac{E^{\frac{1}{2}}A^{\frac{1}{2}}}{\pi B\lambda^{\frac{1}{2}}}J_{\frac{1}{2}}(y)+\frac{2DB^{\frac{1}{2}}}{A^{\frac{1}{2}}\pi}\sum_{\lambda=0}^{\infty}\sum_{\kappa=1}^{\infty}\frac{P_\lambda(-1)^\kappa}{(2\kappa)^{\frac{1}{2}}}U_{\frac{1}{2}}(w, y), \tag{38}$$

where

$$P_\lambda=\begin{cases}1 \text{ for } \lambda=0\\ 2 \text{ for } \lambda\neq 0.\end{cases}$$

The free energy can now be given formally by substituting Eq. (38) into Eq. (5). It is noted that by shifting the cutoff to $n=-\frac{1}{2}$ we have changed E_L from βH to zero. This is very convenient in Eq. (5), since $G(E_L)$ then becomes zero. In fact, this is the second advantage of having chosen $n=-\frac{1}{2}$ instead of some other value for the cutoff. If we now take into account the factor of two due to spin degeneracy, and require $E_0\gg kT$, the free energy can be expressed as

$$F-NE_0=\frac{-16\pi V(2m)^{\frac{1}{2}}E_0^{5/2}}{15h^3}\left[1+\frac{5\pi^2}{8}\left(\frac{kT}{E_0}\right)^2\right]-\sum_{\lambda=1}^{\infty}\frac{4L_xL_y(2m)^{\frac{1}{2}}}{L_z\hbar^{\frac{1}{2}}\lambda^{\frac{1}{2}}}\int_0^\infty E^{\frac{1}{2}}J_{\frac{1}{2}}(y)f(E)dE+\sum_{\lambda=0}^{\infty}\sum_{\kappa=1}^{\infty}P_\lambda(-1)^\kappa\frac{2Ve(2m)^{\frac{1}{2}}\beta^{\frac{1}{2}}H^{5/2}}{\pi^2\hbar^3c\kappa^{5/2}}\times\int_0^\infty U_{\frac{1}{2}}(w, y)\frac{df(E)}{dE}dE. \tag{39}$$[13]

B. Magnetic Moment

The magnetic moment is obtained by substituting Eq. (39) into Eq. (10), and carrying out the indicated differentiation. Since the integrated term and the single

[12] G. N. Watson, *Treatise on The Theory of Bessel Functions* (Cambridge University Press, Cambridge, 1944), pp. 537–550.

[13] It is noted that the terms with $\kappa\neq 0$ have been transformed so as to obtain the derivative of the Fermi function under the integral. The introduction of the 5/2 order Lommel function arises from the relation

$$\int U_{\frac{1}{2}}(w, y)dE=BU_{\frac{1}{2}}(w, y)/2\pi\kappa,$$

which is encountered upon partial integration.

sum on λ in Eq. (39) do not contain H explicitly, they do not contribute anything to the magnetic moment. Differentiating the double sum gives:

$$M=-\sum_{\lambda=0}^{\infty}\sum_{\kappa=1}^{\infty}P_\lambda\frac{(-1)^\kappa 2Ve(2m)^{\frac{1}{2}}\beta^{\frac{1}{2}}}{\pi^2\hbar^3c\kappa^{5/2}}\times\left[\frac{5}{2}H^{\frac{1}{2}}\int_0^\infty U_{\frac{1}{2}}(w,y)\frac{df(E)}{dE}dE\right.$$
$$\times\frac{-\pi\kappa H^{\frac{1}{2}}}{\beta}\int_0^\infty U_{\frac{1}{2}}(w,y)\frac{df(E)}{dE}dE$$
$$\left.\times\frac{-\pi^2\lambda^2\beta H^{3/2}}{\kappa A}\int_0^\infty U_{7/2}(w,y)\frac{df(E)}{dE}dE\right]. \quad (40)$$

The last two integrals in Eq. (40) arise from the relation

$$\partial U_{s/2}(w,y)/\partial H=-\pi\kappa EU_{s/2}(w,y)/\beta H^2 - \pi\lambda^2\beta U_{7/2}(w,y)/\kappa A. \quad (41)$$

Equation (40) is an exact representation of the magnetic moment. But in order to obtain an answer in integrated form, we have to impose some restrictions on the relative magnitudes of E and βH. In addition, we will limit ourselves to the low temperature region.

We now impose the condition

$$E_0\gg\beta H \quad (42)$$

in order to allow the use of the asymptotic expansion of the Lommel function $U_\nu(w,y)$.

1. *Terms with* $\lambda=0$

For purposes of later discussion it is now convenient to break up the sum of Eq. (40) into parts, i.e. $\lambda=0$ and $\lambda\neq0$. For $\lambda=0$, we have the asymptotic expansion[12]

$$U_\nu(w,0)\sim\cos\left(\frac{w}{2}-\frac{\nu\pi}{2}\right)+\sum_{p=0}^{\infty}(-1)^p\Big/\left[\Gamma(\nu-1-2p)\left(\frac{w}{2}\right)^{2p-\nu+2}\right] \quad (43)$$

for $|w|$ large. In our case, Eq. (42) expresses the condition $|w|$ large. Since the series in Eq. (43) is rapidly convergent, we need only retain the first term of the sum. Thus we have

$$U_\nu\left(\frac{4\pi\kappa E}{B},0\right)\sim\cos\left(\frac{2\pi\kappa E}{\beta H}-\frac{\nu\pi}{2}\right)+B^{2-\nu}/[\Gamma(\nu-1)(2\pi\kappa E)^{2-\nu}]. \quad (44)$$

This gives rise to the sum

$$-\sum_{\kappa=1}^{\infty}\frac{(-1)^\kappa 2Ve(2m)^{\frac{1}{2}}\beta^{\frac{1}{2}}}{\pi^2\hbar^3c\kappa^{5/2}}\left[\frac{5}{2}H^{\frac{1}{2}}\int_0^\infty\cos\left(\frac{2\pi\kappa E}{B}-\frac{5\pi}{4}\right)\frac{df(E)}{dE}dE\right.$$
$$\left.+\frac{4\kappa^{\frac{1}{2}}H}{\beta^{\frac{1}{2}}}\int_0^\infty E^{\frac{1}{2}}\frac{df(E)}{dE}dE-\frac{\pi\kappa H^{\frac{1}{2}}}{\beta}\int_0^\infty\cos\left(\frac{2\pi\kappa E}{B}-\frac{3\pi}{4}\right)\frac{df(E)}{dE}dE\right] \quad (45)$$

in the value of M. The second integral of Eq (45) is a standard type Fermi-Dirac integral. At low temperatures we have

$$\int_0^\infty E^{\frac{1}{2}}\frac{df(E)}{dE}dE\cong-E_0^{\frac{1}{2}}\left[1-\frac{\pi^2}{24}\left(\frac{kT}{E_0}\right)^2\right], \quad (46)$$

so that this part of the sum becomes

$$\frac{8Ve(2m)^{\frac{1}{2}}\beta HE_0^{\frac{1}{2}}}{\pi^2\hbar^2c}\left[1-\frac{\pi^2}{24}\left(\frac{kT}{E_0}\right)^2\right]\sum_{\kappa=1}^{\infty}\frac{(-1)^\kappa}{\kappa^2}. \quad (47)$$

But since

$$\sum_{\kappa=1}^{\infty}\frac{(-1)^\kappa}{\kappa^2}=\frac{-\pi^2}{12}, \quad (48)$$

Eq. (47) becomes

$$\frac{-2Ve(2m)^{\frac{1}{2}}\beta E_0^{\frac{1}{2}}H}{3\hbar^2c}\left[1-\frac{\pi^2}{24}\left(\frac{kT}{E_0}\right)^2\right]. \quad (49)$$

This part of the magnetic moment is not periodic in H. In fact, it is identical to the ordinary Landau[1] diamagnetism with the correction due to temperature. The result obtained here agrees with the previous work of Stoner[14] who investigated the temperature dependence of the Landau diamagnetism.

The two other integrals of Eq. (45) give terms in M which are periodic functions of the magnetic field. These integrals can be evaluated by means of contour integration. It is found that their contribution to M is

$$-\sum_{\kappa=1}^{\infty}\frac{(-1)^\kappa 2Ve(2m)^{\frac{1}{2}}\beta^{\frac{1}{2}}}{\pi^2\hbar^2c\kappa^{5/2}}\left[\frac{5\pi^2\kappa kTH^{\frac{1}{2}}\cos\left(\frac{\pi\kappa E_0}{\beta H}-\frac{5\pi}{4}\right)}{2\beta^{\frac{1}{2}}\sinh(\pi^2\kappa kT/\beta H)}\right.$$
$$-\frac{\pi^2\kappa kTH^{\frac{1}{2}}\sin\left(\frac{\pi\kappa E_0}{\beta H}-\frac{3\pi}{4}\right)}{\beta\sinh(\pi^2\kappa kT/\beta H)}$$
$$+\frac{\pi^4\kappa^2(kT)^2\cosh\left(\pi^2\kappa\frac{kT}{\beta H}\right)\sin\left(\frac{\pi\kappa E_0}{\beta H}-\frac{3\pi}{4}\right)}{\beta^2H^{\frac{1}{2}}\sinh^2(\pi^2\kappa kT/\beta H)}$$
$$\left.-\frac{\pi^3\kappa^2kTE_0\cos\left(\frac{\pi\kappa E_0}{\beta H}-\frac{3\pi}{4}\right)}{\beta^2H^{\frac{1}{2}}\sinh(\pi^2\kappa kT/\beta H)}\right]. \quad (50)$$

[14] E. C. Stoner, Proc. Roy. Soc. (London) **A152**, 672 (1935). It is noted that Stoner expresses his result in terms of ϵ_0, the Fermi energy at $T=0°K$ and $H=0$, whereas the E_0 used in the present work is a function of T and H. E_0 can be expressed as a function of ϵ_0, T, H, to bring the two results into coincidence.

If we now invoke our conditions:

$$E_0 \gg kT \quad \text{and} \quad E_0 \gg \beta H,$$

we can neglect the first three terms appearing in the brackets of Eq. (50) compared to the fourth. The significant contribution to M from the terms with $\lambda=0$ therefore becomes (using the definition of β, the Bohr magneton, to transform the nonperiodic term)

$$\frac{-4\pi V(2m)^{\frac{1}{2}}\beta^2 E_0^{\frac{1}{2}}H}{3h^3}\left[1-\frac{\pi^2}{24}\left(\frac{kT}{E_0}\right)^2\right]$$

$$+\sum_{\kappa=1}^{\infty}\frac{(-1)^{\kappa}2\pi kTVe(2m)^{\frac{1}{2}}E_0\cos\left(\dfrac{\pi\kappa E_0}{\beta H}-\dfrac{3\pi}{4}\right)}{\kappa^{\frac{1}{2}}h^2c\beta^{\frac{1}{2}}H^{\frac{1}{2}}\sinh(\pi^2\kappa kT/\beta H)}. \tag{51}$$

2. *Terms with* $\lambda\neq 0$

Before obtaining the contribution from the terms with $\lambda\neq 0$, we must examine the relative magnitudes of y and w appearing in the argument of the Lommel functions. For $\lambda\neq 0$, we find that $y\sim w$ when $E=E_0$ and $H>10$ gauss (if L_z is of order cm). Therefore, if we require $|w|\gg 1$ in our asymptotic solution, we must simultaneously require $|y|\gg 1$. This situation arises from the physical parameters which determine the argument of the Lommel functions. Unfortunately it also means that we cannot use (without caution) the asymptotic development for $U_\nu(w, y)$ given by Watson,[12] in which only $|w|\gg 1$. When both $|y|\gg 1$ and $|w|\gg 1$ we can use the method of critical points (see the appendix) to get the asymptotic development of $U_\nu(w, y)$. The result is dependent upon the relative magnitudes of y and w. The three expansions for $U_{\frac{1}{3}}(w, y)$ are given below:

$$U_{\frac{1}{3}}(w,y)\sim\begin{cases}\cos\left(\dfrac{w}{2}+\dfrac{y^2}{2w}-\dfrac{3\pi}{4}\right)+\left(\dfrac{2}{\pi}\right)^{\frac{1}{2}}\dfrac{w^{\frac{1}{2}}\cosh y}{(w^2-y^2)}, & y<w\\[2ex] \dfrac{1}{2}\cos\left(w-\dfrac{\pi}{4}\right)+\dfrac{\cos w}{2^{\frac{1}{2}}\pi^{\frac{1}{2}}w^{\frac{1}{2}}}, & y=w\\[2ex] \left(\dfrac{2}{\pi}\right)^{\frac{1}{2}}\dfrac{w^{\frac{1}{2}}\cosh y}{(w^2-y^2)}, & y>w.\end{cases} \tag{52}$$

The singular case of $y=w$ is not of great physical significance, since it only occurs at a specific value of H. We are more concerned with the other cases since there H can take on continuous values. Before proceeding to the moments resulting from $\lambda\neq 0$, we note that $y<w$ requires that (for $E=E_0$)

$$\lambda<\kappa hE_0^{\frac{1}{2}}/L_z(2m)^{\frac{1}{2}}\beta H. \tag{53}$$

After carrying out the calculation to get the magnetic moment it is found that only those terms arising from the condition $y<w$ are significant. The specific contribution to M from these terms is

$$-\sum_{\lambda=1}^{\infty}\sum_{\kappa=\kappa_L(H,\lambda)}^{\infty}\frac{(-1)^{\kappa}4\pi kTVe(2m)^{\frac{1}{2}}\beta^{\frac{1}{2}}H^{\frac{1}{2}}}{\kappa^{\frac{1}{2}}h^2c}$$

$$\times\left(\frac{2\lambda^2mL_z^2\beta}{\kappa h^2}-\frac{\kappa E_0}{\beta H^2}\right)\frac{\cos\left(\dfrac{\pi\kappa E_0}{\beta H}+\dfrac{2\pi\lambda^2m\beta L_z^2H}{\kappa h^2}-\dfrac{3\pi}{4}\right)}{\sinh(\pi^2\kappa kT/\beta H)}, \tag{54}$$

where $\kappa_L(H, \lambda)$ is the integral part of

$$\lambda L_z(2m)^{\frac{1}{2}}\beta H/hE_0^{\frac{1}{2}}.$$

C. Discussion of the Magnetic Moment

For the case $E_0\gg\beta H$, the magnetic moment is the sum of Eqs. (51) and (54). We have already discussed the nonperiodic term. The remaining terms are all periodic functions of H. We shall separate the discussion of the single sum in Eq. (51) and the double sum in Eq. (54), but we identify the totality of these sums with the experimentally observed de Haas-van Alphen effect.

Consider now the single sum on κ. If we express our result in terms of the magnetization, M/V, then both the amplitudes and frequencies of all the terms in this sum are independent of the dimensions of the box. These terms are identically those found by Landau[2] in his theory of the de Haas-van Alphen effect.

We now examine the double sum in Eq. (54). The fundamental difference between these terms and those of the single sum is that the amplitudes and frequencies are now functions of the dimension L_z. We will now propose an argument[15] to show that the contribution of this double sum can be neglected. Suppose there is an uncertainty δL_z in the dimension L_z. Then in order for the cosine term to have a definite value (when H is fixed), we require that δL_z should not change the phase by more than $\pi/2$. This leads to the condition:

$$\delta L_z<\kappa h^2/8\lambda^2m\beta L_zH. \tag{55}$$

If we set $\lambda=1$ and κ equal to the lowest possible value compatible with Eq. (53), this condition becomes

$$\delta L_z<2^{\frac{1}{2}}h/8m^{\frac{1}{2}}E_0^{\frac{1}{2}}. \tag{56}$$

If we use the free electron value for m and E_0 as 1 ev, this requires

$$\delta L_z<3\times 10^{-8}\text{ cm}.$$

This severe restriction on the uncertainty in L_z cannot be met in a laboratory specimen. Therefore, the cosine term in the double sum will average to very nearly zero. However, as κ grows, the restriction on δL_z becomes less severe. In fact, the above argument fails completely when $\kappa\gg\lambda$. Under such circumstances we have another factor which will nullify the significance of the double

[15] The author wishes to thank Professor M. H. Johnson for suggesting this argument.

sum. It is the damping factor

$$1/\sinh(\pi^2\kappa kT/\beta H).$$

For κ large the damping factor will make the amplitude of the oscillations negligible. As a result of this analysis we can completely neglect the double sum given by Eq. (54). This is equivalent to saying that the "Landau" counting of states leads to no significant size effect in the magnetic moment. This conclusion is consistent with the fact that we did not include any surface states in this part of the calculation.

IV. SURFACE EFFECTS (SPINLESS ELECTRONS)

The results given in Sec. III are dependent on the use of an eigenvalue degeneracy given by Eq. (22). We have already indicated that there is no *a priori* reason for believing that this degeneracy takes proper account of the surface states in a finite container. In this section we will determine the effect of surface states by means of the WKB approximation and number theoretical methods.

A. Distribution Function $G(E)$

The method we shall follow here is different from that used in the previous section where we utilized an eigenvalue relation with an assumed degeneracy. To find the effect of the surface states with such a method would first require an appropriate eigenvalue relation. Although it is possible to accomplish this by means of the WKB approximation, the resulting expression does not give the energy as an explicit function of the three quantum numbers. Because of this difficulty, it is easier to leave the quantum number n in phase integral form and express $G(E)$ as a triply-periodic Fourier series in the quantum numbers. We shall show that such a procedure will allow us to draw certain general conclusions about the magnetic moment of an electron gas in a finite container.

We start with the WKB quantum condition for the motion in the x direction

$$\oint p dx=(n+\tfrac{1}{2})h. \tag{57}$$

If we suppose x_1 and x_2 are the classical turning points for a given orbit with energy E_1, we have

$$n=\frac{2}{h}\int_{x_1}^{x_2} p dx-\tfrac{1}{2}, \tag{58}$$

where, for our problem,

$$\begin{aligned} p&=[2mE_1-(hn_y/L_y-eHx/c)^2]^{\frac{1}{2}},\\ E&=(h^2n_z^2/2mL_z^2)+E_1. \end{aligned} \tag{59}$$

Our number theory problem is now to count the lattice points within or on the energy surface E in the three-dimensional quantum number space. No assumption is made about a degeneracy. If the counting is done properly, all questions of degeneracy will be automatically answered. Let $G(E)$ be represented by a triply-periodic Fourier series

$$G(E)=\sum_\kappa\sum_\lambda\sum_\mu a_{\kappa,\lambda,\mu}e^{2\pi i(\kappa\alpha_1+\lambda\alpha_2+\mu\alpha_3)}, \tag{60}$$

where α_1, α_2, α_3 correspond to translations along the n, n_y, n_z axes, respectively. In order to avoid a discontinuity in $G(E)$ when α_1, α_2, α_3 are all set to zero we will move the lower limit of n from 0 to $-\frac{1}{2}$. This is done to count all the states in the n_z, n_y plane. Leaving the cut-off plane of the surface at $n=0$ would result in counting only one-half the states in the n_z, n_y plane.

Following the methods in Sec. 3 we find that

$$\begin{aligned} G(E)=a_{0,0,0}&+2\sum_{\kappa=1}^{\infty}R(a_{\kappa,0,0})+2\sum_{\lambda=1}^{\infty}R(a_{0,\lambda,0})\\ &+2\sum_{\mu=1}^{\infty}R(a_{0,0,\mu})+4\sum_{\kappa,\lambda=1}^{\infty}R(a_{\kappa,\lambda,0})\\ &+4\sum_{\lambda,\mu=1}^{\infty}R(a_{0,\lambda,\mu})+4\sum_{\kappa,\mu=1}^{\infty}R(a_{\kappa,0,\mu})\\ &+8\sum_{\kappa,\lambda,\mu=1}^{\infty}R(a_{\kappa,\lambda,\mu}), \end{aligned} \tag{61}$$

where

$$\begin{aligned} R(a_{\kappa,\lambda,\mu})=(-1)^\kappa\int\!\!\int\!\!\int_{\tau(p)}&\cos(2\pi\kappa n)\cos(2\pi\lambda n_y)\\ &\times\cos(2\pi\mu n_z)dndn_ydn_z, \end{aligned} \tag{62}$$

and the integration[16] is over the volume $\tau(p)$, throughout which p is a real number This volume will include both the harmonic oscillator states of Sec. III and our surface states. Consider first the principal coefficient $a_{0,0,0}$ which corresponds to the volume of our energy surface. This coefficient will be by far the largest term in the expansion of $G(E)$. The other terms will represent the number theory corrections to the replacement of a sum by an integral.

1. *The $a_{0,0,0}$ Term*

From Eq. (62) we have

$$a_{0,0,0}=R(a_{0,0,0})=\int\!\!\int\!\!\int_{\tau(p)}dndn_ydn_z. \tag{63}$$

Integrating first over n, using the upper limit

$$\frac{2}{h}\int_{x_1}^{x_2}pdx$$

and the lower limit zero, gives

$$a_{0,0,0}=\frac{2}{h}\int\!\!\int\!\!\int_{\tau'(p)}pdxdn_ydn_z, \tag{64}$$

[16] The lower limit for the n appearing in Eq. (62) is zero. This results from the shift in cutoff as explained in Sec. III.

where $\tau'(p)$ is the volume in x, n_y, n_z space throughout which p is real. It is now more convenient to integrate over n_y first. The limits on n_y are determined by the condition $p=0$. This gives the upper (u) and the lower (l) limits

$$\begin{aligned}(n_y)_u &= eHL_y x/hc+(L_y/h)(2mE_1)^{\frac{1}{2}},\\ (n_y)_l &= eHL_y x/hc-(L_y/h)(2mE_1)^{\frac{1}{2}}.\end{aligned} \tag{65}$$

The limits on x are determined by the extreme values of the classical turning points. By assuming an infinite potential at the walls of the box, these limits become

$$(x)_u=\tfrac{1}{2}L_x, \quad (x)_l=-\tfrac{1}{2}L_x. \tag{66}$$

Finally, the limits of n_z are obtained directly from Eq. (59) with E_1 set to zero. This gives

$$(n_z)_u=L_z(2mE)^{\frac{1}{2}}/h, \quad (n_z)_l=-L_z(2mE)^{\frac{1}{2}}/h. \tag{67}$$

Having thus defined $\tau'(p)$, we carry out the integration of Eq. (64) in the order n_y, x, n_z. This gives

$$a_{0,0,0}=4\pi V(2mE)^{\frac{3}{2}}/3h^3, \tag{68}$$

which is exactly the number of states for free electrons in a box without a magnetic field. In fact, Eq. (68) is identical to the result obtained in Sec. III when we modified the degeneracy to eliminate the need for calculating the effects of surface states. To this extent the calculation given here is a justification of Landau's argument. From a physical point of view, our calculation shows that Landau's overcounting of the harmonic oscillator states exactly compensates his neglecting the surface states.

2. *The $a_{\kappa,0,0}$ Terms*

Although the two methods of counting give the same total volume term, it is evident that the corrections will be different. Qualitatively, the energy surface will approach that of Sec. III as H becomes large, since the harmonic oscillator states then comprise the greatest part of the volume. Under such conditions, one might expect that $G(E)$ would be given by Eq. (38) plus higher order corrections. This conclusion could be made still more plausible by allowing the dimension L_x to be large. However, the situation for low fields and finite L_x does not offer any obvious conclusions. Under such conditions the effect of the surface states is emphasized.

From the results given in Sec. III we know that to compute the magnetic moment we need only consider those correction terms in which the frequency of the oscillatory part is not a function of the dimensions of the box. In the present Fourier expansion, this corresponds to using only the terms $R(a_{\kappa,0,0})$. Our immediate task is therefore to calculate those coefficients. It seems plausible that the results of Sec. III should be identifiable in such a calculation. In this sense we have some control on the validity of the analysis. From Eq. (62), we have

$$R(a_{\kappa,0,0})=(-1)^{\kappa}\int\int\int_{\tau(p)}\cos(2\pi\kappa n)dndn_ydn_z. \tag{69}$$

Integrating first over n, and inserting the limits, gives

$$R(a_{\kappa,0,0})=\frac{(-1)^{\kappa}}{2\pi\kappa}\int\int_{\tau'(p)}\sin\left(\frac{4\pi\kappa}{h}\int_{x_1}^{x_2}pdx\right)dn_ydn_z. \tag{70}$$

Now we break the integral into two parts corresponding to the oscillator states and the surface states. The division is determined by the value of n_y. In Sec. III we found that for

$$0\leqq|n_y|\leqq\left|\frac{eHL_xL_y}{2hc}-\frac{L_y}{h}(2mE_1)^{\frac{1}{2}}\right|$$

we had oscillator states, but for

$$\begin{aligned}|q|=\left|\frac{eHL_xL_y}{2hc}-\frac{L_y}{h}(2mE_1)^{\frac{1}{2}}\right| &\leqq|n_y|\\ &\leqq\left|\frac{eHL_xL_y}{2hc}+\frac{L_y}{h}(2mE_1)^{\frac{1}{2}}\right|=|r|\end{aligned}$$

we got surface states. For the oscillator states the turning points x_1, x_2 are given by the equations

$$\begin{aligned}x_1&=(hcn_y/eHL_y)-(c/eH)(2mE_1)^{\frac{1}{2}},\\ x_2&=(hcn_y/eHL_y)+(c/eH)(2mE_1)^{\frac{1}{2}}.\end{aligned}$$

For the surface states we have (the subscript s denotes surface)

$$x_{1,s}=x_1, \quad x_{2,s}=\tfrac{1}{2}L_x.$$

Thus Eq. (70) can be written as

$$\begin{aligned}R(a_{\kappa,0,0})=\frac{2(-1)^{\kappa}}{\pi\kappa}&\int_0^{(L_x/h)(2mE)^{\frac{1}{2}}}\\ &\times\left[\int_0^{q}\sin\left(\frac{4\pi\kappa}{h}\int_{x_1}^{x_2}pdx\right)dn_y\right.\\ &\left.+\int_q^{r}\sin\left(\frac{4\pi\kappa}{h}\int_{x_{1,s}}^{x_{2,s}}pdx\right)dn_y\right]dn_z. \quad (71)^{17}\end{aligned}$$

If we now impose the restriction $E_0\gg\beta H$, it is possible to obtain the asymptotic value of $R(a_{\kappa,0,0})$. The evaluation of Eq. (71) is dependent on the use of the method of critical points recently introduced by van der Corput.[18] With a plausible interpretation of this method

[17] The factor of 2 appearing in Eq. (71) results from using the symmetry properties of the integral with respect to n_y and n_z to change the limits appropriately.

[18] J. G. van der Corput, Proc. Acad. Sci. (Amsterdam) **51**, 650 (1948).

it is found that

$$R(a_{\kappa,0,0})\sim\Big[(-1)^{\kappa}DB^{\frac{1}{2}}U_{\frac{1}{2}}(w,0)/A^{\frac{1}{2}}\pi(2\kappa)^{\frac{1}{2}}$$
$$-\frac{(-1)^{\kappa}L_yL_z2mE^{\frac{1}{2}}B^{\frac{1}{2}}}{\pi2^{\frac{1}{2}}\kappa^{\frac{1}{2}}h^2}\cos\left(\frac{w}{2}-\frac{3\pi}{4}\right)$$
$$+\frac{(-1)^{\kappa}L_yL_z2mE^{\frac{1}{2}}B^{\frac{1}{2}}}{h^2\kappa^{5/3}}\left(\frac{\Gamma(5/3)\Gamma(11/12)\pi^{\frac{1}{2}}3^{7/6}}{\Gamma(17/12)4^{5/3}}\right)\Big]. \quad (72)$$

The symbols in Eq. (72) have the same values as in Sec. III. Details on the use of the method of critical points for the evaluation of Eq. (71) are given in the appendix.

B. Magnetic Moment

With the restriction $E_0\gg\beta H$, the magnetic moment resulting from $R(a_{\kappa,0,0})$ is

$$M=\frac{-4\pi V(2m)^{\frac{1}{2}}\beta^2E_0^{\frac{1}{2}}H}{3h^3}\left(1-\frac{\pi^2}{24}\left(\frac{kT}{E_0}\right)^2\right)$$
$$+\sum_{\kappa=1}^{\infty}\frac{(-1)^{\kappa}2\pi kTVe(2m)^{\frac{1}{2}}E_0\cos(\pi\kappa E_0/\beta H-\frac{3}{4}\pi)}{\kappa^{\frac{1}{2}}h^2c\beta^{\frac{1}{2}}H^{\frac{1}{2}}\sinh(\pi^2\kappa kT/\beta H)}$$
$$-\sum_{\kappa=1}^{\infty}\frac{(-1)^{\kappa}2\pi kTL_yL_z2mE_0^{\frac{1}{2}}\cos(\pi\kappa E_0/\beta H-\frac{3}{4}\pi)}{\kappa^{\frac{1}{2}}h^2\beta^{\frac{1}{2}}H^{\frac{1}{2}}\sinh(\pi^2\kappa kT/\beta H)}$$
$$-\frac{L_yL_z2mE_0^{5/3}\beta^{\frac{1}{2}}}{h^2H^{\frac{1}{2}}}\left[1-\frac{2\pi^2}{27}\left(\frac{kT}{E_0}\right)^2\right]$$
$$\times\left(\frac{\Gamma(5/3)\Gamma(11/12)\pi^{\frac{1}{2}}3^{7/6}\zeta(5/3)(2^{\frac{1}{2}}-1)}{2^{7/3}\Gamma(17/12)}\right), \quad (73)^{19}$$

where $\zeta(5/3)$ is the Riemann Zeta-function of argument 5/3. The first and second terms of Eq. (73) give exactly the result obtained in Sec. III (Eq. 51). This identification serves to confirm our conjecture that the size effects might appear as a correction to the previous results. The third and fourth terms of Eq. (73) give the effect of the finite size of the box. It is seen that both the oscillatory and nonoscillatory parts of the moment are affected by size.

The two oscillatory parts of Eq. (73) become of the same order of magnitude when

$$H=H_c\sim2c(2mE_0)^{\frac{1}{2}}/eL_z \quad (74)$$

(where H_c denotes a critical field strength). This is exactly the field condition below which our solution fails.

The additional nonoscillatory correction is noteworthy since it varies as $H^{-\frac{1}{2}}$. It is a diamagnetic effect which (for specimen dimensions of order cm) is comparable to the Landau diamagnetism at fields below 1000 gauss. Further discussion of this term will be delayed until after we have considered the effect of electron spin.

V. SURFACE EFFECTS (ELECTRONS WITH SPIN)

In the previous sections we accounted for the electron spin by merely introducing a degeneracy of two in the Fermi summations. Actually, the spin will alter the eigenvalues and give rise to the spin paramagnetism. We now complete the present calculation with a consideration of the influence of both the electron spin and the surface states due to a finite container.

A. Distribution Function $G(E)$

Assuming that the total wave function is separable into a product of a spin function and a spatial coordinate function, we can write the electronic eigenvalues as

$$E=An_z^2+E_1\pm\beta H. \quad (75)$$

The function $G(E)$ must now be written as

$$G(E)=G_+(E)+G_-(E), \quad (76)$$

where the $\pm$ subscripts refer to the eigenvalues obtained from Eq. (75) with $\mp\beta H$, respectively.

1. $G_+(E)$

If we move the cut-off plane to $n=-\frac{1}{2}$ (just as for the spinless case in Sec. IV), we get identically the number theory problem considered in Sec. IV with E replaced by $(E+\beta H)$. By designating the spinless distribution function as $G_{n.s.}(E)$, we can write

$$G_+(E)=G_{n.s.}(E+\beta H), \quad (77)$$

where $G_{n.s.}(E)$ is given by Eq. (61). It must be noted that the minimum value of E for which Eq. (77) holds is $-\beta H$. In other words $G_+(-\beta H)=0$.

2. $G_-(E)$

Following the above reasoning, we can write

$$G_-(E)=G_{n.s.}(E-\beta H), \quad (78)$$

if we move the cutoff again to $n=-\frac{1}{2}$. In Eq. (78) the minimum value of E is βH since $G_-(\beta H)=0$.

B. Free Energy

The free energy for this case is given by

$$F-NE_0=$$
$$-\left(\int_{-\beta H}^{\infty}G_+(E)f(E)dE+\int_{\beta H}^{\infty}G_-(E)f(E)dE\right). \quad (79)$$

[19] The condition $E_0\gg\beta H$ imposes an upper bound on the magnetic field strength. However, it must be emphasized that the result given by Eq. (73) is also dependent on H having a lower bound. Our use of the WKB approximation has not considered states which have turning points determined by the infinite potentials at both walls simultaneously. This imposes the restriction that $H>2c(2mE_0)^{\frac{1}{2}}/eL_z$ for the applicability of Eq. (73).

We transform the first integral by the substitution

$$E+\beta H=\epsilon^+,$$

and the second integral by the substitution

$$E-\beta H=\epsilon^-.$$

This gives

$$F-NE_0=-\left(\int_0^\infty G_+(\epsilon^+-\beta H)f(\epsilon^+-\beta H)d\epsilon^+ + \int_0^\infty G_-(\epsilon^-+\beta H)f(\epsilon^-+\beta H)d\epsilon^-\right). \quad (80)$$

However, from Eqs. (77) and (78), we have

$$G_+(\epsilon^+-\beta H)=G_{n.s.}(\epsilon^+)$$

and

$$G_-(\epsilon^-+\beta H)=G_{n.s.}(\epsilon^-),$$

so that we can write

$$F-NE_0=-\left(\int_0^\infty G_{n.s.}(\epsilon^+)f(\epsilon^+-\beta H)d\epsilon^+ + \int_0^\infty G_{n.s.}(\epsilon^-)f(\epsilon^-+\beta H)d\epsilon^-\right). \quad (81)$$

In Eq. (81) there is no need to distinguish between ϵ^+ and ϵ^- since they are both integration variables. Hence, we have finally

$$F-NE_0=-\int_0^\infty G_{n.s.}(\epsilon)[f(\epsilon-\beta H)+f(\epsilon+\beta H)]d\epsilon. \quad (82)$$

If we again restrict our interest to the terms $a_{0,0,0}$ and $R(a_{\kappa,0,0})$ in $G_{n.s.}(E)$, we can obtain the asymptotic value (when $E_0\gg\beta H$) of the free energy. The methods used for evaluating Eq. (82) have been described in the previous sections and the appendix.

C. Magnetic Moment

After differentiating the resultant expression for the free energy to get the magnetic moment one encounters many factors of the form

$$(E_0\pm\beta H)^{p/q},$$

where p takes on the values 1, 3, 4, 5, while q is 2 or 3. (The combinations occur in such a way that p and q do not contain common factors.) These factors can all be expanded in power series with $(\beta H/E_0)$ as the variable, since in our asymptotic region $\beta H/E_0\ll 1$. After performing these expansions and combining terms, we find that the magnetic moment is

$$M=\frac{4\pi V(2m)^{\frac{1}{2}}\beta^2E_0^{\frac{1}{2}}H}{h^3}\left(1-\frac{1}{24}\left(\frac{\beta H}{E_0}\right)^2-\frac{\pi^2}{24}\left(\frac{kT}{E_0}\right)^2\right)$$
$$-\frac{4\pi V(2m)^{\frac{1}{2}}\beta^2E_0^{\frac{1}{2}}H}{3h^3}\left(1-\frac{\pi^2}{24}\left(\frac{kT}{E_0}\right)^2\right)$$
$$+\sum_{\kappa=1}^{\infty}\frac{2\pi kTVe(2m)^{\frac{1}{2}}E_0\cos(\pi\kappa E_0/\beta H-\frac{3}{4}\pi)}{\kappa^{\frac{1}{2}}h^2c\beta^{\frac{1}{2}}H^{\frac{1}{2}}\sinh(\pi^2\kappa kT/\beta H)}$$
$$-\sum_{\kappa=1}^{\infty}\frac{2\pi kT(2m)L_yL_xE_0^{\frac{1}{2}}\cos(\pi\kappa E_0/\beta H-\frac{3}{4}\pi)}{\kappa^{\frac{1}{2}}h^2\beta^{\frac{1}{2}}H^{\frac{1}{2}}\sinh(\pi^2\kappa kT/\beta H)}$$
$$-\frac{L_yL_x(2m)E_0^{4/3}\beta^{\frac{1}{2}}}{h^2H^{\frac{1}{2}}}\left[1+\frac{8}{9}\left(\frac{\beta H}{E_0}\right)^2-\frac{2\pi^2}{27}\left(\frac{kT}{E_0}\right)^2\right]$$
$$\times\left(\frac{\Gamma(5/3)\Gamma(11/12)\pi^{\frac{1}{2}}3^{7/6}\zeta(5/3)(2^{\frac{1}{3}}-1)}{2^{1/3}\Gamma(17/12)}\right). \quad (83)$$

We shall now identify and discuss each of the five terms which comprise this magnetic moment.

1. The first term is the Pauli spin paramagnetism with higher order temperature and field corrections. (It is noted that the explicit dependence upon temperature and field could be obtained if E_0 were given explicitly in the variables T and H. This could be accomplished through the use of the normalizing condition Eq. (2).)

2. The second term is the ordinary Landau diamagnetism with higher order corrections.

3. The third term is the usual de Haas-van Alphen effect obtained when no surface states are included. It is noted that this part of the moment differs from the spinless case (Secs. III and IV) by having a phase difference of $\pm\pi$ for terms with κ odd. This result is in agreement with the work of Akhieser,[20] Sondheimer and Wilson,[4] and Dingle.[21]

4. The fourth term is the surface state correction to the de Haas-van Alphen effect. It differs from the corresponding term found in Sec. IV by a phase difference of $\pm\pi$ when κ is odd. This correction becomes comparable to the usual de Haas-van Alphen effect when

$$H=H_c\sim 2c(2mE_0)^{\frac{1}{2}}/eL_x. \quad (84)$$

It is re-emphasized here that Eq. (84) expresses the field condition below which the entire solution fails.

5. The fifth term is a nonoscillatory diamagnetic effect arising from the surface states. Since it was also found in Sec. IV we can say that this effect is independent of electron spin. In light of this circumstance we will now focus our attention on this "surface" diamagnetism. For a free electron gas with E_0 of the order of

[20] A. Akhieser, Compt. rend. acad. sci. U.R.S.S. **23**, 874 (1939).
[21] R. B. Dingle, Proc. Roy. Soc. (London) **A211**, 500 (1952).

1 electron volt, the "surface" (s) magnetization is

$$(M/V)_s \sim -10^{-3}/L_z H^{\frac{1}{2}}, \tag{85}$$

while the remaining (r) nonoscillatory magnetization from the Pauli and Landau terms is

$$(M/V)_r \sim 10^{-6} H. \tag{86}$$

For the assumed value of E_0, we also have

$$H_c \sim 10/L_z. \tag{87}$$

From Eqs. (85) and (86) we find that the $|(M/V)_s|$ is about equal to $|(M/V)_r|$ when

$$H = H_0 \sim 3\times 10^8/L_z^{\frac{1}{2}}. \tag{88}$$

In order to comment on the feasibility of finding the surface diamagnetism experimentally, we shall now examine the above quantities for real specimens.

(a) If L_z is of order cm, H_c is of order 10 gauss while H_0 is of order 300 gauss. For 1 cc of material at 300 gauss we would have to be able to measure a magnetic moment of about 10^{-4} cgs unit in order to observe the surface diamagnetism. Although this is feasible experimentally, it is not an easy task.

(b) If L_z were of order 10^{-2} cm, H_c would be of order 10^3 gauss, while H_0 would be of order 6×10^3 gauss. Now we would need to measure moments of about 5×10^{-3} cgs unit in order to observe the surface diamagnetism. Such moments can be measured accurately without elaborate arrangements.

The analysis given above suggests that experiments may be performed to test the theoretical prediction of surface diamagnetism. It would be desirable to use a monovalent metal, such as Cu, Ag, Na, or Au, for such an experiment since these metals are most closely represented by a free electron model. The specimen could be in powder form with individual particles electrically insulated and having dimensions of the order 10^{-2} cm. Finally, the experiment could be performed at room temperature, since even at $T = 300°\text{K}$ the corrections to the moment are small compared to the temperature-independent terms.

The author wishes to thank Professor R. D. Myers for his guidance in this work, and M. F. M. Osborne not only for suggesting the problem but also for many stimulating discussions.

VI. APPENDIX. The Asymptotic Value of $R(a_{s,t,v})$ as Obtained from the Method of Critical Points

A. Transformation of Eq. (71)

We designate by I_1 and I_2 the first and second integrals, respectively, of Eq. (71). Substituting

$$\theta = hn_y/L_y - eHx/c \tag{A1}$$

into I_1 and carrying out the integrations over θ and n_y gives

$$I_1 = \frac{2(-1)^s}{\pi\kappa}\int_0^{(L_x/h)(2mE)^{\frac{1}{2}}}\left(\frac{eHL_xL_y}{2hc} - \frac{L_y}{h}(2mE_1)^{\frac{1}{2}}\right) \times \sin\left(\frac{\pi\kappa E_1}{\beta H}\right) dn_x. \tag{A2}$$

Now consider the first part of this integral. Setting

$$\phi = hn_x/L_x(2mE)^{\frac{1}{2}} \tag{A3}$$

transforms this part to

$$\frac{(-1)^s eHL_xL_yL_x(2mE)^{\frac{1}{2}}}{\pi\kappa h^2 c}\int_0^1 \sin\left[\frac{\pi\kappa E}{\beta H}(1-\phi^2)\right] d\phi. \tag{A4}$$

The value of the integral in Eq. (A4) is given by Watson.[12] In terms of our previously used symbols, Eq. (A4) becomes

$$(-1)^s DB^{\frac{1}{2}} U_{\frac{1}{2}}(w, 0)/A^{\frac{1}{2}}\pi(2\kappa)^{\frac{1}{2}}. \tag{A5}$$

If we again use the substitution given by Eq. (A3), the second part of I_1 becomes

$$\frac{-4(-1)^s L_yL_xmE}{\pi\kappa h^2}\int_0^1 (1-\phi^2)\sin\left[\frac{w}{2}(1-\phi^2)\right] d\phi. \tag{A6}$$

The evaluation of this integral will require the use of the method of critical points.

With appropriate transformations, I_2, the second part of Eq. (71) can be put into the form:

$$I_2 = \frac{4(-1)^s L_yL_xmE}{\pi\kappa h^2}\Bigg[\int_0^1\int_0^1 (1-\phi^2)^{\frac{1}{2}} \times \sin\left[\frac{w}{2\pi}(1-\phi^2)\left(\frac{\pi}{2}+f(\tau)\right)\right] d\tau d\phi + \int_0^1\int_0^1 (1-\phi^2)^{\frac{1}{2}} \times \sin\left[\frac{w}{2\pi}(1-\phi^2)\left(\frac{\pi}{2}-f(\tau)\right)\right] d\tau d\phi\Bigg] \tag{A7}$$

where

$$f(\tau) = \tau(1-\tau^2)^{\frac{1}{2}} + \sin^{-1}\tau.$$

We shall use the method of critical points to evaluate both of the double integrals in Eq. (A7).

B. Details of the Method of Critical Points

Consider the general integral

$$I = \int_a^b g(x)e^{iwf(x)}dx, \tag{A8}$$

where a, b, $f(x)$, and $g(x)$ are independent of the

parameter w. It is further assumed that $f(x)$ and $g(x)$ are infinitely often differentiable in the closed interval $a \leqq x \leqq b$. We seek the value of I for $|w| \gg 1$. Van der Corput[18] asserts that the asymptotic character of I is completely determined if the behavior of $f(x)$ and $g(x)$ is given in the vicinity of the critical points.[22] These points are the end points a and b and the points between a and b where the phase $wf(x)$ is stationary. The contribution of each critical point is called the residue at that point. The residue at a critical point ξ can be developed asymptotically in ascending powers of $1/w^{1/m}$, where m is the smallest positive integer such that the m^{th} derivative of $f(x)$ at ξ is not zero. To establish the nature of the residue at ξ we expand $g(x)$ and $f(x)$ in Taylor series around ξ. It can be shown that the complete residue at ξ may be expressed as

$$(\text{Res})_\xi = e^{iwf(\xi)}\left[\frac{C_1}{w^{1/m}} + \frac{C_2}{w^{2/m}} + \cdots + \frac{C_s}{w^{s/m}} + \cdots\right], \quad \text{(A9)}[23]$$

where

$$C_s = \frac{g^{s-1}(\xi)}{(s-1)!}\left[\frac{m!}{f^m(\xi)}\right]^{s/m} \frac{(s/m)!}{s(-i)^{s/m}} + \frac{i(m+s/m)!}{(m+s)(-i)^{(m+s)/m}}\left(\frac{m!}{f^m(\xi)}\right)^{(m+s)/m} \times \sum_{0<p<s} \frac{g^{p-1}(\xi) f^{m+s-p}(\xi)}{(p-1)!(m+s-p)!}. \quad \text{(A10)}[24]$$

Let us now apply this development to the integral $I_{1,2}$ appearing in Eq. (A6). To put it into the desired form, we write

$$I_{1,2} = \mathcal{I}_m \int_0^1 g(\phi) e^{iwf(\phi)} d\phi, \quad \text{(A11)}$$

where

$$g(\phi) = (1-\phi^2)^{\frac{1}{2}}, \quad f(\phi) = \tfrac{1}{3}(1-\phi^2),$$

and $\mathcal{I}_m$ denotes "the imaginary part of." The critical points are 0 and 1. The point 0 is a stationary phase point as well as an end point. From Eq. (A10) it is found that the residue at the point 0 is

$$(\text{Res})_0 = e^{iw/2}\left[\frac{(\frac{1}{4})!(2!)^{\frac{1}{2}}}{w^{\frac{1}{2}}(i)^{\frac{1}{2}}} - \frac{(2!)^{\frac{1}{2}}(\frac{3}{4})!}{w^{\frac{1}{2}}3(i)^{\frac{1}{2}}}\right]. \quad \text{(A12)}$$

Since the function $g(\phi)$ cannot be expanded into a Taylor series around the point 1, we must make an appropriate transformation to get the residue there. If we let

$$(1-\phi^2)^{\frac{1}{2}} = z, \quad \text{(A13)}$$

we would require the residue at $z=0$. The transformed integral is

$$\int_0^1 \frac{z^2}{(1-z^2)^{\frac{1}{2}}} \exp(iwz^2/2)dz, \quad \text{(A14)}$$

so that we can now expand our functions around $z=0$. Carrying out the details of expansion leads to

$$(\text{Res})_{z=0} = (\text{Res})_{\phi=1} = 2(2!)^{\frac{1}{2}}(\tfrac{3}{4})!/w^{\frac{1}{2}}3(-i)^{\frac{1}{2}}. \quad \text{(A15)}$$

By neglecting the terms $O(1/w^{\frac{1}{2}})$, and taking the imaginary part of the residue, we get

$$I_{1,2} \sim (\pi)^{\frac{1}{2}} \cos(\tfrac{1}{2}w - \tfrac{3}{4}\pi)/(2w)^{\frac{1}{2}}. \quad \text{(A16)}$$

We now consider the double integrals in Eq. (A7). The general philosophy in handling double integrals is to apply the previous development twice. There are additional features which make the double integration more complicated, but rather than discuss them generally we shall note them in solving the specific examples. We designate by $I_{2,1}$ and $I_{2,2}$ the first and second double integrals in Eq. (A7). Then $I_{2,2}$ can be written as

$$I_{2,2} = \mathcal{I}_m \int_0^1 \int_0^1 g(\phi, \tau) e^{iwF(\phi,\tau)} d\tau d\phi, \quad \text{(A17)}$$

where

$$g(\phi, \tau) = (1-\phi^2)^{\frac{1}{2}},$$

$$F(\phi, \tau) = [(1-\phi^2)/2\pi][\tfrac{1}{2}\pi - \tau(1-\tau^2)^{\frac{1}{2}} - \sin^{-1}\tau].$$

The critical points here are first the points within the region of the integration where the phase $wF(\phi, \tau)$ is stationary, i.e., where the $\partial F/\partial\phi = \partial F/\partial\tau = 0$; then the vertices of the boundary of the region; finally those boundary points are critical where $F(\phi, \tau)$, taken along the boundary curve, is stationary. For our integral $I_{2,2}$ the following points (infinite in number) are critical:

$$\phi = 0, \quad \tau = 0$$
$$\phi = 1, \quad 0 \leqq \tau \leqq 1$$
$$0 \leqq \phi \leqq 1, \quad \tau = 1.$$

To get the residue at the point (0, 0) we expand $g(\phi, \tau)$ and $F(\phi, \tau)$ in double Taylor series around that point. Substituting these expansions into the integrand gives

$$(\text{Res})_{0,0} = e^{iw/4} \int_0^\infty \int_0^\infty \left(1 - \frac{\phi^2}{2} - \cdots\right) \times \exp\left\{iw\left[-\frac{\tau}{\pi} - \frac{\phi^2}{4} + \cdots\right]\right\} d\tau d\phi. \quad \text{(A18)}[25]$$

[22] This condition on $f(x)$ and $g(x)$ is weaker than the requirement that $f(x)$ and $g(x)$ be infinitely often differentiable in the closed interval $a \leqq x \leqq b$. In practice we use the weaker condition for the evaluation of integrals.

[23] Van der Corput gives this form for the residue without showing the explicit values of $C_1, C_2, \cdots$.

[24] In getting Eq. (A10) we have assumed that ξ is the lower bound of the interval. If ξ were an interior point or the upper bound of the interval, the value of C_s would be changed to the extent of a factor of 2 or the inclusion of a negative sign.

[25] The extension to infinity for the upper limits of both integrations is justified here since the major contribution of the double integral is around (0, 0). Details on this point can be found in van der Corput's paper.

Integrating first on τ and keeping only the largest terms gives

$$(\text{Res})_{0,0}=\frac{\pi e^{iw/4}}{iw}\int_0^\infty\left(1-\frac{\phi^2}{2}-\cdots\right)\times\exp\left\{iw\left[-\frac{\phi^2}{4}-\cdots\right]\right\}d\phi. \quad \text{(A19)}$$

We now integrate over ϕ to get

$$(\text{Res})_{0,0}=\frac{\pi e^{iw/4}}{iw}\left[\frac{(\frac{1}{2})!}{w^{\frac{1}{2}}(i/4)^{\frac{1}{2}}}\right]. \quad \text{(A20)}$$

Thus, this residue is $O(1/w^{\frac{1}{2}})$.

Next we consider the residue from the points $0\leqq\phi\leqq1$, $\tau=1$. The function $F(\phi,\tau)$ cannot be expanded in a Taylor series around any point having $\tau=1$. Therefore, we must resort to a suitable transformation to accomplish the calculation. If we let

$$\sin^{-1}\tau=\theta, \quad \text{(A21)}$$

we would require the residue from the points $0\leqq\phi\leqq1$, $\theta=\pi/2$. By expanding the functions in the integrand around $\theta=\pi/2$, we can express the residue from this entire boundary [designated as $(\text{Res})_{b_1}$] as

$$(\text{Res})_{b_1}=\int_0^1\int_0^\infty(1-\phi^2)^{\frac{1}{2}}\left(\Theta-\frac{1}{3!}\Theta^3-\cdots\right)\times\exp\left\{i\frac{w(1-\phi^2)}{2\pi}\left[\frac{4}{3!}\Theta^3+\cdots\right]\right\}d\Theta d\phi, \quad \text{(A22)}$$

where

$$\Theta=\tfrac{1}{2}\pi-\theta.$$

The integration over Θ follows from the general development for single integrals. If we keep only the largest term of the resulting expansion, the residue is

$$(\text{Res})_{b_1}=\frac{(\frac{2}{3})!(3\pi)^{\frac{1}{2}}}{w^{\frac{1}{2}}2(-i)^{\frac{1}{2}}}\int_0^1\frac{d\phi}{(1-\phi^2)^{1/6}}. \quad \text{(A23)}$$

The integral in Eq. (A23) is a standard type, so that the final result can be written as

$$(\text{Res})_{b_1}=\frac{(\frac{2}{3})!(3\pi)^{\frac{1}{2}}\pi^{\frac{1}{2}}\Gamma(11/12)}{w^{\frac{1}{2}}(-i)^{\frac{1}{2}}4\Gamma(17/12)}. \quad \text{(A24)}$$

This residue is $O(1/w^{\frac{1}{2}})$.

Using a similar analysis we find that the residue from the boundary $\phi=1$, $0\leqq\tau\leqq1$ is $O(1/w^{\frac{1}{2}})$. The complete evaluation therefore shows that the largest term in $I_{2,2}$ is given by the imaginary part of Eq. (A24), which is $O(1/w^{\frac{1}{2}})$.

The integral $I_{2,1}$ can be evaluated by the same procedure as given above. It is found that the largest term for this integral is $O(1/w^{7/6})$. Combining the results of the two integrations, we find that

$$I_2\sim(3\pi)^{7/6}\Gamma(5/3)\Gamma(11/12)/8\Gamma(17/12)w^{\frac{1}{2}}. \quad \text{(A25)}$$

The sum of Eqs. (A5), (A16), and (A25) is the value for $R(a_{\kappa,0,0})$ given by Eq. (72).

Lattice Vibrations in Graphite*

RONALD W. GURNEY
Institute for Fluid Dynamics and Applied Mathematics, University of Maryland, College Park, Maryland
(Received April 14, 1952)

In both natural and artificial graphites the crystallites are reported to be agglomerates of smaller units, each containing perhaps not more than 12 to 17 well-ordered planes. For atomic displacements perpendicular to a plane the restoring forces are much weaker than for similar displacements in the plane itself. For the latter the restoring forces are so strong that these lattice vibrations will not be excited at low temperatures. In this paper the requisite adaptation of the Debye theory of specific heat is given; it leads to a T^2 law instead of the familiar T^3 law at low temperatures. Unpublished measurements of specific heat between 25° and 60°K by Estermann and Kirkland are cited and compared with the theory; they are found to lead to a value $\theta_D=614°$ for the Debye temperature for the vibrations with weak restoring forces. Combining this with a value $\theta_D=2100°$ for the remaining modes of vibration is found to represent the specific heat over the whole range of temperature.

WHEN a neutron with energy less than 100 ev is being slowed down in a graphite moderator, the principal mechanism for its loss of energy is the excitation of lattice vibrations. In order to estimate the rate of loss of energy by slow neutrons, a knowledge of the frequency spectrum of the lattice is required.

Graphite has a layer-lattice structure, the atoms within each plane forming a network of hexagons. In both natural and artificial graphites the crystallites are reported to be agglomerates of smaller units. In artificial graphites these units are thin plates, each containing perhaps not more than 12 to 17 parallel well-ordered planes.[1] For atomic displacements perpendicular to a plane, the restoring forces are much weaker than for similar displacements in the plane itself. As early as 1911, when comparing specific heat measurements with the Einstein theory, Nernst[2] suggested that for graphite it was necessary to use two "Einstein temperatures" instead of the single temperature characteristic of an isotropic substance.

In the lattice waves of Debye there are three directions of propagation, and in each direction a longitudinal wave and two transverse waves (with their displacements at right angles). In graphite the vibrations which have weak restoring forces will be (a) transverse waves with direction of propagation within the crystal planes and with displacements perpendicular to these planes, and (b) longitudinal waves propagated perpendicular to the planes; if the crystallite units are only from 12 to 17 atoms thick, no waves of long wave length will be associated with these longitudinal waves. At very low temperatures only the transverse waves (a) will be excited, and the problem reduces to a two-dimensional problem.

The usual Debye expressions defining the frequency spectrum are

$$g(\nu)d\nu=\alpha\nu^2d\nu=4\pi V(1/c_l^3+2/c_t^3)\nu^2d\nu,$$

$$3N=\int_0^{\nu_D}\alpha\nu^2d\nu=\tfrac{1}{3}\alpha\nu_D^3,$$

where V is the volume of the crystal, and c the velocity of propagation. These expressions would be replaced by

$$\alpha'\nu d\nu=2\pi A(1/c_l^2+2/c_t^2)\nu d\nu, \tag{1}$$

$$2N=\int_0^{\nu_D}\alpha'\nu d\nu=\tfrac{1}{2}\alpha'\nu_D^2, \tag{2}$$

where A is the area of the crystallite plate, if all types of wave propagated in the planes were to be included. Actually the number of modes will be one-third of this value, to include only the particular transverse waves (a). The expression for the partition function becomes

$$\log k(T)=4/3N\frac{T^2}{\theta^2}\int_0^{\theta/T}\xi\ln(1-e^{-\xi})d\xi, \tag{3}$$

and the usual T^3 law for the specific heat at low temperatures will be replaced by

$$C_v=9.6RT^2/\theta^2. \tag{4}$$

Table I shows the average value of C_v measured by Estermann and Kirkland[3] for four specimens of arti-

TABLE I. The specific heat of graphite.

Temp	C_v	θ^2	
25°K	0.032	385,100	
30	0.046	373,700	
35	0.063	371,400	
40	0.0815	375,000	
45	0.103	375,500	
50	0.126	379,000	
55	0.1525	378,800	
60	0.179	384,100	
			Mean 376,900

* This work was done at the Argonne National Laboratory. Application for declassification was made in 1948, but consent was withheld. A new application was granted in January, 1952.

[1] T. Neubert, *Structure and Properties of Artificial and Natural Graphites*, unpublished.

[2] W. Nernst, Ann. Physik **36**, 395 (1911).

[3] Estermann and Kirkland, unpublished.

ficial graphite. The last column shows the values of θ^2 derived from (4). The constancy of θ^2 shows that the T^2 law is closely obeyed over this range of temperature and leads to a Debye temperature of 614°K for the limit of the frequency of these transverse waves.[4]

In discussing any substance at high temperatures, one usually has to take into account the difference between C_p and C_v. The difference $(C_p - C_v)$ depends on the value of the square of the coefficient of cubic expansion, which in the case of graphite is abnormally small up to 1000°K, since in two directions the linear expansion is nearly zero. The simplest way of representing the specific heat in this range of temperature is to assign another Debye temperature to all the modes not already included in (3), although this is not strictly correct. Good agreement with the experimental values[5] is obtained with $\theta_2 = 2100°$. Below 70°K the contribution from this part is negligible, so that the T^2 law of Table I is unaffected.

[4] V. V. Tarassov [Compt. rend. (U.S.S.R.) **46**, 111 (1945)] arrived at the value 1370°K for this Debye temperature; this seems to be because he used the full number of modes of a three-dimensional lattice.

[5] A. Magnus, Ann. Physik **70**, 303 (1923) and the Landolt Bornstein Tables.

PHYSICAL REVIEW VOLUME 88, NUMBER 3 NOVEMBER 1, 1952

The Scattering of Slow Neutrons in Polycrystalline Media*

RONALD W. GURNEY
Institute for Fluid Dynamics and Applied Mathematics, University of Maryland, College Park, Maryland
(Received April 14, 1952)

When a neutron passing through a crystallite has insufficient energy to eject an atom from its site, excitation of a lattice vibration occurs instead. This paper deals mainly with neutrons having energy between 0.5 and 5.0 electron volts, the range where both the cross section for elastic scattering σ_{el}, and that for inelastic scattering σ_{in} vary rapidly with energy. In order to deal with inelastic collisions in which many phonons are exchanged, Finkelstein replaced the Debye model of the crystal by the Einstein model and gave expressions for $J_n(E)$, the probability that a neutron having energy E colliding with an atom of mass M loses at a collision n quanta. Computations of J_n for large and small M show in detail that in the slowing-down process by this mechanism a heavy element is much less efficient than a light element, as in the familiar case of fast neutrons. Since in this range of energy σ_{el} is inversely proportional to E, and since the observed total cross section is independent of energy, this implies that σ_{in} is of the form $\sigma_{in} = \sigma_0(1 - A/E)$. Computed values of ΣJ_n are found to lead to this form, irrespective of the particular Einstein temperature assumed for the solid.

WHEN a 100-volt neutron, traveling through a crystal or a crystallite, makes a glancing angle collision with an atom of the lattice, the energy transmitted will be less than the binding energy; in this case, the excitation of a lattice vibration occurs instead of the ejection of the atom from its site. For slower neutrons this becomes increasingly important, until finally the neutron becomes incapable of ejecting an atom, even in a head-on collision. This paper deals mainly with neutrons having energy between 5.0 and 0.5 electron-volts, the range of energy where both the cross section for elastic scattering σ_{el} and the cross section for inelastic scattering σ_{in} are varying rapidly with energy.

In order to deal with inelastic collisions in which many phonons are exchanged, Finkelstein[1] replaced the Debye model of the crystal by the Einstein model. If $\hbar\omega$ is the constant energy difference between successive energy levels of the oscillator, a neutron colliding with an atom of the lattice can lose energy $\hbar\omega$, $2\hbar\omega$, $3\hbar\omega$ $\cdots n\hbar\omega$. If $J_n(E)$ is the probability that a neutron having energy E loses at a collision energy $n\hbar\omega$, the total inelastic cross section is obtained by summing over all values of n not greater than $E/\hbar\omega$:

$$\sigma_{in} = (m/\mu)^2 \sigma_f J, \tag{1}$$

$$J = \sum_{n=1}^{n \leq \epsilon} J_n, \tag{2}$$

where m is the mass of the neutron, μ is the reduced mass of the struck nucleus, σ_f is the cross section of the free nucleus, and $\epsilon = E/\hbar\omega$. The expression given by Finkelstein for J_n is the same as that derived by Fermi[2] for the thermalization of neutrons in hydrogenous substances:

$$J_n = (M/4m\epsilon)[f_n(q_1^2) - f_n(q_2^2)], \tag{3}$$

where

$$f_n(x) = e^{-x}(1 + x + \cdots + x^n/n!), \tag{4}$$

$$q_1 = (m/M)^{\frac{1}{2}}[\epsilon^{\frac{1}{2}} - (\epsilon - n)^{\frac{1}{2}}], \tag{5}$$

$$q_2 = (m/M)^{\frac{1}{2}}[\epsilon + (\epsilon - n)^{\frac{1}{2}}], \tag{6}$$

where M is the mass of the struck nucleus.

* This work was done at the Argonne National Laboratory, and the results have been taken from a declassified report by the author.

[1] R. J. Finkelstein, Phys. Rev. **72**, 907 (1947).

[2] E. Fermi, Ricerca sci. **7**, 13 (1936).

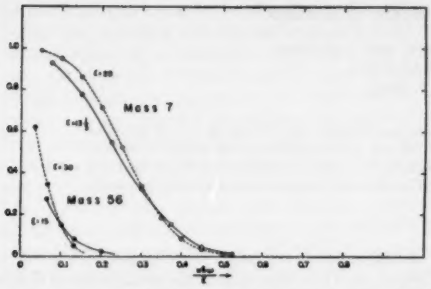

FIG. 1. Relative probabilities for fractional loss of energy $n\hbar\omega/E$.

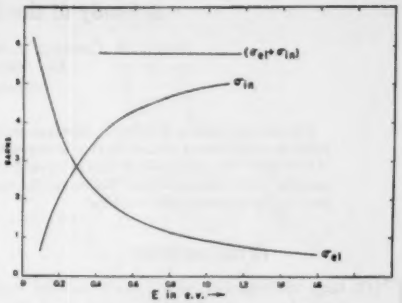

FIG. 2. Elastic and inelastic cross sections.

In the moderation of fast neutrons it is well known that the efficiency of the slowing-down process is much greater for a light element than for a heavy element. It is of interest to know whether this holds likewise for the loss of energy by the other process, the excitation of vibrations by slow neutrons. That it does hold is shown in Fig. 1, which gives the probabilities of various inelastic collisions, computed from (3), (4), (5), and (6), for oscillators of mass 7 and of mass 56 (iron). Here abscissas are ϵ and ordinates are J_n; in each set of points plotted the first is for $n=1$, the second is for $n=2$, and so on. The mass of the struck nucleus determines the character of the oscillator wave functions that are used in the matrix elements: in Fig. 1 it will be seen that for mass 7 the probability of a neutron losing a third of its energy is quite large, whereas for mass 56 the curve falls much more steeply, and the probability that a neutron loses even one-fifth of its energy is very small.

In the range of energy between 0.5 and 5.0 electron-volts, as is well known, the cross section for elastic scattering is inversely proportional to the energy of the neutron—that is, $\sigma_{el}=\sigma_0 A/E$. Now in this range of energy the observed total cross section for many elements is independent of the energy within the experimental error. This implies that the cross section for inelastic scattering is of the form $\sigma_{in}=\sigma_0(1-A/E)$. It does not seem possible to show that, for moderate values of ϵ, the sum (2) is of this form. This is, however, shown by the curves in Fig. 2. These give values of σ_{in} computed from Eqs. (1)–(6) and plotted, omitting the discontinuous structure of the curve, together with values of σ_{el}. Both were computed for mass 7. It will be seen that for energies above 0.4 electron-volt, the one curve is a mirror image of the other, with the result that the total cross section $(\sigma_{el}+\sigma_{in})$ has a value that is independent of the energy, in agreement with experiment.

The values were computed with $\hbar\omega=0.064$ ev, and the question arises whether a different choice of $\hbar\omega$ would lead to a different result. Since at low temperatures σ_{el}, as well as σ_{in}, reduces to a function of ϵ only, a different choice of $\hbar\omega$ would result merely in a change of scale of abscissas in Fig. 2, leaving $(\sigma_{el}+\sigma_{in})$ with the same constant value over the equivalent range of energy.

The computations in this paper were made by M. G. Goldberger.

A Study of the $H^3(d, n)He^4$ Reaction*

J. P. CONNER,† T. W. BONNER, AND J. R. SMITH
Rice Institute, Houston, Texas

(Received July 7, 1952)

The nuclear reaction $H^3(d, n)He^4$ has been studied for deuteron energies from 10 kev up to 1732 kev. The yield curve exhibits a maximum at a deuteron energy of 109 kev, where the total cross section is $5.1\pm0.1 \times 10^{-24}$ cm². The experimental data accurately fit a single level Breit-Wigner resonance curve for deuteron energies below 500 kev. Above this energy the experimental cross section is larger than predicted by a single level in the compound He^5 nucleus.

INTRODUCTION

THE large cross section of the reaction $H^3(d, n)He^4$ makes it interesting both from the standpoint of its use as a neutron source and because the magnitude of the cross section is essentially the maximum possible predicted by nuclear resonance theory. The published data indicate a maximum cross section at around 200 kev triton energy.[1-3] Allen and Poole give the maximum cross section as 5.0 barns.

The purpose of the present work was to make accurate measurements of the cross section over a wide range of particle energies and to compare results with predictions of a single level resonance theory.

EXPERIMENTAL APPARATUS AND PROCEDURE

In the deuteron energy range from 10.3 to 167 kev the Rice Institute Cockroft-Walton machine was used as the accelerator. The energy of the particles was determined by measuring the voltage of the set with a calibrated milliammeter and a calibrated high resistance column of 208.2 megohms. Resistor connections were protected from corona by eliminating sharp edges and by shielding with Lucite. At 180-kev set energy the measured peak to peak ac ripple was 6.5 kev or 3.6 percent, while at 100 kev the ripple was 1.6 kev or 1.6 percent.

The beam from the acceleration tube was deflected about 10° with an electromagnet in order to separate the different mass spots. Apertures of 5 mm diameter were used to define the beam entering and leaving the magnetic field. The ratios of the mass 2, 3, and 4 spots were approximately 1:2:15, respectively, other mass spots being extremely small. Under these conditions the mass 2 beam was about 10 percent to 30 percent molecular hydrogen as determined from the measured cross section using all three beams. Cross section measurements up to 110 kev could be made with the mass 3 beam.

Arrangement of the target chamber is shown in Fig. 1. Targets were mounted so that the resolved beam struck the target at an angle of 20° to the normal of the target surface. The target support extended through the target chamber wall and was insulated with Teflon so that beam current to the target could be measured. The charge striking the target was measured with a beam-current integrator of the type described by Watt.[4] Secondary electrons knocked out of the target were repelled back into it by a potential of −300 volt with respect to ground applied to the target chamber walls; the target itself operated at +40 to +80 volts from ground potential because of the beam integrator. The resulting field between the target chamber and the target was such as to draw to the target secondary electrons knocked out of the analyzing magnet exit aperture. By inserting another electrode (B) between the exit aperture and the target at a negative potential of 600 volts, secondary electron currents either to or from the target were stopped.

In traveling the 35 cm between analyzing magnet and target, some of the beam particles became uncharged and were not counted by the integrator. In order to take account of this effect a large magnetron magnet was placed near the exit aperture so that all charged particles in the beam were deflected away from the target. Disintegrations observed with this arrangement were due to uncharged particles striking the target. This procedure was always executed in every run from 10 kev to 100 kev. The magnitude of the neutral beam correction was 2 to 3 percent at 20 kev, and about 0.5 percent at 100 kev, while at the lowest energy of 10 kev the correction varied widely from 5 to 30 percent. The neutral beam depended on the vacuum in the system, being lower with lower pressure. Operating pressures were in the range of 1.0- to 2.0×10^{-5}-mm Hg.

A liquid air trap was placed near the target in the target chamber in order to reduce carbon formation on the targets. Since the trap would hold liquid air only about two hours, the targets were always removed overnight and at any other time the trap could not be kept cold continuously. No decreases in the yields were observed after 5000 microcoulombs hit the targets. Beam currents were limited to less than 1 μamp.

Alpha-particles from the reaction were counted in a

* Supported by the AEC. A preliminary report of the work has been given at the Denver meeting (June, 1952) of the American Physical Society.

† AEC Predoctoral Fellow.

[1] D. L. Allen and M. J. Poole, Proc. Roy. Soc. (London) **A204**, 488 (1950).

[2] E. Bretcher and A. P. French, Phys. Rev. **75**, 1154 (1949).

[3] Taschek, Hemmendinger, and Jarvis, Phys. Rev. **75**, 1464 (1949).

[4] B. E. Watt, Rev. Sci. Instr. **17**, 334, 338 (1946).

proportional counter at 90° with respect to the incident beam. The counting volume was separated from the vacuum system by a mica window of 1.5-mg/cm² thickness. The aperture defining the solid angle subtended by the counter was accurately one centimeter in diameter and was placed 7.66 cm from the center of the target, therefore subtending a solid angle of 0.0136 steradian. The counter was filled to a pressure of ¼ atmosphere with a gas mixture of argon plus 5 percent CO_2. With this mica window and filling, the alpha-particles just crossed the counter and hit the opposite wall. Pulses from the counter were fed through a cathode follower pre-amplifier to a linear amplifier and a scale of 64. The alpha-particle pulses from the amplifier were 50–60-volts high, and there were no smaller pulses greater than 10 volts. Data were obtained with a bias of 35 volts.

A background count was taken frequently during the runs by reducing the analyzing magnet current to zero, which removed the beam from the target but left all other parts of the set operating. The background counting rate was less than one count per minute, while counting rates of the order of a few thousand per minute were obtained from the reaction at all but the lowest energies.

The Rice Institute Van de Graaff accelerator was used to accelerate deuterons at the higher energy range of 134 to 1732 kev. The energy of the beam was measured with a 90° analyzing magnet, which was calibrated by the 873.5-kev resonance of the $F^{19}(p,\alpha\gamma)O^{16}$ reaction. From 134 to 496 kev, measurements were made with the molecular deuterium beam; from 481 to 1732 kev, the atomic beam was used.

For the molecular beam data, a "long neutron counter" about 4 cm away from the target and at 90° with respect to the beam counted neutrons from the reaction. The counting rate was normalized to the absolute Cockroft-Walton data in the overlapping energy range.

Above about 800 kev, appreciable background neutrons were observed from the $C^{12}(d,n)C^{13}$ reaction. In order to count only high energy neutrons from the $H^3(d,n)He^4$ reaction an anthracene crystal on a 5819 photomultiplier tube was used as the neutron counter for bombarding energies above 481 kev. The anthracene crystal, which was 1½ in. in diameter and 1½-in. long, was placed about 12 cm from the target at 90° to the beam. The neutron pulses cut off at about 75 volts bias at the output of the amplifier; the operating bias for taking data was 50 volts. Such a high bias was used in order to exclude counts from γ-radiation up to 5 Mev. A small correction for the variation of counter efficiency with neutron energy was required. The maximum calculated neutron energy variation at 90° was 500 kev or 3.5 percent. The cross section for neutron-proton collision was assumed constant, and only the increased number of recoil protons recorded above the 50-volt bias has been considered in computing the correction. The correction was 10 percent when the bombarding energy changed from 481 to 1732 kev.

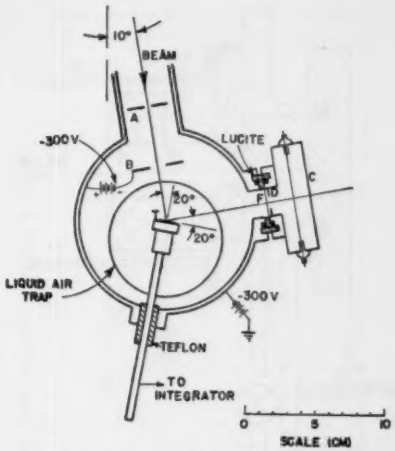

FIG. 1. Target and counter arrangement with the Cockroft-Walton. After being deflected 10° with the analyzing magnet, the beam passed through magnet exit aperture *A*, through the larger opening in secondary electron guard electrode *B* to the target *T*. The alpha-particles from the reaction passed through the mica window *F* into the counter *C*. The counter solid angle was defined by a brass knife-edge aperture *D*. The liquid air trap was placed about 4 cm from the target.

TARGETS

Targets of about 10 μg/cm² of zirconium were used at low energies; in such a layer a 50-kev deuteron loses 1 kev and so the energy of the deuteron is well defined throughout the thin layer. Targets were prepared in a manner similar to that described previously,[5] although certain changes in technique had to be made to get good very thin targets. Since zirconium films of predictable thickness were desired, only a small, definite amount of zirconium was placed on the evaporation filament and all the zirconium was evaporated with a fixed geometry. The mass of the zirconium deposit on the targets could in such a way be determined to about 20 percent without weighing each target. To prevent all of the small amount of zirconium from being used as a getter of gas in the evaporation system, another filament was used to evaporate a larger quantity of zirconium immediately before making the regular evaporation onto the targets.

In filling the zirconium layer with tritium, care was taken to keep the target temperature from becoming too high. According to Gulbransen and Andrew[6] a temperature of 300°C is sufficient to cause hydrogen to go into zirconium at a fast rate, and the hydrogen is actually driven out again in a vacuum if the tempera-

[5] A. B. Lillie and J. P. Conner, Rev. Sci. Instr. **22**, 210 (1951).
[6] E. A. Gulbransen and K. F. Andrew, J. Metals **1**, 515 (1949).

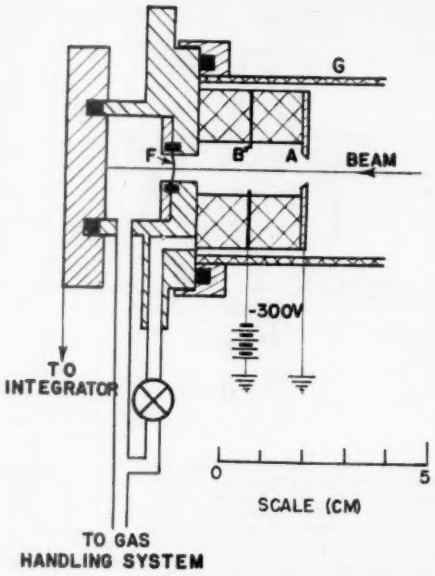

FIG. 2. Gas target arrangement for calibrating tritium targets with the Van de Graaff. The analyzed beam passed through collimator A, through the secondary electron guard electrode B, through the foil F into the gas target. Fluorescent ZnS was placed on the metal body around the foil to make sure none of the collimated beam was lost. Connections to A and B were made by colloidal graphite lines painted on the inside of the glass tube G. The back plate of the chamber could be removed for insertion of targets. Neutrons were detected by a "long neutron counter" placed 4 cm from the gas chamber at 0° to the beam.

ture rises above about 450°C. The temperature of the targets was always kept below that necessary for the targets to have any red color as viewed in a darkened room.

The uniformity of the targets was checked in three different ways. Kodak type 103a-0 spectroscopic plates were exposed to the activity of the tritium in the targets and the developed plates served as a good indicator of uniformity. Targets were also placed in an alpha-ray electroscope, and the activity of different parts of the targets were measured. Tests were also made by making the deuteron beam strike different parts of the target. No target was used which had sharp changes in activity along the surface.

To take account of possible absorption of tritium by backing materials during the filling process, measurements were made on the amount of tritium on the bare metal of the back side of the targets with the alpha-ray electroscope and with the Cockroft-Walton set. All tungsten backed targets had essentially zero tritium on the back side. Aluminum and beryllium backed targets had some tritium primarily as a thin adsorbed layer. An excitation curve taken on the back side indicated the thickness of the layer was less than 10 kev at a deuteron energy of 110 kev. The amount of tritium on the back side of one beryllium backed target was 1 percent of that in the zirconium layer, on the other 3 percent, and on the aluminum backed target 3 percent. Another good reason for filling the targets at a low temperature was that the amount of tritium adsorbed on the backing material was greatly decreased.

To determine the cross section, the number of atoms/cm² of tritium in the targets had to be measured. In order to have a low neutron background, a different nuclear reaction $H^3(p, n)He^3$ was used to produce neutrons from the tritium-zirconium targets and from a tritium gas target whose pressure, temperature, and purity could be measured. Protons were accelerated by the Van de Graaff to an energy of 1.4 Mev and entered the gas target chamber, shown in Fig. 2, through an aluminum foil 1.26-mg/cm² thick. The path length of the beam in the gas was 1.57 cm, the bulge of the foil being taken into account in computing the exact number of atoms/cm² of gas presented to the beam. Tritium-zirconium targets were mounted behind the foil and the chamber filled with ordinary hydrogen gas when taking a counting rate on the targets. The diameter of the beam used for calibration purposes was 5 mm. Neutrons from the reaction were counted by a "long neutron counter" about 5 cm from the target chamber and at 0° to the incident beam. With a fixed geometry the number of tritium atoms/cm² in a tritium-zirconium target was equal to the ratio of counting rates for gas and T-Zr targets times the number of atoms/cm² of gas.

The pressure of tritium gas in the target chamber was measured with a mercury manometer and a traveling microscope. Mercury was used rather than oil to prevent exchange of tritium and hydrogen. The measured values of the pressure were very consistent, having less than one percent spread in the values obtained by reading the manometer several times. Counting rates were always taken at two different pressures. The actual background was measured by putting a blank of the backing material into the target chamber and bombarding with protons. The background was negligible for the tungsten backed targets, 2 percent for the aluminum backed targets, and was 42 percent for one beryllium backed target. This high background is believed to be due to the neutrons from beryllium plus alpha-particles, where the alpha-particles are due to the $Be^9(p, \alpha)Li^6$ reaction. Four sets of calibrations were made, the first being made with tritium gas whose purity was measured afterward and found to be 49-percent tritium. The last three measurements were made with gas which was 99-percent tritium at the start and 88-percent tritium after the last calibration as determined by a Nier-type mass spectrometer. The tritium concentration was assumed to change linearly with use.

In making the target calibration the beam struck the targets normally to the surface; in the Cockroft-Walton set the targets were tilted so that the beam struck at an

angle of 20° with respect to the normal. The effect of the tilt is to increase the target thickness presented to the beam by 6.0 percent.

From the mass/cm² of zirconium on the targets, the thickness in kev of the tritium-zirconium layer has been calculated from results of Warshaw.[7] One-half the thickness has been subtracted from the observed incident deuteron energy to get the average energy of the beam in the target. This correction amounts to only 0.2 kev at 10 kev-deuteron energy, and so a small error in the energy loss is relatively unimportant.

At very low energy some appreciable scattering of the deuterons may take place in the tritium-zirconium layer. A scattered deuteron would travel through a greater thickness of tritium and would lead to too high a value for the measured cross section.

The mean square net scattering angle for multiple scattering was calculated[8] taking into account the fact that the target was tilted at 20° to the normal. This correction amounts to an increase of path length in the target of 2.0 percent at 10 kev and 0.9 percent at 15 kev.

A possible objection to using the tritium-zirconium targets is that some of the incident deuterons might be scattered more than 90° in the backing material, pass through the tritium layer twice, and, if they emerge still charged, not be counted by the current integrator. Both effects would increase the experimentally determined value of the cross section. At the lowest energies, where the backscattering effect would be important, the stopping powers of all atoms are roughly equal. The backscattering effect should then depend on the Z of the scattering material in the same way as Rutherford scattering cross section does, that is, as Z^2. In order to measure experimentally what the backscattering might be, the tritium-zirconium films were prepared on tungsten, aluminum, and beryllium backings polished to a good mirror surface. The plot in Fig. 3 of data obtained from the three kinds of targets indicates the results. A tungsten backing is seen to give about 40 percent larger cross section at 15-kev energy than a target with a beryllium backing. If the backscattering goes as Z^2 then aluminum should give about 1.3 percent effect and beryllium 0.1 percent. The experimental data show no appreciable difference between beryllium and aluminum backings, a result which is consistent with backscattering which varies as Z^2.

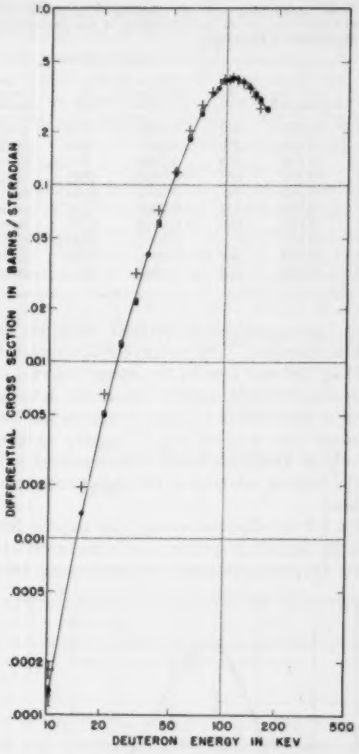

FIG. 3. Effects of target backing on measurements of the $H^3(d,n)He^4$ cross section. Crosses indicate tungsten backed Zr-T targets, open circles aluminum backed targets, and solid circles, beryllium backed targets.

TABLE I. The differential cross section (σ) at 90° *versus* the bombarding deuteron energy at the center of the target (E). Where measurements were made with more than one target at a particular energy, the average value is given, and the targets involved are indicated.

E kev	σ barns per steradian	Targets Al	Be−1	Be−2	E kev	σ barns per steradian	Targets Al	Be−1	Be−2
10.3	0.00013	×	×	×	72.8	0.260	×	×	×
15.4	0.00135	×	×	×	76.2	0.279		×	×
20.7	0.00491	×	×	×	78.0	0.284			×
25.8	0.0125	×		×	83.3	0.330	×	×	×
31.0	0.0233	×	×	×	90.3	0.351			×
34.5	0.0348			×	93.7	0.384	×		
36.3	0.0401	×		×	97.1	0.391		×	×
41.5	0.0593	×	×	×	104	0.404	×	×	×
46.7	0.0845			×	109	0.406	×	×	×
48.5	0.0939			×	111	0.405		×	×
52.0	0.118	×	×	×	115	0.401	×	×	×
55.4	0.141		×	×	125	0.385	×	×	×
57.1	0.141		×	×	136	0.360	×		×
62.3	0.183	×	×	×	146	0.329	×	×	×
67.5	0.224			×	156	0.300	×		×
69.3	0.238		×	×	167	0.272	×	×	×

RESULTS

The variation with energy of the differential cross section at 90° is given in Table I and Table II. Results in Table I were obtained with the Cockroft-Walton and represent data from one aluminum backed target and two beryllium backed targets. The targets were 10-μg/cm² thick. The statistical probable error of the values from each target was about 1 percent except for the points at 10.3 and 15.4 kev. Table II gives the

[7] S. D. Warshaw, Phys. Rev. **76**, 1759 (1949).
[8] E. Fermi, *Nuclear Physics* (University of Chicago Press Chicago, Illinois, 1950), p. 37.

TABLE II. Cross section data at higher energies. The differential cross section (σ) at 90° as a function of the deuteron energy (E) at the center of the target.

E kev	σ barns per steradian	E kev	σ barns per steradian	E kev	σ barns per steradian
134	0.363	302	0.0989	774	0.0230
143	0.339	329	0.0875	864	0.0200
153	0.309	357	0.0766	957	0.0183
162	0.276	402	0.0655	1055	0.0166
173	0.260	448	0.0547	1156	0.0143
183	0.245	481	0.0506	1263	0.0125
205	0.198	496	0.0488	1374	0.0117
227	0.167	533	0.0434	1489	0.0111
251	0.142	607	0.0349	1608	0.0099
276	0.118	689	0.0278	1732	0.0090

data at higher energies as obtained with the Van de Graaff accelerator. A zirconium-tritium target which was 40 μg/cm^2 was used in the energy interval 134 to 496 kev and a thicker target of 200 μg/cm^2 in the higher interval of 481–1732 kev. These zirconium targets were evaporated onto a silver and a tungsten backing, respectively, so that there would be no neutrons or γ-rays from the backing material at the higher energies which were used.

Below 130-kev deuteron energy, the angular distribution of the reaction is symmetrical in the center-of-mass system.[1] Therefore, the total cross section may be determined from measurements at 90°. Several targets have been used to determine the total cross section at 109-kev deuteron energy. The average value is 5.1 barns; the individual values obtained for the different targets are given in Table III. Probable errors in the solid angle, the number of atoms/cm^2 in the target, and the number of incident deuterons are estimated to be about 1 percent each. The probable error in the number of counts is less than $\frac{1}{2}$ percent. Thus, the over-all probable error is about 2 percent or 0.1 barn.

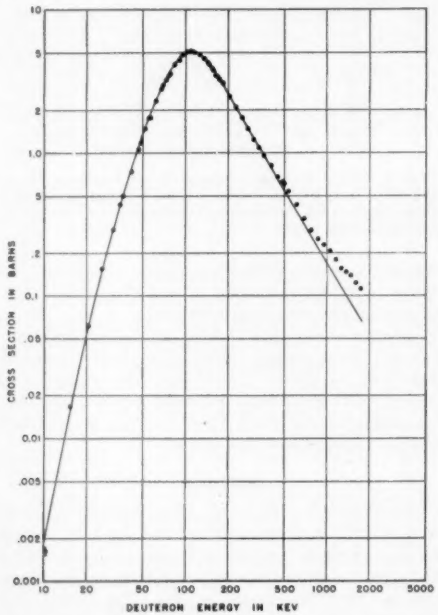

FIG. 4. Theoretical fit to the H^3(d, n)He^4 data. The solid line is the calculated curve, while the circles are the experimental points.

An attempt has been made to fit the experimental data with a single level, Breit-Wigner, formula. It has been found that the fit obtained is very much improved by using the more exact formula[9]

$$\sigma=\frac{2J+1}{(2s+1)(2i+1)}\frac{\pi}{k^2}\frac{\Gamma_d\Gamma_n}{(E_\lambda+\Delta_\lambda-E)^2+\frac{1}{4}(\Gamma_d+\Gamma_n)^2}$$

where J is the angular momentum of the compound nucleus, s and i are the spins of the incident particle and initial nucleus, respectively, k is the wave number of relative motion, Γ_d and Γ_n are deuteron and neutron

TABLE III. Values of the total cross section obtained with different targets at 109 kev deuteron energy.

Target backing	T–Zr thickness μg/cm^2	Total cross section, barns
Al	30	5.20
Al	10	4.96
Al	10	5.00
Al	10	5.10
Al	10	5.13
Al	10	4.99
Be	10	5.29
	Average	5.10±0.03

widths, respectively, E_λ is a constant, Δ_λ is the level shift, and E is the center-of-mass energy. The width Γ equals $2kP\gamma^2$, where P is the penetrability and γ^2 is the reduced width of the particle. The level shift Δ_λ is given by Thomas[10] to be $\gamma_d^2 g/a$, where a is the radius of the interaction and g is a function of the Coulomb wave functions. The penetrability of the deuteron and the values of g have been computed from tables of the Coulomb wave functions.[11]

The maximum possible value of the resonance term is unity and occurs if $(E_\lambda+\Delta_\lambda-E)=0$ and $\Gamma_d=\Gamma_n$. A value of $\frac{3}{2}$ for J, the angular momentum of the intermediate excited He^5 nucleus, is required to obtain a sufficiently large value for the cross section from the formula. Deuterons with $l=0$ are assumed because of the low bombarding energies. Conservation of total angular momentum and parity then requires that the intermediate He^5 nucleus have even parity and that the neutrons given off have $l=2$.

The calculated fit together with the experimental

[9] E. P. Wigner and L. Eisenbud, Phys. Rev. **72**, 29 (1947).
[10] R. G. Thomas, Phys. Rev. **81**, 148 (1951).
[11] Bloch, Hull, Broyles, Bouricius, Freeman, and Breit, Revs. Modern Phys. **23**, 147 (1951).

data are presented in Fig. 4. The parameters are $a=5.0\times10^{-13}$ cm, $E_\lambda=-464$ kev, $\gamma_d^2=10^{-9}$ kev cm, and $\gamma_n^2=2.8\times10^{-11}$ kev cm. The quality of the fit is not sensitive to the value of a which is used if the other parameters are suitably changed. Total cross-section values were obtained from the measured differential cross section by assuming a symmetrical angular distribution in the center-of-mass system. At the higher energies, where the calculated curve falls below the experimental points, the angular distribution is probably not exactly symmetrical. Deviations from a one level formula might be expected at the highest energies because of higher levels in He^5, the compound nucleus. Also at higher energies the stripping process[12] must account for some of the effects since the results of Allred[13] and others at 10 Mev can be almost entirely explained by stripping.

An alternative explanation of the cross-section curve for the $H^3(d,n)He^4$ reaction is that proposed by Flowers.[14] His theory does not make use of an isolated state of the compound nucleus. An experimental study of the inverse process, the scattering of high energy neutrons in He^4, would serve as a means of testing the application of the two theories to this reaction. If an isolated compound state of $^*He^5$ is important in the $H^3(d,n)He^4$ reaction, an anomaly in the scattering cross section of 20–21 Mev neutrons would be expected.

[12] S. T. Butler, Proc. Roy. Soc. (London) **A208**, 599 (1951); S. T. Butler and J. L. Symonds, Phys. Rev. **83**, 858 (1951).

[13] J. C. Allred, Phys. Rev. **84**, 695 (1951); Brolley, Fowler, and Stovall, Phys. Rev. **82**, 502 (1951).

[14] B. H. Flowers, Proc. Roy. Soc. (London) **A204**, 503 (1950).

PHYSICAL REVIEW VOLUME 88, NUMBER 3 NOVEMBER 1, 1952

Cross Section and Angular Distribution of the $He^3(d,p)He^4$ Nuclear Reaction*

T. W. Bonner, J. P. Conner,† and A. B. Lillie
Rice Institute, Houston, Texas

(Received July 7, 1952)

The cross section for the reaction $He^3(d,p)He^4$ has been studied for deuteron energies from 188 kev to 1597 kev. The yield of protons at 0° to the deuteron beam exhibits a maximum at 400-kev deuteron energy. At this energy the angular distribution of the disintegration particles is spherically symmetrical and the total cross section is 0.69×10^{-24} cm². At higher energies there is a preferential emission of protons at 0°. At 1600 kev the ratio of the number of protons at 0° to that at 90° is 1.08. The variation of total cross section with bombarding energy agrees with a calculated single level resonance formula from 188 kev to 600 kev. At higher energies the theoretical values give too small a cross section.

INTRODUCTION

THE reaction $He^3(d,p)He^4$ is quite similar to the reaction[1] $H^3(d,n)He^4$ which has a very large cross section at low deuteron energies. Consequently a large cross section at a low bombarding energy might be expected for this reaction. The double nuclear charge on the He^3 nucleus, however, would decrease the penetrability of the deuterons into this nucleus as compared to a H^3 nucleus. Previous experiments[2] on this reaction which were carried out by slowing down He^3 particles from a cyclotron and sending these into deuterium gas, indicate a large cross section at low bombarding energies. The purpose of the present experiments was to study this reaction with deuterons of a well-defined energy from a Van de Graaff accelerator.

EXPERIMENTAL APPARATUS AND PROCEDURE

Deuterons were accelerated by the Rice Van de Graaff accelerator and passed through a 90° analyzing magnet before reaching the He^3 gas target holder. A diagram of the gas target holder is shown in Fig. 1. The beam of deuterons was collimated by aperture A

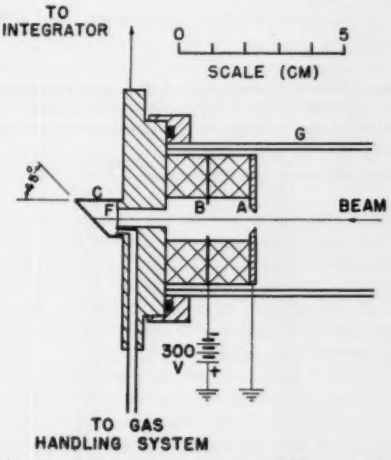

FIG. 1. The gas target holder showing the collimating aperture A, the electron repelling electrode B, the thin aluminum foil F, and the gas chamber C.

* Supported by the AEC. A preliminary report of this work was given at the New York Meeting (January, 1952) of the American Physical Society.

† AEC Predoctoral Fellow.

[1] Conner, Bonner, and Smith, Phys. Rev. **88**, 468 (1952).

[2] Baker, Holloway, King, and Schreiber, Atomic Energy Commission Declassified Report. AECD 2189 (1948) (unpublished).

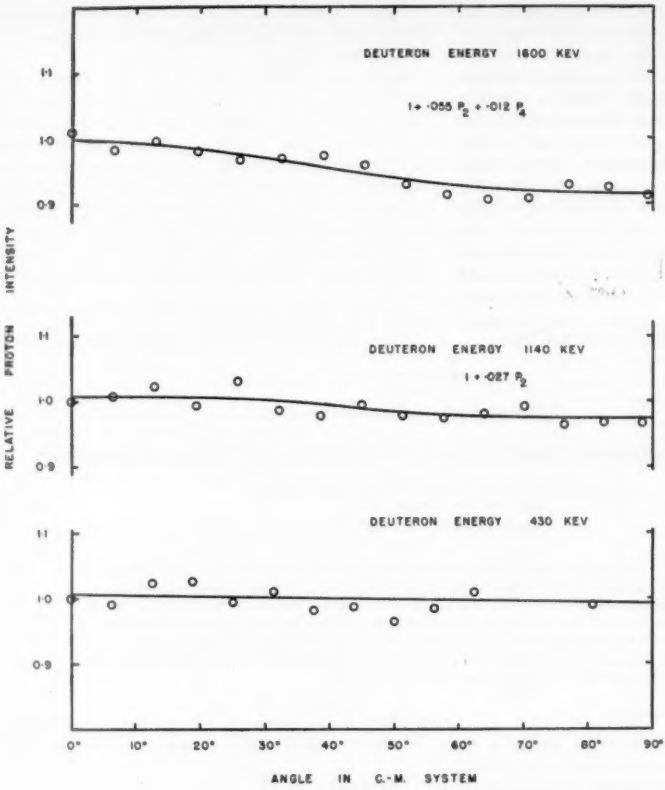

FIG. 2. The angular distribution of the disintegration protons at deuteron energies of 430, 1140, and 1600 kev. The relative intensities at each energy are the counting rates per equal solid angle in the center of mass system. The solid curves are theoretical fits in terms of Legendre polynomials.

TABLE I. Differential cross section at 0°, σ, *versus* the bombarding deuteron energy, E, for the $He^3(d, p)He^4$ reaction.

E kev	σ millibarns/steradian
188	16.6
247	28.8
307	44.4
363	53.6
420	54.4
478	50.8
536	44.4
593	37.6
648	33.4
712	30.4
769	27.7
828	24.4
883	21.8
972	19.2
1102	15.5
1229	14.3
1355	13.4
1487	11.8
1597	10.8

before striking a thin aluminum foil at F. This foil was 1.26 mg/cm² in thickness. After passing through the foil the beam entered a gas chamber which was made of thin aluminum. In the first experiments on cross-section measurements, the gas chamber was cylindrical and 0.973 cm long; in experiments on angular distributions the gas chamber had a diagonal end as indicated in Fig. 1. The energy loss of the deuteron beam in the aluminum foil was calculated from the results of Warshaw[3] and also measured directly at emerging deuteron energies of 313, 370, and 423 kev. The measured losses agreed with the calculated losses within 5 percent. The energy losses at different bombarding energies that were subsequently used were the calculated ones after they were normalized to the experimental values at 400 kev. The gas pressure of He^3 that was used was in the range 0.8–1.0 cm of Hg; this pressure was measured with a mercury manometer.

In the first experiments on cross-section measure-

[3] S. D. Warshaw, Phys. Rev. 76, 1759 (1949).

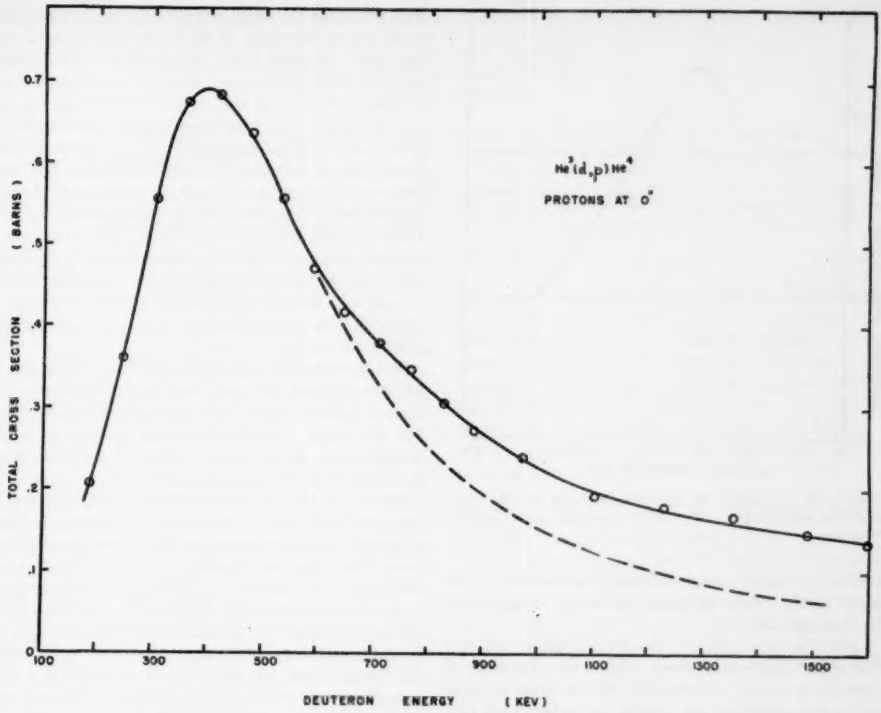

FIG. 3. Experimental values of the total cross section (solid curve) compared to the theoretical curve (dashed), computed with a nuclear interaction distance $a=7.6\times10^{-13}$ cm.

ments, a long proportional counter filled with argon at atmospheric pressure was used to detect protons from the reaction at 0° to the incident beam. The counter aperture of 0.632 cm was placed 5.5 cm from the center of the target and thus subtended a solid angle of 0.0104 steradian. In the experiments to determine the angular distributions, a thin anthracene crystal cemented to a 5819 photomultiplier tube was used as a proton detector. The angular resolution was 4° and points were taken at 6° intervals.

The statistical probable errors of the points were about 1 percent near 400 kev and less than 2 percent elsewhere; the estimated probable errors of the current integrator and number of He^3 atoms were 1 percent each; the solid angle contributed a probable error of 3 percent. Background counts with each type of counter were negligible.

RESULTS

Cross-section data as given in Table I are differential cross sections at 0° to the deuteron beam, after making center-of-mass corrections for the varying solid angle.

The experimental data for the angular distributions at 430-, 1140- and 1600-kev deuteron energy are shown in Fig. 2. The relative proton intensities at different angles (center-of-mass system) are given. At the lowest energy the distribution is symmetrical from 0° to 90° within the experimental accuracy of about 2 percent. At the higher energies there are more protons at 0° than at 90°. The ratio of protons at 0° to that at 90° amounts to about 1.04 at 1140-kev deuteron energy and 1.08 at 1600-kev.

Since the angular distribution is spherically symmetrical at low energies, the total cross section for the reaction can be calculated. This maximum cross section is 0.69 barn at 400-kev deuteron energy. Figure 3 shows the calculated total cross sections for the reaction as a function of the bombarding deuteron energy. The total cross sections were calculated assuming a spherical distribution in center-of-mass coordinates. At the higher energies the total cross section will be in error because the distribution is not exactly spherical. Exact values could not be calculated since our angular distributions did not go to angles greater than 90°. The cross sections below 300 kev are not as accurate

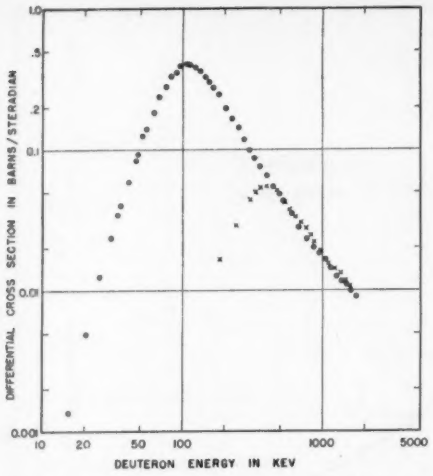

FIG. 4. A comparison of the cross sections for the reactions $H^3(d, n)He^4$ (open circles), and the reaction $He^3(d, p)He^4$ (crosses).

as those at higher energies because of a spread in the energy of the deuteron beam caused by straggling in the aluminum foil.

Figure 4 is a plot of the $He^3(d, p)He^4$ and the $H^3(d, n)He^4$ differential cross section as a function of bombarding energy. Above 500 kev the cross sections for the two reactions are nearly the same. This fact suggests that corresponding states of intermediate nuclei $^*Li^5$ and $^*He^5$ are involved. Since the spin of the intermediate $^*He^5$ nucleus,[1] formed in the reaction $H^3(d, n)He^4$, appears to be $\frac{3}{2}$, a value of $J=\frac{3}{2}$ is assigned to the intermediate $^*Li^5$. The $^*Li^5$ also would be expected to have even parity as does the $^*He^5$. Further, one might expect that the nuclear parameters which are used in the resonance equation for the two reactions to be nearly the same. A fit to the experimental data has been obtained using the modified Breit-Wigner relation[4] using a radius of interaction $a=5.0\times10^{-13}$ cm, a value of $E_\lambda=+175$ kev, $\gamma_d^2=0.7\times10^{-10}$ kev cm, and $\gamma_p^2=2.6\times10^{-11}$ kev cm. These nuclear parameters are of the same order of magnitude but somewhat different from those used in the $H^3(d, n)He^4$ reaction. The value of γ_d^2 is a factor of 14 larger and the value of γ_n^2 is approximately the same as the corresponding γ_p^2. The value of E_λ is larger for the $He^3(d, p)He^4$ reaction as would be expected for these mirror nuclei. A somewhat better fit to the experimental curve was obtained with the slightly different parameters $a=7.6\times10^{-13}$ cm, $E_\lambda=+195$ kev, $\gamma_d^2=5.0\times10^{-10}$ kev cm, and $\gamma_p^2=9.7\times10^{-12}$ kev cm.

Both theoretical curves fit the data within the experimental errors below 600 kev, but both give too small a cross section at the higher energies. Possible reasons for the larger experimental cross sections at higher energies are (1) deuterons with $l=2$ may contribute a considerable amount to the cross section at the higher energies, (2) the "stripping reaction" may account for an appreciable fraction of the cross section at the higher energies. Stripping seems to be the predominant process at 10 Mev,[5] and the results at 3.17 Mev[6] indicate that stripping is beginning to be important at this energy.

As in the case of the $H^3(d, n)He^4$ reaction,[1] an alternative explanation of the cross section curve for the reaction $He^3(d, p)He^4$ is that proposed by Flowers.[7] His theory does not make use of an isolated state of the compound nucleus. If an isolated compound state of $^*Li^5$ is important in this reaction, an anomaly in the large angle scattering cross section of 21–22 Mev protons in He^4 would be expected.

[4] E. P. Wigner and L. Eisenbud, Phys. Rev. **72**, 29 (1947); R. G. Thomas, Phys. Rev. **81**, 148 (1951).
[5] J. C. Allred, Phys. Rev. **84**, 695 (1951); S. T. Butler and J. L. Symonds, Phys. Rev. **83**, 858 (1951).
[6] Wyley, Sailor, and Ott, Phys. Rev. **76**, 1532 (1949).
[7] B. H. Flowers, Proc. Roy. Soc. (London) **A204**, 503 (1950).

The Piezoelectric, Dielectric, and Elastic Properties of $ND_4D_2PO_4$ (Deuterated ADP)

W. P. Mason and B. T. Matthias
Bell Telephone Laboratories, Murray Hill, New Jersey
(Received July 23, 1952)

Measurements of the dielectric constants, piezoelectric constants, and elastic constants have been made for the crystal $ND_4D_2PO_4$ (heavy water ADP). This crystallizes in the same form as normal ammonium dihydrogen phosphate (ADP) but has a transition at $-31°C$ which is 94° higher than that for normal ADP. From the form of the crystal below the transition temperature, it is inferred that the transition is an antiferroelectric one with one of the "a" crystallographic axes as the antiferroelectric axis. The crystal has a zero temperature coefficient of frequency at 0°C, and it may be of use in transducers and mechanical filters.

I. INTRODUCTION

WHEN ammonium dihydrogen phosphate (ADP) is cooled down to $-125°C$ (148°K), a transition occurs which produces a large enough change in volume to shatter the crystal. Dielectric and piezoelectric measurements[1,2] show that the transition is not a ferroelectric transition. On the other hand, the specific heat anomaly[3] is large enough to indicate an order disorder transition. It was generally believed[1,2] that this transition was due to an interaction of the NH_4^+ ions due to their deviation from a spherical symmetrical configuration. However, the specific heat anomaly occurring at this transition is much larger than those observed in other ammonia transitions.

Recently,[4] however, all the hydrogens in the crystal have been replaced by deuterium making the crystal $ND_4D_2PO_4$. The crystal had the same tetragonal structure as ADP, but the transition temperature was shifted from 148°K to 242°K ($-31°C$) an increase of 94°C. This result shows that the transition cannot be an ammonia transition like NH_4Cl, for instance, which changes the transition temperature by only a few degrees, when the hydrogens are replaced by deuterium. From the specific heat data[3] the transition is believed to be an order-disorder transition in the X_2PO_4 (X=H or D) groups, and from the change in crystal structure discussed below it is believed that the crystal goes into an antiferroelectric state below the transition temperature.

In the ferroelectric crystal potassium dihydrogen phosphate (KDP), the crystal changes from tetragonal to orthorhombic form on lowering the temperature through the transition temperature, with the new a and b axes at 45° from the high temperature a axes. This shift of the crystal axes is caused by the piezoelectric strain produced by the spontaneous polarization. For $ND_4D_2PO_4$, as shown by the x-ray and optical work of Dr. E. A. Wood, the structure is orthorhombic below the transition temperature, with the low temperature a and b axes coinciding with the high temperature a axes. The most sensitive test is an optical one, which shows that the crystal has become biaxial in a (100) plane with the two optic axes $\pm 9°$ from the Z axis.[5] It appears that the crystal structure change accompanying the transition in $NH_4H_2PO_4$ and $ND_4D_2PO_4$ is caused by a quadratic distortion proportional to squares and even powers of the spontaneous polarization, and hence the structure is antiferroelectric.

A phenomenological development of this effect is given in a companion paper which makes it appear probable that the antiferroelectric axis lies along one of the a (x or y) crystallographic axes. This agrees also with the x-ray data and makes it appear probable[5] that, below the transition temperature, the hydrogen nuclei take the form of the pattern shown by Fig. 1, which is an antiferroelectric arrangement with the antiferroelectric axis along one of the original a crystallographic axes.

Dielectric, piezoelectric, and elastic measurements have been made over temperature ranges down to the transition temperature. Without protection, the crystal fractured below the transition temperature due to the large volume distortion effects, and no measurements

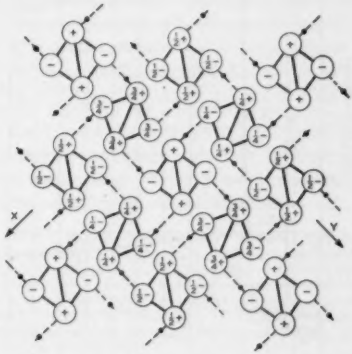

FIG. 1. Arrangement of hydrogen nuclei to produce an antiferroelectric condition.

[1] W. P. Mason, Phys. Rev. **69**, 173 (1946).
[2] Baertschi, Matthias, Merz, and Scherrer, Helv. Phys. Acta **18**, 238 (1945).
[3] C. C. Stephenson and A. C. Zettlemoyer, J. Am. Chem. Soc. **66**, 1405 (1944).
[4] B. T. Matthias, Phys. Rev. **85**, 140 (1952).
[5] Wood, Merz, and Matthias, Phys. Rev. **87**, 544 (1952).

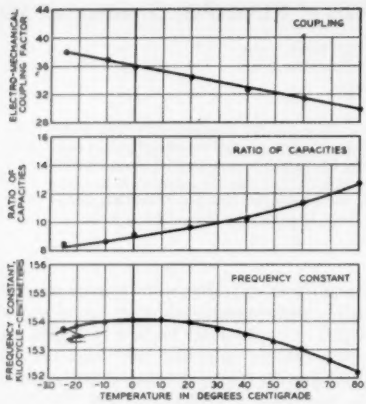

FIG. 2. Properties of a 45°*Z* cut crystal.

could be made of the elastic and piezoelectric constants below the transition temperature. Above the transition temperature, the elastic constants have a very small variation with temperature, and Fig. 2 shows the frequency temperature variation, the ratio of capacities, and the electromechanical coupling factor for one of the principal cuts—the 45° *Z* cut, which has been used considerably in underwater sound equipment. The temperature coefficient of frequency is quite low, and the piezoelectric and dielectric constants are about 50 percent larger than for normal ADP. Hence, it appears that such crystals may have practical applications in electromechanical transducers and in mechanical wave filters. The extra cost of the deuterium can be minimized by saving all cuttings and returning them to the growing bath. The difficulty of cracking at the transition temperature can be overcome by introducing a small amount of thallium[2] or rubidium, both of which have been found to prevent cracking in normal ADP.

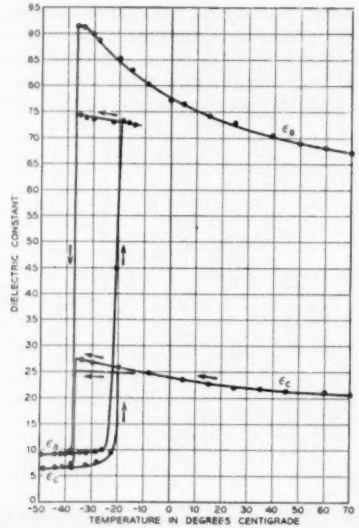

FIG. 3. Dielectric constants along *a* and *c* axes showing drop at transition temperature.

II. MEASUREMENTS OF THE ELASTIC, PIEZOELECTRIC, AND DIELECTRIC CONSTANTS OF $ND_4D_2PO_4$

All of the elastic, dielectric, and piezoelectric constants of ADP and $ND_4D_2PO_4$ can be determined from seven oriented cuts by measuring the dielectric constants, the resonant and antiresonant frequencies. Since this process has been described[1] in connection with measurements for normal ADP, only the measured results will be presented. The cuts were obtained from a small sized crystal grown from a saturated solution by continuously dropping the temperature.

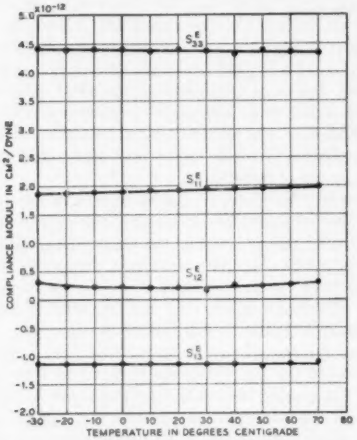

FIG. 4. Elastic compliances s_{11}, s_{33}, s_{12}, and s_{13} as a function of temperature.

Figure 3 shows a measurement of the dielectric constant along the *a* and *c* (*x* and *z*) axes for a crystal covered with a coat of plastic cement. Above the transition point the dielectric constant along both axes increases as the temperature is decreased down to a definite temperature below which the dielectric constant suddenly drops to a low value. With a plastic coating this temperature is about −37°C, whereas for a free crystal it is about −32°C. The value along the *a* axis becomes about 9.0, while along the *c* axis it is about

6.5. On raising the temperature the dielectric constant suddenly increases to nearly its high temperature value at about −20°C. Without coating this temperature is −26°C. This transition can be made to occur repeatedly by temperature cycling.

As shown in the companion paper, there should be three independent dielectric constants below the transition temperature. Since one does not know which *a* axis will become antiferroelectric, two pieces were first tried, one an *x* cut and the other a *y* cut. On taking them below the transition temperature, they had identical dielectric constants. It appears that the mechanical bias put on by the holder determines the direction of the antiferroelectric axis. Next a square piece with two sets of electrodes along the *x* and *y* axes was measured, and it appeared that below the transition temperature one had about 25 percent larger dielectric constant than the other. However, the capacity for this arrangement dropped to such a low value that the measurements were not very reliable.

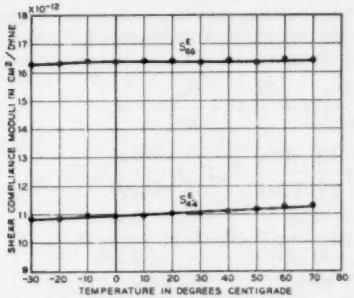

FIG. 5. Shear elastic compliances s_{44} and s_{66} as a function of temperature.

The six elastic compliance moduli are shown by Figs. 4 and 5. Comparing these with similar values for normal ADP,[1] we see that the values are not much changed but the temperature coefficients are much improved. For the two principal cuts, the 45° *Z* cut and 0° *Z* cut shear mode, zero temperature coefficients of frequency are found.

The two piezoelectric constants are shown by Fig. 6. The principal constant is the d_{36} piezoelectric constant, and this is increased 50 percent over that for normal ADP. Hence, it requires only two-thirds the voltage gradient applied to give a determined piezoelectric displacement, and for a given power output from a transducer there is less chance for a voltage breakdown. The other constant d_{14} is about 5 times as large in $ND_4D_2PO_4$ as in normal ADP but is still not large enough to be very useful.

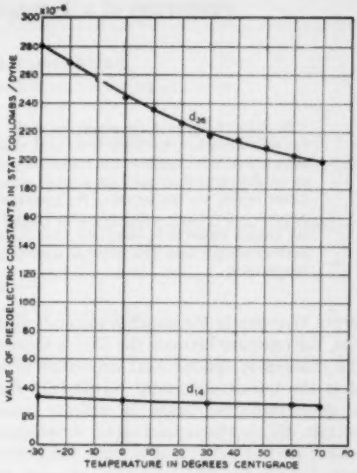

FIG. 6. Piezoelectric constants d_{14} and d_{36} above the transition temperature.

III. DISCUSSION OF RESULTS

Ammonium dihydrogen phosphate and the modification with deuterium $ND_4D_2PO_4$ are interesting technically, due to the large piezoelectric constant and the high electromechanical coupling factor together with freedom from dehydration effects and relatively good mechanical properties. The deuterium modification should be capable of producing more power for the same breakdown voltage gradient. The added frequency-temperature stability may be useful in such devices as mechanical filters which have to remain frequency-stable over a wide temperature range.

On the theoretical side, these crystals are of interest owing to their antiferroelectric properties. The discontinuity[2] in the specific heat is large enough to indicate an order disorder transition which is associated with the ordering of the positions of the hydrogen or deuterium nuclei in an antiferroelectric arrangement below the transition temperature. This interpretation is confirmed by the change in the unit cell from tetragonal to orthorhombic with the low temperature axes coinciding with the high temperature axes.

Note added in proof:—Since this paper originally went to press, a private communication has been received from Professor R. Pepinsky stating that he has a typewritten copy of a paper by Takeo Nagamiya of Osaka University, Japan, entitled "On the Theory of the Phase Transition and the Dielectric, Piezoelectric, and Elastic Behavior of $NH_4H_2PO_4$, I," in which this theory of antiferroelectric behavior is stated, with figures drawn, illustrating the proposed structure.

Properties of a Tetragonal Antiferroelectric Crystal

W. P. Mason
Bell Telephone Laboratories, Murray Hill, New Jersey
(Received July 23, 1952)

In order to interpret the properties of the tetragonal crystal $ND_4D_2PO_4$ (deuterated ADP) a thermodynamic treatment has been developed which relates the observed crystal structure change and the dielectric constant change at the transition temperature to the appearance of spontaneous polarization. For an antiferroelectric crystal, the average spontaneous polarization is zero, being oppositely directed for adjacent layers, but the square of the spontaneous polarization is large. This results in quadratic strain components which cause a change in the crystal structure below the transition temperature. It is shown that the change observed is consistent with an antiferroelectric arrangement with one of the a axes being the antiferroelectric axis. The dielectric constants in all three directions suffer a large drop below the transition temperature.

IN order to evaluate the possible mechanical distortions, the relations between the dielectric constants and the changes in specific heat capacities to be expected in the tetragonal crystal $ND_4D_2PO_4$[1] that becomes antiferroelectric below a definite transition temperature Θ_0, a phenomenological development of the strains, electric fields, and entropy has been made in terms of the independent variables stresses, electric displacements, and temperature Θ. Since as the temperature decreases through the transition temperature Θ_0, the measured changes are strains, remanent polarizations, and entropy changes, this type of formulation is the most useful one for discussing the transition. This requires the use of one of the Gibb's potentials G_1, given in terms of the internal energy function U, by

$$G_1=U-S_{ij}T_{ij}-\sigma\Theta, \tag{1}$$

where S_{ij} are the strains expressed in tensor form, T_{ij} the stresses, σ the entropy, and Θ the temperature. In rationalized mks units the differential form is

$$dG_1=-S_{ij}dT_{ij}+E_m dD_m-\sigma d\Theta, \tag{2}$$

TABLE I. First-order derivatives of the potential G_1 and their physical significance.

Derivative	Relationship between derivatives	Symbol	Name
$\frac{\partial S_{ij}}{\partial T_{kl}}$		$s_{ijkl}^{D,\Theta}$	Elastic compliances at constant displacement and temperature
$\frac{\partial S_{ij}}{\partial D_n}$	$=\frac{-\partial^2 G_1}{\partial T_{ij}\partial D_n}=\frac{-\partial E_m}{\partial T_{ij}}$	g_{ijn}	Piezoelectric constants
$\frac{\partial S_{ij}}{\partial \Theta}$	$=\frac{-\partial^2 G_1}{\partial T_{ij}\partial \Theta}=\frac{\partial \sigma}{\partial T_{ij}}$	α_{ij}	Temperature expansion coefficients
$\frac{\partial E_m}{\partial D_n}$		β_{mn}	Dielectric impermeability coefficients
$\frac{\partial E_m}{\partial \Theta}$	$=\frac{\partial G_1}{\partial D_m\partial \Theta}=-\frac{\partial \sigma}{\partial D_m}$	q_m	Pyroelectric constants
$\frac{\partial \sigma}{\partial \Theta}$		$\frac{\rho C^{T,D}}{\Theta}$	Density times specific heat per unit mass at constant stress and electric displacement divided by the absolute temperature Θ

[1] The data for $ND_4D_2PO_4$ are given by W. P. Mason and B. T. Matthias, preceding paper [Phys. Rev. 88, 477 (1952)].

and hence,

$$S_{ij}=-\partial G_1/\partial T_{ij};\quad E_m=\partial G_1/\partial D_m;\quad \sigma=-\partial G_1/\partial\Theta, \tag{3}$$

where E_m and D_m are, respectively, the electric fields and the electric displacement components.

Developing the strains, electric fields, and entropy in a Maclaurin series about the points of zero stresses, zero displacements, and temperature Θ_0, we have up to second derivatives of the stresses and temperatures, but higher derivatives of the electric displacements:

$$\begin{aligned}S_{ij}=&\frac{\partial S_{ij}}{\partial T_{kl}}T_{kl}+\frac{\partial S_{ij}}{\partial D_n}D_n+\frac{\partial S_{ij}}{\partial\Theta}(\Theta-\Theta_0)\\&+\frac{1}{2!}\Big[\frac{\partial^2 S_{ij}}{\partial T_{kl}\partial T_{qr}}T_{kl}T_{qr}+\frac{2\partial^2 S_{ij}}{\partial T_{kl}\partial D_n}T_{kl}D_n\\&+2\frac{\partial^2 S_{ij}}{\partial T_{kl}\partial\Theta}T_{kl}(\Theta-\Theta_0)+\frac{\partial^2 S_{ij}}{\partial D_n\partial D_o}D_nD_o\\&+\frac{2\partial^2 S_{ij}}{\partial D_n\partial\Theta}D_n(\Theta-\Theta_0)+\frac{\partial^2 S_{ij}}{\partial\Theta^2}(\Theta-\Theta_0)^2\Big]\\&+\frac{1}{3!}\frac{\partial^3 S_{ij}}{\partial D_n\partial D_o\partial D_p}D_nD_oD_p+\cdots,\end{aligned} \tag{4}$$

$$\begin{aligned}E_m=&\frac{\partial E_m}{\partial T_{kl}}T_{kl}+\frac{\partial E_m}{\partial D_n}D_n+\frac{\partial E_m}{\partial\Theta}(\Theta-\Theta_0)\\&+\frac{1}{2!}\Big[\frac{\partial^2 E_m}{\partial T_{kl}\partial T_{qr}}T_{kl}T_{qr}+2\frac{\partial^2 E_m}{\partial T_{kl}\partial D_n}T_{kl}D_n\\&+\frac{2\partial^2 E_m}{\partial T_{kl}\partial\Theta}T_{kl}(\Theta-\Theta_0)+\frac{\partial^2 E_m}{\partial D_n\partial D_o}D_nD_o\\&+\frac{2\partial^2 E_m}{\partial D_n\partial\Theta}D_n(\Theta-\Theta_0)+\frac{\partial^2 E_m}{\partial\Theta^2}(\Theta-\Theta_0)^2\Big]\\&+\frac{1}{3!}\frac{\partial^3 E_m}{\partial D_n\partial D_o\partial D_p}D_nD_oD_p+\frac{1}{4!}\frac{\partial^4 E_m}{\partial D_n\partial D_o\partial D_p\partial D_s}\\&\times D_nD_oD_pD_s+\frac{1}{5!}\frac{\partial^5 E_m}{\partial D_n\partial D_o\partial D_p\partial D_s\partial D_t}\\&\times D_nD_oD_pD_sD_t+\cdots,\end{aligned}$$

TABLE II. Second-order derivatives of the potential G_1 and their physical significance.

Derivative	Relationship between derivatives	Symbol	Name
$\frac{\partial^2 S_{ij}}{\partial T_{kl}\partial T_{qr}}$	$-$assumed zero		Change of elastic compliances with stress
$\frac{\partial^2 S_{ij}}{\partial T_{kl}\partial D_n} = -\frac{\partial^3 G_1}{\partial T_{ij}\partial T_{kl}\partial D_n} = -\frac{\partial^2 E_m}{\partial T_{kl}\partial T_{qr}}$	neglected		Change of elastic compliance with electric displacement
$\frac{\partial^2 S_{ij}}{\partial T_{kl}\partial\Theta} = -\frac{\partial^3 G_1}{\partial T_{ij}\partial T_{kl}\partial\Theta} = -\frac{\partial^2 E_n}{\partial T_{ij}\partial T_{kl}}$	T_{ijkl}		Rate of change of the elastic compliances with temperature
$\frac{\partial^2 S_{ij}}{\partial D_n\partial D_o} = -\frac{\partial^3 G_1}{\partial T_{ij}\partial D_n\partial D_o} = -\frac{\partial^2 E_n}{\partial T_{ij}\partial D_o}$	Q_{ijno}		Quadratic strain components
$\frac{\partial^2 S_{ij}}{\partial D_n\partial\Theta} = -\frac{\partial^3 G_1}{\partial T_{ij}\partial D_n\partial\Theta} = -\frac{\partial^2 E_n}{\partial T_{ij}\partial\Theta} = -\frac{\partial^2\sigma}{\partial T_{ij}\partial D_n}$	T_{qijn}		Rate of change of piezoelectric constants with temperature
$\frac{\partial^2 S_{ij}}{\partial\Theta^2} = -\frac{\partial^3 G_1}{\partial T_{ij}\partial\Theta^2} = \frac{\partial^2\sigma}{\partial T_{ij}\partial\Theta}$	$T\alpha_{ij}$		Rate of change of temperature expansion coefficients with temperature
$\frac{\partial^2 E_m}{\partial D_n\partial\Theta} = \frac{\partial^3 G_1}{\partial D_n\partial D_n\partial\Theta} = -\frac{\partial^2\sigma}{\partial D_m\partial D_n}$	$T\beta_{mn}$		Rate of change of dielectric impermeability with temperature
$\frac{\partial^2 E_m}{\partial\Theta^2} = \frac{\partial^3 G_1}{\partial D_n\partial\Theta^2} = -\frac{\partial^2\sigma}{\partial D_n\partial\Theta}$	$T\zeta_{mn}$		Rate of change of pyroelectric constants with temperature
$\frac{\partial^2\sigma}{\partial\Theta^2}$	$\frac{\partial}{\partial\Theta}\left(\frac{\rho C^{T,\Theta}}{\Theta_0}\right)$		Rate of change of temperature derivative of entropy with temperature

$$(\sigma-\sigma_0)=\frac{\partial\sigma}{\partial T_{kl}}T_{kl}+\frac{\partial\sigma}{\partial D_n}D_n+\frac{\partial\sigma}{\partial\Theta}(\Theta-\Theta_0)$$
$$+\frac{1}{2!}\left[\frac{\partial^2\sigma}{\partial T_{kl}\partial T_{qr}}T_{kl}T_{qr}+\frac{2\partial^2\sigma}{\partial T_{kl}\partial D_n}T_{kl}D_n\right.$$
$$+\frac{2\partial^2\sigma}{\partial T_{kl}\partial\Theta}T_{kl}(\Theta-\Theta_0)+\frac{\partial^2\sigma}{\partial D_n\partial D_o}D_nD_o$$
$$\left.+\frac{2\partial^2\sigma}{\partial D_n\partial\Theta}D_n(\Theta-\Theta_0)+\frac{\partial^2\sigma}{\partial\Theta^2}(\Theta-\Theta_0)^2\right]$$
$$+\frac{1}{3!}\frac{\partial^3\sigma}{\partial D_n\partial D_o\partial D_p}D_nD_oD_p+\cdots.$$

In the differentiations, the conditions for partial differentiation are not written but are understood; for example,

$$\partial S_{ij}/\partial T_{kl}=(\partial S_{ij}/\partial T_{kl})_{D,\Theta}, \quad (5)$$

i.e., the electric field and the temperature are held constant during the differentiation.

In these equations there are some equivalences between the partial derivatives because of the fact that the order of differentiation can be inverted. For example,

$$\partial S_{ij}/\partial D_n=-\partial^2 G_1/\partial T_{ij}\partial D_n=-\partial E_m/\partial T_{ij}=g_{ijn}, \quad (6)$$

a piezoelectric constant relating the strain and the electric displacement. Table I shows all the first-order derivatives, their relationships, the symbols given them, and their names.

Similar relationships and names for the second derivatives are shown by Table II.

All second derivatives involving two differentiations by stresses are neglected as being very small. Also neglected is the change in elastic compliance constants with electric displacement since no measurements have been made of this effect.

The higher derivatives of interest are third, fourth, fifth, and sixth rank tensors representing the additions to the G_1 function due to third, fourth, fifth, and sixth power products of the dielectric displacements. These have been given the designations

$$\frac{\partial^2 E_m}{\partial D_n\partial D_o}=K_{mno}, \quad \frac{\partial^3 E_m}{\partial D_n\partial D_o\partial D_p}=K_{mnop},$$
$$\frac{\partial^4 E_m}{\partial D_n\partial D_o\partial D_p\partial D_s}=K_{mnops}, \quad \frac{\partial^5 E_m}{\partial D_n\partial D_o\partial D_p\partial D_s\partial D_t}=K_{mnopst}. \quad (7)$$

With these symbols, the three equations representing the strains, fields, and the entropy can be written in

the forms

$$S_{ij}=[s_{ijkl}^{D,\Theta}+T_{\varepsilon ijkl}(\Theta-\Theta_0)]T_{kl}+[g_{ijn}+T_{\varepsilon ijn}\times(\Theta-\Theta_0)]D_n+(\alpha_{ij}+\tfrac{1}{2}T\alpha_{ij}(\Theta-\Theta_0))(\Theta-\Theta_0)+\tfrac{1}{2}Q_{ijno}D_nD_o+\cdots, \quad (8)$$

$$E_m=-[g_{mkl}+T_{\varepsilon mkl}(\Theta-\Theta_0)]T_{kl}+[\beta_{mn}+T\beta_{mn}\times(\Theta-\Theta_0)]D_n+\left[q_m+\frac{T_{q_m}(\Theta-\Theta_0)}{2}\right][\Theta-\Theta_0]-Q_{mnkl}T_{kl}D_n+\frac{K_{mno}D_nD_o}{2}+\frac{K_{mnop}}{3!}D_nD_oD_p+\frac{K_{mnops}}{4!}D_nD_oD_pD_s+\frac{K_{mnopst}}{5!}D_nD_oD_pD_sD_t+\cdots$$

$$(\sigma-\sigma_0)=(\alpha_{ij}+T\alpha_{ij}(\Theta-\Theta_0))T_{kl}-(q_m+T_{q_m}(\Theta-\Theta_0))D_m+\left[\frac{\rho C^{T,\Theta}}{\Theta_0}+\frac{1}{2}\frac{\partial}{\partial\Theta}\left(\frac{\rho C^{T,\Theta}}{\Theta_0}\right)\times(\Theta-\Theta_0)\right](\Theta-\Theta_0)+\frac{1}{2!}[T_{\varepsilon ijkl}T_{kl}T_{qr}+2T_{\varepsilon kln}T_{kl}D_n-T\beta_{mn}D_nD_o].$$

Hence, as the temperature increases from below the transition temperature where D_n and D_o are positive to above the transition temperature where $D_n=D_o=0$, an increase in entropy (i.e., a decrease in order) takes place as long as $T\beta_{mn}$ is positive.

These equations can all be derived from a potential G_1 given by

$$G_1=-\tfrac{1}{2}[s_{ijkl}^{D,\Theta}+T_{\varepsilon ijkl}(\Theta-\Theta_0)]T_{ij}T_{kl}-[g_{ijn}+T_{\varepsilon ijn}(\Theta-\Theta_0)]T_{ij}D_n+\tfrac{1}{2}[\beta_{mn}+T\beta_{mn}(\Theta-\Theta_0)]D_mD_n-\left[\alpha_{ij}+\frac{T\alpha_{ij}(\Theta-\Theta_0)}{2}\right]\times T_{ij}(\Theta-\Theta_0)+\left[q_m+\frac{T_{q_m}(\Theta-\Theta_0)}{2}\right]D_m(\Theta-\Theta_0)-\tfrac{1}{2}Q_{ijno}D_nD_oT_{ij}+\frac{K_{mno}}{3!}D_mD_nD_o+\frac{K_{mnop}}{4!}\times D_mD_nD_oD_p+\frac{K_{mnops}}{5!}D_mD_nD_oD_pD_s+\frac{K_{mnopst}}{6!}\times D_mD_nD_oD_pD_sD_t+\left[\frac{\rho C^{T,\Theta}}{\Theta_0}+\frac{1}{2}\frac{\partial}{\partial\Theta}\left(\frac{\rho C^{T,\Theta}}{\Theta_0}\right)\times(\Theta-\Theta_0)\right][\Theta-\Theta_0]. \quad (9)$$

Applying the differentiations of Eqs. (3) to this function, the equations of (8) result.

For tetragonal symmetry $D_{2d}(\bar{4}2m)$ it is well known that the tensors up to the fourth rank have the matrices

$$q_m=0;\ \alpha_{ij};\ \beta_{mn};\ \begin{vmatrix}\alpha_{11}&0&0\\0&\alpha_{11}&0\\0&0&\alpha_{33}\end{vmatrix};$$

$$g_{ijm}=\begin{vmatrix}0&0&0&g_{123}&0&0\\0&0&0&0&g_{123}&0\\0&0&0&0&0&g_{312}\end{vmatrix};$$

$$K_{mno}=\begin{vmatrix}0&0&0&K_{123}&0&0\\0&0&0&0&K_{123}&0\\0&0&0&0&0&K_{123}\end{vmatrix};$$

$$s_{ijkl}=\begin{vmatrix}s_{1111}&s_{1122}&s_{1133}&0&0&0\\s_{1122}&s_{1111}&s_{1133}&0&0&0\\s_{1133}&s_{1133}&s_{3333}&0&0&0\\0&0&0&s_{2323}&0&0\\0&0&0&0&s_{2323}&0\\0&0&0&0&0&s_{1212}\end{vmatrix};$$

$$Q_{ijno}=\begin{vmatrix}Q_{1111}&Q_{1122}&Q_{1133}&0&0&0\\Q_{1122}&Q_{1111}&Q_{1133}&0&0&0\\Q_{3311}&Q_{3311}&Q_{3333}&0&0&0\\0&0&0&Q_{2323}&0&0\\0&0&0&0&Q_{2323}&0\\0&0&0&0&0&Q_{1212}\end{vmatrix};$$

$$K_{mnop}=\begin{vmatrix}K_{1111}&K_{1122}&K_{1133}&0&0&0\\K_{1122}&K_{1111}&K_{1133}&0&0&0\\K_{1133}&K_{1133}&K_{3333}&0&0&0\\0&0&0&K_{1133}&0&0\\0&0&0&0&K_{1133}&0\\0&0&0&0&0&K_{1122}\end{vmatrix}. \quad (10)$$

The fifth rank tensor K_{mnops} for the symmetry $(\bar{4}2m)$ can be determined by applying the two conditions

$$z=-z;\ x=y;\ y=x:\ x=x;\ y=-y;\ z=-z \quad (11)$$

and the equation of tensor transformation

$$K'_{mnops}=\frac{\partial x_m'}{\partial x_m}\frac{\partial x_n'}{\partial x_n}\frac{\partial x_o'}{\partial x_o}\frac{\partial x_p'}{\partial x_p}\frac{\partial x_s'}{\partial x_s}K_{mnops}.$$

The results of applying these two conditions to the tensor K_{mnops} is that all terms are zero except

$$K_{11123}=K_{12223} \quad \text{and} \quad K_{12333}, \quad (12)$$

with all permutations of these terms being equal since all of the D components can be interchanged. Hence, fifth rank terms enter only if polarization exists along all three axes.

For the sixth rank tensor the nonvanishing components when all the subscripts can be interchanged are

for the two conditions

$$K_{111111}=K_{222222};\ K_{111122}=K_{112222};\ K_{111133}=K_{222233},$$
$$K_{113333}=K_{223333};\ K_{112233};\ K_{333333}; \quad (13)$$

and hence the energy terms added by the sixth rank tensor are

$$K^*_{111111}[D^6_1+D^6_2]+K^*_{333332}D^6_3+K^*_{111122}$$
$$\times[D^4_1D^2_2+D^2_1D^4_2]+K^*_{111133}[D^4_1D^2_3+D^4_2D^2_3]$$
$$+K^*_{112233}D^2_1D^2_2D^2_3+K^*_{113333}[D^2_1D^4_3+D^2_2D^4], \quad (14)$$

where the stars indicate that the term is multiplied by the number of different combinations that can be obtained by interchanging the subscripts and dividing by 6!

One fact that is obvious from the form of the quadratic strain constants Q_{ijno} is that if the spontaneous polarization were along the z or 3 direction, the change along x given by Q_{1133} has to equal the change along y given by $Q_{2233}=Q_{1133}$, and hence the crystal will still be tetragonal. On the other hand, if the polarization lies along either x or y, the changes introduced by the quadratic effects are different for all three axes and hence the crystal can change from tetragonal to orthorhombic as observed experimentally. We can rule out the possibility that antiferroelectric polarization occurs simultaneously along both x and z by the fact that no shear displacements of the type generated by terms of the form Q_{2323} are observed.

If all the stresses are zero and we consider only the electric displacements, all the energy terms are represented by the β and K terms. To determine the dielectric constants for small fields we need consider only large spontaneous terms along x and small electric displacements in addition along x, y, and z. We neglect all products of small terms above the second, and hence the only remaining terms are

$$G_1=\tfrac{1}{2}[\beta_{11}+T\beta_{11}(\Theta-\Theta_0)][(D_{1c}+\Delta D_1)^2+D^2_2]$$
$$+[\beta_{33}+T\beta_{33}(\Theta-\Theta_0)]D^2_3+K^*_{1111}[(D_{1c}+\Delta D_1)^4]$$
$$+K^*_{1122}[D_{1c}{}^2D^2_2]+K^*_{1133}[D_{1c}{}^2D^2_3]+K^*_{111111}$$
$$\times[D_{1c}+\Delta D_1]^6+K^*_{111122}[D_{1c}{}^4D^2_2]$$
$$+K^*_{111133}D^2_3D_{1c}{}^4+G_0. \quad (15)$$

In a manner similar to that discussed by Kittel,[2] the polarization along the antiferroelectric axis can be calculated by requiring that the value of G_1 shall be the same below and above the transition temperature and that the first derivative of G_1 by D_1—which equals the field—shall also be zero. This results in two equations:

$$\beta_{11}+2K^*_{1111}D_{1c}{}^2+2K^*_{111111}D_{1c}{}^4=0, \quad (16)$$

$$\beta_{11}+4K^*_{1111}D_{1c}{}^2+6K^*_{111111}D_{1c}{}^4=0. \quad (17)$$

Solving these equations simultaneously, we find

$$D_{1c}{}^2=-\beta_{11}/K^*_{1111}; \quad K^*_{111111}=K_{1111}{}^{*2}/2\beta_{11}. \quad (18)$$

[2] C. Kittel, Phys. Rev. **82**, 729 (1951).

For any temperature, since Eq. (17) is valid, we find

$$D_1{}^2=-\frac{2}{3}\frac{\beta_{11}}{K^*_{1111}}-\frac{2}{3}\frac{\beta_{11}}{K^*_{1111}}$$
$$\left[1-\frac{3}{4}\left(1+\frac{T\beta_{11}(\Theta-\Theta_0)}{\beta_{11}}\right)\right]^{\frac{1}{2}}$$
$$=\tfrac{2}{3}D_{1c}{}^2+\tfrac{2}{3}D_{1c}{}^2\left[1-\frac{3}{4}\left(1+\frac{T\beta_{11}(\Theta-\Theta_0)}{\beta_{11}}\right)\right]^{\frac{1}{2}}. \quad (19)$$

Hence the spontaneous polarization increases below the transition point.

The dielectric constant along the x axis for small applied fields is given by

$$\Delta E_1=[\beta_{11}+T\beta_{11}(\Theta-\Theta_0)][D_{10}+\Delta D_1]$$
$$+4K^*_{1111}[D_{10}{}^3+3D_{10}{}^2\Delta D_1]$$
$$+6K^*_{111111}[D_{10}{}^5+5D_{10}{}^4\Delta D_1]. \quad (20)$$

Since

$$[\beta_{11}+T\beta_{11}(\Theta-\Theta_0)]D_{10}+4K^*_{1111}D_{10}{}^3+6K^*_{111111}D_{10}{}^5$$

is zero for all temperatures, then

$$\Delta D_1/\Delta E_1=\epsilon=\{[\beta_{11}+T\beta_{11}(\Theta-\Theta_0)]+12K^*_{1111}D_{10}{}^2$$
$$+30K^*_{111111}D_{10}{}^4\}^{-1}. \quad (21)$$

Just above the Curie temperature Θ_0,

$$D_{10}=0 \quad \text{and} \quad \epsilon_{11}{}^+=1/\beta_{11}. \quad (22)$$

Just below, introducing the values of $D_{1c}{}^2$ and K^*_{111111} from (18),

$$\epsilon_{11}{}^-=1/4\beta_{11}, \quad (23)$$

and the dielectric constant drops to $\frac{1}{4}$ the value just above the Curie temperature. This is a somewhat arbitrary result which depends on the sixth power term furnishing the potential to limit the increase in polarization. If this term varies as the nth power of D_1 it is readily shown that the dielectric constant below the transition drops to $1/(n-2)$. For $ND_4D_2PO_4$ the ratio along an a axis is about 8 to 1.

The dielectric constants along the y and z axes (i.e., the two nonantiferroelectric axes) can be calculated in a similar manner and are

$$\epsilon_{22}=\{[\beta_{11}+T\beta_{11}(\Theta-\Theta_0)]+2K^*_{1122}D_{10}{}^2$$
$$+2K^*_{111122}D_{10}{}^4\}^{-1};$$
$$\epsilon_{33}=\{[\beta_{33}+T\beta_{33}(\Theta-\Theta_0)]+2K^*_{1133}D_{10}{}^2 \quad (24)$$
$$+K^*_{111133}D_{10}{}^4\}^{-1}.$$

Hence the dielectric constants along y and z will also drop below the transition temperature by amounts depending on the values of the K constants. Along z the drop is about 4 to 1.

An approximate value of the spontaneous polarization of $ND_4D_2PO_4$ can be obtained from the heat of

transition measurements[1] ΔH of Stephenson and Zettlemoyer[2] and the temperature coefficient of the dielectric impermeability constant along the x axis determined from the dielectric measurements of Fig. 2 of the companion paper.[1] The heat of transition ΔH has been found to be $\Delta H = 154 \pm 5$ calories per mole for normal ammonium dihydrogen phosphate. From Eq. (8), the decrease in entropy due to ordering is in cgs units

$$\Delta\sigma = (4\pi/2) T\beta_{11} P_1^2, \tag{25}$$

where P_1 is the polarization per square centimeter.

[2] C. C. Stephenson and A. C. Zettlemoyer, J. Am. Chem. Soc. **66**, 1405 (1944).

The heat of transition in calories per mole is equal to

$$\Delta H = \frac{\Theta_0 \Delta\sigma M}{4.187\times 10^7 \rho} = \frac{2\pi T\beta_{11}\Theta_0 P^2{}_1 M}{4.187\times 10^7 \rho}, \tag{26}$$

where M is the molecular weight and ρ the density. From Fig. 2 of reference 1, $T\beta_{11} = 0.000065$, $M = 115.08$, $\rho = 1.804$, and since $\Delta H = 154$ calories per mole the indicated spontaneous polarization per unit area is

$$P_1 = 32{,}000 \text{ cgs units/cm}^2, \tag{27}$$

which is about twice that measured for potassium dihydrogen phosphate.

PHYSICAL REVIEW VOLUME 88, NUMBER 3 NOVEMBER 1, 1952

A Variational Principle for Scattering*

HERMAN FESHBACH AND S. I. RUBINOW
Physics Department, Massachusetts Institute of Technology, Cambridge, Massachusetts
(Received June 16, 1952)

A variational principle is presented for the phase shifts δ_l of a central force scattering problem. This generalizes the principles of Schwinger and Hulthèn for S-state scattering in that (a) it is applicable to states of higher angular momentum, and (b) it depends explicitly on the "inside" wave function only. The Born approximation may be obtained with the choice of an appropriate trial function. Illustrative calculations have been made for the S- and P-state scattering states for an exponential well nucleon-nucleon interaction potential. A simple one-parameter trial function was utilized. The results are in excellent agreement with previously given exact calculations.

INTRODUCTION

THE theoretical prediction of the scattering cross section for a two-body nuclear scattering process may be reduced, as is well known, to the evaluation of the phase shifts. These are obtained from the solution of the radial part of the Schrödinger wave equation. In general, this may be a tedious numerical task, and in recent years variational procedures have been introduced by both Schwinger[1] and Hulthèn[2] for the case of S-wave scattering which reduce the amount of labor involved. Hulthèn's principle involves the phase shift explicitly, requiring an iterational procedure in solving for $k\cot\delta_0$. Hulthèn has reformulated his method[3] so as to avoid this difficulty, but at the expense of introducing a nonstationary element into the calculation.

In the present paper a variational expression is introduced for the phase shift which utilizes what may be called the "inside" wave function whose value is essentially nonzero only within the range of the potential well under consideration. This expression is stationary and does not involve any explicit dependence upon the quantity sought. Because of its explicit rather than implicit dependence upon the inside wave function the present principle is an improvement over Schwinger's formulation.

* Supported in part by the joint program of the AEC and ONR.
[1] J. Schwinger, Phys. Rev. **78**, 135 (1950); **72**, 742 (1947).
[2] L. Hulthèn, Kgl. Fysiograf. Sällskap. Lund, Förh. **14**, No. 21, 257 (1944); Den 10. Skandinaviske Matematiker Kongres 1946, Copenhagen, 201 (1947).
[3] L. Hulthèn, Arkiv Mat. Astron. Fysik **35A**, 25–1 (1948).

Variational Principle for $k\cot\delta_l$

The radial part (u/r) of the Schrödinger wave function satisfies the equation

$$d^2u/dr^2 + [k^2 - l(l+1)/r^2 + U(r)]u = 0, \tag{1}$$

with

$$k^2 = 2mE/\hbar^2, \quad U(r) = -(2m/\hbar^2)V(r). \tag{2}$$

Here, m is the reduced mass of the two-particle system under consideration (in the case of nucleon-nucleon scattering, m equals $\frac{1}{2}$ mass of a nucleon) and E is the energy in the center-of-mass system. The variable r is the interparticle distance and $V(r)$ is the interaction potential. As usual, the constant l is the orbital angular momentum quantum number.

For scattering, the boundary conditions on $u(r)$ are

$$\begin{aligned} &u(0) = 0, \\ &u(\infty) = \cot\delta_l \sin(kr - \tfrac{1}{2}l\pi) + \cos(kr - \tfrac{1}{2}l\pi). \end{aligned} \tag{3}$$

The problem under consideration is to determine the constant $\cot\delta_l$ from the solution of Eq. (1) consistent with the above boundary conditions.

For nuclear interactions the function $U(r)$ is a short-range potential, so that outside the range of the force the function u attains its asymptotic form w which satisfies the equation

$$d^2w/dr^2+[k^2-l(l+1)/r^2]w=0. \tag{4}$$

The solution of this equation may be written down immediately in the form

$$w=w_1\cot\delta_l+w_2, \tag{5}$$

where $w_{1,2}$ are the spherical Bessel functions

$$w_1=krj_l(kr), \quad w_2=-krn_l(kr). \tag{6}$$

The solutions w_1 and w_2 have been chosen so that they have the asymptotic form required by the boundary conditions,

$$\begin{aligned} &w_1(\infty)\to\sin(kr-\tfrac{1}{2}l\pi),\\ &w_2(\infty)\to\cos(kr-\tfrac{1}{2}l\pi)\equiv w_{2\infty}. \end{aligned} \tag{7}$$

The special notation $w_{2\infty}$ is introduced for the asymptotic form of the function w_2. It obviously satisfies the equation

$$d^2w_{2\infty}/dr^2+k^2w_{2\infty}=0. \tag{8}$$

The "inside" wave function $y(r)$ is defined by the equation

$$u(r)=y(r)+w_1\cot\delta_l+w_{2\infty}. \tag{9}$$

It can be seen from this equation that $y(r)$ differs from zero inside the range of the potential $U(r)$.

It may be noted that the asymptotic function $w_{2\infty}$ is utilized instead of w_2, so that except for the $l=0$ case $y(n)$ does not vanish outside the range of V. The function w_2 is the irregular solution of Eq. (4) and behaves like $r^{-(l+1)}$ in the neighborhood of the origin. While it is nonetheless possible to formulate a variational principle using w_2 instead of $w_{2\infty}$ in Eq. (9), the use of $w_{2\infty}$ instead of w_2 results in a simpler and more elegant formalism. Furthermore, it is more practicable for calculations since the function $y(r)$ is defined by Eq. (9) is analytic at the origin.

If the above expression for $u(r)$ is now introduced into Eq. (1), it can be readily seen with the aid of Eqs. (4) and (8) that the equation satisfied by $y(r)$ is

$$\begin{aligned} d^2y/dr^2+k^2y-[l(l+1)/r^2](y+w_{2\infty})\\ +U(y+w_1\cot\delta_l+w_{2\infty})=0. \end{aligned} \tag{10}$$

The boundary conditions on y are

$$\begin{aligned} &y(0)=w_{2\infty}(0)+O(r^{l+1}),\\ &y(\infty)=0. \end{aligned} \tag{11}$$

In order to obtain a variational expression for $k\cot\delta_l$, Eq. (10) is multiplied by the quantity $(y+\cot\delta_l w_1+w_{2\infty})$ and integrated over all of space. It then follows in a straightforward manner with the aid of integration by parts that

$$\begin{aligned} k\cot\delta_l=\int_0^\infty dr\Big\{-\left(\frac{dy}{dr}\right)^2+k^2y^2-\frac{l(l+1)}{r^2}(y+w_{2\infty})^2\\ +U(y+w_1\cot\delta_l+w_{2\infty})^2\Big\}. \end{aligned} \tag{12}$$

The above integral is a stationary expression for $k\cot\delta_l$. That is, if we introduce for y a varied function $y+\delta y$ which differs by the infinitesimal amount δy from the true solution of Eq. (10) but still satisfies the boundary conditions on y, then all terms of the order of δy vanish as a consequence of the differential Eq. (10) and therefore $\delta(k\cot\delta_l)$ vanishes.

In this form, the expression represents a generalization to states of arbitrary angular momentum of the Schwinger-Hulthèn formalism. In the case of S-state scattering ($l=0$), $w_{2\infty}=w_2=\cos kr$ so that $y=u-w_1\cot\delta_l-w_2=u-w$. The Schwinger formalism may then be obtained directly from Eq. (12) by replacing y by $(u-w)$.

It may be noted that the quantity $\cot\delta_l$ appears as a parameter on the right-hand side, i.e., just the quantity to be solved for. Therefore, when a varied function is introduced, an iterative procedure has to be used for $k\cot\delta_0$, as in Hulthèn's first formulation.[2] To obviate this difficulty, Eq. (12) is rewritten as

$$A(k\cot\delta_l)^2-2B(k\cot\delta_l)+C=0, \tag{13}$$

where

$$\begin{aligned} A&=1/k^2\int_0^\infty drUw_1^2,\\ B&=\tfrac{1}{2}-(1/k)\int_0^\infty drUw_1(y+w_{2\infty}),\\ C&=\int_0^\infty dr\Big\{-(dy/dr)^2+k^2y^2\\ &\qquad+(U-[l(l+1)/r^2])(y+w_{2\infty})^2\Big\}. \end{aligned} \tag{14}$$

Equation (13) is a quadratic in $(k\cot\delta_l)$, a solution of which can be written down immediately, *viz.*,

$$k\cot\delta_l=[B+(B^2-AC)^{\frac{1}{2}}]/A. \tag{15}$$

The point of this is that in Eq. (15), $k\cot\delta_l$ retains its stationary character, and it may be seen directly that the condition for $\delta(k\cot\delta_l)$ to vanish is that

$$\delta(k\cot\delta_l)=\frac{1}{A}\left\{\delta B+\frac{B\delta B-\frac{1}{2}A\delta C}{(B^2-AC)^{\frac{1}{2}}}\right\}=0. \tag{16}$$

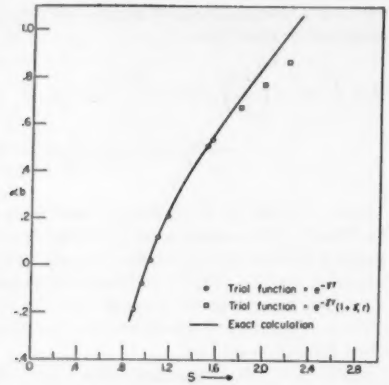

FIG. 1. The reciprocal scattering length plotted against well-depth parameter. The notation b, s is that of Blatt and Jackson and is related to the present notation by means of the relations, $1.4458s = U_0R^2$ and $b = 3.5412R$.

Moreover, the quantity $k\cot\delta_l$ nowhere appears explicitly in any of the integrals on the right-hand side of Eq. (15). Equation (16) may alternatively be written as

$$k\cot\delta_l = \delta C/2\delta B, \tag{17}$$

and the validity of this expression may be verified directly by performing the indicated variations.

In this form (Eq. (17)) the equation has already been given by Hulthèn for the S-state in his second formulation[3] of the variational principle. However, because of the presence of $k\cot\delta_0$ in this equation, he requires another equation to supplement it and suggests the use of an integral expression for $k\cot\delta_0$, which is not stationary. Instead of the latter, Huang[4] has essentially suggested treating $k\cot\delta_0$ on the right side of Eq. (12) as an additional parameter, thereby yielding an additional equation which, however, is likewise nonstationary.[5] It should be mentioned though that Hulthèn is aware of the utility of Eq. (12) in providing a stationary correction to the solution that he obtains.

In Eq. (15), it will be observed that a particular sign for the radical has been chosen. The ambiguity in sign has been resolved by requiring that the solution reduce to the Born approximation which is valid for very weak fields $[U(r)\ll 1]$. It can be seen that with the choice of the trial function $y=-w_{2s}$, $B=\frac{1}{2}$ and $C=0$, so that Eq. (15) reduces to

$$k\cot\delta_l = 1/A, \tag{18}$$

which is just the Born approximation.

If then we insert for y some trial function containing a number of undetermined parameters $\gamma_1, \cdots, \gamma_n$, Eq. (16) yields the following set of equations to determine them:

$$2[B+(B^2-AC)^{\frac{1}{2}}]\partial B/\partial\gamma_\nu = A\partial C/\partial\gamma_\nu, \qquad \nu = 1, 2, \cdots, n. \tag{19}$$

The quantity $k\cot\delta_l$ is, of course, then obtained from Eq. (15). The above constitutes an approximate solution to the problem.

APPLICATION TO S-STATE

As a means of testing the feasibility of the method, application was made to the determination of the S-wave phase shift for an exponential well interaction. In this case it is known that for low energies $k\cot\delta_0$ may be well represented as a power series in k^2,

$$k\cot\delta_0 = -\alpha + \tfrac{1}{2}r_0k^2 + \cdots, \tag{20}$$

where α is the reciprocal "scattering length" and r_0 is the "effective range." It is then desired to find the constants α and r_0. For this purpose, corresponding expansions of the quantities A, B, and C are made; thus,

$$A = A_0 + A_1k^2 + \cdots, \tag{21}$$

where

$$A_0 = \int_0^\infty drUr^2,$$

$$B_0 = \tfrac{1}{2} - \int_0^\infty drUr(y+1), \tag{22}$$

$$C_0 = \int_0^\infty dr\{-(dy/dr)^2 + U(y+1)^2\}.$$

Here, use has been made of the expansions of

$$w_1 = \sin kr, \quad w_{2s} = \cos kr. \tag{23}$$

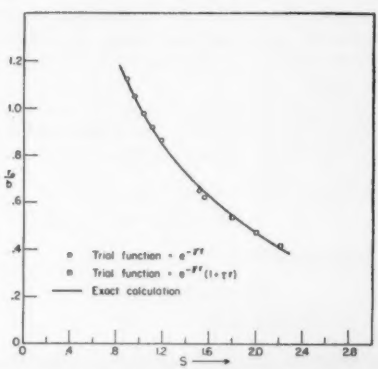

FIG. 2. The effective range as a function of the well-depth parameter.

[4] S. S. Huang, Phys. Rev. **76**, 1878 (1949).
[5] L. Hulthèn and P. O. Olssen, Phys. Rev. **79**, 532 (1950).

It then follows that

$$-\alpha=[B_0+(B_0^2-A_0C_0)^{\frac{1}{2}}]/A_0. \tag{24}$$

Once the values of the variational parameters are obtained from Eq. (19) (with subscript zero appended), these same values determine the value of the effective range, given by the expression

$$r_0=\frac{1}{(B_0^2-A_0C_0)^{\frac{1}{2}}}\left[\frac{A_1}{A_0}C_0+C_1-2B_1\alpha\right]+2\frac{A_1}{A_0}\alpha, \tag{25}$$

where

$$A_1=-\frac{1}{3}\int_0^\infty drUr^4,$$

$$B_1=\frac{1}{6}\int_0^\infty drUr^3(y+4), \tag{26}$$

$$C_1=\int_0^\infty dr[y^2-Ur^2(y+1)].$$

The above considerations have been applied to the case of the exponential well

$$U=U_0e^{-r/R}, \tag{27}$$

for which the exact numerical solution has been given by Blatt and Jackson.[6] The simple trial functions

$$\begin{aligned} y&=e^{-\gamma r},\\ y&=e^{-\gamma r}(1+\gamma_1 r) \end{aligned} \tag{28}$$

were assumed, the latter being used for the deeper wells (larger values of U_0).

In applying Eq. (19), a further numerical simplification may be mentioned. Instead of solving the resulting transcendental Eq. (19) for γ, it is more convenient to choose a particular value of γ and consider the well-depth U_0 to be unspecified. The resulting equation in U_0 is merely a quadratic. In this manner the entire dependence of the phase shift on the well-depth is obtained rapidly. In addition, the same technique can be used for any potential and for arbitrary angular scattering state.

The results obtained are illustrated in Figs. 1 and 2 and indicate excellent agreement with the exact calculations for the simple trial function chosen.

[6] J. M. Blatt and J. D. Jackson, Phys. Rev. **76**, 18 (1949).

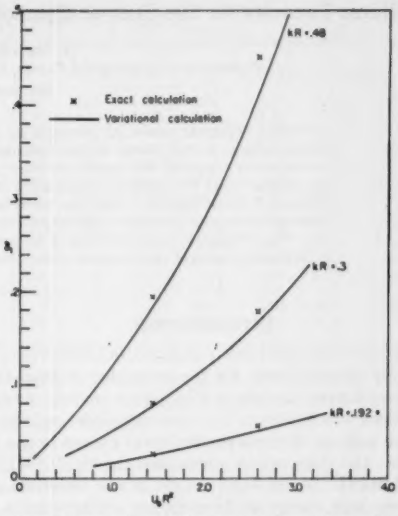

FIG. 3. The P-state phase shift δ_1 as a function of the well-depth parameter U_0R^2. The assumed trial function was $y=-kre^{-\gamma r}$.

APPLICATION TO P-STATE

Application was also made to the calculation of the P-state ($l=1$) phase shift. In this case

$$\begin{aligned} w_1&=\sin kr/kr-\cos kr,\\ w_{2n}&=\sin kr. \end{aligned} \tag{29}$$

A trial function,

$$y=-kre^{-\gamma r}, \tag{30}$$

was chosen, consistent with the boundary conditions on y. The exponential well was again used, and three values of (kR) were chosen in order to compare with some exact calculations made by Massey and Buckingham.[7] The results are illustrated in Fig. 3, and the agreement with the exact calculations can be seen to be again quite good.[8]

[7] H. S. W. Massey and R. A. Buckingham, Proc. Roy. Soc. (London) **A163**, 281 (1937).

[8] *Note added in proof:*—Variational principle (15) has been recently given by L. Hulthén and S. Skavlem, Phys. Rev. **87**, 297 (1952) footnote (17). Use of variational principle (12) to calculate P phase shifts was made by I. Hansson, Kgl. Fysiograf. Sällskap. Lund, Forh **18**, No. 12, 1 (1948).

Plural Theories for the Shower Component in High Energy Nuclear Disintegrations

H. MESSEL AND R. B. POTTS
Department of Mathematical Physics, University of Adelaide, Adelaide, South Australia

(Received July 22, 1952)

Detailed numerical results are presented for the average numbers of protons and mesons emitted as shower particles in high energy nuclear disintegrations. The results for two schemes of plural production of mesons are compared with results previously obtained using the Heitler-Janossy(1) model in which it was assumed that the nucleus is transparent to the mesons emitted in the individual nucleon-nucleon collisions. It is concluded that this latter model best fits the limited experimental data available. The results presented for mesons are based on the assumption that the shower particles consist of π-mesons and protons only. This assumption is not essential, as the energy going into the meson component could be considered as producing mesons of various types. Some recent criticisms of the cascade theory are also answered.

INTRODUCTION

IN a previous publication[1] (henceforth referred to as I) the cascade theory for the production of meson and proton shower particles in high energy nuclear disintegrations was developed for a general model embracing three schemes of plural production of mesons as special cases. The three models were called the HJ(1),[2] HJ(2)[3] and MPM.[1] In the HJ(1) model it was assumed: (1) Every high energy nucleon-nucleon collision leads to the creation of one and only one meson. (2) The primary nucleon makes on the average more than one collision in traversing the nucleus. The effect of recoil nucleons is fully taken into account. (3) Many-body collisions do not occur. (4) The mesons produced are emitted without any interaction with the nucleons of the nucleus in which they were created. In the HJ(2) model the assumptions (1)–(3) were made, but instead of (4) it was postulated that a π-meson may give a large fraction of its energy to a nucleon inside a nucleus and that the nucleon then gives rise to a shower via the cascade process. Finally, in the MPM model, assumptions (1)–(3) were made as well as: (4) Very high energy mesons cascade within a nucleus in a manner entirely analogous to that for nucleons. (5) For high energies, each meson-nucleon collision gives rise to two mesons and one nucleon; thus

(A) meson+nucleon→meson+meson+nucleon.
(B) nucleon+nucleon→nucleon+nucleon+meson.

(6) The cross sections for processes A and B are equal.

TABLE I. The values of the functions q, $l(s)$, $k(s)$, $\lambda_1(s)$, and $\lambda_2(s)$ which are to be used in Eq. (1) when deriving the average numbers of nucleons and mesons for the three schemes of plural production.

Scheme	q	$l(s)$	$k(s)$	$\lambda_1(s)$	$\lambda_2(s)$
HJ(1)	0	0	0	$\alpha(s)$	0
HJ(2)	1	$\frac{6}{(s+2)(s+3)}$	$\frac{6}{(s+2)(s+3)}$	$1-W(0,s)-\frac{1}{2}k(s)$ $+\{W^2(0,s)$ $+\frac{1}{4}k^2(s)\}^{\frac{1}{2}}$	$1-W(0,s)-\frac{1}{2}k(s)$ $-\{W^2(0,s)$ $+\frac{1}{4}k^2(s)\}^{\frac{1}{2}}$
MPM	1	$2W(0,s)$	$W(0,s)$	$1-W(0,s)$	$1-3W(0,s)$

[1] Messel, Potts, and McCusker, Phil. Mag. **43**, 889 (1952).
[2] W. Heitler and L. Janossy, Proc. Phys. Soc. (London) **A62**, 374 (1949).
[3] W. Heitler and L. Janossy, Helv. Phys. Acta **23**, 417 (1950).

In I a full discussion was given of these assumptions in the light of recent experiments carried out on high energy nuclear disintegrations, and detailed numerical results were presented for the average number of shower particles on the HJ(1) model. It is the purpose of this paper to present numerical results for the remaining models, HJ(2) and MPM, thus providing experimentalists with theoretical results with which they may compare their data. Hitherto, mainly because of the lack of detailed theoretical results for various models of meson production, authors have sometimes arrived at conclusions which were not justified. The present results are submitted in an attempt to remedy this situation and not to prove or disprove either the plural or multiple theories of meson production. A recent paper by Treiman[4] is also commented upon.

THEORY AND RESULTS

The expressions[5] for the average number of nucleons $N^{(j)}(E)$ and the average number of π-mesons $\Pi^{(j)}(E)$ with energies greater than E emitted from a nucleus of atomic weight A, due to a collision by a primary particle j ($j=1$ refers to a nucleon, $j=2$ to a meson) of energy E_0 were given in I in matrix form:

$$\begin{bmatrix} N^{(1)}(E) & N^{(2)}(E) \\ \Pi^{(1)}(E) & \Pi^{(2)}(E) \end{bmatrix} = \mathbf{I}_1 \left\{ \frac{V\{D_A\lambda_1(s)\}}{\lambda_2(s)-\lambda_1(s)} \begin{bmatrix} q-\lambda_1(s)-l(s) & k(s) \\ W(0,s) & \alpha(s)-\lambda_1(s) \end{bmatrix} + \frac{V\{D_A\lambda_2(s)\}}{\lambda_1(s)-\lambda_2(s)} \begin{bmatrix} q-\lambda_2(s)-l(s) & k(s) \\ W(0,s) & \alpha(s)-\lambda_2(s) \end{bmatrix} \right\}, \quad (1)$$

[4] S. B. Treiman, Phys. Rev. **86**, 917 (1952).
[5] We assume here that the energy going into the meson component is converted entirely into π-mesons. This assumption is not completely valid, for at very high energies it is well known that mesons with masses greater than that of a π-meson are created. This does not raise any serious difficulty, as one could assume that the energy going into the meson component produces, for instance, kappa-mesons, etc. This would, of course, require a change in the energy ranges used in the calculation.

TABLE II. Theoretical results for high energy nucleon-nucleus collisions in heavy elements (silver and bromine) based on the HJ(2) model ($D_A=3.8$).

E_0 Bev	P_1	P_2	P_3	π_1	π_2	π_3	n_s	$\pi+P$	$P_3+\pi_3$	π_3/n_s	P_3/n_s	$(\pi+P)/n_s$	π_3/n_s	$P_3/(\pi+P)$
5	0.70	0.44	0.26	1.16	0.22	0.94	1.86	0.66	1.20	0.51	0.14	0.35	0.63	0.67
7	0.94	0.60	0.34	1.53	0.30	1.23	2.47	0.90	1.57	0.50	0.14	0.36	0.62	0.67
10	1.29	0.86	0.43	1.99	0.42	1.57	3.28	1.28	2.00	0.48	0.13	0.39	0.61	0.67
12	1.48	1.00	0.48	2.25	0.52	1.73	3.73	1.52	2.21	0.46	0.13	0.41	0.60	0.66
15	1.77	1.23	0.54	2.58	0.65	1.93	4.35	1.88	2.47	0.44	0.12	0.43	0.59	0.65
20	2.17	1.52	0.65	3.07	0.87	2.20	5.24	2.39	2.85	0.42	0.12	0.46	0.59	0.64
30	2.84	2.06	0.78	3.85	1.23	2.62	6.69	3.29	3.40	0.39	0.12	0.49	0.58	0.63
50	3.80	2.85	0.95	4.95	1.75	3.20	8.75	4.62	4.15	0.37	0.11	0.53	0.57	0.62
100	5.50	4.30	1.20	6.83	2.95	3.88	12.33	7.25	5.08	0.31	0.097	0.59	0.55	0.59
200	7.54	6.14	1.40	8.80	4.20	4.60	16.34	10.34	6.00	0.28	0.086	0.63	0.54	0.59
300	8.82	7.30	1.52	10.05	5.15	4.90	18.87	12.45	6.42	0.26	0.081	0.66	0.53	0.59
500	10.65	9.00	1.65	11.70	6.45	5.25	22.35	15.45	6.90	0.23	0.074	0.69	0.52	0.58
1000	13.40	11.50	1.90	14.00	8.40	5.60	27.40	19.90	7.50	0.20	0.070	0.73	0.51	0.58
1500	15.00	13.05	1.95	15.48	9.60	5.88	30.48	22.65	7.83	0.19	0.064	0.74	0.51	0.58
2000	16.16	14.20	1.96	16.45	10.50	5.95	32.61	24.70	7.91	0.18	0.060	0.76	0.50	0.58

where

$$\left.\begin{matrix}\lambda_1(s)\\ \lambda_2(s)\end{matrix}\right\}=\tfrac{1}{2}\{q+\alpha(s)-l(s)\}$$
$$\pm[\tfrac{1}{4}\{q+\alpha(s)-l(s)\}^2+k(s)W(0,s)-\alpha(s)\{q-l(s)\}]^{\frac{1}{2}}, \quad (2)$$

$$\mathbf{I}_1=\frac{1}{2\pi i}\int_{s_0-i\infty}^{s_0+i\infty}(E_0/E)^s ds/s, \quad (3)$$

$$\alpha(s)=1-2W(0,s), \quad (4)$$

$$W(0,s)=120\{(s+2)(s+3)(s+4)(s+5)\}^{-1}, \quad (5)$$

$$V(\lambda)=2[1-(1+\lambda)e^{-\lambda}]/\lambda^2, \quad (6)$$

and D_A is the average number of collisions suffered by a particle in making a diametrical passage through a nucleus of atomic weight A.

If, in the HJ(2) model, we assume that in a meson-nucleon collision the cross section for the production of a nucleon of energy η and a meson of energy $1-\eta$ is $k(\eta)=6\eta(1-\eta)$, then $k(s)=6\{(s+2)(s+3)\}^{-1}$. In Table I the values of q, $l(s)$, $k(s)$, $\lambda_1(s)$, and $\lambda_2(s)$ are tabulated for the three schemes.

Results for the average numbers of protons and mesons for a primary nucleon of energy E_0 are given in Tables II and III for the HJ(2) and MPM models, respectively. The symbols are those used previously,[1] namely:

P_1, P_2 = average number of protons with kinetic energy greater than 500 and 800 Mev, respectively.

π_1, π_2 = average number of charged mesons with kinetic energy greater than 80 and 1100 Mev, respectively.

$P_3=P_1-P_2$, $\pi_3=\pi_1-\pi_2$, $n_s=\pi_1+P_1$, $\pi+P=\pi_3+P_3$.

In deriving the results it was assumed that one-half of the nucleons were protons and two-thirds of the mesons were charged.

The results apply to the heavy nuclei silver and bromine. As has been pointed out by Messel,[6] the value of D_A previously used, *viz.*, $D_A=6.8$, gives for the HJ(1) model a possible total number of nucleons in

TABLE III. Theoretical results for high energy nucleon-nucleus collisions in heavy elements (silver and bromine) based on the MPM model ($D_A=3.3$).

E_0 Bev	P_1	P_2	P_3	π_1	π_2	π_3	n_s	$\pi+P$	$P_3+\pi_3$	π_3/n_s	P_3/n_s	$(\pi+P)/n_s$	π_3/n_s	$P_3/(\pi+P)$
5	0.68	0.43	0.25	1.27	0.24	1.03	1.95	0.67	1.28	0.53	0.13	0.34	0.65	0.64
7	0.89	0.59	0.30	1.69	0.34	1.35	2.58	0.93	1.65	0.52	0.12	0.36	0.65	0.64
10	1.17	0.81	0.36	2.20	0.47	1.73	3.37	1.28	2.09	0.51	0.11	0.38	0.65	0.63
12	1.34	0.94	0.40	2.48	0.56	1.92	3.82	1.50	2.32	0.50	0.10	0.40	0.65	0.63
15	1.54	1.10	0.44	2.86	0.70	2.16	4.40	1.80	2.60	0.49	0.10	0.41	0.65	0.61
20	1.85	1.35	0.50	3.39	0.93	2.46	5.24	2.28	2.96	0.48	0.096	0.42	0.65	0.59
30	2.37	1.78	0.59	4.40	1.35	3.05	6.77	3.13	3.64	0.45	0.087	0.46	0.65	0.57
50	3.16	2.42	0.74	5.82	2.00	3.82	8.98	4.42	4.56	0.43	0.082	0.49	0.65	0.55
100	4.50	3.58	0.92	8.04	3.17	4.87	12.54	6.75	5.79	0.39	0.074	0.54	0.64	0.53
200	6.12	4.92	1.20	10.74	4.82	5.92	16.86	9.74	7.12	0.35	0.071	0.58	0.63	0.51
300	7.28	6.01	1.27	12.40	6.00	6.40	19.68	12.01	7.67	0.33	0.065	0.60	0.63	0.50
500	8.77	7.46	1.31	14.70	7.70	7.00	23.47	15.16	8.31	0.30	0.056	0.64	0.63	0.49
1000	11.04	9.52	1.52	18.22	10.32	7.90	29.26	19.84	9.42	0.27	0.052	0.68	0.62	0.48
1500	12.56	10.88	1.68	20.50	12.00	8.50	33.06	22.88	10.18	0.26	0.051	0.69	0.62	0.48
2000	13.62	11.92	1.70	22.05	13.20	8.85	35.67	25.12	10.55	0.25	0.048	0.70	0.62	0.47

[6] H. Messel, *Progress in Cosmic Ray Physics* (North-Holland Publishing Company, Amsterdam (to be published)), Vol. II.

TABLE IV. Theoretical results for high energy nucleon-nucleus collisions in heavy elements (silver and bromine) based on the HJ(1) model ($D_A=5.8$).

E_0 Bev	P_1	P_2	P_3	π_1	π_2	π_3	n_s	$\pi+P$	$P_1+\pi_1$	π_1/n_s	P_3/n_s	$(\pi+P)/n_s$	π_1/n_s	$P_2/(\pi+P)$
5	0.33	0.22	0.11	2.25	0.55	1.70	2.58	0.77	1.81	0.66	0.04	0.30	0.87	0.28
7	0.45	0.30	0.15	2.76	0.78	1.98	3.21	1.08	2.13	0.62	0.05	0.33	0.86	0.28
10	0.59	0.40	0.19	3.34	1.06	2.28	3.93	1.46	2.47	0.58	0.05	0.37	0.85	0.27
12	0.68	0.47	0.21	3.69	1.24	2.45	4.37	1.71	2.66	0.56	0.05	0.39	0.85	0.27
15	0.80	0.56	0.24	4.12	1.46	2.66	4.92	2.02	2.90	0.54	0.05	0.41	0.84	0.28
20	0.98	0.70	0.28	4.71	1.79	2.92	5.69	2.49	3.20	0.51	0.05	0.44	0.83	0.28
30	1.28	0.94	0.34	5.64	2.32	3.32	6.92	3.26	3.66	0.48	0.05	0.47	0.82	0.29
50	1.72	1.30	0.42	7.03	3.15	3.88	8.75	4.45	4.30	0.44	0.05	0.51	0.80	0.29
100	2.57	1.97	0.60	9.10	4.48	4.62	11.7	6.45	5.22	0.40	0.05	0.55	0.78	0.30
200	3.58	2.84	0.74	11.3	6.00	5.3	14.9	8.84	6.0	0.36	0.05	0.59	0.76	0.32
300	4.23	3.47	0.76	12.8	7.20	5.6	17.0	10.7	6.4	0.33	0.05	0.62	0.75	0.33
500	5.30	4.40	0.90	14.8	8.90	5.9	20.1	13.3	6.8	0.29	0.05	0.66	0.74	0.33
1000	6.90	5.70	1.20	17.8	11.0	6.8	24.7	16.7	8.0	0.28	0.05	0.67	0.72	0.34
1500	8.00	6.70	1.30	19.7	12.5	7.2	27.7	19.2	8.5	0.26	0.05	0.69	0.71	0.35
2000	8.80	7.45	1.35	21.0	13.6	7.4	29.8	21.0	8.8	0.25	0.05	0.70	0.71	0.35

excess of the number available in the nucleus. This phenomenon, explained by "phantom collisions" and the finite size of the nucleus, plays a greater role for the HJ(2) and MPM models because of the greater number of collisions which may occur. Accordingly, the values of D_A were chosen to be $D_A=3.8$ for the HJ(2) model and $D_A=3.3$ for the MPM model, as these values normalized the results to a total number of nucleons equal to 93, the average for silver and bromine. To facilitate direct comparison between the three models, the results for the HJ(1) model with $D_A=5.8$ which normalizes the total number of nucleons to the same value 93 are given in Table IV. (It should be noted that the various ratios tabulated in this table are very much the same as given in I, Table IV for the HJ(1) model with $D_A=6.8$.) The decreasing of the value of D_A in passing from HJ(1)→HJ(2)→MPM and keeping the total numbers of nucleons the same can be roughly explained in the following manner. In the HJ(2) model both the nucleons and the mesons knock out nucleons so that there are fewer nucleons remaining in the nucleus with which the nucleons and mesons can collide. This situation is naturally accentuated in the MPM model.

A further function which has been computed is $G(E_0)$, which expresses the average amount of energy available for the production of particles other than shower particles, that is, gray and evaporation tracks:

$$G(E_0)=-\int_0^{0.5} E\frac{dN^{(j)}(E)}{dE}dE-\int_0^{0.22} E\frac{d\Pi^{(j)}(E)}{dE}dE. \quad (7)$$

The results for $G(E_0)$ for the HJ(1) model with $D_A=5.8$ and a primary nucleon are given in Table V.

DISCUSSION

In I it was pointed out that the surprising feature of the numerical results presented for the HJ(1) model was their apparent agreement with the limited experimental data available on high energy nucleon disintegrations (see Camerini *et al.*[7]). We say "surprising" since experimental evidence[8,9] appeared to support the hypothesis that the π-mesons do interact with nucleons in a manner analogous to that for the nucleons themselves, whereas in the HJ(1) model it was assumed that the nucleus was transparent to the mesons created within it. Heitler (private communication) has suggested that this apparent anomaly would be resolved if the interaction cross section for π-mesons with nucleons were to decrease with increasing primary energy. Although it is true that a large number of meson-nucleus interactions have been observed for primary meson energies $\leqslant 1$ Bev, there is little evidence for such behavior for meson energies >1 Bev.

Since the HJ(1) model *appears* to fit the experimental facts, we shall discuss the results for the HJ(2) and MPM models in relation to those for the HJ(1) model. In I, results for HJ(1) were presented both for light and heavy nuclei. Because the results for heavy nuclei exhibit the main features of the models more strongly than do those for light nuclei, the latter have not been considered in this paper.

Although an inspection of Tables II, III, and IV reveals at first sight a rather strong similarity between the various quantities tabulated, there are a number of outstanding differences which may allow the experimentalist to decide the relative merits of the models. We note that the number of P_1 particles is greatest for the HJ(2) model. This would be expected because in this case the nucleons are given a large preference over the mesons, the mesons themselves contributing to the number of nucleons and at their own expense. In the MPM model the number of P_1 particles is greater than in the HJ(1). This is because the mesons contribute to the number of nucleons. It should be remembered, however, that in this instance the mesons *gain* as well.

[7] Camerini, Lock, and Perkins, *Progress in Cosmic Ray Physics*, edited by J. G. Wilson (North-Holland Publishing Company, Amsterdam, 1952), Vol. I, Chap. I.
[8] W. O. Lock and G. Yekutieli, Phil. Mag. **43**, 231 (1952).
[9] W. G. V. Rosser and M. W. Swift, Phil. Mag. **42**, 856 (1951).

The fact that on the HJ(2) model the nucleons are given preference over the mesons leads to a smaller π_1/n_s ratio than on the HJ(1) model. Furthermore, on the HJ(2) model, the relative number of $\pi+P$ particles is greater and the number of protons among the unidentifiable shower particles is very high. This fact would tend to disagree with the Bristol[7] estimate that the protons constitute roughly 30 percent of the $\pi+P$ particles. The significance which one can attach to this difference depends, of course, upon the amount of confidence one places in the Bristol figure.

The behavior of the $\pi+P$ particles and the P_2 particles on the MPM model is much the same as on the HJ(2) model. One feature of the results makes the validity of this model rather dubious, namely, the constancy of the π_1/n_s ratio. Both the Bristol results and those of Barker and Butler[10] indicate that with increasing primary energy the π_1/n_s ratio decreases.

From the above discussion it is obvious that it is difficult at present to decide between the models. As more accurate experimental results become available it should become relatively simple to decide which of the models, if any, is correct. For the present we conclude that not only is the HJ(1) the simplest of the models of plural meson production considered, but also it gives the most satisfactory agreement with the limited experimental data available.

We now turn our attention to a discussion of the results presented in Table V and a recent paper by Treiman.[4]

It is well known that for nucleon energies below 1.5 Bev, less than one-half of the nucleon-nucleon encounters are inelastic and do not lead to the production of mesons. As the primary energies increase above 1.5 Bev, the probability for inelastic nucleon-nucleon collisions increases, and near 5 Bev practically every nucleon-nucleon collision leads to the creation of mesons. It is evident, then, that in nucleon-nucleus encounters in which the primary nucleon energy $E_0 \leqslant 1$ Bev, practically the total primary energy is dissipated in the production of gray and evaporation tracks. For $1.5 \leqslant E_0 \leqslant 5$ Bev, the percentage of energy going into the production of gray and evaporation tracks will decrease sharply. For energies $E_0 \gtrsim 5$ Bev, one would expect this percentage to remain substantially constant. That this is actually so may be seen from Table V. For a primary energy $E_0 = 10$ Bev there is on the average 1.62 Bev available for the production of gray tracks and evaporation prongs. For $E_0 = 500$ Bev there is, on the average, 10.8 Bev available. If one takes into consideration the gray tracks, which may have energies in the neighborhood of 400 Mev, it will be seen that the actual energy available for the production of evaporation prongs is nearly independent of the primary energy.

[10] K. H. Barker and C. C. Butler, Proc. Phys. Soc. (London) **A64**, 4 (1951).

TABLE V. $G(E_0)$, the energy available for production of gray and evaporation tracks in a nucleon-heavy nucleus collision on the HJ(1) model.

E_0 in Bev	$G(E_0)$ in Bev	$100G/E_0$
10	1.62	16.2
20	2.27	11.3
50	3.28	6.8
100	4.43	4.4
200	6.71	3.4
500	10.82	2.2

Treiman, in a recent paper[4] on the analysis of cosmic-ray experiments on the neutron component, determined a "specific yield" function. This function gave the production rate of disintegration nucleons at a given atmospheric depth arising from a unit flux of vertically incident cosmic-ray primaries of given atomic weight and given energy per nucleon. Disintegration nucleons were defined as evaporation prongs and slow recoil nucleons with $E<50$ Mev. He found, within the experimental error, that over a very limited primary energy range (4 to 12.7 Bev per nucleon) the specific yield function was fairly insensitive to primary energy. For primary energies below 4 Bev per nucleon the specific yield function depended strongly on the energy.

Treiman briefly discussed Messel's theory[11] of a nucleon cascade and stated: "Actually the results obtained by Messel predict a specific yield function for small star production which depends strongly on primary proton energy, even for energies above 4.1 Bev." It is readily seen from Table V that this conclusion was not justified even though $G(E_0)$ applies to the heavy nuclei. Recall that the energy of high energy gray tracks is also included in $G(E_0)$.

It should be mentioned here, once again, that the theory of a nucleon cascade, as such, is independent of the model of meson production. The one and only assumption[6] used in this respect is the homogeneity property of the total cross section with regard to the primary and secondary energies. The theory may, however, be specialized to include various models of meson production, as we have done in I and in this paper.

Finally, we should like to comment on one of Treiman's statements which we believe is incorrect. Trieman states (reference 4, page 922) ". . . Messel has obtained fairly good agreement between theory and experiment for the latitude variations of small stars. This must be considered to be spurious, however, since the primary proton energy spectrum adopted by Messel (integral power law exponent = 1.7) is in serious disagreement with the spectrum deduced from the data of Winckler and Peters (exponent $\simeq$ 1.0)." However, in the papers to which Treiman refers,[12] Messel concluded

[11] H. Messel, Comm. Dublin Inst. Advanced Studies, Series A, No. 7 (1951).

[12] H. Messel, Phys. Rev. **83**, 21 (1951); **83**, 26 (1951).

that using $\gamma=1.7$, the then accepted value, does *not* yield good quantitative agreement with experiment and suggested that better agreement would be obtained with a smaller value of γ. In a further paper[13] (apparently overlooked by Treiman), Messel presented results adopting "the upper limit $\gamma=1.1$." Instead of the agreement between Messel's theory (with $\gamma=1.7$) and experiment being spurious, the facts are, as stated in the literature, that with $\gamma=1.7$ the theory is not in good quantitative agreement but with $\gamma=1.1$ they are.

[13] H. Messel, Proc. Phys. Soc. (London) **A64**, 726 (1951).

PHYSICAL REVIEW VOLUME 88, NUMBER 3 NOVEMBER 1, 1952

The Mechanism of Field Dependent Secondary Emission

HAROLD JACOBS, JOHN FREELY, AND FRANK A. BRAND
Signal Corps Engineering Laboratories, Fort Monmouth, New Jersey

(Received April 3, 1952)

In recent experimental investigations, it was found that secondary emission ratios as high as 10,000 to 1 could be attained utilizing field dependent secondary emission from magnesium oxide. Early tests showed the mechanism causing the high gains to be fundamentally different from the more standard secondary emission phenomenon.

The hypothesis was made that the mechanism of field dependent secondary emission was a process similar to that of the "Townsend avalanche" occurring in gas discharges. As the surface of the dielectric film was bombarded with primary electrons, the high resistivity of the material in combination with the secondary emission current caused the surface to charge to the potential of the collector grid, producing a high field within the dielectric. Electrons released within the material could then gain enough energy to liberate additional electrons, and an avalanche type process resulted.

Experiments were conducted to test this hypothesis and each proved to be consistent with the above theory. The main content of these experiments can be summarized in the following statements:

(1) The high yields appeared to be independent of the base material. This indicated that the surface or volume effects were most important, implying that a Fowler type field emission from the base metal was not a significant factor.

(2) In studying the secondary current as a function of field, the gas discharge equations were found to be correct. These equations predicted a straight line plot of the $\ln \ln \delta$ vs $1/E$, and in addition, gave a close estimate of the magnitude of the secondary emission ratio.

(3) By means of retarding potential measurements, the energies and mean free paths of the emitted secondary electrons were determined. These data were in good agreement with the results in item (2).

(4) The rise time for surface charging was determined by using square wave variations of bombarding currents, and was found to be consistent with the original hypothesis.

I. INTRODUCTION

IN recent years several workers have reported unusually high secondary emission ratios from thin dielectric films. Their investigations have shown that high dc fields applied across these films cause an enhancement of the secondary emission ratio. In the experiments to be described, high fields were applied across thin films of magnesium oxide while the surface was being bombarded with primary electrons. The secondary emission ratio was found to increase exponentially with field over a wide range of bombardment energy.[1] By applying a square wave variation of field and observing the rise time of surface charging, it was concluded that the enhanced ratios were the result of a high field created within the magnesium oxide by the charged surface. It was further postulated that secondary electrons, liberated in the material, would be accelerated to such high velocities that an effect similar to the "Townsend avalanche" could occur.

The following discussion is an attempt to explain the mechanism of electron multiplication in the dielectric film.

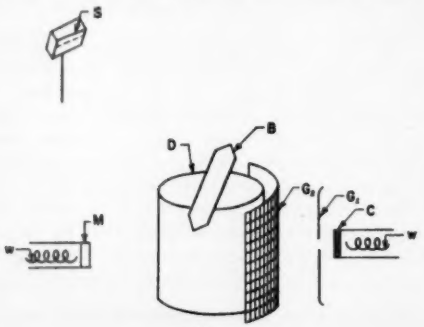

FIG. 1. Experimental tube.

II. EXPERIMENTAL PROCEDURES

Experimental tubes were constructed as shown in Fig. 1. In this design, C represents an oxide coated cathode to be used as the primary emission source; W indicates the tungsten filaments used for heating the cathode sleeves. G_1 is a negatively biased focusing grid consisting of a disk with a small opening. In some tubes, G_1 was omitted with no noticeable difference.

[1] H. Jacobs, Phys. Rev. **84**, 877 (1951).

G_2 consists of a wide mesh nickel grid used as both accelerator and collector. The dynode, D, was rotated by an external magnet coupled to shaft B. M represents a high purity magnesium pellet imbedded in a nickel sleeve, and S refers to a shielded barium getter.

The experimental tube was processed in the following manner. At exhaust, the getter, dynode, and grids were degassed and the cathode activated. After admitting oxygen to a pressure of 80 μ, magnesium was evaporated onto the dynode. Following this step, the surface was further oxidized by induction heating in approximately 2 mm of oxygen. After the oxygen was removed, the cathode was reactivated, the getter flashed, and the tube sealed and removed from the vacuum system. The magnesium oxide formed on the dynode surface was then rotated in front of the cathode, after which the tube was ready for test. The use of the rotating dynode greatly reduced the possibility of contaminating the secondary emission surface, since during cathode activation the surface was shielded.

It should be emphasized that the magnesium oxide deposit had to be quite porous for best results. Porous layers were obtained by the evaporation of magnesium through this low pressure of oxygen. A smooth deposit resulted when the evaporation was carried out in vacuum, rather than through oxygen. These smooth surfaces were then oxidized by heating the dynode in 2 mm of oxygen. The electrical and mechanical properties of the porous and smooth surfaces were found to be radically different.

When examined microscopically, the surfaces evaporated through oxygen appeared to consist of a uniform distribution of small stalactite structures approximately 6×10^{-4} cm long and 2×10^{-4} cm wide. This surface provided much higher secondary emission ratios and stability. In the case of the deposit carried out in vacuum, the shape of the grains after oxidation was generally more spherical and the size not as uniform. This type of surface did not exhibit field dependent secondary emission, despite all efforts at processing. Both surface types did show a high degree of blue luminescence upon electron bombardment. It was concluded from these experiments that field dependent secondary emission is a structure-sensitive phenomenon, and that the surfaces which showed high ratios were very porous.

The thickness of these deposits was determined to be about 10^{-4} cm by three independent methods, i.e., by microscopic measurement, by means of dielectric breakdown fields, and by decay time observations when the surface was operating as an emitter.

The surfaces were tested using the circuit shown in Fig. 2. The cathode was operated at very low temperatures to prevent barium evaporation,[2] the bombardment current being of the order of 1 to 10 μa. With the surface under bombardment, the collector grid was made increasingly positive with respect to the dynode, while measurements were made of the primary and secondary currents. The ratio of secondary to primary current was found to increase nearly exponentially with increasing difference in potential between grid and dynode. Similar results were obtained when the grid potential was kept constant and the dynode voltage lowered, providing the dynode potential was kept over 150 volts. It should be noted that the secondary emission ratios were dependent on the difference in potential between grid and dynode and were independent of bombarding energies above a critical value. This indicates that the high yields were the result of field enhancement.

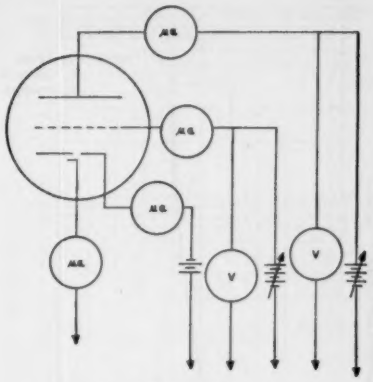

FIG. 2. Static test circuit.

III. EXPERIMENTAL DATA AND INTERPRETATION

The experiments indicated the following factors to be significant in this investigation:

(1) The influence of the base material on the magnitude of the secondary current and the durability of the material.
(2) The dependence of the ratio upon the field within the dielectric film.
(3) The kinetic energy, internal mean free paths, and collision energies of the emitted electrons.
(4) The effect of temperature on the ratios.
(5) The time required for surface charging determined by pulsed bombarding currents.

Since these experimental factors provide the basis for the proposed theory, each item will be discussed in detail.

A. The Role of the Base Material

Tests were conducted with the following dynode base materials: zirconium, tantalum, nickel, barium oxide on nickel, and copper, plated or evaporated on nickel. These experiments showed that variation of the base material had little effect upon the secondary emission properties of the magnesium oxide layers. Figure 3

[2] H. Jacobs, J. Appl. Phys. 17, 596 (1946); J. B. Johnson, Phys. Rev. 73, 1058 (1948); H. Jacobs, Phys. Rev. 85, 441 (1952).

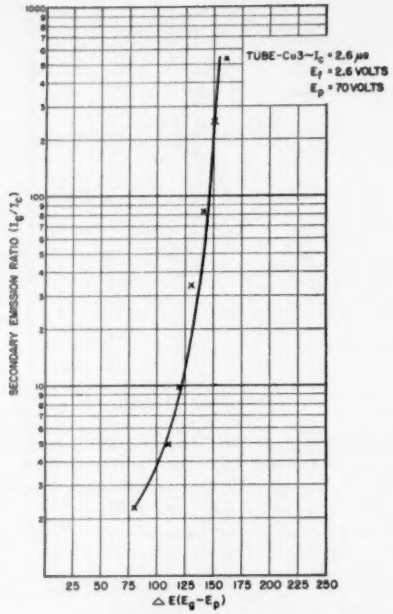

FIG. 3. Secondary emission ratio from magnesium oxide on copper as a function of the potential across the dielectric.

shows the secondary emission characteristics from a dynode which was copper plated and then coated with magnesium oxide. Figures 4, 5, and 6 illustrate similar results from magnesium oxide on pure nickel. Successive tests on the same base material (Fig. 5) showed a greater variation than that from different base materials (Figs. 3 and 4).

The initial secondary emission ratios were evidently independent of base material. However, the power dissipation and lifetime characteristics were found to be quite dependent on the base material. Figure 7 shows the results of a life test using high bombarding currents (1 ma/cm²). The surfaces with zirconium and barium oxide as base materials would not yield ratios greater than 50 to 1 without arcing. The most durable surfaces were those having nickel as a base material. Life test results with bombarding currents of from 10 to 20 μa/cm² are illustrated in Fig. 8.

The fact that the initial secondary emission ratios were independent of the base material indicates that most of the action responsible for the high yields occurs near the surface of the magnesium oxide film since only the material at or near the surface would be chemically similar in all cases. This is a strong indication that field emission from the base material is not a significant factor in the mechanism of field dependent secondary emission.

B. Dependence of Ratio upon Field

In gas discharges there is an effect referred to as the Townsend avalanche.[3] When an electron is accelerated through a gas, new electrons are produced according to the relation

$$N = N_0 e^{\alpha x}, \tag{1}$$

where N_0 is the number of initial electrons, x is the distance traveled by the electron from cathode to anode, α is the number of electrons released per centimeter path per electron, and N is the total number of electrons. With field and distance held constant, the ratio N/N_0 will not vary since α is a function of the applied field.

In these experiments the secondary emission ratios were found to be a function of field, and for constant field, the ratios were independent of bombardment current. This led to the hypothesis that the field dependent secondary emission process was similar to the pre-sparking mechanism in a gas discharge. This can be expressed as

$$\delta = i/i_0 = e^{\alpha x}, \tag{2}$$

where i is the secondary current, i_0 is the primary current, δ is the secondary emission ratio, α the number

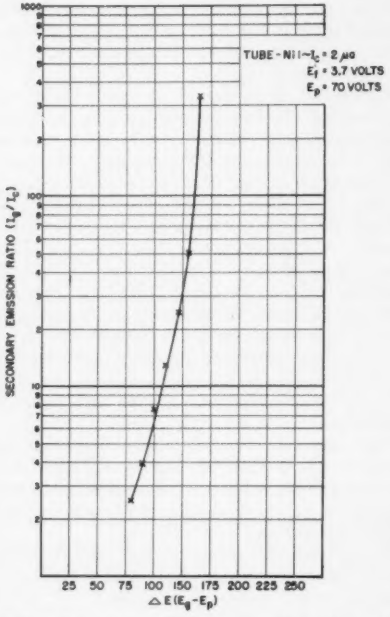

FIG. 4. Secondary emission ratio from magnesium oxide on nickel as a function of potential across the dielectric.

[3] L. B. Loeb, *Fundamental Processes of Electrical Discharges in Gases* (John Wiley and Sons, Inc., New York, 1939), pp. 336–370.

of electrons formed per centimeter of path per electron in magnesium oxide, and x is the depth within the material at which the initial secondary electrons are formed.

Physically, one may describe the mechanism of field dependent secondary emission in the following manner. Primary electrons bombard the uncharged magnesium oxide film liberating electrons by ordinary secondary emission with a ratio greater than unity. As a result of its high resistivity, the surface acquires a large positive charge, and a high field is created across the film. Due to the porosity of the film subsequent bombarding electrons will penetrate a fixed distance into the magnesium oxide. Secondary electrons released within the material are now accelerated towards the surface under the influence of the high field. The secondary electrons travel largely through the pores, gaining sufficient energy from the field to create further electrons by impact. Each new secondary electron creates additional electrons by internal ionization, and a Townsend type avalanche results. The limit of gain is finally reached when the surface of the magnesium oxide film approaches the same potential as that of the collector grid. If the surface potential becomes higher than that of the collector grid, the electrons return to the surface, neutralizing some of the positive charges. If the surface falls below the grid potential, the emission of electrons

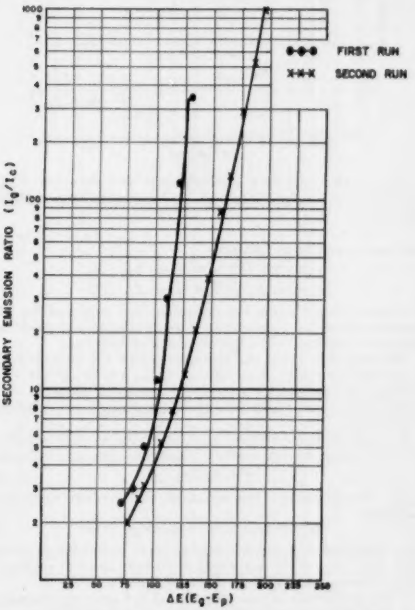

FIG. 5. Secondary emission ratio from magnesium oxide on nickel as a function of potential across the dielectric.

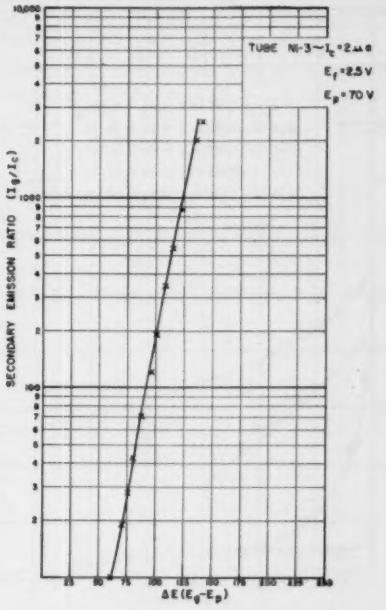

FIG. 6. Secondary emission ratio from magnesium oxide on nickel as a function of potential across the dielectric.

will quickly charge the surface more positively. Therefore an equilibrium potential will be established. The surface of the film thus becomes an unipotential region of positive charges, similar to the condition existing in the cathode glow region of a gaseous glow discharge. This condition implies large mean free paths and mean energies.

An expression for the term α in the factor $e^{\alpha x}$ has been developed by von Engel and Steenbeck[4] and is given by

$$\alpha=\frac{z}{\bar{v}_e}=\frac{600pam}{\bar{v}_e\pi^{\frac{1}{2}}e}C_0^3e^{-eV_i/kT_e}\left(1+\frac{eV_i}{2kT_e}\right), \qquad (3)$$

where α is the number of electrons produced per cm of path per electron, z is the number of electrons produced per second per electron, p is the pressure, $\bar{v}_e$ is the average electron velocity, e/m is the ratio of charge to mass for electrons, V_i is the ionization potential, T_e is the equivalent electron temperature, k is the Boltzmann constant. C_0 is the most probable velocity, or $2\bar{v}_e/\sqrt{\pi}$, and a is a constant of proportionality. Under conditions of very high fields $eV_i/2kT_e \ll 1$, and Eq. (3) becomes

$$\alpha=Ae^{-eV_i/kT_e}, \qquad (4)$$

in which A combines the terms preceding the expo-

[4] See reference 3, p. 368.

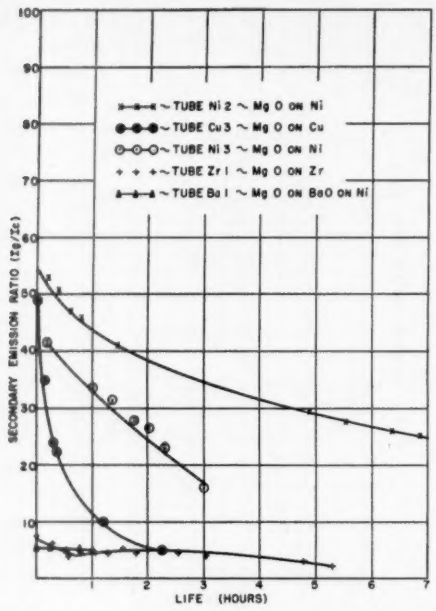
TUBE Ni 2 ~ Mg O on Ni
TUBE Cu 3 ~ Mg O on Cu
TUBE Ni 3 ~ Mg O on Ni
TUBE Zr I ~ Mg O on Zr
TUBE Ba I ~ Mg O on BaO on Ni
SECONDARY EMISSION RATIO (δ/δ₀)
LIFE (HOURS)

FIG. 7. The decay of the secondary emission ratio as a function of time under conditions of high current density bombardment.

nential and is approximately a constant. If we substitute for kT_e its equivalent in field and mean free path,[5] it follows that

$$eV_i/kT_e = 1.64V_i/L_eE, \tag{5}$$

where L_e is the mean free path and E is the field. Equation (5) then becomes

$$\alpha = Ae^{-1.64V_i/L_eE}. \tag{6}$$

Hence, from the Townsend equation, we have

$$\delta = i/i_0 = e^{\alpha x} = \exp(xAe^{-1.64V_i/L_eE}),$$

and

$$\ln\ln\delta = \ln x + \ln A - 1.64(V_i/L_e)(1/E). \tag{7}$$

This equation indicates that if we plot $\ln\ln\delta$ *vs* $1/E$, the result should be a straight line whose slope is of the same order of magnitude as $-1.64V_i/L_e$. Only the order of magnitude of the slope is predicated since A is only approximately constant.[6]

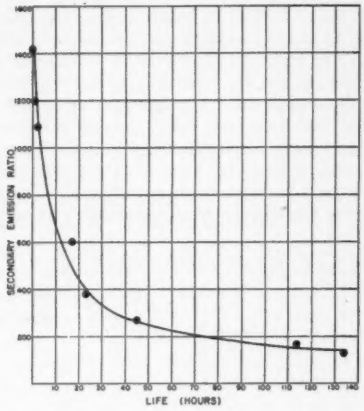

FIG. 8. The secondary emission ratio as a function of time with 10 to 20 microamperes per square centimeter bombarding the surface.

[5] The average energy can be expressed by any one of the following equivalent terms:

$$e\bar{E} = \tfrac{1}{2}m\bar{v}^2 = \tfrac{1}{2}m[(3/2)v_e^2] = \tfrac{1}{2}m(\pi/4)\bar{v}_e^2 = \tfrac{3}{16}\pi m\bar{v}_e^2,$$

where $e\bar{E}$ = average energy, v_e = most probable velocity, $\bar{v}_e$ = average velocity, and $\bar{v}$ = rms velocity. Let us assume that the average velocity can be approximated as

$$\bar{v}_e = (\pi L_eEe/2m)^{\frac{1}{2}}, \tag{14}$$

where E = field and L_e = mean free path. Using Eq. (14), we find

$$e\bar{E} = (3/2)kT_e = \tfrac{3}{16}\pi m\bar{v}_e^2, \quad kT_e = \tfrac{1}{16}\pi^2 L_eEe,$$

or

$$eV_i/kT_e = 1.64V_i/L_eE.$$

Equation (14) is derived under the conditions that the field is strong enough for each collision to be inelastic. That is, the electron starts from rest after each impact, and its terminal velocity is high enough to cause an excited state in the atom with which it collides. For further details, see J. D. Cobine, *Gaseous Conductors* (McGraw-Hill Book Company, Inc., New York, 1941), p. 42.

An alternative derivation of the average velocity, based upon the work of Compton, is described by Loeb (reference 3, p. 368). In this case, the average velocity is determined by

$$\bar{v}_e = (2^{\frac{1}{2}}/\pi^{1/8})[(e/m)EL_ef^{\frac{1}{2}}]^{\frac{1}{2}}, \tag{15}$$

where f = fraction of electron energy lost per collision.

In the limiting case, where $f=1$, all of the electron energy is lost in each collision, and Eq. (15) becomes

$$\bar{v}_e = (2^{\frac{1}{2}}/\pi^{1/8})[(e/m)EL_e]^{\frac{1}{2}}.$$

Numerically then, Eq. (14) and Eq. (15) are in good agreement and can be written as follows:

$$\bar{v}_e = 1.25(eL_eE/m)^{\frac{1}{2}} \quad \text{from Eq. (14)},$$
$$\bar{v}_e = 1.03(eL_eE/m)^{\frac{1}{2}} \quad \text{from Eq. (15)}.$$

We should prefer to use the derivation and results of Eq. (14), however, since the development is more specific and direct with regard to collisions in the magnesium oxide structure.

We have then made the assumption that the internal energy distribution becomes Maxwellian without a large change in the average velocity (as a result of the density of electrons in the magnesium oxide). This assumption is verified by subsequent experiments.

It might further be added that, using the average velocity of Eq. (14), the equivalent electron temperature can be calculated as,

$$kT_e = 0.610(eL_eE). \tag{16}$$

Using the Compton type equation, the electron temperature becomes

$$kT_e = 0.467(eL_eE), \quad \text{assuming } f=1. \tag{17}$$

The differences in $\bar{v}_e$ and kT_e are not great, and although we have used Eq. (14), either one might have been used to predict the order of magnitude of L_e for Eqs. (6) and (7).

[6] The error made in assuming that A is a constant amounts to less than 15 percent for gains ranging from 39 to 365; therefore, it is felt that the use of the approximate form does not seriously affect the theoretical development.

TABLE I. Secondary emission and yield.

Field	Secondary emission ratio
4×10^5	2.6
7×10^5	39.0
10×10^5	365.0

In experiments conducted to test this prediction it was found that $\ln\ln\delta$ does vary as $1/E$, as shown in Figs. 9 and 10. To determine E in this case, dielectric breakdown (or arcing) was assumed to start at 10^6 volts/cm. This generally occurred when there was a potential difference of approximately 100 volts across the magnesium oxide. By varying this potential and assuming proportional changes in field, curves were plotted as indicated in Figs. 9 and 10.

Approximate numerical values could be obtained for the ratio V_i/L_e by using the data in Fig. 9 and rewriting Eq. (7) as

$$\frac{\ln\ln\delta-\ln\ln\delta'}{1/E-1/E'}=1.64\frac{V_i}{L_e}. \tag{8}$$

Substituting experimental values, we find that

$$L_e=0.205V_i\times10^{-5}. \tag{9}$$

If we assume $V_i\cong10$ ev, then $L_e\cong2\times10^{-5}$ cm. For the case of Fig. 10, $L_e\cong1.6\times10^{-5}$ cm. These values are in good agreement with those obtained independently by retarding potential measurements, where $L_e\cong1.1\times10^{-5}$ cm.

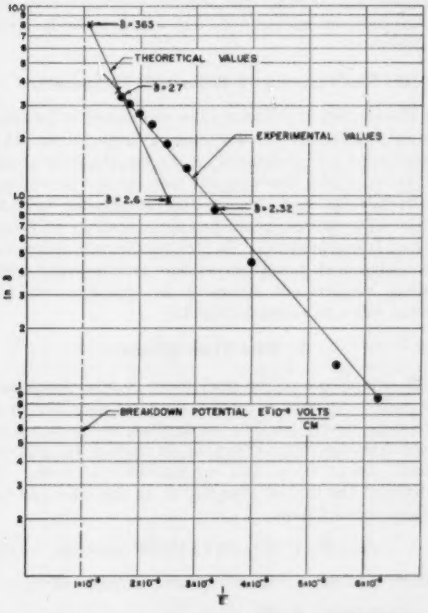

FIG. 9. The ln ln of the secondary emission ratio as a function of the reciprocal of the field.

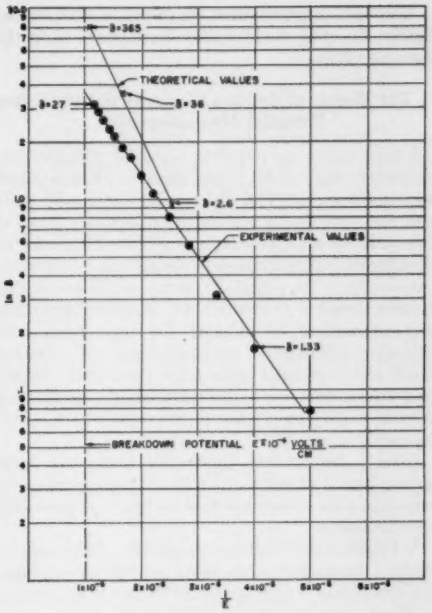

FIG. 10. The ln ln of the secondary emission ratio as a function of the reciprocal of the field.

In addition to predicting a slope, the actual value of the secondary yields can be estimated and shown to be close to the experimental values by referring back to the von Engel and Steenbeck equation,

$$\alpha=\frac{z}{\bar{v}_e}=\frac{600pam}{\bar{v}_e\pi^{\frac{1}{2}}e}C_0^3e^{-eV_i/kT_e}\left(1+\frac{eV_i}{2kT_e}\right). \tag{3}$$

Assume $E\cong10^6$ volts/cm, $L_e\cong10^{-5}$ cm, $a\cong1$, $p=4\times10^5$ mm (the pressure corresponding to a mean free path of 10^{-5} cm in nitrogen), $eV_i=5$ ev, $kT_e=\frac{1}{16}\pi^2L_eE$, and $\bar{v}_e=(\pi L_eEe/2m)^{\frac{1}{2}}\cong1.6\times10^8$ cm/sec. If we now substitute the above factors in Eq. (3), we find that $\alpha=5.9\times10^4$. Since breakdown occurs with approximately 100 volts applied across the film, and assuming $E=10^6$ volts/cm for dielectric breakdown, we find that the film thickness, x, is 10^{-4} cm and

$$\delta=e^{\alpha x}=365 \text{ gain}. \tag{10}$$

Values of δ calculated at this and other fields are shown in Table I. These calculated values are indicated on Figs. 9 and 10 and are in fairly good agreement, with the experimental data, if we consider that V_i and

L_e were only approximated. By changing these values slightly, the slope could readily be adjusted to fit the observed values.

C. The Energy of Emitted Electrons and Retarding Potential Measurements

A tube employing retarding potential principles was designed to analyze the energy spectrum of the emitted electrons (Fig. 11). The grid consisted of a solid sheet with two openings; one allowing the primary beam to enter, and the other permitting a portion of the emitted secondaries to pass through to the collector. Secondary emission from the collector was prevented by coating its inner surface with carbon black. Electron trajectories were determined by dusting the tube parts with willemite. Although it appeared that the primaries struck the magnesium oxide surface in a finely defined spot (about 0.01 cm²), the secondaries were emitted from a much larger area of the film (0.3–0.5 cm², depending on the field).

Some of the electrons leaving the magnesium oxide surface passed through the second opening and were recorded at the collector as various retarding potentials were applied.

A distribution of electron energies was determined by plotting the number of electrons per unit energy range as a function of energy, and from this data, an estimate of the average energy could be made. This average energy $\bar{E}$ of the emitted electrons was found to range between 10 and 20 ev.

A knowledge of the average electron energy allows an estimate to be made of the mean free path, which can then be checked with the values predicted in part B. Assuming that the energy distribution of the electrons on leaving the surface is the same as within the material, it follows that

$$e\bar{E}=(3/2)kT_e=\tfrac{3}{16}\pi m\bar{v}_e^2, \tag{11}$$

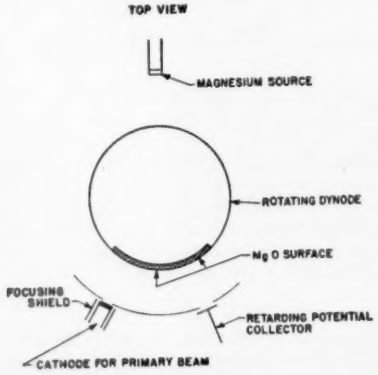

FIG. 11. Experimental tube structure for studying the energy of emitted electrons utilizing retarding potentials.

and

$$\bar{v}_e=(\pi L_eEe/2m)^{\frac{1}{2}} \text{ esu},$$

or

$$e\bar{E}=\tfrac{3}{32}\pi^2L_eEe. \tag{12}$$

Let $e\bar{E}=10$ ev, the average energy of the electron, and $E=10^6$ volts/cm, the field across the dielectric. By substituting these values into Eq. (12), we obtain $EL_e\cong 11$ ev, or $L_e\cong 1.1\times10^{-5}$ cm.

The estimates of the mean free paths given by the retarding potential method are in good agreement with the values estimated by the method described in part B, where the ratios were determined as a function of electric field.

As a refinement of the retarding potential measurements, the natural logarithm of the collector current was plotted *versus* the retarding potential in a procedure similar to that used for probe studies in a plasma.[7] From these plots one observes a linear dependence on energy (indicating a Maxwellian energy distribution), and from the slope a value for the average energy may be determined. The true surface potential is also indicated by methods similar to those measuring contact potentials, making possible a more quantitative determination of the field across the film. The average energy, determined from such plots was found to be approximately 11.1 ev, and the mean free path approximately 1.1×10^{-5} cm. Therefore, the values obtained for the mean free path and average energy, by three independent methods, are found to be in good agreement.

D. The Variation of Ratio with Temperature

The secondary emission ratio was found to be relatively unaffected by variations in temperature. The experiment was performed by placing the entire tube in an oven and observing the primary and secondary currents while slowly raising and lowering the temperature. (The rate of change was approximately 50°C per hour.) It was found that, in general, the ratio decreased somewhat with rising temperature and increased with falling temperature returning to approximately its initial value, as shown in Fig. 12.

E. Rise Time Effects

If our picture of the mechanism of field dependent secondary emission is correct, the yield should show a finite rise time. This time lag results from the fact that with a sudden increase in field, or current, the surface must charge to a new equilibrium. According to McKay,[8] the rate of charging of an insulator can be calculated as follows:

$$E=[(\delta-1)/K]j_pt\times1.13\times10^{13} \text{ volts/cm}, \tag{13}$$

where t=time; j_p=bombardment current, amp/cm²;

[7] See reference 3, p. 240.

[8] K. G. McKay, *Advances in Electronics* (Academic Press, Inc., New York, 1948), Vol. I, p. 109.

and K=dielectric constant. For relatively low ratios, i.e., $\delta=4.5$, $j_p=10^{-5}$ amp/cm², where $K=3.5$ and $E\cong10^6$ volts/cm, we find that $t=10^{-2}$ second. Similarly, for $\delta=3500$, $t=10^{-5}$ second before equilibrium is established.

If we apply this concept to the magnesium oxide surfaces, bombarded with a square wave pulse of primary current, we should expect the following results. If there were no previous charge on the surface (as exists, for instance with no dc bombardment current) the initial secondary emission ratio would be low, and the charging of the surface to equilibrium might require a relatively long time, 10^{-2} to 10^{-3} second. However, if a dc bombardment has been present prior to an increase in bombardment current, the field across the dielectric would already be present and the initial ratios would be higher, i.e., 3500 to 1 rather than 4.5 to 1. This higher ratio would then decrease the time lag by a factor of 10^3, for the new equilibrium to be reached.

Rise time experiments were performed to investigate the conditions mentioned above, and the values predicted by Eq. (13) were found to be quite close to the experimental results.

With a steady state gain of about 130 to 1, $j_p=12\times10^{-5}$ amp/cm², and $E\cong10^6$ volts/cm², the calculated rise time was 1.7×10^{-5} second. The observed rise time under these conditions was approximarely 2.0×10^{-5} second. It was further noted that the rate of rise increased both with field and bombardment current.

Square wave variations of primary current were also made with no initial dc bombardment, and the time lags were found to be greater. For a value of $\delta=70$ after equilibrium, $E\cong10^6$ volts/cm, and with $j_p=4.4\times10^{-6}$ amp/cm², the rise time was calculated to be 2.0×10^{-3} second. Experimentally, the time for equilibrium to be reached was found to be 1.6×10^{-3} second under these conditions. Experiments of this type indicate that the rise time of surface charging can be decreased by increasing the bombardment current, or by maintaining a high field across the surface so that δ is kept high.

IV. CONCLUSIONS

The mechanism of field dependent secondary emission can be described as follows. As a result of conventional secondary emission, the bombarding electrons tend to charge the surface of the dielectric positively creating a high field across the film. Due to porosity (an essential factor in obtaining these high yields), most of the primary electrons can penetrate some distance into the volume of the dielectric releasing secondary electrons. The secondaries, in turn, are accelerated toward the surface of the film, and at sufficiently high fields an electron avalanche will occur.[9]

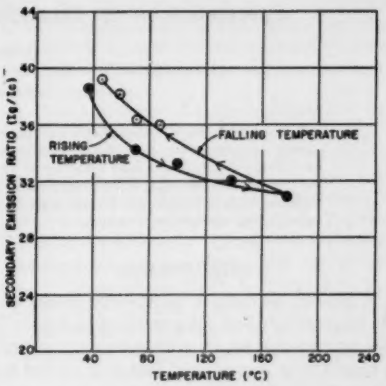

FIG. 12. The secondary emission ratio of magnesium oxide as a function of temperature.

The mean energy of the emitted electrons is roughly 10 to 20 ev and the mean free paths of the secondaries within the dielectric are approximately 10^{-5} cm. Several independent experiments were found to lead to the same conclusions. These include the variation of secondary emission with field, the use of retarding potential measurements, and the measurement of rise times with varying bombarding currents.

Acknowledgment should be made to Dr. J. E. Gorham and Dr. D. Dobischek of the Signal Corps Engineering Laboratories, to Professor A. Van der Ziel of the University of Minnesota and to Dr. E. M. Baroody of Battelle Memorial Institute for their advice during the course of this work.

[9] Considerable theoretical work has been done recently on the mechanism of dielectric breakdown and electron multiplication in solids. [See F. Seitz, Phys. Rev. **76**, 1376 (1949); H. B. Callen, Phys. Rev. **76**, 1394 (1949); H. Frohlich, Phys. Rev. **61**, 200 (1942).] Unfortunately, the emphasis in these works has been on single crystal effects only, and little mention has been made regarding such effects in polycrystalline, nonhomogeneous media. Hence, the concepts and equations developed in these theories do not have a suitable application in the present discussion, where, it is felt, the prime factor is film porosity and not a crystalline breakdown.

Speculation on the Formation of *F*-Centers During Irradiation*

JORDAN J. MARKHAM
Applied Physics Laboratory, Johns Hopkins University, Silver Spring, Maryland
(Received April 7, 1952)

It is suggested in this paper that x-ray and radium radiation cause three effects on alkali halide crystals, namely, to produce free electrons, free holes, and single-ion vacancies. It is further assumed that the single-ion vacancy results from a local distortion of the lattice rather than a diffusion of vacancy pairs from outside the crystal. This postulate explains qualitatively various color center phenomena observed at low temperatures and leads to no obvious contradictions. Some rough calculations on this model have been made. Further experimental verification is required.

I. INTRODUCTION

AT present we have a satisfactory model of the *F*-center based on a suggestion of de Boer.[1,2] This model assumes that an *F*-center is an electron trapped in a negative-ion vacancy and that an *F'*-center is two electrons trapped in such a vacancy. It is generally believed that the number of incipient single-ion vacancies is too small to account for the number of *F*-centers formed during x-radiation. The most convincing evidence, in the author's opinion, regarding the absence of vacancies will be given in the next section (paragraphs 9 and 10).

At present the problem remains as to how lattice vacancies occur during irradiation. One suggestion is that vacancy pairs diffuse into the crystal.[3] A new mechanism suggested by Seitz[4–6] is that ion vacancies are generated at dislocations[7] within the crystals. Recent low temperature data by Dutton, Heller and Maurer,[8] Dorendorf,[9] and others[10] cast doubt on the idea that vacancy pairs diffuse from the surface. This difficulty has prompted a re-examination of the low temperature data on color centers in alkali halides. The re-examination lends strong support to the idea that vacancies are generated at dislocations during x-raying.

In the next section we shall list various low temperature phenomena relating to this problem. Then the data by Pick[11,12] will be re-examined and reinterpreted. Finally, the model suggested by Seitz will be considered and the idea of local heating examined.

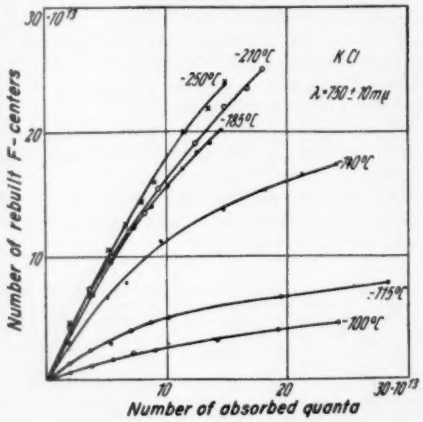

FIG. 1. Plots of the number of rebuilt *F*-centers as a function of the quantum absorbed in the *F'*-band. The data was taken by Pick, reference 12. The notation of the *y* axis corresponds to the present day interpretation (see reference 2).

II. SUMMARY OF LOW TEMPERATURE DATA

We start by listing some of the more interesting properties of color centers in alkali halides:

(1) A very important set of experiments was done by Pick[12] on the formation of *F*-centers from *F'*-centers exposed to light. The data were taken on additively colored synthetic crystals[13] with 80 percent of the *F*-centers converted to *F'*-centers. In the experiment the crystals were exposed to the light in the *F'*-band resulting in the rebuilding of the *F*-centers. Figure 1 is a set of curves taken from Pick, giving the number of

* This work was supported by the U. S. Navy, Bureau of Ordnance.

[1] An experimental review of this subject has been given by R. W. Pohl, Proc. Phys. Soc. (London) **49** (extra part), 4 (1937).

[2] A theoretical review has been given by F. Seitz, Revs. Modern Phys. **18**, 384 (1946). We shall refer to some of the figures in this review since it may be more readily available than the original papers.

[3] As far as the author knows, the diffusion idea was proposed by F. Seitz, reference 2. Calculations on the energy involved in the diffusion process have been made by G. J. Dienes, J. Chem. Phys. **16**, 620 (1948). The local heating idea, to be referred to, was suggested by D. L. Dexter, Science **115**, 199 (1952).

[4] F. Seitz, Phys. Rev. **80**, 239 (1950).

[5] F. Seitz, Revs. Modern Phys. **23**, 328 (1951).

[6] F. Seitz, Advances in Physics **1**, 43 (1952).

[7] Some reviews of the theory of dislocations are A. H. Cottrell, *Progress in Metal Physics* (Interscience Press, Inc., New York, 1949), Vol. 1, p. 77; F. Seitz, "The Theory of Plastic Flow in Single Crystals," in: *A Symposium on the Plastic Deformation of Crystalline Solids, Mellon Institute*, Carnegie Institute of Technology and the Department of the Navy, Office of Naval Research, Pittsburgh, May 19–20, 1950; NAVEXOS-P-834, U.S. Government Printing Office, Washington 25, D. C., 1950, pp. 1–36.

[8] Dutton, Heller, and Maurer, Phys. Rev. **84**, 363 (1951).

[9] H. Dorendorf, Z. Physik **129**, 317 (1951).

[10] W. H. Duerig and J. J. Markham, Conference on the Electrical and Optical Properties of Ionic Crystals, Illinois (1951); Phys. Rev. to be published.

[11] H. Pick, Ann. Physik **31**, 365 (1938).

[12] H. Pick, Ann. Physik **37**, 421 (1940).

[13] That KCl and KBr were additively colored crystals was inferred from reference 11.

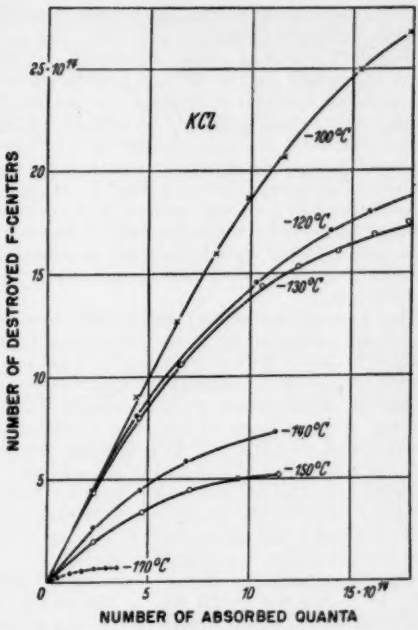

FIG. 2. Plots of the number of destroyed F-centers as a function of the quantum absorbed in the F-band. The data was taken by Pick, reference 11.

rebuilt F-centers as a function of the number of quanta absorbed. The slope of the curves gives the quantum yield $\eta(F'\rightarrow 2F)$, which we define as the number of F-centers formed per quantum absorbed by the F'-band. Our notation does not agree with references 2, 11, and 12. The conclusion we would like to stress is that the slope of the curve, i.e., $\eta(F'\rightarrow 2F)$, varies with time of exposure. The following variation can be estimated from Fig. 1:[14]

At 170°K $\eta(F'\rightarrow 2F)$ drops from 0.3 to 0.1;

at 130°K $\eta(F'\rightarrow 2F)$ drops from 1.4 to 0.4;

and at 23°K $\eta(F'\rightarrow 2F)$ drops from 2 to 1.2.

We shall assume that η changes because the F-center concentration varies with exposure.

(2) Pick[11] has produced F'-centers in additively colored synthetic KCl and KBr by exposing F-centers to light. Here he obtains curves for the number of F-centers destroyed as a function of the number of quanta absorbed. A typical set of curves taken from reference 11 is shown in Fig. 2. For the production of F'-centers from F-centers we define $\eta(2F\rightarrow F')$ as the number of F-centers destroyed when a quantum is absorbed in the F-band. As the concentration of F'-centers increases $\eta(2F\rightarrow F')$ decreases. The concentration dependence is much more pronounced at lower temperature; indeed at 100°K, $\eta(2F\rightarrow F')$ decreases from 0.5 to zero after a short period of radiation.

(3) F-centers form in large concentration at 5°K during an exposure to x-rays.[8,10]

(4) Growth rate curves, i.e., plots of F-center concentration against time of exposure, have been obtained by several observers. Typical growth rate curves for an exposure to x-rays are shown in Fig. 3. The figure is based on observations by Harten[15] on synthetic KCl at temperatures between 90°K and 330°K and by Duerig[10,16] on synthetic NaCl, KCl, and KBr at 5°K, 80°K, and 300°K. From Harten's work, one may assume that a transition in the form of the curve occurs in KCl at about 160°K. Leitner[17] has exposed NaCl at room temperature to x-rays, γ-rays, and β-rays. These data support Fig. 3 with one possible exception. Only a small amount of curvature was observed when a thinner crystal (0.125 cm) is exposed to x-rays from a 130-kv source. For a thicker crystal (0.296 cm) a curvature appears. Growth rate curves have been obtained for the irradiation of natural NaCl (Belar) and natural KCl (Urbach) by a radium source at room temperature.[18] Belar's radium source was shielded by an 0.5-mm glass which should absorb all the α-rays. Urbach's source was in a glass tube so that his crystals were shielded from α-rays. The radium data agree with the high temperature curve.

The actual data are not sufficient at present to establish the complete validity of Fig. 3. Probably the difference is a question of degree.

(5) It has been shown[9,10] that the F'-band is formed upon x-ray bombardment of KCl and KBr at 80°K. While the number of F'-centers is not large, they play

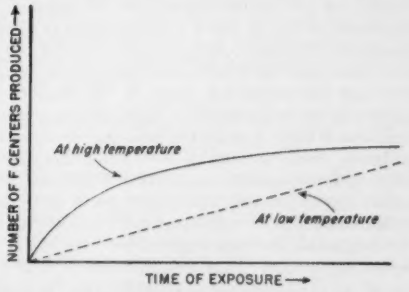

FIG. 3. Schematic plot of the concentration of F-centers as a function of the x-raying time.

[14] Temperatures will be given only approximately.

[15] H. Harten, Z. Physik 126, 619 (1949).

[16] W. H. Duerig (private communication).

[17] Irmberta Leitner, Wien. Ber. IIa 145, 407 (1936). A correction to this paper appears in footnote 1 of a paper by K. Przibram, Z. Physik 107, 709 (1937).

[18] Maria Belar, Wien. Ber. IIa 132, 45 (1923) and 135, 186 (1926); F. Urbach, Wien. Ber. IIa 135, 149 (1926).

a very important role in the formation of color centers under the foregoing conditions. By cooling KBr and KCl to 80°K, Duerig[16] has obtained growth rate curves for the F'-centers. The curves are approximately a linear function of time, indicating that the F'-centers grow simultaneously with the F-centers. We may conclude that the formation of F'-centers requires only a very small concentration of F-centers.

(6) The F'-band has not appeared in KCl during x-raying at 5°K. It has also been observed[10] that the F'-band appeared in x-rayed NaCl at 5°K if the rate of radiation (number of photons per second) is large but not if the rate is small. KBr seems to behave like NaCl, although the F'-band is very small.

(7) Domanic[19] has measured the photoconductivity of F'-centers in KCl as a function of the temperature. His data extend to 20°K. The electrical conductivity depends in part on cross sections, as does the formation of various centers. The essential point of these data is that there is no indication of an abrupt discontinuity in the properties of the material between 80°K and 20°K. Let us therefore assume that the properties remain continuous from 20°K to 5°K, so that conclusions reached at 20°K can be extended to 5°K.

(8) Glaser[20] and others have measured photoconductivity from F-centers between 20°K and 500°K. These data support the conclusion regarding continuity in the low temperature region stated just above.

(9) Smakula[21] has studied the production of F-centers during the irradiating of the crystal (synthetic KBr, KI, RbCl, and RbBr) at the edge of the fundamental ultraviolet absorption region. During this radiation excitons are created which in turn produce F-centers. Two features are to be stressed. First, the number of F-centers produced is very small compared to the number of centers produced by x-rays. Smakula's equation [reference 2, Eq. (1)] indicates that the number of F-centers per unit surface exposed to the radiation is proportional to $\ln I_0/I$, where I_0 is the intensity of the transmitted light before radiation and I is the transmitted light after radiation. An estimate using $\ln I_0/I$ shows that the saturation value of the number of F-centers in crystals colored at liquid air temperature by excitons is about 1 percent of the value obtained by x-radiation. Since the thickness of coloration is unknown, it is impossible to translate this figure into F-center concentrations. The second effect to be noticed is that the growth rate curves in KBr at 300°K and at 90°K resemble the high temperature curve in Fig. 3. The saturation value of the concentration at 90°K is a third of the saturation value at 300°K. The fact that excitons can produce only a small number of F-centers supports the assumption that the number of virgin[22] single-ion vacancies is small.

Schröder[21] performed similar experiments on synthetic and natural NaCl at 300°K. A curve on one synthetic sample is similar to Smakula's. In general the curves on the natural samples do not resemble the high temperature curve of Fig. 3. Schröder shows that past history influences the growth rate cruves. If the crystals are colored uniformly (this is not stated in the paper), then the densities are about 1 percent of the densities obtained by x-rays.[10] An important point to be noted is that some synthetic crystals could not be colored by excitons. Schröder believed these crystals to be exceptionally pure.

(10) Delbecq, Pringsheim, and Yuster[23] have explored and interpreted the α- and β-bands in KI. The α-band is caused by the presence of a negative-ion vacancy. Since the α-band does not appear before the irradiation of the crystals, we must conclude that the number of virgin single-ion vacancies is very small. Further work at 190°K and 80°K indicates that the α-bands appear during x-irradiation, i.e., a number of negative-ion vacancies are frozen into the lattice. At 300°K, however, the α-band, even after irradiation, is hardly visible and the number of vacancies frozen into the lattice must be considerably smaller.

(11) Observations by Harten[15] and Duerig[16] show that by heating the crystal one can remove the ion vacancies formed during irradiation, i.e., one obtains identical growth rate curves on a virgin specimen and on one which has been subject to appropriate heat treatment. Harten heated his crystal (KCl) at 620°K for 5 minutes. Duerig has bleached KBr by exposing it to light at room temperature for 10 hours and KCl by exposing it to light at 600°K for ½ hour. We shall refer to this phenomenon as healing.

In the next section we shall interpret Pick's data and then later we shall speculate on what happens during the x-raying.

III. AN INTERPRETATION OF PICK'S DATA

Let us now use the conventional model[2] of the F- and F'-centers to interpret Pick's results. It will appear that the η's are not unique functions of the temperature, but depend on the concentrations. We will first show that the F-centers formed during the above experiments are produced by two steps: capture of the electron in the excited state, followed by a transition to the ground state. The following notations will be used:

[19] F. Domanic, Ann. Physik **43**, 187 (1943); reference 2, Fig. 12.
[20] G. Glaser and W. Lehfedt, Nachr. Akad. Wiss. Göttingen, Math-physik. Kl. **2**, 91 (1936-37); G. Glaser, Nachr. Akad. Wiss. Göttingen, Math-physik. Kl. **3**, 31 (1937); reference 2, Figs. 6 and 7.
[21] A. Smakula, Z. Physik **63**, 762 (1930); H. J. Schröder, Z. Physik **76**, 608 (1932).

[22] The term "virgin" will be used for vacancies which are in the lattice before the crystal is exposed to the radiation. The term "incipient vacancy" will be reserved for the type of vacancies considered by Seitz, reference 4. This does not agree with the nomenclature recently employed by the author [Phys. Rev. **86**, 433 (1952)] where the term "incipient" means that the vacancies remain as single-ion vacancies, i.e., virgin vacancies in the sense of this paper.
[23] Delbecq, Pringsheim, and Yuster, J. Chem. Phys. **19**, 574 (1951); see also E. Burstein and J. J. Oberly, Phys. Rev. **79**, 903 (1950).

$\sigma(F)$—capture cross section for an electron to form a stable F-center from a negative-ion vacancy; $\sigma(F')$—capture cross section for an electron to form and F'-center from an F-center; n_-—number of negative-ion vacancies per unit volume; n_f—number of F-centers per unit volume; and $n_{f'}$—number of F'-centers per unit volume.

The probability that a free electron forms an F-center can be defined as

$$P(F)=\sigma(F)n_-/[\sigma(F)n_-+\sigma(F')n_f], \quad (1)$$

while the probability that a free electron forms an F'-center is

$$P(F')=\sigma(F')n_f/[\sigma(F)n_-+\sigma(F')n_f]. \quad (2)$$

Since $P(F)+P(F')=1$, we are assuming that the electrons, at low temperatures have only two choices in additively colored crystals. This assumption underlies Pick's work.

If $P(F')$ is unity, then every electron released from an F-center ends up in an F'-center. This destroys two F-centers, the one which released the electron and the second one which captured the electron to form an F'-center. If every photon releases an electron and $P(F')=1$, $\eta(2F\rightarrow F')=2$. If $P(F')$ is smaller than unity, less than two F-centers will be destroyed for every electron released, i.e., $\eta<2$. Likewise if $P(F)=1$, then $\eta(F'\rightarrow 2F)$ will be 2, because every electron released from an F'-center (this forms one F-center) is captured by a vacancy to form a second F-center. In general, $\eta(2F\rightarrow F')=2\varphi(T)P(F')$ and $\eta(F'\rightarrow 2F)=2P(F)$, where φ is the probability of dissociating an excited F-center. The temperature, T, dependence of φ is seen from paragraph 8 of Sec. II. We shall assume that it depends only on T. Thus changes of η during irradiation are due to changes in the P's.

To begin with, we would like to show with the use of Pick's experiments on making F'-centers from F-centers (paragraph 2 of Sec. II) that at high temperatures (about 170°K for KCl), $\sigma(F)$ is very small compared to $\sigma(F')$. At these temperatures the initial value $\eta(2F\rightarrow F')$ is two (see Fig. 2), i.e., $\varphi=P(F')=1$; further, $P(F')$ changes only slightly with irradiation. This means that $\sigma(F')n_f/\sigma(F)n_-$ is large. If $\sigma(F')/\sigma(F)$ is not large, (i.e., n_f/n_- is large), $P(F')$ would start out by being one (since $n_f\gg n_-$) but would decrease with irradiation as n_f/n_- decreases and cause a drop in $\eta(2F\rightarrow F')$. Since there is only a small change in $\eta(2F\rightarrow F')$ during irradiation at these temperatures, it is plausible to assume that $\sigma(F)\ll\sigma(F')$.[24]

At 130°K in KCl the initial value of $\eta(F'\rightarrow 2F)$ is about 1.5 (see Fig. 1) i.e., $P(F)\approx 0.7$ because n_- is large. During the irradiation in the F'-band, n_f increases at the expense of n_- so that $P(F)$ soon drops. As stated, the value of $\eta(F'\rightarrow 2F)$ for KCl at 130°K drops several fold during the radiation. The drop in the η's which occurs when one creates F-centers from F'-centers seems to be due to the drop in n_- during the radiation, i.e., we assume that $n_f+n_{f'}+n_-$ is not affected by the irradiation and that there is no diffusion of vacancies into or out of the crystals.

Pick's experiments (paragraphs 1 and 2 of Sec. II) suggest that $\sigma(F)$ has a marked temperature dependence. Figure 1 shows that $\eta(F)$ changes very little during irradiation below 100°K (approximately) but decreases rapidly with rising temperatures between 100°K and 170°K. The variation in η indicates that the capture cross section in KCl for a vacancy is constant until 100°K and that it decreases rapidly above this temperature. The photoconductivity experiments of Dominic and Glaser (paragraphs 7 and 8 of Sec. II) support this conclusion. The variations in $\sigma(F)$ suggest that the negative-ion vacancy captures the electron in the excited state. When the lifetime of the electron in this state is short, it frees itself and $\sigma(F)$ is small. On the other hand, if the lifetime is long, transitions to the ground state are more probable and $\sigma(F)$ increases. If the electron were captured in the ground state, $\sigma(F)$ could not be small at 170°K for one would strongly expect the F-centers to be stable at these temperatures in KCl.

The above analysis indicates that Pick's quantum yield curves depend on the ratio of n_f to n_-. The composite plots of $\eta(2F\rightarrow F')$ and $\eta(F'\rightarrow 2F)$ against temperature[25] should be used with caution, since the data were not taken under the same condition. (For $\eta(2F\rightarrow F')$, n_f/n_- is large while for $\eta(F'\rightarrow 2F)$, n_f/n_- is small).

Further, we may conclude from Pick's data and the work of Smakula on excitons (paragraph 9 of Sec. II) that the number of vacancies at low temperatures are not affected by irradiation of visible or near visible light. This causes the partial saturation of $\eta(F'\rightarrow 2F)$ at low temperatures.

IV. AN INTERPRETATION OF THE DATA AT LIQUID HELIUM TEMPERATURE

In this section we shall consider the effect x-rays may have on crystals. First, the hypothesis will be stated and its ability to explain low temperature color-center phenomena explored; next, the difficulty with the vacancy diffusion idea will be given; finally, this difficulty will be considered.

The author suggests that energetic ionizing radiation generates:

(1) free electrons;
(2) free holes;
(3) single-ion vacancies.

The new suggestion is the production of vacancies

[24] A complication occurs when making F'-centers from F-centers As pointed out by Pick, during irradiation with F-light, one destroys some F'-centers as well as F-centers. This leads to a saturation of the F'-center concentration (see Fig. 2 for the temperature of 100°K). Part of the curvature observed at 170°K must be due to this effect.

[25] Reference 2, Fig. 9.

by the irradiation and not by the diffusion of vacancies into the crystals. It is to be stressed that the creation of vacancies without diffusion from grain boundaries was first made by Seitz.[4] Here we explore the consequences of the idea and its relation to recent low temperature data. The exact mechanism of vacancy production by irradiation will not be specified in this section but will be considered in detail in the next. The only hypothesis made here is that vacancies are produced by a local perturbation of the lattice. They must be surrounded by a fairly regular lattice, for otherwise F-centers in x-rayed crystals would not be similar to those found in additively colored crystals. Further, since the crystal heals at relatively low temperatures compared to the temperature of melting (paragraph 11 of Sec. II), the vacancies can be removed by a relatively simple process. The perturbation might heal itself by local diffusion at room or slightly higher temperatures. If this is true, vacancies might be produced more efficiently at low temperatures.

We shall use Pick's data on additively colored crystals to arrive at conclusions on x-rayed crystals. Data taken by Duerig[16] indicate that holes combine with F'-centers to reform F-centers during the irradiation. This tends to keep the F'-centers' concentration small. Nevertheless, if Pick's data at 20°K can be extended to 5°K, we would expect F'-centers to form whenever n_- becomes much smaller than n_f and that the absence of F'-centers indicates that n_- is not negligible compared to n_f.

The following observed facts can be explained using the assumption that vacancies form during x-raying.

(1) Formation of F-band and of F'-band at liquid-helium temperature (paragraphs 3 and 6 of Sec. II). The small concentration of F'-centers at liquid helium temperature can be explained on the assumption that enough ion vacancies are produced to keep n_- from getting small. The presence of the α-band at low temperatures, as indicated in paragraph 10 of Sec. II, supports this assumption. Hence one may assume that $\sigma(F)n_- \gg \sigma(F')n_f$ and that by Eq. (1) $P(F)$ is almost equal to unity; thus the F-band forms and the F'-band is suppressed. On the other hand, rough estimates from Pick's curves, Fig. 1, suggest that $\sigma(F)/\sigma(F')$ decreases by a factor of two in going from 20°K (−250°C) to 90°K (−185°C). To keep $P(F)$ at 90°K, the same as its values at 5°K, n_-/n_f would have to increase by a factor of two. The data indicate that this does not happen and that $P(F)$ decreases with rising temperatures. Perhaps n_-/n_f may also decrease with rising temperature if healing is accelerated.

(2) The difference between the growth curves at low and high temperatures (paragraphs 3, 4, and 5 of Sec. II). If the number of electrons liberated from the filled bands does not change radically with temperature, one may assume from the experiments of Harten and Duerig that many more free electrons are produced than F- or F'-centers. Further, the presence of a strong α-band at 80°K (paragraph 10 of Sec. II) indicates that a larger number of stable negative-ion vacancies are produced at low temperatures than F- and F'-centers.[26] A reasonable assumption is that traps with very large macroscopic cross sections form which capture most of the electrons. One possibility is that a hole center captures an electron, e.g., a center made of two holes and a positive-ion vacancy could trap an electron resulting in a center composed of one hole and a positive-ion vacancy. Thus the rate of F-center formation depends on the fraction of free electrons which can be captured in negative-ion vacancies. One would expect this fraction to be temperature dependent as are the V-bands.[9] This may account for the variations in the growth rate curves.

At high temperatures an additional effect must be considered (see also reference 4). Here the x-rays or the free electrons may bleach the F-centers which have been formed. Probably the bleaching effect during the irradiation accounts for the saturation effects which are observed at high temperatures and accounts for the difference between the high and low temperature growth rate curves. At present the data are too meagre to justify detailed calculations. Przibram[27] has made several suggestions as to how this could be done. The bleaching effect should be small at low temperatures where the excited F-center is stable.

(3) Low density of F-centers produced by excitons (paragraph 9 of Sec. II). The low concentration of F-centers produced by excitons can be explained on the above hypothesis, i.e., there are very few negative-ion vacancies present in the crystal at room temperature and only these vacancies can trap excitons to generate F-centers. This assumption of a small number of virgin vacancies is supported by the absence of the α-band before irradiation. If excitons can produce F-centers by dissociating weakly bound vacancy clusters, the number of such clusters must be small, especially in some pure synthetic crystals (see Schröder, reference 21).

(4) Reproducibility of growth rate curves (paragraph 11 of Sec. II). On the picture presented here, one would assume that the ions which have been displaced by the x-ray find their original position by a relatively simple process. This suggests that the ion vacancies may be refilled by a diffusion of a nearby imperfection.

(5) Belar's experiments:[18] Experiments on natural NaCl indicate that a rather complex process occurs during γ-irradiation. Six samples were exposed to

[26] W. Martienssen (see added note at end) has suggested that fewer free electrons are produced at low temperature. This seems possible since excited ionic states may not dissociate at low temperatures. On the other hand, data taken at this laboratory show that only a very small fraction of the electrons released from F'-centers exposed to light are trapped in negative-ion vacancies at low temperature. This latter fact tends to support the idea that only a small fraction of the free electrons are captured by the α-centers. One would expect the probability for a recombination of an electron and a hole to be small. Although the microscopic cross section may be high, the macroscopic cross section is probably small because of the low concentration of free holes and free electrons since they have a short mean free life.

[27] K. Przibram, Wien. Ber. IIa 135, 197 (1926).

radium radiation. They were so placed that the radiation per unit time varied from 100 to 1 on a relative scale. The values observed after long exposure (see Fig. 3) showed that the final level is not directly proportional to the rate of irradiation. Colloidal bands of the type predicted by Savostianowa[28] seem to appear after heating the crystals exposed to intense sources for a year, although the bands did not appear in crystals exposed to the weaker sources. Although more work on this effect is needed, these experiments indicate the complexity of the process.

(6) Appearance of F'-centers in NaCl and KBr at 5°K (paragraph 6 of Sec. II). Since the growth rate of the F-band does not seem to be directly proportional to the radiation intensity, the number of ion vacancies produced does not seem to be a linear function of the number of quanta absorbed. Belar's experiments and the appearance of F'-centers at 5°K in NaCl and KBr suggest that the production of F'-centers during x-radiation depends on a balance between the number of free electrons, number of F-centers, and the way the irradiation produces vacancies. Under some conditions, perhaps larger intensity of radiation, one would expect F'-centers in KCl at 5°K.

(7) Experiments of Etzel and Maurer[29]: Etzel and Maurer estimate the virgin single vacancies at 550°K to be of the order of 10^{17} per cm^3. This would suggest that the free electrons would initially fill these vacancies and subsequently fill vacancies produced during radiation. The growth rate curves at low temperatures should have a change in slope when the virgin vacancies are filled. Rough estimates, from Fig. 2 of reference 10, suggest the virgin vacancy could be of the order of 10^{17} cm^{-3}, in agreement with Etzel and Maurer's value.

Let us now discuss the diffusion idea. At low temperature one must assume that there is local heating which generates enough energy to cause this diffusion. The author sees the following objection to the diffusion idea:

(a) Smakula's data (paragraph 9 of Sec. II) indicates that inward diffusion does not occur in KBr at 300°K, yet the healing process (paragraph 11 of Sec. II) would require, in contradiction, an outward diffusion at the same temperature.

(b) The pair must break up at liquid helium temperatures in order to keep $P(F) \gg P(F')$. In KI the pair must break up at 80°K, since the α-band appears (paragraph 10 of Sec. II), but not at 300°K; this contradicts the stability ideas.

Several other more complicated possibilities exist. One suggestion is that the pair may diffuse into the crystal because of local heating and the following reactions may take place:

$$(V_+V_-)+e_-\rightarrow(V_+V_-e_-); \tag{3}$$

$$(V_+V_-e_-)\rightarrow V_++F \quad \text{due to diffusion.} \tag{4}$$

A hole in turn may cause the reaction

$$F+e_+\rightarrow V_- \tag{5}$$

Here the symbols have the following meaning: V_+ = positive-ion vacancy; V_- = negative-ion vacancy; e_- = free electron in the conduction band; e_+ = free hole; F = F-center, i.e., (V_-e_-); (V_+V_-) = vacancy pair; and (V_+V_-e) = complex made of a negative-ion vacancy, a positive-ion vacancy and an electron. If a strong repulsion exists between an F-center and a positive-ion vacancy, reaction (4) may occur at very low temperatures. Reaction (5) will generate free negative-ion vacancies which will account for the α-band. At high temperatures the positive-ion vacancies could diffuse forming vacancy pairs which will suppress the α-band.

There is also the possibility that pairs of vacancies diffuse into the crystal and dissociate. They remain dissociated in the colder crystals because of rapid cooling but not at room temperature where recombination is possible.

These arguments indicate that it is possible that vacancy diffusions account for the coloration of crystals at low temperatures, although these hypotheses require rather complex reactions to explain the observed data. Tentative calculations to be given in Sec. VI indicate that the amount of local heating is small. Further, it is hard to relate this to Smakula's data. This favors the alternative hypothesis of incipient vacancies to be discussed in the next section.

A difficulty with the model proposed is immediately apparent. Estermann, Leivo, and Stern[30] measured a density change during the radiation. An approximate correlation between density and concentration of F-centers was found which suggests a diffusion of vacancy pairs into the crystals. Perhaps the explanation lies in the fact that diffusion of incipient vacancies, as suggested, causes local strains in the crystal which reduce the density. In the next section we shall show that Seitz's suggestion reduces the density of the crystal (see Fig. 4).

V. THE INTERACTION OF AN X-RAY WITH A DISTORTION

In this section, the author would like to consider how the negative-ion vacancies are produced during x-raying. Calculations to be given in the next section indicate that the local rise in temperature is small so that vacancies do not seem to be produced by local heating which allows diffusion from grain boundaries. Further, recoil energies for 50-kv photons are also too small to produce interstitial ions and vacancies.

Seitz[4] has suggested that the glide plane of a Taylor dislocation may jump from one plane of atoms to another (see Fig. 4). The "extra plane" associated with the edge dislocation has a jog in it, i.e., there is an extra row of ions which does not go along the entire plane.

[28] M. Savostianowa, Z. Physik **64**, 262 (1930).
[29] A. W. Etzel and R. J. Maurer, J. Chem. Phys. **18**, 1003 (1950).
[30] Estermann, Leivo, and Stern, Phys. Rev. **75**, 627 (1949).

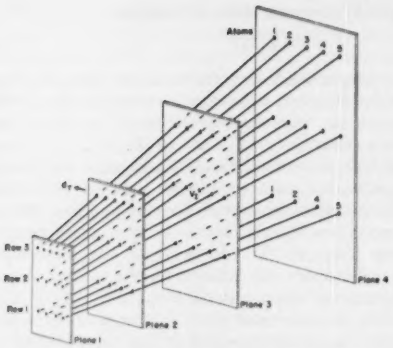

FIG. 4. Schematic drawing of a Seitz jog for a simple cubic crystal. In planes 1 and 2 the extra layer of atoms associated with a Taylor dislocation end in row 3, i.e., atom No. 3 in row 3. In planes 3 and 4 the extra layer reaches row 2, i.e., atoms No. 3 in row 2. Atoms No. 3 are missing in row 1 of all the planes. If atom No. 3 in row 3, plane 2, jumps between atoms No. 2 and No. 4 of row 2 in the same plane, a vacancy will be created in row 3. The jump will cause an expansion of the middle row of atoms in plane 2. This will result in a decrease of the density of the crystal unless row 3 collapses. Note the process considered here causes the dislocation to move at right angles to the Burgers vector, d_T. This should be contrasted to the mechanical problem where the motion occurs along this vector.

It is possible to show that such a jog in an alkali halide has a charge of $\pm\frac{1}{2}e$ associated with it,[21] (e is the charge of an electron). Seitz refers to such a jog as an "incipient vacancy." The term Seitz jog will also be used.

We will now consider a way negative-ion vacancies could be produced in crystals. A slow electron would be attracted to a negative-incipient vacancy and a center (jog center) could be formed at this location. This arrangement is probably not very stable and one of two events may follow:

(1) The center formed at the jog may diffuse away from the dislocation. The diffusion of the center into the lattice causes a negative-ion to jump into the "extra" plane and the Seitz jog moves one lattice distance. Since the charge associated with this jog is half the charge associated with a negative-ion vacancy, one would expect an F-center to be much more stable than a center at the jog. The energy gained by the negative ion which diffuses into the incipient vacancy must also be considered. This will not be attempted here. It is not obvious to the author that energy will be gained by the diffusion of the "jog center"; nevertheless, we shall make this assumption. Some activation energy is probably required to cause the jog center to migrate. This energy probably comes from the electron which is captured at the Seitz jog; or

(2) The jog center, having a negative charge of $\frac{1}{2}e$, may capture a hole, returning the crystal to its original condition. A similarity between the jog center and the F'-center should be noted. Both are charged and tend to attract holes. For this reason one would expect the jog centers which do not migrate to attract holes. This keeps the concentration of jog centers small.

The α-band observed at low temperature during x-radiation seems to be caused by a secondary process. The F-centers form near jogs. Some of these F-centers get bleached by absorbing a hole, thus forming a negative-ion vacancy. These negative-ion vacancies cannot diffuse back to the jog at low temperature and therefore the α-band forms. A period of time may elapse between the formation of the F-center and the formation of the α-center. During this time, the Seitz jog will probably move since more electrons and holes will be captured at the jogs left behind; hence, the α-center need not be near an incipient vacancy although it is near a dislocation.

At low temperatures, about 100°K, the jog center probably does not diffuse very far and remains near the dislocation line. The reason is that the activation energy for diffusion will increase as the center moves away from the jog and the energy the center originally had will be transferred to the lattice. This may account for the difference in the F-centers formed at low and high temperature.[10] The measurements of the width of the F-band formed during x-radiation at low temperature (80°K and below) seem to indicate that it is narrower than when formed at high temperature and cooled to the same low temperature. The change occurs at the long wavelength side of the band. This indicates that the gap between the ground state and excited state of the F-center depends on the position of the centers in the crystal. A possible explanation is that the dislocation affects the frequency spectra of the ionic oscillations which is reflected in the shape of the F-band.

The above hypothesis leads to the following calculations. Assume that next to the surface of a cleaved crystal the density of Taylor dislocations is 10^{10} cm^{-2}. Let us assume the distance between nearest neighbors is $3A$; then the number of vacancies created when a dislocation moves one lattice distance is 3.5×10^{7} cm^{-1}. The motion of interest is at right angles to the dislocation line and the slip direction (see Fig. 4). If every dislocation moves 3 atomic distances, then 10^{18} cm^{-3} F-centers could be produced which agrees roughly with experimental values.[10] If the density of dislocations[4] was as low as 10^{9} cm^{-2}, then the above explanation seems doubtful since the dislocations would move 50 atomic distances. It seems doubtful that the damping of the oscillations will extend over such large distances.

We may summarize the suggestion made as follows:

$$J_-+e_-\rightarrow(J_-e), \qquad \text{(jog centers)} \qquad (7)$$

$$(J_-e_-)\text{ plus diffusion}\rightarrow F, \qquad (F\text{-centers}) \qquad (8)$$

$$F+e_+\rightarrow V_-, \qquad (\alpha\text{-centers}) \qquad (9)$$

or

$$(J_-e_-)+e_+\rightarrow J_-. \qquad (10)$$

J_-, J_+ correspond to negative and positive Seitz jogs.

[21] Reference 5, p. 341, footnote 42.

The large number of negative-ion vacancies postulated in the last section seems to be a result of reaction (9).

Two types of negative-ion vacancies may be considered. One is next to the dislocation and another is in a perfect lattice. It would seem probable that the activation energy for diffusion is lower in the first case than in the second. This may explain why diffusion of negative-ion vacancies seems to occur at room temperature during the healing process (paragraph 11 of Sec. II), although one would not expect such diffusion in a perfect lattice.[32] This further suggests that the stability of some centers depends on where they are located within the crystal which may be a function of the way the alkali halide had been treated.

One must assume that an exciton cannot form *F*-centers from Seitz jogs. The reason may be (1) the exciton is not trapped at an incipient vacancy or (2) the jog center which could form by the dissociation of the exciton does not have sufficient energy to migrate.

VI. LOCAL TEMPERATURE DURING X-RADIATION

The question to be considered in this section is "Does the energy transferred to the lattice raise the local temperature sufficiently to permit the creation of vacancies from Seitz jogs by diffusion?" Since we are interested in a process involving the motion of ions, the temperature of interest is that associated with the vibrational energy of the lattice. Seitz estimates that it takes about 1 ev to produce a vacancy from a jog,[33] so that temperatures of the order of 400°K are required.

If the energy of a 50 kv x-ray were distributed over a sphere of radius 50 atomic units and all of it produced thermal vibrations, then the resulting lattice temperature would be approximately 400°K which is sufficient to produce vacancies from jogs and explains how the crystal increases the number of negative-ion vacancies during x-radiation. If the energy were spread out over a much larger area, however, the local temperature would be too low to account for the vacancies.

The x-rays are attenuated by two processes: scattering from ions and absorption by ions. The second process is followed by the ejection of a photoelectron. The photoelectron further excites secondary electrons into the conduction band. Since the ions have a finite mass, they gain some recoil energy during these processes. This energy is very small and is usually neglected.[34]

The collision between a photon and an ion or between a photoelectron and an ion is a very complex process and a rigorous treatment will not be attempted. It is hoped that the crude approximations made here will give an insight into the problem. We first calculated the recoil energy for various processes occurring within the crystal and then interpreted these results in terms of a temperature. The calculations are based on a 50-kv photon since 50- or 60-kv x-ray tubes have been used to color crystals at low temperatures.[9,10]

(a) Photon and Ion

This situation corresponds to the Compton effect with the electron replaced by an ion. Using the mass of sodium, one finds that the maximum recoil energy is 0.23 ev while the recoil energy averaged over all angles is 0.12 ev.[35] The corresponding values for lithium are 0.76 ev and 0.4 ev.

(b) Electron and Ion

The x-ray may produce photoelectrons of energies equal to the x-ray photon.[36,37] These electrons, 50 kv, will have about ten times the momentum of the photons so that the recoil energies of the ions will be much larger. For a head-on collision the energy transferred to the sodium ion from a 50 kv electron is 4.7 ev. If, however, the electron is deflected 30°, only 0.3 ev are transferred.[38] This value would not be affected if one considers inelastic collisions, provided the ejected electron has a much lower energy than the photoelectron.[39,40]

Seitz[41] estimates that it takes about 25 ev to eject an atom from its normal site; hence, the recoil energy does not create vacancies in a perfect lattice.

Let us now attempt to estimate the rise in temperature due to the scattering of an x-ray by ions. If it is assumed that every ion in a region received 0.12 ev from the photon, the crystal temperature in this region would rise from 5°K to 450°K and various high temperature processes could occur. A highly simplified example will indicate that this assumption is incorrect. Let us assume that the photon is in the middle of a highly condensed gas (i.e., the ions are arranged at random), say at P, and that the scattering is isotropic.[42] Further, we shall assume that the x-ray is not absorbed by an ion before

[32] Reference 2, p. 401.
[33] Reference 6, p. 52.
[34] P. A. Ross and P. Kirkpatrick, Phys. Rev. 45, 223 (1934) have considered a case when the ion has a finite mass.
[35] H. Semat, *Atomic Physics* (Rineheart & Company, New York, 1946), p. 141.
[36] We neglect the binding energy to the ion which for Na is small compared to 50 kv. See for example reference 37, p. 796.
[37] A. H. Compton and S. K. Allison, *X-Rays in Theory and Experiment* (D. Van Nostrand Company, Inc., New York, 1935), second edition.
[38] See H. Soodak and E. C. Campbell, *Elementary Pile Theory* (John Wiley & Sons, Inc., New York, 1950), p. 4.
[39] Mott and Massey (reference 40, p. 227 ff) have considered the inelastic scattering from hydrogen atoms. If the incoming electron has the energy of 300 ev, the most probable value of the ejected electron is 2.5 ev. One might suspect this to be true in our case and that the ejected electrons are of much lower energy. Further the maximum cross section occurs when there is a conservation of momentum between the bombarding electron and the ejected electron, i.e., no recoil ionic momentum.
[40] N. F. Mott and H. S. W. Massey, *The Theory of Atomic Collisions* (Oxford University Press, New York, 1949).
[41] F. Seitz, Disc. Faraday Soc. 5, 271 (1949).
[42] The distinction between modified and unmodified scattering need not be made if the energy absorbed by electrons bound to the ions is small compared to the energy of the x-ray; hence, we are interested in the total cross section for scattering. Although it is not isotropic, (see reference 37, p. 140 ff), a sizable fraction is scattered through 180°.

it makes n_T collisions. This is the random walk problem. The probability that after n collisions the photon is in unit volume at a distance R from P is

$$W(R, n)=\left(\frac{3}{2\pi}\right)^{\frac{1}{2}}\frac{1}{l^3}\frac{1}{n^{\frac{1}{2}}}\exp(-3R^2/2nl^2), \quad (11)$$

where l is the mean free path.[43]

The total number of times the photon is at R during the n_T collisions is

$$N=\int_1^{n_T} W(R, n)dn.$$

Replacing the upper limit by ∞ and making the substitution $3R^2/2nl^2=z^2$, we obtain

$$N=\frac{3}{\pi^{\frac{1}{2}}}\frac{1}{Rl^2}\int_0^{(R/l)\sqrt{(3/2)}}\exp(-z^2)dz.$$

If the further assumption is made that a collision takes place every time the photon is at a distance a from the center of an ion, we have

total number of collisions

$$=\frac{2}{R_0 l_0^2}\frac{2}{\sqrt{\pi}}\int_0^{(R_0/l_0)\sqrt{(3/2)}}\exp(-z^2)dz, \quad (12)$$

where R_0 and l_0 are in units of a. Setting $R_0=l_0=2$ and assuming that the energy transferred per collision is 0.12 ev, we see that the total number of collisions is 0.23, or an ion will receive on the average 0.027 ev of energy corresponding to a rise in temperature of 100°K. Consideration of the nonclassical behavior of the oscillator at low temperature would only raise the temperature slightly.

The large value of the energy transferred when an electron is deflected 180° suggests that the mechanism might account for local heating. Collisions of this type are, however, very rare. Calculations of Mott and Massey[44] based on the Born Approximation and a Fermi-Thomas model of an atom show that the cross section for a deflection through 30° is very small compared to the cross section for a deflection of zero degrees. If $I(\theta)$ is the differential cross section, then for $Z=11$ and a 50-kev electron $I(0)/I(30)$ is about 1.5×10^{-6}; further, if the density of ions is 4×10^{22} per cm^3, the mean free path for scattering through a steradium at 30° is 1.5×10^5 angstroms. Comparison of the tables in reference 44 indicates that consideration of inelastic collision would only decrease the mean path slightly. Evidently the electron occasionally does give some energy to the lattice, but this is not a common occurrence. Since the recoil energy must be shared by many atoms, the actual local heating must be small for a 30° deflection. It would seem that these improbable processes could not explain the darkening at low temperatures.

When an electron is captured by a trapping center or by a hole, some energy must be transferred to the lattice. This energy may be of the order of 5 ev and it would create a local rise in temperature right around the lattice point where the electron was absorbed. This is too localized to cause pair diffusion. It could, however, assist in the evaporation of ion vacancies from a Seitz jog if the trapping was sufficiently near. Trapping at a center resulting from reaction (9) might cause an evaporation of an incipient vacancy. Probably the trapping at the Seitz jog creates the activation energy for the diffusion of the jog centers.

Unquestionably, the above calculations are only approximate and many refinements are possible. The conclusion that the transfer of energy from a 50-kv x-ray to the lattice takes place over many lattice ions, however, seems justified. One would not expect that the local temperatures (over 1000 lattice sites) would vary by several hundred degrees from the macroscopic temperatures.[45] The above arguments do not consider the diffusion of the recoil energy which would tend to lower the local temperature.

VII. CONCLUSIONS AND ACKNOWLEDGMENTS

It has been suggested in this paper that x-radiation and radium radiation produce three effects on the crystals: generation of electrons, generation of holes, and generation of single-ion vacancies by a local perturbation of the lattice rather than by a diffusion of pairs. These vacancies account for the presence of the α-band at low temperature and the very small F'-band at 5°K. This idea seems to explain in a qualitative way the observations on color centers at low temperature. Since the experimental data were gathered from many sources and since these were not designed to test this hypothesis, more experimental work is needed to establish the validity of these suggestions. Theoretical exploration of this idea would be helpful.

The author would like to thank Professor F. Seitz and Professor R. Maurer for a helpful discussion of the paper; Dr. W. H. Duerig for the use of his data; Dr. K. Elder and Miss A. Fogelgren for editorial assistance; and

[43] See S. Chandrasekhar, Revs. Modern Phys. **15**, 1 (1943) especially Eqs. (62), (87), and (93). We assume that our Eq. (11) holds for $n=1$ which is true for Chandrasekhar's Eq. (62). We shall replace a finite sum by an integral which is an approximation.

[44] Reference 40, p. 187, especially Table III, and p. 240, especially Table II.

[45] An insulator heats up during the x-radiation because the material is unable to conduct the heat away. If a 50-kv x-ray tube is run at 50 ma, 600 calories are produced per second. Probably no more than 1 percent fall on the crystal, however. At 5°K alkali halides are good heat conductors so that large macroscopic temperatures would not be expected. See W. J. de Haas and T. Biermasz, Physica **4**, 752 (1937).

Miss D. Rubenfeld for designing Fig. 4. Finally, the author would like to thank his wife for her encouragement.

Note added after completion of the paper: The content of this paper was presented at the Columbus meeting of the American Physical Society, March 22, before which time the details of the paper were worked out. At that meeting, the author obtained a copy of an unpublished paper by W. Martienssen, "Photochemische Vorgänge in Alkalihalogenidkristallen" [see Z. Physik 131, 488 (1952)]. The suggestion is made in this paper that x-rays generate vacancies. Martienssen does not, however, examine in detail the consequences of this idea, nor does he suggest any detail regarding the mechanism of vacancy formation. The production of a strong α-band at 20°K in KBr reported in this paper (see also W. Martienssen, Naturwiss. 38, 482 (1951)) has caused a slight revision of Sec. IV.

PHYSICAL REVIEW VOLUME 88, NUMBER 3 NOVEMBER 1, 1952

Photoproduction of Mesons in Deuterium*

MELVIN LAX
Department of Physics, Syracuse University, Syracuse, New York

AND

HERMAN FESHBACH
Department of Physics and Laboratory for Nuclear Science and Engineering, Massachusetts Institute of Technology, Cambridge, Massachusetts

(Received June 12, 1952)

The production of positive mesons by photons incident on deuterium is calculated in terms of an effective Hamiltonian containing one term which is independent of and another which depends upon the nucleon spin. The meson spectrum at a given angle to the incident photon beam is evaluated at high photon energies by the closure approximation. At low and intermediate energies the closure approximation is not made, but the neutron-neutron force in the final nucleon state is neglected. These spectra have been integrated over a bremsstrahlung spectrum. The total cross section is found at high photon energies and near the threshold for meson production. It is found that the meson spectrum for small angles is sensitive to the relative size of the spin dependent and spin independent terms.

I. INTRODUCTION

THE production of mesons by photons on deuterium is particularly sensitive to the details of the effective Hamiltonian describing the coupling among the photon, meson and nucleon fields. Its charge dependence is revealed by comparing the production of negative and positive mesons. Its spin dependence affects the variation of the total cross section as a function of the energy of the incident photons, the angular distribution and the energy spectrum of the mesons produced at a given angle. These last effects are a consequence of the Pauli exclusion principle[1] and are thus particularly important at small angles where the recoil neutrons have small relative momenta.

On the other hand, the deuteron is the simplest example of a target with structure. It may therefore be employed to test some of the approximate results given earlier for photo-meson production in nuclei.[2] There are, however, some significant differences from the case of heavy nuclei inasmuch as the mass of the residual nucleus is comparable to that of the particle absorbing the photon.

In the present paper we shall employ the same phenomonological treatment as that employed in reference 2, wherein it is assumed that the meson-photon interaction with a nucleus may be treated as a sum of the interactions with the individual nucleons. This clearly neglects cooperative higher order effects such as those given by exchange currents, and the scattering and absorption of the meson produced by one nucleon by another. These should be small in deuterium because of its relatively large structure and the relatively small nucleon scattering amplitude.[3] Once these assumptions are made, it is possible to affect all spin sums and reduce the calculation to quadratures. Further progress requires some statement on (1) the dependence of the effective Hamiltonian on nucleon momenta and (2) on the nature of the interaction of the two residual neutrons. We have omitted both possibilities for reasons of simplicity. The omission of the first of these may be of importance in computing the negative to positive meson production ratio. The second omission is invalid for final states in which the relative kinetic energy of the nucleons is small, i.e., near threshold, at the high energy end of the meson spectrum, or for mesons produced at small angles. A more precise calculation is now in progress.[4]

A similar treatment of this problem has been simul-

* This paper was presented to the American Physical Society. See Phys. Rev. 82, 324 (1951).

[1] H. Feshbach and M. Lax, Phys. Rev. 76, 134, 689 (1949).

[2] M. Lax and H. Feshbach, Phys. Rev. 81, 761 (1951).

[3] G. Chew and H. Lewis, Phys. Rev. 84, 779 (1951).

[4] Feshbach, Goldberger, and Villars, private communication.

taneously developed by Chew and Lewis,[3] in which, however, the attention was focused on the distribution of nucleon recoils whereas our primary interest here will be in the energy spectrum of the mesons at a given production angle. Other theoretical investigations have been made by Machida and Tamura[5] and Morpurgo.[6]

II. GENERAL CONSIDERATIONS

We, as well as Chew and Lewis, employ a notation similar to that developed in reference 2. If $\mathbf{D}$ is the initial deuteron momentum, $D_0=(4M^2+D^2)^{\frac{1}{2}}$ its total energy, and $\mathbf{D}'$ the momentum of the center of gravity of the residual nuclear system, the total cross section takes the form

$$d\sigma=(2\pi)^{-2}(1+(D/D_0))^{-1}\int\int|Q|^2 d\mathbf{q}\,d\mathbf{D}'\,d\mathbf{k}\,\delta(\epsilon+\mu_0+(k^2/M)+(D'^2/4M)-\nu_0-(D^2/4M)), \quad (1)$$

where $\mathbf{q}$ is the meson momentum, μ_0 its energy, k^2/M the final relative kinetic energy, ϵ is the deuteron binding energy, ν_0 is the incident photon energy. The δ-function is just the condition for energy conservation. The matrix element Q is taken between the initial and final nuclear states of the operator:

$$T=T_1+T_2,\qquad T_i=(\boldsymbol{\sigma}_i\cdot\mathbf{K}+L)\exp[i(\mathbf{v}-\mathbf{q})\cdot\mathbf{x}_i]\tau_i^+. \quad (2)$$

$\mathbf{K}$ and L will, in general, depend upon the momentum and energy of the three particles: photon, meson, and proton. This form, i.e., its representation as a sum of two terms involving each particle separately, neglects the possibility that T contain a term which depends, in a nonseparable fashion, on the coordinates of both particles, 1 and 2.

$|Q|^2$ must be summed over the final and averaged over the initial spin and isotopic spin states. The initial deuteron is a spin triple, an isotopic spin singlet:

$$|i\rangle=2^{-\frac{1}{2}}[p(1)n(2)-p(2)n(1)]^3\chi_m(u(\rho)/\rho)(2\pi)^{-\frac{1}{2}}\times\exp[i(\mathbf{D}\cdot\mathbf{R})], \quad (3)$$

where $\mathbf{R}=(\mathbf{x}_1+\mathbf{x}_2)/2$ is the center-of-mass coordinate, $\boldsymbol{\rho}=\mathbf{x}_1-\mathbf{x}_2$ the relative coordinate, and ${}^3\chi_m$ is the triplet spin function, m being the z component of the total spin.

The final state consists of two neutrons, an isotopic triplet, with relative momentum k. The Pauli principle requires separate consideration of the two final states, one that is symmetric and one that is antisymmetric in space:

$$|f_e\rangle=(2\pi)^{-\frac{1}{2}}n(1)n(2)^1\chi_0 u_{f,e}(\mathbf{k}\cdot\boldsymbol{\rho})\exp[i\mathbf{D}'\cdot\mathbf{R}], \quad (4a)$$

$$|f_o\rangle=(2\pi)^{-\frac{1}{2}}n(1)n(2)^3\chi_{m'}u_{f,e}(\mathbf{k}\cdot\boldsymbol{\rho})\exp[i\mathbf{D}'\cdot\mathbf{R}]. \quad (4b)$$

We now introduce (2), (4a), or (4b) into Q. The integration over R leads to requirement of conservation of momentum so that after integration over $d\mathbf{D}'$ in (1) one may make the replacement $\mathbf{D}'=\mathbf{D}+\mathbf{v}-\mathbf{q}$.

The matrix elements for the symmetric and antisymmetric cases become, respectively,

$$Q_e=2^{-\frac{1}{2}}\langle{}^1\chi_0|\,\mathbf{K}\cdot(\boldsymbol{\sigma}_1-\boldsymbol{\sigma}_2)\,|{}^3\chi_m\rangle E, \quad (5a)$$

$$Q_o=i2^{-\frac{1}{2}}\langle{}^3\chi_{m'}|\,\mathbf{K}\cdot(\boldsymbol{\sigma}_1+\boldsymbol{\sigma}_2)+2L\,|{}^3\chi_m\rangle O, \quad (5b)$$

where

$$E=\int u_{f,e}^*(\mathbf{k}\cdot\boldsymbol{\rho})\cos(\mathbf{k}_0\cdot\boldsymbol{\rho})[u(\rho)/\rho]d\boldsymbol{\rho}, \quad (6a)$$

$$O=\int u_{f,e}^*(\mathbf{k}\cdot\boldsymbol{\rho})\sin(\mathbf{k}_0\cdot\boldsymbol{\rho})[u(\rho)/\rho]d\boldsymbol{\rho},\qquad \mathbf{k}_0=\tfrac{1}{2}(\mathbf{v}-\mathbf{q}). \quad (6b)$$

One may already see from (5) that only $\mathbf{K}$ is effective in changing the spin state of the deuteron. Moreover, it is also clear from (6) that O approaches zero at threshold ($\mathbf{k}=0$), so that the presence or absence of a spin-flip term $\mathbf{K}$ will be strongly reflected in the energy dependence of Q.

To proceed further, (5a) and (5b) are squared, summed over final, and averaged over initial spin states with the result

$$|Q|^2=\tfrac{2}{3}|\,\mathbf{K}|^2E^2+[(4/3)|\,\mathbf{K}|^2+2|\,L|^2]O^2. \quad (7)$$

The cross section can according to (1) be written in the form

$$d\sigma=(2\pi)^{-2}(1+D/D_0)^{-1}|H|^2 d\mathbf{q}, \quad (8)$$

where

$$|H|^2=\int|Q|^2 d\mathbf{k}\,\delta,$$

and

$$\delta=\delta(\epsilon+\mu_0+(k^2/M)+(\mathbf{D}+\mathbf{v}-\mathbf{q})^2/4M-\nu_0-(D^2/4M)).$$

Since the final states u_f are either even or odd, it is conventional to carry the integration only over half of k space. We may extend the integration over all of k space providing the normalization of the final states is taken to be

$$\int u_{f,e}^*(\mathbf{k}\cdot\boldsymbol{\rho})u_{f,e}(\mathbf{k}'\cdot\boldsymbol{\rho})d\boldsymbol{\rho}=\tfrac{1}{2}[\delta(\mathbf{k}-\mathbf{k}')+\delta(\mathbf{k}+\mathbf{k}')];$$

$$\int u_{f,e}^*(\mathbf{k}\cdot\boldsymbol{\rho})u_{f,0}(\mathbf{k}'\cdot\boldsymbol{\rho})d\boldsymbol{\rho}=\tfrac{1}{2}[\delta(\mathbf{k}-\mathbf{k}')-\delta(\mathbf{k}+\mathbf{k}')].$$

(Conventional normalization would omit the factor $\frac{1}{2}$ on the right-hand side of these equations.)

III. DIFFERENTIAL SPECTRUM

High Photon Energies

At high photon energies we might expect (1) the deuteron cross section to approach the corresponding

[5] S. Machida and T. Tamura, Prog. Theoret. Phys. **6**, 57 (1951).
[6] G. Morpurgo, Nuovo cimento **7**, 855 (1950).

hydrogen cross section and (2) the struck proton to absorb all the recoil momentum. The second point is verified, in our calculations by the fact that the matrix elements E and O have a strong resonance near $k=k_0=(\nu-\mu)/2$. If we insert $\mathbf{k}=\mathbf{k}_0$, $\mathbf{D}=0$, $\epsilon=0$ into the energy conservation delta-function (8) we obtain the free proton conservation condition: $\delta_p=\delta(\mu_0+(\nu-\mu)^2/2M-\nu_0)$. The delta-function can now be removed from the integral over k space in (8). The integrals over E^2 and O^2 can be performed exactly with the help of the closure properties,

$$\int u_{f,e}^*(\mathbf{k}\cdot\rho)u_{f,e}(\mathbf{k}\cdot\rho')d\mathbf{k}=\tfrac{1}{2}[\delta(\rho-\rho')+\delta(\rho+\rho')],$$

$$\int u_{f,o}^*(\mathbf{k}\cdot\rho)u_{f,o}(\mathbf{k}\cdot\rho')d\mathbf{k}=\tfrac{1}{2}[\delta(\rho-\rho')-\delta(\rho+\rho')].$$

The resulting "closure" matrix element,

$$|H|^2=\{[|\mathbf{K}|^2+|L|^2]-[\tfrac{1}{3}|\mathbf{K}|^2+|L|^2]V\}\delta_p, \quad (9)$$

where

$$V=\int \cos(\nu-\mu)\cdot\rho[u(\rho)/\rho]^2d\rho$$

has a first term exactly in agreement with the corresponding free proton matrix element. The second, "two-particle" term contains the interference integral V. If we use the approximate deuteron wave function given later in Eq. (15), V may be evaluated exactly and is given in Fig. 1. V decreases rapidly as $|\nu-\mu|$ increases so that for a given ν the two-particle term can be important only in the small angle region. It is, therefore, in this region only wherein the spin dependence of the effective Hamiltonian plays a role.

It may be emphasized that the closure results obtained here do not involve any specific assumptions concerning the final neutron-neutron state. However, the resulting closure cross section may be expected to be an overestimate, since it includes contributions from final states that are not energetically permissible. It should be accurate for high photon energies.

Low and Intermediate Photon Energies

In order to obtain an estimate of the cross section at intermediate or low energies, we must abandon the closure approximation. To simplify our calculations, however, we shall neglect the neutron-neutron interaction and use final states of the form:

$$\begin{aligned} u_{f,e}(\mathbf{k}\cdot\rho)&=(2\pi)^{-\frac{1}{2}}\cos(\mathbf{k}\cdot\rho),\\ u_{f,o}(\mathbf{k}\cdot\rho)&=(2\pi)^{-\frac{1}{2}}\sin(\mathbf{k}\cdot\rho).\end{aligned} \quad (10)$$

This approximation affects most seriously the high energy end of the meson spectrum since there the neutrons part with a low velocity. Its effects on the total cross section is not likely to be serious except in the immediate neighborhood of threshold. (This lack of sensitiveness of the cross section to the choice of final state arises because a partial closure sum must be performed. A complete closure is entirely independent of the choice of final state.)

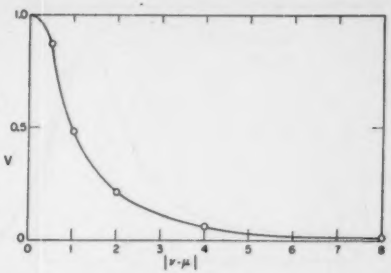

FIG. 1. The function $V(|\nu-\mu|)$.

With the choice (10) E and O may be expressed in the form

$$\begin{aligned} 2E&=C(\mathbf{k}-\mathbf{k}_0)+C(\mathbf{k}+\mathbf{k}_0),\\ 2O&=C(\mathbf{k}-\mathbf{k}_0)-C(\mathbf{k}+\mathbf{k}_0),\end{aligned} \quad (11)$$

where $C(\mathbf{k})$ is the normalized deuteron wave function in momentum space:

$$C(\mathbf{k})=(2\pi)^{-\frac{1}{2}}\int \exp[i\mathbf{k}\cdot\rho][u(\rho)/\rho]d\rho. \quad (12)$$

Referring to (7) and (8), $|H|^2$ takes the form

$$|H|^2=(|\mathbf{K}|^2+|L|^2)\int |C(\mathbf{k}-\mathbf{k}_0)|^2\delta d\mathbf{k}$$

$$-(\tfrac{1}{3}|\mathbf{K}|^2+|L|^2)\int C(\mathbf{k}-\mathbf{k}_0)C(\mathbf{k}+\mathbf{k}_0)\delta d\mathbf{k}. \quad (13)$$

The deuteron wave function in ordinary space may be represented by

$$u(\rho)=\left[\frac{\alpha}{2\pi(1-\alpha\rho_1)}\right]^{\frac{1}{2}}[e^{-\alpha\rho}-e^{-\beta\rho}], \quad (14)$$

where $\alpha^2=M\epsilon$, ρ_1=effective triplet scattering range, 1.74×10^{-13} cm, and β is given by

$$(3/\beta)\simeq\rho_1[1+(4/9)\alpha\rho_1].$$

The corresponding momentum-space wave function is

$$C(\mathbf{k})=\left[\frac{\alpha}{\pi^2(1-\alpha\rho_1)}\right]^{\frac{1}{2}}\frac{\beta^2-\alpha^2}{(\alpha^2+k^2)(\beta^2+k^2)}. \quad (15)$$

We may now determine the energy and angular distribution of the mesons. It is most convenient to

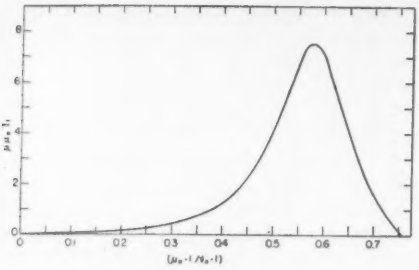

FIG. 2. The function $\mu\mu_0 I_1$ for $\vartheta=90°$ and $\nu=2$.

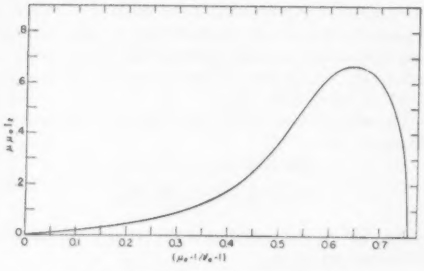

FIG. 3. The function $\mu\mu_0 I_2$ for $\vartheta=90°$ and $\nu=2$.

employ the laboratory system. Hence, from (1) and (3),

$$(d\sigma/d\Omega_\mu d\mu_0)=(2\pi)^{-2}\mu\mu_0[(|\mathbf{K}|^2+|L|^2)I_1 - (\tfrac{1}{2}|\mathbf{K}|^2+|L|^2)I_2], \quad (16a)$$

where

$$I_1=\int |C(\mathbf{k}-\mathbf{k}_0)|^2\delta(\epsilon+\mu_0+(k^2+k_0^2)/M-\nu_0)d\mathbf{k}, \quad (16b)$$

$$I_2=\int C(\mathbf{k}-\mathbf{k}_0)C(\mathbf{k}+\mathbf{k}_0)\delta(\epsilon+\mu_0 +(k^2+k_0^2)/M-\nu_0)d\mathbf{k},$$

where $C(\mathbf{k})$ is given by (15). The integrals I_1 and I_2 may be evaluated exactly:

$$I_1=\frac{2M\alpha k_r}{\pi(1-\alpha\rho_1)}\left[\frac{1}{p_\alpha^4-4k_r^2k_0^2}+\frac{1}{p_\beta^4-4k_r^2k_0^2} -\frac{1}{2k_rk_0(\beta^2-\alpha^2)}\ln\frac{(p_\beta^2-2k_rk_0)(p_\alpha^2+2k_rk_0)}{(p_\beta^2+2k_rk_0)(p_\alpha^2-2k_rk_0)}\right], \quad (17)$$

$$I_2=\frac{M\alpha}{2\pi(1-\alpha\rho_1)}\frac{\beta^2-\alpha^2}{k_0(p_\alpha^2+p_\beta^2)}\left[\frac{1}{p_\alpha^2}\ln\frac{p_\alpha^2+2k_rk_0}{p_\alpha^2-2k_rk_0} -\frac{1}{p_\beta^2}\ln\frac{p_\beta^2+2k_rk_0}{p_\beta^2-2k_rk_0}\right],$$

where

$$k_r^2=M(\nu_0-\mu_0-\epsilon)-k_0^2,$$
$$p_\alpha^2=M(\nu_0-\mu_0-\epsilon)+\alpha^2=M(\nu_0-\mu_0), \quad (18)$$
$$p_\beta^2=M(\nu_0-\mu_0-\epsilon)+\beta^2=M(\nu_0-\mu_0)+\beta^2-\alpha^2.$$

Both I_1 and I_2 go to zero as $k_r=0$, at which μ_0 takes on its maximum value. This maximum value is attained when the maximum available relative energy k_0^2/M is completely converted into meson energy. At this limit,

$$I_1 \underset{k_r\to 0}{\to} \frac{M\alpha}{\pi(1-\alpha\rho_1)}\frac{2(\beta^2-\alpha^2)^2}{p_\alpha^4p_\beta^4}k_r, \quad I_2/I_1 \underset{k_r\to 0}{\to} 1. \quad (19)$$

The fraction of the meson energy spectrum for which these limiting values are valid decreases with increasing ν. Examples[7] of the functions $\mu\mu_0 I_1$ and $\mu\mu_0 I_2$ are given in Fig. 2 and Fig. 3. In agreement with the estimate made in reference 2, $I_2 \ll I_1$, except near the maximum meson energy, near threshold, and for the smaller angles.

Thus at the larger angles and energies the differential spectrum is essentially proportional to $[|\mathbf{K}|^2+|L|^2]$. This combination may also be determined experimentally by measurement of photoproduction of mesons in hydrogen. However, in the hydrogen case this information is available at a given angle for a single meson energy only as given by the Compton relation

$$2\nu(\mu_0-\mu\cos\vartheta)=1+2M(\nu-\mu_0). \quad (20)$$

The experimental results for deuterium are therefore valuable because they extend our knowledge of the value of $|\mathbf{K}|^2+|L|^2$ at a given angle to a range of energies.

At the smaller angles where I_2 is appreciable, a different linear combination of $|\mathbf{K}|^2$ and $|L|^2$ is measured so that at the meson energy given by (20) two different linear combinations of $|\mathbf{K}|^2$ and $|L|^2$ are now available, one from hydrogen and the other from deuterium data. Thus, for meson energies and angles obeying the Compton relation $|\mathbf{K}|^2$ and $|L|^2$ may be determined separately.

These considerations are somewhat academic since the synchrotron does not provide monochromatic x-rays. A direct determination of $|\mathbf{K}|^2$ and $|L|^2$ for a given photon energy from experiment would require data obtained with the bremsstrahlung of electrons with several different energies. The available experimental data are not sufficiently accurate to justify such a direct analysis. We therefore adopt the more realistic approach in which a reasonable dependence of $|\mathbf{K}|^2$ and $|L|^2$ on the energy of the photon and meson is assumed permitting then the integration over a bremsstrahlung spectrum and therefore comparison with experiment.

A reasonable form for this dependence is suggested

[7] Tables of the functions $\mu\mu_0 I_1$ and $\mu\mu_0 I_2$ have been calculated for $\vartheta=26°$, 30°, 45°, 90°, 135° and for values of ν ranging from 1.1 to 2.4. These are available in hectographed form from H.F.

by the pseudoscalar meson theory in the nonrelativistic approximation, which gives

$$|\mathbf{K}|^2 \sim (1/\mu_0\nu_0)\left[1-\frac{\mu^2\sin^2\vartheta[1-(\nu_0-\mu_0)^2]}{2\nu_0^2(\nu-\mu\cos\vartheta)^2}\right]. \quad (21)$$

The dominant term in the energy range of interest is $(1/\mu_0\nu_0)$ which is simply a normalization factor. For the purpose of the integration over ν we may make use of the mean value theorem and replace $|\mathbf{K}|^2$ and $|L|^2$ as follows:

$$|\mathbf{K}|^2 \to \mathcal{K}^2/\mu_0\nu_0, \quad |L|^2 \to \mathcal{L}^2/\mu_0\nu_0. \quad (22)$$

We have inserted these forms into (16) and assumed a $(d\nu/\nu)$ bremsstrahlung spectrum with a maximum ν of 2.4, which is close to currently available synchrotron energies. These results are given in Fig. 4 and Fig. 5 for several different values of ϑ. The sensitivity of the results at small angles to the spin dependence of the effective Hamiltonian is maintained. Comparison of the small angle results with the hydrogen cross section or with the deuterium cross section for large values of the angle ϑ will determine the values of $\mathcal{K}^2$ and $\mathcal{L}^2$. Experimental evidence[8] indicates that $\mathcal{K}^2 \gg \mathcal{L}^2$, that is, the spin dependent term of the effective Hamiltonian is dominant.

Finally we turn to the examination of the spectrum for $\nu \gg \alpha$ and $\nu \gg \beta$, respectively. The results are most easily seen if we consider (17) in the limit $\beta \to \infty$; then

$$I_1 = \frac{2M\alpha}{\pi}\frac{k_r}{[\alpha^2+(k_r-k_0)^2][\alpha^2+(k_r+k_0)^2]},$$
$$I_2 = \frac{M\alpha}{2\pi}\frac{1}{k_0(k_r^2+k_0^2+\alpha^2)}\ln\frac{\alpha^2+(k_r+k_0)^2}{\alpha^2+(k_r-k_0)^2}. \quad (23)$$

For large ν, I_1 approaches the free proton value $\delta_p = \delta[\nu_0-\mu_0-(\nu-\mu)^2/2M]$ while $I_2 \to 0$. Both of these behaviors are apparent from (23). Employing

$$\alpha/[\pi(x^2+\alpha^2)] \to \delta(x),$$

we see that

$$I_1 \to (M/2k_r)[\delta(k_r-k_0)+\delta(k_r+k_0)] = \delta[(k_r^2-k_0^2)/M] = \delta_p,$$

which is the expected result if the deuteron binding energy is placed equal to zero. This derivation indicates that the free proton value is assumed when $|\nu-\psi| \gg \alpha$. This is, of course, true only in the limit $\beta \to \infty$. If β is kept finite, then the deuteron momentum wave function does not have as great an extension in momentum space so that the free proton value is assumed somewhat earlier.

IV. TOTAL CROSS SECTION

The total cross section will be evaluated in two energy regions (1) photon energies well above threshold and (2) photon energies near the threshold for meson production.

[8] Lebow, Feld, Frisch, and Osborne, Phys. Rev. 85, 681 (1952).

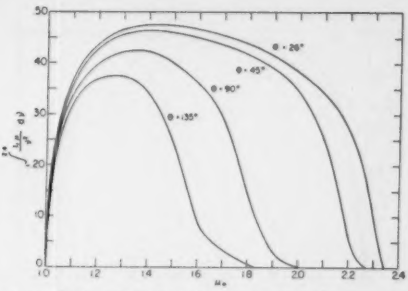

FIG. 4. The integral $\int_1^{\nu_0}(\mu I_1/\nu^2)d\nu$. To obtain the meson spectrum multiply the ordinate by $\mathcal{K}^2+\mathcal{L}^2$ and subtract $\frac{1}{3}\mathcal{K}^2+\mathcal{L}^2$ times the ordinate of the corresponding curve plotted in Fig. 5.

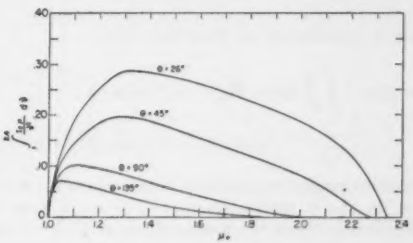

FIG. 5. The integral $\int_1^{\nu_0}(\mu I_2/\nu^2)d\nu$.

Cross Sections for High Photon Energies

A first approximation to the cross section at high energies may be based on the closure approximation (9). Comparison with the free proton cross section gives the ratio

$$\frac{\sigma_D}{\sigma_p} \to 1-\frac{\int(\tfrac{1}{3}|\mathbf{K}|^2+|L|^2)V\delta_p d\psi}{\int(|\mathbf{K}|^2+|L|^2)\delta_p d\psi}. \quad (24)$$

The second term gives the reduction of the cross section for large values of ν because of the Pauli exclusion principle and other interference effects.

There is another reduction of the cross section which enters because of the assumption on the k integration which was made in obtaining (24). It is only asymptotically true that the k integration may be extended over all of k space. Indeed, for energies sufficiently close to threshold the integration in k space is restricted by momentum and energy considerations. We may obtain an estimate of this effect by employing a technique developed in reference 2. Consider first the single

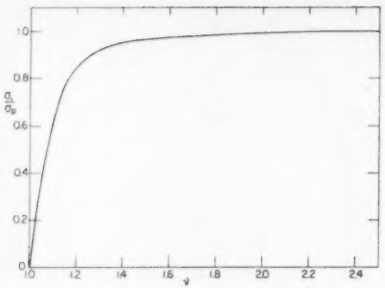

FIG. 6. The ratio of the "single" particle contribution to the total production cross section and the total production cross section in hydrogen.

particle contribution σ_1. Then from (13),

$$\sigma_1=(2\pi)^{-2}\int\int d\mathbf{y}d\mathbf{k}(|\mathbf{K}|^2+|L|^2)|C(\mathbf{k}-\mathbf{k}_0)|^2 \times\delta(\mu_0+\epsilon+(k^2+k_0^2)/M-\nu_0). \quad (25)$$

We now change the variable of integration to $\mathbf{k}'=\mathbf{k}-\mathbf{k}_0$ and do the $\mathbf{y}$ integration first. The result may be expressed in terms of an integration of $|C(\mathbf{k}')|^2$ over an effective cross section:

$$\sigma_1=\int d\mathbf{k}'|C(\mathbf{k}')|^2\sigma(\mathbf{v},\mathbf{k}',\nu_0), \quad (26)$$

where

$$\sigma(\mathbf{v},\mathbf{k}',\nu_0)=(2\pi)^{-2}\int d\mathbf{y}(|\mathbf{K}|^2+|L|^2)\delta(\mu_0+\epsilon +((\mathbf{k}'+\mathbf{k}_0)^2+k_0^2)/M-\nu_0).$$

The range of integration on $\mathbf{k}'$ is limited by the energy delta-function to a sphere,

$$|\mathbf{k}'+(\mathbf{v}/2)|\lesssim[M(\nu_0-\nu_t)]^{\frac{1}{2}}=d, \quad (27)$$

where ν_t is the threshold energy. We note that for large ν, $C(\mathbf{k}')$ has a strong maximum at $k'=0$, so that $\sigma(\mathbf{v},\mathbf{k}',\nu_0)$ may be approximated by $\sigma(\mathbf{v},0,\nu_0)$, in other words, by the free proton cross section. Hence,

$$\sigma_1/\sigma_p\underset{\nu\gg 1}{\rightarrow}\int|C(\mathbf{k}')|^2d\mathbf{k}', \quad (28)$$

where the range of integration is limited according to (27). Roughly speaking, as (27) and (28) show, we are concerned with the overlap between two spheres in momentum space, one centered at the origin and of radius of the order of α, the other centered at $(-\nu/2)$ of radius d. The closure approximation will be valid when these spheres overlap completely, that is, when d is several times greater than $(\alpha+\nu/2)$ or for ν at about 200 Mev. Integration of (28) yields

$$\pi(1-\alpha\rho_1)\frac{\sigma_1}{\sigma_p}=\frac{\beta^2+3\alpha^2}{\beta^2-\alpha^2}\left[\tan^{-1}\frac{d-\frac{1}{2}\nu}{\alpha}+\tan^{-1}\frac{d+\frac{1}{2}\nu}{\alpha}\right] -\frac{\alpha(\alpha^2+3\beta^2)}{\beta(\beta^2-\alpha^2)}\left[\tan^{-1}\frac{d-\frac{1}{2}\nu}{\beta}+\tan^{-1}\frac{d+\frac{1}{2}\nu}{\beta}\right] -\frac{\alpha}{\nu}\left[1+\frac{2(d^2-\frac{1}{4}\nu^2+\alpha^2)}{\beta^2-\alpha^2}\right]\ln\frac{\alpha^2+(d+\frac{1}{2}\nu)^2}{\alpha^2+(d-\frac{1}{2}\nu)^2} -\frac{\alpha}{\nu}\left[1-\frac{2(d^2-\frac{1}{4}\nu^2+\beta^2)}{\beta^2-\alpha^2}\right]\ln\frac{\beta^2+(d+\frac{1}{2}\nu)^2}{\beta^2+(d-\frac{1}{2}\nu)^2}. \quad (29)$$

A curve giving σ_1/σ_p as a function of ν is plotted in Fig. 6, showing that 90 percent of the high energy limit is obtained at $\nu=1.3$ or at $\nu=180$ Mev.

From σ_1/σ_p we must subtract σ_2 as obtained from

$$\sigma_2=(2\pi)^{-2}\int(\tfrac{1}{2}|\mathbf{K}|^2+|L|^2)I_2d\mathbf{y}. \quad (30)$$

It was not possible to evaluate σ_2 analytically. Instead the following approximate evaluation was employed:

$$\sigma_2\simeq\sigma_2(\text{closure})R,$$

where

$$R=\lim(\sigma_2/\sigma_2(\text{closure}))\quad\text{as}\quad\alpha\rightarrow 0\quad\text{and}\quad\beta\rightarrow\infty.$$

The quantity $\sigma_2(\text{closure})$ is given in Eq. (24) as $\int(\frac{1}{2}|\mathbf{K}|^2+L^2)V\delta_2d\mu$ where V is given in Eq. (9). Both $\sigma_2(\text{closure})$ and R may be easily evaluated if Eq. (22) is inserted for $|\mathbf{K}|^2$ and L^2.

The ratio $\sigma_2(\mathfrak{K}^2+\mathfrak{L}^2)/\sigma_p(\frac{1}{2}\mathfrak{K}^2+\mathfrak{L}^2)$ is plotted in Fig. 7. We see that it decreases like a (constant/ν) for ν large, rises to a maximum rather near threshold, and then drops to zero at threshold. We note that σ_2 is much smaller than σ_1, being at most a ten percent correction except near threshold for the case of no spin flip $K=0$, and being at most on third of this for $L=0$. Hence, in the deuteron the effect of the Pauli exclusion principle on the total cross section is negligible except near threshold in accordance with the assumptions made on reference 2.

Cross Section Near Threshold

We shall only quote the results of our calculations, since the approximation neglecting the neutron-neutron interaction is particularly poor here. We find that

$$\sigma_D/\sigma_p\simeq\frac{\pi^2}{3\sqrt{2}}\frac{(M+1)^2}{(2M+1)^{\frac{1}{2}}}\frac{\langle|\mathbf{K}|^2\rangle}{\langle|\mathbf{K}|^2\rangle+\langle|L|^2\rangle} \times|C(-\nu_t/2)|^2(\nu-\nu_t)^{\frac{1}{2}}, \quad (31)$$

where we have neglected the difference between free proton and deuteron thresholds. The quantities $\langle|\mathbf{K}|^2\rangle$

and $\langle|L|^2\rangle$ are the averages over angle. Inserting numerical values, (31) becomes

$$\sigma_D/\sigma_p \simeq 14.3(\nu-\nu_t)^{\frac{1}{2}}\langle|\mathbf{K}|^2\rangle/\langle|\mathbf{K}|^2+|L|^2\rangle. \quad (32)$$

We are indebted to G. Chew for many informative discussions. *Note added in proof:* Calculations similar to those of this paper are reported by Saito, Watanabe, and Yamaguchi, Prog. Theoret. Phys. **7**, 103 (1952).

APPENDIX

A comparison of the experimental ratio of photomeson production in deuterium to that in hydrogen cannot be made directly against the cross-sectional ratio σ_D/σ_p. The theoretical cross sections must first be averaged over a bremsstrahlung spectrum before taking the ratio. Using the assumption of Eq. (22), the experimental ratio of differential cross sections is to be compared with

$$\frac{\int(d\sigma_D/d\Omega_\mu d\mu_0)(d\nu/\nu)}{\int(d\sigma_p/d\Omega_\mu d\mu_0)(d\nu/\nu)} = \frac{\int(\mu I_1/\nu^2)d\nu-\gamma\int(\mu I_2/\nu^2)d\nu}{\int(\mu I_p/\nu^2)d\nu}, \quad (A1)$$

where

$$\gamma=(\tfrac{1}{3}\mathcal{K}^2+\mathcal{L}^2)/(\mathcal{K}^2+\mathcal{L}^2), \quad (A2)$$

$$I_p=\delta((M^2+(\nu-\mu)^2)^{\frac{1}{2}}+\mu_0-\nu_0-M), \quad (A3)$$

and we have used Eq. (5) reference 2 for the proton cross section. (A factor $(2\pi)^{-2}(\mathcal{K}^2+\mathcal{L}^2)$ was cancelled in simplifying the right-hand side of (A1).

The numerator of (A1) is supplied by Eq. (17) and Figs. 4 and 5. The denominator can be integrated immediately:

$$\int(\mu I_p/\nu^2)d\nu = (M+\nu_c-\mu_0)\mu/[(M-\mu_0+\mu\cos\vartheta)\nu_c^2], \quad (A4)$$

where ν_c is the Compton photon energy (20),

$$\nu_c=\frac{\mu_0-(1/2M)}{1-(\mu_0-\mu\cos\vartheta)/M}. \quad (A5)$$

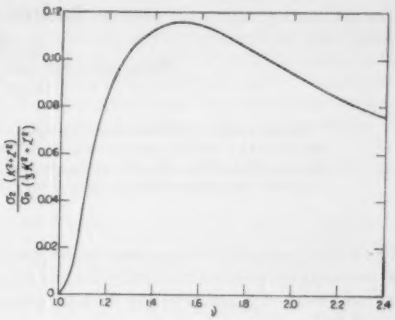

FIG. 7. $\sigma_2(\mathcal{K}^2+\mathcal{L}^2)/\sigma_p(\frac{1}{3}\mathcal{K}^2+\mathcal{L}^2)$.

Inserting (A5) into (A4) we obtain

$$\int(\mu I_p/\nu^2)d\nu = \mu\left(1-\frac{\mu_0}{M}\right)\left(1-\frac{\mu_0-\mu\cos\vartheta}{M}\right)\left(\mu_0-\frac{1}{2M}\right)^{-2} + M^{-1}\mu[\mu_0-(1/2M)]^{-1}, \quad (A6)$$

the lower limit on the spectrum (A6) is $\mu_0=1$. The upper limit is $\bar{\mu}_0=\mu_0{}^c(\bar{\nu},\vartheta)$ where $\mu_0{}^c(\nu,\vartheta)$ is the Compton meson energy obtained by solving (A5) for μ_0:

$$\mu_0{}^c=\frac{[\nu+(1/2M)][1+(\nu/M)] \pm(\nu/M)\cos\vartheta[(\nu+(1/2M))^2-\lambda]^{\frac{1}{2}}}{\lambda}, \quad (A7)$$

where $\lambda=1+2(\nu/M)+(\nu/M)^2\sin^2\vartheta$ and $\bar{\nu}$ is the upper end of the bremsstrahlung spectrum.

A comparison of the angular distribution in the deuteron and proton case requires that we evaluate $\int(\mu I_p/\nu^2)d\nu d\mu_c$. Expanding (A6) in inverse powers of M, the result to terms of order M^{-2} is

$$\begin{aligned}\int(\mu I_p/\nu^2)d\nu d\mu_0 = {}&\ln(\mu+\mu_0)-(\mu/\mu_0)\\ &+M^{-1}[(\mu_0+\mu_0{}^{-1}-2)\cos\vartheta-\mu\\ &+(3/2)\cos^{-1}(1/\mu_0)-(\mu/2\mu_0{}^2)]\\ &+\tfrac{1}{2}M^{-2}[\mu_0\mu-\cos\vartheta(\mu_0{}^2-\mu_0{}^{-2}\\ &-4\ln\mu_0)-\tfrac{1}{2}(\mu/\mu_0)-\tfrac{1}{2}(\mu/\mu_0{}^3)], \quad (A8)\end{aligned}$$

where μ_0 is to be replaced by its upper limit $\bar{\mu}_0=\mu_0{}^c(\bar{\nu},\vartheta)$ using (A7) with $\nu=\bar{\nu}$, and μ is to be replaced by $(\bar{\mu}_0{}^2-1)^{\frac{1}{2}}$.

Excited Levels in Ti^{48}†

MAURICE M. MILLER
Physics Department, Indiana University, Bloomington, Indiana
(Received June 23, 1952)

Excited levels of Ti^{48} have been investigated by means of the radioactive decays of V^{48} and of Sc^{48}. The intensity of a 2.29-Mev gamma-transition in Ti^{48} relative to the total number of V^{48} and Sc^{48} disintegrations is found to be different for the two decays. This evidence that the 2.29-Mev transition in Ti^{48} is not a cross-over is further substantiated by delayed-coincidence measurements and lifetime considerations.

EXCITED levels in Ti^{48} have been investigated by observing the positron and orbital electron capture decay of 16-day V^{48} and also the 44-hour negatron decay of Sc^{48}.

The single crystal scintillation spectrum of V^{48} is shown in Fig. 1. The data were taken with a conventional scintillation spectrometer utilizing a NaI (Tl) crystal and an RCA 5819 photomultiplier. Photopeaks

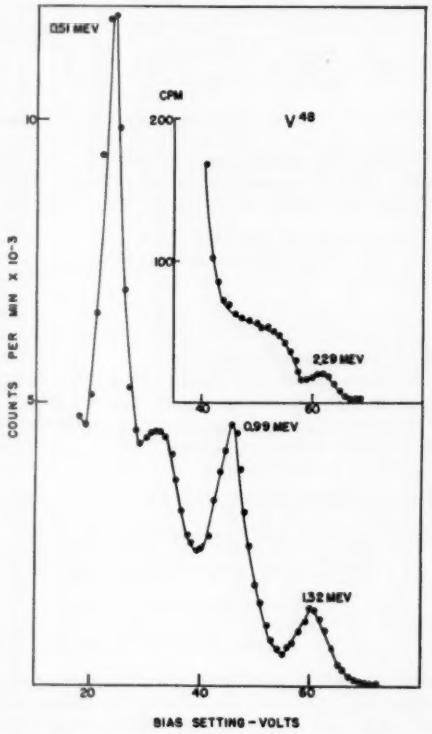

FIG. 1. Scintillation spectrum of V^{48}. Inset shows photopeak and Compton distribution of a 2.29-Mev gamma-ray taken with reduced gain.

† This work was assisted by the joint program of the ONR and AEC.

are observed at 0.51, 0.99, 1.32, and 2.29 Mev on the basis of a calibration with the Cs^{137} 0.661-Mev radiation and the Sc^{46} 1.12-Mev radiation. A similar spectrum is obtained by observing the decay of Sc^{48} in the same geometry. In this case photopeaks are observed at 0.51, 0.99, and 1.32 Mev but not at 2.29 Mev. The 0.51-Mev peak is due, in each case, to the annihilation radiation observed when positrons are stopped in the Pb absorber surrounding the source. The annihilation radiation observed in the spectrum of Sc^{48} is due to the positron decay of Sc^{44} which is fed by a 52-hour isomeric transition. The Sc^{44} was produced along with the Sc^{48} in the deuteron bombardment of calcium.

In each of the decays the lines at 1.32 and 0.99 Mev are of approximately equal intensity. In the V^{48} decay the intensity of the 2.29-Mev radiation (inset of Fig. 1) is found to be 1.7 ± 0.5 percent of the 1.32-Mev radiation. This intensity comparison takes into account the variation of the photoelectric cross section with energy and the contribution to the photopeak intensity due to multiply-scattered Compton gamma-rays which are absorbed completely within the crystal. This intensity ratio compares favorably with the value of one percent obtained by quite different means.[1] Since the search for the corresponding 2.29-Mev gamma-ray in the Sc^{48} decay revealed no discernible line, its intensity is estimated to be no more than 10^{-3} of the intensity of the 1.32-Mev gamma-ray.

Coincidence spectrometer measurements utilizing two single crystal spectrometers[2] showed the 1.32 and 0.99-Mev gamma-rays of V^{48} to be in coincidence with each other and the annihilation radiation. This is in accord with the decay scheme of V^{48} as proposed by Peacock and Deutsch.[3] In addition, coincidences were observed between the annihilation radiation and the 2.29-Mev gamma-ray. All coincidences were found to be "prompt" (with respect to the 10^{-7} second resolving time of the coincidence circuit) by means of the delayed coincidence technique. Co^{60} gamma-coincidences also showed the "prompt" delayed coincidence spectrum.

These results suggest that the high energy gamma-ray does not arise from a cross-over transition. Assuming

[1] R. G. Fluharty and M. Deutsch, Phys. Rev. **76**, 182 (1949).
[2] The spectrometer is described by Miller, Pruett, and Wilkinson, Phys. Rev. **84**, 849 (1951).
[3] W. C. Peacock and M. Deutsch, Phys. Rev. **69**, 306 (1946).

the ground state of the even-even nucleus Ti^{48} is characterized by spin 0, the Weisskopf[4] formula shows that the level giving rise to the 2.29-Mev transition cannot have a spin greater than 3 due to its short lifetime ($<10^{-7}$ seconds). With this limitation, however, no possible spin assignment of the excited levels can yield a cross-over whose intensity relative to the cascade gamma-process is comparable with that measured for the 2.29-Mev gamma-ray. The absence of the 2.29-Mev gamma-ray in the Sc^{48} decay further supports this view. A possible alternative assumption is that the second excited level in Ti^{48} is split into two separate levels differing slightly in energy but differing substantially in spin. The level of lower spin would be characterized by a spin of 3 or less and a higher relative population in the decay of V^{48} as compared with the decay of Sc^{48}. Such a splitting of the second excited state of an even-even nucleus has been previously postulated by Spiers[5] to explain the observed angular correlation in the decay of Pd^{106}.

The author is indebted to Professor R. G. Wilkinson for his suggestion of the problem.

Note added in proof:—A study of the relative intensities of the 1.32-Mev and the 0.99-Mev gamma-rays emitted following the Sc^{48} decay has been reported by Hamermesh, Hummel, Goodman, and Engelkemeier [Phys. Rev. **87**, 528 (1952)].

[4] V. F. Weisskopf, Phys. Rev. **83**, 1073 (1951).

[5] J. A. Spiers, Phys. Rev. **78**, 75 (1950).

PHYSICAL REVIEW VOLUME 88, NUMBER 3 NOVEMBER 1, 1952

Angular Correlations of the Radiations from Deuteron Stripping Reactions*

L. C. Biedenharn,† Keith Boyer,‡ and R. A. Charpie
Oak Ridge National Laboratory, Oak Ridge, Tennessee
(Received July 21, 1952)

The general problem of the angular correlation of the radiations from excited states of nuclei produced in stripping reactions is discussed using the theory of Butler. The $(d,p\gamma)$ correlation is given explicitly.

I.

THE angular distribution of the single particles produced in deuteron stripping reactions[1] has proven to be a powerful tool for obtaining detailed information about the quantum states of the nuclei formed in these reactions. The method has had its greatest success in determining parities; for determining spins, however, it is less useful, and in fact, fails whenever the target nucleus has nonzero spin or the orbital angular momentum transfer is nonzero. If the residual nucleus is left in an excited state, further information on the spin of this state may be inferred from observation of the radiations emitted when the state decays. The specific experiment that seems most practical is to measure the angular correlation of the subsequent radiation in coincidence with stripped particles of a selected energy (in order to specify the energy of the emitting state). The correlations to be expected are found to be quite simple if one uses Butler's theory for the stripping process, and a brief report of the results has been given earlier.[2] Because of the current interest in this type of experiment, a detailed treatment seems to be of some value and is given below.

* This document is based on work performed for the AEC at the Oak Ridge National Laboratory.

† Now at Yale University, New Haven, Connecticut.

‡ Los Alamos Scientific Laboratory, Los Alamos, New Mexico.

[1] S. T. Butler, Proc. Roy. Soc. (London) **A208**, 259 (1951).

[2] Biedenharn, Boyer, and Charpie, Phys. Rev. **86**, 619 (1952); it has come to the authors' attention that W. Cheston and L. Gallaher of Washington University (St. Louis) have independently arrived at similar results. *Note added in proof:*—Professor Spiers has informed us of similar work by G. R. Satchelor and himself to be published in the Proc. Phys. Soc. (London).

II.

In order to calculate the angular distribution of radiations emerging from an excited state of a nucleus formed in stripping, it is sufficient to have the density matrix of the state in question and then apply standard techniques.[3] The required density matrix is implicit in the work of Butler and can be written down immediately if one has evaluated the integrals in his Eqs. (19) and (21) and thereby obtained an explicit form for the wave function that describes the stripping process.

Consider the process whereby an unpolarized deuteron beam, with momentum $\mathbf{K}_d$, bombards a target nucleus of spin j to form a residual nucleus of spin J and a beam of protons which emerges with momentum $\mathbf{K}_p$. (The momenta $\mathbf{K}_d$ and $\mathbf{K}_p$ are measured in the laboratory system.) Then Butler's Eqs. (19) and (21), upon performing the indicated steps, yield the asymptotic wave function

$$\psi\sim\left(\chi_{p}^{\mu_p}\frac{e^{iK_pr_p}}{K_pr_p}\right)\cdot v_J{}^M(K_p)\sum_{l_n,s}i^{l_n}\cdot N(l_n,s;K_p,r_0)$$
$$\cdot Q_{l_n}(\mathbf{K}_d,\mathbf{K}_p)\cdot[Y_{l_n}{}^{M-m-\mu_d+\mu_p}(\mathbf{K}_d-\mathbf{K}_p)]^*$$
$$\cdot(\tfrac{1}{2}\tfrac{1}{2}\mu_p\mu_d-\mu_p|\tfrac{1}{2}\tfrac{1}{2}1\mu_d)$$
$$\cdot(\tfrac{1}{2}j\mu_d-\mu_pm|\tfrac{1}{2}js\mu_d-\mu_p+m)$$
$$\cdot(sl_nm+\mu_d-\mu_pM-m-\mu_d+\mu_p|sl_nJM). \quad (1)$$

We use the notation of reference 1 for convenience,

[3] See for example, U. Fano, National Bureau of Standards Circular No. 1214, or the forthcoming review paper of Biedenharn and Rose on angular correlations.

with only minor changes. Thus M, μ_p, μ_d, m are the magnetic quantum numbers for the spins of the residual nucleus, the emerging proton, the incident deuteron, and the target nucleus, respectively. l_n is the orbital angular momentum carried by the captured neutron, and s is the "channel spin," i.e., the vector sum of the spins of the neutron and target nucleus. r_0 is the radius of the internal region and is taken to be approximately equal to the radius of the initial nucleus plus the range of nuclear forces. The factor $N(l_n, s; K_p, r_0)$ is a (real) nuclear parameter and is a measure of the mixing of the channel spin states and the orbital angular momentum transfers. Finally, $Q_{l_n}(\mathbf{K}_d, \mathbf{K}_p)$ is an explicit function which, if we assume the Hulthén form for the internal motion of the deuteron, i.e.,

$$F(\mathbf{r}_n-\mathbf{r}_p)=F(r)=(e^{-ar}/r)(1-e^{-br}),$$

is

$$Q_{l_n}(\mathbf{K}_d, \mathbf{K}_p)=\left[\frac{1}{K^2+a^2}-\frac{1}{K^2+(a+b)^2}\right]\cdot\left|\sum_{r=0}^{l_n}\frac{(l_n+r)!}{r!(l_n-r)!(2\kappa_s r_0)^r}\left[\kappa_s+\frac{r}{r_n}+\frac{\partial}{\partial r_n}\right]_{r_0}\times\left|\left(\frac{r_n}{Z}\right)^{\frac{1}{2}}J_{l_n+\frac{1}{2}}(Zr_n)\right|\right|,$$

$$K\equiv|\tfrac{1}{2}\mathbf{K}_d-\mathbf{K}_p|, \qquad a=0.23\times10^{13}\ \text{cm}^{-1},$$

$$Z\equiv|\mathbf{K}_d-\mathbf{K}_p|\cdot M_t/(M_t+M_n), \qquad b=1.4\times10^{13}\ \text{cm}^{-1}.$$

The second factor in Q_{l_n} in perhaps more familiar notation is the Wronskian of $j_{l_n}(Zr_n)$ and $h_{l_n}^{(0)}(i\kappa_s[r_n-r_0])$, (spherical Bessel and Hankel functions, respectively) evaluated at $r_n=r_0$.

In Eq. (1), Butler's work has been altered to the extent of introducing explicitly the Clebsch-Gordan or vector addition coefficients, $(j_1j_2m_1m_2|j_1j_2JM)$.[4]

It is now straightforward to determine the density matrix of the residual state, $D(JK_p; MM')$ noting only that the quantum numbers μ_d, μ_p and m are to be averaged, since unpolarized processes are considered. Discarding a multiplicative constant as irrelevant, we have

$$D(JK_p; MM')=\sum_{l_n, l_n', s, \nu} Q_{l_n}Q_{l_n'}N(l_n s; K_p, r_0)\cdot N(l_n' s; K_p, r_0)\cdot i^{l_n-l_n'}(-1)^{s-M}\cdot\left[\frac{(2l_n+1)(2l_n'+1)}{2\nu+1}\right]^{\frac{1}{2}}\cdot Y_\nu^{M'-M}(\mathbf{K}_d-\mathbf{K}_p)\cdot(JJM'-M|JJ\nu M'-M)\cdot(l_nl_n'00|l_nl_n'\nu0)\cdot W(Jl_nJl_n'; \nu s). \quad (2)$$

The function $W(Jl_nJl_n'; \nu s)$ is the so-called Racah coefficient,[5] for which algebraic and numerical tables are available.[6]

Having obtained the density matrix for the desired excited state, one can calculate the angular correlation of succeeding radiations in the standard way.[3] Since in most cases of interest, the excited states have insufficient energy for nucleon emission, attention can be restricted to gamma-radiation. The result for the $(d,p\gamma)$ process with a pure multipole gamma-ray transition is found to be

$$W(\mathbf{K}_d, \mathbf{K}_p, \boldsymbol{\gamma})=\sum_{l_n, l_n', s\nu}[(2l_n+1)(2l_n'+1)]^{\frac{1}{2}}\cdot N(l_n, s; K_p, r_0)N(l_n', s; K_p, r_0)\cdot(l_nl_n'00|l_nl_n'\nu0)(LL1-1|LL\nu0)\cdot i^{l_n-l_n'}\cdot(-1)^{s-J}W(JJLL; \nu J_f)\cdot W(Jl_nJl_n'; \nu s)\cdot Q_{l_n}(\mathbf{K}_d, \mathbf{K}_p)Q_{l_n'}(\mathbf{K}_d, \mathbf{K}_p)\cdot P_\nu\left[\frac{(\mathbf{K}_d-\mathbf{K}_p)\cdot\boldsymbol{\gamma}}{|\mathbf{K}_d-\mathbf{K}_p|}\right]. \quad (3)$$

Here J_f denotes the spin of the final state, while 2^L is the multipolarity of the gamma-ray emitted in the transition from $J\to J_f$. The factor $i^{l_n-l_n'}$ is real since parity restricts the l_n's to differ by an even integer.

III.

The angular correlation given by Eq. (3) shows a number of interesting features. The argument of the legendre polynomial is the cosine of the angle between the gamma-ray direction $(\boldsymbol{\gamma})$ and the direction of the recoil momentum transferred to the nucleus formed in stripping (J). Consequently, the $(d,p\gamma)$ process is azimuthally symmetric about the direction of the recoil momentum. Furthermore, ν is restricted to be an even integer (parity), with the result that the gamma-ray is symmetric about 90°, taking the recoil direction to define the axis. These symmetries are sharply at variance with a (d,p,γ) process that takes place via compound state,[7] since this would in general be a function of three vectors. Thus for fixed $\mathbf{K}_d$ and $\mathbf{K}_p$, a function of two angles would result in contrast to the single angle function that occurs in the analogous case via stripping.

The correlation given in Eq. (3) obeys all the usual rules for limiting ν since these result from the selection rules on the Racah coefficients.[5,6] Hence $\nu_{\max}$ is the largest even integer less than or equal to the minimum of $[2L, 2l_n(\max), 2J]$. It is obvious therefore that l_n must be nonzero for a nonisotropic gamma-distribution to occur. The numerical evaluation of Eq. (3) for specific cases is expedited by the use of tables for the Racah coefficients.[6] Butler has given curves for several cases of $(Q_{l_n})^2$.

[4] E. U. Condon and G. H. Shortley, *Theory of Atomic Spectra* (Cambridge University Press, Cambridge, 1935).

[5] G. Racah, Phys. Rev. **62**, 438 (1942); **63**, 367 (1943).

[6] H. A. Jahn, Proc. Roy. Soc. (London) **A205**, 234 (1951); L. C. Biedenharn, Oak Ridge National Laboratory Report, ONRL 1098 (1952).

[7] Biedenharn, Arfken, and Rose, Phys. Rev. **83**, 586 (1951).

If we integrate Eq. (3) over all directions γ, holding $\mathbf{K}_d$ and $\mathbf{K}_p$ fixed, only $\nu=0$ enters and $l_n=l_n'$. This reproduces exactly the earlier results of Butler, as is to be expected. It is perhaps unnecessary to point out that while the direction of $\mathbf{K}_p$ can be arbitrary, the magnitude, which is determined by energy conservation, will in general depend upon this direction.

Since the mixing of l_n's in Eq. (3) is coherent—in which case the cross-term is proportional to the square root of the percentage of mixing—the $(d,p\gamma)$ process might provide an alternative means of checking shell-model predictions.[8] In all cases where a mixing of l_n's occurs, two channel spins will enter incoherently. This ambiguity could be eliminated if we assumed the j-j coupling model, which would predict definite mixing ratios for the channel spins. On the other hand, one could equally well apply L-S coupling rules to eliminate the ambiguity. Christy[9] has examined both alternatives for a number of light particle reaction angular distributions in which the channel spin ambiguity occurs, and he fails to find a clear-cut advantage for either procedure. Consequently the channel spin ambiguity has been left explicit in Eq. (3) rather than selecting a specific model in order to eliminate it.

IV.

The results given in Eqs. (2), (3) show that the $(d,p\gamma)$ process is formally similar to the familiar resonance capture[10] of a neutron from a plane wave traveling along the recoil momentum direction, $\mathbf{K}_d-\mathbf{K}_p$. This is, of course, implicit in the assumptions of the Butler theory where one has neglected (1) the Coulomb field of the nucleus, (2) the neutron-proton interaction after the splitting of the deuteron, and (3) the formation of a compound nucleus. Hence, one treats the incident deuteron beam as an assembly of neutron and proton plane waves, and at resonance that neutron plane wave which is allowed by momentum conservation interacts, independently of the proton, with the target nucleus. The probability of finding this neutron wave in the incident deuteron beam is just the first factor in the formula for Ql_n. There is, however, one difference in this treatment from the usual (n,γ) process, namely, that the energy of the neutron plane wave is not related in the usual way to the propagation vector, $\mathbf{K}_d-\mathbf{K}_p$, since the proton can carry off energy. In fact, the usual stripping problem involves a "negative" energy neutron wave. This feature of the stripping problem results in a markedly different "penetration factor," which is the second factor in the formula for Ql_n.[11] Aside from these readily interpretable differences, the $(d,p\gamma)$ process is precisely similar in its angular properties to the usual resonance (n,γ) angular distributions. As a result, one can write down immediately the result given by Eq. (3) using the standard angular distribution theory, *mutatis mutandis*.

The particular simplicity of the $(d,p\gamma)$ process is thus an immediate consequence of the approximations of the Butler theory. As to the result of neglecting Coulomb effects, Butler has investigated this point[9] and concludes that for the (d,p) process the error is generally negligible. Specifically for 4-Mev deuterons on target nuclei of $Z\leq 10$ the error in defining the forward maxima of the distribution is of the order of a few degrees. The situation is less favorable for the (d,n) reaction and perhaps one should not expect good results for the $(d,n\gamma)$ process when Coulomb forces are neglected.

As discussed earlier, the particular symmetries of the $(d,p\gamma)$ process are due in part to the neglect of compound nucleus formation. One can, of course, minimize the effect of compound nucleus formation by taking coincidences at the maximum of the proton distribution. The presence or absence of these symmetries should be a critical test of the assumptions of the theory. The effect of neglecting the neutron-proton force after splitting is difficult to estimate, but one may justify this approximation, as indeed all the others, by the experimental confirmation of the predictions of the Butler model of the stripping process. It is probably unnecessary to point out that in addition to these assumptions we have implicitly assumed a short half-life for the excited state ($\tau\lesssim 10^{-11}$ sec) in order to neglect external influences on the correlations. It thus appears that the $(d,p\gamma)$ calculations given in Eq. (3) are quite approximate. Several features mitigate this conclusion: (1) the known success of the Butler theory, (2) the occurrence of easily measured symmetries that will serve as a partial check of the $(d,p\gamma)$ theory, and (3) in favorable cases ($j=0$) we only have to decide between two possibilities ($J=l_n\pm\frac{1}{2}$) which may differ greatly in their predicted correlations. An experimental check of the theory for such a favorable case where $j=0$ would seem to be worthwhile.

[8] H. A. Bethe and S. T. Butler, Phys. Rev. **85**, 1045 (1952).

[9] Conference on Medium Energy Nuclear Physics, University of Pittsburgh, Pittsburgh, Pennsylvania, June, 1952.

[10] E. P. Wigner and L. Eisenbud, Phys. Rev. **72**, 29 (1947); L. Eisenbud, J. Franklin Inst. **251**, 231 (1951); J. M. Blatt and L. C. Biedenharn, Phys. Rev. **82**, 123 (1951) (with minor changes necessitated by γ- instead of particle-emission).

[11] The propagation vector, $\mathbf{K}_d-\mathbf{K}_p$, in the notation employed above is the linear momentum carried by the neutron measured in the laboratory system. To compute the penetration factor in Ql_n the relative momentum of the neutron with respect to the target nucleus is required, and this inserts the factor $M_t/(M_t+M_n)$. Compare the discussion of Bhatia, Huang, Huby, and Newns, Phil. Mag. **43**, 485 (1952).

Elastic Scattering of Protons and Neutrons by Helium*

D. C. Dodder and J. L. Gammel
University of California, Los Alamos Scientific Laboratory, Los Alamos, New Mexico
(Received July 18, 1952)

Proton-alpha elastic scattering experiments at 5.81 and 9.48 Mev are analyzed in terms of phase shifts, and the results, together with earlier ones at lower energies, are used to compute the logarithmic derivatives of the wave functions at a radius of 2.9×10^{-13} cm. These logarithmic derivaties, for $P_{1/2}$ and $P_{3/2}$ states, are found to be linear functions of the energy. From the behavior of the logarithmic derivatives the widths and positions of the $P_{1/2}$ and $P_{3/2}$ energy levels are determined, the most striking results being the large splitting of the two levels and the very broad width of the $P_{1/2}$ level. These results are compared with neutron-alpha experiments and are found to be in sufficiently good agreement to support the conclusions about the $P_{1/2}$ level which differ from those previously expected. Small negative D wave phase shifts are found in the proton-alpha experiments which also show evidence of an inverted doublet spin-orbit splitting.

I. INTRODUCTION

A CONSIDERABLE amount of experimental data[1-5] on the elastic scattering of nucleons by alpha-particles has become available in the last few years. Analysis and interpretation of some of this data have been presented by Critchfield and Dodder[6] in terms of phase shifts and by Adair[3] in terms of resonances associated with virtual energy levels of the compound nuclei He^5 and Li^5. From the information then available it has learned[2] that the S wave phase shifts are very nearly those expected in scattering from an impenetrable sphere of radius 2.6×10^{-13} cm, while the $P_{3/2}$ phase shifts correspond to a resonance level at a few Mev positive energy. The experiments did not make possible a precise determination of the location of the $P_{1/2}$ level or its width, but it was ascertained that any $P_{1/2}$ level must lie at least several Mev above the $P_{3/2}$ level.

It is the purpose of this investigation to extend and amplify the above interpretations by making use of more recent data,[4,5] especially to find the position and width of the $P_{1/2}$ state and to find out something about the D states.

II. PHASE SHIFT ANALYSIS OF PROTON-ALPHA ELASTIC SCATTERING

The differential cross section for elastic scattering as a function of angle scattering, incident energy, and phase shifts is given by the following expression (the notation is that of reference 6).

$$k^2\sigma(\theta)=\left|-\frac{\eta}{2}\csc^2\frac{\theta}{2}\exp\left(i\eta\ln\csc^2\frac{\theta}{2}\right)+\sum_{l=0}^{\infty}\left[(l+1)\exp(i\delta_l^+)\sin\delta_l^+ +l\exp(i\delta_l^-)\sin\delta_l^-\right]\exp(i\phi_l)P_l(\cos\theta)\right|^2+\left|\sum_{l=0}^{\infty}\left[\exp(i\delta_l^-)\sin\delta_l^- -\exp(i\delta_l^+)\sin\delta_l^+\right]\exp(i\phi_l)\sin\theta P_l'(\cos\theta)\right|^2. \quad (1)$$

Because of the complexity of this expression when many angular momenta are included, numerical calculations were made using the I.B.M. card programmed electronic calculators available at the Los Alamos Scientific Laboratory. The criterion used in fitting the experimental data was the same as that of reference 6; namely, minimization with respect to the phase shifts of the sum of the squares of the percentage differences between the experimental and calculated values of the cross sections at the various scattering angles. The method of satisfying this in the present work is different, however, and is the following. Using a set of trial phase shifts, the cross section was computed at each angle where it was measured experimentally. At the same time the gradient with respect to the phase shifts of the sum of the squares of the percent differences between observed and calculated cross sections was computed. A new set of trial phase shifts was then selected by changing the old ones in a direction opposite to that of the gradient, the magnitude of the change being proportional to the magnitude of the gradient. This iterative procedure was carried out until the magnitude of the gradient was a few percent of its value when the agreement with the data was first of the same order of magnitude as the given experimental errors. The calculations were made for three cases: S, $P_{1/2}$, and $P_{3/2}$ waves only, S, $P_{1/2}$, $P_{3/2}$, and D waves (the $D_{5/2}$ and $D_{3/2}$ phase shifts were constrained to be identical), and S, $P_{1/2}$, $P_{3/2}$, $D_{3/2}$, and $D_{5/2}$ waves.

The nature of the method is such that there is always a possibility that there are solutions which fit

* Work done under the auspices of the AEC.
[1] Freier, Lampi, Sleator, and Williams, Phys. Rev. **75**, 1345 (1949).
[2] Bashkin, Mooring, and Petree, Phys. Rev. **82**, 378 (1951).
[3] R. K. Adair, Phys. Rev. **86**, 155 (1952).
[4] T. M. Putnam, University of California Radiation Laboratory Report UCRL-1447, unpublished.
[5] Kreger, Kerman, and Jentschke, Phys. Rev. **86**, 593 (1952).
[6] C. L. Critchfield and D. C. Dodder, Phys. Rev. **76**, 602 (1949).

TABLE I. $E=9.48$ Mev. S and P phase shifts only.

	A		B		C		D	
	$\delta_0 = -57.5°$ $\delta_1^+ = 113.8°$ $\delta_1^- = 61.7°$		$\delta_0 = -57.3°$ $\delta_1^+ = 85.1°$ $\delta_1^- = 137.2°$		$\delta_0 = -90.6°$ $\delta_1^+ = 126.7°$ $\delta_1^- = 84.95°$		$\delta_0 = -90.6°$ $\delta_1^+ = 101.6°$ $\delta_1^- = 143.3°$	
θ	$k^2\sigma$ calc.	% dev.	$k^2\sigma$ calc.	% dev.	$k^2\sigma$ calc.	% dev.	$k^2\sigma$ calc.	% dev.
12.2°	29.27	−11.89	29.36	−11.62	29.59	−10.93	29.61	−10.85
52.0°	6.292	− 6.88	6.281	− 7.04	6.328	− 6.34	6.325	− 6.39
94.5°	1.125	−10.28	1.123	−10.44	1.134	− 9.55	1.134	− 9.61
123.8°	0.7804	− 1.71	0.7806	− 1.68	0.7850	− 1.13	0.7850	− 1.14
174.5°	2.694	− 4.25	2.692	− 4.32	2.701	− 4.00	2.701	− 4.00
rms % dev.		7.94		7.94		7.32		7.32

the experimental values within the experimental error but which were not found because a combination of trial phase shifts sufficiently close to such a solution was not used. However, the procedure was started with a number of initial sets of values of the phase shifts and always converged towards one of a limited number of solutions.

The solutions found for the 9.48-Mev case with S and P waves only are given in Table I. Solutions A and B are mathematically equivalent[7] inverted and normal doublets, as are C and D. In the lower energy work solutions equivalent to all of these were found, but two of them, equivalent to the present C and D, were far worse than the others at small angles. The reasons that this is not so in the present work are that the low angles are given weight in determining the solution, which was not done in the preliminary solutions in the lower energy work, and that the presence of D waves is required by the present experiments, preventing any solution with P waves only from approaching the observed values too closely. The solutions A and C, corresponding to inverted doublets, now modified by the addition of a single D wave phase shift, are given in Table II. It is seen that the presence of D wave phase shifts is definitely indicated. In Table III are given the solutions with $D_{5/2}$ and $D_{3/2}$ phase shifts split. The experimental results do not definitely require splitting, but as discussed later, the direction of splitting indicated is reasonable. In Table IV, for solution A, the results are given at each angle at which the cross section was measured experimentally.

At 5.83 Mev the analysis was not as exhaustive. Initial values of phase shifts used were those given for S, $P_{1/2}$, and $P_{3/2}$ by Kreger *et al.*[5] Eleven angles were used to improve their preliminary fit. Table V gives the result of this. Solutions with a single D phase shift are given in Table VI, while Table VII gives the results with all five phase shifts. In the analysis for split D waves 26 angles were used. It is seen that presence of D waves, and to a lesser degree their splitting, is indicated by this experiment.

[7] The two solutions are found from the parameters of reference 6 by taking the plus and minus signs in the following formulas: $2\delta_1^+ = \tan^{-1}[\rho \sin\beta/(\rho\cos\beta+3)] \pm \cos^{-1}[(\rho^2+6\rho\cos\beta+12)/4(\rho^2+6\rho\cos\beta+9)^{\frac{1}{2}}]$, $2\delta_1 = \sin^{-1}[\rho\sin\beta - 2\sin 2\delta_1^+]$.

It is difficult to set precise limits on the accuracy of the phase shifts. First, if the S phase shift, for example, is varied while the others are held fixed, it might be found that it could be changed only by a few tenths of a degree without destroying the agreement with the experimental data. However, by changing it together with the other phase shifts, it might be possible to change it by say two degrees without damage to the fit. Second, were the experimental cross sections high by say 5 percent at all angles, the S wave phase shifts might be in error, while were the forward angles subject to experimental error, the D wave phase shifts would be in doubt. It seems more pertinent to examine a phase shift as a function of energy for smoothness and reasonableness. However, as a rough estimate based on an examination of the changes in the phase shifts as the procedure described above converged to the final fit, the P phase shifts are accurate to within 2°, while the S phase shifts are somewhat less accurate (5°). Comparison of the results for D wave phase shifts locked and split shows that they are definitely small and negative. As discussed later, this seems reasonable, and even the direction of splitting seems reasonable. But until experiments are performed at still higher energies, conclusions about the D states must remain preliminary, and the values quoted for the D wave

TABLE II. $E=9.48$ Mev. $\delta(D_{5/2}) = \delta(D_{3/2})$.

	A		C	
	$\delta_0 = -65.4°$ $\delta_1^+ = 106.1°$ $\delta_1^- = 47.4°$ $\delta_2 = -7.0°$		$\delta_0 = -94.9°$ $\delta_1^+ = 117.2°$ $\delta_1^- = 78.5°$ $\delta_2 = -4.03°$	
θ	$k^2\sigma$ calc.	% dev.	$k^2\sigma$ calc.	% dev.
12.2°	31.77	−4.37	30.98	−6.73
12.8°	28.39	−1.93	27.78	−4.03
19.0°	15.12	2.18	15.44	4.33
31.3°	10.29	−1.22	10.95	5.09
52.0°	6.341	−6.15	6.787	0.45
63.7°	4.479	−7.72	4.718	−2.80
72.7°	3.255	−6.39	3.353	−3.57
83.8°	2.045	−1.73	2.027	−2.59
94.5°	1.222	−2.51	1.170	−6.73
114.4°	0.6251	−2.32	0.6473	1.14
123.8°	0.7408	−6.70	0.8042	1.29
149.4°	1.889	−2.96	1.891	−2.89
174.5°	2.867	1.90	2.703	−3.91
rms % dev.		4.29		3.98

TABLE III. $E=9.48$ Mev. D phase shifts split.

	A		C	
	$\delta_0 = -70.8°$		$\delta_0 = -98.9°$	
	$\delta_1^+ = 106.2°$		$\delta_1^+ = 115.3°$	
	$\delta_1^- = 53.8°$		$\delta_1^- = 76.6°$	
	$\delta_2^+ = -5.03°$		$\delta_2^+ = -7.16°$	
	$\delta_2^- = -8.84°$		$\delta_2^- = -2.95°$	
θ	$k^2\sigma$ calc.	% dev.	$k^2\sigma$ calc.	% dev.
12.2°	31.48	−5.22	30.96	−6.81
12.8°	28.22	−2.52	27.77	−4.08
19.0°	15.51	4.81	15.48	4.58
31.3°	10.83	3.93	10.98	5.44
52.0°	6.662	−1.41	6.808	0.76
63.7°	4.653	−4.15	4.745	−2.25
72.7°	3.339	−3.98	3.387	−2.57
83.8°	2.059	−1.07	2.067	−0.67
94.5°	1.213	−3.31	1.204	−3.98
114.4°	0.6416	0.25	0.6506	1.66
123.8°	0.7737	−2.56	0.7950	0.12
149.4°	1.900	−2.41	1.899	−2.44
174.5°	2.817	0.12	2.760	−1.92
rms % dev.		3.18		3.44

phase shifts should be thought of as correct in little more than order of magnitude.

III. ENERGY DEPENDENCE OF PROTON-ALPHA PHASE SHIFTS

The energy dependence of the phase shifts is conveniently examined in terms of the energy dependence of the logarithmic derivative Y of the wave function evaluated at a radius taken equal to, or greater than, the distance at which specifically nuclear events become negligible. The logarithmic derivative of a wave function at a given radius plays a central role in the formal description of nuclear reactions of Wigner and Eisenbud[8] being just the reciprocal of their R function if the simplest choice of boundary conditions defining their internal wave functions is made. In the case of the one level approximation the logarithmic derivative is then a linear function of the energy. Breit and Bouricius[9] have discussed the behavior of Y at various radii for the wave function of the S state of two protons. They find that it is possible to find radii at which $\partial Y/\partial E$ can have a wide range of positive and negative values which are independent of energy over the energy region extending up to 3.5 Mev. In the nucleon-alpha P states it is also possible to find a radius at which $\partial Y/\partial E$ is energy independent. However, the range of radii for which this is possible seems to be less than it is in the case of the S state of two protons. The radius a used in the present calculations is 2.9×10^{-13} cm, the same as that of Adair; a radius of 3.5×10^{-13} cm, on the other hand, gave an energy dependent $\partial Y/\partial E$.

The value of the logarithmic derivative at a radius a is given in terms of δ, the phase shift, and F and G, the regular and irregular radial wave functions in the external field, by the well-known formula

$$aY=-\frac{ka}{1+F/G\cot\delta}+\frac{kaF'}{F}. \tag{2}$$

The prime represents differentiation with respect to kr, where k is the wave number. For the case where the external field is Coulombic, aY can be expressed in terms of functions tabulated by Breit and collaborators,[10] and for orbital angular momentum L one obtains

$$aY=\frac{\phi_L'}{\phi_L}-\frac{(2L+1)}{(2L+1)C_L^2\rho^{2L+1}\phi_L^2\cot\delta_L+\phi_L\theta_L}. \tag{3}$$

Equation (2) can be solved for δ_L, giving

$$\delta_L=\tan^{-1}\frac{ka/(F^2+G^2)}{aY-ka[(FF'+GG')/(F^2+G^2)]}-\tan^{-1}\frac{F}{G}.$$

TABLE IV. $E=9.48$ Mev.

A:	$\delta_0=-70.5°$, $\delta_1^+=105.8°$, $\delta_1^-=53.3°$, $\delta_2^+=-3.83°$, $\delta_2^-=-8.42$				
θ	$k^2\sigma$ calc.	% dev.	θ	$k^2\sigma$ calc.	% dev.
12.2°	30.57	−7.97	94.5°	1.216	−3.01
12.8°	27.27	−5.44	99.6°	0.9530	1.71
15.3°	19.62	2.21	104.7°	0.7765	−4.02
15.9°	18.54	1.20	106.8°	0.7281	−0.31
18.4°	15.55	0.13	111.7°	0.6682	−0.25
19.0°	15.06	1.79	114.4°	0.6652	3.94
21.5°	13.57	−0.93	116.4°	0.6760	0.91
25.2°	12.18	2.79	123.8°	0.8032	1.11
27.7°	11.49	4.42	128.3°	0.9388	−3.12
31.3°	10.64	2.13	132.7°	1.105	−3.13
33.9°	10.09	2.47	134.5°	1.181	−4.05
37.4°	9.377	4.09	141.2°	1.492	−2.75
40.0°	8.867	−0.25	145.4°	1.699	3.93
43.5°	8.196	0.44	149.4°	1.897	−2.55
49.5°	7.076	1.65	151.1°	1.980	−0.80
52.0°	6.622	−1.99	157.3°	2.264	−2.99
61.3°	5.025	0.46	159.0°	2.335	−0.79
63.7°	4.642	−4.38	165.0°	2.553	2.76
72.7°	3.335	−4.09	166.7°	2.604	3.23
80.6°	2.385	−0.30	172.6°	2.738	2.04
83.8°	2.058	−1.13	174.2°	2.761	−1.87
86.1°	1.844	−2.97	rms % dev.		2.87

TABLE V. $E=5.81$ Mev. S and P phase shifts only.

	$\delta_0=-46.6°$, $\delta_1^+=112.5°$, $\delta_1^-=40.7°$	
θ	$k^2\sigma$ calc.	% dev.
16.22°	17.50	−3.24
28.64°	8.509	−3.01
43.32°	6.186	1.68
55.28°	4.708	0.43
66.88°	3.426	−0.12
80°	2.233	−1.62
95°	1.321	−1.22
115°	0.9196	−0.74
125°	1.017	−2.37
140°	1.390	2.74
154°	1.809	−2.08
rms % dev.		2.01

[8] E. P. Wigner and L. Eisenbud, Phys. Rev. **72**, 29 (1947). See also Feshbach, Peaslee, and Weisskopf, Phys. Rev. **71**, 145 (1947).

[9] G. Breit and W. G. Bouricius, Phys. Rev. **75**, 1029 (1949). Y in the present article is equal to Y/r of this reference.

[10] Bloch, Hull, Broyles, Bouricius, Freeman, and Breit, Revs. Modern Phys. **23**, 147 (1951). References to earlier work and to other tables of coulomb functions are given here.

Using the simple boundary condition in the Wigner-Eisenbud formalism, $Y=1/R$, and the aY term becomes, in the one-level approximation, just $(a/\gamma_\lambda^2)(E_\lambda-E)$ where E_λ is the characteristic energy of the level and γ_λ^2 is the reduced width of the level; the term $-ka(FF'+GG')/(F^2+G^2)$ becomes $a\Delta_\lambda/\gamma_\lambda^2$ where Δ_λ is the level shift. This Δ_λ differs by $\gamma_\lambda^2 L/a$ from that evaluated by Thomas[11] because of the different choice of boundary conditions defining the E_λ and the resulting different relationship between R and Y.

Graphs of aY as a function of the center-of-mass energy for the $P_{1/2}$ and $P_{3/2}$ states in Li^5 are given in Fig. 1. The points for energies less than or equal to 3.5 Mev were obtained using the phase shift analysis of Critchfield and Dodder.[6] The two most noticeable features are the markedly different slopes, corresponding to different reduced widths, γ_λ^2, and the large splitting between the E_λ's for the two states. This is much greater than that previously indicated, and these results may be hard to reconcile with experiments showing two sharply defined P levels a few Mev apart.[12,13] The best values of E_λ and γ_λ^2 are: $P_{1/2}$: $E_\lambda=2.7$ Mev, $\gamma_\lambda^2=85\times10^{-13}$ Mev cm and $P_{3/2}$: $E_\lambda=-3.3$ Mev, $\gamma_\lambda^2=20.0\times10^{-13}$ Mev cm. The $P_{3/2}$ E_λ is different from that of Adair because of the different Δ_λ. Figure 2 is a corresponding graph for the S waves. It is seen that due to the large uncertainties in the values of the points, it is hard to determine exactly the energy dependence of aY.

TABLE VI. $E=5.81$ Mev. $\delta(D_{5/2})=\delta(D_{3/2})$.

$\delta_0=-47.6°$, θ	$\delta_1^+=112.1°$, $\delta_1^-=39.9°$, $k^2\sigma$ calc.	$\delta_2=-0.52°$ % dev.
16.22°	17.91	−0.96
28.64°	8.643	−1.49
43.32°	6.226	2.34
55.28°	4.714	0.56
66.88°	3.416	−0.40
80°	2.220	−2.19
95°	1.315	−1.64
115°	0.9271	0.06
125°	1.029	−1.28
140°	1.402	3.65
154°	1.818	−1.56
rms % dev.		1.75

TABLE VII. $E=5.81$ Mev. D phase shifts split.

$\delta_0=-48.2°$, θ	$\delta_1^+=112.3°$, $k^2\sigma$ calc.	$\delta_1^-=39.8°$, % dev.	$\delta_2^+=-0.42°$, θ	$\delta_2^-=-1.7°$ $k^2\sigma$ calc.	% dev.
16.22°	17.98	−0.58	72.6°	2.863	−1.98
18.70°	13.82	−1.14	80°	2.230	−1.75
21.80°	11.20	−0.50	85°	1.870	−1.42
24.93°	9.747	−0.18	95°	1.326	−0.85
28.64°	8.675	−1.12	105°	1.019	−2.14
31.11°	8.145	−0.02	115°	0.9317	0.57
35.05°	7.448	0.39	125°	1.026	−1.54
37.25°	6.802	−3.20	130°	1.124	1.06
43.32°	6.243	2.62	134°	1.221	0.64
49.30°	5.463	2.63	140°	1.384	2.34
55.28°	4.726	0.81	145°	1.530	−1.02
61.13°	4.047	0.44	150°	1.674	−0.12
66.88°	3.426	−0.12	154°	1.785	−3.36
			rms % dev.		1.58

Wigner and Eisenbud have shown that under very general assumptions regarding the interaction in the internal region, $R=\sum_\lambda \gamma_\lambda^2/(E_\lambda-E)$. From this it is seen that $\partial Y/\partial E=(\partial 1/R)/\partial E$ is always a negative quantity. The graph for aY for the S wave shows either an approximately constant value or a slightly negative slope. This is to be interpreted that the S wave scattering is nearly that expected from an impenetrable sphere and that there is no evidence for a nearby S resonance level. This agrees with the conclusion of Adair.

At both of the present energies the D wave phase shifts are small and negative and show a splitting, the $D_{5/2}$ wave being less negative than the $D_{3/2}$. The potential scattering associated with a radius of $a=2.9\times10^{-13}$ cm is small and negative, and any nonpotential effect caused by an inverted doublet type of effective spin-orbit forces similar to those acting in the P states would make the $D_{5/2}$ phase shift more positive than the $D_{3/2}$. The apparent agreement with this picture is not conclusive, however, since a distant level with a large width could produce more effect at a given energy than a closer one with a narrow width, and the fact that the widths can be quite different is seen from the P-state widths.

The $D_{7/2}$ state in the mirror nucleus He^5 is also effective in producing the resonance in the D-T reaction

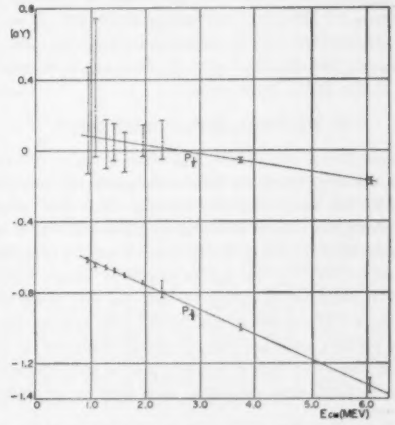

FIG. 1. Logarithmic derivative times radius evaluated at a radius of 2.9×10^{-13} cm for the P states in proton-alpha elastic scattering as a function of center-of-mass energy. For points below 3.5 Mev, the errors are those of reference 6. Above 3.5 Mev, an error of $\pm1°$ is shown.

[11] R. G. Thomas, Phys. Rev. **80**, 136 (1950).
[12] W. J. Leland and H. M. Agnew, Phys. Rev. **82**, 558 (1951).
[13] W. E. Titterton and T. A. Brinkley, Proc. Phys. Soc. (London) **A64**, 212 (1951).

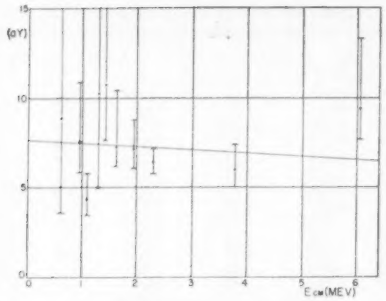

FIG. 2. Logarithmic derivative times radius evaluated at a radius of 2.9×10^{-13} cm for the S state in proton-alpha-elastic scattering as a function of center-of-mass energy. For points below 3.5 Mev, the errors are those of reference 6. Above 3.5 Mev, an error of $\pm2°$ is shown.

cross section at 165-kev triton energy, which can be identified with a state of $J=3/2$ and even parity.[14] The values of E_λ and of the reduced widths which agree with the energy dependence of the D-T cross section are not uniquely determined; however, the range of values of E_λ and the neutron width γ_λ^2 are in agreement with a small deviation from potential scattering for the n-He^4 $D_{3/2}$ phase shift at energies corresponding to the 5.81 and 9.48 p-He^4 energies. If the $D_{5/2}$ level does lie lower there should be a resonance associated with this state lying between 10 Mev and 22 Mev, the energy corresponding to the D-T reaction resonance. This could be detected either by an experiment measuring the total cross section for n-He^4 elastic scattering as a function of energy over the region, or by an angular distribution of the elastic scattering of protons or neutrons by helium at an energy sufficiently close to the resonant energy. A determination of the proton-alpha angular distribution at 32 Mev has been made[15] and is now being investigated.

IV. NEUTRON-ALPHA SCATTERING

Since the width of the $P_{1/2}$ level is quite different from the one chosen by Adair, the predicted contribution to the total cross section for the n-He^4 elastic scattering from this level at energies above 2 Mev would be somewhat different. Using Adair's assumptions that the E_λ's differ for the mirror nuclei by about 1 Mev, the difference being chosen so that the $P_{3/2}$ phase shift for the n-He^4 scattering will be 90° near the maximum cross section, and that the γ_λ^2 are the same for the two nuclei, the n-He^4 elastic scattering total and differential cross sections were computed as a function of energy.

[14] Argo, Adair, Agnew, Hemmendinger, Leland, and Taschek, Phys. Rev. **87**, 205 (1952); Argo, Taschek, Agnew, Hemmendinger, and Leland, Phys. Rev. **87**, 612 (1952).

[15] Bruce Cork, University of California Report UCRL 1673, unpublished.

Figure 3 shows the total cross section together with the experimental points and Adair's[3] calculated total cross section. From this it is clear that the experiment is in better agreement with the broader $P_{1/2}$ level, corroborating the results from the p-He^4 scattering. The calculations at 14.1 Mev, using S and P phase shifts obtained from extrapolating the lower energy values, assuming the $D_{3/2}$ phase shift to be that due to potential scattering, and assuming the $D_{5/2}$ phase shift to be zero, gives a total cross section of 1.05 barns as compared with an experimental value of 1.02 ± 0.03 barns.[16] The angular distribution is in qualitative agreement with preliminary experiments of Seagrave.[17] The choice of zero for the $D_{5/2}$ phase shift was made assuming that the effect of a $D_{5/2}$ level would just cancel the potential scattering effect at this energy. This is in rough agreement with the trend shown by the p-He^4 experiments at 5.81 and 9.48 Mev.

V. CONCLUSION

It is seen that the experiments on the elastic scattering of protons and neutrons by He^4 are very well explained on the basis of the resonance theory of nuclear interactions, and afford considerable information on the level scheme of the He^5 and Li^5 compound nuclei. Due to the wide spacing of the levels they can be studied almost individually, and due to their large widths their shapes can be investigated. These seem so far to be quite well described by the expressions of Wigner and Eisenbud and others. The widths of the P state levels are of particular interest, the $P_{3/2}$ level being just about as broad as expected from the single particle model, and the $P_{1/2}$ level being surprisingly broader as if due either to some type of "surface" reaction where the internal wave function is concentrated closer to the boundary than is a particle in a potential well, or to a much smaller internal region for the interaction. Fortunately it does not seem impossible to investigate the dependence of the five nucleon

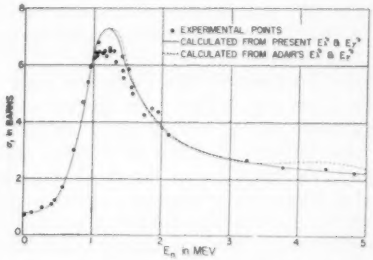

FIG. 3. Neutron-alpha total elastic cross section as a function of neutron energy in the laboratory system.

[16] J. Coon, private communication.

[17] John Seagrave, private communication.

system on the nucleon-nucleon forces. It is hoped that such an investigation will be able to explain the observed results. Further experiments at higher energies should reveal in a similar manner detailed information about the higher levels.

We are indebted to members of group T-1 of the Los Alamos Scientific Laboratory for assistance with the hand calculations. Drs. Coon, Seagrave, Barschall, Argo, Cork, Putnam, and Kreger furnished us with experimental data from various laboratories. Dr. Rosen and Dr. Barschall discussed with us the reliability and weights to be assigned experimental results.

PHYSICAL REVIEW VOLUME 88, NUMBER 3 NOVEMBER 1, 1952

Iterative Procedures and the Helium Wave Equation

JAMES H. BARTLETT
Department of Physics, University of Illinois, Urbana, Illinois
(Received July 16, 1952)

In an attempt to solve the helium wave equation exactly, study of a 180-point mesh shows the need for an improved difference operator to approximate the Laplacian. Such an operator has been developed, allowing one to express the value of the function at one point in terms of the values at 26 neighboring points (in three dimensions).

SINCE the wave equation for the ground state of the helium atom is nonseparable, analytic methods for obtaining a solution have been so far unsuccessful, and it has seemed worthwhile to try to solve the equation by numerical methods. If such a solution can be obtained, it will demonstrate whether or not the formulation of the many-body problem of quantum mechanics is correct. Also, a solution for the first excited state ($^3S_1$) would afford an opportunity to check the theory of hyperfine structure, using the spectrum of He^3 I.

Until a successful analog machine for partial differential equations in more than two dimensions is developed, it is probably necessary to replace the continuum of points by a mesh, and the differential equation by a difference equation. A prototype calculation was made[1] in one dimension for the hydrogen radial wave equation, and we shall show how these methods can be extended to several dimensions, with prospects of considerable accuracy.

The wave equation that is to be solved is of the form

$$\nabla^2\psi+\frac{1}{z}\frac{\partial\psi}{\partial z}+\frac{1}{4r}(E-V)\psi=0, \tag{1}$$

where, if r_1 and r_2 are the electron-nucleus distances and θ is the angle between the corresponding radius vectors, the coordinates x, y, and z are given by the relations $4x=2r_1r_2\cos\theta$, $4y=r_1^2-r_2^2$, $4z=2r_1r_2\sin\theta$. (Note that $z\geq 0$.) The radius in this system is $r=\frac{1}{4}(r_1^2+r_2^2)$, and V is the potential energy. If the substitution $\psi=Wz^{-\frac{1}{2}}$ is made, Eq. (1) is transformed into the equation

$$\nabla^2W+\left(\frac{E-V}{4r}+\frac{1}{4z^2}\right)W=0, \tag{2}$$

which is of the type $\nabla^2u+f(xyz)u=0$, where f is singular along the $+x$ axis and the whole y axis. However, we expect ψ to be finite everywhere and, consequently, W to be zero when $z=0$. Also, the solution is to be symmetric with respect to exchange of the electron space coordinates, so that $\psi(-y)=\psi(y)$. Hence the boundary conditions are

$$W=0, \quad z=0,$$
$$\partial W/\partial y=0, \quad y=0,$$
$$W\to 0, \quad r\to\infty.$$

In an attempt to construct an approximate solution of Eq. (2), the differential equation was replaced by a difference equation. This was done by equating the second partial derivative in each direction to the corresponding second partial difference, i.e., $\partial^2W/\partial x^2\cong\Delta_{xx}W$. A coarse mesh consisting of 180 points was chosen as follows:

$$x=0, \pm1, \pm3, \pm7, \pm15; \quad y=0, 1, 3, 7, 15;$$
$$z=1, 3, 7, 15.$$

(W was taken to equal zero for values of x, y, or z equal to 31.) Then the iterative procedure of Liebmann,[2] regarding each point as influenced by its six neighbors along the axes, was applied, and the solution of the 180-point mesh was obtained.[3] The eigenvalue turned out to be $E=-1.14$, but this could be lowered to $E=-1.33$ by drawing smooth curves through the mesh points and integrating by planimeter. This indicates that the procedure is much too crude and that one must use a better way of approximating the Laplacian. That this is possible will now be shown.

[1] G. E. Kimball and G. H. Shortley, Phys. Rev. **45**, 815 (1934).

[2] See G. H. Shortley and R. Weller, J. Appl. Phys. **9**, 334 (1938).

[3] This was done on the SEAC, the digital computer at the National Bureau of Standards by Mr. Joseph H. Wegstein, who also remarked that Eq. (2) might be simpler than Eq. (1) to solve numerically.

First, let us consider the one-dimensional case and suppose we are given three points $x_1>x_2>x_3$, and denote the intervals by $t=x_1-x_2$ and $s=x_2-x_3$. If the function W be expanded in a power series $W=a_0+a_1(x-x_2)+a_2(x-x_2)^2+\cdots$, then it may be shown easily that

$$\frac{tW(x_3)+sW(x_1)-(s+t)W(x_2)}{st(s+t)} = a_2+(t-s)a_3+(t^2-st+s^2)a_4+\cdots. \quad (3)$$

The left-hand side approaches a_2 when t and s go to zero, and so it is one-half the second difference, i.e., $(\frac{1}{2})\Delta^2W$. The ordinary procedure is to equate this to the second derivative at the point x_2, but a much better approximation can be found[4] if it is taken to be a linear combination of the second derivatives at the points x_1, x_2, and x_3, respectively, *viz.*,

$$\tfrac{1}{2}\Delta^2W=\tfrac{1}{2}(X_1W''|_1+X_2W''|_2+X_3W''|_3), \quad (4)$$

where X_1, X_2, and X_3 are constants to be determined. Substitute the expansion of W'' in the right-hand side of (4) and equate to the right-hand side of (3). The a_i's are arbitrary, and so their coefficients can be equated. The results are

$$X_1=\tfrac{1}{6}-\frac{s^2}{6t^2+6st},$$
$$X_3=\tfrac{1}{6}-\frac{t^2}{6s^2+6st}, \quad (5)$$
$$X_2=1-X_1-X_3.$$

The value of the second difference is now accurate up to and including the term in a_4, so should be much better than the value $2a_2$ alone. This is as good as can be done if one sticks to a difference equation of second order. Difference equations of higher order are unsafe to introduce, because unwanted solutions may come in.

If we have a differential equation $W''=-fW$, this may be substituted in (4), so that

$$\sum_{i=1}^{3}\xi_iW(x_i)=-\sum_{i=1}^{3}X_if(x_i)W(x_i), \quad (6)$$

where

$$\xi_1=2/[t(s+t)]; \quad \xi_3=-2/st; \quad \xi_2=2/[s(s+t)]. \quad (7)$$

In Eq. (6), we may solve for $W(x_2)$ in terms of $W(x_1)$ and $W(x_3)$. This is the basic calculation of the modified Liebmann procedure and will now be generalized.

In three dimensions, one may write the equations

$$\sum_{i=1}^{3}\xi_iW(x_iy_jz_k)=\sum_i X_i(\partial^2W/\partial x^2)_{x_iy_jz_k}, \quad (8a)$$

$$\sum_{j=1}^{3}\eta_jW(x_iy_jz_k)=\sum_j Y_j(\partial^2W/\partial y^2)_{x_iy_jz_k}, \quad (8b)$$

$$\sum_{k=1}^{3}\eta_kW(x_iy_jz_k)=\sum_k Z_k(\partial^2W/\partial z^2)_{x_iy_jz_k}. \quad (8c)$$

Apply the operator $\sum_{jk}Y_jZ_k$ to (8a), $\sum_{ik}X_iZ_k$ to (8b), $\sum_{ij}X_iY_j$ to (8c), and add. The result is

$$\sum_{ijk}(\xi_iY_jZ_k+X_i\eta_jZ_k+X_iY_j\zeta_k)W(x_iy_jz_k) = \sum_{ijk}X_iY_jZ_k\nabla^2W|_{x_iy_jz_k} = -\sum X_iY_jZ_k(fW)_{x_iy_jz_k}. \quad (9)$$

Equation (9) is the desired extension of Eq. (6) to three dimensions. The value of $W(x_2y_2z_2)$ may be found in terms of all the other $W(x_iy_jz_k)$, where i, j, and k go from 1 to 3. There are now 26 neighbors instead of the 6 that were used previously. Although the work involved is somewhat greater, this may be compensated by greater speed in arriving at an accurate solution, and the eigenvalue should certainly be much nearer the true value, since the Laplacian is now adequately represented.

The numerical work was made possible by generous support by the University of Illinois Research Board, to whom the author is deeply indebted. Appreciation is also expressed to Mr. John Todd and to Dr. Ralph Slutz of the National Bureau of Standards for making the SEAC available and for their interest in the problem and to Mr. Joseph H. Wegstein for much valuable research assistance, for coding and programing the problem, and for solving it with the machine.

The improved approximation to the Laplacian was developed while the author was spending the summer at the Brookhaven National Laboratory. The opportunity to use its facilities was most welcome.

[4] This was kindly pointed out by Dr. Hartland Snyder.

Quantum Corrections to Classical Nonlinear Meson Theory

DONALD R. YENNIE*†
Institute for Advanced Study, Princeton, New Jersey
(Received July 8, 1952)

For a linear Einstein-Bose field of large amplitude it is well known that the classical approximation is quite good for treating certain problems; the validity of this conclusion for the case of a nonlinear field is investigated here. In order to compare the classical and quantized versions of a nonlinear meson theory, we consider the problem of calculating the energy of interaction of the field with a given static source distribution. The quantized theory is treated in such a way that the classical result appears as a first approximation; the quantum corrections then include infinite renormalizations of the original parameters of the theory plus finite corrections to the energy. Part of these corrections are estimated and are found to become increasingly important with increasing source strength, contrary to the usual assumption. Since only a small part of the total quantum correction can be estimated by the present methods, a complete calculation might give a value very much larger or very much smaller than that given here; nevertheless, it is possible to conclude that the nature of quantum corrections is such that they cannot be treated as small perturbations.

I. INTRODUCTION

RECENTLY Schiff[1] and Malenka[2] have suggested the possibility of accounting for certain nuclear properties such as nuclear saturation and shell structure by means of forces derived from a nonlinear meson theory. In these calculations the meson field is treated classically under the assumption that quantum fluctuations can be neglected because the meson field has a large amplitude and obeys Einstein-Bose statistics. Such an assumption is certainly valid for a linear meson field because a large field amplitude in the classical theory corresponds to the presence of a large number of mesons in the quantized theory, and quantum fluctuations are unimportant in such a situation. In this paper we shall be concerned with the energy of interaction of the field with a static source; for a linear field it will be apparent that this energy is actually the same in the quantum theory as in the classical theory, independent of the source strength. In the nonlinear meson theory, however, new features arise because of the infinities introduced by the interaction of the field with itself. From the power series expansion of this interaction, we know that these infinities lead to renormalizations of the original parameters of the theory plus finite residues which are taken to be physically meaningful. There seems to be no *a priori* reason to expect that finite quantities obtained in this way should be small compared to the corresponding quantities calculated with the classical theory. The object of the present paper is to treat the quantized theory in such a way that the classical theory appears as a first approximation and to investigate the relative importance of the quantum corrections to this classical approximation.

Let us first review briefly the general features of the classical theory. We consider as a particular example the following Lagrangian density[3]

$$\mathfrak{L}=\tfrac{1}{2}(\partial\phi/\partial t)^2-\tfrac{1}{2}(\nabla\phi)^2-\tfrac{1}{2}\kappa^2\phi^2-\tfrac{1}{4}\alpha^2\phi^4+f\phi, \quad (1)$$

where $f(\mathbf{r})$ is the nucleon source density, which we take to be time-independent (thus neglecting the dynamics of the source). We use units in which $\hbar=c=1$. From this Lagrangian density are deduced the Hamiltonian density and the Hamiltonian

$$\mathfrak{IC}=\tfrac{1}{2}\pi^2+\tfrac{1}{2}(\nabla\phi)^2+\tfrac{1}{2}\kappa^2\phi^2+\tfrac{1}{4}\alpha^2\phi^4-f\phi, \quad (2)$$

$$H=\int\mathfrak{IC}(dx)^3, \quad (3)$$

where $\pi=\partial\phi/\partial t$ is the momentum canonically conjugate to ϕ. The wave equation deduced from the Lagrangian or Hamiltonian is

$$\partial^2\phi/\partial t^2-\nabla^2\phi+\kappa^2\phi+\alpha^2\phi^3=f. \quad (4)$$

For a given source distribution $f(\mathbf{r})$, one has to solve the wave equation to obtain the static field ϕ_s (in practice this may be done only approximately). Inserting ϕ_s into (3), the classical energy associated with the given source distribution is obtained. By considering different source distributions, information about nuclear forces, the potential energy of a nucleon in a nucleus, etc., is deduced. The present note is concerned not with any of these particular nuclear problems, but only with the general method of calculation.

In the next section the field is quantized according to the usual commutation rules, and by means of a canonical transformation the Hamiltonian is expressed in a form which clearly reveals the classical approximation. Part of the quantum corrections to the energy are then easily estimated by calculating the zero point

* National Research Fellow.
† Now at Stanford University, Stanford, California.
[1] L. I. Schiff, Phys. Rev. **80**, 137 (1950); **83**, 239 (1951); **84**, 1 (1951), referred to here as SI; Phys. Rev. **84**, 10 (1951).
[2] B. J. Malenka, Phys. Rev. **85**, 686 (1952); **86**, 68 (1952).
[3] This particular Lagrangian density has been considered classically by Schiff in SI (see reference 1) and by Malenka (see reference 2); as shown by Malenka (see reference 2) the form of the nonlinearity in (1) is suggested by the pseudoscalar interaction of a quantized nucleon field with a classical pseudoscalar field. The sign of the nonlinearity in (1) has been chosen so that its contribution to the energy will be positive definite. This excludes from our consideration the case in which there is a classical particle-like solution, as treated by Finkelstein, LeLevier, and Ruderman, Phys. Rev. **83**, 326 (1951).

energy of the part of the Hamiltonian which is quadratic in the meson variables; this estimation involves the dropping of infinite κ- and α-renormalizations and the interpretation of the finite remainder as physically meaningful. These quantum corrections are found to increase in relative importance with increasing source strength, thus showing that quantum corrections are important and may not be treated as a perturbation. In order to see how to calculate higher order corrections and to show that the renormalization prescription used in this estimation is correct, we turn in Sec. III to a proof of the existence of a consistent renormalization program by means of a power series expansion. The main result of this program is that the energy is a functional of a variable ϕ_0 which obeys a complicated nonlinear differential-integral equation. The energy functional and the equation for ϕ_0 are related by the condition that a solution of the equation minimizes the energy functional. To the zeroth order in the quantum corrections, ϕ_0 is, of course, the same as ϕ_s, and the energy functional is the same as (3). In Sec. IV, the results of Sec. II are shown to result from summing a certain subset of the power series expansion. To investigate whether quantum corrections will be reduced by including a larger portion of the total quantum contribution, we sum the contribution from a somewhat larger subset of the power series expansion. It is found that the effect of including this larger subset is to increase the estimate of the quantum corrections, thus confirming the conclusions of Sec. II.

II. QUANTIZATION OF THE FIELD

The field is quantized according to the usual rules

$$[\pi(\mathbf{x}), \phi(\mathbf{x}')] = -i\delta(\mathbf{x}-\mathbf{x}'), \tag{5}$$

where π and ϕ are Schrödinger representation operators. We make a canonical transformation[4]

$$S = \exp\left[i\int \phi_0(\mathbf{x})\pi(\mathbf{x})(dx)^3\right], \tag{6}$$

where ϕ_0 is a c-number function of position to be specified later. Under this transformation, the field quantities and the Hamiltonian are transformed in the following way

$$\begin{aligned} &S\phi S^* = \phi_0+\phi, \quad S\pi S^* = \pi, \\ &SHS^* = H_{cl}+H_1+H_2, \end{aligned} \tag{7}$$

$$H_{cl} = \int \{\tfrac{1}{2}(\nabla\phi_0)^2+\tfrac{1}{2}\kappa^2\phi_0^2+\tfrac{1}{4}\alpha^2\phi_0^4-f\phi_0 + \phi(-\nabla^2\phi_0+\kappa^2\phi_0+\alpha^2\phi_0^3-f)\}(dx)^3,$$

$$H_1 = \int \{\tfrac{1}{2}\pi^2+\tfrac{1}{2}(\nabla\phi)^2+\tfrac{1}{2}\kappa^2\phi^2+\tfrac{3}{2}\alpha^2\phi_0^2\phi^2\}(dx)^3,$$

$$H_2 = \int \{\tfrac{1}{4}\alpha^2\phi^4+\alpha^2\phi_0\phi^3\}(dx)^3.$$

[4] This transformation was used previously by L. I. Schiff, Phys. Rev. **86**, 625 (1952).

The choice of ϕ_0 will be discussed in more detail in Sec. III. In this section we shall make the working assumption that quantum corrections are small when the classical field strengths are large. Under this assumption, ϕ_0 is approximately equal to ϕ_s, the classical static field. In the Hamiltonian the term linear in ϕ is then small and H_{cl} is approximately the usual classical energy. The quantized field interacts with the source mainly through the dependence of H_1 and H_2 on ϕ_0. Since we are assuming that ϕ_0 is in some sense large compared to ϕ, we try to treat H_1 exactly, with H_2 as a perturbation.

The field equation derived from H_1 is

$$\partial^2\phi/\partial t^2 - \nabla^2\phi+\kappa^2\phi+3\alpha^2\phi_0^2\phi = 0. \tag{8}$$

In this equation it is seen that $3\alpha^2\phi_0^2$ serves as an effective potential through which the ϕ field moves. Considered as a classical equation with periodic boundary conditions, the field equation has fundamental solutions of the form

$$\exp(\pm i\omega_n t)\phi_n(\mathbf{x}), \quad \omega_n > 0 \tag{9}$$

satisfying

$$(-\omega_n^2-\nabla^2+\kappa^2+3\alpha^2\phi_0^2)\phi_n = 0. \tag{10}$$

This enables us to define the operator $\omega = (-\nabla^2+\kappa^2+3\alpha^2\phi_0^2)^{\frac{1}{2}}$ by the equation

$$\omega\phi_n = \omega_n\phi_n. \tag{11}$$

We may now expand ϕ and π in terms of the complete set of functions ϕ_n:

$$\begin{aligned} &\phi = \textstyle\sum_n (2\omega_n)^{-\frac{1}{2}}(a_n\phi_n+a_n^*\phi_n^*), \\ &\pi = \textstyle\sum_n (\omega_n/2)^{\frac{1}{2}}i(a_n^*\phi_n^*-a_n\phi_n), \end{aligned} \tag{12}$$

where the a's obey the following commutation rules

$$[a_n, a_{n'}^*] = \delta_{nn'}. \tag{13}$$

Expressing H_1 in terms of these expansions, we obtain the usual result

$$\begin{aligned} &H_1 = \textstyle\sum_n N_n\omega_n + \frac{1}{2}\sum_n \omega_n, \\ &N_n = a_n^* a_n, \end{aligned} \tag{14}$$

where the operators N_n have the eigenvalues 0, 1, 2, 3, $\cdots$. The vacuum is defined as the state of lowest energy: all $N_n = 0$. Normally the infinite zero-point energy $(\frac{1}{2}\sum\omega_n)$ is neglected because it is an infinite additive constant. In the present case, however, the zero-point energy may not be neglected because it depends on the source strength through ϕ_0; in fact, it varies by an infinite amount when the source is changed. We shall show that part of this infinite dependence on the source can be interpreted as a change in the values of κ and α appearing in H_{cl}. After this renormalization, we shall have a finite remainder which may be interpreted as physically meaningful (within the spirit of the usual renormalization treatment) and compared with terms already occurring in the classical energy. The zero-

point energy is

$$\begin{aligned}\tfrac{1}{2}\sum\omega_n&=\tfrac{1}{2}Tr\omega\\&=\frac{1}{2}\int\int\delta(\mathbf{x}-\mathbf{x}')(-\nabla^2+\kappa^2+V_0)^{\frac{1}{2}}\delta(\mathbf{x}'-\mathbf{x})\\&\qquad\times(dx)^3(dx')^3\\&=\frac{1}{16\pi^3}\int\int\int\delta(\mathbf{x}-\mathbf{x}')(-\nabla^2+\kappa^2+V_0)^{\frac{1}{2}}\\&\qquad\times\exp[i\mathbf{k}\cdot(\mathbf{x}-\mathbf{x}')](dx)^3(dx')^3(dk)^3,\end{aligned}\tag{15}$$

where $V_0=3\alpha^2\phi_0^2$.

We cannot evaluate this expression exactly because ∇^2 may act on the V_0 under the square root; we accordingly make the approximation that V_0 is a slowly varying function of position and that we may neglect its derivatives. Even though this approximation may not be good in general, we expect it to give us an estimate of the order of magnitude of the correction to the energy. In the Appendix we use the WKB approximation to estimate the fundamental frequencies for the case of a one-dimensional source distribution and show that it agrees with the following result except for possible ambiguities in the renormalization; surface effects arising from sharp discontinuities in V_0 are also estimated there. With this approximation, the zero-point energy becomes

$$\begin{aligned}\tfrac{1}{2}\sum\omega_n&=\frac{1}{16\pi^3}\int\int(dx)^3(dk)^3(k^2+\kappa^2+V_0)^{\frac{1}{2}}\\&=\lim_{K\to\infty}\frac{1}{4\pi^2}\int(dx)^3\int_0^K k^2dk(k^2+\kappa^2+V_0)^{\frac{1}{2}}\\&=\int(dx)^3\{A+B\alpha^2\phi_0^2+C\alpha^4\phi_0^4+\frac{1}{64\pi^2}\\&\qquad\times[(V_0+\kappa^2)^2\ln(1+V_0\kappa^{-2})\\&\qquad-\kappa^2V_0-1.5V_0^2]\},\end{aligned}\tag{16}$$

where A, B, and C are infinite constants, independent of α and ϕ_0. A is the zero-point energy of the field in the absence of a source and B and C give renormalizations of the κ and α appearing in the first line of H_{el}. The finite part has been made unique by the requirement that its series expansion in powers of ϕ_0 contains no terms in ϕ_0^2 or ϕ_0^4. The consistency of this renormalization prescription will be discussed in Secs. III and IV. Interpreting the finite part as physically meaningful, the energy of the vacuum is given approximately by

$$\begin{aligned}E_0\cong\int\{&\tfrac{1}{2}(\nabla\phi_0)^2+\tfrac{1}{2}\kappa^2\phi_0^2+\tfrac{1}{4}\alpha^2\phi_0^4-f\phi_0\\&+\frac{1}{64\pi^2}[(3\alpha^2\phi_0^2+\kappa^2)^2\ln(1+3\alpha^2\phi_0^2\kappa^{-2})\\&-3\kappa^2\alpha^2\phi_0^2-13.5\alpha^4\phi_0^4]\}(dx)^3.\end{aligned}\tag{17}$$

It is easily seen that for small field strengths the new contribution is unimportant since the leading term in a power series expansion is proportional to ϕ_0^6. For large field strengths, however, the logarithmic term becomes more important than other terms in the energy. As an example, we take the following parameters for the interior of a nucleus from Schiff's paper:[4] $\kappa=1$; $\alpha=7.96$, $\phi_0=0.149$. With these parameters the nonlinear term in the energy has the value $\frac{1}{4}\alpha^2\phi_0^4=0.0078$, while the quantum correction just obtained has the value 0.023. For larger field strengths, quantum corrections will become relatively more important.

In addition to these energy corrections, we may also desire to determine the corresponding quantum corrections to the equation which ϕ_0 must satisfy. To the order of approximation of the present section, these corrections arise from the term $\alpha^2\phi_c\phi^3$ which occurs in H_2. Before this term can be used in a perturbation expansion, it is necessary to rewrite it as an ordered product[5] plus another term which is linear in ϕ. Because of (12), the definition of the creation and destruction operators, and hence of the ordered product, depends on ϕ_0. The ordered product is used in the perturbation expansion, while the other term gives a contribution to the equations which ϕ_0 must satisfy. The correction to the equation of ϕ_0 is

$$\begin{aligned}3\alpha^2\phi_0\langle\phi^2\rangle_0&=3\alpha^2\phi_0\textstyle\sum_n(1/2\omega_n)\phi_n^*\phi_n\\&=(\tfrac{3}{2})\alpha^2\phi_0(\mathbf{x}|(-\nabla^2+\kappa^2+V_0)^{-\frac{1}{2}}|\mathbf{x}).\end{aligned}\tag{18}$$

Now it is easily derived from (10) that

$$\omega_n\delta\omega_n/\delta\phi_0(\mathbf{x})=3\alpha^2\phi_0(\mathbf{x})\phi_n^*(\mathbf{x})\phi_n(\mathbf{x}).\tag{19}$$

Hence, the corrected equation for ϕ_0 may be written

$$-\nabla^2\phi_0+\kappa^2\phi_0+\alpha^2\phi_0^3+\tfrac{1}{2}\delta(\textstyle\sum\omega_n)/\delta\phi_0=f.\tag{20}$$

From this equation it is apparent that the κ- and α-renormalizations occurring in the equation for ϕ_0 are the same ones that occurred in the energy, Eq. (17). The renormalization is thus consistent to this order of approximation. The finite correction to the equation satisfied by ϕ_0 is obtained simply by taking the functional derivative of the corresponding finite correction to the classical energy. In the following section, this relation will be seen to be generally true, although it appears there as a simplifying choice rather than a necessary requirement.

It is now evident that our working assumption is not valid; for having assumed that quantum corrections were small, we have found that to a certain order of approximation they are large. In fact, the quantum corrections seem to become relatively more important as the classical field strength increases, contrary to the usual assumptions that the effect of lack of commutativity may be neglected when the field magnitudes

[5] In an ordered product, all creation operators are written to the left of all destruction operators; the use of the ordered product was introduced by A. Houriet and A. Kind, Helv. Phys. Acta 22, 319 (1949).

are large. We have not actually proved that quantum corrections are large, because we have not treated the whole Hamiltonian exactly. It is conceivable, although it seems to be very unlikely, that the net effect of all the perturbations we have neglected would be to reduce the quantum corrections to a small value. In any case, we have shown that we may not assume at the start that quantum corrections will be small enough to be calculable by the sort of perturbation techniques used here.

III. THE RENORMALIZATION PROGRAM

In the preceding section, a finite result was extracted from an infinite quantity by applying a certain prescription for renormalizing the original parameters of the theory. This renormalization took place with respect to the lowest possible order of the parameter of nonlinearity. In order that the result obtained in this way should have a physical meaning, it is necessary to show that the result of the preceding section is the first stage of some renormalization program which can be carried through consistently to all orders of approximation. It must be shown, for instance, that each of the five quantities α^2 appearing in the Hamiltonian will be renormalized in exactly the same way; similarly for the three quantities κ^2. In carrying out this demonstration, it will be necessary to make a power series expansion of the energy so that the techniques developed for handling the renormalization of the S-matrix may be employed.[6,7] We shall rely heavily on the results of Ward's paper[7] because the set of interacting fields treated by him includes, as a special case, the nonlinear field of this paper. Only the features arising because of the presence of a source will be treated in this note.

Before proceeding, we note that the canonical transformation (6) is time-independent and therefore does not alter the eigenvalues of H. This means that if we calculate the energy from (7) using perturbation theory, the net effect of all contributions involving ϕ_0 will be identically zero; this will be seen explicitly when the perturbation method is presented. For the quantum-mechanical calculation, it is therefore simplest to set ϕ_0 equal to zero at the start and proceed with a perturbation treatment of the original Hamiltonian (3). In the perturbation treatment it will be seen that the various contributions to the energy can be represented by Feynman graphs. The classical approximation to the energy is represented by the set of graphs in which there are no closed loops; the contribution of the last section is represented by the set of graphs with one closed loop; etc. The results of Ward's paper[7] can be applied immediately, and with a suitable renormalization of the source, they lead to a well-defined power series expansion for the energy. However, because of the closer connection with the classical theory, we prefer to make the canonical transformation involving ϕ_0. To avoid having all the contributions from ϕ_0 cancel each other out, we calculate the part of the energy represented by a small (but infinite) subset of the Feynman graphs and then choose ϕ_0 in such a way that the remaining contribution vanishes identically. In this way the quantum corrections appear as a modification of the classical problem.

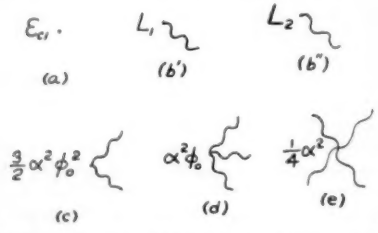

FIG. 1. Types of vertices which may appear in Feynman graphs.

In order to apply perturbation theory, we separate the Hamiltonian (7) into a free field part H_0 and a perturbation H_i

$$SHS^*=H_0+H_i,$$

$$H_0=\int\{\tfrac{1}{2}\pi^2+\tfrac{1}{2}(\nabla\phi)^2+\tfrac{1}{2}\kappa_c^2\phi^2\}(dx)^3,$$

$$H_i=H_{ci}+\int\{\tfrac{1}{4}\alpha^2\phi^4+\alpha^2\phi_0\phi^3+(\tfrac{3}{2})\alpha^2\phi_0^2\phi^2+(\kappa^2-\kappa_c^2)\phi^2\}(dx)^3. \quad (21)$$

The quantities κ^2, α^2, f, and ϕ_0 appearing in (21) are not finite but must be related to the corresponding finite quantities κ_c^2, α_c^2, f_c, and ϕ_{0c} in such a way that the final results are unique and finite (aside from any possible lack of convergence of the perturbation expansion itself). Notice that H_0 contains the finite mass κ_c; the last term of H_i cancels out mass corrections explicitly as they arise from the perturbation expansion of the other parts of H_i. It is easily seen that the mass corrections for H_{ci} cancel in the same way term by term, so we shall take no further account of mass renormalization.

We are interested in the energy of the state in which there are no freely propagating mesons present. This energy is easily calculated by averaging the rate of change of phase of the U-matrix over a long period of time and is found to be

$$E_{vac}=\sum_G\sum_{n=0}^{\infty}[(-i)^n/(n+1)!]\int_{-\infty}^{\infty}\cdots\int_{-\infty}^{\infty}(dx_0)^3\times(dx_1)^4\cdots(dx_n)^4P[H_i(x_0),\ H_i(x_1)\cdots H_i(x_n)]. \quad (22)$$

The sum is over all Feynman graphs G which are connected with the point x_0 and which have no external

[6] F. J. Dyson, Phys. Rev. 75, 1736 (1949).
[7] J. C. Ward, Phys. Rev. 84, 897 (1951).

meson lines. The operators occurring in $H_i(x_j)$ are interaction representation operators; that is, they have the time dependence of free field operators and reduce to Schrödinger representation operators at zero time. P is the usual chronological ordering operator. Since ϕ_0 is independent of time, the result of the integrations in (22) is independent of the time assigned to $H_i(x_0)$; for definiteness, we set this time equal to zero.

The types of vertices which may occur in Feynman graphs are shown in Fig. 1. We have used the abbreviations:

$$\begin{aligned}\mathcal{E}_{cl}&=\tfrac{1}{2}(\nabla\phi_0)^2+\tfrac{1}{2}\kappa_c{}^2\phi_0{}^2+\tfrac{1}{4}\alpha^2\phi_0{}^4-f\phi_0,\\ L_1&=(-\nabla^2+\kappa_c{}^2)\phi_0,\\ L_2&=\alpha^2\phi_0{}^3-f.\end{aligned}\tag{23}$$

Terms involving mass renormalizations have already been dropped. The two types of vertices (b') and (b'') have been distinguished to aid in proving the statement made previously that the net effect of all contributions involving ϕ_0 will be identically zero. The vertex (a) appears in one Feynman graph, consisting only of itself $(n=0)$.

Corresponding to each line of a graph there is a factor

$$\begin{aligned}\langle P[\phi(x),\phi(y)]\rangle_0&=\tfrac{1}{2}\Delta_F(x-y)\\ &=[(-i)/(2\pi)^4]\int_C (dk)^4(k^2+\kappa_c{}^2)^{-1}\\ &\quad\times\exp[ik_\mu(x-y)_\mu],\end{aligned}\tag{24}$$

where the contour C is defined by imagining κ_c to have a small negative imaginary part which displaces the poles from the real axis.

It is now easy to show that the net effect of all contributions involving ϕ_0 is zero. Consider a particular graph which does not contain any vertices of type (b'), but has the quantity ϕ_0 occurring a certain number of times. Any ϕ_0 may be replaced by a contribution involving a vertex of type (b'), yielding a new graph which must be considered in the enumeration. The net result is that if ϕ_0 occurs at the place x in the original graph, in the new graph it is to be replaced by

$$\tfrac{1}{2}(-i)\int\Delta_F(x-y)(-\nabla^2+\kappa_c{}^2)\phi_0(y)(dy)^4=-\phi_0(x).$$

Since this replacement takes place independently of all others, all contributions involving ϕ_0 are canceled out identically. The only contributions which do not cancel in this way are those which are made up purely of the perturbation expansion of $(-f\phi+\frac{1}{4}\alpha^2\phi^4)$.

In order to make the use of the canonical transformation (6) nontrivial, it is necessary to choose ϕ_0 in such a way that the energy may be evaluated from a subset of all possible Feynman graphs. It may be possible to choose such a subset in more than one way, but we make

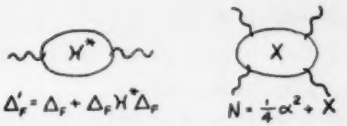

FIG. 2. The two types of primitive divergences.

the following choice which seems to make the subset as small as possible, at the expense of complicating the equation which ϕ_0 must satisfy. We define the subset Ω' to consist of all graphs G' which have the property that they cannot be bisected by cutting a single meson line. ϕ_0 must then be chosen so that the net contribution from all remaining graphs is zero. This is easily done, for each of these graphs must contain at least two subgraphs of the type (β), which have the properties that they are connected to the remainder of the graph by a single line and may not be bisected by cutting a single internal line. The simplest examples of this type of subgraph are the vertices (b') and (b''). In order that the net contribution from graphs not in Ω' be zero, we require simply that the sum of all contributions represented by the subgraphs (β) vanish. This gives a complicated nonlinear differential integral equation which ϕ_0 must satisfy; the classical field equation is the first approximation to this more general equation.

There is obviously a close structural relationship between the graphs G' and the subgraphs (β); for if we replace a ϕ_0 acting at some point in G' by an external line attached to the point, the result is a contribution to one of the subgraphs (β). If this is done in all possible ways, several subgraphs of the type (β) will be obtained from the same G', and inspection shows that all these contributions will have the proper weight factor associated with them. This graphical process is a representation of the mathematical process of taking the functional derivative with respect to $\phi_0(x)$ of the integral corresponding to G'. Letting $A[\phi_0]$ be the contribution to the energy arising from graphs in Ω', the condition that the sum of all contributions from subgraphs of type (β) vanishes is then expressed by the equation

$$\delta A[\phi_0]/\delta\phi_0(x)=0.\tag{25}$$

We are now ready to discuss the renormalization program. Except for the terms involving ϕ_0, Ward[7] has already discussed a more general case than that of this paper; and we shall make full use of his results, which we review briefly. In this theory there are two types of primitive divergences, self-energy parts and four-vertex parts, shown in Fig. 2. Every graph G' has a "skeleton" which may be obtained by omitting all self-energy and four-vertex parts from G'. Corresponding to a given skeleton there is a whole set of graphs which may be built up by all possible insertions of self-energy and four-vertex parts. The net effect of all these insertions is to modify the propagation and scat-

tering of mesons in the following way

$$\Delta_F(x-x') \rightarrow \Delta_F'(x-x')$$
$$\tfrac{1}{4}\alpha^2\delta(x_1-x_2)\delta(x_1-x_3)\delta(x_1-x_4) \rightarrow$$
$$\tfrac{1}{4}\alpha^2\delta(x_1-x_2)\delta(x_1-x_3)\delta(x_1-x_4)+X(x_1, x_2, x_3, x_4)$$
$$=N(x_1, x_2, x_3, x_4). \quad (26)$$

Because of the divergences of the theory, these quantities are given by power series with infinite coefficients. Δ_F' and N are called the infinite functions. If at each stage of the power series expansion we define finite quantities by the unique subtraction procedure specified in Ward's paper, we arrive at a corresponding set of finite functions which we designate Δ_c and N_c. It then turns out that the infinite functions, expressed in terms of α^2, are simply numerical multiples of the finite functions, expressed in terms of α_c^2.

$$\begin{aligned}\Delta_F' &= Z\Delta_c, \\ N &= Z^{-2}N_c.\end{aligned} \quad (27)$$

Z and α^2 are given by certain power series in α_c^2 (with infinite coefficients).

In order to apply these results to the present problem, we distinguish the various contributions to A according to the number of times that ϕ_0 acts in the contributing graphs; $A_m[\phi_0]$ is the total contribution from all graphs in which ϕ_0 acts m times. The cases $m=1$, $m=2$ and $m=4$ which occur in $\mathcal{S}_{cl}$ are somewhat special and will be discussed last. For $m \geq 6$, Ward's work shows us that

$$A_m[\phi_0]=Z^{-m/2}A_{mc}[\phi_0], \quad (28)$$

where A_{mc} is defined by inserting the finite functions Δ_c and N_c (expressed in terms of α_c and κ_c) into the various skeletons of graphs which contribute to A_m. From (28), it is obvious that the field strength should be renormalized in the following way

$$\phi_0=Z^{\frac{1}{2}}\phi_{0c}. \quad (29)$$

We have to show that (28) is also correct for $m=1$, $m=2$, and $m=4$. To make (28) correct for $m=1$, we are required to renormalize the source strength as follows

$$f=Z^{-\frac{1}{2}}f_c. \quad (30)$$

This is in agreement with the renormalization of the meson-nucleon interaction constant in Ward's paper.

The $m=2$ and $m=4$ contributions are special cases because they are primitively divergent. For $m=4$, it is obvious from (26) that the total contribution is given by

$$A_4=\int\cdots\int N(x_1, x_2, x_3, x_4)\phi_0(x_1)\phi_0(x_2)\phi_0(x_3)$$
$$\times\phi_0(x_4)(dx_1)^3(dx_2)^4(dx_3)^4(dx_4)^4.$$

By virtue of (27), it is obvious that A_4 satisfies (28). For $m=2$, we may express the result in terms of the proper self-energy part $\mathfrak{K}^*$

$$A_2=\int\tfrac{1}{2}\phi_0(-\nabla^2+\kappa_c^2)\phi_0(dx)^3$$
$$+i\int\phi_0(x_1)\mathfrak{K}^*(x_1, x_2)\phi_0(x_2)(dx_1)^3(dx_2)^4.$$

From Ward's paper

$$\mathfrak{K}^*(x_1, x_2)=\tfrac{1}{2}i(Z-1)Z^{-1}(-\Box^2+\kappa_c^2)\delta(x_1-x_2)$$
$$+Z^{-1}\mathfrak{K}_c^*(x_1, x_2),$$

where $\mathfrak{K}_c^*$ is the finite part of $\mathfrak{K}^*$, expressed in terms of the finite parameters. When this is substituted into the expression for A_2, it is found that the result satisfies (28). This completes the proof of the consistency of the renormalization program.

We may summarize the results of this section by the following set of rules for calculating the energy: (1) calculate the functional $A_c[\phi_{0c}]$ by summing the contributions from all graphs of type G' and dropping the infinite κ and α renormalizations in the manner specified by Ward;[7] (2) minimize this functional by requiring ϕ_{0c} to satisfy

$$\delta A_c[\phi_{0c}]/\delta\phi_{0c}(x)=0. \quad (31)$$

This minimum value of the functional is the energy associated with the given source distribution.

IV. NEARLY-UNIFORM SOURCE DISTRIBUTION

In this section we shall make the approximation, used previously in Sec. II, that the source is such a slowly varying function of position that its derivatives may be neglected. Such an approximation is probably not valid in practical problems; nevertheless, features which arise in such an approximation will probably have a counterpart in a more exact calculation. Strictly speaking, the results of this section will apply only to a source which is independent of position. Because of the great complexity that graphs of type G' may have, we shall sum the contributions from only a certain simple subset of all possible graphs. The method of summation is as follows: for sufficiently small f, the series expansion for A_c may converge, defining an analytic function; the analytic continuation of this function along the real f axis, if it exists and is unique, is taken to represent the sum of the infinite series, even outside the original radius of convergence.

It was mentioned in Sec. II that the quantity[8] $V_0=3\alpha^2\phi_0^2$ plays the role of a potential through which the ϕ-field moves; we shall now calculate some of the quantum corrections to this potential. The simplest type of correction is shown in Fig. 3(b). The potential V_0 must act one or more times on the closed loop because the graph with no such interactions corresponds

[8] In this section we shall drop the subscript c to denote the finite quantities; infinite quantities will be dropped as they arise according to the prescriptions of Ward.

to a mass renormalization which must be dropped. If V_0 acts only once, it yields a renormalization of the α^2 occurring in the contribution from Fig. 3(a). It is obvious that the result of summing all contributions (including zero interactions of V_0) will be, before renormalization, simply the propagation function for a particle in a potential V_0, which we call Δv_0. The net effect of all these contributions, including renormalizations, is the following correction to the original potential V_0

$$V_1(x)=(\tfrac{3}{2})\alpha^2\Delta v_0(x,x)-(\tfrac{3}{2})\alpha^2\Delta_F(x-x)$$
$$-(-3i/4)\alpha^2V_0\int[\Delta_F(x-y)]^2(dy)^4. \quad (32)$$

(Note that this corresponds to the addition of a term $\frac{1}{2}V_1\phi^2$ to the Hamiltonian.) Expressing Δv_0 in terms of the normal mode expansion (12), we obtain

$$V_1(x)=3\alpha^2\textstyle\sum_n(1/2\omega_n)\phi_n^*\phi_n$$
$$-[3\alpha^2/2(2\pi)^3]\int(dk)^3(k^2+\kappa^2)^{-\frac{1}{2}}$$
$$+[3\alpha^2/4(2\pi)^3]\int(dk^3)(k^2+\kappa^2)^{-1}V_0. \quad (33)$$

This is in agreement with Eq. (18), with the proper renormalization rule now specified. This shows that the results of Sec. II correspond to the sum of contributions from all graphs with one closed loop.

We may now extend this result to a somewhat larger class of graphs by a simple iteration procedure. For example, we may replace the quantities V_0 of Fig. 3(b) in arbitrary ways by the quantities V_1; the result will be the quantity V_2, given by an expression like (32), but with V_0 replaced by V_0+V_1. It is obvious that V_2 consists of V_1 plus additional contributions, so the next step of the iteration procedure is to replace the quantities V_0 of Fig. 3(b) in arbitrary ways by V_2 (not V_1+V_2), thus producing the quantity V_3. In this way we define V_{n+1} in terms of V_n, as indicated in Fig. 3(c). It is obvious that the renormalization procedure is precisely analogous to that employed in (31), so that we have the following recursion relation for $W_n=V_0+V_n$.

$$W_{n+1}=V_0+\tfrac{3}{2}\alpha^2(\mathbf{x}|(-\nabla^2+\kappa^2+W_n)^{-1}|\mathbf{x})-\tfrac{3}{2}\alpha^2(\mathbf{x}|(-\nabla^2+\kappa^2)^{-1}|\mathbf{x})+\tfrac{3}{4}\alpha^2(\mathbf{x}|(-\nabla^2+\kappa^2)^{-1}|\mathbf{x})W_n, \quad (34)$$
$$W_0=V_0.$$

So far this is an exact expression for the graphs considered in the iteration process. In order to proceed further, we take advantage of the approximation that the quantity ϕ_0 is a slowly varying function of position. Then the various W_n will also have this property and

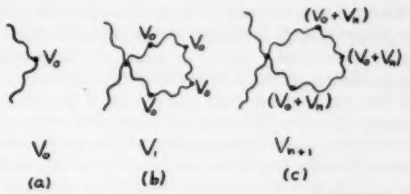

FIG. 3. Some contributions to the effective potential for the meson field.

Eq. (34) can be evaluated by the methods of Sec. II, yielding

$$W_{n+1}=V_0+(3\alpha^2/16\pi^2)[(\kappa^2+W_n)\times\ln(1+\kappa^{-2}W_n)-W_n], \quad (35)$$
$$W_0=V_0.$$

Examination of this recursion relation shows that for $V_0>0$:

$$0<W_0<W_1\cdots<W_n<\cdots. \quad (36)$$

Thus, either W_n approaches a finite limit W, or it approaches infinity. In the first case, W must satisfy the equation

$$V_0=W-(3\alpha^2/16\pi^2)[(\kappa^2+W)\ln(1+\kappa^{-2}W)-W]. \quad (37)$$

If, for a given V_0, no real solutions of this equation exist, the iteration process is divergent. Considered as a function of W, V_0 is zero for W equal to zero, has a maximum value when

$$\ln(1+\kappa^{-2}W)=16\pi^2/3\alpha^2, \quad (38)$$

and approaches minus infinity when W approaches infinity. This implies that the iteration process diverges when V_0 is greater than a certain value, which is the maximum of the right side of (37)

$$(V_0)_{\max}=\kappa^2[(3\alpha^2/16\pi^2)\{\exp(16\pi^2/3\alpha^2)-1\}-1]. \quad (39)$$

For $V_0<(V_0)_{\max}$, there are two solutions of Eq. (37); inspection shows that the recursion relation (35) converges to the smaller of these two solutions.

We may now calculate the energy and the correction to the classical field equation associated with graphs of the type shown in Fig. 3. Neglecting derivatives of ϕ_0, the corrected field equation is simply

$$\kappa^2\phi_0+\alpha^2\phi_0^3+\phi_0(W-V_0)=f. \quad (40)$$

Equations (37) and (40) are to be solved simultaneously for ϕ_0 and W. Equation (37) may be used to eliminate ϕ_0 from Eq. (40), thus giving f as an analytic function of W. As W increases from zero, this function increases from zero to a maximum at a value of W somewhat greater than given by (38), and then decreases to zero at the value of W for which the right side of (37) vanishes. The inverse function, which gives W as a function of f, is obviously analytic from zero

to the maximum value of f where it has a branch point; the proper branch is chosen by the condition that W must vanish when f does. For values of f larger than this maximum, no real solution to these equations exists and the contribution from this subset of graphs presumably diverges. This does not necessarily mean that the complete power series expansion diverges however, because if other graphs are included in the calculation in a suitable way the result as a whole may be finite.

We calculate the contribution to the energy by applying (31) in reverse; we now know a term in the equation for the classical field and wish to find the corresponding contribution A', which must satisfy

$$\delta A'/\delta\phi_0=\phi_0(W-V_0). \tag{41}$$

Assuming

$$A'=\int[B(W)-(\tfrac{3}{4})\alpha^2\phi_0^4](dx)^3, \tag{42}$$

we find

$$(dB/dW)(dW/d\phi_0)=\phi_0 W.$$

But from (37)

$$6\alpha^2\phi_0=(dW/d\phi_0)[1-(3\alpha^2/16\pi^2)\ln(1+\kappa^{-2}W)]. \tag{43}$$

Therefore,

$$dB/dW=(\tfrac{1}{6}\alpha^2)W[1-(3\alpha^2/16\pi^2)\ln(1+\kappa^{-2}W)]. \tag{44}$$

Integrating this equation, we find

$$B=(W^2/12\alpha^2)-(1/64\pi^2)[(W^2-\kappa^4)\ln(1+\kappa^{-2}W) -\tfrac{1}{2}W^2+\alpha^2W]. \tag{45}$$

This calculation of A' by means of (41) is much simpler than by the original definition of A' because of the difficulty of properly enumerating the various contributions to A' in the direct calculation.

These results seen to reinforce the views of Sec. II that quantum corrections to the energy associated with a source distribution become relatively more important as the source strength is increased. It certainly seems to be unlikely that the net effect of all the contributions omitted would be just sufficient to make the total effect very small, although such a possibility cannot definitely be ruled out. In any case, we are justified in saying that quantum corrections are not so small that they may be treated as a perturbation. The results of this section also suggest the possibility that the relation of the energy to the source strength may be changed qualitatively as well as quantitatively. For example, the contribution of A' to the energy increases with f until a critical value of f is reached beyond which the problem can no longer be solved. For this value of f, the energy is still finite, which means that such a source could be built up without an infinite expenditure of energy; if, instead, the energy became infinite as f approached its critical value, then we would have a saturation effect which would prevent the source from being built up. Since we are considering only one class of graphs out of an infinite number of classes, it is hard to predict whether a final complete calculation would show either of these effects, or possibly other effects not yet revealed in the calculation to this stage of approximation; however, we should be prepared to expect such effects.

Unfortunately the results of this paper do not shed too much light on the question of convergence of the power series expansion. The functional A is a power series expansion in both α^2 and ϕ_0; each power of ϕ_0 has a coefficient which is an infinite series in powers of α^2; each power of α^2 has a coefficient which is a polynomial in ϕ_0. According to Hurst,[9] the coefficients of each power of ϕ_0 are divergent series for all values of α^2. This result is perhaps to be expected because the whole nature of the physical problem changes when α^2 changes sign, and this situation should not be capable of representation by a power series expansion with a nonvanishing radius of convergence (compare the remarks of Dyson[10] for the case of quantum electrodynamics). It is quite possible that the unusual result found in the calculation of A' is simply due to the fact that we have selected out a certain finite part of a divergent series. This divergent series as a whole may be meaningless, in which case the theory is meaningless; or it may be some sort of an asymptotic representation of an analytic function which is not expandable as a power series about the origin in the α^2 plane.

The order of magnitude of the corrections given by (42) is not to be taken too seriously; the particular form of the odd qualitative features in the calculation of A' is not to be taken seriously either, although the existence of some qualitative changes in the relation between the energy and the source strength does seem to be plausible. The present results therefore can be taken only as an indication that quantum corrections are relatively important for a nonlinear boson field with a large classical strength.

The author wishes to express his thanks to Dr. J. R. Oppenheimer for his interest and encouragement in this work. He is also indebted to Dr. M. Gell-Mann and Dr. K. V. Roberts for many stimulating discussions and for constructive criticism of the manuscript.

APPENDIX

It is the purpose of this Appendix to derive Eq. (16) for a one-dimensional source distribution by means of the WKB approximation for the normal mode frequencies. Consider such a source leading to a classical field $\phi_0(x)$ which depends only on the x-coordinate, but not on y and z, and assume periodic boundary conditions. The normal mode solutions (9) then take the form

$$\phi_n=\exp(i\omega_{n_1n_2n_3}t+ik_{n_1}y+ik_{n_2}z)u_{n_1}(x), \tag{A1}$$

[9] C. A. Hurst (private communication).
[10] F. J. Dyson, Phys. Rev. 85, 631 (1952).

where

$$[-\omega_{n_1n_2n_3}^2-(d^2/dx^2)+k_{n_2}^2+k_{n_3}^2+\kappa^2+3\alpha^2\phi_0^2]u_{n_1}(x)=0. \quad \text{(A2)}$$

The one-dimensional eigenvalue problem for the frequencies is therefore

$$[-(d^2/dx^2)+3\alpha^2\phi_0^2]u_n(x)=\Omega_n^2u_n(x), \quad \text{(A3)}$$

with

$$\omega_{n_1n_2n_3}=(\kappa^2+k_{n_2}^2+k_{n_3}^2+\Omega_{n_1}^2)^{\frac{1}{2}}. \quad \text{(A4)}$$

If the period of the functions is L, the zero-point energy is

$$\tfrac{1}{2}\sum\omega_n=\tfrac{1}{2}\left(\frac{L}{2\pi}\right)^2\int dk_2dk_3\sum_n(\kappa^2+k_2^2+k_3^2+\Omega_n^2)^{\frac{1}{2}}. \quad \text{(A5)}$$

The WKB approximation to the frequencies is

$$\int_R dx(\Omega_n^2-3\alpha^2\phi_0^2)^{\frac{1}{2}}+\beta_n=2\pi n, \quad \text{(A6)}$$

where R is the region of integration for which $\Omega_n^2>3\alpha^2\phi_0^2$. β_n is a phase factor which must be introduced if there are classical turning points for the given value of Ω_n^2. If ϕ_0^2 is a slowly varying function of position in the region of the turning point, the effects of β_n will be averaged out and β_n may be neglected in (A6). We shall treat this case first, and later modify it for the case in which there are discontinuities in ϕ_0^2. From (A6), the number of states in a range $d\Omega_n$ is given by

$$dn=\frac{2}{(2\pi)}\int_R dx\Omega_nd\Omega_n(\Omega_n^2-3\alpha^2\phi_0^2)^{-\frac{1}{2}}. \quad \text{(A7)}$$

The zero-point energy accordingly becomes

$$\tfrac{1}{2}\sum\omega_n=\frac{L^2}{(2\pi)^3}\int_{-\infty}^{\infty}dk_2dk_3\int_R dx\int_0^{\infty}\Omega d\Omega \times(\kappa^2+k_2^2+k_3^2+\Omega^2)^{\frac{1}{2}}(\Omega^2-3\alpha^2\phi_0^2)^{-\frac{1}{2}}. \quad \text{(A8)}$$

With the change of variable,

$$k_1^2=\Omega^2-3\alpha^2\phi_0^2,$$

this is seen to be identical with (16):

$$\tfrac{1}{2}\sum\omega_n=\frac{L^2}{2(2\pi)^3}\int dx\int_{-\infty}^{\infty}dk_1dk_2dk_3 \times(\kappa^2+k_1^2+k_2^2+k_3^2+3\alpha^2\phi_0^2)^{\frac{1}{2}}. \quad \text{(A9)}$$

We now turn to the case in which there are discontinuities in the function ϕ_0. For simplicity, we assume

$$\begin{aligned}3\alpha^2\phi_0^2&=0, \quad -L/2<x<-a;\\ &=U, \quad -a<x<a;\\ &=0, \quad a<x<L/2.\end{aligned} \quad \text{(A10)}$$

We further assume that the distance a is so large that for all except a negligible fraction of the frequencies we may assume

$$\begin{aligned}(\Omega_n^2-U)^{\frac{1}{2}}a&\gg1, \quad \Omega_n^2>U;\\ (U-\Omega_n^2)^{\frac{1}{2}}a&\gg1, \quad \Omega_n^2<U.\end{aligned} \quad \text{(A11)}$$

Under this assumption the phase shifts β_n for $\Omega_n^2>U$ will average out in a more or less random fashion, while those for $\Omega_n^2<U$ will not. Distinguishing the phase shifts for even and odd functions of x, we find for $\Omega_n^2<U$

$$\begin{aligned}\beta_{n\ \mathrm{odd}}&\cong2\tan^{-1}[\Omega_n^2/(U-\Omega_n^2)]^{\frac{1}{2}},\\ \beta_{n\ \mathrm{even}}&\cong-\pi+2\tan^{-1}[\Omega_n^2/(U-\Omega_n^2)]^{\frac{1}{2}}.\end{aligned} \quad \text{(A12)}$$

On the average,

$$\bar{\beta}_n\cong-\pi/2+2\tan^{-1}[\Omega_n^2/(U-\Omega_n^2)]^{\frac{1}{2}}. \quad \text{(A13)}$$

From (A6) we see that each Ω_n used in calculating the zero-point energy must be shifted by an amount $\delta\Omega_n$ given by

$$\int_R dx\frac{\Omega_n\delta\Omega_n}{(\Omega_n^2-U)^{\frac{1}{2}}}+\bar{\beta}_n=0. \quad \text{(A14)}$$

The resulting shift in the zero-point energy itself is then

$$\tfrac{1}{2}\sum\delta\omega_n=\frac{L^2}{(2\pi)^3}\int dk_2dk_3\int_R dx\int_0^{U^{\frac{1}{2}}}\Omega d\Omega(\Omega^2-U)^{-\frac{1}{2}} \times\Omega\delta\Omega(\kappa^2+k_2^2+k_3^2+\Omega^2)^{-\frac{1}{2}}. \quad \text{(A15)}$$

Combining these results, we obtain

$$\tfrac{1}{2}\sum\delta\omega_n=\left(\frac{L}{2\pi}\right)^2\lim_{K\to\infty}\int_0^K kdk\int_0^{U^{\frac{1}{2}}}\Omega d\Omega \times\left\{\frac{\pi}{2}-2\tan^{-1}\left(\frac{\Omega^2}{U-\Omega^2}\right)^{\frac{1}{2}}\right\}(\kappa^2+k^2+\Omega^2)^{-\frac{1}{2}}. \quad \text{(A16)}$$

Carrying out the k integration and using the fact that

$$\int_0^{U^{\frac{1}{2}}}\Omega d\Omega\left\{\frac{\pi}{2}-2\tan^{-1}\left(\frac{\Omega^2}{U-\Omega^2}\right)^{\frac{1}{2}}\right\}=0,$$

we find

$$\tfrac{1}{2}\sum\delta\omega_n=-\left(\frac{L}{2\pi}\right)^2\int_0^{U^{\frac{1}{2}}}\Omega d\Omega \times\left\{\frac{\pi}{2}-2\tan^{-1}\left(\frac{\Omega^2}{U-\Omega^2}\right)^{\frac{1}{2}}\right\}(\kappa^2+\Omega^2)^{\frac{1}{2}}. \quad \text{(A17)}$$

Making the substitution,

$$\Omega=U^{\frac{1}{2}}\sin(\tfrac{1}{2}\theta+\tfrac{1}{4}\pi),$$

we find after some simple manipulations

$$\tfrac{1}{2}\sum\delta\omega_n=\left(\frac{L}{2\pi}\right)^2\frac{U^2}{8}\int_{-\pi/2}^{\pi/2}\theta\cos\theta I(\sin\theta)d\theta, \quad \text{(A18)}$$

$$I(\sin\theta)=\sin\theta/[\kappa^2+\tfrac{1}{2}U+\tfrac{1}{2}U\sin\theta)^{\frac{1}{2}}+(\kappa^2+\tfrac{1}{2}U-\tfrac{1}{2}U\sin\theta)^{\frac{1}{2}}].$$

From the form of $I(\sin\theta)$, we are able to place the following upper and lower bounds on the change in the zero-point energy

$$\tfrac{1}{2}\sum\delta\omega_n<\left(\frac{L}{2\pi}\right)^2\frac{\pi U^2}{32}[(\kappa^2+U)^{\frac{1}{2}}+\kappa]^{-1}$$
$$>\left(\frac{L}{2\pi}\right)^2\frac{\pi U^2}{32}\cdot\tfrac{1}{2}(\kappa^2+U/2)^{-\frac{1}{2}}. \quad \text{(A19)}$$

For $U\gg\kappa^2$, $I(\sin\theta)$ reduces to

$$I(\sin\theta)=(2/U)^{\frac{1}{2}}\sin(\theta/2),$$

which gives

$$\tfrac{1}{2}\sum\delta\omega_n=(L/2\pi)^2(\pi U^{\frac{1}{2}}/32)(0.806). \quad \text{(A20)}$$

Under this condition, the surface energy per unit area is then approximately

$$(0.806/2^7\pi)U^{\frac{1}{2}}=[(3a^2)^{\frac{1}{2}}(0.806)/2^7\pi]\phi_0^3. \quad \text{(A21)}$$

Since in actual practice ϕ_0 will not have sharp discontinuities, the actual surface energy will be somewhat less than (A21).

PHYSICAL REVIEW VOLUME 88, NUMBER 3 NOVEMBER 1, 1952

The Angular Distribution of Prompt Neutrons Emitted in Fission

J. S. FRASER
Chalk River Laboratory, Atomic Energy of Canada Limited, Chalk River, Ontario, Canada
(Received July 9, 1952)

The angular distribution, relative to the direction of motion of the fragments, of the prompt fast neutrons emitted in the thermal neutron fission of U^{233}, U^{235}, and Pu^{239} has been measured. Collimated fission fragments were selected in energy in a gridded ionization chamber and coincident prompt neutrons in a given direction were counted by proton recoils in an electron collecting chamber filled with methane. The distributions obtained selecting only light fragments have been compared with curves computed on the basis of the evaporation of the neutrons from the moving fragments of the most probable mode. Reasonably good agreement is obtained if one postulates that in the fission of each of the three nuclides studied, the neutron emission probability is about thirty percent greater for the light fragment than for the heavy one. An upper limit of 4×10^{-14} sec following fission may be placed on the time of emission of the neutrons.

I. INTRODUCTION

IN 1945, Wilson[1] measured the correlation between the direction of the prompt neutrons and the fragments in the fission process. The results were consistent with the view that the neutrons are evaporated isotropically in the frame of reference of the moving fragments.

The angular dependence of coincidences between fission neutrons has been studied by De Benedetti *et al.*,[2] who concluded that there are twice as many neutron pairs emitted by opposite fragments than by the same fragment.

Prior to the work of Leachman[3] on the ionization yields of fission fragments, it was suggested by Brunton and Hanna[4] that preferential emission of neutrons from one group of fragments may contribute to the disagreement between the distributions in fission fragment mass derived from the ionization and chemical yield measurements. This discrepancy has been shown recently by Leachman[3,5] to be due to a variation in ionization yield with fragment mass and to a dispersion arising from instrumental errors and poor resolution.

The experiment to be described, essentially an extension of Wilson's experiment, was designed to investigate the possibility of preferential emission of neutrons by one of the fragments. It was also found possible to place a much lower limit on the time of emission of the neutrons than the figure of 8×10^{-9} sec given by Snyder and Williams.[6]

II. APPARATUS

A. The Fission Chamber

A cross section of the fission chamber is shown schematically in Fig. 1. A layer of fissile material, approximately 180 $\mu g/cm^2$ thick was deposited on a 2.5-cm diameter nickel or aluminum plate which was then cemented to the cathode. Over the source was placed a 0.081-in. thick Dural plate with $\frac{1}{32}$-in. holes drilled in an hexagonal array to act as a collimator. The average angle of emission of the fragments was, therefore, approximately 9° from the normal. The position of the neutron counter was such that the angular uncertainty of the neutron direction was equal to that of the fission fragments passing through the collimator. A

[1] R. R. Wilson, Phys. Rev. **72**, 189 (1947).
[2] De Benedetti, Francis, Preston, and Bonner, Phys. Rev. **74**, 1645 (1948).
[3] R. B. Leachman, Phys. Rev. **83**, 17 (1951).
[4] D. C. Brunton and G. C. Hanna, Can. J. Research **A28**, 190 (1950).
[5] R. B. Leachman, Los Alamos Report LADC 1058 (revised, unpublished).
[6] T. M. Snyder and R. W. Williams, Phys. Rev. **81**, 171 (1951).

Frisch grid of No. 35 B and S copper wires spaced $\frac{1}{16}$ in. apart was used to provide a shielding efficiency of 96 percent.[7] The distance from the source layer to the grid was 2.65 cm; the grid-collector spacing was 0.80 cm. With a gas filling of 1.5 cm of CO_2 and 100-cm argon, saturation of the fission fragment pulses was obtained with a field of 550 volts per cm. A field of 1500 volts per cm between collector and grid was required for zero grid interception. The rise time of the electron collection pulses was about 0.7 μsec. The electrode assembly was mounted in a cylindrical chamber which could be rotated about an eccentric axis through the plane of the fissile layer. A $1\frac{1}{2}$-in. diameter beam of slow neutrons from the thermal column of the *NRX* reactor could thus be made to pass through the source for all angular positions of the chamber.

The U^{233} and U^{235} sources were electrodeposited on nickel disks and the Pu^{239} was put down by the zapon layer technique.[8]

B. The Neutron Counter

In the fission process there are approximately as many γ-rays emitted as there are neutrons. The fast neutron counter in this experiment must therefore be relatively insensitive to these γ-rays. An electron collecting chamber filled to a moderately high pressure with methane fulfills the requirements. The chamber used is shown schematically in Fig. 1. The walls are of $\frac{1}{8}$-in. stainless steel, the end plate being $\frac{1}{2}$ in. thick. The inside diameter is 2.0 in. The 0.040-in. diameter collecting electrode is supported by a $\frac{1}{2}$-in. diameter copper-glass seal and a $\frac{1}{8}$-in. diameter Kovar guard ring. The exposed length of the central electrode is 4.5 in. An earlier model of the chamber included an "O"-ring seal for the endplate. It was found necessary, however, to use welded or soldered joints in order to maintain saturated electron collection over a period of several months. The chamber was heated to about 200°C and pumped for 20 hours before filling. After filling the chamber, the copper pumping tube was pinched off and soldered.

The pressure of the filling, 100 pounds per square inch absolute, was chosen so that the energy lost by a fast electron traversing the length of the counter would be about 200 kev. Since the average fission neutron energy is about 2 Mev, the operating bias could be set to reject most of the γ-ray counts with only a small loss of efficiency for the average neutron. The methane used was of very high purity, prepared at A.E.R.E., Harwell.

The electron collection was tested by measuring the counting rate of Po—Be neutrons at a fixed bias as a function of collecting electrode voltage. Throughout the experiment, the saturation curve remained flat from 3500 volts to at least 8500 volts.

[7] Buneman, Cranshaw, and Harvey, Can. J. Research, **A27**, 191 (1949).

[8] B. Rossi and H. Staub, *Ionization Chambers and Counters* (McGraw-Hill Book Company, Inc., New York, 1949), p. 210.

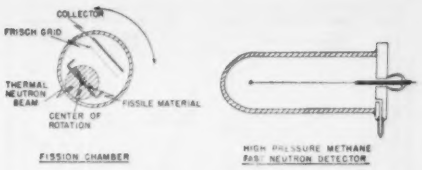

FIG. 1. Schematic diagram of the experimental apparatus.

The variation of neutron counting efficiency with neutron energy was required for the analysis of the experimental results. This was estimated by comparing the methane chamber with a long boron counter using 0.8-Mev neutrons produced by Na^{24} γ-rays on Be, 2.4-Mev neutrons from the D+D reaction, and 14-Mev neutrons from the D+T reaction. The efficiency of the counter at these three energies was (3.25±0.20) percent, (3.26±0.20) percent, and (0.83±0.06) percent, respectively. Between 2.4 Mev and 14 Mev, it was assumed that the efficiency varied as the neutron-proton scattering cross section. The efficiency at 0.8 Mev is approximately one-half of that expected from the variation of the cross section. As the neutron energy is decreased, a greater fraction of the proton recoil pulses are lost below the threshold level of approximately 380 kev. A smooth interpolation of the efficiency curve was made between 2.4 Mev and the threshold energy.

With the bias set at a level corresponding to a proton recoil energy of 380 kev, the counting efficiency for the Na^{24} γ-rays was 0.1 percent of that for the average fission neutron.

C. Electronic Equipment

At the output of the fission pulse linear amplifier, two discriminators were used. The lower one accepted all fission pulses and the upper one those above the valley between the two peaks of the fission fragment energy spectrum. The pulses which triggered the upper discriminator then, are almost entirely due to light fragments entering the chamber. The output pulses from the lower discriminator and from the discriminator on the neutron pulse linear amplifier were fed into a coincidence circuit employing delay line shaped pulses and having a resolving time $2\tau = 2.5$ μsec. The output from the coincidence circuit was fed to a scalar and to a gate circuit which passed the pulse to a second scaler only when the upper fission pulse discriminator was triggered. In this way, the angular distribution of neutron-fragment coincidences was recorded (a) with all fragments selected and (b) with only light fragments. The outputs from the two discriminators on the fission pulse amplifier and from the discriminator on the neutron pulse amplifier were recorded continually on scalers.

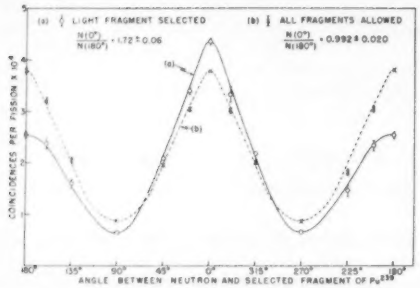
(a) LIGHT FRAGMENT SELECTED
(b) ALL FRAGMENTS ALLOWED
N(0°)/N(180°) = 1.72 ± 0.06
N(0°)/N(180°) = 0.992 ± 0.020
(a)
(b)
COINCIDENCES PER FISSION X 10⁴
ANGLE BETWEEN NEUTRON AND SELECTED FRAGMENT OF Pu²³⁹

FIG. 2. Experimental prompt neutron angular distribution curves for Pu^{239}.

III. EXPERIMENTAL RESULTS

The first nuclide studied was Pu^{239}. The complete angular distribution curves obtained are shown in Fig. 2. The vertical bars through the points represent the standard errors due to the counting statistics. The solid curve (a) was taken with light fragments only selected. It yields a ratio of the number of coincidences at 0° from the light fragment direction to the number at 180° of 1.72 ± 0.06. 180° from the light fragment corresponds to the direction of motion of the heavy fragment. The dashed curve (b) was obtained with fragments of all energies detected in the fission chamber. For this curve the ratio of the number at 0° to the number at 180° is 0.992 ± 0.020. The symmetry of this curve provides a check on the alignment of the apparatus and demonstrates that there is no measureable difference in the number of neutrons counted per unit solid angle when emitted from a fragment that passes through the gas of the fission chamber and from a fragment that penetrates the source backing.

One would expect no difference between curves (a) and (b) at the 90° and 270° positions. With the neutron counter in a direction perpendicular to the line joining the two fragments, it should be immaterial whether the light or the heavy fragment were detected in the chamber. The source used for these measurements was so non-uniform in thickness that 25 percent of the light fragments were decreased in energy below the upper discriminator level. This, together with the observation that fission modes with low energy light fragments have a greater than average neutron emission probability,[9] may account for the deviation. A subsidiary set of measurements on a uniform source with well-resolved peaks and the same average thickness (190 $\mu g/cm^2$) showed no significant difference in the two curves at 90° and 270°, and the value of the ratio $N(0°)/N(180°)$ was within the stated standard error of that for the first source.

Similar measurements were then made on sources of U^{233} and of uranium enriched to about 15 percent in U^{235}. The results are shown in Figs. 3 and 4 and are similar to those for Pu^{239}. In these figures, the complete angular distribution curves have been folded over the 0°–180° axis and weighted averages taken of the data at corresponding points; the comparison with theory, to be described in Sec. IV, is made only over the 0° to 180° range. In the curves obtained when the light fragments only were selected, values for the ratio $N(0°)/N(180°)$ are 2.05 ± 0.07 and 1.85 ± 0.06, respectively, for the two isotopes.

IV. DISCUSSION

A. Angular Distribution Predicted by the Evaporation Model

The experimental angular distribution may be compared with that calculated on the basis of the following simplifying assumptions: (1) The prompt neutrons are evaporated isotropically in the frame of reference of a moving fission fragment, (2) the neutrons are all emitted in the most probable fission mode, (3) the energy distribution of the neutrons in the frame of reference of a fragment is the same for the light and heavy fragments, and (4) this energy spectrum is the same for the fission fragments of U^{233}, U^{235}, and Pu^{239}.

If η is the energy of a neutron in the fragment's frame of reference, the energy of the same neutron in the laboratory system is[2]

$$E(\eta,\theta)=\eta[1-r^2+2r^2\cos^2\theta \pm 2r\cos\theta(1-r^2+r^2\cos^2\theta)^{\frac{1}{2}}], \quad (1)$$

where θ is the angle between the direction of the fragment and that of the neutron measured in the laboratory system, and r is the ratio of the fragment velocity to the neutron velocity in the fragment's system. The $\pm$ sign applies only when $r>1$ and corresponds to the fact that the neutron may be emitted at either one of two angles in the fragment's system and appear at the same laboratory angle but with different energies E.[10] It can

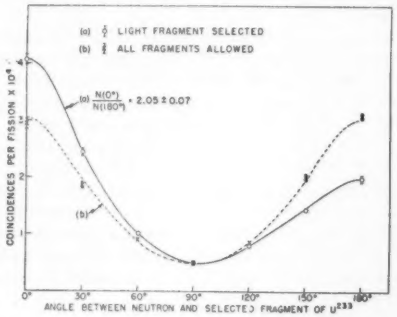
(a) LIGHT FRAGMENT SELECTED
(b) ALL FRAGMENTS ALLOWED
(a) N(0°)/N(180°) = 2.05 ± 0.07
(b)
COINCIDENCES PER FISSION X 10⁴
ANGLE BETWEEN NEUTRON AND SELECTED FRAGMENT OF U²³³

FIG. 3. Experimental prompt neutron angular distribution curves for U^{233}.

[9] J. S. Fraser and J. C. D. Milton (to be published).

[10] N. Feather, BR 335A (unpublished).

be shown that neutrons with the smaller of the two possible energies E make a negligible contribution to the observed angular distribution. For $r \leq 1$, E is single valued.

The probability per unit solid angle that neutrons of emission energy η appear at an angle θ in the laboratory system is[2,11]

$$f(\eta, \theta) = (1/4\pi)(E/\eta)^{\frac{1}{2}} |1 + r[(E/\eta)^{\frac{1}{2}} \cos\theta - r]|^{-1}. \quad (2)$$

The coincidence counting rate per unit solid angle of neutrons at a laboratory angle θ emitted by a fragment is[2]

$$F(\theta) = \int_0^\infty \phi(\eta) f(\eta, \theta) \epsilon[E(\eta, \theta)] d\eta, \quad (3)$$

where $\phi(\eta)$ is the energy distribution of the neutrons in the fragment's system, and $\epsilon(E)$ is the known efficiency of the neutron counter for neutrons of energy E. If θ is measured from the direction of the light fragment and if R denotes the ratio of the neutron emission probability of the light fragment to that of the heavy, then the angular distribution of coincidences will be given by

$$F(\theta) = \text{const} \times \left\{ R \int_0^\infty \phi(\eta) f_L(\eta, \theta) \epsilon_L[E(\eta, \theta)] d\eta + \int_0^\infty \phi(\eta) f_H(\eta, \pi - \theta) \epsilon_H[E(\eta, \pi - \theta)] d\eta \right\}. \quad (4)$$

This equation, with $R = 1$, gives that part of the angular distribution which can be ascribed solely to the effects of the motion of the fragments; the asymmetry is expected to vary in the same sense as the ratio of the most probable velocities of the two groups of fragments. Thus, if one knows the form of $\phi(\eta)$, a value for R may be found by fitting the computed angular distribution of neutron-fragment coincidences to the experimental curve.

B. The Emission Spectrum of the Neutrons

The choice of the emission spectrum $\phi(\eta)$ used in this calculation is guided by the fact that it must also give the laboratory energy distribution of fission neutrons, for which the experimental data is available for U^{235}.[12] The laboratory neutron spectrum $\Phi(E)$ given in terms of the emission spectrum, $\phi(\eta)$ is[10]

$$\Phi(E) = \frac{1}{1+R} \left\{ \frac{R}{4} \left(\frac{M_L}{mE_L} \right)^{\frac{1}{2}} \int_{\eta_1^L}^{\eta_2^L} \phi(\eta) \eta^{-\frac{1}{2}} d\eta + \frac{1}{4} \left(\frac{M_H}{mE_H} \right)^{\frac{1}{2}} \int_{\eta_1^H}^{\eta_2^H} \phi(\eta) \eta^{-\frac{1}{2}} d\eta \right\}, \quad (5)$$

[11] For example, see L. I. Schiff, *Quantum Mechanics* (McGraw-Hill Book Company, Inc., New York, 1949), first edition, p. 99.
[12] B. E. Watt, AEC Report 3073 (unpublished, 1951).

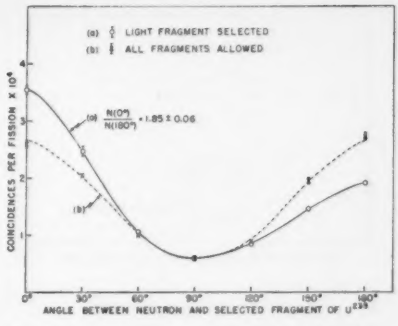
(a) ½ LIGHT FRAGMENT SELECTED
(b) ½ ALL FRAGMENTS ALLOWED
N(0°)/N(180°) = 1.85 ± 0.06
COINCIDENCES PER FISSION X 10⁴
ANGLE BETWEEN NEUTRON AND SELECTED FRAGMENT OF U²³⁵

FIG. 4. Experimental prompt neutron angular distribution curves for U^{235}.

where m, M_L, M_H are the masses of the neutron, light, and heavy fragments, respectively, E, E_L, E_H their kinetic energies, respectively, and

$$\eta_1' = E|(mE_f/M_fE)^{\frac{1}{2}} - 1|^2, \quad \eta_2' = E[(mE_f/M_fE)^{\frac{1}{2}} + 1]^2. \quad (6)$$

As a first approximation R was set equal to one, since the fitting of $\Phi(E)$ to the experimental data in the energy range below 8 Mev is not very sensitive to small changes in the values of R. It was found, in agreement with Watt,[12] that a good fit could not be obtained with a single "Maxwellian" distribution[10,13] of the form

$$\phi(\eta) = (a\eta/\eta_m) \exp[-(a/\eta_m)^{\frac{1}{2}}\eta], \quad (7)$$

where a is an exponential level density constant, and η_m the maximum possible neutron energy. This is, however, the distribution predicted by Weisskopf's statistical theory for a nucleus excited sufficiently to emit only one neutron. The number of neutrons emitted in the thermal neutron fission of a U^{235} nucleus is 2.5 ± 0.1,[14] i.e., an average of about 1.25 per fragment. The appropriate theoretical spectrum, therefore, should be that for a nucleus with sufficient internal excitation for the evaporation of between one and two neutrons. This has been given by Feld *et al.*,[15] and in the notation used here is

$$\phi(\eta) = \frac{a\eta}{\eta_m} \exp\left[-\left(\frac{a}{\eta_m} \right)^{\frac{1}{2}} \eta \right] + \frac{a^2\eta}{\eta_m} \int_0^{\eta_m - E_b - \eta} \frac{\eta' \exp\left[-\left(\frac{a}{\eta_m} \right)^{\frac{1}{2}} \eta' - \left(\frac{a}{\eta_m - E_b - \eta'} \right)^{\frac{1}{2}} \eta \right]}{\eta_m - E_b - \eta'} d\eta', \quad (8)$$

[13] V. F. Weisskopf, Phys. Rev. **52**, 295 (1937).
[14] Nucleonics **8**, 78 (1951).
[15] Feld, Feshbach, Goldberger, Goldstein, and Weisskopf, AEC Report NYO-636 (unpublished, 1951).

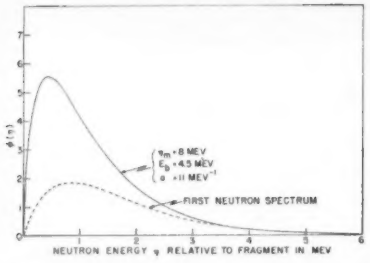

FIG. 5. Calculated prompt neutron emission spectrum for an average primary fission fragment.

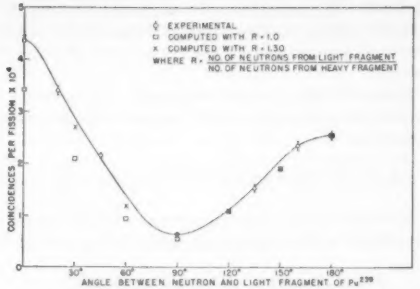
EXPERIMENTAL
COMPUTED WITH R = 1.0
COMPUTED WITH R = 1.30
WHERE R = NO. OF NEUTRONS FROM LIGHT FRAGMENT / NO. OF NEUTRONS FROM HEAVY FRAGMENT
COINCIDENCES PER FISSION X 10^4
ANGLE BETWEEN NEUTRON AND LIGHT FRAGMENT OF Pu^{239}

FIG. 7. Comparison of the calculated and the experimental angular distributions of the prompt neutrons in the fission of Pu^{239}.

where a and η_m are as given in (7), and E_b is the binding energy of the second neutron. The two terms represent the spectrum of "first" and "second" neutrons, respectively. The parameters chosen were $\eta_m = 8$ Mev, $E_b = 4.5$ Mev for the binding energy of a neutron in an average primary fission fragment, and $a = 11$ Mev^{-1} for the exponential level density constant for a medium weight nucleus. The computed emission spectrum $\phi(\eta)$ is shown in Fig. 5 and the comparison of the laboratory energy distribution computed by means of Eq. (5) with the experimental curve given by Watt is shown in Fig. 6. The agreement in the energy range below about 8 Mev is adequate for the present purpose. The contribution to the angular distribution of neutrons whose laboratory energies are greater than 8 Mev is clearly unimportant when the relatively small number involved and decreasing efficiency of the neutron detector with increasing energy are considered. The choice of parameters is not unique. The value of a and E_b are reasonable estimates and $\eta_m = 8$ Mev may represent the average value corresponding to a distribution of initial excitation energies. The spectrum given in Fig. 5 was then used in Eq. (4) to compute the angular distribution with the assumption that it is approximately correct for fission fragments of U^{233} and Pu^{239} as well as for those of U^{235}.

C. Relative Neutron Emission Probabilities for Light and Heavy Fragments

The result of the calculation for Pu^{239} with $R = 1.0$ is indicated by the squares in Fig. 7, the normalization having been done arbitrarily at $\theta = 180°$. The points in the region 0° to 90° fall considerably below the experimental curve. The computed curve cannot be brought into agreement with the experimental one by choosing a different spectrum for the neutrons emitted by the light fragment. For example, a spectrum with a lower mean energy than that used would give higher values of $F(\theta)$ near 0°, but lower ones near 90°. The choice of a higher velocity for the light fragment would have a similar effect on $F(\theta)$. A fairly good fit, however, is obtained if one sets $R = 1.30$. The curve so obtained is indicated by the x's. It may be concluded, therefore, that the neutron emission probability for the light fragment is on the average about thirty percent greater than that for the heavy fragment. The computed and experimental curves for U^{233} and U^{235} are shown in Figs. 8 and 9; where in both cases a value of $R = 1.30$ was found to give a satisfactory fit. The results are summarized in Table I. The ratio V_L/V_H of the most probable velocities for the two fragments is taken from

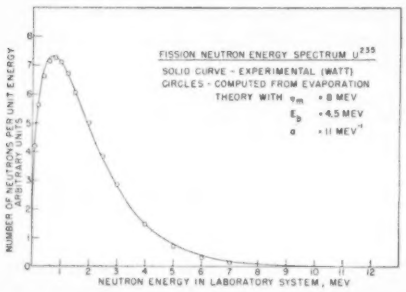
FISSION NEUTRON ENERGY SPECTRUM U^{235}
SOLID CURVE - EXPERIMENTAL (WATT)
CIRCLES - COMPUTED FROM EVAPORATION THEORY WITH η_m = 8 MEV
E_b = 4.5 MEV
a = 11 MEV^{-1}
NUMBER OF NEUTRONS PER UNIT ENERGY INTERVAL PER FISSION
NEUTRON ENERGY IN LABORATORY SYSTEM, MEV

FIG. 6. Comparison of the calculated and the experimental neutron spectrum in the laboratory system for U^{235}.

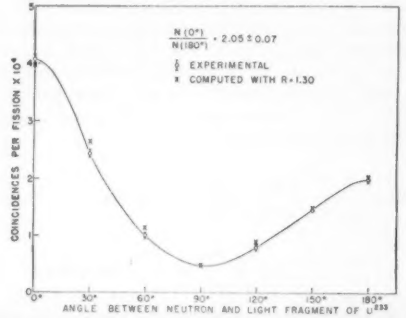
$\frac{N(0°)}{N(180°)}$ = 2.05 ± 0.07
EXPERIMENTAL
COMPUTED WITH R = 1.30
COINCIDENCES PER FISSION X 10^4
ANGLE BETWEEN NEUTRON AND LIGHT FRAGMENT OF U^{233}

FIG. 8. Comparison of the calculated and the experimental angular distributions of the prompt neutrons in the fission of U^{233}.

Leachman's velocity measurements. The experimental curves have not been corrected for the angular resolution of the apparatus. The part of the curves near 0° where the curvature is greatest would be raised by 5 to 10 percent by such a correction. In view of the limited accuracy of the model used for the calculations, no adjustment in the values of R has been made. The errors stated for R are those in fitting the computed to the experimental curves. It appears that the ratio of neutron emission probabilities for the two fragments is approximately the same for the three nuclides investigated. The trend of the angular distribution towards greater symmetry with increasing mass of the fissile nuclide is evidently associated with the decreasing velocity ratio of the fragments.

D. Time between Fission and the Emission of Neutrons

In Fig. 2 it may be seen that on the dashed curve, representing the angular distribution taken with no energy selection of the fragments, the coincidence rates at the 0° and 180° positions are equal to within 2 percent. The calculated angular distributions discussed in the preceding sections suggest that there is a negligible probability of a neutron being detected in a direction opposite to that of the fragment from which it was emitted. In the 0° position, therefore, the detected neutrons come from fragments entering the gas filling of the chamber, whereas in the 180° position they are from fragments penetrating the aluminum source backing. The number of coincidences at 0° from a fragment may be represented by Eq. (3) with $\theta=0°$. For simplicity suppose that there are ν_f neutrons per fragment all of the average energy $\bar{\eta}$. Then

$$F(0°)=\nu_f f(\bar{\eta}, 0°)\epsilon[E(\bar{\eta}, 0°)]. \tag{9}$$

If the fragment were to lose a few Mev of kinetic energy before emitting a neutron, the factor in (9) which changes most rapidly is

$$f(\bar{\eta}, 0°)=\frac{1}{4\pi}\left[1+\left(\frac{E_f m}{\bar{\eta}M_f}\right)^{\frac{1}{2}}\right]^2. \tag{10}$$

TABLE I. Summary of results. V_L/V_H is the ratio of most probable velocities for the two fragments given by Leachman (see reference 6).

Fissile nuclide	$N(0°)/N(180°)$	V_L/V_H	R
U^{233}	2.05±0.07	1.53	1.30±0.08
U^{235}	1.85±0.06	1.47	1.30±0.08
Pu^{239}	1.72±0.06	1.37	1.30±0.08

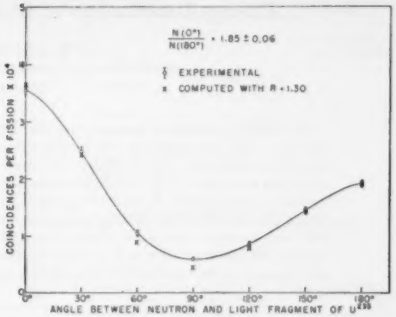

FIG. 9. Comparison of the calculated and the experimental angular distributions of the prompt neutrons in the fission of U^{235}.

A difference in coincidence counting rate of 2 percent, then, in the two positions would correspond to $\delta f/f=0.02$. For $\bar{\eta}=1$ Mev and an average fission fragment, this would occur with a decrease in E_f of $\delta E_f \sim 5$ Mev. The initial specific ionization of an average fission fragment in argon at N.T.P. is about 6 Mev per mm.[16] If one assumes that the initial specific ionization expressed in Mev/(mg/cm²) in aluminum is related to that of argon as the inverse ratio of the maximum ranges of fission fragments,[17,18] then it follows that the distance traveled in the aluminum by a fragment before it has lost 5 Mev of kinetic energy is about 5×10^{-3} cm. Since the average velocity of a Pu^{239} fission fragment is about 1.2×10^9 cm/sec, the time elapsed in traveling this distance is about 4×10^{-14} sec. It is probable, therefore, that if the time between fission and the emission of prompt neutrons exceeded about 4×10^{-14} sec, the consequent distortions of the prompt neutron angular distribution would have been observed in this experiment.

I wish to express my appreciation to Dr. K. W. Allen (now at the University of Liverpool, Liverpool, England) for valuable discussion in the early stages of this work, to Professor J. D. Jackson of McGill University, Montreal, Quebec, for helpful discussions on the evaporation model, and to Miss M. F. MacGregor and Miss A. R. Rutledge for the numerical computations. The continued interest and encouragement of Mr. G. C. Hanna and of Dr. B. W. Sargent and Dr. L. G. Elliott is gratefully acknowledged.

[16] N. O. Lassen, Phys. Rev. **70**, 577 (1946).
[17] C. Wiegand and E. Segrè, AEC Report MDDC-134 (unpublished).
[18] Flammersfeld, Jensen, and Gentner, Z. Physik **120**, 405 (1943).

Energy Distribution of Slow Neutrons Scattered from Solids

B. N. Brockhouse and D. G. Hurst
Atomic Energy of Canada Limited, Chalk River, Ontario, Canada
(Received July 21, 1952)

The sharp dependence on energy of the cadmium cross section for neutrons of energies near 0.35 ev has been used to investigate the energy distribution of 0.35-ev neutrons scattered through 90° by lead, aluminum, diamond, and graphite. The transmission of the scattered neutrons by cadmium filters was measured as a function of cadmium thickness and compared with cadmium transmissions calculated for an Einstein crystal model. In all cases agreement was obtained. For lead and aluminum at room temperature the simpler model of a gas of free atoms gave equally good agreement, a well-known behavior at high energies, but here applying when the temperature and neutron energy were only moderately greater than the Einstein temperature and much less than the binding energy. Theoretical formulas for the partial differential scattering cross sections for the two models are given in convenient form.

I. INTRODUCTION

When slow neutrons are scattered by a crystal, energy is exchanged between the neutron and the vibrational states of the crystal. The scattered neutrons have an energy distribution which depends on the properties of the crystal, on its temperature, and on the angle of scattering. The only previous experimental work on this problem has been done by Egelstaff.[1] He determined the mean energy changes of very slow neutrons scattered by polycrystalline scatterers, but the large number of multiple scatterings precluded comparison with theory.

This paper describes an investigation of the energy distribution of neutrons scattered singly through 90° by polycrystalline diamond, graphite, aluminum, and lead. Before scattering, the neutrons had an energy of 0.35 ev. The work was originally undertaken to determine the general features of the energy distribution for use in correcting scattering measurements on resonant absorbers.[2] It has established the applicability of simple theoretical formulas and has proved to be a useful approach to a more detailed experimental study of the scattering by single crystals.

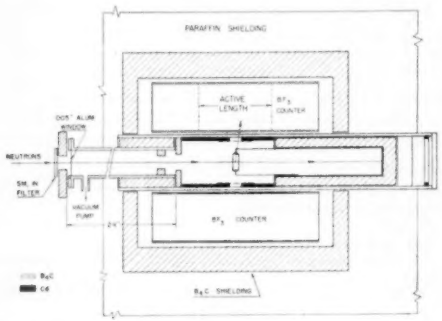

FIG. 1. The apparatus. In this figure the horizontal dimensions are compressed relative to the vertical in the ratio 2:1.

The theory of neutron scattering by crystals has been discussed by many authors in particular by Weinstock,[3] Finkelstein,[4] and Cassels.[5] Weinstock and Cassels took into account the normal modes of the crystal, but because of the complexity treated fully only those collisions in which a single phonon is transferred. Finkelstein discussed the scattering from an Einstein model of a crystal and included collisions with multiple phonon transfers. The neutron energy used in the present experiment is so high that a theory restricted to single phonon transfers is inadequate. On this account, the experimental results were first compared with predictions based on an extension of Finkelstein's work. As the agreement was satisfactory, only the Einstein model was considered in detail, the greater complexity associated with the more exact model not being warranted in the present case.

II. APPARATUS

The apparatus is shown in Fig. 1. It was mounted on the arm of the spectrometer previously described,[6] replacing the neutron counter and its shield. The NaCl crystal of the spectrometer was set to select neutrons of energy 0.35 ev, which were passed through filters of indium and samarium oxide to remove second-order and diffusely scattered thermal neutrons contaminating the beam. The resulting monoenergetic neutron beam was collimated by two $\frac{1}{2}$-inch diameter apertures in boron carbide blocks. The collimated beam then passed through a $\frac{3}{4}$-inch diameter aperture, which removed neutrons scattered by the collimating system, into an evacuated scattering chamber.

The scattering chamber was surrounded by a ring of six BF_3 proportional counters which were shielded everywhere except for a short cylindrical opening surrounding the scatterer. This opening accepted neutrons

[1] P. A. Egelstaff, Nature **168**, 290 (1951).
[2] J. Tittman and C. Sheer, Phys. Rev. **83**, 746 (1951); Brockhouse, Hurst, and Bloom, Phys. Rev. **83**, 840 (1951).
[3] R. Weinstock, Phys. Rev. **65**, 1 (1944).
[4] R. J. Finkelstein, Phys. Rev. **72**, 907 (1947).
[5] J. M. Cassels, Proc. Roy. Soc. (London) **A208**, 527 (1951).
[6] Hurst, Pressesky, and Tunnicliffe, Rev. Sci. Instr. **21**, 705 (1950).

that had been scattered through 90°±30°. Cylindrical cadmium absorbers of various thicknesses could be placed over the opening. The counting rates with and without the cadmium absorber, corrected for background and variations in incident neutron flux, gave the transmission by the cadmium. As virtually no counts were produced by the beam in the absence of a scatterer, the background was taken to be the counting rate with the scatterer in position and the counters shielded from the scatterer by a thick cadmium absorber (~2 g/cm²). The neutron beam included a small third-order component (about 1.5 percent of energy 9×0.35 ev) for which all the cadmium absorbers were nearly transparent. This was included in the background. The total background was about 10 percent of the scattered intensity, and this set a limit upon the accuracy which could be obtained for thick absorbers with reasonable counting times. Corrections for fluctuations in the neutron flux from the reactor were found by means of a BF_3 counter which monitored the original undiffracted beam.

The specimens were held in position by a thin aluminum tube, no part of which was in the beam. All had about the same scattering power (≈12 percent) and occupied the same volume. The aluminum specimen was in the form of a cylinder $\frac{1}{2}$ inch long and $\frac{3}{4}$ inch in diameter. The lead specimen consisted of lead turnings contained between two lead foils in a thin aluminum case. The graphite specimen was made up of five individual graphite disks spaced over a length of $\frac{7}{16}$ inch. The diamond consisted of five layers of diamond powder held between thin aluminum foils at the same positions as the five graphite disks. These constructions avoided large multiple scattering effects which would have arisen in compact cylindrical specimens.

III. ANALYSIS AND CORRECTION OF THE MEASUREMENTS

Between neutron energies of 0.2 ev and 0.5 ev the cadmium cross section falls rapidly from over 6000 barns to less than 150 barns. The cadmium cross section is thus a sensitive indicator of the energy near 0.35 ev. For a cadmium foil having n atoms/cm², the transmission for neutrons having an energy distribution $F(E)$ is

$$T(n)=\int_0^\infty F(E)E^{-\frac{1}{2}}\exp\{-n\sigma(E)\}dE \Big/ \int_0^\infty F(E)E^{-\frac{1}{2}}dE, \quad (1)$$

where $\sigma(E)$ is the cross section as a function of neutron energy E. The factor $E^{-\frac{1}{2}}$ is introduced to allow for the energy dependence of the detector (assumed to be thin and obeying a $1/v$ law as is the case with the BF_3 counters).

Provided the neutron energies lie entirely in a region like that between 0.2 ev and 0.5 ev where the cross section is a single valued function of the energy, it may be useful to replace the energy by the cross section as the independent variable. Equation (1) then has the form of a Laplace transform of a function $f(\sigma)$ which is related to $F(E)$. In principle, $T(n)$ could then be inverted to obtain $f(\sigma)$ and thence $F(E)$, but unless the values of $T(n)$ were known over a wide range with high accuracy, this would hardly be justified. The alternative procedure of comparing measured values of $T(n)$ with values calculated from theoretically predicted energy distributions has been used in the present work.

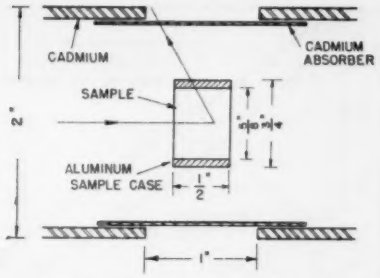

FIG. 2. Dimensions and arrangement of the scatterer and counter aperture.

The total cross section of cadmium has been measured[7] on the same spectrometer with the result

$$\sigma(E)=24.9(0.180/E)^{\frac{1}{2}}((E-0.180)^2+0.00319)^{-1} \times 10^{-24}\ \text{cm}^2. \quad (2)$$

This has been used for $\sigma(E)$ in (1).

To insure that the energy setting of the scattering apparatus was in satisfactory agreement with that used in (2), the total cross section of cadmium for the incident neutrons was measured and found to be in almost exact agreement with the cross section predicted by (2) at 0.35 ev.

Before the measured transmissions of the cylindrical cadmium absorbers could be compared with (1), some small corrections were necessary. The formula for $T(n)$ supposes normal incidence of the neutrons on the absorber, but in the apparatus deviations from normal incidence were possible. The dimensions of aperture and specimen are given in Fig. 2. The correction for angular spread was found by a calculation of the effective transmission for an isotropic distribution of neutrons, taking into account the thicknesses of cadmium and counter traversed at each angle. The result of averaging over the specimen and aperture was that all geometrical effects could be accurately accounted for if the thickness of cadmium absorber used in (1) was taken as 1.055 times the measured thickness.

The measurements had to be corrected for a small scattering effect. A fraction of the neutrons which were

[7] B. N. Brockhouse (to be published).

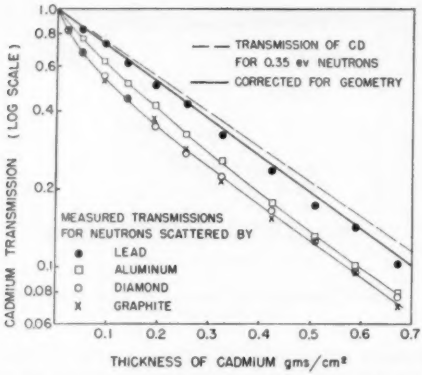

FIG. 3. The measured transmissions of the cadmium absorbers plotted against the thickness of the absorbers. The thick solid line shows the expected transmission for neutrons of unchanged energy.

finally counted was first scattered by the window of the scattering chamber and the walls of the counters. Those which were scattered back through the scattering chamber in such directions as to reach the counters traversed the cadmium absorber three times instead of once, possibly at a considerable inclination to the normal. A correction, which varied with the transmission but did not exceed $2\frac{1}{2}$ percent, was computed from the geometry and applied to the measurements.

The energy distribution for scattering through 90° was used in (1) in all cases. Use of the mean energy distribution for scattering over the range 60° to 120° made no significant difference in the results.

IV. THEORY

The crystal model chosen for the calculation of the energy distribution function $F(E)$ is that due to Einstein. In the Einstein approximation for a simple crystal containing only one type of atom, each atom is regarded as bound in a harmonic potential well. The wells are identical and are not affected by the motions of the atoms. The inelastic scattering cross section per atom is simply the cross section for a single oscillator[4] averaged over the thermal excitation according to the Boltzmann distribution. The elastic scattering includes interference effects and is made up of terms arising from diffraction and a disorder term, owing to differences in the thermal excitation of the oscillators, which may correspond to small energy losses in a real crystal. At high energies, the elastic scattering from a polycrystalline specimen produces many Debye-Scherrer diffraction rings. If the detector is not too restricted in angle, it will include a number of such rings. Under these conditions, the scattering per atom approaches the scattering from a single oscillator. Because some thirty or forty Debye rings were accepted by the detector in the present work, interference effects in the elastic scattering have been ignored.

The energy levels of an oscillator are separated by equal energy intervals $k\Theta$, Θ being the Einstein temperature of the crystal and k Boltzmann's constant. Consequently, the neutron gains or loses energy only in amounts $\gamma k\Theta$, where γ is an integer or zero. Finkelstein[4] has given the cross section for neutron scattering by an oscillator initially in state n which undergoes a transition to a state $n+\gamma$ as a result of the collision. The neutron loses energy of amount $\gamma k\Theta$. For comparison with the present experiment, it is necessary to calculate the cross section for loss of energy $\gamma k\Theta$ by the neutron irrespective of the value of n. That is, Finkelstein's expression for the cross section must be averaged according to the probability of thermal excitation of the initial states. If the crystal is at a temperature T, this probability is $\{1-\exp(-\Theta/T)\}\exp(-n\Theta/T)$. The average for any value of γ has been found by a method due to Pope,[5] with the result that the differential cross section for scattering of a neutron of initial energy E through an angle φ with loss of energy $\gamma k\Theta$ is

$$\sigma_\gamma(\varphi)=(\sigma_B/4\pi)(1-\gamma/\epsilon)^{\frac{1}{2}}I_{|\gamma|}(q^2/\sinh(\Theta/2T)) \times\exp\{-q^2\coth(\Theta/2T)+\gamma\Theta/2T\}. \quad (3)$$

In this formula, σ_B is the bound scattering cross section of the atoms, i.e., $\sigma_B=\sigma_{\text{free}}/(\text{reduced mass of the neutron relative to the atom})^2$,

$$\epsilon=E/k\Theta,$$
$$q^2=(1/2Ak\Theta)|\text{vector change in momentum}|^2,$$
$$=(m/A)\{2\epsilon-\gamma-2[\epsilon(\epsilon-\gamma)]^{\frac{1}{2}}\cos\varphi\},$$

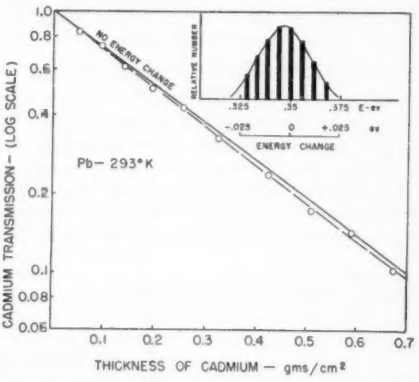

FIG. 4. Results for a lead scatterer. The insert shows the theoretical energy distribution of initially monoenergetic (0.35 ev) neutrons after scattering from a gas (solid line), and an Einstein crystal with $k\Theta=0.00565$ ev (line diagram). In the main diagram the experimental points are plotted together with the transmissions calculated for neutrons with unchanged energy (thick solid line) and with the energy distribution produced by scattering from the Einstein crystal (broken line).

[5] N. K. Pope, Can. J. Phys. (to be published).

where m = mass of neutron, A = mass of atom, and $I_{|\gamma|}(x)$ = modified Bessel function of first kind $= i^{-|\gamma|}J_{|\gamma|}(ix)$. With the introduction of variables $\beta=\frac{1}{2}\Theta/T$ and $x=q^2/\sinh(\frac{1}{2}\Theta/T)$, the cross section may be written

$$\sigma_\gamma(\varphi)=(\sigma_B/4\pi)(1-\gamma/\epsilon)^{\frac{1}{2}}I_{|\gamma|}(x)\exp(-x\cosh\beta+\gamma\beta). \quad (4)$$

Before the application of this formula to the experimental results is discussed, another model of the scatterer will be considered. During calculations on the Einstein crystal model, it was noticed that some of the cross sections and energy losses were almost equal to the corresponding values for free atoms at rest. To improve the free atom model, the free atoms were assumed to form a gas with a Maxwellian distribution of velocities corresponding to the temperature T. The gas gives a closer parallel to the crystal at a temperature T than would an atom at rest; in particular, the neutron can gain energy from the gas. The differential cross section for scattering by a gas of atoms (isotropic scattering in the center-of-mass system) was obtained by suitable modification of formulas given by Spiers.[9] For comparison with the Einstein crystal the energies are written in units of $k\Theta$, although Θ has no significance in the gas. The differential cross section for scattering of a neutron through an angle φ with loss of energy $\gamma k\Theta$ is, per unit interval in γ,

$$\sigma_\gamma(\varphi)(\text{gas})=(\sigma_B/4\pi)[(1-\gamma/\epsilon)(\beta/2\pi)]^{\frac{1}{2}}q^{-1} \times\exp\{-\tfrac{1}{2}\beta(\gamma/q-q)^2\}. \quad (5)$$

The gas cross section is a continuous function of γ with a maximum very close to the point where the energy loss is the same as that due to recoil of an atom initially at rest. The cross section decreases on either side of the maximum. If ΔE is the energy of the scattered neutron measured from the maximum of the cross section, the cross section is small for $(\Delta E)^2/(kTE) \gg 8(1-\cos\varphi)m/A$. The value of x in the region of large cross sections is roughly $(8m/A)(T/\Theta)(E/k\Theta)\sin^2(\varphi/2)$.

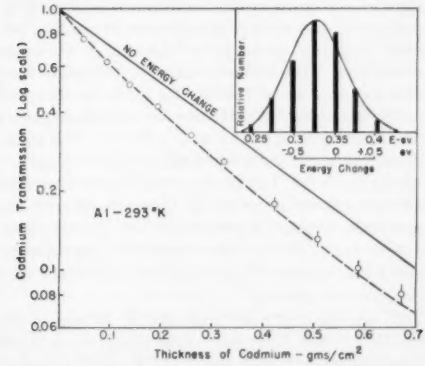

FIG. 5. Results for an aluminum scatterer. The insert shows the theoretical energy distribution of initially monoenergetic (0.35 ev) neutrons after scattering from a gas (solid line), and an Einstein crystal with $k\Theta=0.0259$ ev (line diagram). In the main diagram the experimental points are plotted together with the transmissions calculated for neutrons with unchanged energy (thick solid line), and with the energy distribution produced by scattering from the Einstein crystal (broken line).

[9] J. A. Spiers, National Research Council (Canada) Report CRT-417 (April, 1949) (N.R.C. No. 1940) (unpublished).

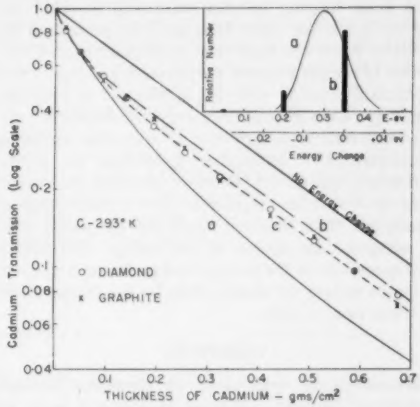

FIG. 6. Results for carbon scatterers. The insert shows the theoretical energy distributions of initially monoenergetic (0.35 ev) neutrons after scattering by a gas (solid line) and by an Einstein crystal with $k\Theta=0.150$ ev (line diagram). In the main diagram the experimental points for diamond and graphite are plotted together with the transmissions calculated for neutrons with unchanged energy (thick solid line) and with energy distributions produced by scattering from (a) the gas, (b) the Einstein crystal with $k\Theta=0.150$ ev, and (c) an Einstein crystal with $k\Theta=0.122$ ev.

The crystal cross section exists only for integral values of γ and is appreciable in the same region as the gas cross section. For $x\gg1$, the two models are indistinguishable by experiments which cannot resolve energies separated by $k\Theta$. This criterion may be approximately expressed as

$$E/k\Theta\gg(A/8m)(\Theta/T)/\sin^2\tfrac{1}{2}\varphi \quad (6)$$

and applies at smaller energies than has previously been assumed.[10]

If $\Theta\gg T$, most of the oscillators will be in the ground state, for which the gas has no analog. Also energy exchange between the neutron and crystal will occur in multiples of $k\Theta$, which is large compared to the dominant exchanges with the gas. Clearly, one would not expect comparison of a gas with such a crystal to be fruitful. Carbon (diamond) is a case in point.

The comparison of the gas and crystal models shows that even when only a few low-lying levels are excited the atoms of the crystal act in scattering neutrons very much like a gas. The specific properties of the binding

[10] G. Placzek, in a recent paper [Phys. Rev. 86, 377 (1952)] has compared the scattering from a bound atom with that from a free atom having the same momentum distribution. He also finds that the generally accepted criterion $E/k\Theta\gg A/m$ is too restrictive.

have little bearing on the scattering provided the binding is not too tight. It is as if the motion in the oscillator levels was equivalent in Doppler effect to the motion of the gas atoms of corresponding energy. From a practical point of view, for application to problems requiring a knowledge of the energy distribution of scattered neutrons, e.g., correction of resonance scattering measurements,[2,7] incomplete knowledge of crystal parameters will have little effect provided the parameters are of suitable magnitude. Over a wider range of parameters than that for which the gas model gives an adequate description of the energy distribution, such quantities as the average energy loss and differential cross section are closely given by the simple model of a free atom at rest.

V. RESULTS

Measurements were made on specimens of lead, aluminum, diamond, and graphite. Figure 3 shows the results where the transmission of the cadmium absorbers is plotted against the thickness of cadmium in g/cm^2. The dashed line shows the transmission for neutrons of unchanged energy (0.35 ev) incident normally on the absorber; the thick solid line shows the expected transmission for neutrons of unchanged energy, after correction for the geometry of the apparatus.

Results for lead are shown as solid circles. Here the energy change is very small, as expected, because of the great mass of the lead atom. The order of the mean energy changes is indicated by the initial slopes of these curves—largest for carbon, next largest for aluminum, and smallest for lead in order of their atomic weights. The results show no significant difference between the two forms of carbon—diamond and graphite. The shapes of the curves for carbon and for aluminum are different indicating that their energy distributions have different forms.

VI. DISCUSSION

Lead

The results for lead are shown again in Fig. 4, together with the expected transmission for neutrons of unchanged energy. The insert shows (as vertical lines) the energy distribution calculated for an Einstein crystal according to Eq. (3). The Einstein temperature was taken to be 0.75 times the Debye temperature obtained from specific heat measurements,[11] and corresponded in this case to $k\Theta = 0.00565$ ev.[11] The energy distribution for a monatomic gas, calculated from Eq. (5) is shown in the insert as a solid line. The two distributions are indistinguishable by experiments which cannot resolve energy changes smaller than $k\Theta$, corresponding to the fine structure of the Einstein crystal.

[11] N. F. Mott and H. Jones, *The Theory of the Properties of Metals and Alloys* (Oxford University Press, London, 1936), Chapter 1.

Using this common energy distribution, the transmissions have been calculated from Eqs. (1) and (2), and the theoretical transmission curve is shown in Fig. 4 as a dashed line. Good agreement is obtained, although in this case the agreement is chiefly evidence that the various corrections have been correctly applied.

In this and the following cases, the calculated energy distributions were modified slightly to take account of multiple scattering before computing the theoretical transmissions. This was done by assuming that a fraction $n\sigma_s/2$ of the scattered neutrons of each energy were rescattered with an appropriate energy distribution (σ_s is the scattering cross section of the atoms in the sample, n is the number of atoms per cm^2). Since $n\sigma_s$ has values of from 0.10 to 0.15, this correction was small.

Aluminum

The results for aluminum are shown in Fig. 5, again with the expected transmission for neutrons of unchanged energy. The insert shows the energy distribution for an Einstein crystal ($k\Theta = 0.0259$ ev[11]) as vertical lines and that for a gas as a solid line. The two distributions are not exactly the same, since in this case the Einstein temperature was about the same as room temperature, i.e., $T/\Theta \simeq 1$. The cadmium transmissions computed from the distribution for the Einstein crystal are shown as a dashed line. The theoretical and measured transmissions are in agreement within the errors of this experiment.

Carbon

Figure 6 shows the results for diamond and graphite. In the insert the energy distribution for an Einstein crystal of carbon atoms ($k\Theta = 0.150$ ev) is shown as vertical lines. This Einstein energy corresponds to a Debye temperature of 2340°K, the generally accepted value.[12] The energy distribution for a carbon gas at room temperature is shown as a solid line. The transmissions calculated from the distribution for a gas are shown as curve (a). This is not at all in agreement with the measurements as is to be expected because the temperature was much lower than the Einstein temperature, i.e., $T/\Theta \ll 1$. The calculated transmissions for the Einstein crystal [curve (b)] are in fair agreement with the measurements.

This agreement can be improved if, instead of defining the Einstein frequency as the simple mean of the Debye frequency distribution,[11] the Einstein temperature is chosen with particular reference to scattering experiments. If $k\Theta$ is taken to be 0.122 ev, the elastic cross section of diamond at room temperature is the same for the Einstein crystal[4] as for a Debye crystal[3] with a Debye temperature of 2340°K. Curve (c) shows

[12] This value is given in reference 11 and elsewhere. Other (somewhat lower) values are also to be found in the literature.

the calculated transmissions for $k\Theta=0.122$ ev, and is in agreement with the experimental points.

VII. CONCLUSIONS

The experimental results show that over a wide range of crystal parameters the Einstein model of a crystal gives sufficiently accurate information about neutron scattering to be of use where the fine details of the scattering are not required. It can give no information about actual energy transfers smaller than $k\Theta$, or angular variations of the order of the separation of Debye-Scherrer rings.

The agreement of the gas model with the Einstein model over a wide region of conditions shows how little influence the binding has on the general scattering pattern; energy and momentum conservation between the neutron and individual nuclei are, in most cases, the over-riding factors. The gas model fails when Bragg scattering, i.e., interference, is important or when the Einstein temperature is large compared with either the temperature or the half-width of the energy distribution.

The authors wish to thank Dr. N. K. Pope for communicating his results prior to publication and for several helpful discussions.

PHYSICAL REVIEW VOLUME 88, NUMBER 3 NOVEMBER 1, 1952

Nuclear Reactions in the Stars. I. Proton-Proton Chain

E. E. SALPETER
Newman Laboratory of Nuclear Studies, Cornell University, Ithaca, New York
(Received July 24, 1952)

The rates are calculated for the main reactions making up the "proton-proton chain," whose net effect is the conversion of four hydrogen atoms into one helium atom. These calculations are carried out for temperatures and densities corresponding to central conditions in main sequence stars.

The mean reaction rate for the beta-decay conversion of two protons into one deuteron is calculated accurately, using the latest data on the two-nucleon system and on beta-decay. It is shown that, under normal stellar conditions, the reaction chain is completed by the radiative capture of a proton by a deuteron and by the collision between two of the resultant He^3 nuclei to form one He^4 nucleus and two protons. Values are given for the rate of energy production and for the concentrations of deuterium and He^3 at various temperatures.

I. INTRODUCTION

DETAILED calculations on nuclear reactions in main-sequence stars were presented over a decade ago in two papers by Bethe[1] and by Bethe and Critchfield,[2] hereafter referred to as B and BC, respectively. The present paper is largely a continuation of these papers and, wherever possible, the same notation will be used.

The main aim of the present paper is to revise the work of B and BC on the reaction rates for the chain of reactions starting with the combination of two protons in main-sequence stars, in the light of the most recent experimental information on nuclear reaction rates and Q-values. No detailed calculations on the stellar hydrodynamics of the problem, using any specific stellar model, are carried out. The results are presented largely in the form of reaction rates as a function of temperature, density, and relative abundance of the nuclear species. In later papers, the carbon cycle and reactions in stars which have exhausted their hydrogen supply will be discussed.

Many of the reactions we shall discuss are of the thermonuclear type, i.e., an exothermic reaction undergone by two nuclear species with a Maxwellian velocity distribution colliding with each other. Under stellar conditions, the mean thermal energy kT (of the order of 1 kev for the sun) is extremely small compared with the kinetic energies at which the Coulomb-barrier is negligible (of the order of a few Mev). Consequently, most of the reactions are undergone by nuclei in a fairly narrow energy-region in the tail of the Maxwell distribution (10 to 50 kev for the sun), which we shall call the "stellar energy-region," E_{st}. An approximate formula for p, the number of reactions per second per nucleus of type 2, is then obtained (see for instance B) which can be written in the form

$$p=(4\rho x_1 N_0 \Gamma a_0 R_0^2/3^{5/2}\hbar) \times[(A_1+A_2)^{5/2}/A_1^2 A_2 Z_1 Z_2]\tau^2 e^{(\lambda-\tau)}, \quad (1)$$

where

$$\tau=3\left[\frac{\pi^2 e^4 M_0}{2\hbar^2 kT}\frac{Z_1^2 Z_2^2 A_1 A_2}{(A_1+A_2)}\right]^{\frac{1}{3}} \quad (2)$$

and

$$\lambda=4[R_0 A_1 A_2 Z_1 Z_2/a_0(A_1+A_2)]^{\frac{1}{2}}. \quad (3)$$

In (1) x_1, x_2 are the concentrations (by weight), A_1, A_2 the atomic weights and Z_1, Z_2 the atomic charges of the two reacting nuclear species. N_0 is Avogadro's number, M_0 one atomic mass unit, ρ the density in g cm^{-3}, and Γ

[1] H. A. Bethe, Phys. Rev. **55**, 434 (1939); B.
[2] H. A. Bethe and C. L. Critchfield, Phys. Rev. **54**, 248 (1938); BC.

the "reaction width," i.e., $\Gamma/\hbar$ is the reaction probability (for energy E_{st}) in sec^{-1} after penetration. R_0 is the "nuclear radius per nucleon,"[3]

$$R_0=(1.45\pm0.20)\times10^{-13}\text{ cm}, \tag{4}$$

and a_0 is the "Bohr radius" for one amu,[4]

$$a_0=\hbar^2/M_0e^2=2.904\times10^{-12}\text{ cm}. \tag{5}$$

The considerations leading to (1) are valid only if the compound nucleus formed in the collision of particles 1 and 2 has no resonance levels for excitation energies corresponding to the neighborhood of the stellar energy-region, E_{st}.

If Γ is expressed in volts and T in units of 10^6 degrees, the expression for p becomes, using DuMond and Cohen's[4] values for the atomic constants (for $\alpha^{-1}=137.036$),

$$p=2.59\times10^4\times\rho x_1\Gamma[(A_1+A_2)/A_1]\times(Z_1Z_2/A_1A_2)^{\frac{1}{3}}T^{-\frac{1}{3}}e^{(\lambda-\tau)}\text{ sec}^{-1}, \tag{1a}$$

$$\tau=42.48[Z_1^2Z_2^2A_1A_2/(A_1+A_2)]^{\frac{1}{3}}T^{-\frac{1}{3}}, \tag{2a}$$

$$\lambda=1.26(Z_1Z_2A_1A_2)^{\frac{1}{3}}(A_1+A_2)^{-\frac{1}{3}}. \tag{6}$$

In many cases, the cross sections σ for such reactions have been measured in the laboratory as a function of energy for fairly low energies (100 kev and up). If the compound nucleus formed has no resonance levels in the region corresponding to these kinetic energies, then the cross section is approximately of the form

$$\sigma=(S/E)\exp(-2\pi e^2Z_1Z_2/\hbar v), \tag{7}$$

where E and v are the kinetic energy and velocity, respectively, of particle 1 (relative to particle 2) and S is a constant (in units of ev barn). A simple formula [see B, Eq. (11)] then expresses Γ (for the energy region E) in terms of the constant S. The experimental energies E are usually larger than E_{st}. But, if $(E-E_{st})$ is small compared with the difference of E_{st} and the energy corresponding to the nearest resonance level, then the values of the width Γ will be approximately the same in the energy regions E and E_{st}. Using Eq. (11) of B, we can eliminate Γ and the poorly known R_0 from expression (1) for p, and we obtain an expression for p in terms of the experimentally determined constant S,

$$p=(8\rho x_1N_0Sa_0/3^{\frac{1}{2}}\pi\hbar)(A_1^2Z_1Z_2)^{-\frac{1}{3}}\tau^2e^{-\tau}. \tag{8}$$

If S is measured in units of ev barn, we have

$$p=434\rho x_1S(A_1^2Z_1Z_2)^{-\frac{1}{3}}\tau^2e^{-\tau}\text{ sec}^{-1}. \tag{9}$$

If there is one or more levels in or near the stellar energy-region, then the above formulas are not valid. The expression (9) is then usually a gross underestimate, since the nearest resonance level will usually give overwhelmingly the biggest contribution and destructive interference should be unimportant. If in particular there is a resonance level corresponding to a positive kinetic energy E_r between zero and about 50 kev, then this level gives the biggest contribution and p depends mainly on the ratio (E_r/kT) and hardly on the width of the resonance level.

If Q is the energy in Mev liberated in one reaction between a nucleus of type 1 and one of type 2, then the energy ϵ liberated per g per sec is

$$\epsilon=(N_0x_2/A_2)pQ, \tag{10}$$

or

$$\epsilon=4.19\times10^{20}(\rho x_1x_2S(Q)(A_1^2A_2Z_1Z_2)^{-\frac{1}{3}}\tau^2\times e^{-\tau}\text{ erg g}^{-1}\text{ sec}^{-1}. \tag{11}$$

II. THE PROTON-PROTON REACTION. ORBITAL MATRIX ELEMENT

For main sequence stars, which consist to a large extent of hydrogen, two chains of nuclear reactions were shown to be the main source of energy (see B), each of these chains having the net effect of converting four hydrogen atoms into one helium atom plus two neutrinos. The reaction governing the rate of one of these chains, the "proton-proton chain," is the initial and slowest reaction, the formation of a deuteron in the collision of two protons:

$$H^1+H^1\rightarrow D^2+e^++\nu+0.42\text{ Mev}. \tag{12}$$

Formulas for the reaction rate for this process were derived in BC. Our knowledge of the properties of the two-nucleon system and of beta-decay phenomena has improved so greatly, that a much more accurate re-evaluation of this reaction-rate is made possible. The formula for the reaction rate p can be written in the form

$$p=16\pi\times3^{-5/2}gf(W)|M_{sp}|^2\gamma^{-3}\Lambda^2N_0A_H^{-1}\rho x_H\tau^2e^{-\tau}F_\tau. \tag{13}$$

Here g is the Gamow-Teller part of the beta-decay constant, $f(W)$ is the well-known beta-decay f-function [see BC Eq. (8)], x_H is the concentration (by weight) of hydrogen, F_τ is a correction factor approximately equal to unity. Λ is a dimensionless quantity which is proportional to the orbital part of the matrix element and is almost independent of energy, M_{sp} is the spin part of the matrix element, and γ^{-1} is the radius of the deuteron,

$$\gamma^{-1}=(4.314\pm0.003)\times10^{-13}\text{ cm}. \tag{14}$$

Equation (13) is the same as the Eq. (32) derived by BC, except for the factor[5] $|M_{sp}|^2$, which is omitted in the original derivation, and the correction factor F_τ.

The orbital matrix element Λ is of the form

$$\Lambda=(\gamma^3/8\pi C_0^2)^{\frac{1}{2}}\int\psi_D^*\psi_p d^3r, \tag{15}$$

[3] H. Feshbach and V. F. Weisskopf, Phys. Rev. **76**, 1550 (1949).
[4] J. W. M. DuMond and E. R. Cohen, Phys. Rev. **82**, 556 (1951).
[5] G. Gamow and C. L. Critchfield, *Theory of Atomic Nucleus* (Oxford University Press, Oxford, 1949).

where ψ_D is the normalized wave function for the deuteron ground state and ψ_p is the S-part of the wave function for the two-proton system with a particular wave number k. Let R be the "Bohr radius" for one proton,

$$R=\hbar^2/Me^2=2.881\times10^{-13}\text{ cm}, \tag{16}$$

and

$$\eta=e^2/\hbar v=(2kR)^{-1};\quad y=r/R. \tag{17}$$

C_0 in (15) is the Coulomb-barrier factor,

$$C_0=[2\pi\eta/(e^{2\pi\eta}-1)]^{\frac{1}{2}}. \tag{18}$$

The two-proton wave function ψ_p is normalized per unit density at infinity. Outside of the range of nuclear forces, ψ_p has the form

$$\bar{\psi}_p(y)=e^{i\delta}\sin\delta C_0^{-1}\{\Theta(y)+C_0^2\cot\delta(kR)y\Phi(y)\}/kr. \tag{19}$$

In (19) δ is the nuclear phase-shift constant for S-scattering of two protons with wave number k, Θ and Φ are functions of k and y, defined by Yost, Wheeler, and Breit,[6] which are proportional to the irregular and regular Coulomb wave functions, respectively, and have the value unity for $y=0$.

The matrix element (13) has recently been evaluated very accurately by Frieman and Motz,[7] using accurate explicit wave functions ψ_p and ψ_D which are based on specific assumptions about the potential shape of nuclear forces with the constants chosen to fit low energy experimental data for the two-nucleon system. In such a calculation it is difficult to evaluate the inaccuracy in the final result due to the uncertainty in the potential shape and the experimental errors. For this reason, an approximate re-evaluation of Λ seems worthwhile, using the theory of the effective range,[8–10] from which the effect of the present uncertainties in the theory of nuclear forces can be derived very simply.

The nuclear phase shift δ is of the form[8,11]

$$\pi\cot\delta/(e^{2\pi\eta}-1)=K(\eta), \tag{20}$$

where K is a slowly varying function of η (or k),

$$K(\eta)=(K_\infty+\tfrac{1}{2}r_{0S}Rk^2\cdots)-h(\eta), \tag{21}$$

and $h(\eta)$ is a function defined by Jackson and Blatt.[11] An analysis[11] of low energy proton-proton scattering data gives the following values for the two constants K_∞ and r_{0S}:

$$r_{0S}=(2.65\pm0.07)\times10^{-13}\text{ cm}, \tag{22}$$

$$K_\infty=3.76\pm0.03. \tag{23}$$

We now make use of the fact that the range of nuclear forces is small compared with the deuteron radius, γ^{-1}, with the "Bohr radius" R and with the wavelength k^{-1}. We write the matrix element Λ in the form

$$\Lambda^2=F_r\Lambda_0^2, \tag{24}$$

where Λ_0 is the value obtained for expression (15) by replacing ψ_D by its normalized asymptotic expression and ψ_p by $\bar{\psi}_p$, Eq. (19). Λ would be exactly equal to Λ_0 if the range of nuclear forces were zero, and hence the correction factor F_r is only slightly different from unity.

At a temperature T of about $15(\times10^6\,^\circ\text{K})$ (central temperature of the sun), the main contribution to the reaction comes from proton pairs of relative kinetic energy about 6 kev corresponding to $\eta\approx1.5$. At these energies both δ and $e^{-2\pi\eta}$ are of the order of magnitude of 10^{-4} and hence negligible compared with unity. Using this fact, considering only the S-part of ψ_D and neglecting tensor forces completely, we get an accurate approximation to Λ_0, using (19) and (20),

$$\Lambda_0=(2R\gamma/K)J;\quad J=\int_0^\infty dre^{-\gamma r}\{\Theta+(Kr/R)\Phi\}. \tag{25}$$

Using the expansions for Θ and Φ for small values of r, (21), (22), and (23), the expression (25) can be evaluated for a particular value of η. For zero relative energy ($\eta=\infty$), one finds

$$J=1.40\gamma^{-1},\quad \Lambda_0^2=6.18\pm0.06, \tag{26}$$

the main uncertainty in the value of Λ_0 coming from the uncertainty in the experimental value for K_∞. The expressions for Θ, Φ, and K for energies in the stellar region differ only very slightly from those for zero relative energy: For $\eta=1.5$, one finds $h=0.04$, $K=3.73$, and $\Lambda_0^2=6.21$.

The factor F_r, correcting for the finite range of nuclear forces, consists of the product of two terms:

$$F_r=(1-\rho_t'\gamma)^{-1}(1-DJ^{-1}). \tag{27}$$

The first term is due to the difference between the normalization integrals of ψ_D and of its asymptotic expression, ρ_t' being the effective range[10] $\rho_t(-\epsilon,-\epsilon)$ for the deuteron ground state. The second term takes care of the difference D between J as defined in (25) and the equivalent integral involving the correct wave functions normalized such that the asymptotic form of the integrand is equal to the integrand of J. In two previous papers[8,10] an integral D was defined and evaluated (in connection with photomagnetic neutron-proton capture) which is identical with the expression D occurring in (27), except that the singlet wave functions for the neutron-proton (instead of the proton-proton) system occur. The main contribution to D comes from the range of integration less than the range of nuclear forces (0 to 3×10^{-13} cm). In this region it was shown by Bethe[8] (see Fig. 5) that both the correct and asymptotic singlet wave functions are very similar

[6] Yost, Wheeler, and Breit, Phys. Rev. **49**, 174 (1937).
[7] E. Frieman and L. Motz, Phys. Rev. **83**, 202 (1951) and private communication.
[8] H. A. Bethe, Phys. Rev. **76**, 38 (1949).
[9] H. A. Bethe and C. L. Longmire, Phys. Rev. **77**, 647 (1950).
[10] E. E. Salpeter, Phys. Rev. **82**, 60 (1951).
[11] J. D. Jackson and J. M. Blatt, Revs. Modern Phys. **22**, 77 (1950).

for the p–p and n–p systems, except for the slight difference between the singlet ranges r_{0s} for the two systems. We therefore get a fairly good approximation to D by using the expression (20) of reference 10 for the various potential shapes, using the value (22) for r_{0s} and the latest value[10] for the triplet range

$$\rho_t=(1.704\pm0.030)\times10^{-13}\text{ cm}. \tag{28}$$

Equation (27) then gives for F_r a value of about 1.15 for a Yukawa (Hulthén), 1.13 for an exponential, and 1.12 for a square well shape for both the triplet and singlet potential. This gives, for these three potential shapes and for $\eta=\infty$,

$$\Lambda^2=7.11(\text{Y}),\quad 7.00(\text{E}),\quad 6.92(\text{S}). \tag{29}$$

Frieman and Motz,[7] using accurate wave functions for a specific potential shape find a value of 6.79 for Λ^2. The experimental errors in ρ_t and r_{0s} contribute probable errors of about ±3 percent and ±1 percent, respectively, to the factor F_r. From the numerical values of (29), we estimate a further probable error in Λ^2 due to the uncertainty in the potential shape of about ±3 percent, the uncertainty in Λ_0^2 contributes another ±1 percent. These four sources of error are also present in the calculations of Frieman and Motz. The numerical values in (29) contain an uncertainty of another 5 or 10 percent (due to the neglect of tensor forces and the approximation used for D), which is not present in the more accurate calculations. We therefore shall use the value for Λ^2 obtained by Frieman and Motz plus the small correction due to $\eta\approx1.5$ instead of infinity, calculated above (and with the four errors of 3.3, 1, and 1 percent estimated above). Since the sources of these errors are independent, we finally get

$$\Lambda^2=6.82(1\pm0.05). \tag{30}$$

III. THE PROTON-PROTON REACTION. OTHER FACTORS

In the beta-decay factor $f(W)$, W is the maximum beta-particle energy (including rest mass) in units of mc^2. Using a value[12] for the H_2-D doublet of

$$H_2-D=(1.551\pm0.002)\text{mMU}, \tag{31}$$

we have

$$W_0=1.827(1\pm0.002), \tag{32}$$

where W_0 is the value of W for zero relative kinetic energy of the two protons. The main contribution to the cross section comes from relative velocities.

$$v\approx(4\pi e^2kT/hM)^{\frac{1}{2}},$$

which corresponds to a relative kinetic energy of 5.9 kev for $T=15$. We evaluate $f(W)$ for a value of W equal to W_0 plus this "most probable" relative kinetic energy. Using the very accurate approximations for $f(W)$ given by Feenberg and Trigg,[13] we find

$$f(W)=0.145[1+0.054(T/15)^{\frac{1}{2}}](1\pm0.03). \tag{33}$$

The reaction involves a transition from a singlet S-state of the two-nucleon system and hence requires Gamow-Teller selection rules. If these selection rules are valid, then the factor $|M_{sp}|^2$ (which takes care of the summation over spin-states and of the fact that either proton can turn into a neutron) becomes equal[14] to $\frac{3}{4}$.

A lower limit for g, the Gamow-Teller beta-decay constant used in Eq. (13), can be obtained from experimental data on those super allowed beta-decays which can only proceed by means of Gamow-Teller selection rules. For such a decay[14]

$$g=\ln2/[f(W)t_{\frac{1}{2}}|M|^2|M_{sp}|^2], \tag{34}$$

where $t_{\frac{1}{2}}$ is the half-life in seconds, and M is the orbital matrix element, which is equal to or slightly less than unity. The most suitable decay of this type is that of He^6 into Li^6, which is a process quite analogous to our p–p reaction.[15] Using for the energy end point the latest experimental value[16] of (3.50 ± 0.05) Mev and for the half-life[14] (0.823 ± 0.013) sec, we get a value of (1270 ± 90) sec^{-1} for $[f|M|^2|M_{sp}|^2]$. Since the factor $|M|^2$ cannot exceed unity, we get from Eq. (34) and the upper limit of this value the inequality

$$g>5.1\times10^{-4}\text{ sec}^{-1}. \tag{35a}$$

The beta-decay of the neutron, on the other hand, provides an *upper* limit for g. For this decay the orbital factor $|M|^2$ is identically equal to unity, the energy end point[12] is (0.782 ± 0.001) Mev, the half-life[17] is (12.8 ± 2.5) min. If no Fermi type of beta-interaction existed, this would give a value of (930 ± 180) sec for $[f|M|^2|M_{sp}|^2]$. Since part of the neutron decay probably proceeds by means of Fermi selection rules, Eq. (34) and the lower limit of this value furnish an inequality for the Gamow-Teller decay constant,

$$g<9.4\times10^{-4}\text{ sec}^{-1}. \tag{35b}$$

In addition to these two inequalities, actual estimates for g can be obtained[18] from the decay of H^3 and other beta-transitions between mirror nuclei. We therefore take

$$g=7.5(1+\Delta)\times10^{-4}\text{ sec}. \tag{36}$$

The error factor Δ lies between about ±0.20 at the moment, and it is hoped that further advances in beta-decay investigations will furnish a better value for it.

[12] Li, Whaling, Fowler, and Lauritsen, Phys. Rev. **83**, 512 (1951).

[13] E. Feenberg and G. Trigg, Revs. Modern Phys. **22**, 399 (1950).

[14] Using the notation of C. S. Wu, Revs. Modern Phys. **22**, 386 (1950).

[15] The decay of He^6 can be considered qualitatively as the transition of two neutrons in a singlet state to a deuteron in a triplet state, all in the field of an α-particle. The value of $|M_{sp}|^2$ is $\frac{3}{4}$, the same as for the $p-p$ reaction. (See reference 14.)

[16] C. S. Wu, Phys. Rev. (to be published).

[17] J. M. Robson, Phys. Rev. **83**, 349 (1951).

[18] G. L. Trigg, Phys. Rev. **86**, 506 (1952).

The correction factor F_τ, which occurs in (13) [also (1), (4), (8), and (9) should be multiplied by F_τ] is of the form

$$F_\tau=(\tau/\pi)^{\frac{1}{2}}e^\tau\int_0^\infty dx\exp\{-(\tau/3)[(2/x)+x^2]\}. \quad (37)$$

The quantity τ, defined in (2), is greater than 10 for all cases of interest and is about 13.7 for the proton–proton reaction at a temperature of 15×10^6 °K. On putting $x=(1+y)$, Eq. (37) becomes

$$F_\tau=(\tau/\pi)^{\frac{1}{2}}\int_{-1}^\infty dy\exp(-\tau y^2)\times\{(1+y)\exp[2\tau y^2/3(1+y)]\}.$$

We replace the lower limit of integration by $(-\infty)$, which introduces only errors of the order of magnitude of $e^{-\tau}(<10^{-4})$, expand the expression inside the curly bracket in positive powers of y and integrate. This gives

$$F_\tau=1+(5/12\tau)-(35/288\tau^2)+\cdots. \quad (38)$$

For a temperature of $T=15$, the numerical value of F_τ for the proton–proton reaction is 1.030.

In the formulas derived above, the screening due to the electron charge cloud surrounding a proton has been neglected. But for a relative kinetic energy of about 6 kev, the classical turning point corresponds to a distance between the two protons of only about 2.5×10^{-11} cm. The electron charge cloud, on the other hand, is spread out over distances as large as the mean distance between neighboring nuclei, which is about 2×10^{-9} cm for a density ρ of about 100 g cm^{-3}. Under these circumstances the correction to the reaction rate due to screening is less than 1 in 10^4 and hence will be neglected.

Substituting all the quantities calculated in this section into Eq. (13), we obtain for the mean reaction rate per proton

$$p=1.73(1+\Delta\pm0.06)\times10^{-16}\rho x_H\tau^2e^{-\tau}\times[1+(5/12\tau)+\cdots][1+0.054(T/15)^{\frac{1}{2}}]\ \text{sec}^{-1}. \quad (39)$$

The largest source of error in this expression is still the 20 percent error Δ in the beta-decay constant.[19]

For temperatures in the neighborhood of 15 million degrees, we obtain the following approximation for p,

$$p=3.9_4(1+\Delta\pm0.06)\times10^{-18}\times(\rho x_H/100)(T/15)^{3.96}\ \text{sec}^{-1}. \quad (40)$$

IV. REACTIONS INVOLVING DEUTERONS

Once deuterons are formed by the proton–proton reaction, they are quickly converted into He^3 by the reaction

$$H^1+D^2\rightarrow He^3+\gamma+5.5\ \text{Mev}. \quad (41)$$

We first consider the contribution to this reaction from protons of zero orbital angular momentum, which contributes practically the whole reaction rate at the low stellar energies.

A recent measurement of the capture cross section of thermal neutrons by deuterium[20] gives

$$\sigma=(0.57\pm0.01)(2200\ \text{m sec}^{-1}/v)\times10^{-27}\ \text{cm}^2. \quad (42)$$

H^3 and He^3 are mirror nuclei which are extremely similar except for the Coulomb repulsion. We therefore assume that the cross section for reaction (41) for low energy S-state protons is the same as Eq. (42), except for the Coulomb-barrier penetration factor C_0^2, Eq. (18).* This gives a cross section of the form of Eq. (7) with

$$S=9.0\times10^{-2}\ \text{ev barn}.[21] \quad (43)$$

Substituting into Eq. (9), we find for the reaction rate p,

$$p=39(\rho x_H)\tau^2e^{-\tau}\ \text{sec}^{-1}. \quad (44)$$

At temperatures T near 15 (in 10^6 °K) this can be written as

$$p=0.25(\rho x_H/100)(T/15)^{4.3}\ \text{sec}^{-1}. \quad (44a)$$

The biggest uncertainty in the numerical values in Eqs. (44) and (44a) comes from the assumption that the matrix elements for neutron and proton capture are the same except for the Coulomb barrier. This uncertainty in p should not be more than about ±40 percent.

The cross section for reaction (41) has been measured directly[22] for proton energies E between 400 kev and 1.5 Mev. The observed angular distribution indicates that most of the cross section at these energies is contributed by P-state protons. By means of the well-known Coulomb barrier penetration formula[23] for orbital angular momentum unity, the energy dependence of the partial cross section for reaction (41) for P-state protons can be calculated at all energies. For energies of a hundred kev or more, this cross section rises sharply with energy. In the 1 Mev region, this theoretical energy dependence was found to agree very well with the measured one,[22] confirming the fact that the bulk of the reaction comes from P-state protons in this energy region. For much lower energies, however, the P-state cross section becomes smaller than that for the S-state. At energies of about 20 kev or less the energy dependence of the P-state cross section is of the form of Eq. (7) with S about 2×10^{-3} ev barn, which is negligible compared with Eq. (43). We therefore neglect any P-state corrections to Eqs. (44) and (44a).

The mean life for reaction (41) is of the order of

[19] The expression (39) is much larger than the value given originally by BC. This is mainly due to the fact that too low a value for g was used and the factor $|M_{rp}|^2$ omitted in BC.

[20] Kaplan, Ringo, and Wilzbach, Phys. Rev. **87**, 785 (1952).

* *Note added in proof.*—As was kindly pointed out by Dr. W. A. Fowler, Eqs. (43) and (44) have to be multiplied by an additional factor resulting from the finite size of the nuclei involved. This factor was estimated to be about (1.3 ± 0.3). The numbers in the second lines of Tables II and III should be divided by this factor.

[21] Corresponding to a width Γ of about 0.25 ev.

[22] Fowler, Lauritsen, and Tollestrup, Phys. Rev. **76**, 1767 (1949).

[23] N. F. Mott and H. S. Massey, *The Theory of Atomic Collisions* (Clarendon Press, Oxford, 1949), second edition, p. 54.

seconds or minutes for normal stellar conditions (see Table III). Dynamic equilibrium between the concentrations x_D of deuterium and x_H of hydrogen will therefore be established very quickly; the ratio (x_D/x_H) is then equal to the ratio of the mean lifetimes of reactions (12) and (41) (formation and destruction, respectively, of deuterons) multiplied by the ratio of atomic weights. Because of the high speed of reaction (41), the concentration x_D is extremely low and values for x_D are given in Table II. No spectroscopic measurements of x_D in stellar atmospheres are available as yet, but terrestrial deuterium concentrations are enormously larger than those given in Table II. This fact may suggest that the material from which the earth was formed could not have come from the interior of a main sequence star (like our sun).

There are a few reactions involving deuterons which might compete with reaction (41), but these were all found to be much slower. Collisions between two deuterons are negligible under stellar conditions, because of the extremely small concentration x_D. Collisions between a deuteron and an alpha-particle are unimportant because of the high Coulomb barrier and small gamma-ray width Γ. The reaction between one deuteron and one He^3 nucleus is somewhat more important, because of a resonance[24,25] near the stellar energy region. Using the experimental cross sections[24,25] and the equilibrium concentrations of He^3 (calculated in the next section), this reaction was found to be slower than reaction (41) by a factor of at least 50 at temperatures of 5×10^6 °K or more.

V. REACTIONS INVOLVING He^3

Since Li^4 is unstable to particle disintegration, no direct (p,γ) reaction on He^3 is possible. There are, however, a number of competing reactions which use up He^3. Of these the reaction

$$He^3+He^3\rightarrow He^4+2H^1+12.8\ \text{Mev}, \qquad (45)$$

first suggested by Schatzman[26] and by Fowler and Lauritsen,[27] turns out to be the fastest and most important. This reaction has been detected experimentally,[28] but no accurate cross-sectional measurements are available as yet. But cross sections for the similar reaction involving two H^3 nuclei have been measured[29] for energies of 100 kev and up. For energies between 100 kev and 500 kev, the experimental cross section is of the form of Eq. (7) with

$$S=(3.2\pm1.5)\times10^6\ \text{ev barn}. \qquad (46)$$

H^3 and He^3 being very similar, we assume that the cross sections for reaction (45) and for the reaction involving two tritons are the same except for the different Coulomb barrier factors. This gives for reaction (45) a value for S of four times (ratio of the values for Z^2) the expression (46), if the nuclear radii are assumed to be zero. The finite size of the nuclei involved introduces an additional correction factor, which cannot yet be calculated accurately. This factor was estimated to be between two and eight (but may even lie slightly outside these limits) and a value of four was adopted for it. Using Eq. (9), the rate p of reaction (45) becomes

$$p=6\times10^7(\rho x_3)\tau^2e^{-\tau}\ \text{sec}^{-1}, \qquad (47)$$

where x_3 is the concentration (by mass) of He^3. The numerical factor in Eq. (47) should not be in error by a factor of more than five.

When dynamical equilibrium has been set up, the concentration x_3 adjusts itself such that the number of He^3 nuclei created per cm^3 per sec by means of reactions (12) and (41) equals the number destroyed by means of reaction (45). The ratio (x_3/x_H) can then be computed using Eqs. (39) and (47). Values computed for x_3 in this manner are given in Table II for different temperatures. For temperatures T about 10 to 15 (central portions of the sun), x_3 is very low, which agrees with the fact that He^3 has not yet been detected with certainty in solar spectra.[30] But at temperatures T of the order of 5 or lower (extremely cool stars), the equilibrium concentration of He^3 is quite appreciable and it would require a very long time to build up this concentration (starting from pure hydrogen).

A list of reactions involving He^3 which compete with reaction (45) is given in Table I, together with the estimated mean reaction times at two temperatures which respresent lower and upper limits to central temperatures of main sequence stars. Although the stated estimates for the reaction times for all reactions except (45) could be in error by a factor of as much as

TABLE I. Mean life of He^3 corresponding to various competing reactions for $\rho x_H=100$ and for two temperatures T (in 10^6 °K).

Reaction	Mean life (years) $T=5$	$T=30$
$He^3+He^3\rightarrow He^4+2H^1$	6×10^{10}	240
$D^2+He^3\rightarrow He^4+H^1$	7×10^{12}	3×10^5
$He^4+He^3\rightarrow Be^7+\gamma$	1×10^{13}	8×10^5
$H^1+He^3\rightarrow He^4+e^++\nu$	5×10^{14}	2×10^6
$e^-+He^3\rightarrow H^3+\nu$	2×10^{23}	3×10^6

TABLE II. Concentrations (by mass) of deuterium, x_D, and of He^3, x_3, relative to that of hydrogen for various temperatures T (in 10^6 °K).

T	5	8	15	30
x_D/x_H	5.6×10^{-17}	4.1×10^{-17}	3.0×10^{-17}	2.2×10^{-17}
$2x_3/x_H$	0.2_2	0.01_3	8×10^{-5}	1.8×10^{-6}

[24] D. L. Allen and M. J. Poole, Nature **164**, 102 (1949).
[25] C. P. Baker *et al.*, Atomic Energy Commission Declassified Report AECD 2189 (1948) (unpublished).
[26] E. Schatzman, Compt. rend. **232**, 1740 (1951).
[27] W. A. Fowler and T. Lauritsen, private communication; and Phys. Rev. **81**, 655 (1951).
[28] Good, Kunz, and Moak, Phys. Rev. **83**, 845 (1951).
[29] H. M. Agnew *et al.*, Phys. Rev. **84**, 862 (1951).
[30] J. L. Greenstein, Astrophys. J. **113**, 531 (1951).

TABLE III. Mean reaction times, p^{-1}, and the rate of energy production ϵ (in ergs g^{-1} sec^{-1}) at various temperatures T (in 10^6 °K).

Reaction	Mean reaction times*	$T=5$	$T=8$	$T=15$	$T=30$
$H^1+H^1\rightarrow D^2+e^++\nu$	$(100/\rho x_H)p^{-1}$	1.7×10^{10} yr	1.3×10^{9} yr	8.1×10^{7} yr	7.6×10^{6} yr
$H^1+D^2\rightarrow He^3+\gamma$	$(100/\rho x_H)p^{-1}$	23 min	80 sec	4 sec	0.3 sec
$He^3+He^3\rightarrow He^4+2H^1$	$(200/\rho x_H)p^{-1}$	2.5×10^{11} yr	1.3×10^{9} yr	4×10^{6} yr	1.5×10^{5} yr
Rate of energy production	$(100/\rho x_H^2)\epsilon$	0.2_4	3.1	50	530

* The "mean lives" of H^1 and He^3 are one-half of the mean reaction times for the first and third reaction respectively. ρ is the density in g/cm^3, x_H the concentration (by mass) of H^1.

ten or twenty, Table I shows that the competing reactions are probably much slower than reaction (45) for all temperatures T between 5 and 30 (in 10^6 °K) and almost certainly slower for T between 10 and 20. The reaction rates were estimated as follows.

The rate of the reaction involving a deuteron was calculated from the experimental cross section[24,25] near resonance as described in the preceding section. The rate of the reaction involving He^4 was estimated as described by B, using an estimate for the γ-ray width of $\Gamma\sim0.1$ ev and an upper limit of $x_{He^4}\sim0.5$ in Eq. (1a).

The rate of the reaction involving capture of a proton and a beta-decay was estimated in analogy with the proton–proton reaction, (12). An approximate one-particle model was used, considering the He^4 nucleus as made up of one neutron moving in the field of a core of the same type as a He^3 nucleus. The matrix element for the transition of the incident proton to this neutron was then calculated, using the theory and constants of the effective range of nuclear forces.

Finally, the inverse beta-decay involving the absorption of an electron was calculated using the formulas of Gamow and Schönberg.[31] A value[12] of (18.5 ± 0.2) kev for the energy end point and a half-life of 3.9×10^{8} sec for the normal beta-decay of H^3 into He^3 was used and the electron gas was assumed to be nondegenerate. This nondegeneracy applies to the interior of all main sequence stars, but not to the interior of white dwarf stars. In fact, at densities of the order of 10^6 g cm^{-3} the Fermi energy is of the same order as the energy difference between H^3 and He^3 and the inverse beta-decay proceeds enormously faster than for a nondegenerate gas and would be faster than reaction (45) under these circumstances.

VI. ENERGY PRODUCTION

The three reactions making up the proton–proton chain are given in Table III, together with their mean reaction times for four different temperatures corresponding to central conditions of different main sequence stars. The corresponding concentrations of deuterium and of He^3, under conditions of dynamic equilibrium, are given in Table II. The probable errors for the reaction times given in Table III are of the order of 40 percent for each of the first two reactions and of a factor of two or three for the third reaction.[32]

As pointed out before,[1,2] the net result of the proton–proton chain is the conversion of four hydrogen atoms (ionized) into one helium atom (ionized He^4) plus two neutrinos (the two positrons created quickly annihilating with two electrons of the ionized gas). Note that, since two He^3 nuclei are involved in reaction (45), two reactions of type (12) are required to form one He^4 nucleus. A fraction of about 0.6 of the energy release of reaction (12) escapes from the star in the form of kinetic energy of the neutrino. Allowing for this loss and using the known binding energy of an α-particle,[12] one gets an energy release of 26.2 Mev for every He^4 nucleus formed [i.e., for two reactions of type (12)]. Substituting this into Eq. (10), one gets for the energy release ϵ

$$\epsilon=1.26\times10^{19}(x_H p)\ \text{erg/g sec}, \qquad (48)$$

where x_H is the hydrogen concentration and p is the reaction rate given by Eqs. (39) or (40). For temperatures near 15×10^6 °K, we get

$$\epsilon=49.4(1+\Delta\pm0.06)(\rho x_H^2/100)\times(T/15)^{3.96}\ \text{erg/g sec}. \qquad (48a)$$

It should finally be emphasized that all the calculations of this paper were carried out under the assumption of a perfectly Maxwellian distribution of thermal energies, fixed and uniform chemical composition, density and temperature and complete dynamic equilibrium. The carbon nitrogen cycle and its relation to the proton–proton chain will be discussed in a later paper.

The author wishes to thank Professors H. A. Bethe, W. A. Fowler, E. Frieman, J. Greenstein, T. Lauritsen, P. Morrison, L. Motz, M. Schwarzschild, C. S. Wu, and W. Whaling for valuable discussions and correspondence.

[31] G. Gamow and M. Schönberg, Phys. Rev. **59**, 539 (1941).

[32] For the lower two temperatures in Table III the errors may be somewhat larger than those stated above.

Gamma-Rays from Sn^{125}†

C. E. MANDEVILLE, E. SHAPIRO, R. I. MENDENHALL, E. R. ZUCKER,* AND G. L. CONKLIN
Bartol Research Foundation of the Franklin Institute, Swarthmore, Pennsylvania
(Received June 23, 1952)

An inner beta-spectrum at ~0.5 Mev, coincident with gamma-radiation, constitutes 10±2 percent of the total beta-radiation of the 10-day Sn^{125}. The gamma-rays have a maximum energy of 1.67±0.10 Mev.

THE ten-day activity in tin has been assigned[1] to Sn^{125}. Spectrometric measurements[2] have yielded maximum beta-ray energies of 2.37±0.02 Mev and 0.40±0.01 Mev. The spectrum of lower energy was estimated to contain five percent of the total beta-radiation. A search was made for the gamma-radiation which should accompany the beta-rays of the inner group, but because of low intensity, none was detected by the spectrometric method. It was mentioned, however, that absorption measurements in lead indicated the "possible presence" of a gamma-ray at 1.5 Mev.

During the past four years, four different quantities of metallic tin, two isotopically concentrated in Sn^{124} and two of naturally occurring tin, have been irradiated in the Oak Ridge pile.[3] The following chemical procedure has been followed. Irradiated metallic tin was dissolved in HCl and carrier Sb and Te solutions were added. Metallic Te precipitated at once, and Sb was precipitated as a metal by addition of powdered Fe to the hot 6.*N*−HCl solution. Sn and some Fe were precipitated from the filtrate by addition of metallic zinc. This precipitate was dissolved by HCl, oxidized with H_2O_2, and Sn and Fe were separated by addition of NaOH to excess to form soluble Na_2SnO_3 and insoluble $Fe(OH)_3$. The filtrate was acidified with HCl, then made slightly ammoniacal, precipitating $SnO_2 \cdot xH_2O$ which was ignited to SnO_2.

A gamma-ray at 1.7 Mev was noted in the tin fraction in 1948 but was dismissed as the intense hard gamma-ray of Sb^{124}. More recently this gamma-ray has been observed in a coincidence absorption counting arrangement, and the quantum energy has been measured as 1.67±0.10 Mev. This coincidence absorption curve (Fig. 1) of the secondary electrons of the gamma-ray was observed repeatedly for forty days, and the ordinate values were observed to decay with a half-life of ten days.

A source of the ten-day tin was placed in a beta-gamma coincidence counting arrangement, and beta-

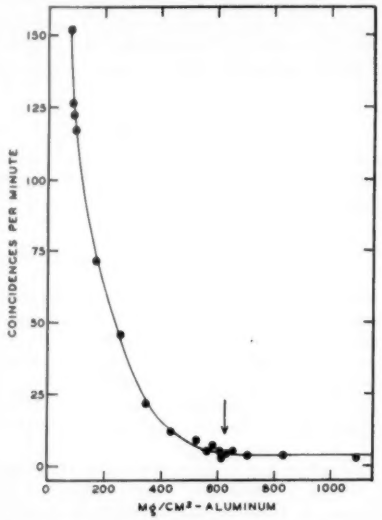

FIG. 1. Coincidence absorption of the secondary electrons of the gamma-rays from Sn^{125}.

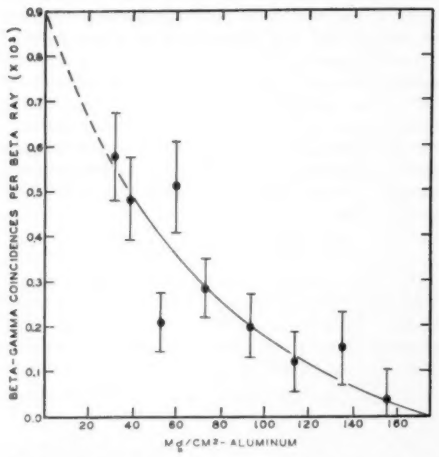

FIG. 2. Beta-gamma coincidence rate of Sn^{125} as a function of the surface density of aluminum before the beta-ray counter.

† Assisted by the joint program of the ONR and AEC.
* Frankford Arsenal, Philadelphia, Pennsylvania.
[1] J. C. Lee and M. L. Pool, Phys. Rev. **76**, 606 (1949).
[2] R. W. Hayward, Phys. Rev. **79**, 409 (1950).
[3] Isotopically concentrated Sn^{124} supplied by Y-12 Research Laboratory, Carbide and Carbon Chemicals Division, Union Carbide and Carbon Corporation, Oak Ridge, Tennessee.

gamma coincidences were measured as a function of aluminum absorber thickness before the beta-ray counter. The data are shown in Fig. 2 where the beta-gamma coincidence rate is seen to decrease to zero at 180 mg/cm² of aluminum, indicating an inner beta-ray group at ~0.5 Mev. These beta-gamma coincidences were observed to decay over a period of 40 days with the 10-day period. On calibration of the beta-gamma coincidence counting arrangement with the beta-gamma coincidence rate of Sc^{46}, the beta-gamma coincidence rate of Fig. 1 indicated, on extrapolation to zero absorber thickness, that the gamma-ray at 1.67 Mev is coincident with 10±2 percent of the beta-rays of the 10-day Sn^{125}.

The 15-day Sn^{117m}, a possible contaminant, has been observed to decay with the emission of γ-rays at 159 kev and 162 kev in cascade, and $\gamma-e^-$ coincidences have been noted.[4] In the present measurements, sufficient lead was placed before the gamma-ray counter to reduce the intensity of a gamma-ray of energy 160 kev by a factor of four. However, the beta-gamma coincidence rate of Fig. 2 remained unchanged, further confirmation of the assignment of the coincidences to Sn^{125}.

Measurements by Boyd and associates[5] at Oak Ridge, employing a scintillation spectrometer, yield a quantum energy of ~1.9 Mev for this gamma-ray.

Note added in proof.—The orbital of the 60-day level in Te^{125} is $h_{11/2}$. The beta-spectrum of Sb^{125} terminating at that level obeys the selection rule $\Delta I=2$, yes!, suggesting that the ground state of Sb^{125} is $g_{7/2}$. Since the 2.4-Mev spectrum of Sn^{125} is of the form[3] $\Delta I=2$, yes!, an orbital of $h_{11/2}$ is predicted for the ground state of Sn^{125}. For the inner spectrum of Sn^{125}, log ft is 7.2 ($\Delta I=0$, 1, yes!). No satisfactory orbital assignment appears to be available for the 1.67-Mev level in Sb^{125}, suggesting excitation of the nuclear core so that the single particle model breaks down, or that the harder beta-spectrum leads to a metastable level in Sb^{125} rather than to the ground state.

[4] J. W. Mihelich and R. D. Hill, Phys. Rev. **79**, 781 (1950).

[5] *Nuclear Data*, National Bureau of Standards Supplement 2 to Circular 499 (1951).

PHYSICAL REVIEW VOLUME 88, NUMBER 3 NOVEMBER 1, 1952

The *V*-Particle and the Composite Pion

R. J. FINKELSTEIN
University of California, Los Angeles, California
(Received June 30, 1952)

It is assumed that the *V*-particle is described by a spinor wave function, and that the pion may be treated as a nucleon-antinucleon pair. The rates of the following reactions

$$\left.\begin{matrix}\pi\rightarrow\mu+\nu\\ V^0\rightarrow\pi+P\end{matrix}\right\},\quad \text{now written as}\quad \begin{cases}(P+\bar{N})\rightarrow\mu+\nu\\ V^0\rightarrow(\bar{P}+N)+P'\end{cases}$$

are then compared under the assumption that both reactions are governed by the same form and strength of β-interaction. The ratio of the two lifetimes is independent of all numerical details of the pion structure. Putting in the observed lifetime of the pion, one finds for the lifetime of the V: 5×10^{-10} sec for $Q=35$ Mev; and 2×10^{-10} sec for $Q=75$ Mev. The two Q values have been interpreted in terms of a mass doublet.

THE attractive hypothesis that the bosons are composite, previously suggested in connection with the neutrino theory of light, has been introduced into the problem of the pion by Fermi and Yang,[1] who consider the possibility that this particle is a nucleon bound to an antinucleon by a square well, having a radius $\sim\hbar/Mc$ and a depth ~25 Bev. As emphasized by them, however, relativity permits only zero-range interactions, and for such interactions no bound two-particle solutions exist. The two-particle model, therefore, has to be interpreted either as an approximation to a much more complicated structure in the usual field theory, or as an approximately permissible structure in a modified field theory, which is not based on the usual singular commutators and light-cone interactions. The possible origins and limitations of such a two-particle model are here ignored and attention is directed toward some consequences which result from the further assumption of similar Fermi interactions between all spinor particles.[2] It is known that the fundamental reactions

$$N\rightarrow P+e+\nu \tag{1}$$

$$\mu\rightarrow e+\nu+\nu \tag{2}$$

$$\mu+P\rightarrow N+\nu \tag{3}$$

can be correlated, at least approximately, in terms of the same spinor coupling, namely:

$$g\sum_{c=0}^{4}\sum_{\rho}a_c(\psi_1 T\Gamma_\rho{}^c\psi_2)(\psi_3 T\Gamma_\rho{}^c\psi_4), \tag{I}$$

where $g\cong3\times10^{-49}$ erg cm³; T is a charge conjugate operator:

$$T\gamma_\mu T^{-1}=-\bar{\gamma}_\mu;\quad \Gamma_\rho{}^0=1,\quad \Gamma_\rho{}^1=\gamma_\mu,\quad\cdots\quad \Gamma_\rho{}^4=\gamma_1\gamma_2\gamma_3\gamma_4,$$

[1] E. Fermi and C. N. Yang, Phys. Rev. **76**, 1739 (1949).

[2] C. N. Yang and J. Tiomno, Phys. Rev. **79**, 495 (1950).

and

$$\sum_0^4 a_\sigma = 1,$$

with the individual a_σ still in doubt.

(In addition, our extremely meager knowledge of the κ meson is compatible with the view that it is a fermion, and with the decay scheme: $\kappa \to \mu + \nu + \nu$. The approximate lifetime is 10^{-9} sec, also in rough agreement with (I) and the stated value of g.)

Consider now the possibility that the π and V decays can also be understood in terms of (I). These reactions are if the pion is composite.

$$(P^- + N) \to \mu^- + \nu, \tag{4a}$$

or

$$\to e^- + \nu, \tag{4b}$$

and if the V is a fermion,

$$V^0 \to P + (P^- + N).$$

Both (4a) and (4b), as well as (5), are first-order processes. The rates are therefore finite in contrast to the results of earlier calculations which introduce the nucleon pair only in an intermediate state. The competition between (4a) and (4b), as well as their absolute rates and that of (5), of course depend upon the wave function of the nucleon-antinucleon system which is interpreted as the pion. This wave function will now be considered without making any very special assumptions about the interaction responsible for the bound state.

THE WAVE FUNCTION OF THE PION

Denote the probability amplitude for annihilating a positive meson by $\Phi_{\alpha\alpha}$ and require that it transform like the product $(N_>)_\alpha (P_<)_\alpha{}^*$ the amplitude for annihilating a positive ($>$) energy N and creating a negative ($<$) energy P. Then under the Lorentz rotation, S,

$$\Phi' = S\Phi\bar{S}^* = S\Phi(\gamma_4 S^{-1}\gamma_4)$$

or

$$(\Phi\gamma_4)' = S(\Phi\gamma_4)S^{-1}. \tag{1a}$$

Define the positive energy wave function $(\bar{P}_>)$ of the antiproton by

$$\bar{P}_> = (CP_<)^* = P_<{}^* C^{-1},$$

where

$$C^{-1}\gamma_4{}^* C = -\gamma_4, \quad C^{-1}\gamma_k C = \gamma_k.$$

Then the wave function Ψ of the pair $(N_>\bar{P}_>)$ may be defined as

$$\Psi = \Phi C^{-1}.$$

For it, one has

$$(\Psi T)' = S(\Psi T)S^{-1}, \tag{1b}$$

where

$$T = C\gamma_4 \quad (\text{and} \quad T\gamma_\mu T^{-1} = -\tilde{\gamma}_\mu).$$

Under inversions

$$(\Phi\gamma_4)' = \epsilon_{N>}\epsilon_{P<}{}^*\gamma_4(\Phi\gamma_4)\gamma_4, \quad (\Psi T)' = \epsilon_{N>}\epsilon_{P<}{}^*\gamma_4(\Psi T)\gamma_4,$$

where $\epsilon_{N>}$, for example, $= \pm 1$, depending on the inversion properties assigned to a neutron wave function of positive energy. Now expand $\Phi\gamma_4 = \Psi T$ in the set of sixteen independent matrices, $\Gamma_\rho{}^\sigma$, previously introduced

$$\Phi\gamma_4 = \Psi T = \sum_1^{16} \lambda_\rho{}^\sigma \Gamma_\rho{}^\sigma. \tag{2}$$

Then

$$(\Phi\gamma_4)' = (\Psi T)' = \sum_1^{16} \lambda_{\rho'}{}^{\sigma'} \Gamma_{\rho'}{}^{\sigma'},$$

where

$$\lambda_{\rho'}{}^{\sigma'} = \sum a_{\rho'\rho}{}^{\sigma'\sigma} \lambda_\rho{}^\sigma,$$

and the tensor transformation coefficients $a_{\rho'\rho}{}^{\sigma'\sigma}$ are appropriate to $\Gamma_\rho{}^\sigma$. If P and N are both of type A (Yang and Tiomno[2])

$$\epsilon_{N>}\epsilon_{P<}{}^* = -1.$$

Then $\lambda_\rho{}^\sigma$ is ρ-component of tensor of rank $4-\sigma$. In general, the structure of a meson will be specified by the 16 tensor functions $\{\lambda_\rho{}^\sigma\}$. These tensor properties result from the intrinsic spin of the component particles. If, in addition, there is orbital angular momentum of $\bar{P}$ with respect to N in the proper frame of the pion, then the coefficients $\lambda_\rho{}^\sigma$ will transform in the manner indicated by the composition rules for angular momentum.

To construct a particle having zero proper angular momentum, one must either put $\lambda_k{}^1 = \lambda_{\mu\nu}{}^2 = \lambda_k{}^3 = 0$ or assign p-orbitals to them. In either case one has

$$\lambda_k{}^1(0) = \lambda_{\mu\nu}{}^2(0) = \lambda_k{}^3(0) = 0,$$

where the argument indicates a zero separation of $\bar{P}$ and N in the proper system. Because the pair interactions are δ-functions, it follows for pions of zero spin that the only contributing parts of Ψ are $\lambda_0{}^0$, $\lambda_4{}^1$; $\lambda_{123}{}^5$, $\lambda_{1234}{}^4$. The first two functions are odd; the second pair, even; all are spherically symmetric.

THE PAIR INTERACTIONS

The following matrix element (densities) and associated processes will be considered:

Matrix element	*Process*	
$G\Sigma A_\sigma (P_<{}^+\Gamma_\rho{}^\sigma N_>)(N_>{}^+\Gamma_\rho{}^\sigma P_>) b_{P<}{}^* b_{N>} b_{N>}{}^* b_{P>}$	$P + \pi^- \to N$	(a)
$g\Sigma a_\sigma (P_<{}^+\Gamma_\rho{}^\sigma N_>)(V_>{}^+\Gamma_\rho{}^\sigma P_>) b_{P<}{}^* b_{N>} b_{\nu>}{}^* b_{P>}$	$P + \pi^- \to V^0$	(b)
$g\Sigma a_\sigma (P_<{}^+\Gamma_\rho{}^\sigma N_>)(e_>{}^+\Gamma_\rho{}^\sigma \nu_<) b_{P<}{}^* b_{N>} b_{e>}{}^* b_{\nu<}$	$\pi^- \to e^- + \nu$	(c)
$g\Sigma a_\sigma (P_<{}^+\Gamma_\rho{}^\sigma N_>)(\mu_>{}^+\Gamma_\rho{}^\sigma \nu_<) b_{P<}{}^* b_{N>} b_{\mu>}{}^* b_{\nu<}$	$\pi^- \to \mu^- + \nu$	(d)

where b and b^* indicate annihilation and creation operators. The interactions (b)–(d) may tentatively be regarded as special cases of (I), but it is clear that (a) is different. One may say either that the universal Fermi coupling does not have the form I or that the composite pion does not fit simply into this scheme. On the other hand, one is not forced, but the existing evidence, to take GA and ga of different orders of

magnitude even though interaction (a) is much stronger than the others (see below).

It is convenient to rewrite (a)–(d) in terms of the tensors previously introduced. In each case the covariant factor belonging to the pion is

$$\begin{aligned} P_<{}^*\gamma_4\Gamma_\rho{}^\sigma N_> &= (N_>)_\alpha (P_<)_\alpha{}^*(\gamma_4\Gamma_\rho{}^\sigma)_{\alpha\alpha} \\ &= (N_>)_\alpha (\bar{P}_>)_\alpha (C\gamma_4\Gamma_\rho{}^\sigma)_{\alpha\alpha} \\ &= \mathrm{Tr}\Psi T\Gamma_\rho{}^\sigma. \end{aligned}$$

This form is now adopted even when Ψ cannot be factored. By (2)

$$\mathrm{Tr}\Psi T\Gamma_\rho{}^\sigma = \sum \lambda_{\rho'}{}^{\sigma'}\,\mathrm{Tr}\Gamma_{\rho'}{}^{\sigma'}\Gamma_\rho{}^\sigma = 4\epsilon_\rho{}^\sigma\lambda_\rho{}^\sigma,$$

where

$$\epsilon_\rho{}^\sigma = 1 \quad \text{if} \quad \sigma = 0, 1, 4; \quad \epsilon = -1 \quad \text{if} \quad \sigma = 2, 3.$$

The matrix elements are of the form

$$\int\int\int\int \sum a_\sigma [4\epsilon_\rho{}^\sigma \lambda_\rho{}^\sigma(x_1, x_2)][\varphi_3{}^*(x_3)\gamma_4\Gamma_\rho{}^\sigma\varphi_4(x_4)] \times \delta(1, 2, 3, 4)dx_1dx_2dx_3dx_4, \quad (3)$$

where

$$\delta(1, 2, 3, 4) = \delta(x_1 - x_2)\delta(x_2 - x_3)\delta(x_3 - x_4).$$

Write $\lambda_\rho{}^\sigma(1, 2) = (e^{iP_\mu X_\mu}/\Omega^{\frac{1}{2}})\mu_\rho{}^\sigma(x_1 - x_2)$, where $e^{iP_\mu X_\mu}/\Omega^{\frac{1}{2}}$ is the external wave function of the pion. Then the matrix element for pion annihilation according to (b), (c), or (d) and (3) is

$$(g/\Omega^{\frac{1}{2}})\sum 4a_\sigma\epsilon_\rho{}^\sigma\mu_\rho{}^\sigma(0)(u_3{}^*\gamma_4\Gamma_\rho{}^\sigma u_4)b_\sigma b_3{}^*b_4, \quad (4)$$

where u_3 and u_4 are constant spinors, and $b_\sigma = b_{P<}{}^*b_{N>}$. The form (4) in the usual Yukawa theory would refer to more than one species of meson. But here all tensors appearing in (4) are to be associated with the same particle.

For absorptions according to (a) substitute $g \to G$ and $a_\sigma \to A_\sigma$ in (4). Present evidence indicates $A_\sigma = \delta_{\sigma 4}$. The corresponding tensor is $\mu_{1234}{}^4$. The other tensors do not contribute to (a), but they do not vanish, and in fact determine the rates of (b), (c), and (d). In the following, we continue to consider a particle of zero spin and therefore need keep only the contributions from $\mu_\rho{}^0(0)$, $\mu_4{}^1(0)$, $\mu_{123}{}^2(0)$, and $\mu_{1234}{}^4(0)$. These numbers are partially determined by experiment as follows:

(a) Nuclear Forces, Pion Production, etc.

$$G\varphi_{1234}{}^4(0) \cong a^{\frac{1}{2}}(Mc^2)^{\frac{1}{2}}(h/Mc)^2(Mf^2/2m_\pi hc)^{\frac{1}{2}}, \quad (5)$$

where f is Yukawa's coupling constant. Then

$$G\varphi_{1234}{}^4(0) \cong a^{\frac{1}{2}} \times 10^{-44} \text{ erg cm}^2,$$

where the radius of the pion is $a(h/Mc)$ and $\varphi(0)$ is the dimensionless amplitude at the origin

$$\varphi(0) = (ah/Mc)^{\frac{1}{2}}\mu(0).$$

If one takes $G = g$, then

$$\varphi_{1234}{}^4(0) \cong (a^{\frac{1}{2}}/2) \times 10^{13}.$$

(b) Lifetime of Charged Pion

Assume that

$$a_0, a_1 \ll a_3, a_4. \quad (6)$$

This assumption is probably not in disagreement with our knowledge of nuclear β-decay. The decay of the charged pion may go according to either (c) or (d). The matrix element (4) may be used directly. The spin sums appearing in case (c) are

$$\sum_{\text{spin}} |e_>{}^*\gamma_4\Gamma_4{}^1\nu_<|^2 = 1 - \frac{V}{c} \sim \frac{1}{2}\frac{1}{\gamma^2}. \quad (7a)$$

$$\sum_{\text{spin}} |e_>{}^*\gamma_4\Gamma_0{}^0\nu_<|^2 = 1 + V/c. \quad (7b)$$

The interference term between a_1 and a_0 contains the factor $1/\gamma$. Exactly the same results are, of course, obtained if e is replaced by μ. The competition between the $\pi - \mu$ and the $\pi - e$ decay will be decided in favor of the former, in agreement with experiment, only if the dominant contributing coefficient is a_1. Therefore, assume also that

$$a_1 \gg a_0,$$

i.e., that the vector part is large compared to the scalar part. From this analysis nothing can be concluded about the tensor contribution, which has been emphasized by recent β-evidence. (A similar argument was given earlier under the assumption that the decay progressed through a virtual nuclear pair, but then both the electron and the muon decay have infinite rates and only the ratio is finite.[2])

The lifetime for the $\pi\mu$-decay may now be written if we tentatively put $a_0 = 0$

$$\tau_\pi{}^{-1} = (16g^2/\pi\hbar^4)p_\nu f_1{}^\pi f_2{}^\pi m_\pi[a_1\mu_4{}^1(0)]^2(1 - V/C), \quad (9)$$

where f_1, f_2 = fraction of energy taken by particles (1) and (2), P_ν is momentum of neutrino and the index π has been introduced to differentiate this case from the V-decay, which we consider next. From the observed decay one finds

$$a_1\mu_4{}^1(0) \cong 5.2 \times 10^{-8} \times (Mc/\hbar)^{\frac{1}{2}} \text{ cm}^{-\frac{1}{2}}. \quad (10)$$

(c) Lifetime of the V-Particle

Assume that the neutral V-particle is a fermion (of inversion type A or B). Attribute its instability to the Fermi coupling (b). To determine the lifetime assume that the initial V^0 is at rest and therefore that the pion is created in motion. The tensors contributing to (4) are again $\mu_\rho{}^0(0)$ and $\mu_\rho{}^1(0)$ and in this case also we put $a_0 = 0$, so that only $\mu_\rho{}^1(0)$ survives; however, all components of $\mu_\rho{}^1$ are now important since the pion has a relativistic energy. One then finds for the lifetime

$$\tau_V{}^{-1} = (16g^2/\pi\hbar^4)p_P f_1{}^V f_2{}^V m_V[a_1\mu_4{}'(0)]^2 \times \left\{1 - \frac{V_\pi}{c}\frac{V_P}{c} - \frac{1}{2}\frac{1}{\gamma_\pi{}^2}\left(1 - \frac{1}{\gamma_P}\right)\right\}, \quad (11)$$

[2] M. Ruderman and R. Finkelstein, Phys. Rev. **76**, 1458 (1949).

where the additional factor comes from

$$\tfrac{1}{2}\sum_{\text{spin}}|P^{+}\gamma_4\mu_\rho'(0)\gamma_\rho V^0|^2.$$

The ratio τ_V/τ_π is independent of a_1 and $\mu_4^1(0)$

Using the observed value of τ_π, one finds

$$\tau_V=5.2\times10^{-10}\text{ sec for } Q=35\text{ Mev},$$
$$\tau_V=2.2\times10^{-10}\text{ sec for } Q=75\text{ Mev},$$

where Q is the energy released in the disintegration.[4] We have tentatively interpreted the two Q values to mean that there are two neutral V particles differing in mass by $\sim$80 electron masses. (The mass spectrum of spinor particles would then be extended to include at least two more eigenvalues—in addition perhaps to that of the κ.) The calculated lifetimes are in approximate agreement with the experimental value $\sim2\times10^{-10}$ sec. The data permit, but do not require, one to associate different lifetimes with the two Q values.

Decays such as

$$V^0\rightarrow\begin{cases}\mu^+\\ e^+\end{cases}+\overset{\pi}{(\bar{P}+N)}\quad\text{and}\quad V^0\rightarrow\mu^++e^-+\nu\qquad(12)$$

would be excluded by our assumption that the V is of type A or B, since the light particles are C or D; that is, the V is one of the conserved heavy particles. On the other hand there would seem to be no selection rules forbidding

$$V^0\rightarrow P+\mu^-+\nu,\qquad(13a)$$
$$V^0\rightarrow P+e^-+\nu,\qquad(13b)$$

and in fact it has been suggested that the Q-histogram consists of a line at 35 Mev, corresponding to $V\rightarrow P+\pi^-$, superimposed on a continuous spectrum centered at 75 Mev, corresponding to (13a). However, an estimate of these lifetimes according to the usual β-formulas yields $\tau=4\times10^{-9}$ sec for (13b) and a longer lifetime for (13a). Neither would be expected to compete with the two-particle decay, and in addition (13b) is faster than (13a). If it is found that the peak at 75 Mev is indeed associated with the continuous spectrum of (13a), then one could, of course, postulate a new β-coupling with $g\cong3\times10^{-13}$; and, if it is either vector or axial vector, then the relative rates of (13a) and (13b) could be accounted for by the argument previously used in connection with the $\pi\mu/\pi e$ branching. At present, however, this proposal does not appear to be very attractive, and for this reason we assume that the rates of (13a) and (13b) are too slow to play an important role in the shape of the Q-histogram.

[4] Leighton, Wanloss, and Alford, Phys. Rev. **83**, 843 (1951).

(d) Production of the *V*-Particle

Nothing definite can be said at present about this process, although there now appears to be some evidence against a large cross section for the production of either charged or neutral V-pairs. If that result stands, one might consider $\pi^-+P\rightarrow V^0$. To exhibit this coupling as a pair interaction one might write

$$(V^0+\bar{P})+P\rightarrow V^0,$$

where the associated interaction must be strong [like (a)].

Absolute Lifetimes

The argument so far is independent of the force binding the nucleons together. We have studied some pion structures arising when the invariant interaction (J) is a functional of Ψ; then the equation determining Ψ is nonlinear:

$$[\gamma_\mu{}^1\hat{p}_\mu{}^1+\gamma_\mu{}^2\hat{p}_\mu{}^2-2iM+J(\Psi)]\Psi=0.$$

Such a theory is covariant, but deviates from the relativity as well as quantum theory. One case worked out in detail leads to an acceptable lifetime only if the vector contribution to I is of the order of $10^{-1}\times$tensor contribution.[5] Quite different conclusions result from other variants of this theory.

The Neutral Pion

The radius of the nucleon-antinucleon system turns out to be $\sim\hbar/Mc$ on either the square well or the nonlinear model. This is satisfactory if the mass difference, charged minus neutral, which is about 10 electron masses, is attributed to electromagnetic mass, provided that the observed neutral pions are identified as proton-antiproton systems and the charge independence of nuclear forces is assumed for particles *vs* antiparticles. This idea is supported by the observed approximate charge independence of the pi-nucleon interaction.

The instability of the proton-antiproton may be described in just the same way as the two-quantum annihilation of positronium, although the lifetime now depends significantly on the internal wave function. The calculated lifetime is convergent but very short $\sim10^{-19}$ sec.[5] The lifetime of the neutron-antineutron might be much longer. Suppose that the decay goes according to the scheme

$$N+\bar{N}\rightarrow P+\bar{P}\rightarrow2\gamma,$$

and that transitions between the two neutral structures are regulated by interaction (a); then the lifetime is of the order of $a^{-3}\times10^{-16}$ sec.[5]

[5] S. Gasiorowicz and P. Kaus (to be published).

Spin Paramagnetism of Cr^{+++}, Fe^{+++}, and Gd^{+++} at Liquid Helium Temperatures and in Strong Magnetic Fields

WARREN E. HENRY
Naval Research Laboratory, Washington, D. C.
(Received May 1, 1952)

A quantitative experimental study of space quantization of magnetic dipoles and quenching of orbital angular momentum has been made by measuring the fractional variation of the magnetic moment of paramagnetic ions with magnetic field strength at fixed temperatures. The study of trivalent chromium ion ($^4F_{3/2}$ state for free ion) in potassium chromium alum up to 99.5 percent saturation at 1.29°K and in a field of 50,000 gauss gave a close confirmation of space quantization of magnetic dipoles through compatibility of experimental results with the Brillouin function and very marked incompatibility with the Langevin function. The quenching of orbital angular momentum by the crystalline electric field was demonstrated by the agreement of experimental measurements with a Brillouin function for $g=2$ ($L=0$) as against $g=2/5$ ($L=3$). The paramagnetic saturation of iron ($^6S_{5/2}$ for free ion) ammonium alum and gadolinium ($^8S_{7/2}$ for free ion) sulfate octahydrate was achieved, thus permitting of speculation as to a small contribution of the crystalline field to the magnetic moment. Some preliminary calculations were made of this effect for iron ammonium alum and compared with experiment. Experimental study of moments consisted in moving a spherical sample with respect to a double coil system and measuring the flux change ballistically. Magnetic moments were reproducible to ~0.2 percent in mid-range and the magnitude of H/T is known to ~1.5 percent.

ANALYSIS of measurements[1] of magnetic moments of the trivalent chromium ion in potassium chromium alum in the range near paramagnetic saturation has made possible a critical examination of existing simple theories of paramagnetism. In particular, evaluation of ideas regarding the space quantization[2] of magnetic dipoles and the quenching[3] of orbital angular momentum has been made. The idea of space quantization is examined by comparison of the variation of experimental magnetic moments with theoretical predictions, using H/T as independent variable. Two simple formulas, taking into account saturation effects, are the Langevin[4] formula, based on a classical dipole which can assume all orientations in space and the Brillouin[2] function, limited to discrete values of spatial orientation.

The method of checking the idea of quenching of orbital angular momentum is to compare the array of experimental moments with an array of calculated moments for a substance for which $L\neq 0$ for the free ion and in which a nonlinear aggregate[3] of atoms (i.e., not lying on a straight line) contribute to the crystalline field. The trivalent chromium ion in potassium chromium alum meets these requirements, since it exists in a $^4F_{3/2}$ state for the free ion and in the alum the ion is at the center of an octahedron in which water molecules are at the corners. Thus, in one experiment, answers to the questions on space quantization and the quenching of orbital angular momentum are simultaneously obtained.

The investigation of the magnetic field dependence of magnetic moments was extended to trivalent iron ($^6S_{5/2}$ state for free ion) in iron ammonium alum and to trivalent gadolinium ($^8S_{7/2}$ state for free ion) in gadolinium sulfate octahydrate. Since $L=0$ for these ions, interpretation of small, second-order departures of moments from simple functions is made easier, in that the question of incomplete quenching does not arise.

EXPERIMENTAL WORK

The relative magnetic moments were measured with a magnetic moment differential fluxmeter as a function of static magnetic fields for fixed values of temperatures in the liquid helium range. A schematic diagram of the general experimental arrangement is shown in Fig. 1.

The Temperature

The sample (a solid sphere) of potassium chromium alum 2 cm in diameter was kept in contact with liquid helium in a metal Dewar (the vacuum chamber around the sample having been removed), Fig. 1, similar to one previously[5] described. A cylindrical space 6 cm in diameter was available. The value of the initial temperature, 4.21°K, was determined by the local atmospheric pressure and the distance from the sample to the helium level. This temperature varied only slightly with the normal variations of atmospheric pressure or the change in level of the liquid helium. Other temperatures were produced by reduction of pressure above the liquid helium and were kept constant by means of a manostat,

[1] W. E. Henry, Phys. Rev. **87**, 229 (1952) and **85**, 487 (1952); Gorter, de Haas, and van den Handel, Amsterdam Acad. Sci. **36**, 158 (1933).

[2] L. Brillouin, J. phys. et radium **8**, 74 (1927); K. F. Niessen Phys. Rev. **34**, 253 (1929); R. H. Fowler and E. A. Guggenheim, *Statistical Thermodynamics* (Cambridge University Press, Cambridge, 1939), p. 629.

[3] H. A. Kramers, Proc. Koninkl. Nederland, Akad. Wetenschap. **33**, 959 (1930); H. A. Jahn and E. Teller, Proc. Roy. Soc. (London) **A161**, 220 (1937).

[4] P. Langevin, J. phys. et radium, **4**, 678 (1905); E. C. Stoner, *Magnetism* (Methuen and Company, Ltd., London, 1947), p. 42; J. C. Slater, *Quantum Theory of Matter* (McGraw-Hill Book Company, Inc., New York, 1951), p. 383.

[5] W. E. Henry and R. L. Dolecek, Rev. Sci. Instr. **21**, 496 (1950); W. E. Henry, J. Appl. Phys. **22**, 1439 (1951).

FIG. 1. Schematic diagram of assembly of metal Dewar for liquid helium and sample; displacement lift is shown at top.

except at the lowest temperature. The temperatures were obtained from vapor pressures and monitored by a carbon resistance thermometer.[6] Mercury manometers were used to read vapor pressures in the high pressure range, while oil manometers were used for the low pressure range. In general, the temperatures were decreased monotonically with time to insure temperature equilibrium in the helium I range. However, if temperature inversion occurred with accompanying temperature gradients, variation of the magnetic field could be used to restore equilibrium through eddy current heating of the Dewar metal. The temperatures could be determined to within 0.2 percent for 4.21°K and to 0.5 percent for 1.30° and 2.00°K.

Magnetic Fields

A Bitter[7] type solenoidal magnet, capable of producing fields of over 50,000 gauss, was used. There was available a 10-cm opening with the center and most homogeneous portion of the field 32.5 cm from the top. The magnet was calibrated in gauss produced at a point per ampere of current passing through the magnet; a standardized coil was connected in series with a ballistic galvanometer which was standardized for each set of conditions. Flux change through the coil was generated by moving the coil from the field to be measured to nearly zero field in a time short compared with the period of the galvanometer. Thus, after calibration, the magnetic field was determined by potentiometric measurement of the current through a calibrated shunt resistance in series with the magnet. Fields could be reproduced to within 0.2 percent in the middle of the range, as indicated by reproducibility of magnetic moments. The magnitude of field was known to better than 1 percent.

The Magnetic Moment Differential Fluxmeter[8]

This device consisted of a sample displacement lift (Fig. 1), and a flux change indicator comprised of a self-bucking coil system in series with a controllable resistance and a ballistic galvanometer with a 27-second period. The sample displacer was designed to avoid mechanical shock and motion of the coil system with respect to the magnet. The coil system consisted of about 2000 turns of No. 40 wire on each of the oppositely would bobbins (3.5 cm in diameter). The measurements were made by causing the sample to shuttle, in about 0.5 second, from the middle of one coil to the middle of the other. The positions at the ends of the 4-cm excursions were reproduced to ± 0.003 cm. The net flux change in the coils (due to the motion of the sample), and accordingly the deflection of the ballistic galvanometer, was proportional to the moment of the sample.

INTERPRETATION OF RESULTS

A plot of the experimental results, in which the relative magnetic moment M_r is plotted against H/T, is given in Fig. 2. The interpretation of these results embraces their analysis in the light of space quantization of the ionic moments and the quenching of orbital angular momentum with the idea of detecting departures from known theoretical functions. Since the Langevin and Brillouin functions are unique and proper functions of (H/T), it is sufficient to use relative mag-

TABLE I. Comparison of theoretical and experimental moments for two sets of values of H and T corresponding roughly to the same value of H/T.

	Calculated moments		
	Brillouin $g=2$ $S=5/2$	Space quantized model with cubic field splitting	Experimental moments
$H=35{,}770$ g $T=4.21$°K	4.074	4.067	4.0_6
$H=12{,}200$ g $T=1.32$°K	4.20	4.17	4.1_4

[6] J. R. Clement and E. H. Quinnell, Proc. International Conf. on Low Temperature Physics, Oxford, 1951, p. 51; Rev. Sci. Instr. **23**, 213 (1952).

[7] F. M. Bitter, Rev. Sci. Instr. **10**, 373 (1939).

[8] W. E. Henry, paper presented at the National Bureau of Standards 50th Anniversary Low Temperature Physics Symposium, March 1951.

netic moments for our analysis. This analysis consists of normalizing the calculated and experimental values at chosen values of H/T. Although space quantization and the quenching of orbital angular momentum are unmistakably indicated by the good agreement of simple theory and experiment for the ${}^4F_{3/2}$ state of the free chromium ion, there appears to be a small, second-order departure of the experimental results from the Brillouin function. In searching for the source of the small systematic deviation, one must consider the following: (1) experimental error in the measurement of M, H, and T, (2) dipole-dipole interaction, (3) exchange interaction, (4) incomplete quenching, and (5) the effect of the crystalline field splitting on the magnetic energy levels. The diamagnetic contribution is, of course, too small to affect the results.

It is felt that since the moment can be reproduced to 0.2 percent and the magnitude of H/T is known to less than 1 percent, especially for 4.21°K, experimental error as a complete explanation must be discarded. It is true that the field seen by the ion is the applied

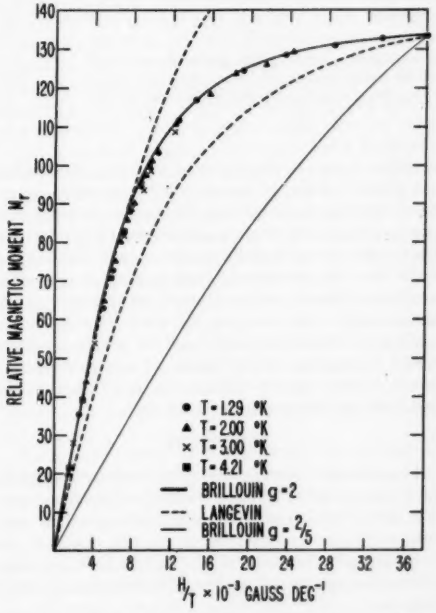

FIG. 2. Plot of relative magnetic moment, M_r, *vs* H/T for potassium chromium alum. The heavy solid line is for a Brillouin curve for $g=2$ (complete quenching of orbital angular momentum) and $J=S=3/2$, fitted to the experimental data at the highest value of H/T. The thin solid line is a Brillouin curve for $g=2/5$, $J=3/2$ and $L=3$ (no quenching). The broken lines are for a Langevin curve fitted at the highest value of H/T to obtain the lower curve and fitted at a low value (slope fitting) of H/T to obtain the upper curve.

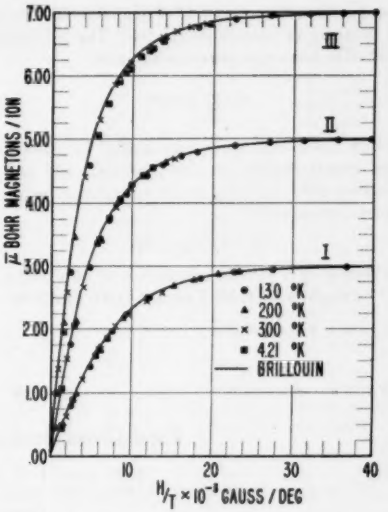

FIG. 3. Plot of average magnetic moment per ion, $\bar{\mu}$ *vs* H/T for (I) potassium chromium alum ($J=S=3/2$), (II) iron ammonium alum ($J=S=5/2$), and (III) gadolinium sulfate octahydrate ($J=S=7/2$). $g=2$ in all cases, the normalizing point is at the highest value of H/T.

field with corrections due to the demagnetization factor[9] and the Lorentz polarization[10] (effect of field of neighboring ions). However, since the sample is spherical, these two opposing corrections cancel[11] each other in first approximation. Therefore, any error thus introduced is a second-order correction to a second-order effect which is negligible. For potassium chromium alum, the chromium ions are greatly separated, practically eliminating dipole-dipole and exchange interactions (ignoring the possibility of superexchange based on the existence of excited states of normally diamagnetic atoms).

Experiments which were carried out with iron ammonium alum[12] (iron in ${}^6S_{5/2}$ state for the free ion) and gadolinium (${}^8S_{7/2}$ state for free ion) sulfate octahydrate show (Fig. 3) slight departures from the Brillouin functions for free spins. Since L is zero for both free ions, these slight departures which remain for the two ions are not attributable to incomplete quenching. Energy levels taken from Kittel and Luttinger[13] and based on the effect of a crystalline cubic field through spin-orbit interaction,[14] have been used to calculate magnetic moments at a few points for iron ammonium alum in

[9] C. Breit, Amsterdam Acad. Sci. **25**, 293 (1922).
[10] H. A. Lorentz, *Theory of Electrons* (G. E. Stechert and Company, New York, 1909).
[11] C. J. Gorter, Arch. du Musee Teyler **7**, 183 (1932).
[12] Contamination and decomposition were carefully avoided.
[13] C. Kittel and J. M. Luttinger, Phys. Rev. **73**, 162 (1948).
[14] J. H. Van Vleck and W. G. Penney, Phil. Mag. **17**, 961 (1934).

mid-range as a function of H, T and the total electric field splitting in zero magnetic field. The calculations consisted in forming a partition function

$$Z=\sum_{i=1}^{6} e^{-E_i/kT},$$

in which the E_i are the energy levels[12] for cubic symmetry which depend on the magnetic field and on crystalline field splitting in zero magnetic field. The magnetic moment is

$$M=kT\partial \ln Z/\partial H.$$

The results of a sample calculation of two points for Fe^{+++} are given in Table I for the (100) direction.

The experimental determination of relative magnetic moments for potassium chromium alum in fields up to 50,000 gauss has shown with precision the creditability of space quantization of magnetic dipoles and the quenching of orbital angular momentum by compatibility of the Brillouin function, for $g=2$, with experiment. Even the small, second-order departure of the magnetic moment from the Brillouin function can probably be attributed, at least in part, to an effect of the crystalline field splitting on the magnetic energy levels, as is suggested by a preliminary calculation of the moment for Fe^{+++} at a few points. More detailed calculations of the effect of the crystalline field are being made and will be reported later.

PHYSICAL REVIEW VOLUME 88, NUMBER 3 NOVEMBER 1, 1952

Total Cross Sections for 14-Mev Neutrons*

J. H. Coon, E. R. Graves, and H. H. Barschall
University of California, Los Alamos Scientific Laboratory, Los Alamos, New Mexico
(Received July 21, 1952)

The total cross sections of over 50 elements were measured in good geometry for 14-Mev neutrons. A plot of the square root of the total cross section *versus* the one-third power of the atomic weight shows deviations from the linear relationship predicted by statistical theory. The deviations are most pronounced for the heaviest elements.

INTRODUCTION

ONE of the methods for determining nuclear radii is based on measurements of the total cross sections of nuclei for fast neutrons. Nuclear radii are most likely to be calculable from such measurements if the neutron wavelength divided by 2π is small compared to the nuclear radius, but not small enough that the nucleus is transparent for the neutrons used. Neutrons of energies of the order of 20 Mev satisfy these conditions. Several measurements using[1] neutrons of energies between 13 and 25 Mev have been published,[1-6] and have served to determine nuclear radii. Each investigation covers a relatively small number of elements. Measurements performed at different neutron energies and in different geometries are difficult to compare particularly because of the strong angular dependence of diffraction scattering about which only very limited experimental information is available.

All the published measurements at neutron energies of the order of 20 Mev are compatible with the assumption that for nuclei heavier than Be the nuclear radius is a linear function of the one-third power of the number of nucleons in the nucleus. The present investigation was undertaken to study possible deviations from this relationship as might perhaps occur in nuclei with closed shells. For this purpose the cross sections of all readily available elements were measured for neutrons of the same energy and in about the same geometry. The uniformity of the technique used for all the elements serves to increase the precision of the cross section *versus* atomic weight relationship and hence might facilitate the interpretation of the data.

PROCEDURE

Fast neutrons were produced by bombarding a thick Zr-T target with 220-kev diatomic deuterium ions. The direction of observation was at an angle of 88° with respect to the deuteron beam. In this direction the neutrons have an energy of 14.12 ± 0.04 Mev, assuming a reaction energy of 17.58 ± 0.02 Mev for the d-T reaction.

A *trans*-stilbene scintillator served as neutron detector. It was placed at a distance of 165 cm from the neutron source. In order to check the sensitivity of the detector to γ-rays or neutrons which do not come directly from the target, a copper bar, 1 in. in diameter and 25 in. long, was inserted between source and detector. It was found that the background counting

* Work performed under the auspices of the AEC.
[1] Amaldi, Bocciarelli, Cacciapuoti, and Trabacchi, Nuovo cimento 3, 203 (1946).
[2] R. Sherr, Phys. Rev. 68, 240 (1945).
[3] A. H. Lasday, Phys. Rev. 81, 139 (1951).
[4] Coon, Bondelid, and Phillips (to be published).
[5] Poss, Salant, and Yuan, Phys. Rev. 85, 703 (1952).
[6] D. I. Meyer and W. Nyer, Los Alamos report LA-1279 (1951) (unpublished).

rate in the presence of the bar divided by the counting rate produced by the direct neutron flux decreased as the setting of the pulse-height discriminator was increased. The discriminator bias was set high enough to keep the background below one percent. This setting corresponded to a proton recoil energy of about 10 Mev.

The neutron source strength was monitored both by counting associated α-particles from the d-T reaction and by a second scintillation neutron detector. No systematic differences between the two monitors were observed.

Total cross sections were measured by simple transmission experiments in good geometry. The samples were placed half-way between the source and detector. The thickness of the samples was chosen to give transmissions of about fifty percent. Most of the samples had a diameter of one inch. In this geometry the transmission experiment measures the total cross section except for neutrons scattered elastically (or inelastically with small energy loss) through angles less than about 2°. It is assumed that within this angle the neutrons scattered into the detector by the sample compensate those neutrons which are scattered out of the direct path from source to detector. If the scattering were isotropic, 0.02 percent of the scattered neutrons would hit the detector. The diffraction scattering will produce a forward maximum in the distribution of the elastically scattered neutrons which results for the heaviest nuclei in an intensity about seventy times larger than if the neutrons were scattered isotropically, so that the largest inscattering correction to be expected would be about 0.8 percent, assuming that elastic scattering constitutes one-half of all the interactions. A correction for inscattering of 0.13 σ_t percent was applied to the data, where σ_t is the measured total cross section in barns. This correction is based on a value of $k^2R^4/4$ for the differential scattering cross section in the forward direction[7] where k is the wave number of the incident neutrons and R the nuclear radius. Use of the value $(kR+1)^4/4k^2$, instead of $k^2R^4/4$, as indicated in a summary report by other authors,[8] would make the corrections for the heavy elements approximately a factor of two larger.

Whenever possible the samples were made of the pure element. In Table I the elements investigated are listed together with the form in which the element was used. Gas samples were contained in cylinders 40 in. long and $1\frac{5}{16}$-in. inner diameter of stainless steel of $\frac{1}{32}$-in. wall thickness. The inscattering corrections for these samples, although larger than for nongaseous samples of similar atomic weight, were still negligible.

RESULTS

In Table I the measured total cross sections corrected for background and scattering into the detector are

TABLE I. Total cross sections for 14-Mev neutrons.

Z	Element	A	Sample form	σ_t (barns)	Previous reports	Reference
1	H	1	Gas		0.686±0.007	4
					0.689±0.005	5
2	He	4	Gas		1.02 ±0.02	4
3	Li	6	Cast	1.39±0.05		
3	Li	7	M[a]	1.45±0.03		
4	Be	9	M	1.53±0.03	0.65 ±0.04	1
					1.41 ±0.11	3
5	B	10	Powder	1.47±0.03		
5	B	11	Powder	1.40±0.03	1.16 ±0.13	1
6	C	12	Graphite	1.32±0.02	1.23 ±0.02	1
					1.24 ±0.06	3
					1.279±0.004	5
					1.29 ±0.02	6
7	N	14	Gas	1.59±0.03	1.7 ±0.1	5
					1.39 ±0.05	6
8	O	16	Gas	1.59±0.03	1.64 ±0.04	5
					1.61 ±0.04	6
8	O	16	H_2O	1.56±0.04		
9	F	19	CF_4	1.70±0.05		
11	Na	23	Compacted	1.71±0.03		
12	Mg	24.3	M	1.75±0.03	1.83 ±0.10	1
13	Al	27	M	1.73±0.03	1.92 ±0.09	1
14	Si	28.1	Compacted	1.83±0.04		
14	Si	28.1	SiO_2	1.90±0.13		
15	P	31	Cast	1.97±0.04		
16	S	32.1	Cast	1.92±0.04	1.58 ±0.10	1
17	Cl	35.5	CCl_4	2.00±0.05		
19	K	39.1	Compacted	2.24±0.04		
20	Ca	40.1	Compacted	2.19±0.04		
22	Ti	47.9	M	2.28±0.04	2.24 ±0.29	3
24	Cr	52.0	Compacted	2.45±0.04		
25	Mn	54.9	Compacted	2.54±0.05		
26	Fe	55.9	M	2.60±0.05	2.75 ±0.09	1
27	Co	58.9	Compacted	2.72±0.05		
28	Ni	58.7	M	2.67±0.05	2.62 ±0.09	1
29	Cu	63.5	M	2.96±0.06	2.86 ±0.15	1
					2.85 ±0.05	6
30	Zn	65.4	Cast	3.06±0.06	3.03 ±0.17	1
31	Ga	69.7	Cast	3.19±0.06		
34	Se	79.2	Powder	3.56±0.07	3.35 ±0.20	1
35	Br	79.9	Liquid	3.52±0.07		
38	Sr	87.6	Compacted	3.68±0.07		
39	Y	88.9	Y_2O_3	3.88±0.14		
40	Zr	91.2	Compacted	4.00±0.08	2.37 ±0.35	3
41	Nb	93.3	Compacted	4.02±0.08		
42	Mo	96.0	M	4.04±0.08		
47	Ag	107.9	Cast	4.34±0.09	3.82 ±0.13	1
48	Cd	112.4	Cast	4.44±0.09	4.25 ±0.13	1
49	In	114.8	Cast	4.53±0.09		
50	Sn	118.7	Compacted	4.68±0.09	4.52 ±0.14	1
51	Sb	121.8	Compacted	4.71±0.09	4.35 ±0.15	1
52	Te	127.6	Compacted	4.85±0.10		
53	I	126.9	Compacted	4.74±0.10		
56	Ba	137.4	Compacted	5.17±0.10		
57	La	138.9	Compacted	5.18±0.10		
58	Ce	140.1	M	5.08±0.10		
59	Pr	140.9	M	4.93±0.25		
73	Ta	180.9	M	5.24±0.10		
74	W	183.9	M	5.30±0.11		
78	Pt	195.2	Cast	5.36±0.11		
79	Au	197.2	M	5.31±0.11	4.68 ±0.9	1
80	Hg	200.6	Liquid	5.36±0.11	5.64 ±0.24	1
81	Tl	204.4	Cast	5.36±0.11		
82	Pb	206	Cast	5.40±0.11		
82	Pb	207.2	M	5.48±0.11	5.05 ±0.15	1
					4.97 ±0.27	3
83	Bi	209.0	Cast	5.46±0.11	5.17 ±0.17	1
90	Th	232.1	M	5.69±0.11	6.11 ±0.33	3
92	U	238.1	M	5.87±0.12		

[a] M denotes samples which were machined from bulk metal. Most of the cast and compacted samples were also machined to accurate dimensions.

[7] G. Placzek and H. A. Bethe, Phys. Rev. **57**, 1075 (1940).

[8] Feld, Feshbach, Goldberger, Goldstein, and Weisskopf, Atomic Energy Commission report NYO-636 (1951).

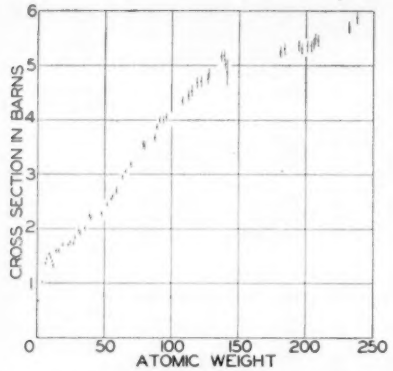

FIG. 1. The total cross sections of the elements for 14-Mev neutrons plotted against atomic weight.

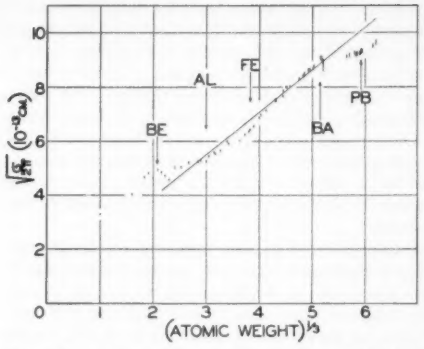

FIG. 2. Square root of the total cross sections divided by 2π plotted against the cube root of the atomic weight. The solid line represents the behavior predicted by the theory of Feshbach and Weisskopf under the assumption that the nuclear radius is given by $1.5\times A^{\frac{1}{3}}\times 10^{-13}$ cm.

tabulated, and in Fig. 1 the results are plotted against atomic weights. The statistical accuracy of the measurements is about one percent, except in the cases in which compounds were used and in the case of Pr where only a very thin sample was available. While precautions were taken to obtain samples of high purity and uniform density, errors introduced by the properties of the samples may be of the same order of magnitude as the statistical errors.

In the last two columns of Table I the results obtained previously by others are listed. While the agreement with the present data is within the experimental error in most cases, there are a few instances of rather large differences. These discrepancies may be due to the fact that some of the elements have only recently become available in pure form.

Feshbach and Weisskopf[9] have proposed a schematic theory of nuclear cross sections which should be applicable for neutrons of the energy used in the present experiment. According to this theory the square root of the total cross section should be approximately a linear function of the nuclear radius. To facilitate a comparison between the calculated and observed cross sections $(\sigma_t/2\pi)^{\frac{1}{2}}$ is plotted in Fig. 2 against the cube roots of the atomic weights, A. The solid line shown in Fig. 2 shows the dependence of the cross sections on nuclear radius calculated according to reference 9 with the assumption that the nuclear radius is related to the atomic weight by $R=1.5\times 10^{-13}\times A^{\frac{1}{3}}$ cm.

While the experimental points lie on a fairly smooth curve, systematic deviations from the calculated relationship between σ and A are apparent in Fig. 2. No appreciable improvement in the fit is obtained by changing the coefficient in the dependence of R on $A^{\frac{1}{3}}$. Deviations from the predicted curve might be expected for the lightest elements, since statistical theory is probably not applicable to them. Apart from the lightest elements the largest differences between calculated and observed cross sections occur for the elements above the rare earths.

There is no apparent effect of closed shells on the nuclear radius; for example, Tl, Pb^{206}, and Pb^{208} have within the experimental error the same total cross sections. This finding is at variance with the results of Lasday[3] and with the analysis by Curie[10] based on data taken at higher neutron energies.

It should perhaps not be surprising that the theory of Feshbach and Weisskopf does not give a precise quantitative fit to the experiments, since this theory is based on a rather special assumption about the radial dependence of the neutron wave function inside the nucleus. It would probably be possible to fit the data more quantitatively by a theory which has more adjustable parameters, as was done for example by Fernbach, Serber, and Taylor[11] to account for the experimental results at 90 Mev.

We are indebted to Professor F. H. Spedding for the loan of samples of yttrium oxide and praseodymium metal. We wish to thank Mr. L. K. Goodwin for help in preparing most of the samples and Dr. J. S. Wahl for building the detector.

[9] H. Feshbach and V. F. Weisskopf, Phys. Rev. **76**, 1550 (1949).

[10] D. Curie, J. phys. et radium **12**, 941 (1951).

[11] Fernbach, Serber, and Taylor, Phys. Rev. **75**, 1352 (1949).

The Ground-State Parity of N^{14}†

D. A. BROMLEY
University of Rochester, Rochester, New York
(Received June 16, 1952)

Four-Mev deuterons from the Rochester 27-inch cyclotron have been used to determine the angular distribution of the neutrons from the $C^{13}(d,n)N^{14}$ ground-state reaction for laboratory angles less than 45°. Similar measurements have been made on the $Be^{9}(d,n)B^{10}$ and $F^{19}(d,n)Ne^{20}$ ground-state reactions, primarily to confirm the applicability of the Butler stripping theory at this energy and with this particular experimental arrangement. Comparison of the experimental results with the predictions of the theory shows that there is a parity change in the $C^{13}(d,n)N^{14}$ and $Be^{9}(d,n)Ne^{20}$ reactions and no parity change in the $F^{19}(d,n)Ne^{20}$ reaction. Since the C^{14} and C^{13} ground states have been previously shown to have opposite parity, there can be no parity change in the C^{14} beta-decay.

I. INTRODUCTION

THE C^{14} beta-decay is one of the few cases which has not yet been reconciled with modern beta-decay theory. This spectrum has an apparently allowed shape[1] but the logft value for the transition[2] is 9.05, indicating a forbidden transition.

The spins of C^{14} and N^{14} have been measured[3,4] to be 0 and 1, respectively; hence, the spin change in the transition is known to be 1. Although the shell theories predict that both the C^{14} and N^{14} ground states should have even parity, several authors have suggested a parity change in the transition as a possible explanation for the anomalously long lifetime. If this were the case, the decay could be first forbidden, but with an allowed spectrum shape, for Fermi or Gamow-Teller selection rules.

A similar difficulty had once existed for the Be^{10} beta-decay, since a spin change of 1 and no parity change had been assumed for the transition. Under these conditions an allowed transition would be predicted, whereas the observed spectrum had a shape corresponding to a highly forbidden transition and a logft value[2] of 13.65 indicating a second or third forbidden transition. This difficulty was resolved when the spin change was measured to be 3.[5]

Since the spin change is known for the C^{14} beta-decay, it was considered of interest to determine whether or not a parity change occurs.

The study of the angular distributions of the neutrons and protons from the $C^{13}(d,n)N^{14}$ and $C^{13}(d,p)C^{14}$ ground-state reaction was chosen as a method for determining the N^{14} and C^{14} ground-state parities, since this made possible not only the determination of the relative parities but also the determination of these parities relative to that of C^{12}. In the remainder of this paper, unless otherwise specified, all reactions and parities will be those corresponding to the ground states of the nuclei in question. The parity of C^{12} will be assumed even. The spin of C^{13} has been measured[3] to be $\frac{1}{2}$ and a study of the angular distribution of the protons from the $C^{12}(d,p)C^{13}$ reaction[6] has shown that C^{12} and C^{13} have opposite parities. The values of the orbital angular momentum which could be transferred to the C^{13} nucleus by the absorbed nucleon were thus limited to 0, 1, and 2 units, and the experimental distributions had only to be compared with the three distributions predicted by the Butler theory[7] corresponding to these angular momentum transfers. The results of the $C^{12}(d,p)C^{14}$ experiment have been published previously,[8] and the experimental method will be described elsewhere.[9] The C^{14} parity was found to be opposite to that of C^{13}, hence even as expected. This paper will describe the $C^{13}(d,n)N^{14}$ experiment

When this research was begun, it seemed advisable to carry out an experiment to determine the angular distributions of neutrons from two different reactions, one of which would be expected to show a parity change and the other no parity change. The results of this experiment served to check the apparatus and method against the effects of wall-scattering and similar possible sources of error. They also confirmed the applicability of the Butler theory for the relatively low energy deuterons available. The $Be^{9}(d,n)B^{10}$ and $F^{19}(d,n)Ne^{20}$ reactions were chosen for this experiment on the basis of shell model predictions.

Thick targets were used to give adequate counting rates. Since the Q value for the $C^{12}(d,n)N^{13}$ reaction is -0.26 Mev and that for the $C^{13}(d,n)N^{14}$ reaction is 5.38 Mev,[10] it was simple to discriminate against the neutrons from the first reaction in the carbon target enriched to 53.7 percent in C^{13} (see Appendix I).

† Presented in part as a post-deadline paper at the Washington meeting of the American Physical Society, May 3, 1952. This work has been supported by the AEC.

[1] L. Feldman and C. S. Wu, Phys. Rev. **75**, 1286 (1949).
[2] A. M. Feingold, Revs. Modern Phys. **23**, 10 (1951).
[3] F. Jenkins, Phys. Rev. **73**, 639 (1948).
[4] Kusch, Millman, and Rabi, Phys. Rev. **55**, 1176 (1939).
[5] Gordy, Ring, and Burg, Phys. Rev. **74**, 1191 (1948).
[6] J. Rotblat, Proceedings of the International Conference on Nuclear Physics, Chicago, Sept. 17–22 (1951).
[7] S. T. Butler, Proc. Roy. Soc. (London) **A208**, 559 (1951).
[8] D. A. Bromley and L. M. Goldman, Phys. Rev. **86**, 790 (1952). In the caption for Fig. 1 of this letter, it was incorrectly stated that the value $l_p=2$ is excluded for both the $C^{13}(d,n)N^{14}$ and $C^{13}(d,p)C^{14}$ ground-state reactions.
[9] L. M. Goldman, Doctoral dissertation, to be submitted to the Physics Department, University of Rochester, August, 1952.
[10] Hornyak, Lauritsen, Morrison, and Fowler, Revs. Modern Phys. **22**, 291 (1950).

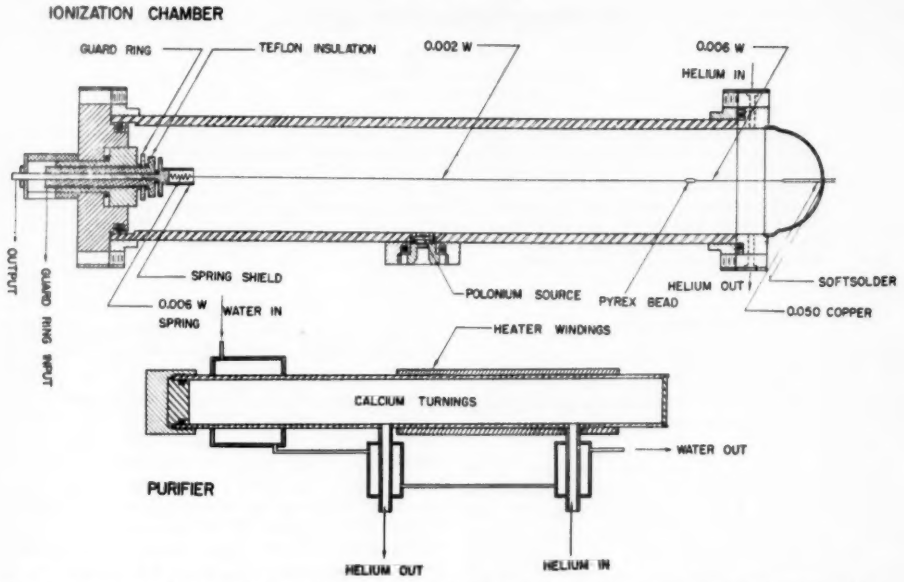

FIG. 1. The ionization chamber and hot calcium purifier. The filling valve and Bourdon pressure gauge which are mounted on the chamber are not shown.

II. EXPERIMENTAL METHOD

A high pressure ionization chamber was chosen as the neutron detector in preference to the more usual photographic plate because it combines the high detection efficiency of the photographic plate with the possibility of continuous checking and the much more rapid rate of obtaining data available with electronic equipment. Helium was used in the chamber rather than hydrogen, because of its greater atomic stopping power, although the maximum energy transfer from the neutrons was 64 percent instead of the 100 percent possible with hydrogen.

Figure 1 shows a section through the ionization chamber. The outer, stainless-steel cylinder is 2 inches in internal diameter and $\frac{3}{16}$-inch thick. The hemispherical copper cap on the front end of the chamber was made $\frac{1}{16}$-inch thick to minimize scattering and attenuation of the incident neutrons. A polonium alpha-source was mounted, as shown, for use in calibrating the system and for checking its operation.

When first assembled and filled to 20 atmospheres pressure with tank helium it was found that sufficient contaminants were present to prevent observation of the calibration alpha-pulses.

The helium was passed through a cold trap consisting of a spiral wound from 10 feet of $\frac{1}{8}$-inch copper tubing which was completely immersed in a Dewar flask of liquid nitrogen. Since sufficient contaminants remained to prevent energy resolution, a hot-calcium, convection-flow purifier was constructed, as shown in Fig. 1, and attached to the chamber. It was found that 6 to 8 hours treatment with the purifier removed all observable contaminants provided that the helium had been first passed through the cold trap. The purifier was operated continuously to avoid possible poisoning of the helium due to the gradual evolution of gases from the gaskets and walls of the chamber.

Figure 2 shows the experimental arrangement. The circular scattering chamber will be described in detail elsewhere.[9] The first and last collimator apertures were $\frac{3}{8}$ inch in diameter, and the antiscattering center aperture

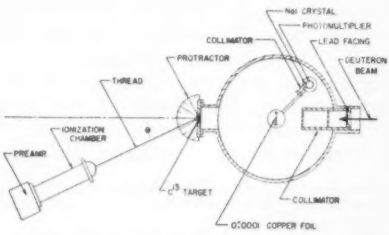

FIG. 2. The experimental arrangement. The scattering chamber is about 15 feet from the cyclotron at the end of the external focusing section. A common vacuum system is used for the cyclotron, exit section, and scattering chamber.

was 41/64 inches in diameter: The apertures were 2 inches apart. The collimated deuteron beam passed through a 0.0001-inch copper foil (1 mg/cm^2), mounted at the center of the scattering chamber and perpendicular to the beam, before strking the thick target. The scintillation counter, set at 132° to the beam direction, detected backscattered deuterons and served as a monitor. This was calibrated by replacing the target-holding plate with a Faraday cage connected to an integrating circuit and measuring the total charge required for a given number of monitor counts.

The targets (see Appendix I) were spring mounted in a well milled at the center of the chamber end plate. The bottom of the well was 0.035 inch thick; hence the neutron scattering and attenuation due to it was negligible.

The ionization chamber was mounted on a simple tripod stand and was moved in an arc of radius 36 inches centered on the target with its axis always pointing toward the target.

Figure 3 is a block diagram of the electronic equipment. All units, with the exception of the 30-channel pulse-height analyzer, are of standard design. The analyzer has been described elsewhere.[11] The rf power supply had degenerative regulation both on the input and output of the oscillator and was conveniently adjustable from 500 to 2000 volts. The internal power supply filter was supplemented by an *RC* external filter and an *LC* filter mounted directly on the ion chamber. The positive high voltage was applied to the guard ring, which was connected to the central wire through a 10-megohm resistor. The model 500 preamplifier was mounted directly on the chamber in a shield box. The clipping time of the amplifier was adjusted to 20 μsec and an *RC* filter inserted between the two loops of the amplifier set the rise time at 2.5 μsec.

The amplified photomultiplier output was connected to a second discriminator and scaler for use in monitoring the beam.

Before each run a pulse-height *versus* chamber voltage curve was obtained for the polonium alphas to check on the operating point of the system. A typical curve had a plateau extending from about 850 to 1150 volts, hence the operating voltage was set at 1000 volts. No appreciable change in the chamber characteristics was observed during the experiment.

Before and after each run, 15-minute calibration spectra were taken on the polonium alphas. Figure 4 shows typical spectra. The full curve was taken at the beginning of an eight-hour run and the dashed curve at the end. The increased background at low energies was assumed due to the build-up of neutron-induced beta-activity in the chamber. The longest half-life expected in this activity was that of the 12.9-hour beta-emitter Cu^{64}; rough measurements of the decrease of this activity were in agreement with this value.

[11] Fulbright, McCarthy, and McCutchen, Phys. Rev. **87**, 184 (1952).

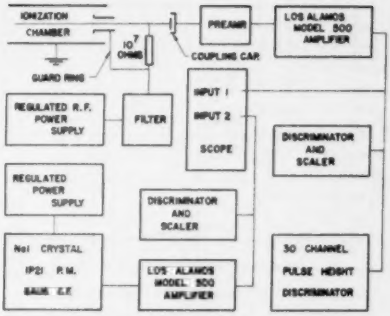

FIG. 3. Block diagram of the electronic equipment.

Since all the pulses of interest corresponded to at least 5 Mev, this activity caused no difficulty.

In any particular run the angle of observation was increased stepwise from 0° to 45° and then reduced stepwise to 0° to check on the internal consistency of the measurements. In all runs used this consistency was within the expected statistical errors. As a check on the angular symmetry of the system, measurements were

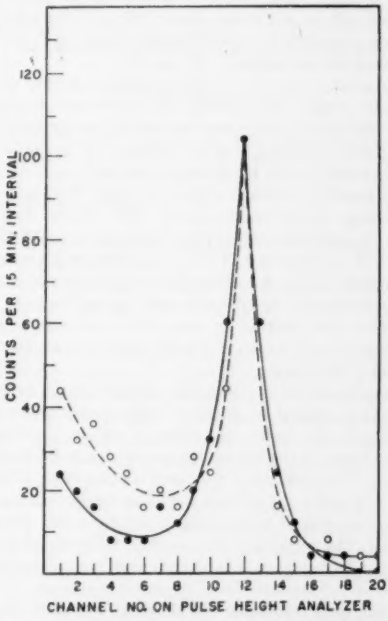

FIG. 4. Polonium alpha-pulse-height spectra. The zero of the distribution is at minus 6 channels. The solid line is the spectrum at the beginning of an 8-hour run; the dashed line is the spectrum at the end of the run.

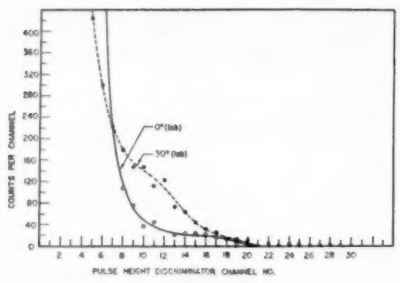

FIG. 5. $C^{13}(d,n)N^{14}$ pulse-height spectra.

made at equal angles on either side of 0°. These measurements also agree within statistical error.

At each angle the detector output was transformed into an energy spectrum by the pulse-height analyzer. A background run was carried out with only the target frame and tantalum backing foil in place. All data have been corrected for this background.

III. RESULTS

Four acceptable runs were taken on the $C^{13}(d,n)N^{14}$ reaction and three on each of $F^{19}(d,n)Ne^{20}$ and $Be^{9}(d,n)B^{10}$. Typical pulse-height spectra obtained with the pulse-height analyzer are shown in Fig. 5. Each of the runs corresponds to a total deuteron charge of 3.0×10^{-5} coulomb at each angle.

In order to identify the ground-state neutron group at each angle, the corresponding alpha-recoil energy was calculated. Since only the highest energy neutrons from each reaction were of interest the variation of alpha-energy with recoil angle was neglected. It was thus possible to select a range of pulse heights corresponding to the neutron group under study. For the N^{14}, neutrons were accepted in the range 7.0 to 9.0 Mev; for Ne^{20}, in the range 11.75 to 13.5 Mev, and for B^{10} in the range 7.75 to 8.5 Mev. The total number of counts between these energy levels was proportional to the relative cross section at each angle and was plotted against the corresponding angle to give the observed angular distribution.

Because of the finite angular aperture of the detector it was necessary to apply a small correction to this observed distribution in order to obtain the "true" distribution in the laboratory system. Since the detector was symmetrical about a vertical median plane a "line" in the angular distribution would be observed as a symmetrical peak of width roughly equal to the chamber width. The correction was assumed to be equal to the second derivative of the observed distribution multiplied by a factor estimated from the detector geometry.[12] The largest such correction (7.5 percent) was at 0° in the $F^{19}(d,n)Ne^{20}$ distribution. For all other points the correction was less than the statistical error.

[12] H. Primakoff and G. Owen, Phys. Rev. **74**, 1406 (1948).

All distributions were transformed to the center-of-mass system for comparison with the Butler theory. Figure 6 shows the $F^{19}(d,n)Ne^{20}$ and the $Be^{9}(d,n)B^{10}$ distributions. The angular distribution sfor the $C^{13}(d,n)N^{14}$ neutrons and the $C^{13}(d,p)C^{14}$ protons were normalized to the same peak height and are plotted together in Fig. 7 for comparison.

The predicted angular distributions of the neutrons in the center-of-mass system were calculated from Eq. (34) in Butler's paper.[7] The curves were calculated specifically for the $C^{13}(d,n)N^{14}$ reaction assuming a Q of 5.38 Mev and an r_0 of 4.3×10^{-13} cm.

These curves are qualitatively correct for the Be^{9} and F^{19} results. Figure 8 shows these curves normalized to the same peak heights as the experimental distributions.

Comparison of the $C^{13}(d,n)N^{14}$ experimental results with the predicted distributions indicates a parity change and an angular momentum transfer of one unit. Consequently, the parity of N^{14} is opposite to that of C^{13}, hence even.

Similar comparisons indicate a parity change in the

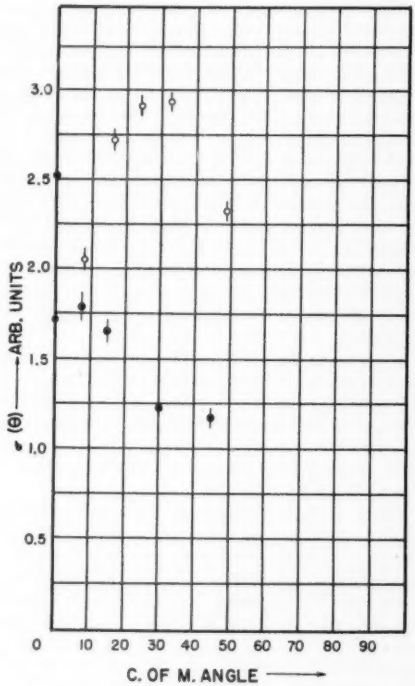

FIG. 6. The closed circles give the angular distribution of the neutrons from the $F^{19}(d,n)Ne^{20}$ ground-state reaction, and the open circles give the angular distribution of the neutrons from the $Be^{9}(d,n)B^{10}$ ground-state reaction (4-Mev deuterons).

$Be^9(d,n)B^{10}$ reaction and no parity change in the $F^{19}(d,n)Ne^{20}$ reaction. These latter results are considered as evidence supporting the validity of the N^{14} parity assignment. The forward maximum in the $F^{19}(d,n)Ne^{20}$ angular distribution is much less pronounced than that predicted. This may be due to the low deuteron energy and relatively higher Z. Ajzenberg has obtained a similar distribution for the $O^{16}(d,n)F^{17*}$ (536-kev level) transition using 3-Mev deuterons.[13]

IV. CONCLUSIONS

The B^{10} parity has been shown to be opposite to that of Be^9, in agreement with previous results.[14] The F^{19} parity has been shown to be the same as that of Ne^{20} and is therefore presumably even, in agreement with the predictions of the Mayer shell model.

The ground state of N^{14} has been shown to have even parity. This result is also in agreement with the predictions of the shell model.

Since the study of the $N^{14}(d,p)N^{15}$ reaction[15] has shown a parity change, this work shows that N^{15} has odd parity.

The agreement between the neutron and proton angular distribution in Fig. 7 indicates that for 4-Mev incident deuterons, the Coulomb effects on the angular distribution of the emitted nucleon are relatively unimportant. Finally, and most important, this agreement is conclusive evidence that there is no parity change in the C^{14} beta-decay.

The author wishes to express his gratitude to Professor H. W. Fulbright for suggesting the problem and for his very valuable advice and assistance. He also wishes to thank Mr. L. M. Goldman for his cooperation during the course of the experiment.

He is indebted to the National Research Council of Canada for the award of a Special Scholarship during the early stages of this work.

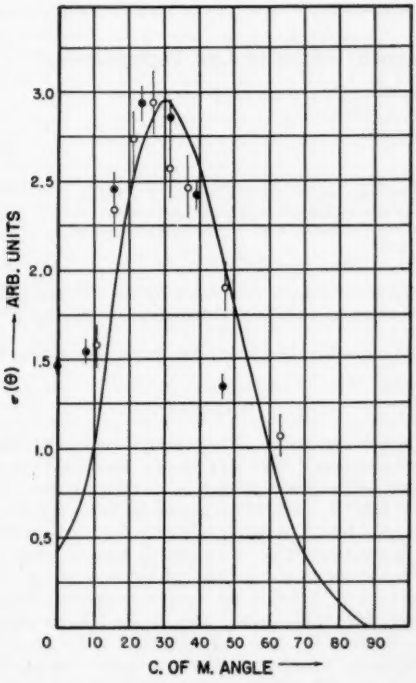

FIG. 7. The closed circles give the angular distribution of the neutrons from the $C^{13}(d,n)N^{14}$ ground-state reaction and the open circles give the angular distribution of the protons from the $C^{13}(d,p)C^{14}$ ground-state reaction, normalized to the same peak height. The theoretical curve $l_p=1$ (4.00 Mev) is included for comparison.

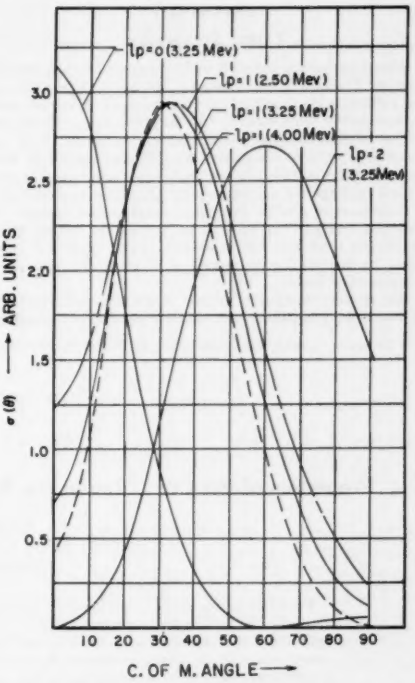

FIG. 8. Neutron angular distributions predicted by the Butler theory for the $C^{13}(d,n)N^{14}$ reaction. l_p is the angular momentum transferred to the target nucleus by the absorbed proton. The indicated energies are the laboratory energies of the deuterons used in the calculations. The Q value assumed was 5.38 Mev and r_0 was taken as 4.3×10^{-13} cm.

[13] F. Ajzenberg, Phys. Rev. **83**, 693 (1951).
[14] F. Ajzenberg, Phys. Rev. **87**, 205 (1952).
[15] J. Rotblat, as quoted by S. T. Butler (reference 7).

APPENDIX I

Target Preparation

Barium carbonate, enriched to 53.7 percent C^{13}, was obtained from the Eastman Kodak Company, Rochester, New York, and was reduced to the elemental form by means of a technique similar to that used by Anderson *et al.*[16] for the production of C^{14} samples.

The barium carbonate was doubly decomposed with lead chloride, to yield carbon dioxide, by prolonged heating at 360°C in a potassium nitrate and sodium nitrate bath. The fine magnesium turnings and cadmium metal catalyst were contained in a stainless steel reaction boat in a stainless steel furnace. The reduction reaction was initiated by flaming the furnace with a gas-oxygen torch and was completed, over a period of several hours, by maintaining the furnace at about 1000°C with an external electric heater.

The resultant mixture of carbon, magnesium oxide, and magnesium metal was treated with boiling concentrated hydrochloric acid, washed, and the filtrate was removed using a sintered glass filter and aspirator. This was repeated three times with concentrated hydrochloric acid and three more times with concentrated nitric acid. The carbon residue was evaporated to dryness, finely ground in an agate mortar, and weighed. An 80 percent recovery efficiency was found; the 20 percent loss was largely mechanical resulting from the difficulty in completely recovering the charge from the furnace and from the considerable handling which followed.

Tantalum foil of 0.003-inch thickness was used as a target backing because of its availability, high Z, and consequent low yield of neutrons from low energy deuteron bombardment. In preparing the C^{13} target it was found that if the fine carbon powder was made into a slurry with benzene and spread evenly on the tantalum, foil it did not crack or separate from the backing when the benzene was slowly removed by evaporation. This method was used to prepare a target of areal density 20 mg/cm². The Be^9 target consisted of a sheet of beryllium metal $\frac{1}{16}$-inch thick. The F^{19} target consisted of a 0.012-inch sheet of Teflon (CF_2).

[16] Anderson, Arnold, and Libby, Rev. Sci. Instr. **22**, 225 (1951(.

PHYSICAL REVIEW VOLUME 88, NUMBER 3 NOVEMBER 1, 1952

Properties of the Cr^{+++} Ion in the Paramagnetic Alums at Low Temperatures*

RALPH P. HUDSON
National Bureau of Standards, Washington, D. C.
(Received July 14, 1952)

Formulas for the entropy and magnetic moment as functions of temperature and magnetic field are derived for the paramagnetic chromic alums at liquid helium temperatures, taking into account the Stark splitting of the magnetic energy levels by the electric field of the crystal lattice. A comparison is made between values of the magnetic moment derived therefrom and the results of recent experimental work on paramagnetic saturation in potassium chromic alum by Henry.

I. INTRODUCTION

IN experiments on the magnetic properties of matter below 1°K it is often necessary to calculate the entropy of the paramagnetic salt as a function of external magnetic field at constant temperature, the adiabatic-demagnetization starting temperature. One makes use of the thermodynamic relation $(\partial S/\partial H)_T = (\partial M/\partial T)_H$, whence

$$S = S_0 - S_m = S_{0,T} - S_{H,T} = R\log_e(2J+1) + \int_0^H \left(\frac{\partial M}{\partial T}\right)_H dH, \quad (1)$$

and for M as a function of T and H it is customary to use the Brillouin formula,

$$M = NgJ\mu\left[\frac{2J+1}{2J}\coth\frac{2J+1}{2J}a - \frac{1}{2J}\coth\frac{a}{2J}\right], \quad (2)$$

where $a = gJ\mu H/kT$, the symbols having their usual meanings. Since the orbital quenching is practically complete in the magnetic alums at liquid helium temperatures, we have $J=S=3/2$ (for Cr^{+++}) and g has the value 2. Combining (1) and (2) we obtain, for Cr^{+++}

$$S/R = x\coth x - 4x\coth 4x + \log_e\sinh 4x - \log_e\sinh x, \quad (3)$$

where

$$x = \mu H/kT.$$

The fact that the ion, in zero field, is not in a $(2J+1)$-fold degenerate state but has its degeneracy partly lifted by the Stark splitting due to the crystalline electric field, is taken into account by correcting S_0 to $S_0 - S_e$. Here, S_e is simply related to the Stark splitting δ, if the temperature is sufficiently high to bring one into the region of the "tail" of the zero-field specific heat curve. Thus, in the case of potassium chromic alum $\delta/k \sim 0.25$ degree,[1] and if $T = 1$°K or higher $C_e/R = \frac{1}{4}(\delta/kT)^2$ and $-S_e/R = -\frac{1}{8}(\delta/kT)^2$. At 1°K, therefore, $-S_e/R = -0.00781$; actually, use of this approximation still introduces a small error, and exact calculation gives 0.00775.

Strictly speaking, however, the application of this correction is valid only up to quite small external fields, such that $\mu H \ll \delta$. In large fields, where $\mu H \gg \delta$, the effect of the Stark splitting is negligible and the

* Supported by the ONR, Contract NAonr 12-48.

[1] de Klerk, Steenland, and Gorter, Physica **15**, 649 (1949).

"Brillouin entropy curve" is correct to a high order of accuracy.[2]

In the following, the entropy in a magnetic field at 1°K is calculated taking into account the initial splitting δ and also the magnetic moment as a function of H and T. The latter is of interest in the light of recently reported small deviations from the Brillouin curve in potassium chromic alum, etc.[3]

II. ENERGY LEVELS

The energy levels of the Cr^{+++} ion as a function of magnetic field have been given by Broer:[4]

$$W^4+2\delta W^3+W^2(\delta^2-10\mu^2H^2)-2\delta\cdot W\mu^2H^2(7-6c)+9\mu^4H^4-\delta^2\mu^2H^2(4-3c)=0, \quad (4)$$

where $c=\cos^2\theta$ and θ is the angle between the direction of the field and the trigonal axis. The four Cr^{+++} ions in unit cell have different values of θ for an arbitrary direction of the magnetic field and Eq. (4) only has a simple solution for the case $c=1$. If H is applied along a trigonal axis (111), $c=1$ for one in four ions and $c=1/9$ for the other three; if the magnetic field is applied along a crystal cubic axis (100), $c=1/3$ for all ions. For $c\neq 1$, one can develop W in a power series for the two cases $\mu H\ll\delta$ and $\mu H\gg\delta$,[4] or graphical solutions may be obtained[5] by treating (4) as a quadratic in H^2.

It may be noticed, however, that with $c=1/3$ the pattern of energy levels is symmetrical about a line $W=-\delta/2=-\Delta$. By transferring to the origin $W=-\Delta$, $H=0$, we find

$$W^4-(2\Delta^2+10\mu^2H^2)W^2+\Delta^4-2\Delta^2\mu^2H^2+9\mu^4H^4=0, \quad (4a)$$

and the solutions are

$$W_{4,1}=\pm[\Delta^2+5\mu^2H^2+2\mu H(3\Delta^2+4\mu^2H^2)^{\frac{1}{2}}]^{\frac{1}{2}},$$
$$W_{3,2}=\pm[\Delta^2+5\mu^2H^2-2\mu H(3\Delta^2+4\mu^2H^2)^{\frac{1}{2}}]^{\frac{1}{2}}. \quad (5)$$

III. ENTROPY

We take $\delta/k=0.25°$, i.e., $\Delta/k=0.125°$, as derived from specific heat measurements, assuming that this is the unique value of δ (see below). Values of μH (in "degrees") may now be inserted in (5) and the partition function Z may be written down. Making use of the relation $S=Nk(\partial/\partial T)(T\log_e Z)$, we find

$$S/R=\log_e 2\left(\cosh\frac{W_4}{kT}+\cosh\frac{W_3}{kT}\right)-\frac{1}{kT}\frac{W_4\sinh(W_4/kT)+W_3\sinh(W_3/kT)}{\cosh(W_4/kT)+\cosh(W_3/kT)}. \quad (6)$$

Values of S/R have been calculated for $T=1°$K and μH varying between 0 and 1.5 "degrees" (0–22 kilogauss), and some of these are shown in Table I. The difference S_c/R between the "Brillouin entropy" $(S/R)_B$ and that calculated from (6) decreases steadily as a function of increasing magnetic field, or decreasing entropy. (Over the range of entropy $0.2<(S/R)_B<1.3$ the variation is represented quite closely by the relation

$$S_c/R=0.00574[(S/R)_B-0.046].$$

TABLE I. Entropy for $J=3/2$.

$\mu H/k$ degrees	Brillouin	This paper ($\delta/k=0.25°$)	Difference
0	1.3862_9	1.3785_4	0.0077_5
0.05	1.3800_7	1.3723_6	0.0077_1
0.10	1.3617_1	1.3441_1	0.0076_0
0.20	1.2926_6	1.2854_8	0.0071_8
0.40	1.0717_9	1.0659_2	0.0058_7
0.50	0.9475_4	0.9423_8	0.0051_6
1.00	0.4554_2	0.4530_7	0.0023_5
1.50	0.2081_8	0.2072_1	0.0009_7

IV. MAGNETIC MOMENT

Since we are here concerned with a differentiation of (5) with respect to H $[M=NkT(\partial/\partial H)(\log_e Z)]$, the rather complicated form of these expressions for the energy W_1, etc., results in a somewhat unwieldy final reltion for M as a function of H and T. It is

$$\frac{M}{N\mu}=\frac{\left[\frac{5\mu H+A+4\mu^2H^2/A}{W_4}\sinh\frac{W_4}{kT}+\frac{5\mu H-A-4\mu^2H^2/A}{W_3}\sinh\frac{W_3}{kT}\right]}{\cosh(W_4/kT)+\cosh(W_3/kT)}, \quad (7)$$

where $A=(3\Delta^2+4\mu^2H^2)^{\frac{1}{2}}$.

The labor of calculation is much reduced again, however, by choosing "simple" values of μH and also by making use of some of the computation already made in III.

In Table II we list corresponding values of $M/N\mu$ for the Brillouin treatment and for the above method, calculated for a temperature of 1°K. Since the modified formula (7) is not a simple function of H/T, we have also calculated $M/N\mu$ in a few cases for 2°K. It may be seen that the deviations from the Brillouin curve are very small, e.g., a maximum of -0.2 percent at $\mu H/kT=0.10$, and the deviations are considerably smaller for 2°K than for 1°K.

V. SUSCEPTIBILITY

For very small magnetic fields, such that $\mu H\ll kT$, the Brillouin formula reduces to an expression of

[2] Casimir, de Haas, and de Klerk, Physica **6**, 365 (1939).
[3] W. E. Henry, Phys. Rev. **85**, 487 (1952); Phys. Rev. **87**, 229 (1952).
[4] L. J. F. Broer, Physica **9**, 547 (1942).
[5] D. M. S. Bagguley and J. H. E. Griffiths, Proc. Roy. Soc. (London) **204**, 193 (1950).

TABLE II. Magnetic moment for $J=3/2$.

$\mu H/kT$ \ $M/N\mu$	Brillouin	This paper $T=1°K$	$(\delta/k=0.25°)$ $T=2°K$
0.05	0.2493_0	0.2487_8	0.2491_8
0.10	0.4944_2	0.4934_2	0.4941_6
0.20	0.9572_7	0.9553_9	0.9568_1
0.40	1.7080_7	1.7050_9	...
0.50	1.9853_1	1.9821_1	1.9845_0
1.00	2.6896_8	2.6868_1	...
1.50	2.8952_4	2.8932_4	...

Curie's law $\chi_0=M/H=a/T$, where a is the Curie constant. Specifically, $\chi_0=N\mu^2g^2J(J+1)/3kT$ and for $J=3/2$, $g=2$ we have $\chi_0=5N\mu^2/kT$. The effect of the crystalline field splitting δ is to cause deviations from the Curie law (unless $T\gg\delta/k$), and this has been studied in detail by Hebb and Purcell[6] for the temperature range below 1°K. Taking H to be of the order of a few oersteds or less and assuming $\delta\ll kT$, we may expand the hyperbolic functions in (7) and approximate to obtain the result

$$\chi_0\approx(5N\mu^2/kT)[1-\delta^2/30T^2]. \tag{8}$$

The same expression may be derived as a high temperature approximation of the pertinent Hebb and Purcell formula.

The expressions for the magnetic moment in the foregoing take no account of the magnetic coupling between ions which reinforces the aligning effect of the external magnetic field. Thus H (above) is to be taken as the field acting upon the ions and this may be derived from the external field by correcting for the interaction an 1 for the demagnetizing effect of the shape of the specimen.

VI. DISCUSSION

In measurements of the magnetic saturation curve of potassium chromic alum at liquid helium temperatures Henry[3] finds deviations from the Brillouin curve (up to three percent) over a wide range of H/T values. The experimental points lie below the Brillouin curve between $H/T=3000$ and about 16,000 gauss/degree (corresponding to $\mu H/kT$ values between 0.2 and 1.1), and the deviation apparently becomes greater as the temperature of measurement increases. Henry suggests that the cause of the deviations is the interaction of the crystalline electric field with the paramagnetic ions, but the aforementioned treatment indicates that the deviations to be expected from this cause are much smaller than are found experimentally; in any case, they should be smaller at higher temperatures, for a given value of H/T.

In deriving Eqs. (6) and (7) we have made the simplifying assumption of a unique value of δ, the crystalline-field Stark splitting of the ground state of the Cr^{+++} ion. In the potassium alum, however, paramagnetic resonance spectra[7] indicate that below 160°K two splittings of 0.27 cm^{-1} and 0.15 cm^{-1} (0.38 and 0.21 degree) are found, but no simple division of the ions into two groups each having one or other of these two possible splittings can explain both the shape of the tail of the specific heat curve and the spectrum intensities. The former might be accounted for by ascribing the smaller splitting to 85 percent of the ions, but the latter require roughly equal proportions.[7] Until this problem is resolved one can only seek the best approximation in the calculation of the magnetic moment by making the assumption of a single splitting, the value of which is derived from the specific heat measurements. [The variation of the calculated magnetic moment with δ may be demonstrated by using the formula derived above to find what would be the effect of all the ions having the larger splitting (0.38 degree), and it is found that even then the deviations would be quite small. Thus for 1°K and $\mu H/k=0.1$ and 0.5 degree, the corresponding values of $M/N\mu$ are 0.4886_8 and 1.9731_0, or deviations of, respectively, 1.2 percent and 0.6 percent from the corresponding points on the Brillouin curve.]

A much more desirable situation obtains in the case of the chromic alums of caesium, rubidium, and methylamine inasmuch as these alums exhibit only one splitting at low temperatures.[8] For these substances, Eqs. (6) and (7) would apply more rigorously and permit one to examine the corresponding experimental results more critically. (The experiments should be made preferably upon a single crystal and with the magnetic field along a cubic axis. In this case the energy level pattern is the same for all ions, and it is this case which is treated above.) There remain to be discussed, of course, the deviations from the "ideal curves" to be expected as a result of other interaction effects such as magnetic dipole-dipole and exchange (or "super exchange") coupling between the ions, although these effects are presumably very much smaller than that due to the action of the crystalline electric field, at the temperatures considered.

[6] M. H. Hebb and E. M. Purcell, J. Chem. Phys. **5**, 338 (1937).

[7] B. Bleaney, Proc. Roy. Soc. (London) **204**, 213 (1950).

[8] B. Bleaney, Proc. Roy. Soc. (London) **204**, 222 (1950).

Production of P^{33} with Thermal Neutrons

TORBJÖRN WESTERMARK
Division of Physical Chemistry, Royal Institute of Technology, Stockholm 70, Sweden
(Received June 23, 1952)

A soft beta-activity was found in old P^{32} samples from the Harwell reactor. It was established that it definitely is due to a P isotope, probably P^{33}, thus confirming the findings by Jensen and Sheline. The amount of P^{33} and P^{32} samples from a 14-day irradiation of sulfur has been found to 1.4±0.2 percent. The following data were found: half-life 25±2 days, maximum beta-energy 246±5 kev, number of gamma-rays at most 3.5 percent of the betas, cross section for the presumed $S^{33}(n,p)P^{33}$ reaction 0.03 barn. From energy considerations the latter reaction was found to be exothermic, whereas the reaction leading to P^{32} is endothermic, and this was supported by getting a P activity as rich as 30 percent in P^{33} by means of a purer thermal neutron flux. The cross section for the $S^{32}(n,p)P^{32}$ reaction for thermal neutrons was found to be 2.3×10^{-3} barn.

RECENTLY Jensen *et al.*[1] and Sheline *et al.*[2] announced the discovery of the radionuclide P^{33}. Similar work was at that time in progress in this laboratory, and later the work was extended and has yielded the following results: (1) confirmation of the physical data of P^{33} and its production with reactor neutrons; (2) a method of its production from sulfur in a purer state by means of thermal neutrons only; (3) a chemical proof that the activity is due to a phosphorus isotope. The most significant facts will be stated briefly here.

The half-life of a strong P^{32} sample (Harwell) showed (in 1950) too large a value, namely, 14.68±0.08 days (14.3 days was the accepted value[3]); but when aged for 15 months a soft beta-component, present as a negative ion inseparable from P^{32}, remained. This was taken as evidence for a P isotope, which was fully confirmed when the American publications appeared.[1,2] Our data confirmed the results of these authors quite well: The half-life was preliminarily found to be 25±2 days (Sheline[2]: 25±2 days; Jensen[1]: 24.8±0.5 days). The maximum beta-energy was found to be very close to that of Ca^{45}. An absorption comparison, however, using only the first 2/5 of the practical range, was made with S^{35} and Ca^{45}, yielding an energy of 246±5 kev for P^{33}; but it should be noted that this result presumes that the spectra are of very similar form and that the upper energy limit of Ca^{45} is 250 kev.[3] (Jensen's figure for P^{33} is 0.26±0.02 Mev; Sheline's is 0.26±0.01 Mev.) The activity found in aged reactor-produced P^{32} (Harwell) gave a figure of 1.4±0.2 percent P^{33} activity after a 14-day irradiation of the sulfur sample in the usual, central position of the reactor.[4] Taking the cross section for the $S^{32}(n,p)P^{32}$ reaction as 0.012 barn,[5] a cross section of 0.03 barn was found for the presumed reaction $S^{33}(n,p)P^{33}$ for this neutron energy distribution. The P^{33} content of old P^{32} samples (0–250 days) was found to increase with age according to the rate expected using the above-mentioned figures. The P^{33}/P^{32} ratio was determined using an absorption method (see Fig. 1).

No gamma-rays were detected in P^{33}, the experimental limit being that less than 3.5 percent gammas were present. (The figure was based on a calibration of the counter with Co^{60} 1.2-Mev gamma-rays.)

It was of interest to look for a method of producing pure P^{33} directly, instead of by aging P^{32} samples. As the Q-values of an (n,p) reaction is simply 750 kev minus the beta-energy of the product nuclide, the $S^{33}(n,p)P^{33}$ reaction is exothermic by about 500 kev. This suggested that P^{33} might be produced by means of thermal neutrons, and since the $S^{32}(n,p)P^{32}$ reaction is endothermic by about 900 kev the activity should be purer the better the fast neutrons are cut off. A sulfur sample was therefore irradiated for 14 days near the reflector in the Harwell reactor, where the thermal/fast ratio should be very high (the total flux being 5×10^{10} neutrons/cm² sec). The purified P-activity showed about 30 percent P^{33} (see Fig. 1), the rest being P^{32};

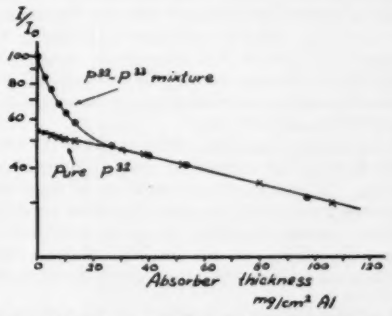

FIG. 1. Absorption curves taken with a 1.4-mg/cm² mica end-window counter, showing the presence of about 50 percent P^{33} (upper curve) in a sample obtained after irradiating sulfur with thermal neutrons. (The curve was taken 6 weeks after irradiation.) The lower curve represents almost pure P^{32}.

[1] Jensen, Nichols, Clement, and Pohm, Phys. Rev. 85, 112 (1952).
[2] Sheline, Holtzman, and Fan, Phys. Rev. 83, 919 (1951).
[3] *Nuclear Data*, National Bureau of Standards Circular 499 (1950).
[4] L. B. Emlet, Chem. Eng. Progress 46, 591 (1950); W. J. Arrol, AERE-I/R-748 (Harwell) (unpublished).

this is much higher than the 1.4 percent found in the center and supports the view that the reaction is exothermic. (The presence of P^{32} shows that a fast neutron flux is still present, of order 10^8 neutrons/cm^2 sec.) The specific activity calculated for sulfur is 0.1 μC/gram, giving a thermal cross section of only 2.3×10^{-3} barn for the $S^{33}(n,p)P^{33}$ reaction. This is about 7 percent of the cross section found for the neutrons in the center. It seems safe to assume that the fast neutron flux might be simply reduced by at least a factor of ten by means of moderating material, thus directly making P^{33} at least 90 percent pure. It is possible, moreover, to use a much higher neutron flux (e.g., in Chalk River), where the order of one millicurie P^{33} per kg sulfur might be produced.

The chemical identity proof for P^{33} involved dissolving of the sulfur in CS_2, filtering through a pile of filter papers (more than 60 percent of the P-activity was found on the first paper, whereas S^{35} went through), treating the paper with HNO_3 and a 0.1-mg phosphate carrier, lanthanum precipitation,[4] dissolving and cation-exchange processing,[4] and finally a molybdate precipitation. Absorption curves for samples from the filter paper, lanthanum precipitation, and the molybdate all showed the same P^{33}/P^{32} ratio within experimental error. The chemical steps should eliminate all cations and most of the anions, except possibly arsenate and silicate. Even if the latter is true, some separation would likely have been observed and, moreover, Si or As isotopes are not likely to be produced from sulfur, for physical reasons.

I thank Mr. J. L. Putman and the AERE, Harwell, for their kindness in performing the irradiation in the reactor.

PHYSICAL REVIEW VOLUME 88, NUMBER 3 NOVEMBER 1, 1952

Magnetic Analysis of the Proton Groups from the $Na^{23}(d,p)Na^{24}$ Reaction*†

A. SPERDUTO AND W. W. BUECHNER
Physics Department and Laboratory for Nuclear Science and Engineering, Massachusetts Institute of Technology, Cambridge, Massachusetts
(Received July 10, 1952)

Thin targets of sodium iodide evaporated onto platinum and thin nickel backings have been bombarded with deuterons accelerated to energies ranging from 1.5 to 2.2 Mev by the large M.I.T. air-insulated electrostatic generator. Proton groups emitted at 90 degrees to the incident deuterons were analyzed with a 180-degree magnetic spectrograph. Twenty of the observed proton groups are assigned to the $Na^{23}(d,p)Na^{24}$, Na^{24*} reaction and correspond with energy levels in Na^{24} up to 4.5 Mev. Several of the groups are closely spaced, and level spacings in Na^{24} as low as 17.0±3 kev have been observed.

I. INTRODUCTION

THE element sodium, atomic number 11, exists in nature as a single isotope of mass number 23. Thus, the protons emitted from the interaction of deuterons on sodium are associated with the formation of Na^{24} in various states of excitation according to the reaction $Na^{23}(d,p)Na^{24}$. Na^{24} subsequently decays with a half-life of 14.9 hours to Mg^{24} by emission of 1.390-Mev beta-particle, accompanied by two cascade gamma-rays of 2.758 and 1.380 Mev.[1]

At the present time, the determination of the lower energy levels in Na^{24} can best be made by either of two methods. The gamma-ray spectra observed from slow neutron capture in Na^{23} can give information regarding radiative transitions between the levels of the residual nucleus, according to the reaction $Na^{23}(n,\gamma)Na^{24}$. Although not uniquely fixing the positions of the excited levels, such gamma-ray measurements do provide confirmatory evidence for levels assigned from other nuclear reactions. Some recent measurements of gamma-transitions in Na^{24} by Kinsey and his collaborators are discussed later in this paper and are compared with the results obtained here. Measurement of the proton energies from the $Na^{23}(d,p)Na^{24}$ reaction, as done in the present work, yields more directly the energy levels of the residual nucleus.

A number of proton groups from the deuteron bombardment of sodium have been reported by other investigators. Lawrence,[2,3] using deuterons of 2.15 Mev, first observed two proton groups with Q-values of 4.92 and 1.72 Mev. Murrell and Smith,[4] using deuterons of 0.85 Mev, found four groups they attributed to $Na^{23}(d,p)Na^{24}$ with Q-values of 4.76, 4.58, 3.50, and 1.38 Mev. Recently, Whitehead and Heydenburg[5] have made a more

* A portion of this work was reported at the New York meeting of the American Physical Society, Phys. Rev. **82**, 304 (1951).

† This work has been supported by the joint program of the ONR and AEC.

[1] *Nuclear Data*, National Bureau of Standards Circular 499, 19 (1950).

[2] E. O. Lawrence, Phys. Rev. **47**, 17 (1935).

[3] M. S. Livingston and H. A. Bethe, Revs. Modern Phys. **9**, 245 (19437).

[4] E. B. Murrell and C. L. Smith, Proc. Roy. Soc. (London) **A173**, 410 (1939).

[5] W. D. Whitehead and N. P. Heydenburg, Phys. Rev. **79**, 99 (1950).

exhaustive investigation at deuteron bombarding energies of 2.0, 2.5, and 3.0 Mev. They report ten groups from the $Na^{23}(d,p)$ reaction. The arithmetic average of their Q-values at the three bombarding energies are listed in Table I.

II. EXPERIMENTAL METHOD

The large air-insulated Van de Graaff generator was used for accelerating deuterons up to 2.2 Mev. After magnetic deflection through 90 degrees, the beam was made to enter a gap in a 180-degree magnetic spectrograph and was focused on the target material, placed at 45 degrees to the direction of the incident deuterons and also at 45 degrees to the main gap of the spectrograph. Charged particles emitted at 90 degrees to the incident beam were thus deflected in the annular gap, and those particles with momentum corresponding to 180-degree deflection for a particular field setting were focused on nuclear emulsions (25-micron Eastman NTA plates) which were placed diametrically opposite to the target and at 30 degrees to the plane of the gap. Further details on the general technique, including experimental arrangement, interpretation of the data, corrections of the measurements, and over-all precision, have been discussed in recent publications.[6-8]

The magnetic spectrograph, since it is a momentum analyzer, will focus protons, deuterons, tritons, and alpha-particles of the same momentum at the same point. Distinction between the particles is then made by observing their ranges in the nuclear emulsion. When a thin target supported on a thick backing is bombarded with deuterons, a continuous distribution of deuterons scattered from the backing material is recorded in the emulsion, starting at the high energy side where the magnet field setting corresponds to the $H\rho$ of the deuterons elastically scattered from the target. The density of these tracks in the emulsion is so great as to make difficult the observation of other particles in this momentum range. For detecting protons in this region, we have generally resorted to a technique in which a sheet of aluminum foil is placed directly in front of the emulsions, the foil thickness being sufficient to stop the deuterons but thin enough for protons to penetrate it and enter the emulsion. An alternative technique is to use a sufficiently thin target backing so that the scattered deuterons obscure only a small region of the momentum spectrum. Although both of these methods have been employed in the present investigation, the results reported are based primarily on the measurements made from targets deposited onto thick supports.

A preliminary survey of the proton groups resulting from the $Na^{23}(d,p)Na^{24}$ reaction was made at a deuteron bombarding energy of 1.5 Mev. A rather thick target was made by depositing a drop of NaOH solution on a thick platinum backing. This made possible rapid survey of the approximate energies and relative yields of the various groups. Because of the deliquescent properties of NaOH, no attempt was made to prepare thinner targets of NaOH for the more exhaustive study. Instead, thin targets of approximately 5-kev thickness were prepared by evaporating NaI onto a 0.010-inch platinum sheet. Several targets were prepared at the same time in order to have available equivalent targets for repeated bombardments, thereby making possible yield comparisons among the various groups. It was found that the amount of NaI on the targets decreased during prolonged bombardment. Hence, the region of bombardment on a particular target was changed or a fresh target was used whenever the exposure exceeded a few microampere hours. This procedure also tended to minimize the effects of surface contaminations on the energy measurements, since it is observed that the thickness of surface layers, such as that from carbon, increases with bombardment time. For the observation of the low energy proton groups, targets prepared on 0.1-micron nickel foils[9] were also used in the region of $H\rho$ below 290 kilogauss-centimeters, but the results obtained were unsatisfactory for precision measurements. A broad proton distribution was usually observed even with the thinnest NaI layers. This effect would be expected if the NaI reacted with the nickel foil and caused the sodium to be distributed throughout the volume of the nickel. The protons emitted from the interaction of deuterons on sodium then would originate from within the volume as well as from the front surface of the nickel and, hence, give rise to the broad peaks observed. No attempt was made to evaporate other sodium salts onto the nickel foils.

TABLE I. Q-values for $Na^{23}(d,p)Na^{24}$ and energy levels in Na^{24}. Columns (a) and (d) = present investigation; Columns (b) and (e) = Whitehead and Heydenburg; Columns (c) and (f) = Kinsey, Bartholomew, and Walker.

Group	Relative intensity (±20 percent) E_d=2.0 Mev	Q-values (Mev) (a)	(b)	(c)	Energy levels in Na^{24} (d)	(e)	(f)
(0)	1.0	4.731±0.007	4.77	···	0	0	···
(1)	0.7	4.259±0.007	···	···	0.472±0.008	···	···
(2)	1.4	4.167±0.007	4.23	4.18±0.03	0.564±0.008	0.54	0.55±0.03
(3)	7.0	3.390±0.006	3.45	3.38±0.03	1.341±0.008	1.32	1.35±0.03
(4)	2.5	2.887±0.006	2.94	2.90±0.03	1.844±0.008	1.83	1.83±0.02
(5)	1.4	2.847±0.006	···	···	1.884±0.008	···	···
(6)	0.4	2.267±0.006	···	···	2.464±0.008	···	···
(7)	0.6	2.170±0.006	2.22	···	2.561±0.008	2.55	···
(8)	4.0	1.322±0.005	1.33	1.33±0.05	3.409±0.008	3.44	3.40±0.05
(9)	0.8	1.149±0.006	···	1.13±0.03	3.582±0.009	···	3.60±0.03
(10)	0.7	1.108±0.006	···	···	3.623±0.009	···	···
(11)	0.8	1.083±0.006	···	···	3.648±0.009	···	···
(12)	4.0	0.993±0.005	0.96	···	3.738±0.008	3.81	···
(13)	1.1	0.881±0.005	···	0.88±0.05	3.850±0.008	···	3.85±0.05
(14)	0.9	0.832±0.005	···	···	3.899±0.008	···	···
(15)	1.2	0.802±0.005	0.78	0.77±0.03	3.929±0.008	3.99	3.96±0.03
(16)	0.8	0.547±0.006	···	···	4.184±0.008	···	···
(17)	3.5	0.529±0.005	0.50	···	4.202±0.008	4.27	···
(18)	0.3	0.512±0.006	···	···	4.219±0.008	···	···
(19)	0.2	0.173±0.008	0.13	···	4.558±0.009	4.64	···

[6] Buechner, Strait, Stergiopoulos, and Sperduto, Phys. Rev. **74**, 1569 (1948).

[7] Buechner, Strait, Sperduto, and Malm, Phys. Rev. **76**, 1543 (1949).

[8] Strait, Van Patter, Buechner, and Sperduto, Phys. Rev. **81**, 747 (1951).

[9] S. Baskin and G. Goldhaber, Rev. Sci. Instr. **22**, 112 (1951).

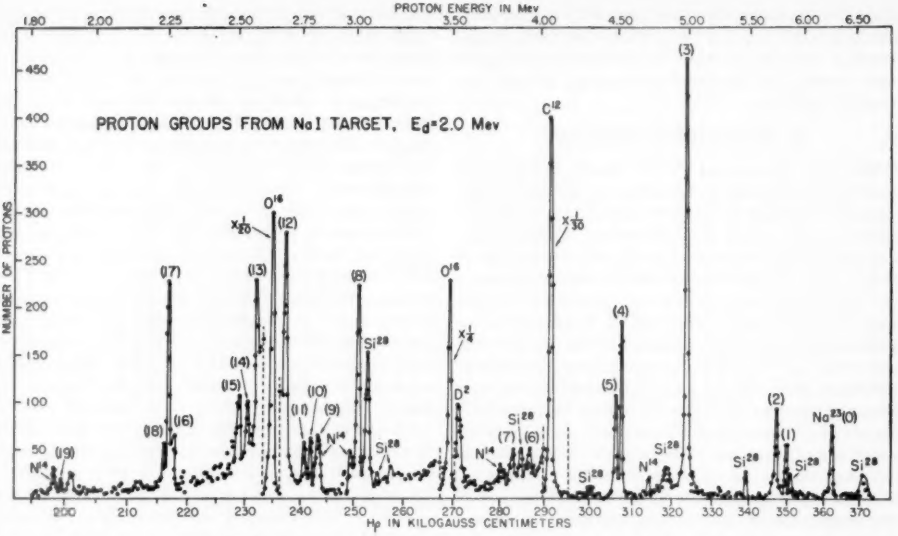

FIG. 1. Proton spectrum observed from deuteron bombardment of thin NaI targets evaporated onto platinum backings. Contamination groups are indicated by the chemical symbol of the target nucleus. Groups from sodium are numbered (0) through (19).

At a deuteron energy of 1.995 Mev, a complete survey was made by bombarding the thin NaI targets for various settings of the magnetic field in the spectrograph. These settings were such that the energy intervals recorded on successive plates overlapped so that a complete spectrum of the particle groups from these targets was obtained on fifteen plates, covering proton energies from 1.8 to 6.5 Mev.

A separate survey was made at a bombarding energy of 1.512 Mev. The observed shift in energy of the various groups was used to assist in the assignment of the groups to the target nuclei responsible. Also, in several instances, bombardments were made at 1.807, 2.105, and 2.214 Mev in the cases where particle groups were not completely resolved for definite identification at 1.995 Mev. The plates were given the same exposure from equivalent targets so that relative yields of the various groups could be estimated. The exposures were measured in terms of amount of charge collected by a fine mesh grid placed just ahead of the target. This charge was related directly to the number of deuterons impinging on the target. A microcoulomb integrating circuit[10] was used for this purpose, and a total of 1000 microcoulombs exposure was used for each plate at the 1.995-Mev run, the time of each exposure being of the order of 1 to 1½ hours. Although both proton and alpha-particle groups were observed, only the proton groups are reported here.

[10] H. A. Enge, Rev. Sci. Instr. (to be published).

II. RESULTS AND DISCUSSION

The complete spectrum of all the proton groups observed at the 1.995-Mev bombarding energy is shown in Fig. 1. The aluminum-foil technique mentioned previously was used in this case for the plates exposed between 195 and 290 kilogauss-centimeters. The peaks identified with reactions from contaminations on the targets are indicated by the chemical symbol of the contaminant nucleus; the peaks assigned to the $Na^{23}(d,p)Na^{24}$ reaction are indicated by the numbers starting with (0), the ground state, through (19), the nineteenth excited level in Na^{24}.

The evidence for assignment for each of the groups was based chiefly on two factors. First, the known contamination groups were identified both by comparing yield ratios of the groups from a particular contaminant observed in the present investigation with those observed in earlier work in this Laboratory from targets enriched in these contaminants and also by comparing the measured Q-values with those previously determined. Second, with the one exception of group (19), the remaining groups assigned to the $Na^{23}(d,p)Na^{24}$ reaction were all observed at least at one other bombarding energy. In each instance, the observed change in proton energy for a given change in deuteron energy was found in excellent agreement with the expected shift.

A total of twenty groups was attributed to various impurities on the target backing; namely, one from the $D^2(d,p)T^3$ reaction, apparently from incident deuterons reacting with other deuterons sticking in the target

backing, one from the $C^{12}(d,p)C^{13}$ reaction, two from the $O^{16}(d,p)O^{17}$ reaction, six from the $N^{14}(d,p)N^{15}$ reaction,[11] nine from the $Si^{28}(d,p)Si^{29}$ reaction,[12] and one from a contaminant group that was not identified. Some of the silicon peaks were found troublesome because of their proximity to two of the sodium peaks at the 2.0-Mev bombarding energy.

Many targets were rejected on the basis of having a high silicon contamination relative to the NaI layer. The criterion for acceptance of a target for use in making final measurements from the various groups was based on two factors. First, the sodium-iodide layer had to be sufficiently thin to resolve the close $Na(d,p)$ groups (4) and (5), and second, the silicon contaminant also had to be sufficiently low so that, at the 2.0-Mev bombarding energy, the sodium group (1) was resolved from the close silicon group. The latter separation, at 2.0-Mev bombardment, is 30.8±4 kev, while that of the groups (4) and (5) is 38.7±3 kev. The evidence for the existence of the two sodium groups (1) and (2) was first observed from a target with relatively high silicon content, where group (1) was not resolved from the silicon group and was thus at first attributed to the silicon. However, the presence of an irregularity observed in the shape of the proton-distribution curve gave evidence of the structure later observed from thin-target bombardment. Similar irregularities were also at first observed with groups (4) and (5) and with group (8) and the Si^{28} group at $H\rho$ of about 250 kilogauss-centimeters. Group (9) is broader than the other groups and bombardments at other deuteron energies have shown it consists of two nearly coincident groups, one of which is due to Na^{23} and the other to N^{14}.

The ground-state group (0) was observed at 1.5, 1.8, and 2.0 Mev. Several measurements from different targets gave Q-values agreeing to ±3 kev, the weighted average being 4.731±0.007 Mev. Groups (1) and (2) were also observed at bombarding energies of 1.5, 1.8, and 2.0 Mev, the first excited state observed in Na^{24} being 0.472±0.008 Mev above the ground state. The spacing between the levels corresponding to these two groups is 92.0±3 kev. The fourth group (3) attributed to the $Na(d,p)$ reaction is the most intense of the twenty sodium groups. With 2-Mev deuterons, this group is about 7 times more intense than the ground-state group and about 35 times more intense than the weakest group (19). The level spacing between groups (4) and (5) is 40.3±3 kev. Groups (6) and (7) are relatively weak groups superimposed on the background of protons from the $C^{12}(d,p)C^{13}$ reaction. At the 2.0-Mev bombarding energy, the yield of protons from C^{13} was more than 500 times the proton yield from either sodium group (6) or (7). Despite the presence of these C^{13} protons and the close proximity of Si^{29} and N^{14} groups, groups (6) and (7) were observed also at the 1.5- and 1.8-Mev bombardment. The level spacing between (6) and (7) is 97.1±4 kev.

Between groups (7) and (8), there is a level spacing of 848±8 kev, which is the largest gap in the energy range investigated. This region was also observed at other bombarding energies ranging from 1.5 to 2.2 Mev, so that the likelihood of a proton group from sodium coinciding with a contaminant group may be ruled out. The presence of the two weakest of the Si^{28} groups over the background of protons from O^{16} also indicates that even a fairly weak sodium group would have been detected within this energy range. Therefore, it is concluded that, for the region of excitation in Na^{24} between 2.56 and 3.41 Mev, there is no sodium group with a yield more than about 15 percent of the ground-state group.

In the region of $H\rho$ between 227 and 244 kilogauss-centimeters, there have been identified a total of seven proton groups which are assigned to levels in Na^{24} between 3.582 and 3.929 Mev in excitation, a total separation of only 347 kev. The three groups (9), (10), and (11) were observed at 1.8, 2.0, and 2.2 Mev. At the 2.0-Mev bombarding energy, group (9), which is also labeled N^{14} (Fig. 1), is not resolved from a $N^{14}(d,p)N^{15}$ group. The large half-width and asymmetrical distribution observed at this bombarding energy gave first evidence that this group was complex. It was found that the shape of this group depended on the bombarding energy. With 2.2-Mev deuterons, it separated into two groups, and from the changes in the peak shape with deuteron energy, the higher energy group was assigned to sodium, the Q-value being 1.149±0.006 Mev. That this was the case was confirmed by an exposure at 2.2 Mev on a target free of Na. The high energy group was not observed under these conditions, although the low energy group was seen. Both from the shifts in energy of the groups and the excellent agreement with previous measurements,[11] this low energy peak was assigned to N^{14}. The separation between the levels corresponding to groups (9) and (10) is 41.2±3 kev and is 24.8±3 kev between the levels corresponding to groups (10) and (11).

Groups (12), (13), (14), and (15) were observed at deuteron bombarding energies of 1.5, 1.8, 2.0, and 2.2 Mev. Here again, three of the four groups are observed

TABLE II. Energy-level spacings in Na^{24}.

Level interval (group numbers)	Level spacing (in kev)	Level intervals (group numbers)	Level spacing (in kev)
(0)–(1)	472 ±8	(10)–(11)	24.8±3
(1)–(2)	92 ±3	(11)–(12)	89.9±3
(2)–(3)	777 ±8	(12)–(13)	112 ±2
(3)–(4)	503 ±8	(13)–(14)	49.1±2
(4)–(5)	40.3±3	(14)–(15)	30.5±2
(5)–(6)	580 ±8	(15)–(16)	255 ±8
(6)–(7)	97.1±4	(16)–(17)	18.3±3
(7)–(8)	848 ±8	(17)–(18)	17 ±3
(8)–(9)	173 ±4	(18)–(19)	339 ±8
(9)–(10)	41.2±3		

[11] R. Malm and W. W. Buechner, Phys. Rev. **80**, 771 (1950).
[12] Endt, Van Patter, Buechner, and Sperduto, Phys. Rev. **83**, 491 (1951).

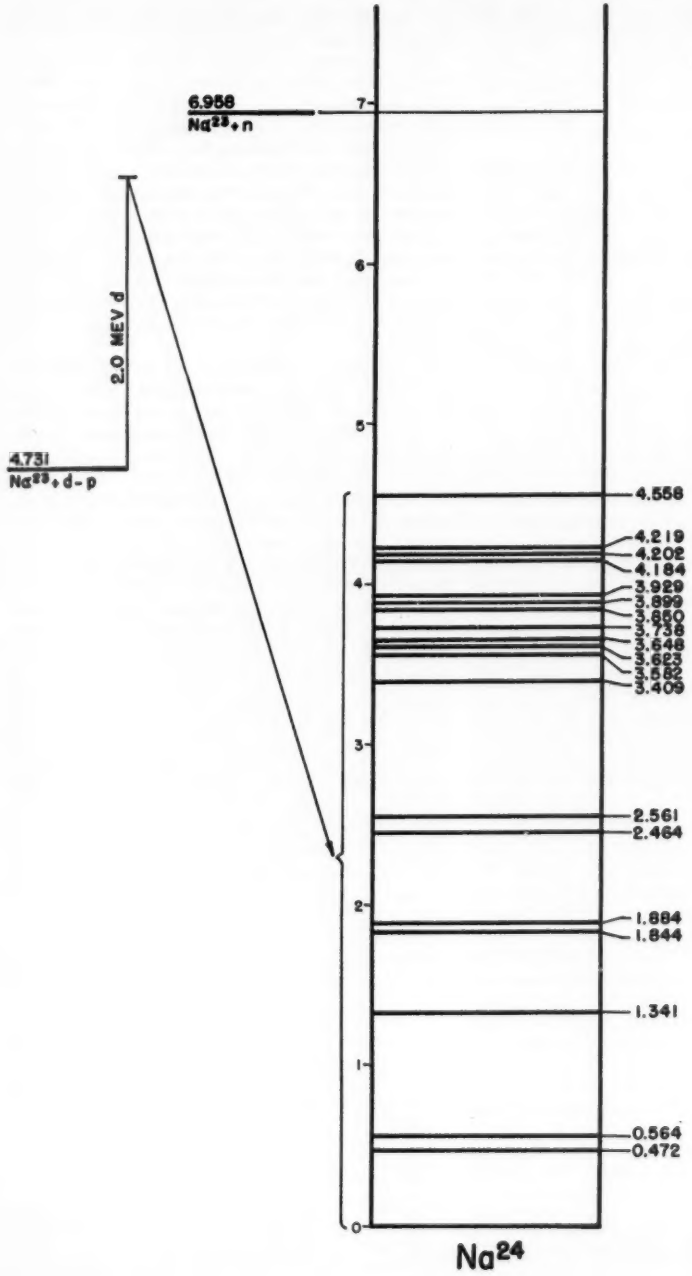

FIG. 2. Energy-level diagram for Na^{24}.

over the background of scattered protons from an $O^{16}(d,p)O^{17}$ group. The Q-values and level spacings are tabulated in Tables I and II.

Measurements on the remaining groups (16) through (19) were based on data from the 2.0-Mev bombardment only. In the region of group (17), several runs were made at 1.8-Mev bombardment with the nickel-foil targets, but because of the target difficulties mentioned earlier, the results were not suitable for precise measurement. Each of two measurements at the 2.0-Mev bombardment of the platinum-backed targets showed three closely spaced groups. Although the three groups were not completely resolved, appropriate adjustments in the peak shapes permitted sufficiently accurate measurements of the Q-values and level separations. The level spacings of 18.3 ± 3 kev and 17.0 ± 3 kev on the two sides of the main group are the closest spacings observed in the present investigation. Because no energy-shift measurement was made in connection with these groups, assignment to $Na^{23}(d,p)Na^{24}$ is based chiefly on the evidence that no common contaminant has been observed in this region at the 2.0-Mev bombardment.

Group (19) is reported here on the basis of a single measurement made at the 2.0-Mev deuteron bombarding energy. It is the weakest of the groups identified with the $Na^{23}(d,p)Na^{24}$ reaction, being of the order of 20 percent the intensity of the ground-state group. Group (19) has not been observed from other targets. The unidentified group to the right of group (19) is presumed to arise from a target contaminant. It has been observed from other targets bombarded in this laboratory, but no definite assignment has been made.

IV. CONCLUSIONS

In Table I, the results of this investigation are summarized and compared with the results of Whitehead and Heydenburg and those of Kinsey, Bartholomew, and Walker. In column 1 are listed the twenty individual groups observed in the present experiment. Column 2 lists the relative yields normalized to the ground-state group. The Q-values and probable errors tabulated in column (a) are the weighted averages of several measurements made at least at two different bombarding energies, except in the cases of groups (9), (16), (17), (18), and (19), as noted above. In column (b) are listed the Q-values obtained by Whitehead and Heydenburg from range measurements and for which no probable errors were given. The figures are the numerical averages of the values they reported at the three bombarding energies 2.0, 2.5, and 3.0 Mev, except for groups (15), (17), and (19), in which cases no values were reported for the 2.0-Mev bombardment. In column (c) are listed the Q-values as deduced by combining the binding energy of the deuteron[13,14] and the ground-state Q-value from the present investigation with certain gamma-ray transitions observed by Kinsey, Bartholomew, and Walker.[15] In columns (d), (e), and (f) are listed the resultant levels in Na^{24} as obtained from columns (a), (b), and (c), respectively.

As can be seen from Table I, there is reasonable agreement between the ten energy levels in Na^{24} found by Whitehead and Heydenburg and ten of the values measured in the present work. The additional ten levels found in this investigation are close to those previously measured and probably would not have been resolved by the range method employed in the earlier work.

In Table II are tabulated the level spacings between successive levels in Na^{24}, as determined from this investigation. In certain instances, it is noticed that the probable error is much less than that for the energy level indicated in column (d) of Table I. This is because the groups in question were observed on the same photographic plate where the major source of error in the level spacing arose from the measurement of the peak location.

In Fig. 2 is shown the energy-level scheme for Na^{24}, incorporating the results of the present investigation. The horizontal lines represent the excitation energies in Mev above the ground state.

We are happy to acknowledge the assistance of the various members of the High Voltage Laboratory during the course of this work. We are especially grateful to Mr. W. A. Tripp, Mrs. Cecilia Bryant, and Mrs. Clara Stucky for reading the photographic plates.

[13] R. C. Mobley and R. A. Laubenstein, Phys. Rev. **80**, 309 (1950).
[14] R. E. Bell and L. G. Elliott, Phys. Rev. **79**, 282 (1950).
[15] Kinsey, Bartholomew, and Walker, Phys. Rev. **83**, 519 (1951).

The Configuration Interaction between the Odd Terms in the Iron Group*

NORBERT ROSENZWEIG†
Department of Physics, Cornell University, Ithaca, New York
(Received July 7, 1952)

Using Racah's methods, the matrix components of the electrostatic interaction between the terms of the configurations $d^{n-2}sp$ and $d^{n-1}p$ are expressed as linear combinations of Slater integrals. The result consists of two parts. One part represents the interaction between the terms of the parent configurations. The second part results from the coupling of the p electron to the parent groups and contains the Slater integrals $R^2(sp,dp)$ and $R^1(sp,pd)$. The appropriate linear combinations of these integrals are formed by means on the coefficients of fractional parentage, the Racah coefficients, and a spin-dependent factor. A tabulation of coefficients sufficient for the construction of the matrix components for the entire iron group is given.

I. INTRODUCTION

THE principal lines observed in the spectra of the elements in the iron group arise from the combinations of the levels belonging to the deep even configurations $3d^{n-2}4s^2$, $3d^{n-1}4s$, $3d^n$ with the levels of the deep odd configurations $3d^{n-2}4s4p$ and $3d^{n-1}4p$. Analyses of many of these spectra have been carried out, and assignments of the spectroscopic levels have been made with respect to configuration, spin, and orbital and total angular momenta.[1]

However, whereas the identification of the angular momenta is rather reliable, the specification of the configuration is sometimes not. Under such circumstances it is desirable to settle doubtful assignments by means of theoretical calculations. A twofold attack on this problem is possible[2] namely, the calculation of energy levels and the calculation of line strengths.

This paper deals with the energy level problem[3] and more particularly with the matrix components of the electrostatic interaction which connect different configurations.

If the configurations are well separated, the matrix components of the configuration interaction (CI) are usually small compared to the difference between the diagonal elements which they connect. In such a case these matrix elements have no appreciable effect on the determination of the eigenvalues and they may be neglected. The configuration label then is a set of good quantum numbers to a high degree of accuracy. If, on the other hand, the configurations overlap, the matrix components of CI can frequently not be neglected. In this case the energy eigenfunction may contain more than one configuration to a considerable extent, so that the assignment of a term to only one configuration, if at all meaningful, is a rough approximation.

The configurations of the elements in the iron group overlap considerably. A theoretical study of their term values must therefore include a consideration of CI. The matrix components connecting the even configurations have been derived for d^3, d^2s, and ds^2 by Ufford[4] and for configurations containing many equivalent electrons by Racah.[5] Their results have been applied to specific spectra by various authors.[6]

It is desirable to make available also the matrix components connecting the odd configurations. Rohrlich[2] in his work on the classification of the odd terms of Ti I treated the CI to some extent by considering the interaction between the even parent configurations only. He found that the CI had an appreciable effect on the eigenvalues. Ishidzu and Obi[7] attribute at least partly to the CI, the disagreement between the calculated and observed values of several terms assigned to the configuration d^6p in the spectrum of Fe II. A study[8] of the odd terms of Fe I indicates that CI is even more important in this case than for Ti I or Fe II. This is not surprising in view of the almost complete overlapping of the configurations d^6sp and d^7p and the relatively small energy differences which separate the many like terms

In this paper we shall obtain the matrix components of the electrostatic interaction which connect the terms of $d^{n-2}sp$ and $d^{n-1}p$. As usual this means we shall express the interaction in the Russell-Saunders scheme in terms of the solutions of the central field problem, i.e., in terms of the Slater integrals R^k. The methods given by Racah[5,9] for dealing with many equivalent electrons will be employed. We refer to his papers for

* Based on Sec. V of the author's Ph.D. thesis, Cornell University, 1951, unpublished. Some of the work was carried out at the Argonne National Laboratory.

† Now at Argonne National Laboratory, Chicago, Illinois.

[1] *Atomic Energy Levels*, Vol. I, National Bureau of Standards Circular 467 (1949). Volume II to appear in the near future.

[2] See F. Rohrlich, Phys. Rev. **74**, 1381 (1948).

[3] We are concerned here with the traditional attack on the problem as described by E. U. Condon and W. Shortley, *Theory of Atomic Spectra* (Cambridge University Press, Cambridge, 1935). It consists of constructing the matrix of the electrostatic interaction in the Russell-Saunders scheme. The matrix elements are expressed in terms of the solutions of the approximating central field problem, i.e., in terms of Slater integrals. Extensions which make the theory applicable to configurations containing many equivalent electrons (e.g., filling of the d shill) have been made by G. Racah (see reference 5).

[4] C. W. Ufford, Phys. Rev. **44**, 732 (1933).

[5] G. Racah, Phys. Rev. **63**, 367 (1943), hereafter referred to as RIII.

[6] See, for example, C. W. Ufford (reference 4), Ti II and Zr II; A. Many, Phys. Rev. **70**, 511 (1946), Ti-I and -II, V-II and -III; A. A. Schweizer, Phys. Rev. **80**, 1080 (1950), V I and Cr II; R. E. Trees, Phys. Rev. **83**, 756 (1951), Mn II.

[7] T. Ishidzu and S. Obi, J. Phys. Soc. Japan **5**, 124 (1950).

[8] N. Rosenzweig, thesis, Cornell, 1951, unpublished.

[9] G. Racah, Phys. Rev. **62**, 438 (1942), referred to as RII.

an exposition of the underlying theory as well as for definitions and notation.

II. THE ELECTROSTATIC INTERACTION BETWEEN $d^{n-2}sp$ AND $d^{n-1}p$

In order to be able to distinguish all the observed terms in the configurations $d^{n-1}p$ and $d^{n-2}sp$, the Russell-Saunders scheme must include not only S and L, the spin and orbital angular momenta of the entire configuration, but also the following quantum numbers: $\alpha_1 S_1 L_1$ representing respectively the seniority number, spin, and orbital angular momenta of the d^{n-2} group; S_2 spin of the parent $d^{n-2}s$; and $\alpha_3 S_3 L_3$ of the parent d^{n-1}. The matrix elements which are of direct interest are the following:

$$\left[d^{n-2}(\alpha_1 S_1 L_1)sS_2 L_1 pSL\left|\sum_{i<j}^{n}\frac{e^2}{r_{ij}}\right|d^{n-1}\alpha_3 S_3 L_3 pSL\right]. \quad (1)$$

However, to begin with, we shall consider the somewhat more general configurations $l^{n-2}l'l''$ and $l^{n-1}l''$. The identification of l, l', and l'' with d, s, and p electrons will not be made until this specialization results in a simplification. Thus, we wish to express

$$C=\left[l^{n-2}(\alpha_1 S_1 L_1)l'S_2 L_2 l''SL\left|\sum_{i<j}^{n}\frac{e^2}{r_{ij}}\right|l^{n-1}\alpha_3 S_3 L_3 l''SL\right] \quad (2)$$

in terms of Slater integrals. This can be accomplished because we know, as a result of Racah's work, how to expand the antisymmetric eigenfunctions in the above scheme in terms of one-electron eigenfunctions. The reduction of (2) will, in fact, consist largely of exhibiting explicitly (but only to the extent necessary) the construction of the eigenfunctions and the application of orthogonality conditions.

The following expanded forms of the eigenfunctions will be used:

(A) Explicit antisymmetrization with respect to a particular inequivalent electron.

$$\Psi[l^{n-1}\alpha_3 S_3 L_3 l''SL]=n^{-\frac{1}{2}}\sum_{q=1}^{n}(-1)^Q\Psi[l^{n-1}\alpha_3 S_3 L_3 l_q''SL].$$

Q is the parity of the permutation which exchanges q with n.

(B) Addition of two angular momenta.

$$\psi[l^{n-1}\alpha_3 S_3 L_3 l_q''SL]$$
$$=\sum_{MS_2ML_2}\sum_{m_s''m_l''}\psi[l^{n-1}\alpha_3 S_3 L_3 M_{S_1}M_{L_1}]\Phi[n''l_q''m_{l''}m_{s''}]$$
$$\times[MS_2ML_2m_{s''}m_{l''}|M_SM_LSL].$$

The coefficients of the transformation are well known. We shall need only the general properties of the unitary transformation.

(C) Expansion in terms of fractional parentage.

$$\psi[l^{n-1}\alpha_3 S_3 L_3]=\sum_{\alpha_3' S_3' L_3'}\psi[l^{n-2}\alpha_3' S_3' L_3' l_{n-1}S_3 L_3]$$
$$\times[l^{n-2}\alpha_3' S_3' L_3' lS_3 L_3|l^{n-1}\alpha_3 S_3 L_3].$$

The coefficients in this expansion are the coefficients of fractional parentage as introduced by Racah in RIII. It should be noted that the equivalent l electron which is added to the parent angular momenta in the manner (B) is numbered $n-1$. However, the linear combination is determined in such a way as to make it antisymmetric in all pairs of coordinates.

(D) Transformation between two schemes of coupling three angular momenta.

$$\psi[l^{n-1}\alpha_3' S_3' L_3' l_{n-1}(S_3 L_3)l_q''SL]$$
$$=\sum_{S_4 L_4}\psi[l^{n-1}\alpha_3' S_3' L_3' l_{n-1}l_q''(S_4 L_4)SL]$$
$$\times[S_3' L_3' l l''(S_4 L_4)SL|S_3' L_3' l(S_3 L_3)l''SL].$$

The coefficients of the transformation have been given by Racah in RIII in terms of his W function and are called the Racah coefficients.

Naturally, the eigenfunction

$$\psi[l^{n-2}\alpha_1 S_1 L_1 l'(S_2 L_2)l''SL]$$

can also be expanded in the various forms described above. We are now ready to proceed with the reduction of the matrix component (2). In view of the symmetry of the operator and the antisymmetry of the states, we may write

$$C=\tfrac{1}{2}n(n-1)\left[l^{n-2}\alpha_1 S_1 L_1 l'S_2 L_2 l''SL\left|\frac{e^2}{r_{n,n-1}}\right|l^{n-1}\alpha_3 S_3 L_3 l''SL\right]. \quad (3)$$

Indicating explicitly the antisymmetrization with respect to the l'' electron in the manner (A), we have

$$C=\tfrac{1}{2}(n-1)\sum_{p,q}(-1)^{p+q}\left[l^{n-2}\alpha_1 S_1 L_1 l'(S_2 L_2)l_p''SL\left|\frac{e^2}{r_{n,n-1}}\right|l^{n-1}\alpha_3 S_3 L_3 l_q''SL\right]. \quad (4)$$

The expression (4) is a sum of n^2 terms, an advantageous grouping of which is the following:

(a) C': $p=n-1, n$; $q=1, 2\cdots n-2$
and $p=1, 2\cdots n-2$; $q=n-1, n$.
(b) C'': $p=1, 2\cdots n-2$; $q=1, 2\cdots n-2$.
(c) C''': $p=n-1, n$; $q=n-1, n$
and $C=C'+C''+C'''$. (5)

Let us consider one part at a time.

(a) In each term of C' one and only one of l_p'' and l_q'' has the same coordinate as the operator; the other one is orthogonal to the parent eigenfunction. Therefore, each term of C' vanishes.

(b) The coordinates of both l_p'' and l_q'' differ from those of the operator in every term of C''. Therefore, the terms of C'' vanish unless $p=q$. It should be noted that

$$(-1)^{P+Q}=1$$

for every term. There are $n-2$ nonvanishing terms, all of which have the same value. Thus,

$$C''=\tfrac{1}{2}(n-1)(n-2)\left[l^{n-2}\alpha_1 S_1L_1l'S_2L_2l_1''SL \times\left|\frac{e^2}{r_{n,\,n-1}}\right|l^{n-1}\alpha_3S_3L_3l_1''SL\right]. \quad (6)$$

This expression can be simplified by considering the coupling of the electron to its parent angular momenta in the manner (B). Thus,

$$\begin{aligned}C''=\tfrac{1}{2}(n-1)(n-2)&\sum_{MS_1ML_1}\sum_{m'l'm's'}\sum_{MS_2ML_2}\sum_{m_1''m_s''}\\ &\times\Phi[l_1''m_{l''}'m_{s''}'][M_SM_LSL\,|\,m_{l''}'m_{s''}'MS_2ML_2]\\ &\times\left[l^{n-2}\alpha_1S_1L_1l'S_2L_2MS_2ML_2\right.\\ &\times\left.\left|\frac{e^2}{r_{n,\,n-1}}\right|l^{n-1}\alpha_3S_3L_3MS_3ML_3\right]\\ &\times[MS_2ML_3m_{s''}m_{l''}\,|\,M_SM_LSL]\Phi[l_1''m_{l''}m_{s''}]. \quad (7)\end{aligned}$$

However, the matrix element of the electrostatic interaction is diagonal with respect to $S_2L_2MS_2ML_2$, and its value is independent of MS_2ML_2. Hence, the matrix element can be taken outside the summation sign. The summation gives unity. Also, we may make the replacement

$$\tfrac{1}{2}(n-1)(n-2)\frac{e^2}{r_{n,\,n-1}}\rightarrow\sum_{i<j}^{n-1}\frac{e^2}{r_{ij}}.$$

The result of these considerations is

$$C''=\left[l^{n-2}\alpha_1S_1L_1l'S_2L_2\left|\sum_{i<j}^{n-1}\frac{e^2}{r_{ij}}\right|l^{n-1}\alpha_3S_2L_2\right]\times\delta(S_2S_3)\delta(L_2L_3). \quad (8)$$

Thus, C'' is precisely the matrix component of the electrostatic interaction between the parent configurations. The reduction of (8) for the configurations $d^{n-2}s$, d^{n-1} is dealt with in RIII. All of these matrix components can be expressed in terms of the single radial integral $R^2(dd,ds)$. The coefficients needed for the left side of the periodic table are tabulated in RIII.

In the next section we shall extend these results to the right side of the periodic table. Let us now turn our attention to C'''.

(c) We shall subdivide C''' into two parts as follows:

$$\begin{aligned}&C_1''':\ p=n,\ q=n;\ p=n-1,\ q=n-1;\\ &C_2''':\ p=n,\ q=n-1;\ p=n-1,\ q=n;\\ &C'''=C_1'''+C_2'''.\end{aligned}$$

Inspection of (4) shows that the two terms comprising C_1''' are equal, and so are the two terms making up C_2'''. However, C_1''' and C_2''' differ in several important respects, as we shall see. We study C_1''' first. Since $(-1)^{P+Q}=1$, we have

$$C_1'''=(n-1)\left[l^{n-2}\alpha_1S_1L_1l'S_2L_2l_n''SL\times\left|\frac{e^2}{r_{n,\,n-1}}\right|l^{n-1}\alpha_3S_3L_3l_n''SL\right]. \quad (9)$$

Considering the antisymmetrization of the inequivalent electron l' in the manner (A) and its orthogonality to the eigenfunction on the right leads to

$$C_1'''=(n-1)^{\frac{1}{2}}\left[l^{n-2}\alpha_1S_1L_1l_{n-1}'S_2L_2l_n''SL\times\left|\frac{e^2}{r_{n,\,n-1}}\right|l^{n-1}\alpha_3S_3L_3l_n''SL\right]. \quad (10)$$

We progress in the reduction of (10) by expanding the left eigenfunction in the scheme in which the resultant angular momenta of l_{n-1}' and l_n'' are coupled to the angular momenta of the group of equivalent electrons [see Sec. (D)]. The right eigenfunction can be treated in the same way after it has been expanded in terms of fractional parents [see Sec. (C)]. Thus,

$$\begin{aligned}C_1'''=\sum_{S_4L_4}\sum_{S_5L_5}\sum_{\alpha_3'S_3'L_3'}&[S_1L_1l'(S_2L_2)l''SL\,|\,S_1L_1l'l''(S_4L_4)SL]\\ &\times(n-1)^{\frac{1}{2}}\left[l^{n-2}\alpha_1S_1L_1l_{n-1}'l_n''(S_4L_4)SL\right.\\ &\left.\left|\frac{e^2}{r_{n,\,n-1}}\right|l^{n-2}\alpha_3'S_3'L_3'l_{n-1}l_n''(S_5L_5)SL\right]\\ &\times[l^{n-2}\alpha_3'S_3'L_3'lS_3L_3]l^{n-1}\alpha_3S_3L_3]\\ &\times[S_3'L_3'll''(S_5L_5)SL\,|\,S_3'L_3'l(S_3L_3)l''SL]. \quad (11)\end{aligned}$$

Next, we observe that the matrix element occurring in (11) is equal to

$$\left[l_1'l_2''S_4L_4\left|\frac{e^2}{r_{12}}\right|l_1l_2''S_4L_4\right]\times\delta(\alpha_1S_1L_1;\alpha_3'S_3'L_3')\delta(S_4L_4;S_5L_5). \quad (12)$$

Thus, we obtain

$$C_1''' = (n-1)^{\frac{1}{2}}[l^{n-2}\alpha_1 S_1 L_1 l S_3 L_3 \| l^{n-1}\alpha_2 S_2 L_2]$$
$$\times \sum_{S_4 L_4} [S_1 L_1 l'(S_2 L_2) l'' SL | S_1 L_1 l' l''(S_4 L_4) SL]$$
$$\times \left[l_1' l_2'' S_4 L_4 \left| \frac{e^2}{r_{12}} \right| l_1 l_2'' S_4 L_4 \right]$$
$$\times [S_1 L_1 l l''(S_4 L_4) SL | S_1 L_1 l (S_3 L_3) l'' SL]. \quad (13)$$

It should be noted that the matrix element in expression (13) is actually independent of S_4; it has the same value for singlet and triplet states.

Next we will identify $ll'l''$ with dsp electrons and thereby achieve a considerable simplification of (13) because $L_1 = L_2$ and L_4 can be a P state only. Thus,

$$[L_1 s(L_1) pL | L_1 s p(P) L] = 1.$$

The sum over S_4 amounts to

$$\sum_{S_4} [S_1 \tfrac{1}{2}(S_2) \tfrac{1}{2} S | S_1 \tfrac{1}{2} \tfrac{1}{2}(S_4) S]$$
$$\times [S_1 \tfrac{1}{2} \tfrac{1}{2}(S_4) S | S_1 \tfrac{1}{2}(S_3) \tfrac{1}{2} S] = \delta(S_2 S_3), \quad (14)$$

in accordance with the general property of unitary transformations. Therefore, we have

$$C_1''' = (n-1)^{\frac{1}{2}}[d^{n-2}\alpha_1 S_1 L_1 d S_3 L_3 \| d^{n-1}\alpha_2 S_2 L_2]$$
$$\times [L_1 d p(P) L | L_1 d(L_2) p L] \delta(S_2 S_3) R_d \quad (15)$$

in which we have put

$$R_d = \left[s_1 p_2 P \left| \frac{e^2}{r_{12}} \right| d_1 p_2 P \right]. \quad (15')$$

By the use of Racah's tensor calculus R_d can readily be expressed in terms of Slater integrals. The result, obtained in Appendix I, is

$$R_d = -(\sqrt{2}/5) R^2(s p_1 d p). \quad (16)$$

Next we must consider C_2'''. Since $(-1)^{P+Q} = -1$, we have

$$C_2''' = -(n-1)^{\frac{1}{2}} \left[l^{n-2}\alpha_1 S_1 L_1 l' S_2 L_2 \| l_n'' SL \right.$$
$$\left. \times \left| \frac{e^2}{r_{n,\,n-1}} \right| l^{n-1}\alpha_2 S_2 L_2 \| l_{n-1}'' SL \right]. \quad (16')$$

This is treated in the same way as expression (9) for C_1''' and leads to an expression corresponding to (13), *viz.*,

$$C_2''' = -(n-1)^{\frac{1}{2}}[l^{n-2}\alpha_1 S_1 L_1 l S_3 L_3 \| l^{n-1}\alpha_2 S_2 L_2]$$
$$\times \sum_{S_4 L_4} [S_1 L_1 l'(S_2 L_2) l'' SL | S_1 L_1 l' l''(S_4 L_4) SL]$$
$$\times \left[l_1' l_2'' S_4 L_4 \left| \frac{e^2}{r_{12}} \right| l_2 l_1'' S_4 L_4 \right]$$
$$\times [S_1 L_1 l l''(S_4 L_4) SL | S_1 L_1 l (S_3 L_3) l'' SL]. \quad (17)$$

TABLE I. $[d^2 \alpha' S' L' {}_1 SL | {}^2/_{r_{ij}} | d^2 \Sigma e^2 \alpha SL]$.

$d^2{}_2$	d^2	H_2
$(^3P)^3P$	^3P	$-(210)^{\frac{1}{2}}$
$(^1P)^3P$	^3P	0
$(^1D)^1D$	^1D	$-(35)^{\frac{1}{2}}$
$(^3D)^1D$	^3D	$3(15)^{\frac{1}{2}}$
$(^3F)^3F$	^3F	$2(15)^{\frac{1}{2}}$
$(^1F)^3F$	^3F	0
$(^3G)^1G$	^1G	-10

TABLE II. $[d^3 \alpha' S' L' {}_2 SL | \Sigma e^2/r_{ij} | d^3 \alpha SL]$.

$d^3{}_2$	d^3	H_3	$d^3{}_2$	d^3	H_3
$(^3P)^3P$	^3P	$(105)^{\frac{1}{2}}$	$(^1F)^3F$	^3F	$(15/2)(2)^{\frac{1}{2}}$
$(^3P)^3P$	^3P	$-(30)^{\frac{1}{2}}$	$(^3F)^3F$	^3F	$-(30)^{\frac{1}{2}}$
$(^3P)^1P$	^1P	0	$(^3F)^3F$	^3F	$(3/2)(30)^{\frac{1}{2}}$
$(^3P)^5P$	^5P	$-(210)^{\frac{1}{2}}$	$(^3F)^5F$	^5F	0
$(^1D)^3D$	^3D	$(1/2)(210)^{\frac{1}{2}}$	$(^3F)^5F$	^5F	$2(15)^{\frac{1}{2}}$
$(^1D)^3D$	^3D	$(3/2)(10)^{\frac{1}{2}}$	$(^3G)^3G$	^3G	$-(5/3)(6)^{\frac{1}{2}}$
$(^1D)^3D$	^3D	$-6(5)^{\frac{1}{2}}$	$(^1G)^3G$	^3G	$-(5/6)(66)^{\frac{1}{2}}$
$(^3D)^3D$	^3D	$-2(30)^{\frac{1}{2}}$	$(^3G)^3G$	^3G	$(3/2)(30)^{\frac{1}{2}}$
			$(^3H)^3H$	^3H	$-(30)^{\frac{1}{2}}$

TABLE III. $[d^3 \alpha' S' L' {}_3 SL | \Sigma e^2/r_{ij} | d^3 \alpha SL]$.

$d^3{}_2$	d^3	H_3	$d^3{}_2$	d^3	H_3
$(^3S)^1S$	^4S	$8(10)^{\frac{1}{2}}$	$(^3F)^1F$	^4F	$(7/2)(10)^{\frac{1}{2}}$
$(^3P)^3P$	^2P	$-2(35)^{\frac{1}{2}}$	$(^3F)^3F$	^4F	$(3/2)(10)^{\frac{1}{2}}$
$(^3P)^3P$	^4P	$-(10)^{\frac{1}{2}}$	$(^3F)^3F$	^2F	$2(10)^{\frac{1}{2}}$
$(^1P)^3P$	^2P	0	$(^3F)^3F$	^2F	$-(15/2)(2)^{\frac{1}{2}}$
$(^1P)^3P$	^4P	$2(35)^{\frac{1}{2}}$	$(^1F)^1F$	^2F	0
$(^1D)^1D$	^2D	$-(70)^{\frac{1}{2}}$	$(^1F)^3F$	^4F	$-2(10)^{\frac{1}{2}}$
$(^3D)^1D$	^2D	$3(10)^{\frac{1}{2}}$	$(^2G)^1G$	^2G	$-(10/3)(6)^{\frac{1}{2}}$
$(^3D)^1D$	^4D	$6(5)^{\frac{1}{2}}$	$(^2G)^1G$	^4G	$(5/6)(66)^{\frac{1}{2}}$
$(^3D)^1D$	^4D	$-(10)^{\frac{1}{2}}$	$(^2G)^1G$	^4G	$-(9/2)(10)^{\frac{1}{2}}$
$(^3D)^3D$	^4D	$-2(10)^{\frac{1}{2}}$	$(^2G)^3G$	^2G	$(3/2)(10)^{\frac{1}{2}}$
$(^3D)^3D$	^2D	$6(5)^{\frac{1}{2}}$	$(^2G)^3G$	^4G	$(5/6)(66)^{\frac{1}{2}}$
$(^1D)^3D$	^2D	$-3(10)^{\frac{1}{2}}$	$(^1G)^3G$	^4G	$(10/3)(6)^{\frac{1}{2}}$
$(^1D)^3D$	^4D	$(70)^{\frac{1}{2}}$	$(^3H)^3H$	^4H	$-(10)^{\frac{1}{2}}$
$(^3F)^1F$	^3F	$-(15/2)(2)^{\frac{1}{2}}$	$(^3I)^1I$	^4I	$(10)^{\frac{1}{2}}$

C_2''' differs from C_1''' in that the direct integral is replaced by the exchange integral with a minus sign. Furthermore, the exchange integral is not independent of spin; the singlet and triplet states differ by a minus sign. Specializing to dsp electrons, we have

$$\left[s_1 p_2 {}^1P \left| \frac{e^2}{r_{12}} \right| d_2 p_1 {}^1P \right] = -\left[s_1 p_2 P \left| \frac{e^2}{r_{12}} \right| d_2 p_1 P \right] = -R_e$$
$$\left[s_1 p_2 {}^3P \left| \frac{e^2}{r_{12}} \right| d_2 p_1 {}^3P \right] = \left[s_1 p_2 P \left| \frac{e^2}{r_{12}} \right| d_2 p_1 P \right] = R_e. \quad (18)$$

Therefore,

$$C_2''' = (n-1)^{\frac{1}{2}}[d^{n-2}\alpha_1 S_1 L_1 d S_3 L_3 \| d^{n-1}\alpha_2 S_2 L_2]$$
$$\times [L_1 d p(P) L | L_1 d(L_2) p L] R_e$$
$$\times \sum_{S_4} (-1)^{S_4} [S_1 \tfrac{1}{2}(S_2) \tfrac{1}{2} S | S_1 \tfrac{1}{2} \tfrac{1}{2}(S_4) S]$$
$$\times [S_1 \tfrac{1}{2} \tfrac{1}{2}(S_4) S | S_1 \tfrac{1}{2}(S_3) \tfrac{1}{2} S]. \quad (18')$$

The sum over S_4 is evaluated in Appendix II:

$$\sum_{S_4}=\delta(S_1S)(-1)^{S_2-S_3}\frac{[(2S_2+1)(2S_3+1)]^{\frac{1}{2}}}{2S+1}-\delta(S_2S_3). \quad (19)$$

The exchange integral R_e is evaluated in terms of Slater integrals in Appendix I with the result

$$R_e=-(\sqrt{2}/3)R^1(sp,pd). \quad (20)$$

Finally, we form the desired matrix component from the partial results (5), (8), (15), (18′), and (19), *viz.*,

$$\left[d^{n-2}\alpha_1S_1L_1sS_2L_2\right)pSL\left|\sum_{i<j}^{n}\frac{e^2}{r_{ij}}\right|d^{n-1}\alpha_3S_3L_3pSL\Big]$$

$$=\left[d^{n-2}\alpha_1S_1L_1sS_2L_2\left|\sum_{i<j}^{n-1}\frac{e^2}{r_{ij}}\right|d^{n-1}\alpha_3S_3L_2\right]\delta(S_2S_3)\delta(L_2L_3)$$

$$+(n-1)^{\frac{1}{2}}[d^{n-2}\alpha_1S_1L_1dS_3L_3][d^{n-1}\alpha_3S_3L_3]$$

$$\times[L_1dp(P)L|L_1d(L_3)pL]$$

$$\times[(R_d-R_e)\delta(S_2S_3)+g_eR_e], \quad (21)$$

in which

$$g_e=\delta(S_1S)(-1)^{S_2-S_3}\{[(2S_2+1)(2S_3+1)]^{\frac{1}{2}}/(2S+1)\}.$$

R_d and R_e are given by (16) and (20), respectively.

The result has certain obvious features. If the parent orbital angular momenta are different, the interaction between the parents (first term) vanishes. If, in addition, the parent spins differ, the term containing R_d-R_e also vanishes. Finally, if the grandparent spin S_1 and the total spin are also different, the entire matrix component vanishes.

It should also be noted that the consideration of the configuration interaction introduces three radial integrals, none of which occurs in the part of the matrix labeled by one configuration only. In addition to R_d and R_e, which appear explicitly in formula (21), the integral $R^2(dd,ds)$ arises from the first term of (21) [see Sec. III, part (1) below]. Thus, in the usual procedure of adjusting parameters there will be three more independent parameters. In practice it will be convenient to adopt as independent the combination R_d-R_e and R_e.

TABLE IV. $[d^3\alpha_2S_2L_2[d^7(\alpha_1S_1L_1)dS_3L_3]$. A particular N is the normalizing factor for the coefficients in its column.

d^7 / d^8	^1S	^3P	^1D	^3F	^3G
^2P	0	$-14^{\frac{1}{2}}$	$-126^{\frac{1}{2}}$	4	0
^4P	0	-8	0	$-56^{\frac{1}{2}}$	0
^1D	1	$-15^{\frac{1}{2}}$	$-35^{\frac{1}{2}}$	$-35^{\frac{1}{2}}$	$-21^{\frac{1}{2}}$
^3D	0	$-35^{\frac{1}{2}}$	$135^{\frac{1}{2}}$	$15^{\frac{1}{2}}$	-5
^3F	0	$-56^{\frac{1}{2}}$	$84^{\frac{1}{2}}$	$-14^{\frac{1}{2}}$	$70^{\frac{1}{2}}$
^4F	0	$-56^{\frac{1}{2}}$	0	$224^{\frac{1}{2}}$	0
^3G	0	0	$-180^{\frac{1}{2}}$	$90^{\frac{1}{2}}$	$66^{\frac{1}{2}}$
^3H	0	0	0	$110^{\frac{1}{2}}$	$-154^{\frac{1}{2}}$
N	1	$240^{-\frac{1}{2}}$	$560^{-\frac{1}{2}}$	$560^{-\frac{1}{2}}$	$336^{-\frac{1}{2}}$

We shall now discuss the quantities in the formula (21).

III. TABULATION OF COEFFICIENTS AND MATRIX COMPONENTS

In this section we shall discuss the availability and tabulation of the matrix elements and coefficients occurring in the result (21). We shall point out that many of these quantities are already listed in RIII; the remaining ones are supplied in this section.

(1) Interaction between the Parent Configurations $d^{n-1}s$ and d^n

The matrix components of the electrostatic interaction between the parent configurations $d^{n-1}s$ and d^n are discussed fully in Sec. 7 of RIII. We merely wish to reiterate certain features of these matrix elements and extend the tabulation given in RIII.

The matrices of the electrostatic interaction are, of course, diagonal with respect to S and L. For the particular matrix components under consideration, we have the additional rule that an element will vanish unless the seniority numbers of d^{n-1} and d^n differ by unity. The nonvanishing matrix elements depend on the single Slater integral $R^2(dd,ds)$. Racah introduces the more convenient parameter $H_2=R^2(dd,ds)/35$. The coefficients of H_2 are given in Tables XX, XXI, and XXII of RIII for the left side of the periodic table ($n=3$, 4, and 5). There is a simple relationship[10] connecting the matrix components of the left and right sides of the periodic table, *viz.*,

$$\left[d^{n-1}\alpha_1S_1L_1sS_3L_3\left|\sum\frac{e^2}{r_{ij}}\right|d^n\alpha_3S_3L_3\right]$$

$$=(-1)^{S+\frac{1}{2}-S'}\left(\frac{2S_1+1}{2S+1}\right)^{\frac{1}{2}}\Big[d^{11-n}\alpha_1S_1L_1$$

$$\times\left|\sum\frac{e^2}{r_{ij}}\right|d^{10-n}\alpha_3S_3L_3sS_1L_1\Big]. \quad (22)$$

TABLE V. $[d^7\alpha_2S_2L_2[d^8(\alpha_1S_1L_1)dS_2L_2]$.

d^7 / d^8	^2P	^4P	^2D	^2F	^4F	^2G	^2H
^1S	0	0	$8^{\frac{1}{2}}$	0	0	0	0
^3S	0	0	$56^{\frac{1}{2}}$	0	0	0	0
^2P	$7^{\frac{1}{2}}$	$-16^{\frac{1}{2}}$	$27^{\frac{1}{2}}$	$-49^{\frac{1}{2}}$	$112^{\frac{1}{2}}$	$-14^{\frac{1}{2}}$	0
^4P	$-50^{\frac{1}{2}}$	$-14^{\frac{1}{2}}$	0	$56^{\frac{1}{2}}$	$200^{\frac{1}{2}}$	$16^{\frac{1}{2}}$	0
^1D	$15^{\frac{1}{2}}$	0	$15^{\frac{1}{2}}$	$45^{\frac{1}{2}}$	$-40^{\frac{1}{2}}$	0	$-200^{\frac{1}{2}}$
^3D	$-30^{\frac{1}{2}}$	0	0	$40^{\frac{1}{2}}$	$-180^{\frac{1}{2}}$	0	$100^{\frac{1}{2}}$
^4D	$-20^{\frac{1}{2}}$	$-35^{\frac{1}{2}}$	0	$-240^{\frac{1}{2}}$	$-120^{\frac{1}{2}}$	$15^{\frac{1}{2}}$	$-600^{\frac{1}{2}}$
^2D	0	$75^{\frac{1}{2}}$	0	0	0	$175^{\frac{1}{2}}$	0
^2F	$30^{\frac{1}{2}}$	0	0	$-140^{\frac{1}{2}}$	$-105^{\frac{1}{2}}$	0	$7^{\frac{1}{2}}$
^3F	$-8^{\frac{1}{2}}$	$-14^{\frac{1}{2}}$	$63^{\frac{1}{2}}$	$21^{\frac{1}{2}}$	$28^{\frac{1}{2}}$	$56^{\frac{1}{2}}$	$420^{\frac{1}{2}}$
^4F	$50^{\frac{1}{2}}$	$-56^{\frac{1}{2}}$	0	$84^{\frac{1}{2}}$	$175^{\frac{1}{2}}$	$-14^{\frac{1}{2}}$	$-945^{\frac{1}{2}}$
^2G	0	0	$27^{\frac{1}{2}}$	$-25^{\frac{1}{2}}$	$-100^{\frac{1}{2}}$	0	$220^{\frac{1}{2}}$
^4G	0	0	0	$44^{\frac{1}{2}}$	$-275^{\frac{1}{2}}$	0	$-845^{\frac{1}{2}}$
^6G	0	0	0	$-180^{\frac{1}{2}}$	$405^{\frac{1}{2}}$	$90^{\frac{1}{2}}$	$-891^{\frac{1}{2}}$
^4H	0	0	0	0	$-220^{\frac{1}{2}}$	$110^{\frac{1}{2}}$	$-924^{\frac{1}{2}}$
^4I	0	0	0	0	0	$728^{\frac{1}{2}}$	$-182^{\frac{1}{2}}$
N	$210^{-\frac{1}{2}}$	$210^{-\frac{1}{2}}$	$140^{-\frac{1}{2}}$	$980^{-\frac{1}{2}}$	$1960^{-\frac{1}{2}}$	$490^{-\frac{1}{2}}$	$5880^{-\frac{1}{2}}$	$770^{-\frac{1}{2}}$

[10] The author is indebted to Professor G. Racah for pointing this out to him.

TABLE VI. $[d^n\alpha_2 S_2 L_2 \| d^n(\alpha_1 S_1 L_1) d S_3 L_3]$.

d^n / d^n	^1S	^3S	^1P	^3P	^1D	^3D	^1F	^3F	^1G	^3G	^1H	^3I
^1S	0	0	0	0	0	$-280^{\frac{1}{2}}$	$42^{\frac{1}{2}}$	0	0	0	0	0	0	0	0	0
^3S	0	0	0	0	0	0	0	$0^{\frac{1}{2}}$	0	0	0	0	0	0	0	0
^1P	0	0	$-14^{\frac{1}{2}}$	-5	$-42^{\frac{1}{2}}$	$-210^{\frac{1}{2}}$	$14^{\frac{1}{2}}$	0	$-120^{\frac{1}{2}}$	8	$200^{\frac{1}{2}}$	0	0	0	0	0
^3P	0	0	-8	$14^{\frac{1}{2}}$	0	0	-7	$-3^{\frac{1}{2}}$	0	$-224^{\frac{1}{2}}$	$448^{\frac{1}{2}}$	0	0	0	0	0
^1D	1	0	$-45^{\frac{1}{2}}$	0	$-35^{\frac{1}{2}}$	0	0	0	$-420^{\frac{1}{2}}$	0	$-63^{\frac{1}{2}}$	0	0	0	0	0
^3D	0	-1	$-35^{\frac{1}{2}}$	$-10^{\frac{1}{2}}$	$45^{\frac{1}{2}}$	-10	$-60^{\frac{1}{2}}$	0	$-200^{\frac{1}{2}}$	$60^{\frac{1}{2}}$	-120	-5	$-968^{\frac{1}{2}}$	$-200^{\frac{1}{2}}$	0	0
^1D	0	$-2^{\frac{1}{2}}$	0	$45^{\frac{1}{2}}$	0	$450^{\frac{1}{2}}$	$-30^{\frac{1}{2}}$	0	-10	0	$540^{\frac{1}{2}}$	0	$4356^{\frac{1}{2}}$	-10	0	0
^1D	0	0	0	$-90^{\frac{1}{2}}$	0	0	$-135^{\frac{1}{2}}$	$5^{\frac{1}{2}}$	0	0	$480^{\frac{1}{2}}$	0	0	$800^{\frac{1}{2}}$	0	0
^1F	0	0	$-56^{\frac{1}{2}}$	5	$28^{\frac{1}{2}}$	$-315^{\frac{1}{2}}$	$21^{\frac{1}{2}}$	0	$105^{\frac{1}{2}}$	$-56^{\frac{1}{2}}$	$175^{\frac{1}{2}}$	$70^{\frac{1}{2}}$	$-4235^{\frac{1}{2}}$	$-315^{\frac{1}{2}}$	$-55^{\frac{1}{2}}$	0
^3F	0	0	0	$-45^{\frac{1}{2}}$	0	$175^{\frac{1}{2}}$	$105^{\frac{1}{2}}$	0	$-525^{\frac{1}{2}}$	0	$315^{\frac{1}{2}}$	0	$-7623^{\frac{1}{2}}$	$-7^{\frac{1}{2}}$	$99^{\frac{1}{2}}$	0
^1F	0	0	$-56^{\frac{1}{2}}$	-4	0	0	$21^{\frac{1}{2}}$	$-7^{\frac{1}{2}}$	0	$896^{\frac{1}{2}}$	$112^{\frac{1}{2}}$	0	0	$560^{\frac{1}{2}}$	$-220^{\frac{1}{2}}$	0
^3G	0	0	0	0	$-60^{\frac{1}{2}}$	$-75^{\frac{1}{2}}$	$-45^{\frac{1}{2}}$	0	$3^{\frac{1}{2}}$	$360^{\frac{1}{2}}$	$405^{\frac{1}{2}}$	$66^{\frac{1}{2}}$	$5577^{\frac{1}{2}}$	$-297^{\frac{1}{2}}$	$99^{\frac{1}{2}}$	$-33^{\frac{1}{2}}$
^1G	0	0	0	0	0	$495^{\frac{1}{2}}$	$-33^{\frac{1}{2}}$	0	$495^{\frac{1}{2}}$	0	$825^{\frac{1}{2}}$	0	$-3645^{\frac{1}{2}}$	$845^{\frac{1}{2}}$	$-15^{\frac{1}{2}}$	$-45^{\frac{1}{2}}$
^3G	0	0	0	0	0	0	$75^{\frac{1}{2}}$	3	0	0	$1200^{\frac{1}{2}}$	0	0	$-880^{\frac{1}{2}}$	$-660^{\frac{1}{2}}$	0
^1H	0	0	0	0	0	0	0	$13^{\frac{1}{2}}$	$440^{\frac{1}{2}}$	$-220^{\frac{1}{2}}$	$-154^{\frac{1}{2}}$	$308^{\frac{1}{2}}$	$-308^{\frac{1}{2}}$	$-286^{\frac{1}{2}}$	$-77^{\frac{1}{2}}$
^3I	0	0	0	0	0	0	0	0	0	0	0	0	$-6552^{\frac{1}{2}}$	$-728^{\frac{1}{2}}$	$546^{\frac{1}{2}}$	$-175^{\frac{1}{2}}$
N	1	$3^{-\frac{1}{2}}$	$270^{-\frac{1}{2}}$	$270^{-\frac{1}{2}}$	$210^{-\frac{1}{2}}$	$2100^{-\frac{1}{2}}$	$630^{-\frac{1}{2}}$	$30^{-\frac{1}{2}}$	$1680^{-\frac{1}{2}}$	$2520^{-\frac{1}{2}}$	$5040^{-\frac{1}{2}}$	$378^{-\frac{1}{2}}$	$33264^{-\frac{1}{2}}$	$5040^{-\frac{1}{2}}$	$1980^{-\frac{1}{2}}$	$330^{-\frac{1}{2}}$

This follows directly from (79) in view of (81) of RIII and (74) of RII. We have used Eq. (22) to obtain the results for the right side of the periodic table and have listed these in Tables I, II, and III.

(2) Coefficients of Fractional Percentage

Equation (19) of RIII relates the coefficients of fractional parentage of the left side to the corresponding ones on the right side of the periodic table. For d electrons this relationship is

$$[d^{9-n}(\alpha' S' L') dSL \| d^{10-n}\alpha SL] = (-1)^{S+S'+L+L'-5/2}\left[\frac{(n+1)(2S'+1)(2L'+1)}{(10-n)(2S+1)(2L+1)}\right]^{\frac{1}{2}} \times [d^n(\alpha SL) dS'L' \| d^{n+1}\alpha' S'L']. \quad (23)$$

We have applied the above to the results given in Tables II, III, and IV in RIII and have thus obtained the coefficients for the conjugated configurations. The fact that the calculation yielded normalized coefficients served as a valuable check. Our results are given in Tables IV, V, and VI.

(3) Racah Coefficients

The Racah coefficients are given in terms of Racah's W function. Thus Eq. (4) of RIII applied to the Racah coefficient occurring in our equation (21) gives

$$[L_1 dp(P)L \,|\, L_1 d(L_3) pL] = [3(2L_3+1)]^{\frac{1}{2}} W[L_1 2L1; L_3 1]. \quad (24)$$

An explicit algebraic formula for the W function in terms of its six arguments is given in Eq. (36′) of RII. There are altogether fifty-four different coefficients of this type in the entire iron group. We have evaluated these and have listed them in Table VII. The evaluation is best carried out by first reducing the general form of the W function to more specialized expressions.[11] For example, there are six cases of the type in which $L_3 = L_1$ and $L = L_1 + 1$. For this case the Racah coefficient becomes

$$[L_1 dp(P)L \,|\, L_1 d(L_1) pL_1+1] = \left[\frac{L_1(2L_1-1)}{10(L_1+1)(2L_1+3)}\right]^{\frac{1}{2}}.$$

The fifty-four coefficients listed in Table VII were obtained by means of nine similar formulas.[12]

It should be noted that all the quantities which enter in the configuration interaction (21) are now available in either RIII or this section.

IV. CONCLUDING REMARKS

It need hardly be emphasized that in order to study the term values of a spectrum one must obtain also the matrix components of the electrostatic interaction within configurations. However, it should be pointed out that these matrices are amenable to treatment by the methods given by Racah, and many of these matrices have been obtained by various authors. In RII there are given the matrices of d^2p and d^8p. Rohrlich[13] has calculated the matrices for d^3p, d^7p, and also for d^25p. Ishidzu and Obi[14] have made available the matrices of d^4p, d^5p, and d^6p. The author has obtained the matrices of d^6ps.[8]

It is expected and hoped that the configuration interaction which we have treated in this paper will be sufficient for an elucidation of the odd terms in the spectra of the iron group. However, the possibility of interactions with other configurations, notably $d^{n-2}s^2p$ and the higher configuration of the type $d^{n-1}n'p$, is by no means ruled out. If we include the word "hope," it is because the matrices are already close to being unmanageably large.

The author wishes to express his gratitude to Dr. F. Rohrlich both for suggesting this work and for many helpful discussions.

[11] Compare H. A. Jahn, Proc. Roy. Soc. (London) **A205**, 234 (1951). In this paper there are given a large number of specialized expressions. See also reference 12.

[12] The W function and related coefficients have recently been evaluated and compiled at the Oak Ridge National Laboratory for a wide range of the arguments. The results are contained in Oak Ridge National Laboratory Report ORNL-1098 (April, 1952), by L. C. Biedenharn. We have checked our results (Table VII) against the entries in that collection.

[13] F. Rohrlich, Phys. Rev. **74**, 1372 (1948).

[14] See reference 7. We wish to draw attention to a misprint in that paper. In the ^1D matrix in Table I, p. 126, the off-diagonal element should be $12(2)^4B$ instead of $12(12)^4B$.

TABLE VII. Racah coefficients $[L_1 d\rho(P) L | L_1 d(L_2) \rho L]$.

L_1	L_2	L	Coeff.
0	2	1	1
1	1	0	1
1	1	1	$-\frac{1}{2}$
1	2	1	$\frac{1}{2}[3]^{\frac{1}{2}}$
1	1	2	1/10
1	2	2	$-(1/10)[15]^{\frac{1}{2}}$
1	3	2	$(1/5)[21]^{\frac{1}{2}}$
2	0	1	$(1/5)[5]^{\frac{1}{2}}$
2	1	1	$-(3/10)[5]^{\frac{1}{2}}$
2	2	1	$(1/10)[35]^{\frac{1}{2}}$
2	1	2	(3/10)
2	2	2	$-(1/10)[35]^{\frac{1}{2}}$
2	3	2	$(1/5)[14]^{\frac{1}{2}}$
2	2	3	$(1/35)[35]^{\frac{1}{2}}$
2	3	3	$-(1/5)[5]^{\frac{1}{2}}$
2	4	3	$(3/35)[105]^{\frac{1}{2}}$
3	1	2	3/5
3	2	2	$-(1/5)[10]^{\frac{1}{2}}$
3	3	2	$(1/5)[6]^{\frac{1}{2}}$
3	2	3	$(1/7)[7]^{\frac{1}{2}}$
3	3	3	$-\frac{1}{2}[6]^{\frac{1}{2}}$
3	4	3	$(3/28)[42]^{\frac{1}{2}}$
3	3	4	$(1/12)[6]^{\frac{1}{2}}$
3	4	4	$-(3/20)[10]^{\frac{1}{2}}$
3	5	4	$(1/15)[165]^{\frac{1}{2}}$
4	2	3	$(1/7)[21]^{\frac{1}{2}}$
4	3	3	$-\frac{1}{2}[6]^{\frac{1}{2}}$
4	4	3	$(1/28)[154]^{\frac{1}{2}}$
4	3	4	$(1/20)[70]^{\frac{1}{2}}$
4	4	4	$-(1/20)[154]^{\frac{1}{2}}$
4	5	4	$(1/5)[11]^{\frac{1}{2}}$
4	4	5	$(1/55)[154]^{\frac{1}{2}}$
4	5	5	$-(1/5)[6]^{\frac{1}{2}}$
4	6	5	$(1/55)[2145]^{\frac{1}{2}}$
5	3	4	$(1/15)[105]^{\frac{1}{2}}$
5	4	4	$-(3/5)$
5	5	4	$(1/15)[39]^{\frac{1}{2}}$
5	4	5	$(3/55)[66]^{\frac{1}{2}}$
5	5	5	$-(1/10)[39]^{\frac{1}{2}}$
5	6	5	$(1/110)[5005]^{\frac{1}{2}}$
5	5	6	$(1/26)[39]^{\frac{1}{2}}$
5	6	6	$-\frac{1}{2}$
5	7	6	$(3/13)[13]^{\frac{1}{2}}$
6	4	5	$(3/55)[165]^{\frac{1}{2}}$
6	5	5	$-(1/10)[35]^{\frac{1}{2}}$
6	6	5	$(1/22)[77]^{\frac{1}{2}}$
6	5	6	$(1/26)[143]^{\frac{1}{2}}$
6	6	6	$-(1/14)[77]^{\frac{1}{2}}$
6	7	6	$(6/91)[91]^{\frac{1}{2}}$
6	6	7	$(1/35)[77]^{\frac{1}{2}}$
6	7	7	$-(3/35)[35]^{\frac{1}{2}}$
6	8	7	$(1/5)[17]^{\frac{1}{2}}$

APPENDIX I

We shall express R_d and R_e in terms of Slater integrals R^k. Applying the well-known development

$$\frac{1}{r_{12}} = \sum_{k=0}^{\infty} \frac{r_<^k}{r_>^{k+1}} P_k(\cos\theta_{12})$$

to R_d gives

$$R_d = \left(s_1 p_2 P \left| \frac{e^2}{r_{12}} \right| d_1 p_2 P\right) = \sum_{k=0}^{\infty} \left(s_1 p_2 P \left| \frac{r_<^k}{r_>^{k+1}} P_k \right| d_1 p_2 P\right).$$

The integration over r_1 and r_2 may be separated from the rest giving

$$R_d = \sum_{k=0}^{\infty} R^k(sp, dp)(s_1 p_2 P | P_k | d_1 p_2 P).$$

The matrix element multiplying R^k differs from zero for only one value of k, *viz.*, $k=2$. This follows from the triangular conditions. Hence,

$$R_d = R^2(sp, dp)(s_1 p_2 P | P_2 | d_1 p_2 P).$$

Racah's matrix methods for tensor operators enable us to evaluate the coefficient of R^2. P_2 is a scalar product of tensors, and a straightforward application of RII (38) gives

$$(s_1 p_2 P | P_2 | d_1 p_2 P) = (0 \| T^{(2)} \| 2)(1 \| U^{(2)} \| 1) W(0121; 12).$$

Using RII (51) and (50′) we find

$$(0 \| T^{(2)} \| 2) = 1, \quad (1 \| U^{(2)} \| 1) = -(6/5)^{\frac{1}{2}},$$

and for RII (36′) we obtain

$$W(0121; 12) = (15)^{-\frac{1}{2}}.$$

Hence,

$$R_d = -(2)^{\frac{1}{2}}/5 R^2(sp, dp).$$

Similarly, we have

$$R_e = [s_1 p_2 P | e^2/r_{12} | d_2 p_1 P] = R^1(sp, pd)(s_1 p_2 P | P_1 | d_2 p_1 P),$$

$$(s_1 p_2 P | P_1 | d_2 p_1 P) = -(0 \| T^{(1)} \| 1)(1 \| U^{(1)} \| 2) W(0112; 11),$$

$$(0 \| T^{(1)} \| 1) = -1, \quad (1 \| U^{(1)} \| 2) = -(2)^{\frac{1}{2}},$$

$$W(0112; 11) = \tfrac{1}{3},$$

and

$$R_e = -(\sqrt{2}/3) R^1(sp, pd).$$

APPENDIX II

The sum over spin in Eq. (18) is evaluated here. We have

$$\sum_{S_4} = \sum_{S_4} (-1)^{S_4} [S_1 \tfrac{1}{2}(S_2) \tfrac{1}{2} S | S_1 \tfrac{1}{2} \tfrac{1}{2}(S_4) S] \times [S_1 \tfrac{1}{2} \tfrac{1}{2}(S_4) S | S_1 \tfrac{1}{2}(S_3) \tfrac{1}{2} S].$$

S_4 assumes the values 0 and 1 corresponding to singlet and triplet states. If the factor $(-1)^{S_4}$ is replaced by unity, the sum becomes simply $\delta(S_2 S_3)$. Therefore,

$$\sum_{S_4} = 2[S_1 \tfrac{1}{2}(S_2) \tfrac{1}{2} S | S_1 \tfrac{1}{2} \tfrac{1}{2}(0) S] \times [S_1 \tfrac{1}{2} \tfrac{1}{2}(0) S | S_1 \tfrac{1}{2}(S_3) \tfrac{1}{2} S] - \delta(S_2 S_3).$$

Now let us consider the various possibilities. In the first place, the Racah coefficients occurring in the above vanish unless

$$S_1 = S.$$

The only possibilities for S_2 and S_3 are $S+\frac{1}{2}$ or $S-\frac{1}{2}$. Evaluating the Racah coefficients by means of RIII (4) and RII (36′), one finds

$$[S \tfrac{1}{2}(S_2 = S+\tfrac{1}{2}) \tfrac{1}{2} S | S \tfrac{1}{2} \tfrac{1}{2}(0) S] = [(2S_2+1)/2(2S+1)]^{\frac{1}{2}}$$

and

$$[S \tfrac{1}{2}(S_3 = S-\tfrac{1}{2}) \tfrac{1}{2} S | S \tfrac{1}{2} \tfrac{1}{2}(0) S] = -[(2S_3+1)/2(2S+1)]^{\frac{1}{2}}.$$

All possibilities for $\sum_{S_4}$ can thus be summarized by

$$\sum_{S_4} = \delta(S_1 S)(-1)^{S_2 - S_3} [(2S_2+1)(2S_3+1)]^{\frac{1}{2}}/(2S+1) - \delta(S_2 S_3).$$

Negative Pion Activation of Bromine*†

T. T. SUGIHARA‡ AND W. F. LIBBY
Institute for Nuclear Studies and Department of Chemistry, University of Chicago, Chicago, Illinois
(Received June 23, 1952)

Radiochemical studies of the reactions of π^- mesons with bromine, silver, and the light elements present in photographic emulsions should assist considerably in the interpretation of data obtained with photographic plates. The results for bromine with 122-Mev negative pions expending their full range in the element include: Peak yield of about 7 percent for As^{70} (ejection of 1 proton and 2 or 4 neutrons depending on which Br isotope absorbs the pion); the ratio of the number of neutrons to the number of protons ejected was three to four in the most probable cases; the distribution of radioactivities appears to be reconcilable with photographic plate data if one guesses that the silver data will resemble those for bromine.

THE very considerable intensity of negative pions available from the 170-inch synchrocyclotron at the University of Chicago makes possible radiochemical studies of meson reactions.[1] Such studies with the elements bromine, silver, and the light elements carbon, nitrogen, and oxygen should be of great assistance in the interpretation of data obtained with photographic plates. The results for the element bromine are reported in this communication.

The initial intensity of mesons at the beryllium target is of the order of 1 curie. An appreciable fraction of this intensity is available as negative pions. Deflection by the magnetic field of the main cyclotron magnet allows selection of a 122-Mev beam by the use of a channel several square inches in cross section traversing a 6-foot thick iron shield. (This shield was increased to 12 feet in thickness toward the end of this research.) The pion beam emerging from the iron shield is further purified by deflection with an auxiliary magnet. The target bromine was placed just beyond this auxiliary magnetic field. The usual intensity ran between 200,000 and 600,000 mesons per minute, and irradiation was conducted for periods between 1 and 6 hours. Background experiments were performed by turning off the auxiliary deflecting magnet and operating the cyclotron at its usual meson output.

The sample itself consisted of about 6 pounds of liquid bromine in the standard commercial bottle. This gave a cylindrical target about 8 cm in diameter and about 20 cm long. The range of 122-Mev negative pions is about 55 grams per cm^2 in bromine, so the target is thicker than the range of the incident beam. Carriers of selenium, arsenic, germanium, gallium, and zinc were added to the irradiated bromine and subsequently separated by shaking with a hydrochloric acid solution. The various elements then were separated chemically from the aqueous layer and the individual isotopes identified by half-life and absorption curves. Table I presents the results. Percent yields are quoted in terms of the activity that would have been observed had all of the negative pions formed the individual isotope in question. The yields shown in column 4 are the mean of at least two determinations.

The samples were counted on a large cylindrical counter of thin wall (2.7 mg/cm^2), developed for this research. The counter was 1.5 inches in diameter and 10 inches long. On the inner surface of the thin plastic wall gold had been deposited to the extent of about 0.1 mg/cm^2. This foil is commercially available, its principal use being for gilding. By the use of an atmospheric pressure filling such as "*Q* gas" the wall was supported by a slight excess pressure of gas in the counter. The sample was placed intimately around the counter with a geometry of 35 percent. Anticoincidence shielding was used to keep the background rate at about 6 cpm. Absolute assays were obtained by calibration with absolute standards, and the use of the general methodology of correction for self-absorption were observed to hold for close geometries of the type involved in this counting arrangement.

An experiment was performed to test for possible deleterious activation effects of the 5 or 6 neutrons emitted per pion captured. This experiment consisted in irradiating a stack of solid bromine cylindrical disks, each of which was 15 g/cm^2 thick and had a cross-section diameter of about 3.5 inches. The results of this experi-

TABLE I. Absolute yields for negative pions on bromine.

Isotope	Observed half-life	Literature half-life	Yield (%)
Se^{72}	9.5 days	9.5 days	3.2±0.9
Se^{73}	6.7 hr	6.7 hr, 7.1 hr	3.6±1.0
As^{77} (+As^{71})	40 hr	40 hr, 50 hr	3.6±1.0
As^{76} (+As^{72})	26.8 hr	26.8 hr, 26 hr	6.3±1.7
As^{74}	17.5 days	17.5 days	7.0±1.8
As^{73}	80 min	90 min	0.8±0.3
Ge^{69}	40 hr	39.6 hr	0.6±0.15
Ge^{75}	90 min	82 min	0.3±0.08
Ga^{66}	68 min	68 min	1.2±0.4
Ga^{72}	14.1 hr	14.1 hr	0.6±0.15
Ga^{73}	5.0 hr	5.0 hr	0.4±0.1

* This research was supported in part by the Air Research and Development Command of the U. S. Air Force. The 170-inch synchrocyclotron was supported jointly by the ONR and AEC.
† This paper is taken in major part from the thesis submitted by T.T.S. in partial fulfillment of the requirements for the Ph.D. degree in the Division of Physical Sciences of the University of Chicago. Full details are available in the thesis.
‡ Now at Department of Chemistry, Massachusetts Institute of Technology, Cambridge, Massachusetts.
[1] A. Turkevich and J. B. Niday, Phys. Rev. **84**, 1253 (1951).

TABLE II. Activation *vs* range data.

Br traversed (g/cm²)	Yield in % for As isotopes: 17.5-day As^{74}	40-hr As^{77} (+As^{71})	26.8-hr As^{76} (+As^{73})
0–15	1.16	0.56	0.92
15–30	1.36	0.65	1.06
30–45	2.0	0.95	1.58
45–60	2.8	1.39	2.27
60–75	...	...	0.22
75–90	...	...	0.08

ment are given for three arsenic isotopes in Table II. It should be observed that these data were obtained with a somewhat divergent pion beam, so the exact shape of the yield *vs* range curve should not be taken too seriously. It is clear, however, from these data that the arsenic activities are formed by the negative pions and only slightly by the secondary neutrons. Some small correction has been made for the secondary neutron formation in compiling the data in Table I.

By chemical group separations an upper limit was set on the yield of all isotopes other than those of selenium, arsenic, germanium, and gallium. For those having a half-life in the range 30 min to 15 days and which do not decay exclusively by K capture, the total maximum yield is estimated to be less than 3 percent.

By plotting arsenic isotope yields against mass number, a curve is obtained that is roughly symmetrical about a vertical axis. The peak seems to be at mass 74 or 75. As a first approximation it is assumed that selenium and germanium yield curves will have the same shape as the arsenic curve. The arsenic curve is chosen as the standard since more data are available for it. The gallium curve is taken to be somewhat flatter and broader. When such interpolation and extrapolation are used to obtain yields of the stable isotopes, the total yields per element can be calculated. These are shown in Table III.

TABLE III. Element yields for negative pion activation of bromine.

Element	Yield (%)
Selenium	34
Arsenic	31
Germanium	21
Gallium	7

These values appear to correspond roughly with those obtained in photographic plate studies when emulsion data are corrected to consider heavy nuclei capture only. However, this point will be more conclusively settled when the data for silver and the lighter elements in the emulsion are determined more completely.

Mr. Wataru Goishi helped with the chemical separations in an invaluable way. The authors are very grateful.

Energy Loss of Cosmic-Ray Mu-Mesons in Sodium Iodide Crystals*

ALVIN HUDSON AND ROBERT HOFSTADTER
Department of Physics and Microwave Laboratory, Stanford University, Stanford, California
(Received June 20, 1952)

A scintillation counter telescope, employing three NaI(Tl) crystals in coincidence, has been used to study the energy losses experienced by mu-mesons in traversing one of the crystals. The magnitude of the light flash in NaI(Tl) has been assumed to be proportional to the energy lost in the crystal by the meson. The observed pulse distribution is compared with one calculated on the basis of the Bethe-Bloch theory without the density correction and also with the Halpern-Hall theory which includes the effect of the dielectric shielding. Each calculated curve employs a fold of the Landau straggling theory with the cosmic-ray mu-meson spectrum. Comparison of the data with the two theories definitely favors the Halpern-Hall theory both in respect to absolute value of the most probable energy loss as well as the shape of the distribution.

INTRODUCTION

THE energy loss suffered by charged particles in passing through absorbing layers has been the subject of many calculations since the original classical treatment of Bohr.[1] Quantum-mechanical calculations were first made by Bethe[2] for hydrogen, and by extension, to other materials. Bloch[3] has also calculated the mean energy loss using the methods of quantum mechanics and showed how Bohr's classical result could be reconciled with Bethe's formula. Bloch also extended the energy loss formulas to materials of any atomic number by employing the Thomas-Fermi atomic model in a particularly successful and practically useful way. Further significant ideas and calculations were contributed by Williams[4] who showed, as Bohr previously had done for the classical case, how modifications of the energy loss formula had to be made in order to include the effects of relativity.

The particular expression for the mean energy loss now commonly employed is taken from the work of Bethe and Bloch and is termed the Bethe-Bloch formula. The practical way of using the formula is described in the well-known paper of Rossi and Greisen.[5] The validity of the formula has been established for gases in and near the minimum of the energy loss curve although the accuracy with which the formula has been checked in the region above the minimum is not high. Further, there is some disagreement as to whether the Bethe-Bloch result applies to μ-meson losses.[6]

Additional contributions to the theory of energy loss have been made in connection with the passage of charged particles through dense media, i.e., liquid or solids. In such cases the dielectric behavior of the material introduces a shielding effect in the region of relativistic energies of the primary particle, and produces a reduction of energy loss. The original suggestion of a dielectric shielding effect is due to Swann.[7] The problem was first treated by Fermi[8] who proposed a simple theory embodying a dispersion model of the atom based on a single resonant frequency.

The Fermi model is perhaps a bit too simple since, in actuality, electrons in all shells corresponding to many "frequencies" are involved in the shielding. The calculation has been improved by Halpern and Hall[9] who take the multifrequency model as a basis of the theory. The Fermi model and the Halpern-Hall theory give identical results in the region of very high particle energies. The two theories give similar results in all regions provided a suitable "effective" dielectric constant can be used in the Fermi formulation. The weakness of the Fermi theory is that one must essentially guess a value of the dielectric constant. The Halpern-Hall theory, in effect, calculates this value for a reasonable model of the atom. The calculated values differ in most cases only a little from the value unity.

Further calculations on the dielectric effects have been made by Wick[10] and by A. Bohr[11] and by Schoenberg.[12] A. Bohr discusses the connection between Čerenkov radiation, energy loss, and the dielectric shielding effects. Recently, the experimental reality of the ideas and calculations on dielectric shielding have been demonstrated through the work of Bowen and Roser[13] on a light material, anthracene. Earlier experiments on AgCl indicated similar results.[14]

The theoretical treatments discussed above are con-

* This work was partially supported by the joint program of the ONR and AEC.

[1] N. Bohr, Phil. Mag. **25**, 10 (1913); **30**, 581 (1915).
[2] H. Bethe. Ann. Physik **5**, 325 (1930); Z. Physik **76**, 293 (1932); Handbuch der Physik **24**, Part 1, 491 (1933).
[3] F. Bloch, Ann. Physik **16**, 285 (1933); Z. Physik **81**, 363 (1933).
[4] E. J. Williams, Proc. Roy. Soc. (London) **135**, 108 (1932); **139**, 163 (1933); **169**, 531 (1931); Phys. Rev. **58**, 292 (1940).
[5] B. Rossi and K. Greisen, Revs. Modern Phys. **13**, 240 (1941).
[6] Goodman, Nicholson, and Rathgeber, Proc. Phys. Soc. (London) **A64**, 96 (1951); J. E. Kupperian, Jr., and E. D. Palmatier, Phys. Rev. **85**, 1043 (1952); H. D. Rathgeber, Z. Naturforsch. **6a**, 598 (1951).
[7] W. F. G. Swann, J. Franklin Inst. **226**, 598 (1938).
[8] E. Fermi, Phys. Rev. **56**, 1242 (1939); **57**, 485 (1940).
[9] O. Halpern and H. Hall, Phys. Rev. **57**, 459 (1940); **73**, 477 (1948).
[10] G. C. Wick, Ricerca sci. **11**, 273 (1940); **12**, 858 (1941); Nuovo cimento **1**, 302 (1943).
[11] A. Bohr, Kgl. Danske Videnskab. Selskab Mat.-fys. Medd. **24**, No. 19 (1948).
[12] M. Schoenberg, Nuovo cimento **8**, No. 3 (1951); Nuovo cimento **9**, No. 4 (1952).
[13] T. Bowen and F. X. Roser, Phys. Rev. **85**, 992 (1952).
[14] W. L. Whittemore and J. C. Street, Phys. Rev. **76**, 1786 (1949).

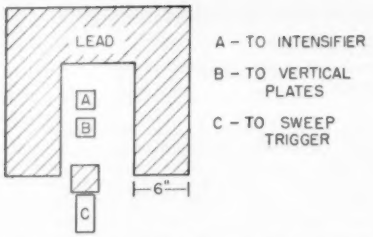

FIG. 1. Schematic drawing of counter telescope and shielding arrangement.

cerned with mean energy losses. As Bohr[1] early pointed out in his second paper, we usually measure the most probable energy loss rather than the mean; the two values are significantly different. If, for example, the energy loss of individual particles can be studied, one may expect to find a most probable energy loss and a straggling of the individual losses around this value. The most probable energy loss will be the same as the mean only in those cases of a symmetrical straggling curve, e.g., for low energy alpha-particles. On the other hand, for large energy transfers, when the straggling curve is unsymmetrical, the most probable value will differ from the mean value. The Rutherford-Bohr relation giving the energy transfer in collision of a heavy particle with an atomic electron implies that the straggling curve will not be symmetrical. This relation states that the probability for a given energy to be transferred to an electron depends inversely on the square of the energy imparted to the electron. This type of probability function produces a long and unsymmetrical tail on the high energy side of the straggling curve and is due to projected electrons of high energy which are conventionally called δ-rays.

This situation was known to Bohr and Williams and calculations were made by the latter on the form of the straggling curve.[15] A discussion of straggling including the work of Williams is given by N. Bohr[15] in his comprehensive treatment of atomic energy loss problems.

It remained for Landau[16] to calculate the straggling function in closed form and to bring to it the renewed attention it has recently received. Landau has given both an expression for the most probable energy loss and the shape of a universal straggling curve when the energy loss is small compared with the particle's energy. The universal Landau curve may be applied to particular materials, thicknesses of sample, particular energy, etc. Symon[17] has extended the theory to intermediate cases where the energy loss may be a large fraction of the total energy.

[15] N. Bohr, Kgl. Danske Videnskab. Selskab Mat.-fys Medd. **18**, No. 8 (1948). (See pp. 50 ff.)
[16] L. Landau, J. Phys. (U.S.S.R.) **8**, 201 (1944).
[17] K. R. Symon, (unpublished) Harvard University thesis (1948).

Recently, Jauch[18] has calculated the effect of a radiative correction to the energy loss formula. The experimental information now available is unable to distinguish small virtual or real radiative effects.

It is generally appreciated that cosmic-ray μ-mesons at sea level offer an attractive source of particles for testing the various proposed energy loss theories. The facts that μ-mesons are poor radiators and that their nuclear interactions are small are important points in their favor in such applications. In present day high energy physics many situations are encountered in which energetic charged particles are not stopped by conventional thicknesses of absorbers. We are forced, at best, to sample a particle's behavior as it passes through an absorbing slab of matter. Hence, we feel that it is of some importance to study the exact laws of interaction, energy loss, and straggling. Bowen and Roser have made a beginning in this direction by investigating anthracene absorbers (carbon) at specific meson energies. We have chosen to study NaI(Tl) because of its availability, high Z, high density and good proportionality between energy loss and light pulse output.[19] This publication presents a summary of our work to date.

APPARATUS

A sketch of the experimental layout is shown in Fig. 1. A, B, and C represent three NaI(Tl) crystals arranged in the form of a μ-meson telescope. Each of the three crystals is viewed by an appropriate photomultiplier. A C7157 photomultiplier is used with crystal B; 5819 photomultipliers are used with the other crystals. The photosurface of the C7157 is large enough so that the whole area of contact of the crystal B is viewed directly through a close-fitting light pipe. Crystals A and B are approximately two-inch cubes. The length of crystal B along the telescope axis is 2.17 inches. Crystal C is 2 in.×2 in.×4 in. Above and on the sides of the three-crystal-telescope are layers of

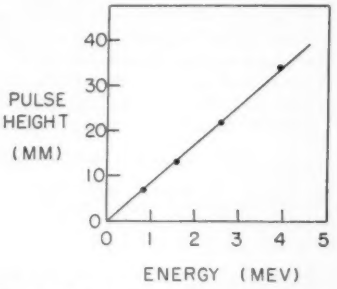

FIG. 2. The linearity curve used in this experiment.

[18] J. M. Jauch, Phys. Rev. **85**, 950 (1952).
[19] R. Hofstadter, Phys. Rev. **75**, 796 (1949); R. Hofstadter and J. A. McIntyre, Phys. Rev. **80**, 631 (1950).

lead six inches thick. The lead is used to separate, in a conventional way, the hard from the soft component. Between crystals B and C a three-inch layer of lead prevents mesons with energy less than 120 Mev from tripping the counter telescope. Connections are indicated schematically on the side of the figure and show that the pulses in the middle crystal become visible on the oscilloscope tube face when and only when a triple scintillation coincidence of all crystals occurs; the oscilloscope face is used as a coincidence device. A triple coincidence implies that each of the three crystals has been traversed, presumably by a μ-meson (see below). Biases are applied to the discriminator circuits of crystals A and C. Experiments with different biases above a minimum showed no changes in the pattern of pulses in crystal B.

The energy loss of the μ-meson in crystal B can be measured by the height of the light pulse.[19] Calibration of crystal B was achieved with the well-resolved pair and photolines of ThC″ (2.62 Mev) and C^{12*} (4.45 Mev) gamma-ray lines. The latter was obtained from a weak Po-Be source.

It will be assumed that the process of energy loss of mesons in NaI(Tl) is similar to that of electrons and therefore results in a linear relationship between energy loss and pulse height of the scintillation. Evidence obtained with electrons up to energies of $9mc^2$ (m = electron mass) completely supports such a linear relationship.[19] By using the stated pair and photolines a linearity curve could be constructed. Figure 2 shows such a linearity curve. For actual calibration, the sharp peak due to the ThC″ photoline was used.

The ordinate of Fig. 2, namely, the vertical deflection of the oscilloscope, was carefully examined for linearity with respect to magnitude of the input voltage pulse by using two independently calibrated artificial pulse sources. Up to deflections of 70 mm the deviation from linearity was less than 1 percent, which was about the experimental error in making measurements. To obtain 70 mm deflections on the Tektronix 511 AD oscilloscope, a single stage, push-pull supplementary amplifier was employed in addition to a Model 501 amplifier. The attenuator of the 501 amplifier was calibrated both with artificial pulses and with the photolines of known gamma-rays. Since the largest gamma-ray energy obtainable conveniently is 4.45 Mev, (the corresponding pair lines are at 3.43 and 3.94 Mev) and the range of cosmic-ray pulses centers about 27 Mev, an extrapolation of the photoline calibration had to be made. The actual factor used was 8.07. While we have made a careful attempt to avoid error in making this extrapolation to higher energies, the largest source of possible error in the experiment rests here. We believe that energies in the range 27 Mev can be measured to within 1.0 Mev or perhaps a bit less. The relative values of energy loss are not affected by an error in absolute calibration.

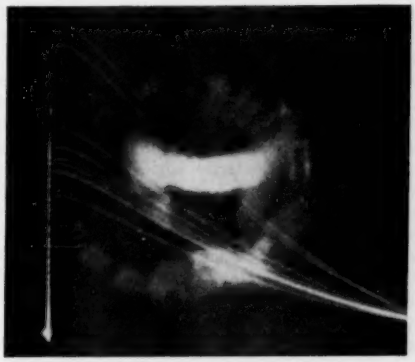

FIG. 3. A sample of exposed film showing representative traces. The tail of a very large pulse may be seen at the right. The irregular bright pattern in the center and the surrounding bright patch are due to glow from the filament of the oscilloscope tube.

In order to test whether different parts of the crystal cube B produced pulses of varying sizes, we have taken pictures of the pulse distribution produced by a collimated Co^{60} gamma-ray source. The gamma-beam was directed at different areas of the crystal, but in all cases the pulse distributions were found to be very similar. The sharp lines of the calibration photographs provide further confirmation of the uniformity of different parts of the crystal.

Single traces of oscilloscope pulses in the middle crystal were photographed by an f2.5 10-in. focal length lens on 3 in.×4 in. sheets of cut film. Each exposure lasted fifteen minutes and on the average eight traces appeared. The traces were measured directly against ruled millimeter paper and the pulse heights so obtained were grouped into seventy channels each one millimeter wide. Figure 3 shows a sample of an exposed film with several traces visible. Occasionally, more than one pulse of the same height was recorded during a fifteen-minute exposure. A little practice in observation soon showed that the greater opacity of a double trace could easily be distinguished from that of a single trace. Very rarely, a triple trace was observed. In addition to these types of multiple traces, two examples in about 3000 traces were observed in which a time coincidence occurred within the sweep duration of 100 microseconds.

In order to detect possible changes of pulse heights due to drift of photomultiplier voltage supply, amplifier gain, etc., approximately once every four hours a calibration point was taken with a ThC″ source. Over the eighty hours of running time (actual operating time ~200 hours) a gradual drift towards smaller pulses occurred. At the end of operating time the accumulated drift amounted to 3 percent. The data were corrected according to the two calibrations between which the data were sandwiched. Therefore, it is felt that no systematic error has occurred due to drift.

We have checked the observed triple coincidence counting rate against the known meson flux at sea level (0.82 meson/cm² per steradian in the vertical direction under six inches of lead[20]) in the following way. A full scale skeleton model was constructed of the three cross-sectional areas of the crystals in the telescope. With this model meson traces could be projected through all crystals. The effective solid angle accepted by the telescope for each 0.6 cm² area of crystal B could be measured by measuring areas in the model. Furthermore, the mean path length traversed by mesons in crystal B could also be found. This length exceeds the thickness of crystal on the average by only one part in two hundred, due to the slight obliquity of some meson paths. Using the solid angles measured on the model and the known meson flux quoted above, the expected meson counting rate was 8.3 counts per 15 minutes. Figure 4 shows a histograph of the observed counting rate. The mean observed value is 8.0±0.5 count per 15 minutes. The agreement is good and indicates that the triple coincidences are indeed due to μ-mesons.

Preliminary experiments were carried out with a crystal of NaI(Tl), 0.53-in. thick, under conditions of better geometry but lower counting rate. In this case only a small extrapolation of pulse height is required to calibrate the crystal. The results of this earlier work are in agreement with those obtained with the 2.17-in. crystal B. However, the experiment was carried on for a shorter time and the statistical accuracy is considerably less than that obtained with the 2.17-in. crystal. For this reason the detailed results with the 0.53-in. crystal will not be reported.

It is to be noted that the μ-meson range is not measured in this experiment and, consequently, mesons of all energies exceeding a minimum contribute to the observed pulse spectrum. In this respect our experiment differs from that of Bowen and Roser[13] in which several distinct energy intervals were simultaneously studied. However, our results do not require correction for scattering in lead absorbers, as in the work of Bowen and Roser.

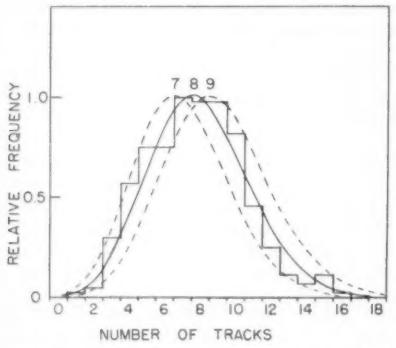

FIG. 4. Histograph of the observed counting rate and Poisson curves for mean counting rates of 7, 8, 9 counts per fifteen minutes.

[20] B. Rossi, Revs. Modern Phys. **20**, 537 (1948).

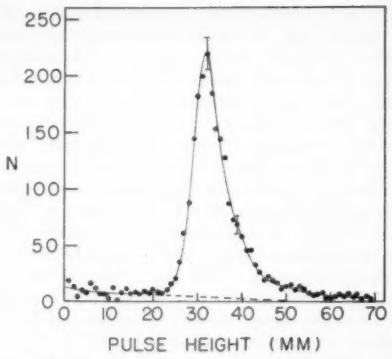

FIG. 5. The pulse distribution after 80 hours of running time. The ordinate represents the number of pulses in a one-millimeter channel.

RESULTS

The pulse distribution obtained after 80 hours of running time is shown in Fig. 5. The units of abscissas are actual millimeters of trace on the oscilloscope screen. When the data are translated into energy loss by means of the calibration curve, the experimental pulse distribution has the appearance of the solid line of Fig. 6. If it is assumed that the errors are purely statistical in nature, representative limits of error may be found. Such limits are shown at two points on the curve.

In Fig. 6 a small background effect has been subtracted from the data of Fig. 5. The dashed line in Fig. 5 represents the background effect, which is believed to be due to two causes: (1) showers which activate all crystals simultaneously are occasionally counted and (2) the middle crystal B was $\frac{3}{32}$ in. out of exact alignment with the other two crystals. The shower effect has been estimated by an independent experiment and is represented by the black circles in Fig. 7. These points were obtained in an 80-hour background run when the middle crystal was deliberately placed $2\frac{3}{32}$ in. out of line with the other crystals. It may be noted that there are virtually no pulses in the region of the peak of Figs. 5 or 6. This behavior is very satisfactory and is an additional check on the fact that single particles (μ-mesons) produce the observed triple coincidences.

In the actual experiment the alignment was not exact and, as stated above, the middle crystal was $\frac{3}{32}$ in. out of line. This can account for a small number of pulses due to μ-mesons passing through corners and edges of the middle crystal. These pulses will naturally also be small in magnitude.

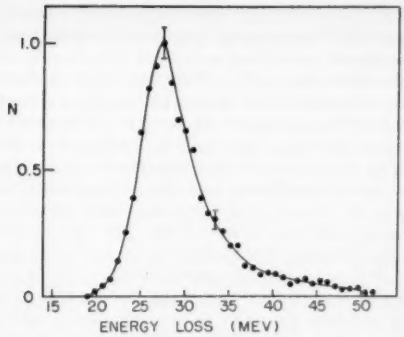

FIG. 6. The pulse distribution after calibration and correction for background pulses.

If we assume that the shower contribution to the pulse distribution when the crystals are in line is about the same or possibly a little larger than the black circles measured in the out-of-line experiment, then the contribution of showers and small pulses ($\frac{3}{32}$ in. out-of-line effect) will account completely for the background. Our best estimate for this combined effect is shown by the dotted line in Fig. 5. Although the choice is a bit arbitrary, the correction is quite small and has no important influence on the final results.

We have considered the possible effect of protons in producing distortion of the meson pulse distribution, but from the work of Miller *et al.*[21] the number of protons at sea level is too small to be observed in this experiment.

COMPARISON WITH THEORY

In order to compare these results with theory we have had to compute various pulse distributions based on (a) the Landau straggling theory, (b) the cosmic-ray μ-meson spectrum, (c) the assumed nature of the energy loss curve, *viz.*, Bethe-Bloch or Halpern-Hall, etc. In each case the assumed theory (c) was folded together with (a) and (b) in numerical integrations.

The Landau formula[22] for the most probable energy loss Δ_0 for monoenergetic heavy charged particles of velocity v, ($\beta=v/c$) and charge e, has the form,

$$\Delta_0=\xi[\ln(\xi/\epsilon')+0.37], \tag{1}$$

where

$$\xi=(2\pi Ne^4\rho x/mv^2)(\textstyle\sum Z/\sum A), \tag{2}$$

and

$$\ln\epsilon'=\ln\frac{(1-v^2/c^2)I^2}{2mv^2}+\frac{v^2}{c^2}. \tag{3}$$

In these formulas m is the mass of the electron, N is Avogadro's number, x is the thickness of the crystal in cm, ρ its density, Z and A the atomic number and mass number of the crystal material. $I=13.5Z$ ev has been used by Landau and others and is a constant which measures the average ionization energy of the atom in the Bethe-Bloch theory.

The mean energy loss α is expressed as

$$\alpha=\xi\ln(E_0/\epsilon'), \tag{4}$$

where E_0 is the maximum energy that a meson can transfer to an electron in a single collision, i.e., it is the maximum energy of a δ-ray. E_0 is given by a formula of Bhabha. The Bhabha formula may be approximated for incident meson energies less than 20 Bev by the quite accurate but more suggestive formula,[23]

$$E_0=2mc^2\beta^2/(1-\beta^2). \tag{5}$$

If we wish to calculate the mean energy loss of a meson, we must use expression (4), substituting for E_0 the value given in Eq. (5). However, if we wish to calculate the mean energy deposited in the crystal slab, we must use Eq. (4) but must now substitute for E_0 the maximum transferable energy E_1 of those δ-rays that can be completely absorbed in the crystal. For a sample of the size of crystal B, E_1 might be 10 or 20 Mev allowing for radiation losses. On the other hand, E_0 is quite different from E_1 and might be $E_0=100$ Mev for a 1-Bev meson and $E_0=300$ Mev for a 10-Bev meson. Thus the mean energy deposited in the crystal will be limited by the value E_1.

It has been shown by Bohr, the result being fairly intuitive, that we may use the mean value formula in computing the most probable value of energy loss if we substitute for E_0 in Eq. (4) that upper bound of δ-ray energy E_2, which occurs once on the average as the meson traverses the crystal. Bohr has shown that $E_2=\xi$. By substituting $E_2=\xi$ for E_0 we shall obtain the Landau expression for Δ_0 except for the constant 0.37ξ

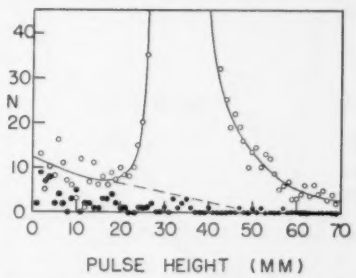

FIG. 7. The lower part of the observed pulse distribution is given by the open circles. The full circles represent the results of an 80-hour run with the middle crystal offset by $2\frac{3}{32}$ in. from the telescope axis.

[21] Miller, Henderson, Potter, and Todd, Phys. Rev. **84**, 981 (1951).

[22] The effect of using Symon's calculations in place of Landau's is negligible in this experiment. For example, even in the lowest bracket (225–500 Mev/c) the average fractional energy lost is not more than 10 percent.

[23] See reference 5, formulas (1.5) and (1.5a).

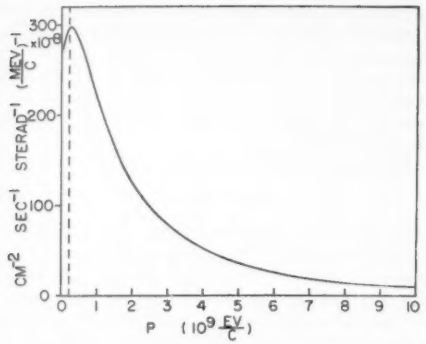

FIG. 8. The cosmic-ray spectrum when filtered by six inches of lead. The dashed line on the left cuts off all those mesons with momenta insufficient to pass through the three inch lead absorber and still give a pulse larger than the bias of crystal C (12 Mev).

which is generally small. Thus the exact Landau result may be made more readily understandable. In the case of crystal B, $\xi = 1.35$ Mev and falls within a range easily absorbed by the crystal.

Now the Landau theory may be used with and without a density correction. Without a density correction we shall refer to Δ_0 and resulting curves as the Bethe-Bloch values. With the density correction we shall refer to these as the Halpern-Hall values. The Halpern-Hall (and also Fermi) density correction essentially removes the factor $1/(1-\beta^2)$ from the logarithm of Eq. (1). The exact correction factor which we have used has been taken, however, from the published curves of Halpern-Hall[9] (their Fig. 1), and is applied to the most probable value Δ_0 directly as we would have applied it to the mean energy loss. After Δ_0 is calculated, the straggling curve is taken directly from Landau's universal curve. Individual straggling curves for selected momentum intervals are folded together

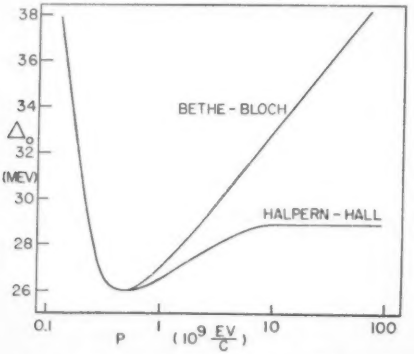

FIG. 9 A plot of the most probable energy loss Δ_0 against momentum for crystal B.

according to the weight of the corresponding momentum interval in the cosmic-ray spectrum. Nineteen momentum intervals were used.

In calculating the final theoretical curves, it is necessary to consider three further points: (A) the cosmic-ray spectrum is modified by the 6 in. of Pb above the counter telescope. The modified distribution is shown in Fig. 8. The final effect of the filtered distribution is not noticeably different from that of the original spectrum. (B) Some of the δ-rays may have high enough energies, and may be formed near the crystal surfaces so that they may emerge from the crystal before giving up all their energy. The experimental straggling curve may be distorted for this reason on the high energy side and may appear to be narrower than it really is. However, it may be seen from Figs. 5 and 6 that all the significant observations (those with better statistics) and comparisons with theory are made in the neighborhood of the most probable energy loss and just a few Mev larger. A rough evaluation of the solid angle available to those mesons traveling near the faces of the crystal which might produce δ-tracks of 5 Mev or larger in the proper directions to escape the crystal shows that this effect is of the order of about 5 percent at 5 Mev from the peak. This effect is therefore rather small in making the comparisons of theory with our present experiments. Further, the choice of ξ in the theory of Landau is consistent with these considerations. (C) Since NaI(Tl) has the two components Na and I,[24] the separate effects of each must be evaluated and combined. The combination has been effected by using a common[25] value of ξ for the compound material, NaI, in front of the logarithm of Eq. (1) and by adding

TABLE I. The momentum intervals of the modified mu-meson spectrum and the corresponding values of Δ_0.

Momentum interval (Mev/c)	Mean momentum (Mev/c)	Bethe-Bloch (Mev)	Halpern-Hall (Mev)	Percentage of modified mu-meson spectrum
225– 250	240	28.2	28.2	0.9
250– 500	375	26.1	26.05	9.5
500– 1000	750	26.5	26.05	16.3
1000– 1500	1250	27.8	26.9	12.2
1500– 2000	1750	28.4	27.3	9.2
2000– 3000	2500	29.3	27.6	13.0
3000– 4000	3500	30.2	28.15	8.5
4000– 5000	3400	30.8	28.35	5.6
5000– 6000	5500	31.4	28.58	4.0
6000– 7000	6500	31.9	28.7	2.8
7000– 8000	7500	32.3	28.8	2.1
8000–10,000	9000	32.7	28.8	3.1
10,000–12,500	11,250	33.3	28.9	2.8
12,500–16,000	14,000	34.0	28.9	2.5
16,000–20,000	18,000	34.2	28.9	1.8
20,000–30,000	25,000	35.9	28.9	2.5
30,000–40,000	35,000	36.4	28.9	1.3
40,000–60,000	50,000	37.3	28.9	1.3
60,000–80,000	70,000	38.2	28.9	0.6

In addition to the most probable energy loss, the mean energy loss is also of interest. The mean energy loss is given by the Bethe-Bloch formula. Values of the mean energy loss for the momentum intervals of Table I are given in the fourth column. The Bethe-Bloch values are given in the third column. The Halpern-Hall values are given in the fifth column. The last column gives the percentage of the modified mu-meson spectrum in each momentum interval.

[24] The percentage of thallium (<0.5 percent) is considered negligible.

[25] We wish to thank Mr. T. Bowen for suggesting this procedure.

the two separate contributions for each material with the appropriate values of I in each case. The latter differ according to the values of the mean ionization potentials of sodium and iodine. The values of the mean ionization potentials were taken as $11.8Z=130$ ev for sodium and $9.7Z=514$ ev for iodine according to the recent work of Bakker and Segrè and Mather and Segrè.[26] When the combination is made in this way, the mean ionization potential for NaI is obtained as:

$$(\bar{I})^2=I_{\mathrm{Na}}{}^{2(0.172)}I_{\mathrm{I}}{}^{2(0.828)}, \tag{6}$$

where 0.172 and 0.828 are the respective electronic compositions of Na and I, respectively. The calculation of Halpern-Hall, of course, has not been made specifically for NaI and a similar combination of effects has been made for the density correction. In the case of this correction, the difference between assuming pure

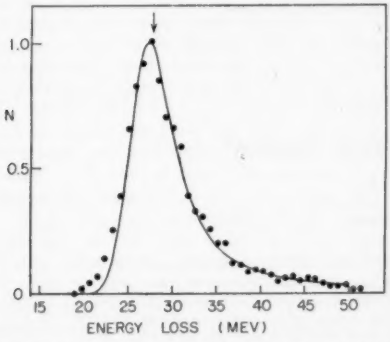

FIG. 10. The solid line gives the result of the calculated distribution based on the Halpern-Hall theory. The black circles are the experimental points. The theoretical curve actually shows a peak 0.4 Mev to the right (arrow position) but has been shifted to permit better comparison with experiment.

iodine and the actual compound is barely worth considering.

When the effects of (A), (B), and (C) above are taken into account, two theoretical curves are obtained according as one uses the Bethe-Bloch formula (uncorrected for the density effect) or that of Halpern-Hall. For further reference the experimental curves may also be compared with the Landau relation for a single energy in the neighborhood of the mean energy of the cosmic-ray spectrum. Table I and Fig. 9 show the various values of Δ_0 which have been calculated in the appropriate cases. The effect of making the various choices for comparison is shown in Figs. 10, 11, and 12. The energy loss is observed to show a saturation in Fig. 9 because of the density effect and because of the cut-off δ-ray energy in the neighborhood of ξ. When the contributions of all energy intervals in the cosmic-

[26] C. J. Bakker and E. Segrè, Phys. Rev. **81**, 489 (1951); R. Mather and E. Segrè (to be published).

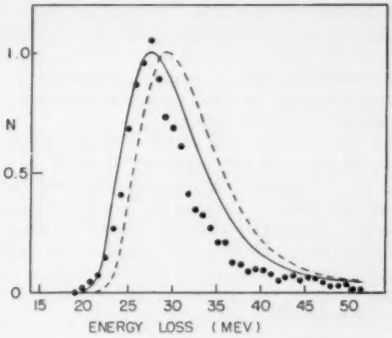

FIG. 11. The dashed curve gives the result of the calculated distribution based on the Bethe-Bloch theory without inclusion of a density correction. The solid line gives the same curve shifted by two Mev to permit better comparison with experiment.

ray spectrum are added together, the Halpern-Hall theory gives the solid curve of Fig. 10 and the Bethe-Bloch theory gives the dashed curve of Fig. 11. A single Landau curve for the meson energy 2.0 Bev (Halpern-Hall curve) is given by the solid line in Fig. 12.

Because of the small experimental uncertainty in the peak values (originating in the uncertainty of the extrapolation of the calibration data), the Bethe-Bloch and Halpern-Hall theoretical curves have been shifted to fit the experimental curve more closely. The shift required is 2 Mev for the Bethe-Bloch curve and 0.4 Mev for the Halpern-Hall theory. It is believed that a 2.0-Mev shift is outside our experimental error but a 0.4-Mev shift would be well inside our limits of precision. It is therefore observed that the fit with the Halpern-Hall theory is much better than with Bethe-Bloch both as regards the absolute value of the most probable energy loss as well as the shape of the straggling curve. In the latter case the Bethe-Bloch theory without the density effect shows a wide divergence

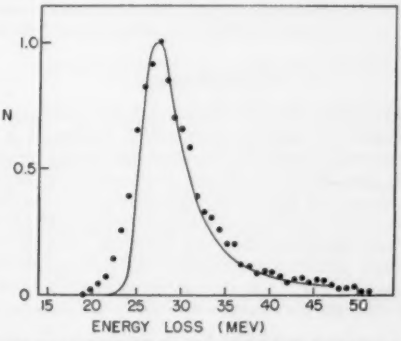

FIG. 12. The solid line gives the distribution calculated for a single meson energy of 2.0 Bev, using the Halpern-Hall theory.

from the experimental shape. The single Landau curve, Fig. 12, also fits less well than the Halpern-Hall theory although the difference here is not so striking. It seems quite interesting that, to a good approximation for these experiments, the entire cosmic-ray spectrum may be replaced by a single energy.

The fact that the peak of the Halpern-Hall curve agrees so well with the experimental curve may be taken as an indication that a small relativistic rise is present (see Table I). Thus our results are in agreement with those of Bowen and Roser who find evidence of saturation in the Halpern-Hall model of anthracene. Our experimental curve does, however, show a small divergence from the theoretical Halpern-Hall curve. The reason for this is not known at present.

CONCLUSION

It appears that the density or polarization effect is observed in NaI(Tl) as well as in anthracene (Bowen-Roser) and that a small relativistic rise probably exists in NaI(Tl). It would be desirable to improve the measurements of absolute energy-loss, the statistical accuracy of the data, and to use monoenergetic mesons, so that folding-in of the cosmic-ray spectrum will become unnecessary. We hope to do further work along all these directions. It is interesting that NaI(Tl) appears to be linear in the range of high meson energies in the cosmic rays, a result that might have been anticipated from previous experiments with other charged particles.

We wish to thank Dr. Sidney Drell for his very kind help in considering many of the theoretical aspects of this problem and also for his independent calculations of energy loss. We also wish to thank Dr. J. A. McIntyre for help in packaging the NaI(Tl) crystals. Finally we appreciate greatly the kindness of Dr. Burton Moyer, of the University of California, in lending us, from time to time, his Po-Be source.

PHYSICAL REVIEW VOLUME 88, NUMBER 3 NOVEMBER 1, 1952

Electron Diffraction from Small Crystals*

CHESTER R. BERRY
Kodak Research Laboratories, Rochester, New York
(Received April 14, 1952)

Small crystals of silver and silver bromide were studied by electron diffraction. Small crystals of these materials are of interest because published experimental and theoretical considerations indicate changes in their structure which may occur. Since the diffraction theory which is applicable to large crystals cannot always be used in interpreting the photographs from materials of small size, computations were made for crystal structures and shapes which might be expected for silver and silver bromide. As a result of the computations, it was found that positions of diffraction peaks of substances having the sodium chloride structure depend on the crystal shape. It was also shown that the determination of particle size by the usual method of the Scherrer equation may give values which are much too small. Comparison of experimental and theoretical diffraction effects indicates that small silver particles have the same structure as the large particles, but that there is a real contraction of the lattice in the smaller particles which amounts to 2.7 percent for particles with a diameter of about 31A. The small silver bromide particles have the same structure as the large particles, and an apparent expansion of the silver bromide lattice of about 1.0 percent appears to be best explained not as an expansion but as a particle-shape effect which changes the position of the diffraction peak. The crystals appear to be plates bounded by (111) faces, just as in many photographic emulsions, although this is not the usual form of crystals having this structure.

INTRODUCTION

BECAUSE there are differences between the surface and the internal properties of crystals, it is of interest to compare the characteristics of large crystals with those of very small crystals in which the surface to volume ratio is relatively high. Scattering of electrons from small crystals is sufficiently strong to permit an electron-diffraction study to be made. Boswell[1] has recently published some results obtained by electron diffraction from small crystals of alkali halides, gold, and bismuth. He reports a decrease in lattice constant with decrease in particle size in the diameter range below 100A. The decrease is attributed to a surface-tension effect predicted by Lennard-Jones and Dent.[2]

The substances studied here are silver and silver bromide. Silver is of particular interest in view of Quarrell's[3] observation of many cubic close-packed metals which appeared to begin their growth with the hexagonal close-packed structure. A theoretical study of the lattice energies of the silver halides by Huggins[4] indicates a small difference in the energies of silver

* Communication No. 1488 from the Kodak Research Laboratories.

[1] F. W. C. Boswell, Proc. Phys. Soc. (London) **A64**, 465 (1951).

[2] J. E. Lennard-Jones and B. M. Dent, Proc. Roy. Soc. (London) **A121**, 247 (1928).

[3] A. G. Quarrell, Proc. Phys. Soc. (London) **49**, 279 (1937).

[4] M. L. Huggins, J. Chem. Phys. **11**, 412 (1943).

bromide in the sodium chloride type of structure and in the zinc sulfide types of structure, and he suggests that under some circumstances, particularly at the surface, a transition from the normal sodium chloride structure may be expected. Silver bromide is also of interest because of its photographic behavior and because of its abnormally large number of lattice defects.

In interpreting electron-diffraction patterns from thin films of gold and copper, Germer and White[5] have calculated the diffraction effects to be expected from small spherical particles of face-centered cubic structure in random orientation. This type of analysis has been extended to crystals of various structures, shapes, sizes, and orientations to permit more detailed interpretation of the experimental results.

EXPERIMENTAL

Small crystals of silver or silver bromide were formed by vacuum evaporation in the electron-diffraction instrument. The deposits were collected on thin cellulose membranes and were observed by transmission. No attempt was made to determine the average thickness of the deposits, since it was considered that the size of the crystals was the important factor and this could best be determined from the diffraction patterns. A calibrating substance, usually potassium bromide, was formed on the reverse side of the cellulose support by vacuum evaporation.

It was found that a considerable concentration of small particles of silver could be readily produced. Control of the amount of material evaporated could be conveniently managed merely by observing the silver-diffraction pattern on the fluorescent screen. Diffraction patterns from crystallites having diameters of about 30A could be seen clearly. However, this was not the case with silver bromide, which tended to form a small number of relatively large particles.

It was possible to obtain satisfactory microphotometer traces of the (111) reflection from the small silver particles and to compare its position with the lines of the potassium bromide calibrating substance, whose lattice constant was assumed to be 6.586 Kx as given by Wyckoff.[6] To determine the breadth of the reflection at half-maximum intensity, it was assumed that density on the photographic plate was proportional to exposure. The positions of many (111) reflections from silver particles of various sizes were also determined visually on a plate-measuring device. The Bragg spacing of the (111) reflection was as small as 2.292 Kx in some cases, compared to the value for large particles of 2.355 Kx. This difference in values agrees with the observations of Boswell[1] on many materials, although the decrease of 2.7 percent is larger than in any of the materials which he studied.

The half-maximum intensity breadth of a reflection may be conveniently expressed as $2\Delta\theta/2\theta$, where 2θ is the scattering angle for the reflection and $2\Delta\theta$ is the angular breadth of the reflected beam at half-maximum intensity.

For the broadest (111) reflection observed, the half-intensity breadth expressed as $2\Delta\theta/2\theta$ was about 0.11. The geometrical breadth due to instrumental factors was about 0.02.

Since most of the patterns of small silver bromide particles were not sufficiently strong to give good microphotometer traces, the peak position of the innermost (200) ring was determined by visual estimation. There was considerable variation in the results obtained for particles of a given apparent size, but the observations of a large number of plates were used in determining the final results. It was found that the Bragg spacing of the reflection increased with decreasing particle size, quite the opposite effect from that occurring with silver and from that observed by Boswell for a large number of substances having the sodium chloride structure. The maximum effect observed was an increase of about 1.0 percent. This unusual behavior made it desirable to reconsider the experimental conditions for a possible source of the discrepancy. The only possibility which suggested itself was that some of the potassium bromide calibrating substance had come in contact with the silver bromide on the support and had expanded the silver bromide lattice by solid solution or by strained epitaxial growth of silver bromide on the potassium bromide. To detect any lattice expansion by the calibrating material, several exposures were made using, in place of KBr, LiF, in which each ion is smaller than the corresponding ions in silver bromide. Since, in this case, the Bragg spacing of the (200) silver bromide reflection again increased with decreasing particle size, it was concluded that the behavior was characteristic of silver bromide.

One particularly good plate having an intense, broad silver bromide pattern could be examined with the microdensitometer, and the measurement gave a Bragg spacing which was 0.8 percent greater than the normal value for large particles and a half-intensity breadth of about $2\Delta\theta/2\theta = 0.08$.

CALCULATED DIFFRACTION EFFECTS FOR SMALL CRYSTALS

Germer's[7] experiments on the diffraction of electrons from small metal particles gave results which could not be interpreted readily in terms of diffraction theory for large particles. However, Germer and White[5] were able to explain some of the effects on the basis of calculations, using the gas-scattering equation, which gives the intensity of electrons scattered from small groups of atoms in random orientation. The equation for this scattering is of the form given by Debye[8] for the scat-

[5] L. H. Germer and A. H. White, Phys. Rev. **60**, 447 (1941).
[6] R. W. G. Wyckoff, *Crystal Structures* (Interscience Publishers, Inc., New York, 1948), Vol. I.
[7] L. H. Germer, Phys. Rev. **56**, 58 (1939).
[8] P. Debye, Ann. Physik (4) **46**, 809 (1915).

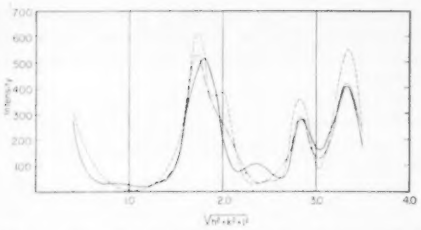

FIG. 1. Calculated diffraction patterns for silver crystals. – – – Sphere of 201 atoms, cubic structure; —— Plate of 183 atoms, cubic structure; —— Plate of 183 atoms, hexagonal structure.

tering of x-rays and may be written as:

$$I = f(\theta)\sum_j \sum_k f_j f_k \sin(4\pi l_{jk}\sin\theta/\lambda)/(4\pi l_{jk}\sin\theta/\lambda),$$

where θ is half the scattering angle; $f(\theta)$ is a monotonically decreasing function on which are superimposed the maxima and minima of the double summation; f_j and f_k are the scattering amplitudes of the jth and kth atoms; l_{jk} is the separation of the jth and kth atoms within an individual crystal; and λ is the wavelength of the radiation. This relation has been used here in making similar computations and the values of $f(\theta)$, f_j, and f_k have been made equal to unity.

In addition, it was desirable to consider the diffraction effects to be expected from crystals in uniaxial orientation in the direction of the electron beam. This type of orientation will occur when crystals having well-developed faces are deposited on a smooth support, the face being always parallel to the support and perpendicular to the electron beam. In this case, it can be shown that the scattered intensity may be written:

$$I = f(\theta)\sum_j \sum_k f_j f_k \cos[2\pi S_{jk}(1-\cos 2\theta)/\lambda] \times J_0(2\pi D_{jk}\sin 2\theta/\lambda),$$

where the quantities are defined as above, and in addition S_{jk} and D_{jk} are the components of separation of the jth and kth atoms along the direction of the electron beam and perpendicular to the direction of the electron beam, respectively; and J_0 is the Bessel function of zero order. In the case of a single layer of atoms, S_{jk} is zero, and the summation contains only the Bessel function. Also, for small particles of only a few layers thickness and at small angles, $S_{jk}(1-\cos 2\theta)$ is so small that the intensity is dependent only on D_{jk}.

Since the position, intensity, and breadth of a diffraction line can be determined experimentally, the dependence of these characteristics on particle size, shape, and structure was calculated. For the close-packed cubic structure and particles of spherical shape, Germer and White[5] made the calculations plotted in Fig. 3 of their paper for particles of many sizes. For 379 atoms, corresponding to an external diameter of 26.0A for silver, having the normal lattice constant, the pattern begins to look much like that for infinitely large particles. The first peak occurs at a position 1.73 in terms of $(h^2+k^2+l^2)^{\frac{1}{2}}$ and has a half-intensity breadth of 0.13. If the Scherrer[9] equation is used to compute the particle size from this value of line breadth, the particle size obtained is too small. For example, if the coefficient 1.11 is used in the Scherrer equation, which Patterson[10] computed for a spherical particle, the resultant size is 20.1A. If Boswell's scheme of using the coefficient 0.9 is followed, a particle size of only 16.4A is obtained.

In order to determine the effect of particle shape and structure on the diffraction curves, computations were made here for three kinds of particles in random orientation: a sphere of 201 atoms (exterior diameter of 21.2A for silver) in the cubic close-packed structure, a plate of 183 atoms consisting of three 61-atom close-packed layers (having breadth of 27A and thickness of 7.6A) in cubic stacking, and a plate of 183 atoms consisting of three 61-atom close-packed layers in hexagonal stacking. The number of atoms in these particles is apparently somewhat less than in the smallest silver particles observed experimentally, but this was done to reduce somewhat the very lengthy computations involved. The results are shown in Fig. 1. For both the cubic structures, the first maximum occurs at $(h^2+k^2+l^2)^{\frac{1}{2}}=1.73$, and the next peak at $(h^2+k^2+l^2)^{\frac{1}{2}}=2.00$ begins to appear. It is difficult to distinguish between the spherical and platelike shape from the diffraction patterns. The hexagonal structure gives a peak position and shape which are quite different from those of the cubic structure. Computations for the platelike crystals with uniaxial orientation showed a first maximum of intensity only at $(h^2+k^2+l^2)^{\frac{1}{2}}=2.83$. The diffraction patterns from the smallest particles of silver observed showed partial resolution of the (200) peak, thereby eliminating the possibility of a hexagonal structure in these crystals. The smallest particles of silver observed were therefore of the usual cubic structure, the lattice constant was about 2.7 percent smaller than that of bulk material, and the size was that expected for spheres of about 31A diameter.

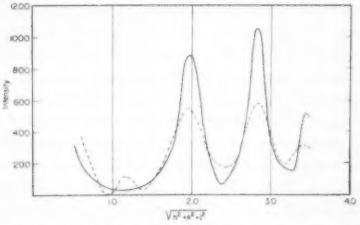

FIG. 2. Calculated diffraction patterns from crystals with sodium chloride structure. Hexagonal plates bounded by (111) faces. – – – Four 19-atom layers (intensity scale expanded four times); —— Six 61-atom layers.

[9] P. Scherrer, Nachr. Ges. Wiss. Göttingen, Math.-physik. Klasse, No. 2, p. 98 (1918).
[10] A. L. Patterson, Phys. Rev. **56**, 972 (1939).

Computations were also made for the diffraction patterns to be expected for small crystals of the NaCl structure in random orientation for flat plates with (100) faces and with (111) faces, as well as for more nearly spherical particles. To simplify the computations, $f(\theta)$, f_j, and f_k were again taken as unity. This means that the scattering of the positive and negative ions in the structure is assumed to be equal. In contrast with the situation for the silver structure, the particle shape has a definite effect on the position of the first maximum. In Fig. 2, there is shown the diffracted intensity from hexagonal-shaped plates containing alternate (111) planes of anions and cations, which is often the shape of grains observed in photographic emulsions. The two curves are for the cases of four 19-atom layers (20A in breadth and 7.8A thick) and for six 61-atom layers (37A in breadth and 11.2A thick). The (200) peak positions are shifted to smaller values of angle from that for large particles and occur at $(h^2+k^2+l^2)^{\frac{1}{2}}=1.97$ and $(h^2+k^2+l^2)^{\frac{1}{2}}=1.98$ for the 76-atom and 366-atom particles, respectively. Further computations indicate, for about 100 atoms in the particle, that the peak position shifts to smaller angles the greater the departure from spherical toward plate shape. The effect of the (111) plate shape is to give an apparent increase in lattice constant.

In Fig. 3 are given curves for the diffraction from plates in random orientation made up of (100) planes in the NaCl structure. The cases considered are for two 25-atom layers in a square array (15.4A edge length and 6.8A thick) and for three 25-atom layers (15.4A edge length and 9.7A thick). Here, the (200) peak positions are shifted to larger values of angle from that for large particles and occur at

$$(h^2+k^2+l^2)^{\frac{1}{2}}=2.02 \quad \text{and} \quad (h^2+k^2+l^2)^{\frac{1}{2}}=2.01$$

for the 50-atom and 75-atom arrays, respectively. Computations for small crystals having uniaxial orientation about the (100) and (111) axes show maxima which are not noticeably displaced from those observed for large crystals with the same orientations.

Hence, the apparent increase of lattice parameter of small silver bromide crystals is the result of their crystallization as plates bounded by (111) faces. Electron micrographs of 350A silver bromide crystals formed by vacuum evaporation were prepared to check this conclusion concerning crystal shape. There was a definite tendency for the hexagonal shape to occur, although regular hexagons were observed in only about one crystal in ten. It is interesting that this shape of

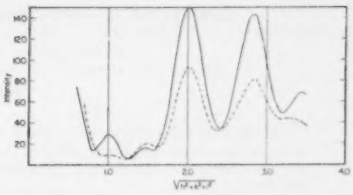

FIG. 3. Calculated diffraction patterns from crystals with sodium chloride structure. Square plates bounded by (100) faces. – – – Two 25-atom layers; —— Three 25-atom layers.

the silver bromide crystals occurs, since Mitchell[11] suggests that crystallization with (100) faces would be expected except when the crystals are formed from solutions under special conditions. Since the half-intensity breadth of the experimental diffraction curve of the smallest particles is only about half as great as that calculated for the 366-atom particle, the crystals observed experimentally must be somewhat larger than 500 atoms. Another conclusion which is derived from consideration of the curves in Fig. 3 is that the apparent decrease in lattice constant of small crystallites of the alkali halides observed by Boswell may be caused, at least in part, by their crystallization as plates bounded by (100) faces.

Possible reasons for an actual lattice expansion of small particles of silver bromide were considered. According to Huggins, an expansion of the lattice would be expected in the transition from the NaCl to the ZnS cubic structure. However, the relative intensities of the diffraction lines in these two structures are quite different, and the existence of the NaCl structure is indicated by the strong (200) reflection and the absence of the (111) reflection. The presence of Frenkel defects in the crystals would cause a lattice expansion. If we assume, according to Lawson,[12] that the production of 2 percent Frenkel defects in silver bromide causes a volume increase of 0.2 percent, then a lattice constant increase of 1 percent would require an impossible number of about 30-percent defects. The particle-shape effect appears to give the most logical explanation for the peak position observed in the silver bromide patterns, but there may be in addition real changes in the lattice constant which are obscured by the shape effect.

[11] J. W. Mitchell, "The nature of sensitivity centers and the formation of the latent image in the grains of chemically non-sensitized emulsion," contribution to Paris Photographic Conference, 1951 (to be published).

[12] A. W. Lawson, Phys. Rev. **78**, 185 (1950).

Inelastic Collision Cross Sections for 14-Mev Neutrons*

D. D. PHILLIPS, R. W. DAVIS, AND E. R. GRAVES
University of California, Los Alamos Scientific Laboratory, Los Alamos, New Mexico
(Received July 21, 1952)

The inelastic collision cross sections of a number of elements for 14-Mev neutrons have been measured, using threshold detectors inside spherical shells of the scattering material. Reactions in copper, aluminum, and phosphorus with thresholds at approximately 11.5 Mev, 2.6 Mev, and 1.4 Mev were used as threshold detectors.

I. INTRODUCTION

THE purpose of the present experiment is to measure the neutron cross section of various elements for processes other than elastic scattering. This type of cross section will be referred to as inelastic collision cross section. The method used was essentially the same as that described by Gittings, Barschall, and Everhart for their measurement of the inelastic collision cross section of lead for 14.5-Mev neutrons.[1] In this method the neutron transmission through spherical shells of the material under investigation is observed. The neutrons are detected by means of threshold detectors. It is assumed that the threshold detector has the same sensitivity for elastically scattered neutrons as for the primary neutrons and does not detect neutrons which have been inelastically scattered to energies below the threshold of the detector. For a thin shell the effect of elastic scattering on the transmission should be small since the neutrons scattered into the detector should compensate those neutrons which are scattered out of the direct path between the source and the detector. A detailed analysis of this assumption has been made and estimates of its rigor derived.[2] The analysis justifies the use of the assumption.

In the past several investigators have used threshold detectors for measurements of inelastic collision cross sections for fast neutrons. Grahame and Seaborg[3] used reactions in iron and aluminum for a study of the inelastic scattering of neutrons from a RaBe source. Amaldi *et al.*[4] studied the inelastic scattering of Li+d neutrons by Al, Fe, Hg, and Pb by means of the $Cu^{63}(n,2n)Cu^{62}$ reaction.

In the present experiment the following three threshold reactions were used: $P^{31}(n,p)Si^{31}$, $Al^{27}(n,p)Mg^{27}$, $Cu^{63}(n,2n)Cu^{62}$, with thresholds at 1.4 Mev, 2.6 Mev, and 11.5 Mev, respectively. Since the reaction cross sections for the various threshold detectors rise slowly above the threshold, the effective thresholds are somewhat higher, i.e., approximately 2 Mev, 3 Mev, and 12.5 Mev. The use of different threshold detectors enables one to get a rough idea of the energy distribution of the inelastically scattered neutrons.

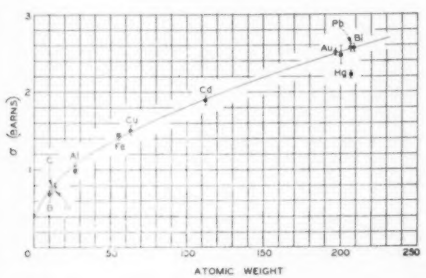

FIG. 1. Inelastic collision cross sections for 14-Mev neutrons measured with copper threshold detectors plotted against atomic weights. The smooth curve was calculated from the empirical relation $\sigma=\pi R^2$, where $R=(2.5+1.1\,A^{\frac{1}{3}})\times10^{-13}$ cm. The squares are values of Amaldi *et al.* taken from reference 4.

II. EXPERIMENTAL

Neutron Source

Neutrons were obtained from the $T(d,n)He$ reaction by bombarding a thick tritium target with 220-kev deuterons. The target consisted of a tungsten disk to which was fused a zirconium foil in which tritium had been absorbed.[5] The intensity of the neutron source was monitored by counting α-particles from the d-T reaction. Neutrons emitted at 90° with respect to the incident deuteron beam were used in the present experiment. These neutrons have an average energy of 14.15 Mev and an energy spread of approximately ±0.05 Mev.

Threshold Detectors

Cu^{62} formed in the $Cu^{63}(n,2n)$ reaction was found to have a half-life of 9.9±0.1 min. The yield of this reaction as a function of energy has been measured by Fowler and Slye,[6] and Forbes has measured the isotopic cross section at 14 Mev to be 0.506±0.035 barn.[7] Other activities which are induced in normal copper by neutrons are the 12.8-hr activity of Cu^{64} and the 5-min activity of Cu^{66}. The Cu^{64} activity may arise from an $(n,2n)$ reaction in Cu^{65} or an (n,γ) reaction in Cu^{63}. In

* Work performed under the auspices of the AEC.
[1] Gittings, Barschall, and Everhart, Phys Rev. **75**, 1610 (1949).
[2] D. D. Phillips, AEC Report AECU-404 (1949) (unpublished).
[3] D. C. Grahame and G. T. Seaborg, Phys. Rev. **53**, 795 (1938).
[4] Amaldi, Bocciarelli, Cacciapuoti, and Trabacchi, Nuovo cimento **3**, 203 (1946).
[5] Graves, Rodrigues, Goldblatt, and Meyer, Rev. Sci. Instr. **20**, 579 (1949).
[6] J. L. Fowler and J. M. Slye, Jr., Phys. Rev. **77**, 787 (1950).
[7] S. G. Forbes, Phys Rev. (to be published).

TABLE I. Effects of source distance and shell thickness on measured cross sections.

Sphere	Detector	Distance source to detector cm	Sphere Outer radius cm	Sphere Thickness cm	Transmission T	σ barns	Av σ barns
Bi	Cu	16.6	5.5	4.22	0.740±0.006	2.53±0.07	2.56±0.05
Bi	Cu	16.6	7.0	5.72	0.660±0.006	2.58±0.06	
Bi	Al	16.6	5.5	4.22	0.765±0.012	2.25±0.13	2.28±0.08
Bi	Al	16.6	7.0	5.72	0.689±0.012	2.31±0.11	
Bi	Al	27.4	5.5	4.22	0.761±0.015	2.30±0.15	
Fe	Cu	16.6	7.62	6.82	0.4315±0.005	1.45±0.02	1.45±0.02
Fe	Cu	16.6	7.62	6.24	0.463±0.029	1.46±0.12	
Fe	Cu	15.0	7.62	5.02	0.535±0.006	1.47±0.03	
Fe	Cu	35.5	7.62	5.02	0.541±0.008	1.44±0.04	
Fe	Al	15.0	7.62	5.02	0.595±0.007	1.22±0.03	1.21±0.03
Fe	Al	16.6	7.62	6.24	0.539±0.013	1.17±0.05	

spite of several attempts to observe the 5-min activity, no evidence for its presence was found in the present experiment. Since irradiations were carried out for only 10 or 15 minutes, the effect of the 12.8-hr activity was negligibly small compared to the 9.9-min activity.

The copper was used in the form of strips about 12 in. long and $\frac{3}{8}$ in. wide, which could be wound in the form of a helix and fitted into a cylindrical brass holder about 1.5 in. long and 1 in. in diameter. This holder could then be placed on a Geiger counter in a reproducible geometry. Foils of different thicknesses were tried. The best results were obtained with foils 0.003 in. thick. The foils were rolled up in tight spirals for irradiation.

The $Al^{27}(n,p)$ reaction leads to Mg^{27}, which has a half-life of 9.6±0.1 min.[8] The yield of this reaction has been measured by Bretscher and Wilkinson.[9] In addition to the (n,p) reaction, (n,γ) and (n,α) reactions may be produced in aluminum. Of these, only the effect of the (n,α) reaction was observed which leads to Na^{24} with a half-life of 14.8 hr. Since no irradiations longer than 20 minutes were used, the effect of the 14.8-hr activity was negligible. Al foils of the same size as the Cu foils were used except that a thickness of 0.008 in. was employed.

The (n,p) reaction of P^{31} leads to Si^{31}, the half-life of which has been variously quoted from 146 min to 3 hr. The present experiment indicated a half-life of 160±10 min. The yield of this reaction as a function of energy has been measured by Taschek.[10] In addition to the 160-min activity, an activity with a half-life of 2 or 3 min was observed which could have been produced by an $(n,2n)$ reaction or an (n,α) reaction. The irradiation times used varied from 80 minutes to 2 hours. By waiting about 20 minutes after an irradiation before counting was started, it was possible to eliminate the effect of the short-lived activity.

Phosphorus foils were prepared by impregnating polythene with red phosphorus.[11] Such foils contained 49.5 percent P by weight. They were cut in strips $\frac{1}{2}$ in. wide and about 0.005 in. thick.

Some difficulties were encountered in the use of the P foils. The initial activity of the foils after 2 hours of bombardment was only 4 to 6 times the background counting rate of these foils. Each foil had a small amount of long-life activity which may have been caused by some impurity. A particular foil had a constant background but different foils had different backgrounds which varied appreciably.

Another difficulty was caused by non-uniformity of the foils which was due partly to non-uniform distribution of the P through the foil and partly to variation of thickness of the polythene. Consistent results could be obtained only by using the same foil both for the measurement with the sphere and for the measurement of the direct intensity.

III. PROCEDURE

If I denotes the activity of the detector in the presence of the sphere and I_0 the activity without the sphere, the inelastic collision cross section is given by

$$\sigma = -(1/nx)\ln(I/I_0),$$

where n is the number of nuclei per unit volume and x

TABLE II. Inelastic collision cross sections for 14-Mev neutrons.

Element	Atomic weight	Density g/cc	Cross section in barns Cu detector	Al detector	P detector
B*	10.20	1.08 ±0.06	0.69±0.10	0.24±0.04	
C shell 1s	12.01	1.58 ±0.04	0.76±0.04	0.28±0.04	
C shell 2s		1.50 ±0.04			
N	14.01	0.812±0.004	0.79±0.05	0.46±0.05	
Al	26.97	2.61 ±0.02	1.06±0.05	0.62±0.07	
Fe	55.85	7.88 ±0.04	1.45±0.02	1.21±0.03	0.78±0.03
Cu	63.57	8.92 ±0.02	1.51±0.06	1.32±0.05	0.87±0.06
Cd	112.41	8.61 ±0.05	1.89±0.06	1.66±0.07	1.14±0.04
Au	197.2	19.1 ±0.2	2.51±0.04	2.06±0.09	1.47±0.10
Pb	207.2	11.3 ±0.1	2.56±0.05	2.29±0.04	0.91±0.06
Bi	209.0	9.74 ±0.08	2.56±0.05	2.28±0.08	1.03±0.11

* 82 percent B^{11}, 18 percent B^{10}.

[8] S. Eklund and N. Hole, Arkiv Mat. Astr. fys. **A29**, No. 26, 4, (1943).

[9] E. Bretscher and D. H. Wilkinson, Proc. Cambridge Phil. Soc. **45**, 141 (1949).

[10] R. F. Taschek, Atomic Energy Commission unclassified report MDDC-360 (1946) (unpublished).

[11] These foils were prepared by Mr. James S. Church of the Chemistry and Metallurgy Division of the Los Alamos Laboratory.

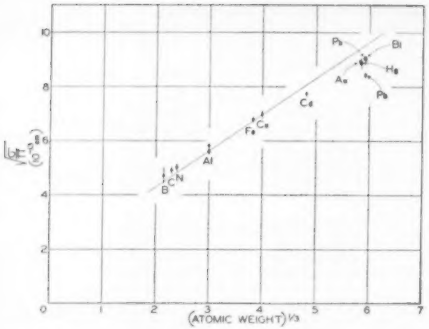

FIG. 2. Experimental values of $(\sigma/\pi)^{\frac{1}{2}}$ as a function of the one-third power of the atomic weights. Solid circles represent data presented here. Crosses represent the data of Amaldi *et al.* taken from reference 4. The curve is calculated from the theory of Feshbach and Weisskopf.

is the thickness of the shell. In order to eliminate the effect of fluctuation of the intensity of the neutron source, two identical foils were irradiated at different positions with respect to the source. If these two foils are irradiated through the same time interval and then counted simultaneously on two counters, the ratio of the observed counts will give the ratio of neutron intensity except for differences in counter efficiency. When the sphere is placed in position, the ratio of observed counts on the detector and monitor foils is reduced by the transmission of the sphere. This transmission is given by

$$T=I/I_0=C_s/C_0,$$

where C_s is the ratio of observed counts from the detector foil to those from the monitor foil after the detector foil has been irradiated within a sphere, and C_0 is the ratio when no sphere has been used. If the same two counters are used for determining C_0 and C_s, effects due to differences in counter efficiencies are eliminated.

Transmission was measured for certain materials and detectors as a function of distance from source to detector and as a function of shell thickness. Results of these measurements are given in Table I. Although the variation in shell thickness is limited to 36 percent, the fact that this produced no significant variation in the calculated cross section either in the range of transmission of 43 to 53 percent (for Fe) or 66 to 76 percent (for Bi) is taken as assurance that multiple scattering is not appreciably influencing the results. In addition, the fact that elastic scattering[4] is almost entirely within 30° leads to the conclusion that certainly the Cu detector results are not appreciably affected by multiple scattering.

IV. RESULTS

The results obtained by using the three threshold detectors in spheres of various elements are shown in Table II. All spherical shells had transmissions of greater than 0.43, as measured by Cu detectors. Inelastic collision cross sections obtained by using copper foils are plotted against atomic weight A in Fig. 1. The data are best fitted empirically by the relation $\sigma=\pi R^2$, where $R=(2.5+1.1A^{\frac{1}{3}})\times10^{-13}$ cm. This equation is shown as the solid curve and may be useful for interpolation. Values of Amaldi *et al.* are also shown.

V. DISCUSSION

Feshbach and Weisskopf[12] have published a schematic theory of nuclear cross sections. Their "reaction cross section," σ_r, may be identified with the inelastic collision cross section reported here, measured with copper detectors. They have calculated σ_r using values of the nuclear raidus, R obtained from analysis of measurements of σ_{tot}. Since recent measurements[13] of σ_{tot} for 14-Mev neutrons are in disagreement with the values used by Feshbach and Weisskopf, the values of σ_r have been recalculated according to their theory upon the assumption that $R=1.5\times10^{-13}\times A^{\frac{1}{3}}$ cm.

Figure 2 shows the measured values of $(\sigma/\pi)^{\frac{1}{2}}$ plotted against $A^{\frac{1}{3}}$. The values of Amaldi *et al.* are also shown. The curve represents the theoretical values derived as stated. The slope of the theoretical curve is steeper than desirable for the best fit to the data. This depends on the choice of r_0, the nuclear radius for $A=1$. However, the absolute values of the σ's change faster with r_0 than does the slope so that the best fit seems to be as chosen.

The results with the lower threshold detectors indicate that the neutrons emerging from inelastic events for all the elements observed have an energy spectrum which is quite low compared to the primary energy. Uncertainties in the knowledge of the response of the detectors prevent detailed analysis of these results.

[12] H. Feshbach and V. F. Weisskopf, Phys. Rev. **76**, 1550 (1949).
[13] Coon, Graves, and Barschall, Phys. Rev. **87**, 562 (1952).

Diffusion of Neutrons*

GEORGE JAFFÉ
Louisiana State University, Baton Rouge, Louisiana

(Received May 5, 1952)

It is the object of the present investigation to include the thermal motion of the medium in the treatment of neutron diffusion, under the simplifying assumption that the collisions are such as between hard elastic spheres. The methods used are those previously established by the author in radiative and gas-kinetic transfer. They only have to be adapted to the present purpose. This is done in Sec. II. Boltzmann's original equation which is quadratic in the distribution functions is linearized by the assumption that the velocity distribution of the molecules is Maxwellian. The treatment of the resultant transport equation is different for "thermal" and for "fast" neutrons. Section III deals with thermal neutrons by the method of "moments." The distribution function is assumed to be of the form: Maxwellian factor times arbitrary function of direction, the latter written as a series of general spherical harmonics. Thereby, and by the use of a theorem due to Maxwell, the fundamental equation may be reduced to an infinite system of linear differential equations which have been previously treated. The case of arbitrary geometry is treated to second-order moments (inclusive). For the case of cylindrical symmetry a recurrence relation for the moments, to any order, is derived. In Sec. IV the case of fast neutrons is treated by the method of iterated integrations. In order to make them straightforward the kernel of the integral equation is transformed into the standard form. This is achieved by characterizing the collisions in a way which is different from that usually applied. A simple example for the working of the method is given and the results are discussed.

I. INTRODUCTION

DURING the last decade important progress has been made in the theory of neutron diffusion by a variety of methods.[1] As far as the author is aware, however, all previous treatments are subject to an important restriction. They do not take into account the thermal motion of the ambient medium, the "moderator," since they invariably assume that the molecules of this medium are at rest when they are hit by the neutrons. As long as this assumption is made, it is evidently impossible to investigate the influence of temperature on the diffusion process, or even to derive in a rational way the simple fact that the neutrons are not slowed down indefinitely but arrive ultimately at "thermal velocities." It is the object of the present investigation to close this gap of the theory.

Methods for dealing with the problem have been available for a good many years. As early as 1930 the author[2] treated the fundamental Boltzmann equation in a way which makes it directly applicable to the present purpose. By considering what happens in a molecular beam directed in a given direction, rather than dealing with a certain neighborhood in the field, the author transformed the Boltzmann equation to the form which is now frequently called a transport equation. Furthermore, he treated this equation by two methods, the method of "moments" and the method of "iteration," which he had developed still earlier in his theory of the anisotropic radiation field.[3]

Neither the author's work on gas-kinetic transfer, nor the earlier work on radiative transfer, seem to have been noticed by the later workers in the field, and some work has been duplicated. Naturally, important results which have been derived since then are not to be found in those early papers. However, in some regards they go considerably beyond what has been achieved since that time, such as by not being restricted to specific geometric conditions,[4] by including time-dependent processes (A, p. 624; B, p. 458; J, p. 249), and even the existence of a given external force field (J, p. 248), which case corresponds to an inhomogeneous medium in radiation theory (B, p. 501; C, p. 470).

It is the object of the author in the present paper to establish methods for dealing with the problem, not to arrive at results of practical applicability.

II. THE FUNDAMENTAL EQUATION

If the thermal motion of the medium is to be included in the theory, it becomes imperative to go back to the original form of the Boltzmann equation which is quadratic in the distribution functions and not to start from a linear transport equation as occurs in the theory of radiative transfer. We shall write the fundamental equation in the form which was obtained in J, but for the sake of simplicity we shall restrict ourselves to the simple case of elastic collisions between spherically shaped particles. Furthermore, we shall assume that there is no external force field.

We refer the index 1 to the neutrons of mass m_1 and the index 2 to the molecules of mass m_2 of the medium. Let $f(\mathbf{r}_1, \mathbf{c}_1, t)$, abbreviated by f_1, be the distribution function for the former, and $F(\mathbf{r}_2, \mathbf{c}_2, t)$, abbreviated by F_2, the corresponding distribution function for the

* Work supported in part by the ONR.

[1] For a summary of the work done see R. E. Marshak, Revs. Modern Phys. **19**, 185–238 (1947).

[2] G. Jaffé, Ann. Physik **6**, 195–252 (1930). We refer to this paper in the text with J.

[3] G. Jaffé, (A) Ann. Physik **68**, 583 (1922); (B) Physik. Z. **23**, 500 (1922); (C) Ann. Physik **70**, 457 (1923). We refer to these papers in the text with the symbols A, B, and C.

[4] The linear problem was treated merely as an instance for various aspects of the general theory (A, p. 608, 619; C, p. 465), and the case of spherical symmetry was developed by a pupil of the author in Leipzig: H. W. Becker, Ann. Physik **81**, 1 (1926).

molecules of the medium.[5] Furthermore, let σ be the radius of the "sphere of action," i.e., the sum of the radii of m_1 and m_2, $\mathbf{g}$ the relative velocity of m_1 *versus* m_2, and ϑ, $(0 \leq \vartheta \leq \pi/2)$, the angle between $\mathbf{g}$ and the line of centers $\mathbf{z}$, drawn from m_1 to m_2, at the moment of collision. This line is to be contained within an infinitesimal solid angle $d\Omega_z$ in order to make the collision well defined. Finally, $d\omega_1$ and $d\omega_2$ are the "cells in velocity space" containing the velocities $\mathbf{c}_1$ and $\mathbf{c}_2$ before collision. Primes, wherever they appear, refer to variables after collision.

With all these conventions the rate of change of f_1 along any straight line s of given direction may be written in the form (see J, pp. 207–208, with the changes appropriate to elastic collisions)

$$(1/c_1)\partial f_1/\partial t + \partial f_1/\partial s = J(f_1, F_2), \tag{1}$$

where the integral operator

$$J(f_1, F_2) = (1/c_1)\int (f_1'F_2' - f_1F_2)\sigma^2 g \cos\vartheta d\Omega_z d\omega_2 \tag{2}$$

represents in the well-known way the excess of gains over losses by collisions between neutrons and molecules.

In general, Eq. (1) should contain a second term referring to collisions between neutrons themselves [Bo, Eq. (25)]. However, at this point the first simplification of the neutron problem as compared with the general gas-kinetic problem, may be introduced. Under observable conditions, the collisions between neutrons are such rare events that the term referring to them may be omitted.

Of equal importance is the second simplifying assumption which we introduce, namely, that the distribution function of the molecules may be considered to be given independently of their collisions with the neutrons. Again, the collisions of neutrons with molecules occur at such relatively long intervals of time that after each collision the molecule can restore its thermal equilibrium before it is hit again. This means that we may assume F_2 to be a given function, and no second equation for F_2 besides (1) is required.

It will depend on the physical circumstances which form for F_2 is adequate. We shall assume that the temperature is high enough to eliminate quantum effects and that the influence of the binding of the molecules in the lattice may be disregarded. The latter assumption, implicit already in Eq. (2), is rather far reaching;[6] however, it certainly represents a first approximation in dealing with the thermal motion of the medium.

With these assumptions the velocity distribution of the molecules may be considered to be Maxwellian, i.e., of the form

$$F_2 = A_2 \exp(-h_2 c_2^2), \tag{3}$$

with

$$A_2 = n_2(h_2/\pi)^{\frac{3}{2}}, \quad h_2 = m_2/(2kT), \tag{4}$$

and, thereby, our fundamental Eq. (1) becomes linear with regard to the unknown distribution function f_1.

For some purposes it is desirable to generalize Eq. (1) so as to include true absorption, characterized by a coefficient of absorption α_{abs}, and formation of new neutrons, characterized by a source function $S_1(\mathbf{r}_1, \mathbf{c}_1, t)$, which is not necessarily isotropic. Then the fundamental equation takes the form

$$(1/c_1)\partial f_1/\partial t + \partial f_1/\partial s = J(f_1, F_2) - \alpha_{abs} f_1 + S_1. \tag{5}$$

It was shown by the author that, in the theory of anisotropic radiation, the treatment has to be different according to whether absorption is "strong" or "weak," and in the treatment of Boltzmann's original equation the cases of "short" and "long" free path have to be distinguished.[7] Correspondingly, in the present case the treatment of the fundamental equations (1) or (5) becomes different for "thermal" and for "fast" neutrons. This distinction introduces in a most natural way the two methods of moments and of iterated integrations.

III. THERMAL NEUTRONS

If the neutrons are supposed to be of thermal velocities, but not by any means isotropically distributed, it is reasonable to represent the distribution function as the product of a Maxwellian distribution into a series progressing with general spherical harmonics. In order to simplify the writing we shall use the notation previously introduced (J, pp. 211–212).[8]

Thus, we assume for f_1 a representation of the form

$$f_1(\mathbf{r}_1, \mathbf{c}_1) = \exp(-h_1 c_1^2) f_1^*(\mathbf{r}_1, \lambda_1, \mu_1), \tag{6}$$

with

$$f_1^*(\mathbf{r}_1, \lambda_1, \mu_1) = \sum_{m=0}^{\infty} \sum_{\mu=0}^{2m} A_m{}^{\mu} \Pi_m{}^{\mu}(\lambda_1, \mu_1), \tag{7}$$

and

$$h_1 = m_1/(2kT), \quad \int f_1 d\omega_1 = n_1. \tag{8}$$

This expresses that we have represented the vector $\mathbf{c}_1$ by polar coordinates, c_1, λ_1, μ_1, with regard to any fixed system of coordinates in velocity space.

Limiting ourselves to the stationary case we assume that the coefficients $A_m{}^{\mu}$ depend on the position vector $\mathbf{r}_1$ only, and neither on time nor on the quantity c_1. This latter assumption is an important restriction as compared with the more general treatment in *J* and will be discussed later.

[5] Our notation follows as closely as feasible the one used in J and in L. Boltzmann's classical *Vorlesungen über Gastheorie* (I. Teil, Joh. Ambr. Barth, Leipzig, 1896). We refer to the latter with the symbol Bo.

[6] See reference 1, p. 186.

[7] Naturally it has to be defined accurately what is meant by strong and weak absorption (A, pp. 601, 614) and by short and long mean free path (*J*, p. 226).

[8] The $\Pi_m{}^{\mu}$ introduced by us are, except for the normalization, essentially the same with the Y_{lm} frequently used in wave mechanics (e.g., see Leonard I. Schiff, *Quantum Mechanics* (McGraw-Hill Book Company, Inc., New York, 1949), pp. 72, 73. We were forced to use the old notation and normalization in order to retain agreement with the older papers.

When the expressions (3) and (6) are substituted into the integral operator (2) the sum of the kinetic energies after collisions can be replaced by the corresponding sum before collision, and the factor $\exp(-h_1c_1^2)$ can be drawn before the sign of integration. Thereby Eq. (5), with $\partial/\partial t=0$, reduces to

$$df_1^*/ds=J_1-(\alpha(c_1)+\alpha_{\text{abs}})f_1^*+S^*. \tag{9}$$

Here we have introduced the following abbreviations:

$$J_1=(A_2\sigma^2/c_1)\int \exp(-h_2c_2^2)$$

$$\times(\sum_{m,\mu} A_m{}^\mu\Pi_m{}^\mu(\lambda_1',\mu_1'))g\cos\vartheta d\Omega_z d\omega_2, \tag{10}$$

$$\alpha(c_1)=(A_2\sigma^2/c_1)\int \exp(-h_2c_2^2)g\cos\vartheta d\Omega_z d\omega_2, \tag{11}$$

and

$$S^*=S_1(\mathbf{r}_1,\mathbf{c}_1)/(\exp(-h_1c_1^2)). \tag{12}$$

It is our object to transform Eq. (9) into an infinite system of partial differential equations for the coefficients $A_m{}^\mu$. In order to do that we have to develop the left-hand side into a series of general spherical harmonics and to perform the integrations in (10) and (11) in such a way that the corresponding terms in (9) also become series of this type. Finally the coefficients of equal harmonics on both sides of (9) have to be equated.

The integral in (11) is well known (Bo. p. 62), namely

$$\alpha(c_1)=1/\lambda(c_1)=(n_2\sigma^2\pi^{\frac{1}{2}}/\xi^3)$$

$$\times\left\{\xi\exp(-\xi^2)+(2\xi^2+1)\int_0^\xi \exp(-y^2)dy\right\}, \tag{13}$$

with

$$\xi^2=h_2c_1^2. \tag{14}$$

Its reciprocal, $\lambda(c_1)$, represents the mean free path of a molecule m_1 of speed c_1 traveling through a gas of molecules m_2, n_2 in number per cc. The mean free path so defined appears here without any ambiguity, and its dependence on c_1 will prove to be of importance in the later work. For $(m_2/m_1)\to\infty$, or for $T\to 0$, $\alpha(c_1)$ reduces to

$$\alpha_\infty=1/\lambda_\infty=n_2\sigma^2\pi, \tag{15}$$

which is larger than the Maxwellian value by the factor $2^{\frac{1}{2}}$.[9]

The integral in (10) is not as simple, since it contains the angles λ_1', μ_1' after collision. Fortunately, these can be eliminated by the use of a theorem on spherical harmonics due to Maxwell.

Since $\mathbf{c}_1$ is to be kept constant for the integrations in (10) we may fix $\mathbf{c}_2$ in polar velocity coordinates, c_2, ϕ, χ, *versus* $\mathbf{c}_1$ as polar axis. Thereby $d\omega_2$ becomes

$$d\omega_2=c_2^2\sin\phi d\phi d\chi dc_2. \tag{16}$$

[9] The function in (13) is tabulated in: J. Jeans, *An Introduction to the Kinetic Theory of Gases* (The Macmillan Company, New York, 1940), Appendix V.

The direction of the line of centers, $\mathfrak{z}$, may be fixed in the usual way by two angles, ϑ and ϵ, relatively to $\mathfrak{g}$, with the result

$$d\Omega_z=\sin\vartheta d\vartheta d\epsilon. \tag{17}$$

Now we perform the integrations in the order $d\chi$, $d\epsilon$, $d\vartheta$, $d\phi$, dc_2. The first of these integrations can be achieved by the use of Maxwell's theorem already mentioned. In our notation it states (Bo. p. 171)

$$\int \Pi_m{}^\mu(\lambda_1',\mu_1')d\chi=2\pi\Pi_m{}^\mu(\lambda_1,\mu_1)P_m(\cos\phi), \tag{18}$$

where P_m is the Legendre polynomial of order m. When the integration with regard to $d\chi$ is performed, those with regard to $d\epsilon$ and $d\vartheta$ become immediate and we obtain

$$J_1=(2\pi A_2\sigma^2/c_1)\sum_{m,\mu} A_m{}^\mu\Pi(\lambda_1,\mu_1)$$

$$\times\int_0^\infty \exp(-h_2c_2^2)c_2^2dc_2\int_{-1}^{+1} P_m(x)g dx. \tag{19}$$

In order to integrate with regard to $dx=\sin\phi d\phi$ we develop the relative velocity

$$g=(c_1^2+c_2^2-2c_1c_2\cos\phi)^{\frac{1}{2}} \tag{20}$$

into a series progressing with Legendre polynomials

$$g=\sum_{n=0}^{\infty} b_n(c_1,c_2)P_n(\cos\phi),$$

$$b_n(c_1,c_2)=[(2n+1)/2]\int_{-1}^{+1} g(x)P_n(x)dx. \tag{21}$$

If this development is substituted into (19) only the term with $n=m$ remains on account of the orthogonality of the Legendre polynomials, and we obtain

$$J_1=\sum_{m,\mu}\alpha_m A_m{}^\mu\Pi_m{}^\mu(\lambda_1,\mu_1), \tag{22}$$

where we have set

$$\alpha_m=[4\pi^2\sigma^2A_2/((2m+1)c_1)]$$

$$\times\int_0^\infty \exp(-h_2c_2^2)b_m c_2^2dc_2. \tag{23}$$

Thereby we have obtained our object of representing the integral J_1 in form of a series like (7). It remains to evaluate the coefficients b_m and α_m. This can be done by quite straightforward procedures based on the definitions (21) and (23).

The first coefficient, α_0, is identical with $\alpha(c_1)$ as defined by (13). The subsequent ones become increasingly more involved. Therefore, we shall be satisfied to state the results for ξ [see Eq. (14)] larger than about 3.

Neglecting terms of the order $\exp(-\xi^2)$ we find

$$\alpha_0=\alpha_\infty(1+1/\xi^2), \tag{24a}$$

$$\alpha_1=[\alpha_\infty\{4/(3\pi^{\frac{1}{2}})\}/\xi][-1+1/(5\xi^2)], \tag{24b}$$

$$\alpha_2=[\alpha_\infty/(10\xi^2)][-1+15/(14\xi^2)]. \tag{24c}$$

These results indicate that, with the exception of α_0, all α's are negative and become rapidly smaller as ξ increases. Now ξ increases with m_2 and, in the limiting case of $(m_2/m_1)\gg 1$, α_0 becomes α_∞ and all other α's vanish. In that case our results become identical with those of our old radiation theory where the "emission," i.e., the term corresponding to the gain J_1, is treated as isotropic.

This leads to an important remark regarding a generalization of our theory. The factor g in (10) expresses, by its dependence on ϕ, how the gain in the beam $\mathbf{c}_1$ depends on the angle between the velocities $\mathbf{c}_1$ and $\mathbf{c}_2$ of the two colliding particles. This dependence is, of course, limited to the specific nature of the collisions, i.e., elastic collisions in our case. If the nature of the collision is changed the angular dependence may vary and may be expressed by any other function of c_1, c_2, and ϕ, say one suggested by experimental results. This would not invalidate our method as long as the function in question shows cylindrical symmetry and, therefore, may be written as a series like (21). This would change only the values of the constants b_m and α_m. Thus any kind of anisotropic scattering, in gas-kinetic as in radiative transfer, may be treated by the same method, if only the scattering is cylindrically symmetrical.

Following the program given above, we have now to develop the left-hand side of Eq. (9) into a series of harmonics. This has been carried through completely in the author's radiation theory [A, Eqs. (24) to (26)], and there is no need for reproducing the lengthy formulas. Nor is it necessary to write down the differential equations which are obtained by the comparison of the two sides of (9). They are identical with those given in the old paper [A, Eqs. (27), (42), (43)] with only one exception. In the case of isotropic scattering to which the older theory applies the absorption coefficient (there called α_r) is the same in all orders. In the present case the effective absorption coefficient, $\alpha_m{}^*$, which replaces α_r, will be different for each group of $(2m+1)$ equations of order m, namely,

$$\alpha_m{}^*=\alpha_{\text{abs}}+\alpha_0-\alpha_m. \tag{25}$$

Therefore also the treatment of the linear differential equations remains exactly the same as exposed in *A*, and we shall only quote the generalized results. In first approximation the series (7) is broken off after the four first terms. This means restricting the representation to the local density, n_c, and the (vector) flux, $\mathbf{F}_c$, both referring to neutrons of specified velocity c_1. These physical quantities are related to the coefficients $A_m{}^\mu$ in the following manner:

$$n_c=4\pi\exp(-h_1c_1^2)c_1^2A_0{}^0, \tag{26}$$

and

$$(F_c)_i=(4\pi/3)\exp(-h_1c_1^2)c_1^3A_1{}^i, \quad i=0, 1, 2. \tag{27}$$

The differential equations of zero and first order lead to the equation

$$\nabla^2n_c=3\alpha_1{}^*(\alpha_{\text{abs}}n_c-4\pi c_1^2S_1) \tag{28}$$

for the density n_c. The flux is given by

$$\mathbf{F}_c=-(c_1/3\alpha_1{}^*)\,\text{grad}n_c. \tag{29}$$

The treatment can be carried through in a similar way if the five moments of second order are added,[10] which means taking into consideration the pressure tensor (J, p. 221).

So far the treatment is entirely general concerning the geometry of the field. Whenever a solution of Eq. (28) can be found, Eq. (29) yields the flux. However, the boundary conditions can be given only in a rather restricted form, by prescribing either the density, or the normal component of the flux at the boundaries.

A more general, and more rational way of giving the boundary conditions is to prescribe the distribution function itself at the boundaries in all directions leading into the field (A, p. 592). In order to treat this more comprehensive problem higher moments have to be introduced. The more anisotropic the incoming radiation is, the more terms have to be considered.

From here on we shall restrict ourselves to problems of cylindrical symmetry, i.e., to cases where the distribution function reduces to a simple series of Legendre polynomials. We shall prove a theorem which permits of calculating all moments by a recurrence relation.

Since we are assuming cylindrical symmetry now there will be a distinguished direction. This we choose as x axis and measure the angles, λ_1, μ_1, with respect to the x axis as polar axis. Then Eq. (9) can be written in the form

$$\cos\lambda_1\,df_1{}^*/dx=\int\varphi(c_2)f_1{}^*(\lambda_1',\mu_1')g \times\cos\vartheta d\Omega_\varepsilon dc_2d\Omega_1'-\alpha f_1{}^*+S^*, \tag{30}$$

where we have introduced the abbreviations

$$\varphi(c_2)=(A_2\sigma^2/c_1)\exp(-h_2c_2^2)c_2^2, \tag{31}$$

and

$$\alpha=\alpha(c_1)+\alpha_{\text{abs}}, \tag{32}$$

and where $d\Omega_1'$ signifies an infinitesimal solid angle which contains the direction λ_1', μ_1'.

Now we multiply Eq. (30) by $P_m(\cos\lambda_1)$ and integrate over

$$d\Omega_1=\sin\lambda_1d\lambda_1d\mu_1. \tag{33}$$

This yields

$$\frac{d}{dx}\int P_m(\cos\lambda_1)f_1{}^*d\Omega_1=C_m-\alpha K_m+S_m, \tag{34}$$

[10] See Appendix I.

if the mth moment, K_m, is defined by

$$K_m=\int f_1^* P_m d\Omega_1=(4\pi/(2m+1))A_m^0, \quad (35)$$

and if the abbreviations

$$C_m=\int \varphi(c_2)P_m\cos\vartheta d\Omega_x dc_2 d\Omega_1\int g f_1^* d\Omega_1', \quad (36)$$

and

$$S_m=\int S^* P_m d\Omega_1 \quad (37)$$

are introduced. If S^* is isotropic all S_m's vanish with the exception of S_0.

Transforming the left-hand side of (34) by the recurrence relation of the Legendre polynomials we obtain

$$((m+1)/(2m+1))dK_{m+1}/dx = -(m/(2m+1))dK_{m-1}/dx-\alpha K_m+C_m+S_m. \quad (38)$$

Now we treat the integral C_m in exactly the same way as we treated J_1 above introducing a series of form (7) for f_1^*, making use of the Maxwell theorem (18), and adding in the end one integration with regard to $d\Omega_1$ (Eq. (33)). This yields

$$C_m=\alpha_m K_m. \quad (39)$$

If this is introduced into Eq. (38) and the integration with regard to x performed we obtain the recurrence relation

$$((m+1)/(2m+1))K_{m+1}=-(m/(2m+1))K_{m-1} -\alpha_m^*\int_0^x K_m dx+\int_0^x S_m dx+B_{m+1}, \quad (40)$$

where α_m^* is defined by Eq. (25), and where B_{m+1} is a constant of integration.

It should be remarked again that the recurrence relation remains valid if $g(\phi)$ is replaced by a different function of ϕ, provided this function has cylindrical symmetry and can be developed into a series like (21). Only the values of the constants b_m and α_m^* are changed.

The recurrence relation (40) can serve to calculate successively any number of moments, and thereby the distribution function, provided the first two, K_0 and K_1 are known. These two can be obtained from the first-order solution given above [Eqs. (28) and (29)].[11] Since each step introduces a new constant of integration, sufficient constants may be obtained to satisfy the boundary conditions to any desired degree of accuracy. The procedure has been shown at length in the older paper (A, pp. 607–612).

It is easy to extend the method of this section to the more general case where the temperature of the medium is a prescribed function of space. It becomes necessary only to combine the coefficients A_m^μ of Eq. (7) with the exponential factor of Eq. (6) into new coefficients. All transformations remain the same, and the system of differential equations for the new coefficients is unaltered.

The contents of this entire section are, however, limited to neutrons which are already slowed down to thermal velocities, though they may still exhibit anisotropy to any amount.[12] This restriction is due to our assumption that the A_m^μ's are independent of c_1. If this assumption were dropped the development (6), (7) could represent distribution functions which depart much more strongly from the Maxwellian distribution (as in J, p. 213). However, Maxwell's theorem, which proved to be essential for the treatment in this Section, would not be applicable any more, since c_1' would be dependent on χ, and the first integration in J_1 or C_m could not be performed by the aid of that theorem. Therefore, another approach is indicated for "fast" neutrons.

IV. FAST NEUTRONS

The method which lends itself to the treatment of this case, and even to the treatment of all velocities, is that of iterated integrations (A, Sec. 2(b), p. 615 and J, Sec. 4, p. 238). However, the Boltzmann equation in its original form (1) makes the actual performance of the necessary integrations very inconvenient, since in the "gain term" the integration is over $d\omega_2$, i.e., over the velocities of m_2 *before* collision, whereas the distribution functions depend on the velocities *after* collision. Therefore, we shall first transform the gain term in such a way that it corresponds to the standard form in the theory of integral equations. This transformation will prove to be the crucial step in this section.

We limit ourselves again to stationary problems, we retain the assumption (3) for F_2 (with much better justification now) and add a term for true absorption and a source function, as in (5). Then the fundamental equation takes the form

$$df_1/ds=J_1-\alpha f_1+S_1, \quad (41)$$

where α is given by (32), and J_1 is now defined by

$$J_1=(A_2\sigma^2/c_1)\int \exp(-h_2 c_2'^2) f_1' g\cos\vartheta d\Omega_x d\omega_2, \quad (42)$$

f_1 being not expressed in any specific form.

Since the integral J_1 "collects" the gains out of all directions and velocities we wish to represent it as an integral with regard to $d\omega_1'$. This, however, cannot be

[11] It has been shown by the author (A, pp. 609–610) that in the plane problem which we are dealing with now $A_0^0=-\alpha_x C_1 x+C_2$, $A_1^0=C_1$, (with C_1 and C_2 constants), is a rigorous solution of the infinite set of differential equations in the case $S_1=0$. It is easy to generalize this solution for a nonvanishing source function, and it may serve as a starting point for the application of (40). Also the higher approximation for the first four moments (A, pp. 610–613) may be used for this purpose.

[12] A beam of thermal neutrons emerging from a reactor would present such a behavior.

achieved by transforming $d\omega_2$ into $d\omega_1'$ by the use of the collision equations: the Jacobian becomes zero.

This is readily understood by examination of the well-known Maxwell vector diagram for an elastic collision (Bo. Fig. 2). It is then seen that the definition of the collision gets lost by the indicated transformation. A collision can be specified in a variety of ways. The only one used until now is that underlying the integral operator (2), i.e., the collision is characterized by $\mathbf{c}_1$, $\mathbf{c}_2$, and the direction of the line of centers, $\mathbf{z}$, at the moment of collision. This represents eight independent parameters altogether. If, now, it is attempted to replace $\mathbf{c}_2$ by $\mathbf{c}_1'$ the collision cannot be specified any more by the direction of $\mathbf{z}$, since this direction is given already by that of $\mathbf{c}_1'-\mathbf{c}_1$. Therefore it becomes necessary to specify the collision in a new way. This can be done by giving, besides $\mathbf{c}_1$ and $\mathbf{c}_1'$, the direction of the relative velocity $\mathbf{g}$ before collision. Then Maxwell's diagram can again be constructed in a unique way.

It follows from this consideration that $d\Omega_z$, i.e., the infinitesimal solid angle containing $\mathbf{z}$, has to be replaced by $d\Omega_g$, i.e., an infinitesimal solid angle containing $\mathbf{g}$. Then the collision is again specified by eight independent parameters. Consequently we have to calculate the Jacobian in the equation

$$d\Omega_z d\omega_2 = \Delta d\Omega d_g\omega_1'. \tag{43}$$

This calculation is somewhat lengthy but straightforward and yields

$$\Delta = (\mu/\cos\vartheta)^3, \tag{44}$$

where

$$\mu = (m_1+m_2)/(2m_2), \tag{45}$$

and ϑ is the angle between the relative velocity, $\mathbf{g}$, and the line of centers, $\mathbf{z}$, as heretofore.[13]

Furthermore, it follows from Maxwell's diagram that the relative velocity can be expressed in the new variables by

$$g = \mu c_{11}/\cos\vartheta, \tag{46}$$

where

$$c_{11} = |\mathbf{c}_1'-\mathbf{c}_1|. \tag{47}$$

In consequence of (44) and (46) the integral (42) can be written in the form

$$J_1 = (\sigma^2\mu^4/c_1)\int f_1' K(\mathbf{c}_1, \mathbf{c}_1')d\omega_1', \tag{48}$$

where the kernel, K, has the desired representation and is given by

$$K(\mathbf{c}_1, \mathbf{c}_1') = A_2\int \exp(-h_2c_2'^2)c_{11}(\sin\vartheta/\cos^3\vartheta)d\vartheta d\eta. \tag{49}$$

Here ϑ and η are the polar angles for $\mathbf{g}$ with regard to $\mathbf{c}_1-\mathbf{c}_1'$ as polar axis.

The kernel can be simplified by performance of the two integrations. The integration with regard to η leads to the result[14]

$$K(\mathbf{c}_1, \mathbf{c}_1^*) = 2\pi A_2 c_{11}\exp(-h_2X_0) \times\int_0^\infty J_0(i\gamma\zeta)\exp(-\beta^*\zeta^2)\zeta d\zeta, \tag{50}$$

with the abbreviations

$$X_0 = \mu^2c_1^2-(1-\mu)^2c_1'^2+2\mu(1-\mu)c_1c_1'\cos\phi, \tag{51}$$

and

$$\beta^* = h_2\mu^2c_{11}^2, \quad \gamma = 2h_2\mu c_{11}c_1'\sin\vartheta_1'. \tag{52}$$

The angle ϑ_1' is the one between $\mathbf{c}_1'$ and $(\mathbf{c}_1'-\mathbf{c}_1)$, ϕ is the angle between $\mathbf{c}_1$ and $\mathbf{c}_1'$ as previously, and $J_0(iy)$ is the Bessel function of order zero and purely imaginary argument.

The integration in (50) cannot be performed in closed form, but two important limiting cases can be obtained. If the velocity of the neutrons, $\mathbf{c}_1$, is of the thermal order the factor γ will be of the order 1 in the domain where the integrand contributes essentially. Therefore $J_0(i\gamma\zeta)$ may then be replaced by unity and the remaining integration is immediate.

We are not interested in thermal neutrons at present. On the other hand, if $\mathbf{c}_1$, and therefore also $\mathbf{c}_1'$ are large compared to the thermal velocity$\approx(1/h_2)^{\frac{1}{2}}$, $\gamma\zeta$ will be large in the important region[15] and $J_0(i\gamma\zeta)$ may be replaced by its asymptotic value. Then the integration can be performed again[16] and leads to the final form of the kernel for *fast neutrons*, namely

$$K(\mathbf{c}_1, \mathbf{c}_1') = n_2(h_2/\pi)^{\frac{1}{2}}\exp(-h_2X)/c_{11}, \tag{53}$$

where

$$X = X_0-c_1'^2\sin^2\vartheta_1' = [\mu c_1^2-(1-\mu)c_1'^2+(1-2\mu)c_1c_1'\cos\phi]^2/c_{11}^2. \tag{54}$$

Combining (53) with (48) and (41) we obtain the fundamental equation in the form

$$df_1/ds = \beta\int \mathbf{K}(\mathbf{c}_1, \mathbf{c}_1')f_1'd\omega_1'-\alpha f_1+S_1, \tag{55}$$

with

$$\mathbf{K}(\mathbf{c}_1, \mathbf{c}_1') = \exp(-h_2X)/c_{11}, \quad \beta = \sigma^2\mu^2n_2(h_2/\pi)^{\frac{1}{2}}/c_1. \tag{56}$$

Since the kernel has the standard form now, Eq. (55) can be solved by a Neumann series[17]

$$f_1 = \sum_{i=0}^{\infty}\beta^i f_1^{(i)}. \tag{57}$$

---

[13] See Appendix II.

[14] See Appendix III.

[15] Since, under our assumption, $\zeta\exp(-\beta^*\zeta^2)$ has its steep and narrow maximum at $\zeta_{\max} = (1/2\beta^*)^{\frac{1}{2}}$, $\gamma\zeta_{\max}$ will have the value $(2h_2)^{\frac{1}{2}}c_1'\sin\vartheta_1'$.

[16] We have neglected terms of the order $(1/(h_2\mu^2c_{11}^2))$.

[17] The singularity of the kernel, c_{11}^{-1}, does not affect the applicability of the theory of integral equations. Compare: D. Hilbert, *Grundzüge einer allgemeinen Theorie der linearen Integralgleichungen* (B. G. Teubner, Leipzig und Berlin, 1912), pp. 267, 276.

This leads to the zero approximation

$$f_1^{(0)} = f_1 \exp(-\alpha s) + \exp(-\alpha s)\int_{s_0}^{s} \exp(\alpha y) S_1(y)\,dy, \quad (58)$$

along a straight line s of any direction in the field, if f_1 is the given value of f_1 at the point s_0 where the line enters the field.

The subsequent approximations are given by

$$f_1^{(i)} = \exp(-\alpha s)\int_{s_0}^{s} \exp(\alpha y - h_2 X) c_{11}^{-1} (f_1^{(i-1)})' d\omega_1' dy, \quad i = 1, 2, \cdots. \quad (59)$$

The method can be extended to time-dependent problems by taking the integrations in a "retarded" way (C, Sec. 5, p. 458 ff.), and also the case of an external force field can be included (J, p. 248). It should be pointed out, furthermore, that the solution (58), (59) remains valid if the temperature is a prescribed function of space. This generalization affects only the quadratures to be performed.

Before the method is applied to a simple example it may be of interest to point out two limiting cases to which (55) leads. If $m_2 \gg m_1$, the parameter μ becomes $\frac{1}{2}$, and $h_2 \to \infty$. The exponent $h_2 X$ [Eq. (54)] reduces to

$$h_2 X = (h_2/4)(c_1'^2 - c_1^2)^2/c_{11}^2, \quad (60)$$

indicating that the integral will contribute only for $c' = c_1$, as it should be. In performing the integration we may treat c_{11} as a constant for any fixed angle ϕ and obtain

$$df_1/ds = (\alpha_s/4\pi)\int (f_1')_{c_1'=c_1} d\Omega_1' - \alpha f_1 + S_1. \quad (61)$$

Thus the gain, i.e., the scattering into the direction of s is isotropic and we have obtained one of the forms of the fundamental equation of our old radiation theory[18] with the absorption coefficient $\alpha_s = \alpha_\infty$.

We shall treat $m_2 = 1$, i.e., hydrogen, as the second limiting case, and we shall, furthermore, assume that the molecules are at rest when they collide. This means $\mu = 1$ and $T \to 0$, or $h_2 \to \infty$. Then the exponent becomes

$$h_2 X = h_2 c_1^2 (c_1 - c_1' \cos\phi)^2/c_{11}^2. \quad (62)$$

Consequently the integral contributes only for

$$c_1 = c_1' \cos\phi, \quad 0 \le \phi \le \pi/2,$$

as it should be. The integration yields

$$df_1'/ds = (1/4\pi)\int \sigma^*(f_1')_{c_1'=c_1/\cos\phi} d\Omega_1' - \alpha f_1 + S_1, \quad (63)$$

with σ^*/n_2, the "differential cross section for gain," given by

$$\sigma^*/n_2 = 4\pi\alpha_\infty/(n_2 \cos^3\phi). \quad (64)$$

[18] Compare A, p. 618 Eq. (IId) combined with the subsequent equation.

The cross section just introduced has to be distinguished from the cross section for scattering which is usually considered and which might be obtained by the same procedure from the expression (11). The difference is caused by the fact that, in the process of scattering, it need not be considered what change the speed undergoes, whereas for the gain the change in speed has to be just such that the neutron is brought into the velocity group $\mathbf{c}_1$. This is the essential circumstance which makes the gain term so much more difficult to handle than the loss term, and it results in a different angular dependence of the differential cross section for gain as stated above. The result (63) can be verified by direct derivation.

As a simple example for our method we treat the case of a parallel, monochromatic beam of neutrons impinging normally on the plane surface of a semi-infinite scattering medium. The beam is to have equal density over the entire surface.

We choose the normal to the surface, pointing inward, as x axis with its origin in the surface. Directions will be fixed by the polar angles, Θ and Φ, with the x axis as polar axis. Thus s in the fundamental equation (55) signifies a straight line forming an angle Φ with the x axis.

We describe the incident beam by a δ-function

$$f_1(c_1, \Theta_1) = C\delta(c_1 - c^*, \Theta_1), \quad (65)$$

with

$$\int \delta(c_1 - c^*, \Theta_1) c_1^2 dc_1 d\Omega_1 = 1 \text{ (cm/sec)}^3. \quad (66)$$

Hence $c_1 = c^*$ is its speed and $\Theta_1 = 0$ its direction. We disregard true absorption and formation processes ($\alpha_{abs} = 0$, $S_1 = 0$).

Then the zero solution becomes

$$f_1^{(0)} = C \exp(-\alpha(c^*)s)\delta(c_1 - c^*, \Theta_1). \quad (67)$$

Substituting this into (59) (with $i = 1$), we obtain for the first-order solution

$$f_1^{(1)} = K(\mathbf{c}_1, \mathbf{c}^*)\int \delta(c_1' - c^*, \Theta_1') d\omega_1' \Psi_1^{(1)}(x, \Theta_1), \quad (68)$$

where we have set

$$\Psi_1^{(1)}(x, \Theta_1) = \exp(-\alpha(c_1)s) \times \int_{s_0}^{s} \exp[(\alpha(c_1) - \alpha(c^*)\cos\Theta_1)y]dy. \quad (69)$$

The integral in (69) is easily performed though the cases $\Theta_1 \le \pi/2$ have to be distinguished. For $\Theta_1 < \pi/2$ the integration begins in the surface ($s_0 = 0$), for $\Theta_1 > \pi/2$ at infinity. This yields

$$\Psi_1^{(1)}(x, \cos\Theta_1) = [\exp(-\alpha(c^*)x) - \exp(-\alpha(c_1)x/\cos\Theta_1)]/N, \quad 0 \le \Theta_1 \le \pi/2, \quad (70a)$$

$$\Psi_1^{(1)}(x, \cos\Theta_1) = [\exp(-\alpha(c^*)x]/N, \qquad \pi/2 \leq \Theta_1 \leq \pi, \quad (70b)$$

with the denominator

$$N = \alpha(c_1) - \alpha(c^*)\cos\Theta_1.^{19} \quad (70c)$$

Now the final expression for the first-order solution takes the form

$$f_1^{(1)} = C[\exp(-h_2 X^*)/c_{1*}]\Psi_1^{(1)}(x, \Theta_1), \quad (71)$$

with

$$X^* = [\mu c_1^2 - (1-\mu)c^{*2} + (1-2\mu)c_1 c^* \cos\Theta_1]^2/c_{1*}^2, \quad (72a)$$

and

$$c_{1*}^2 = c_1^2 + c^{*2} - 2c_1 c^* \cos\Theta_1. \quad (72b)$$

It should be pointed out that the solution (71) has a singularity at $\mathbf{c}_1 = \mathbf{c}^*$ (i.e., at $c_1 = c^*$, $\Theta_1 = 0$), but the singularity is integrable if integrated over $d\omega_1$.

The velocity distribution is given by the factor $K(\mathbf{c}_1, \mathbf{c}_*)$; the distribution of intensity in the scattered beam, in its dependence on position, x, and direction, Θ_1, by $\Psi_1^{(1)}$. It is easy to show that the latter factor would reduce to $\exp(-\alpha(c^*)x)$ if an incident beam of negligible cross section would be considered.

The first order solution represents conditions as they result from the consideration of neutrons which have undergone one collision (J, p. 252). Therefore it would be valid if a slab of absorbent medium were to be considered whose thickness is appreciably smaller than the mean free path $\lambda^* = 1/\alpha(c^*)$.

We briefly discuss the two cases $m_2 \gg m_1$, and $m_2 = m_1$. In the former case $h_2 \to \infty$ and the exponent is given by (60). Hence the velocity spectrum in the scattered beam contracts to a narrow line about $c_1 = c^*$ as m_2/m_1 increases indefinitely. Integrating over $c_1^2 dc_1$ we start from $\beta f_1^{(1)}$ (which is the contribution to $f_1^{(0)}$) and find

$$\beta \int f_1^{(1)} c_1^2 dc_1 = (C/4\pi)\alpha_x \Psi_1^{(1)}(x, \Theta_1). \quad (73)$$

Therefore the angular distribution is determined by $\Psi_1^{(1)}$ exclusively and becomes isotropic if a narrow incident beam is considered (see above). In the case $m_1 = m_2$ the exponent is given by (62) and the velocity distribution is somewhat involved. We treat the two cases that the velocity c_1 is either "thermal" (i.e., $c_1 \approx 1/(h_2)^{\frac{1}{2}}$) or "fast" (i.e., $c_1 \approx c^*$). For thermal neutrons[20] we have $h_2 = h_1$, $h_1 c_1^2 \approx 1$. Consequently the kernel boils down to

$$K^* = \exp(-h_1 c_1^2 \cos^2\Theta_1)/c^*. \quad (74)$$

[19] It is in the expression for N where the distinction between $\alpha(c_1)$ and $\alpha(c^*)$ becomes of importance. However, this fact makes itself felt only in the calculation of the higher approximations, i.e., for $i > 1$. For $i = 1$ the second term in (70a) prevents a singularity at $\Theta_1 = 0$ even if $\alpha(c_1) = \alpha(c^*)$.

[20] It might appear contradictory to apply our result to thermal neutrons since we used a kernel limited to fast neutrons (see p. 606). It should be pointed out, however, that for the calculation of the kernel in the first-order solution the value of c^* is relevant, as is shown by Eq. (68), and we still assume that c^* is much larger than $1/(h_1)^{\frac{1}{2}}$.

Hence there will be a finite contribution of thermal neutrons, even after the first collision. By integrating over the velocity spectrum (for a given direction) we find

$$\beta \int f_1^{(1)} c_1^2 dc_1 = (C/4\pi)\alpha_x \times [1/(h_1 c_1 c^* \cos^3\Theta_1)]\Psi_1^{(1)}(x, \Theta_1). \quad (75)$$

In the case $c_1 \approx c^*$, i.e., $h_1 c_1^2 \gg 1$, the kernel will be different from zero only for

$$c_1 \approx c_1' \cos\Theta_1, \quad \Theta_1 \leq \pi/2, \quad (76)$$

and the velocity spectrum contracts for every direction to a narrow line about the velocity (76). The total number of neutrons in this beam is found to be

$$\beta \int f_1^{(1)} c_1^2 dc_1 = (C/4\pi)4\alpha_x \Psi_1^{(1)}(x, \Theta_1) \quad (77)$$

relative to the contribution of $f_1^{(0)}$. Hence the number of fast neutrons is larger than that of the thermal ones by a factor of the order c^*/c_{therm}. There are no other groups of velocity in the scattered beam except the two discussed, since the exponent in K^* makes all other contributions negligible.

We shall not enter here into the calculation of higher approximations. They are all performed easily in an approximate way by treating the kernel in the preceding solution as a δ-function (on account of the denominator c_{11}); then this kernel reproduces itself. Otherwise lengthy calculations become necessary and it is difficult to obtain the asymptotic solution for $x \to \infty$ by the addition of the series (57). It can, however, be obtained by a more direct procedure by assuming it to be of the form

$$f_1 = \exp(-\alpha x)K(\mathbf{c}_1, \mathbf{c}^*)\Psi(\Theta_1), \quad (78)$$

where the kernel for thermal neutrons has to be used (see Eq. (49)).

The case of a point source in an infinitely extended medium can be treated in a way very similar to the linear problem.

Note added in proof:—The author is obliged to Dr. Richard K. Osborn for pointing out to him that the integral (50) is known in explicit form (see G. N. Watson, *Theory of Bessel Functions* (Cambridge University Press, Cambridge, 1944), Sec. 13.3, Eq. (1), p. 393). If the correct formula is used the result is the same as the one obtained by the author who used an asymptotic procedure. Hence the final form of the kernel, Eq. (56), is not limited to "fast neutrons." but holds for all values of the parameters.

APPENDIX I

If the series (7) is broken off after the second-order terms, the problem can still be treated in a general way if a potential function, Φ, (called in A the "radiation potential") is introduced. By similar calculations as in the old paper (A, pp. 605 to 607) it can be shown that the differential equation for Φ becomes

$$\nabla^2\Phi - a_1\Phi + a_2 S_1 = 0, \quad (79)$$

with the abbreviations

$$a_1=3\alpha_1^*\alpha_2^*\alpha_{\text{abs}}/a_3, \tag{80a}$$

$$a_2=4\pi c_1^3\alpha_2^*/a_3, \tag{80b}$$

and

$$a_3=\alpha_2^*+(4/5)\alpha_{\text{abs}}. \tag{80c}$$

When Φ is determined from this differential equation the first four moments are obtained in the following way

$$n_c=(3\alpha_1^*\alpha_2^*/c_1a_3)\Phi+(16\pi c_1^2/5a_3)S_1, \tag{81}$$

and

$$\mathbf{F}_c=-\text{grad}\Phi. \tag{82}$$

The five second-order moments $A_2^i(i=0, 1, 2, 3, 4)$ can be expressed in terms of partial second differential coefficients of Φ. For $\alpha_{\text{abs}}=0$, $\alpha_1^*=\alpha_2^*=\alpha_r$, Eq. (81) reduces to the result of the old paper [A, Eq. (46)].

APPENDIX II

In the calculation of the Jacobian in Eq. (43) the following considerations should be taken into account. It is customary to fix the direction of the line of centers, $\mathbf{z}$, relatively to the relative velocity, $\mathbf{g}$. In a similar way in our choice of collision parameters the direction of $\mathbf{g}$ may be fixed relatively to $(\mathbf{c}_1'-\mathbf{c}_1)$. This is perfectly legitimate as long as integrations are to be performed which keep $\mathbf{c}_1$ and $\mathbf{c}_2$ in the old system, or $\mathbf{c}_1$ and $\mathbf{c}_1'$ in the new system, constant. However, if the five variables $\mathbf{c}_2$, $\mathbf{e}_z$ (with e_z a unit vector in the direction of z) are to be transformed into $\mathbf{c}_1'$, $\mathbf{e}_g$, the unit vectors $\mathbf{e}_z$ and $\mathbf{e}_g$ may not be fixed any longer relatively to $\mathbf{g}$ or $(\mathbf{c}_1'-\mathbf{c}_1)$, since these vectors are varied themselves in the procedure. Consequently all five variables of either system have to be defined in one and the same fixed coordinate system.

Let the components of $\mathbf{c}_1$ in this system be u_1, v_1, w_1, etc.; furthermore, let ϑ_z, η_z be the polar angles for $\mathbf{z}$, and ϑ_g, η_g the corresponding ones for $\mathbf{g}$. Then the five expressions relating the old set of variables with the new set become

$$u_2=u_1+\mu c_{11}^2\cos\vartheta_g/V', \tag{83a}$$

$$v_2=v_1+\mu c_{11}^2\sin\vartheta_g\cos\eta_g/V', \tag{83b}$$

$$w_2=w_1+\mu c_{11}^2\sin\vartheta_g\sin\eta_g/V', \tag{83c}$$

$$\cos\vartheta_z=(u_1'-u_1)/c_{11}, \tag{83d}$$

$$\tan\eta_z=(w_1'-w_1)/(v_1'-v_1). \tag{83e}$$

Here the abbreviations

$$c_{11}=((u_1'-u_1)^2+(v_1'-v_1)^2+(w_1'-w_1)^2)^{\frac{1}{2}}, \tag{84a}$$

$$V'=(u_1'-u_1)\cos\vartheta_g+(v_1'-v_1)\sin\vartheta_g\cos\eta_g +(w_1'-w_1)\sin\vartheta_g\sin\eta_g, \tag{84b}$$

have been introduced. The angle ϑ between $\mathbf{g}$ and $\mathbf{z}$ is given by

$$\cos\vartheta=V'/c_{11}. \tag{85}$$

Now the calculation of Δ is straightforward (some work may be shortened by introducing $x_z=\cos\vartheta_z$ and $x_g=\cos\vartheta_g$ as new variables).

A further remark may not be out of place. We have based our calculation of the gain term in (2) on Boltzmann's original expression, which makes use of the concept of "inverse collisions." One might think that this represents a detour and that the gain term could be calculated in a more direct manner by first setting up the usual expression for the number of direct collisions, by then expressing g in terms of c_{11} by Eq. (47), and by finally integrating over $d\Omega_g d\omega_1'$. The last step of this procedure would be erroneous because it would assume arbitrarily $\Delta=1$, in contradiction with the result in the text. In replacing g by c_{11} a change of variables is implied which necessitates a corresponding Jacobian. Therefore, the laborious calculation of the latter cannot be avoided by starting from direct collisions.

APPENDIX III

In order to perform the integration with regard to η in (50) we first have to obtain an expression for c_2' in our variables of integration. Now we have

$$\mathbf{c}_2'=\mathbf{c}_1'-\mathbf{g}', \tag{86}$$

or, by the aid of (46),

$$c_2'^2=c_1'^2+(c_{11}\mu/\cos\vartheta)^2 -2c_1'(c_{11}\mu/\cos\vartheta)\cos(\mathbf{g}', \mathbf{c}_1'). \tag{87}$$

For the integration with regard to ϑ and η, $\mathbf{c}_1$ and $\mathbf{c}_1'$, hence also $\mathbf{c}_{11}=\mathbf{c}_1'-\mathbf{c}_1$ are being kept constant. Consequently we may fix the directions of $\mathbf{g}'$ and $\mathbf{c}_1'$ with regard to $\mathbf{c}_{11}$ as polar axis. Let the polar angles be ϑ', η', and ϑ_1', η_1', respectively. Now the angle between $\mathbf{g}'$ and $(\mathbf{c}_1'-\mathbf{c}_1)$ is the same as the angle between $\mathbf{g}$ and $(\mathbf{c}_1-\mathbf{c}_1')$, and the vectors $\mathbf{g}$, $\mathbf{g}'$ and $(\mathbf{c}_1-\mathbf{c}_1')$ are in the same plane; consequently ϑ', η' may be replaced by ϑ, η. This leads to the final expression for $(c_2')^2$, namely,

$$c_2'^2=c_1'^2+(c_{11}\mu/\cos\vartheta)^2 -2\mu c_1'c_{11}[\cos\vartheta_1'+\tan\vartheta\sin\vartheta_1'\cos(\eta-\eta_1')]. \tag{88}$$

If now $\tan\vartheta=\zeta$ is introduced as a new variable the result (5) is obtained, since

$$\int_0^{2\pi}\exp(\gamma\zeta\cos(\eta-\eta_1'))d\eta=2\pi J_0(i\gamma\zeta). \tag{89}$$

Absorption of 5.3-Mev, 10.3-Mev, and 17.6-Mev Gamma-Rays*

E. S. Rosenblum,† E. F. Shrader, and R. M. Warner, Jr.‡
Case Institute of Technology, Cleveland, Ohio

(Received June 10, 1952)

Gamma-ray absorption cross sections have been measured for Cu, Sn, Pb, and U at each of the gamma-ray energies, 5.3-Mev, 10.3-Mev, and 17.6-Mev. Betatron radiation collimated to give "good" geometry is used for the transmission measurements. The energy sensitive detector used is a 180° homogeneous magnetic field pair spectrometer with crystal-and-photomultiplier detectors. The measured cross sections in units of barns per atom are at 5.3 Mev, 3.244 (Cu), 7.05 (Sn), 15.07 (Pb), and 18.43 (U); at 10.3 Mev, 3.285 (Cu), 7.95 (Sn), 17.83 (Pb), and 21.73 (U); and at 17.6 Mev, 3.688 (Cu), 9.22 (Sn), 20.47 (Pb), and 25.32 (U). The statistical errors range from 0.5 percent to 1.5 percent.

The pair cross sections are inferred by subtracting the best-known values of the cross sections for the Compton, nuclear, and photoelectric effects from the total cross section. The ratio of this pair cross section to the value calculated from the Bethe-Heitler theory is given as a function of energy. The present results give the transition of this ratio which is greater than unity for low energy gamma-rays to a value less than unity at extremely high gamma-ray energies.

I. INTRODUCTION

RECENT experimental data on gamma-ray absorption coefficients[1–5] from 11 to 280 Mev indicate that the Bethe-Heitler[6] calculation for the contribution due to pair production is in error for elements of high atomic number, being about 10 percent too high for lead and slightly higher for uranium, probably due to failure of the Born approximation. Within the accuracy of these experiments, the error appears to be independent of the energy.

No accurate experimental determination of absorption coefficients appears to have been made below 11 Mev and above the energy of conveniently obtainable natural gamma-rays.[7] Agreement of experimentally determined absorption coefficients with theoretical values has been good below 2.5 Mev. However, the contribution of the coefficient in this region becomes small and vanishes at 1.02 Mev, so that a relatively large percentage error in the theoretically determined value of this component may be undetected in the total coefficient.

In contrast to the high energy case, the exact calculation by Hulme and Jaeger[8] of the pair production cross section near threshold for elements of high atomic number indicates that the value of this cross section calculated from the Bethe-Heitler theory will be too low. The observations of Hahn *et al.*[9] on pair production at 2.0 Mev show this to be the case. The 5- to 17.6-Mev region has been chosen for this investigation because it is in this energy region that the pair cross section must go from the low energy case to the high energy case. For reasons discussed later in this paper, we have not yet found it practicable to measure the absorption coefficients below 5 Mev. The present paper gives results at 5.3 Mev, 10.3 Mev, and 17.6 Mev for four elements, copper ($Z=29$), tin ($Z=50$), lead ($Z=82$), and uranium ($Z=92$).

The method used for determining the total absorption cross section for gamma-rays is similar to that used by previous investigators[3,4] using the bremsstrahlung spectrum from an electron accelerator, differing, however, in that the measurements were not restricted to gamma-ray energies in the region of the maximum energy in the spectrum. The energy sensitive detector is a pair spectrometer of the type first used by Walker and McDaniel,[10] with the modification of replacing the Geiger counters with stilbene scintillation detectors. This modification makes possible higher counting rates without bothersome accidental coincidence background which unfortunately is enhanced in pulsed type accelerators. The source of the radiation used is the Case field-biased, flux-forced betatron.

The geometry and energy resolution of the detector insure that the effect of measuring the degraded radiation produced when an absorber is introduced is small enough to be neglected. It is estimated that for the present experimental arrangement the reduction in cross section from this cause is less than 0.1 percent in every case.

III. EXPERIMENTAL ARRANGEMENT

The arrangement of equipment is shown schematically in Fig. 1, which is drawn approximately to scale.

* Work supported by the AEC.

† Now at Lincoln Laboratory, Massachusetts Institute of Technology, Cambridge, Massachusetts.

‡ Now at the Bell Telephone Laboratories, Murray Hill, New Jersey.

[1] G. D. Adams, Phys. Rev. **74**, 1707 (1948); conclusions modified by Walker (reference 2).

[2] R. L. Walker, Phys. Rev. **76**, 527 (1949).

[3] J. L. Lawson, Phys. Rev. **75**, 443 (1949).

[4] DeWire, Ashkin, and Beach, Phys. Rev. **82**, 447 (1951).

[5] A. I. Berman, Phys. Rev. **85**, 774 (1952).

[6] H. Bethe and W. Heitler, Proc. Roy. Soc. (London) **146**, 83 (1934).

[7] For a summary of results obtained at all energies prior to about June 1949, see W. S. Snyder and J. L. Powell, AEC Report, AECD-2739 (1949) (unpublished). For a more recent review, see C. M. Davisson and R. D. Evans, Revs. Modern Phys. **24**, 79 (1952).

[8] H. R. Hulme and J. C. Jaeger, Proc. Roy. Soc. (London) **153**, 443 (1936).

[9] Hahn, Baldinger, and Huber, Helv. Phys. Acta **24**, 324 (1951).

[10] R. L. Walker and B. D. McDaniel, Phys. Rev. **74**, 315 (1948).

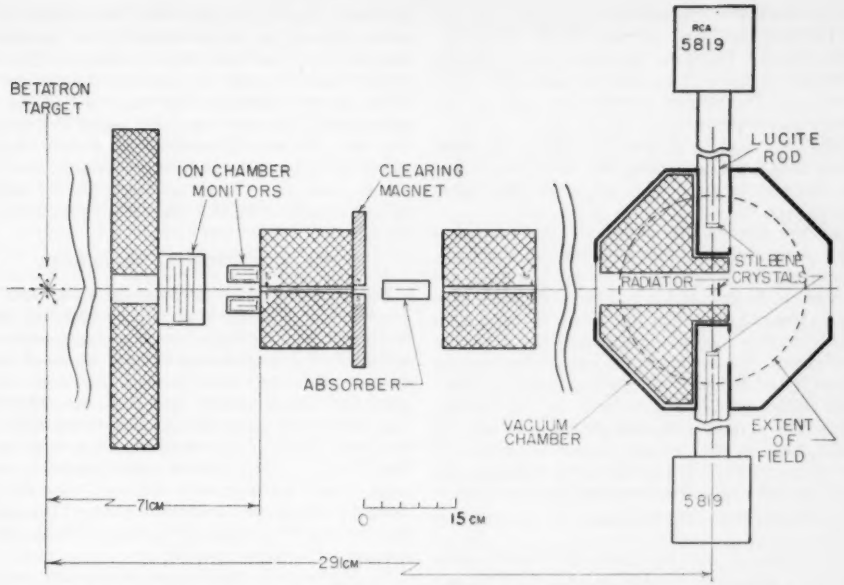

FIG. 1. Experimental arrangement for making gamma-ray transmission measurements at various energies.

A block diagram of the electrical equipment is shown in Fig. 2.

The Case betatron, used as the source of radiation and operated with orbit self-expansion, gives a gamma-ray output consisting of 180 pulses per second, each 150–250 μsec long.[11] A peak energy of 12 to 14 Mev was used for the measurements at 5.3 and 10.3 Mev and a peak energy of 20 Mev for the measurements at 17.6 Mev.

The thin-walled transmission ion chamber is used by the betatron operator for instantaneous monitoring of the beam while the annular thick-walled chamber is used to obtain a continual chart record of the beam intensity.

The lead collimator consists of two sections, each 6 inches thick, separated by 6 inches. The circular hole in the two section collimator tapers from $\frac{3}{16}$ in. to $\frac{3}{8}$ in. in diameter. The apex of the cone defined by this hole is thus 45 cm in front of the collimator. However, the collimator is located about 70 cm from the betatron target, because of clearance requirements. The collimator limits the beam to a cone of about 0.3° half-angle.[12]

The absorber is mounted between the halves of the collimator, in such a manner that it can be moved by remote control in and out of the beam. The maximum angle through which betatron gamma-rays that are incident on the absorber can be scattered by Compton recoil and still fall on the detector is less than 1°.

The energy-sensitive, gamma-ray detector is a 180° magnetic pair spectrometer. The pole pieces are 12 in. in diameter with a gap of $1\frac{5}{8}$ in. The magnetic field is uniform within ±0.5 percent out to 0.8 pole radius. The magnet is energized by a voltage stabilized *MG* set, resulting in an output current which does not vary more than a fraction of one percent over the running time. The current is monitored visually and corrected manually if necessary. The magnet exhibits no notice-

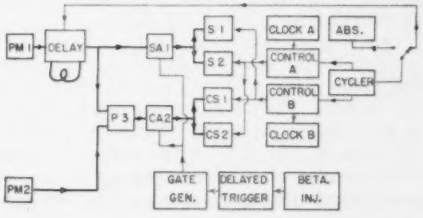

FIG. 2. Block diagram of cycling and recording system for transmission measurements. Either absorber or electrical delay may be cycled to obtain transmission ratio or accidental coincidences.

[11] E. C. Gregg, Jr., Rev. Sci. Instr. **22**, 176 (1951).

[12] Although experiments by J. Robson of this laboratory indicate that charged particles do not get through a small collimating hole which is centered on the betatron target, the clearing magnet shown was inserted as an added precaution. It consists of a magnetron magnet with suitably modified pole faces and flux path.

able hysteresis over the current range used, and the field strength was found to vary linearly with magnetizing current. Therefore, the magnet was calibrated by the proton-resonance technique at one value of the current, and the magnet current then used as the measure of field strength.

Radiators are strips of lead foil about 2 cm wide. One-mil foils have been used, but at 5 Mev, it has been necessary to use a 4-mil foil to get the desired counting rate.

Detectors are two stilbene crystals, each approximately 6 mm wide, 30 mm high, and 15 mm deep. Center-to-center separation is 20 cm. Crystals are mounted on the ends of Lucite rods of the same cross section. One-mil aluminum foil covers all open faces of the crystals to improve the light-gathering properties of the system. A space of one cm was left between the stilbene crystal and the Lucite rod to avoid the scattering of electrons and positrons from the rod into the crystal. The crystals and rods are inserted into reentrant ports in the vacuum chamber; windows in these ports are two thicknesses of one-mil aluminum foil, as are the entrance and exit windows for the betatron beam. Approximate distance from foil to crystal is 1.7 cm.

The Lucite rods butt up against RCA 5819 photomultipliers, which are mounted so that the long axis of the dynodes is horizontal, to minimize defocusing effects due to fringing fields. This precaution is probably unnecessary, as the photomultipliers are shielded electrostatically and magnetically by iron cylinders with walls $\frac{7}{32}$ in. thick; this is sufficient to eliminate difficulties due to fringing fields, under the conditions of this experiment.

Signals from the photomultipliers are fed through cathode followers to a coaxial line, shaped by 1.0-meter lengths of RG8U cable terminated by resistances of 5 ohms, and then into a fast coincidence circuit (P3) which has been described elsewhere.[13] The resolving time of this arrangement is about 5×10^{-9} sec, although it is somewhat dependent on the voltage applied to the photomultiplier tubes and on the discrimination level used in the coincidence amplifier (CA 2). Single pulses from photomultiplier No. 1 can be obtained with an amplifier (SA 1). No use is made of the singles counting rate other than as a check on the system.

The singles and coincidence amplifiers include voltage discriminators whose outputs are gated to give no signal except during a 200-μsec interval, including the betatron pulse. The gating arrangement is shown in Fig. 2, and is adjusted by displaying the betatron x-ray pulse (obtained from a 931-A photomultiplier exposed to the beam) on an oscilloscope along with the gate pulse. The gate can then be varied in time and length so as to bracket the x-ray pulse.

The output pulses from the amplifiers are recorded on scalers S1, S2, CS1, and CS2. These scalers can be made to record or not as desired by an appropriate electrical signal from the cycling mechanism described in the following section on experimental procedure.

The energy calibration and resolution of the pair spectrometer has been calculated taking into account the 180° focusing properties, the natural angular spread in pair particles and the scattering in the radiator, windows, etc. The energy resolution is 5 percent at 17.6, 6 percent at 10.3 Mev, and 9 percent at 5.3 Mev.[14]

III. EXPERIMENTAL PROCEDURE

Preliminary experiments indicated that, when the betatron is in operation and with the shielding shown in Fig. 1, almost all singles counts coming from sources other than the spectrometer radiator consist of pulses small compared to wanted pulses.[15] The former can be eliminated almost entirely at a given photomultiplier high voltage setting by suitable adjustment of the discriminator levels of the amplifiers. Then, with any of the following variations from normal operating conditions, singles counting rates are quite low and coincidence counting rates are essentially zero: (1) beam on, but blocked from radiator by 16 in. of lead; (2) no radiator; (3) magnetic field off.

An approximate pulse-height distribution was obtained of counts originated from the radiator. The results indicate that the differential pulse-height distribution is nearly rectangular, neglecting noise.

When operating with a radiator in place accidental coincidence rates are determined by inserting 10 meters of RG8U cable in the signal lead from one photomultiplier (see Fig. 2). Apparently accidental coincidences are of three types: (1) Rate proportional to square of beam intensity—from accidental coincidences due to random nature of singles caused by events at the radiator; (2) rate proportional to beam intensity; (3) rate nearly independent of beam intensity, but zero with beam blocked from the radiator.

It was found impractical to take the time necessary to separate these types of background. For operation at 10 Mev and at 17.6 Mev, it was found sufficient to decrease the sensitivity of the detection system, so that the background with no absorber averages a few percent, of the coincidence rate. Under these circumstances, the desired statistical accuracy in absorption coefficient can be obtained, even with a background whose statistics are quite poor.

[13] E. F. Shrader, Rev. Sci. Instr. **21**, 883 (1950).

[14] For more complete discussion of factors affecting resolution and energy calibration see E. S. Rosenblum, AEC Report AECU-1825 (unpublished).

[15] In the course of another experiment, it was found that the total integrated light output per unit volume caused by betatron x-rays incident on Lucite rods is less than 8 percent of that with a scintillation crystal in the beam. This light output from the Lucite, furthermore, must consist of individual pulses which are far smaller than pulses from electrons. Therefore, in an experiment such as the present one, in which discrimination against small pulses is employed, contributions from scintillations in the Lucite should be entirely negligible.

At 5.3 Mev, for various reasons the background rate is higher and more time must be devoted to background measurements. At this energy, the number of pairs per quantum is about half that at 10 Mev, and angular spread of pair particles is practically doubled, as is the angular scattering of electrons in a given radiator. This angular spread causes a much lower detection efficiency in a 180° focusing system. For these reasons, operation below 5 Mev is impractical.

Because of fluctuations in betatron beam intensity and possible drifts in the sensitivity of the detection system, a cycling mechanism is employed. It has a 60-sec cycle during which the following steps occur: (1) 3 sec—all clocks and scalers off—absorber moved out of beam; (2) 10 sec—clock B and scalers S1 and CS1 activated, counting singles and coincidences with absorber out of beam; (3) 3 sec—all clocks and scalers off—absorber moved into beam; (4) 44 sec—clock A and scalers S2 and CS2 activated, counting singles and coincidences with absorber in beam; (5) Repeat step 1.

The ratio of running time with absorber in the beam to that with absorber out of the beam was selected, together with absorbers whose transmission is about 10 percent, to give a desired accuracy in absorption coefficients in a minimum running time.[16] As shown by Rose and Shapiro, a rather large variation in time ratio and/or transmission can be allowed, as long as both are near optimum values, without a large increase in running time.

IV. ABSORPTION RUNS

A typical run lasts from one to four hours, with the absorber, clocks, and scalers cycled automatically, as described above. Every ten cycles (ten minutes), the scaler readings are recorded, and the clock time noted on the continuous chart of the betatron output. This record is later examined, and all intervals rejected in which the betatron intensity varied significantly during the interval.

Accidental background determinations are made at various times, in ten-cycle runs with delay in one signal lead throughout the interval and with the absorber cycled in the normal manner. This background data, normalized for running time and beam intensity, is used to correct the transmission data.

The absorbers used were copper, tin, lead, and uranium. The copper used was highly pure electrical bus rod. The tin absorber was cast from chemically pure mossy tin. The lead was obtained from the National Lead Company, Cleveland, Ohio and the uranium was obtained on loan from the AEC.[17] The purity of all materials is greater than 99.9 percent based on information furnished by the suppliers.

[16] M. E. Rose and M. M. Shapiro, Phys. Rev. **74**, 1853 (1948).

[17] The authors wish to thank the Research Service Division of the Chicago Operations Office, USAEC for making available the uranium and for arranging for it to be machined to a form suitable for our measurements.

TABLE I. Experimental cross sections.

Absorber element	Thickness (cm)	Density (g/cm³)	Absorption coeff. (cm⁻¹)	Absorption cross section (10^{-24} cm²)
		(a) 5.3-Mev gamma-rays		
Cu	8.638	8.898	0.2735±0.0027	3.244±0.032
Sn	8.365	7.275	0.260 ±0.004	7.05 ±0.10
Pb	4.742	11.34	0.497 ±0.005	15.07 ±0.15
U	2.056	18.70	0.872 ±0.009	18.43 ±0.18
		(b) 10.3-Mev gamma-rays		
Cu	8.638	8.898	0.2770±0.0025	3.285±0.030
Sn	8.365	7.275	0.2933±0.0029	7.95 ±0.079
Pb	3.983	11.34	0.599 ±0.007	
Pb	3.005	11.34	0.581 ±0.005	
Pb (Av)			0.588 ±0.006	17.83 ±0.18
U	2.506	18.70	1.026 ±0.004	
U	3.005	18.70	1.040 ±0.010	
U (Av)			1.028 ±0.004	21.73 ±0.11
		(c) 17.6-Mev gamma-rays		
Cu	7.817	8.878	0.3103±0.0034	3.688±0.040
Sn	8.365	7.275	0.3404±0.0034	9.222±0.092
Pb	3.005	11.34	0.6750±0.0068	20.47 ±0.21
U	2.000	18.70	1.198 ±0.012	25.32 ±0.25

V. EXPERIMENTAL RESULTS

The results of transmission measurements made on the four absorbers at each of three gamma-ray energies is given in Table I. The densities listed for the absorbers are from measurements made in our laboratory and in each case are within a few tenths of one percent of the theoretical density. Both the absorption coefficient in cm^{-1} and the total cross section per atom are given. The energies at which the measurements were made were to a certain extent arbitrary with, however, the object of comparing directly our results with those of Walkers[2] at 17.6 Mev. The considerations entering into the energy calibration of the pair spectrometer are given in reference 14. Two thicknesses of the lead and uranium absorbers were measured at 10.3 Mev to check the internal consistency of the measurements.

VI. THEORETICAL ABSORPTION COEFFICIENTS

The important contributions to the absorption coefficients are the photoelectric effect, the Compton effect, and pair production both in the field of the nucleus and the electrons. The photonuclear contributions are estimated on the basis of our present best knowledge of these processes.

These contributions to the cross sections for the four elements at three energies are tabulated in Table II. The photoelectric cross section has been calculated by formula due to Hall.[18]

A factor of 5/4 is included to take account of the fact that the K electrons contribute about 80 percent of the total coefficient.[19]

The Compton cross section per atom is given by the

[18] H. Hall, Phys. Rev. **45**, 620 (1934). The equation used here is the one valid for higher energies ($\gamma \gg 1$).

[19] W. Heitler, *Quantum Theory of Radiation* (Oxford University Press, London, 1944), p. 127.

TABLE II. Theoretical cross sections.

Element	Photoelectric cross section (10^{-24} cm^2)	Compton cross section (10^{-24} cm^2)	Pair-production (nucleus screened) (10^{-24} cm^2)	Pair production (electrons) (10^{-24} cm^{-2})	Photonuclear (10^{-28} cm^2)	Total cross section (10^{-24} cm^2)
			(a) 5.3-Mev gamma-rays			
Cu	0.0042	2.2822	0.9717	0.0115	≃0	3.2696
Sn	0.054	3.935	2.880	0.020	≃0	6.889
Pb	0.515	6.453	7.714	0.033	≃0	14.715
U	0.862	7.240	9.690	0.037	≃0	17.829
			(b) 10.3-Mev gamma-rays			
Cu	0.002	1.447	1.787	0.034	<0.01	3.275
Sn	0.029	2.495	5.268	0.059	0.10 ±0.07	7.951
Pb	0.279	4.093	14.07	0.096	0.25 ±0.10	18.79
U	0.469	4.592	17.64	0.108	0.34 ±0.07	23.15
			(c) 17.6-Mev gamma-rays			
Cu	0.0013	0.9691	2.496	0.059	0.14 ±0.03	3.665
Sn	0.0174	1.6708	7.347	0.102	0.38 ±0.07	9.517
Pb	0.168	2.7402	19.53	0.167	0.50 ±0.10	23.11
U	0.281	3.074	24.51	0.187	0.56 ±0.12	28.61

Klein-Nishina formula for the cross section per electron,[20] multiplied by Z.

The pair cross section has been calculated by the method described by Walker,[2] using an approximate formula due to Hough[21] modified to include a screening correction and pair production in the field of an electron.

Borsellino's values are used for the electronic pair production factor and are 0.32 at 5 Mev, 0.55 at 10 Mev, and 0.68 at 17.6 Mev.[22]

The screening corrections to the nuclear pair cross section are given in Table III.

In estimating the contribution to the total cross section due to nuclear absorption, one must rely on extremely incomplete experimental data and theory. Our best knowledge of the magnitude of the nuclear absorption is at 17 Mev, where the various gamma-ray processes have been studied using the Li gamma-rays. The neutron yield at this energy for Sn, Pb, and U relative to Cu has been measured by Walker, McDaniel, and Stearns.[23] The ratios are 3.3, 4.5, and 9.0 for Sn, Pb, and U, respectively. Heidman and Bethe[24] have calculated the neutron multiplicity per gamma-ray absorbed for a number of elements including Cu and U, and an estimate can be made for Sn and Pb. Knowing the relative neutron yields and multiplicity, we can calculate the total nuclear cross section for gamma-ray capture for Sn, Pb, and U if we know the (γ, n) cross section for Cu.[25] The $Cu^{63}(\gamma, n)Cu^{62}$ cross section has been measured by a number of investigators. Using the Li gamma-rays, Wäffler and Hirzel[26] give for this cross section $\sigma = 1.2 \pm 0.12 \times 10^{-25}$ cm^2, while Walker, *et al.*[23] give a much lower value of $\sigma = 0.55 \pm 0.12 \times 10^{-25}$ cm^2. From bremsstrahlung activation, Johns *et al.*[27] have measured this cross section as $\sigma = 1.1 \times 10^{-25}$ cm^2 at 17.5 Mev. Measurements made by Krohn and one of the authors (EFS),[28] of the Cu^{62} cross section relative to the deuteron photodisintegration cross section, give a value at 17.5 Mev of $\sigma = 1.0 \pm 0.1 \times 10^{-25}$ cm^2. Johns *et al.*[27] have also measured the $Cu^{65}(\gamma, n)Cu^{64}$ cross section at 17.5 Mev and find a value approximately 1.5 times as large as the $Cu^{63}(\gamma, n)Cu^{62}$ cross section at the same energy. Using a value of $\sigma = 1.0 \times 10^{-25}$ cm^2 for the $Cu^{63}(\gamma, n)Cu^{62}$ reaction, the total gamma-ray nuclear capture cross section for Cu, Sn, Pb, and U have been calculated and listed in Table II(c). A possible error of ±20 percent has been allowed in these values.

At 5.3 Mev only (γ, γ) processes are possible, with cross sections of at most a few millibarns, so their contribution to the total gamma-ray absorption cross section has been neglected.

At 10.3 Mev, however, other processes are possible, of which however only (γ, n) and fission reactions can make appreciable contributions to the total cross section. From the $Cu^{65}(\gamma, n)Cu^{64}$ cross section as a function of gamma-ray energy as determined by Johns *et al.*,[27] we can make an estimate that the Cu nuclear cross section at 10.3 Mev will be less than 10 percent of its value at 17.6 Mev. Ogle and McElhinney[29] have measured the relative photofission cross section as a function of energy. Their cross section at 10.3 Mev is approximately 0.6 that at 17.6 Mev. We will assume approximately the same ratio for Pb, while for Sn we can use the curve for Sb published by Johns *et al.*[27] The assumed ratios for Sn and Pb are 0.3 and 0.5, respectively, with large allowance for errors. The resulting nuclear cross sections at 10.3 Mev are listed in Table II(b).

VII. DISCUSSION OF RESULTS

Our experimental values of the total gamma-ray absorption cross section per atom for Cu, Sn, Pb, and U at gamma-ray energies of 5.3, 10.3, and 17.6 Mev are listed in Table I. At 10.3 Mev, two thicknesses each of Pb and U were measured to check the internal consistency of the measurement. Our values for Cu and Pb at 17.6 Mev agree with those of Walker[2] well within the experimental error. For Sn, however, at this same

TABLE III. Screening corrections.

Energy (Mev)	5.3	10.3	17.6
Cu	−0.011	−0.018	−0.029
Sn	−0.014	−0.026	−0.039
Pb	−0.019	−0.032	−0.050
U	−0.020	−0.036	−0.053

[20] See reference 19, p. 157.
[21] P. V. C. Hough, Phys. Rev. **73**, 266 (1948).
[22] A. Borsellino, Helv. Phys. Acta **20**, 136 (1947).
[23] Walker, McDaniel, and Stearns, Phys. Rev. **80**, 807 (1950).
[24] J. Heidman and H. A. Bethe, Phys. Rev. **84**, 274 (1951).
[25] We must make the further reasonable assumption that $(\gamma, 2n)$ processes are negligible at this energy for Cu.
[26] H. Wäffler and O. Hirzel, Helv. Phys. Acta **21**, 200 (1948).
[27] Johns, Katz, Douglas, and Haslam, Phys. Rev. **80**, 1062 (1950).
[28] V. E. Krohn and E. F. Shrader, Phys. Rev. **87**, 685 (1952).
[29] W. Ogle and J. McElhinney, Phys. Rev. **81**, 344 (1951).

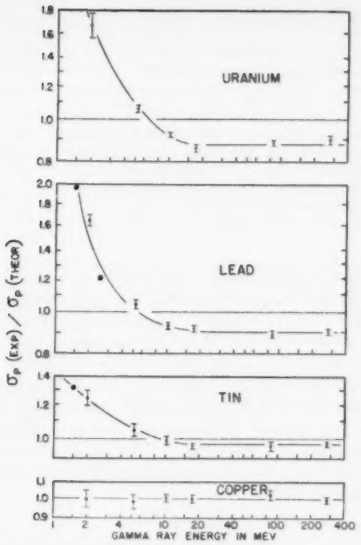

FIG. 3. The ratio of the experimental nuclear pair production cross section to the theoretical (Bethe-Heitler) cross section plotted as a function of energy for Cu, Sn, Pb, and U. The values at 1.5 and 2.5 Mev are from Hulme and Jaeger (reference 8), at 2 Mev from Hahn *et al.* (reference 9), at 88 Mev from Lawson (reference 3), and at 280 Mev from DeWire *et al.* (reference 4).

energy there is disagreement of the order of two standard deviations.

At high gamma-ray energies, where pair production is the only major contributor to the total cross section, the discrepancy between the Bethe-Heitler theory and experiment has been blamed on the failure of the Born approximation. In the limiting case of extremely high energies, the Born approximation requires that $Z/137 \ll 1$, which certainly is not the case for elements in the upper part of the periodic table. The failure is presumably worse as the gamma-ray energy is decreased. However, at low gamma-ray energies, there is fair agreement between the experimental and theoretical values of the total cross section since the pair cross section becomes a successively smaller fraction of the total cross section. In order, therefore, to investigate the behavior of the pair cross section, we have obtained an "experimental" pair cross section by the expedient of subtracting from the experimental value of the total cross section the contributions due to the photoelectric and Compton effects, electronic pair production, and our best estimate of photonuclear processes. The ratio of this "experimental" value to the theoretical cross section for pair production is plotted as a function of energy in Fig. 3. The values of Lawson[3] at 88 Mev and of De Wire *et al.*[4] at 280 Mev have been included to show the limiting values of this ratio. It has been assumed that at 88 Mev and 280 Mev all other processes are small compared to pair production.

At low energies Hulme and Jaeger[8] have calculated the pair production cross section using the proper wave function. The ratio of their value to the corresponding Bethe-Heitler value are plotted in Fig. 3 for Pb at 1.5 and 2.5 Mev and Sn at 1.5 Mev. Hahn *et al.*[9] have measured the relative pair production cross section as a function of Z at a mean energy of 2 Mev. They give the value of $\sigma_p(Z)/Z^2$, where $\sigma_p(Z)$ is the cross section as a function of Z with $\sigma_p(1)$ set equal to the theoretical Bethe-Heitler value for $Z=1$. Their values of σ_p/Z^2 are also plotted in Fig. 3 at an energy of 2 Mev.

For Cu there is good agreement between the Bethe-Heitler theory and experiment at all energies. However, a discrepancy appears for Sn and is larger the higher the Z value. The present data show the expected smooth transition from the previously obtained results at high energies to those at low energies.

The authors wish to acknowledge the help of Professor E. C. Gregg, Jr., and Mr. W. C. Voelker and Mr. P. French of the betatron crew in providing the long self-expanded beam which has made counting experiments possible. We would like also to thank Mr. D. G. Proctor for his help in the construction and maintenance of the electronic equipment.

$(n,2n)$ Reactions in C^{12}, Cu^{63}, and Mo^{92}†

J. E. Brolley, Jr., J. L. Fowler,* and L. K. Schlacks
Los Alamos Scientific Laboratory, University of California, Los Alamos, New Mexico

(Received July 17, 1952)

Using the method of induced radioactivity we have measured the $(n,2n)$ cross sections of C^{12}, Cu^{63}, and Mo^{92} as a function of energy from threshold to 27 Mev. The positron activities of 20, 10, and 15.5 min, respectively, were employed. K-capture corrections were applied to the copper and molybdenum data. We have compared the copper and molybdenum data with the statistical theory of Weisskopf and collaborators and find satisfactory agreement from threshold to the onset of tertiary reactions.

INTRODUCTION

THE statistical theory[1,2] gives an account of $(n,2n)$ reactions for nuclei with mass number greater than about 50, in terms of a rather simple model. If the variation of cross section with energy for this type of reaction is known, deductions about the effective energy level densities in the nuclei concerned can be made. Radioactivities produced by the $(n,2n)$ reactions are frequently employed as fast neutron detectors. For these reasons we have investigated $(n,2n)$ cross sections as a function of energy for C^{12}, Cu^{63}, and Mo^{92}. The associated half-lives are of convenient duration and K-capture corrections are small. In the case of Cu^{63} this study extended the range of measurements which have been performed at lower energies.[3–5] The cross section of C^{12} has been measured with 90-Mev neutrons.[6]

EXPERIMENT

The source of neutrons was the $T(d,n)He^4$ reaction. Tritium gas contained in a thin-walled target cell was bombarded by 10.5-Mev deuterons from the 42-in. cyclotron. The energy of the neutrons produced at different angles to the deuteron beam can be calculated from the measured deuteron energy and the known energy release from the $T(d,n)He^4$ reaction, 17.6 Mev. A description of the target cell and alignment procedure has been given in a paper on (n,p) scattering at 27 Mev.[7]

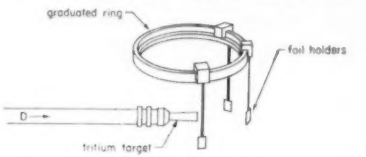

FIG. 1. Arrangement of foils around the tritium target.

The absolute differential cross section as a function of angle for the reaction $T(d,n)He^4$ has been measured by counting the neutrons and α-particles; results are given in the paper by Brolley, et al.[8] The samples, which in the case of copper and molybdenum were enclosed in thin cadmium jackets were supported around the target cell in such a way that there was negligible scattering material in the vicinity of the target. The arrangement is schematically shown in Fig. 1. The general bombardment and counting techniques have been discussed in an earlier report.[4]

RESULTS

In the curves of experimental data (Figs. 2–4) the total spread in energy of the neutrons intercepted by the foils is indicated by horizontal lines. It is calculated from the angular resolution as well as from the spread in energy resulting from the slowing down of the deuterons in the tritium target.

$C^{12}(n,2n)C^{11}$

The threshold of this reaction as calculated from mass tables[9] and taking into account the recoil energy of the carbon nucleus is 20.2 Mev. C^{11} decays by positron emission with a half-life of 20.3 min.[10] The samples irradiated were in the form of polyethylene foils about 11 mg/cm² thick. A lamina of two thicknesses of polyethylene was irradiated and counted as a single foil.

Since the end-point energy of the positron emitted by C^{11}(0.95–0.98 Mev)[10] is approximately the same as the end-point energy of the beta-particles from the RaD+E National Bureau of Standards source (1.17 Mev), it is convenient to calibrate the Geiger counters by use of the RaD+E Standard. Due to the low intensity of the C^{11} activity the following experimental procedures were adopted.

Rectangular foils, of polyethylene 2.54×5.08 cm, were folded into a 2.54-cm square and supported about 15 cm away from the center of the target cell. Similar 2.54×5.08 cm foils were folded and placed between two circular foils 1.43 cm in diameter (the diameter of the radioactive layer of the RaD+E standard). This

† Work done under the auspices of the AEC.
* Now at Oak Ridge National Laboratory, Oak Ridge, Tennessee.
[1] V. F. Weisskopf and D. H. Ewing, Phys. Rev. **57**, 472 (1940).
[2] J. M. Blatt and V. F. Weisskopf, ONR Technical Report No. 42 (1950) (unpublished); see also AEC documents NYO-632, NYO-636 (unpublished).
[3] D. D. Phillips (unpublished); S. Forbes (to be published).
[4] J. L. Fowler and J. M. Slye, Jr., Phys. Rev. **77**, 787 (1950).
[5] Hermann Wäffler, Helv. Phys. Acta **22**, 239 (1950).
[6] E. M. McMillan and H. F. York, Phys. Rev. **73**, 262 (1948).
[7] Brolley, Coon, and Fowler, Phys. Rev. **82**, 190 (1951).
[8] Brolley, Fowler, and Stovall, Phys. Rev. **82**, 502 (1951).
[9] H. A. Bethe, *Elementary Nuclear Theory* (John Wiley and Sons, Inc., New York, 1947).
[10] *Nuclear Data*, National Bureau of Standards Circular No. 499 (1950).

arrangement of foils was fastened directly on the end of the target cell. After the bombardment the circular disks were counted with end-window counters with the same geometry and with the same type of silver backing as supported the RaD+E source. The rectangular foils were all counted on a set of three glass-walled Geiger counters. Since the activity per unit mass of all the foils next to the target cell was the same, the rectangular foils activated in juxtaposition with the disks could be used to calibrate the cylindrical counters in terms of the end-window counters, which in turn were calibrated against the RaD+E standard.

In order to compensate to some extent for the effects of self-absorption and scattering in the sample, a single thickness of inactive polyethylene was placed over the RaD+E source during a calibration run. A relative correction of 7.5 percent had to be applied in the efficiency calculations due to the difference in energy of the beta-particles from C^{11} and those from the RaD+E

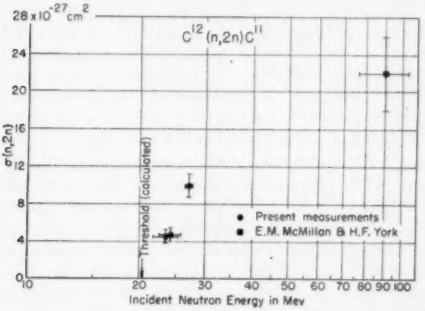

FIG. 2. Cross section of the $C^{12}(n,2n)C^{11}$ reaction as a function of neutron energy. The ordinate represents the absolute cross section for the production of the 20.3 minute positron emitter C^{11} from the C^{12} isotope. The data has not been corrected for K-capture competition.

standard and due to the difference of thickness of polyethylene involved in the two different cases. This correction was calculated from the absorption coefficients as well as effects resulting from fore- and backscattering estimated from the measurements of Zumwalt.[11] As a check on these calculations, a curve was taken of the counting rate of an end-window counter as a function of thickness of polyethylene placed over the RaD+E standard, which was 2.8 cm away from the counter window. The curve calculated by using Zumwalt's measurements of self-absorption, self-scattering, and backscattering effects agreed fairly well with the measurements. The 8 percent correction to the value of the RaD+E standard found necessary by Burtt[12] was applied to the data.

Figure 2 gives the absolute cross section for production of C^{11} by the $(n,2n)$ reaction as a function of the energy of the incident neutrons. The circles denote the present measurements. The vertical spread indicated is the estimated standard error of the measurements. Besides the standard deviations from the mean of a number of measurements, the errors indicated in Fig. 2 also include the errors in the neutron counting (11 to 15 percent) as well as errors involved in the absolute beta-counting, which were estimated to be about 6 percent. The values plotted have been corrected for the isotopic abundance of C^{12} in normal C. For comparison, the reported value at 90 Mev is included in Fig. 2.[8] For this point the horizontal spread is quoted as the width of the neutron energy distribution at half-maximum. The cross sections in Fig. 2 have not been corrected for K-capture competition with positron emission and therefore represent only the cross section for production of the positron activity.

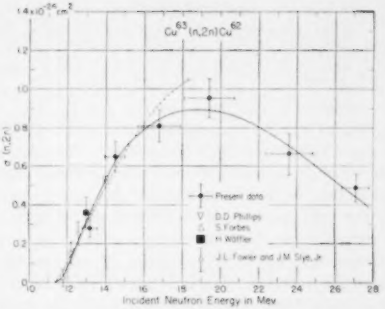

FIG. 3. The cross section of the $Cu^{63}(n,2n)Cu^{62}$ reactions as a function of neutron energy. The data has been corrected for isotopic abundance of Cu^{63} and for K-capture competition with positron emission. The broken line gives the predictions of the statistical theory, ignoring competitive proton emission.

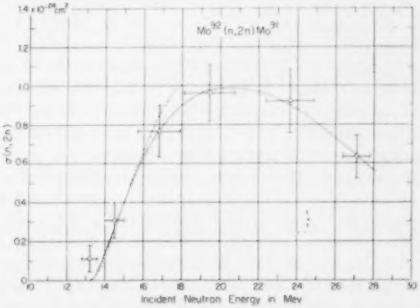

FIG. 4. The cross section of the $Mo^{92}(n,2n)Mo^{91}$ (15.5-minute period) reaction as a function of neutron energy. The data has been corrected for isotopic abundance of Mo^{92} as well as K-capture competition with positron emission. The broken line gives the prediction of the statistical theory, ignoring competitive proton emission.

[11] L. R. Zumwalt, Oak Ridge National Laboratory Document ORNL 397 (1949) (unpublished).

[12] B. P. Burtt, Nucleonics 5, 28 (1949).

$Cu^{63}(n,2n)Cu^{62}$

The threshold of this reaction calculated from reported values of (γ,n) thresholds as well as $(n,2n)$ thresholds[10,13] is 11.1±0.2 Mev. Cu^{62} decays with positron emission of maximum energy 2.8–2.9 Mev and period of 10 min.[10] The samples irradiated were Cu foils 2.54 cm×5.08 cm and 0.0127 cm thick. The data were made absolute in terms of the known thermal capture cross section of Cu^{65} by calibrating the Geiger counters with the beta-particles from Cu^{66} produced from Cu^{65} by thermal neutrons.[4] A recent and somewhat more accurate measurement of the $Cu^{65}(n,\gamma)Cu^{66}$ cross section reduces the uncertainty in this type of calibration over that given in reference 4.[14] Cu^{66} decays with the emission of electrons of maximum energy 2.6–2.9 Mev.[10]

The results for the $Cu^{63}(n,2n)Cu^{62}$ cross section are shown in Fig. 3, together with results of other investigators. The points of previous experiments due to Phillips and to Fowler and Slye[4] have been corrected for the new value of the capture cross section in Cu^{65}. All of the points in Fig. 3, with the exception of the value due to Wäffler,[5] have been corrected by us for K-capture competition with positron emission. This correction raises the points approximately 1.7 percent in value and was calculated from Feenberg and Trigg's[15] curves with the end-point energy of the positron taken as 2.9 Mev. Wäffler had already applied a K-capture correction to his measurement.

The standard errors indicated by the vertical lines are estimated from the standard deviations of a number of runs, the uncertainty in the absolute beta-counting (about 10 percent), and the uncertainties in the measurement of the neutron flux. It is apparent that the various measurements are consistent with each other within the limits of error.

The statistical theory of Weisskopf and collaborators[1,2] should apply to copper; we have therefore computed the theoretical $(n,2n)$ cross section for Cu^{63} using the value $a=2.2$ Mev^{-1} [nuclear temperature $=(E/2.2)^{\frac{1}{2}}$], suggested by Feld *et al.*[16] The theoretical cross section is indicated by the dashed curve in Fig. 3. The agreement with experiment is good from the threshold up to 16 Mev. At 18 Mev it is rather higher than the experimental curve but still consistent. In the neighborhood of 18-Mev tertiary reactions compete and therefore the $(n,2n)$ cross section will drop.

It should be noted that the theoretical calculation we have used takes no cognizance of competitive proton emission. This process may well occur in the second emission. From considerations of reactions and beta-ray kinetics, as well as from theoretical mass calculations, a proton binding energy of about 6.5 Mev in Cu^{63} may be inferred. Since this is significantly lower than the binding energy of a neutron to Cu^{63}, some proton emission might be expected from Cu^{62} in its highest excitation states.

$Mo^{92}(n,2n)Mo^{91}$

The threshold of the $Mo^{92}(\gamma,n)Mo^{91}$ reaction has been measured as 13.28±0.15 Mev[17] and 13.1±0.1 Mev.[18] An earlier direct measurement of the $(n,2n)$ threshold for the production of the 15.5-min period gave a value between 12 and 13 Mev.[19] The average of these measurements, weighted according to their errors, the (γ,n) threshold being corrected for the recoil energy for the case of $(n,2n)$ reactions, gives the $(n,2n)$ threshold as 13.2±0.1 Mev. Mo^{92} is a magic number nucleus with a closed shell of 50 neutrons. The Mo^{91} isotope has two isomeric states and decays with two periods: One has a half-life of 15.5 min and emits a positron with end-point energy of about 3.3 Mev; the other has a half-life slightly over one minute (75 sec,[20] 65.5 sec[18]) and emits a positron with end-point energy of about 2.6 Mev.[17,18,20]

The sample in the case of this element consisted of foils of normal molybdenum 2.54×5.08 cm and 0.0127 cm in thickness. For obtaining relative values of the cross section, these foils were counted on three glass-walled cylinder type Geiger counters. The shorter period reported for Mo^{91} produced by betatron irradiation was not observed in this experiment.[18,20] In order to normalize the cross section to absolute values, 1-cm diameter disks of copper and molybdenum were irradiated simultaneously in juxtaposition with neutrons coming off in the forward direction from the $(D+T)$ reaction, and the activities produced in these disks were compared by use of an end-window Geiger counter. By extrapolating the measurements of Zumwalt[11] in the manner which he suggests, one can make an estimate of the relative effects of beta-ray absorption and self-scattering. When this was done it was found that the relative efficiencies for counting were the same within one percent. The range of extrapolation, however, was such that one concludes the estimate of the relative efficiency of counting may be in error as much as 7 percent

Thus, the cross section of the $Mo^{92}(n,2n)Mo^{91}$ reaction for neutrons in the forward direction was calculated in terms of the cross section of the $Cu^{63}(n,2n)Cu^{62}$ reaction for these neutrons.

Figure 4 gives the results of the $Mo^{92}(n,2n)Mo^{91}$ measurements. The data have been corrected for K-capture competition with positron emission (4.5 percent) assuming an end-point energy of the positron 3.3 Mev. The uncertainties indicated by the vertical spread are estimated from the reproducibility of measurements, the uncertainty in determining the molybdenum cross

[13] J. McElhinney and W. E. Ogle, Phys. Rev. **78**, 63 (1950).
[14] H. Pomerance, Phys. Rev. **83**, 641 (1951).
[15] E. Feenberg and G. Trigg, Revs. Modern Phys. **22**, 399 (1950).
[16] B. T. Feld *et al.*, AEC Report NYO-636, p. 153 (unpublished).
[17] Hanson, Duffield, Knight, Diven, and Palevsky, Phys. Rev. **76** 578 (1949).
[18] Measurements of R. Montalbatti, communicated to us by Professor L. Katz, University of Saskatchewan.
[19] R. Sagane, Phys. Rev. **53**, 492 (1938).
[20] R. B. Duffield and J. B. Knight, Phys. Rev. **76**, 573 (1949).

sections relative to the copper cross sections, the uncertainty in the copper cross section, and the uncertainty of the neutron measurements.

The dashed curve in Fig. 4 is a theoretical calculation of the $Mo^{92}(n,2n)Mo^{91}$ cross section based on the statistical theory[1,2] with $a=3.1$ Mev^{-1} (nuclear temperature$=(E/3.1)^{\frac{1}{2}}$ Mev). The value $a=3.1$ Mev^{-1} is reasonable for this region of the periodic table. It was chosen to give the best fit to the data. As in the case of copper, agreement with the statistical model is satisfactory up to about 18 Mev, where tertiary reactions began to compete.

PHYSICAL REVIEW VOLUME 88, NUMBER 3 NOVEMBER 1, 1952

The Impulse Approximation and Field Theoretical Calculations. I

JOHN S. BLAIR* AND BENJAMIN SEGALL†
Department of Physics, University of Illinois, Urbana, Illinois
(Received June 5, 1952)

The reaction α+nucleus$\rightarrow\beta$+nucleons is considered where α and β are particles of quantized fields and the coupling to nucleons is assumed linear in the fields. By an extension of the recent work of Chew and Goldberger on potential scattering, the collision matrix has been manipulated into a term representing the impulse approximation plus three correction terms which are, respectively: The error in the impulse assumption arising from nuclear potentials; the "multiple scattering" which is at least fourth order in the coupling; and finally, a small term representing the effect of lowest order absorption. It is significant that there is no large term present, of the order of the impulse approximation term, which represents processes, second order in the coupling, where one nucleon absorbs α and another nucleon emits β.

I. INTRODUCTION

THE impulse approximation, introduced by Chew[1] in a study of the inelastic scattering of neutrons by the deuteron, has proved useful for a variety of nuclear problems. The essence of this approximation is that the scattering amplitude for a nucleus can be written as the sum of the free scattering amplitudes of the single nucleons whose momentum distribution is determined by the initial nuclear state function. The conditions under which the impulse approximation can be expected to hold were stated first by Chew and Wick[2] and recently were more rigorously demonstrated by Ashkin and Wick[3] and Chew and Goldberger[4] for the case of potential scattering.

These conditions are[4] (A) the incident particle interacts only with one particle at a time; (B) the amplitude of the incident wave is not appreciably reduced in crossing the nucleus; (C) the nuclear binding potential U has a negligible effect during the interval of strong interaction. Condition (C), the so-called "impulse assumption," was shown equivalent[2] to the requirement that the "collision time" τ be short compared to a time characteristic of the nuclear binding $(1/U)$.

The applications of the impulse approximation have not been limited to potential scattering; they have also been extended to field theoretical calculations such as photomeson production[5-8] and π meson scattering.[9-14] It has been qualitatively argued[9,12,2] that condition (C) is satisfied for the case of meson-deuteron scattering as treated by conventional weak coupling theory, but a more quantitative argument justifying the impulse approximation in a field theoretical calculation has not been published. To repeat the qualitative argument: The reciprocal of the "collision time" $(1/\tau)$ can be equated to the amount by which energy conservation is violated in the intermediate state; this energy violation is of the order of the total meson energy, ω, which is large compared to the nuclear potential U. It is not immediately obvious, however, that this qualitative argument implies that the term in the collision matrix will vanish, which represents, to second order in the coupling, absorption of a field particle by one nucleon and emission by another nucleon.

The purpose of this note is then to discuss formally the impulse approximation when applied to field theoretical calculations such as meson scattering; the task

* Assisted by the joint program of the ONR and AEC. Presently at the Department of Physics, University of Washington, Seattle, Washington.

† Illinois postdoctoral fellow; presently at The Institute for Theoretical Physics, Copenhagen, Denmark.

[1] G. F. Chew, Phys. Rev. **80**, 196 (1950).
[2] G. F. Chew and G. C. Wick, Phys. Rev. **85**, 636 (1952).
[3] J. Ashkin and G. C. Wick, Phys. Rev. **85**, 686 (1952).
[4] G. F. Chew and M. L. Goldberger **87**, 778 (1952).
[5] M. Lax and H. Feshbach, Phys. Rev. **81**, 189 (1951).
[6] S. Machida and T. Tamura, Prog. Theoret. Phys. **6**, 572 (1951).
[7] G. Morpurgo, Nuovo cimento **8**, 552 (1951).
[8] G. F. Chew and H. W. Lewis, Phys. Rev. **84**, 779 (1951).
[9] B. Segall, Phys. Rev. **83**, 1247 (1951).
[10] Fernbach, Green, and Watson, Phys. Rev. **84**, 1084 (1951).
[11] V. B. Berestesky and I. J. Pomeranchuk, Compt. rend. (U.S.S.R.) **77**, 803 (1951); also Compt. rend. (U.S.S.R.) **81**, 1019 (1951).
[12] W. B. Cheston, Phys. Rev. **85**, 952 (1952).
[13] J. S. Blair and B. Segall, Phys. Rev. **86**, 626 (1952).
[14] Isaacs, Sachs, and Steinberger, Phys. Rev. **85**, 803 (1952).

is facilitated by the recent work of Chew and Goldberger[4] for potential scattering. In a separate paper, labeled Part II, we explicitly estimate the term which measures the validity of the impulse assumption (C) for the case of meson-deuteron scattering as predicted by typical weak coupling theories. Further, some detailed consideration of the term expressing "multiple scattering" is given in Part II.

II. THEORY

In this section we shall use much of the notation and many of the results of Chew and Goldberger[4] (abbreviated C.&G.). We wish to consider the reaction:

$$\alpha+\text{nucleus}\rightarrow\beta+\text{nucleons}, \tag{1}$$

where α and β are particles of a quantized field.

The total Hamiltonian for the system of field particles and target nucleus is [C.&G., Eqs. (1) and (2)]:

$$H=H_0+V=K+U+V. \tag{2}$$

K is re-interpreted as the kinetic energy operator for the nucleons and the total energy operator for the field particles. U is still the nuclear potential. The interaction between the field and the nucleons V is assumed to be linear in the field and will contain a part creating β, v_β^*, and a part annihilating α, v_α. Further, $V=\sum_k V_k$, where k labels the nucleons, it is crucial in what follows to assume that V_k is a function of the coordinates (spatial and spin) and momenta of the kth particle alone. It is desirable to assume that the reaction proceeds through positive energy states; nuclear pair terms occurring to second order in V are discussed in Part II.

The scattering (or production) cross section will be proportional to the square of the operator $T^{(+)}$ [C.&G., Eq. (12)]:

$$T^{(+)}=V+V(E_a+i\eta-H_0-V)^{-1}V, \tag{3}$$

where E_a is the energy of the initial state. The matrix elements of $T^{(+)}$ are defined between the initial state Φ_a and the final state Φ_b, both of which are eigenfunctions of H_0; each state function is a product of a field functional and a nuclear wave function. Since V is assumed linear in the fields, the first term in $T^{(+)}$ will not contribute to our reaction. The corresponding free nucleon collision matrix for the kth particle, $t_k^{(+)}$, is [C.&G., Eq. (15a)]:

$$t_k^{(+)}=V_k(K_a+i\eta-K-V_k)^{-1}V_k, \tag{4}$$

with K_a, the kinetic energy operator on the initial state. When the above operator acts on the initial state Φ_a, it is equivalent to

$$t_k^{(+)}\Phi_a=\sum_l V_k(K_l+i\eta-K-V_k)^{-1}V_k\chi_l(\chi_l,\Phi_a), \tag{4'}$$

where χ_l is the eigenfunction of K with eigenvalue K_l. Then it is shown [C.&G., Eq. (21) with some rearrangement] that

$$T^{(+)}\equiv A+B+C+D$$
$$=\sum_k a_k+\sum_k b_k+\sum_{k\neq k'} c_{kk'}+\sum_{k\neq k'} d_{kk'}, \tag{5}$$

$$a_k=t_k^{(+)}, \tag{5a}$$

$$b_k=V(E_a+i\eta-H_0-V)^{-1}\times[U,(K_a+i\eta-K-V_k)^{-1}V_k], \tag{5b}$$

$$c_{kk'}=V_{k'}(K_a+i\eta-K-V_k)^{-1}V_k, \tag{5c}$$

$$d_{kk'}=V(E_a+i\eta-H_0-V)^{-1}V_{k'}\times(K_a+i\eta-K-V_k)^{-1}V_k. \tag{5d}$$

The commutator notation is that used by Chew and Wick,[2] Eq. (28); when the initial state is expanded in plane wave states, Eq. (5b) is equivalent to

$$b_k\Phi_a=\sum_l V(E_a+i\eta-H_0-V)^{-1}\times\{U(K_l+i\eta-K-V_k)^{-1}V_k\chi_l(\chi_l,\Phi_a)-(K_l+i\eta-K-V_k)^{-1}V_k\chi_l(\chi_l,U\Phi_a)\}. \tag{5b'}$$

Let us re-examine the meaning of this formula: Term A is the impulse approximation and B again represents some of the error associated with assumption (C). Term C, however, cannot now be called a "multiple scattering" term in the sense of C.&G.; to lowest order in V it represents a process in which one nucleon absorbs α and another emits β. The last term D may more properly be thought of as a "multiple scattering" term since its lowest nonvanishing contribution is fourth order in V. On the other hand, C appears to contain terms second order in V and might, at first glance, be expected to be of the same order of magnitude as the impulse term A. It will be our major task to show that this is not so. More precisely, we will prove in the next few paragraphs that C leads only to terms of the order B and D plus a small term reflecting first-order absorption processes.

With the aid of the operator relation,

$$(P-Q)^{-1}=P^{-1}+(P-Q)^{-1}QP^{-1}, \tag{6}$$

we can write

$$c_{kk'}=V_{k'}(K_a+i\eta-K)^{-1}V_k+V_{k'}(K_a+i\eta-K-V_k)^{-1}V_k(K_a+i\eta-K)^{-1}V_k. \tag{7}$$

The second term above can be grouped with $d_{kk'}$ and the combination will be discussed in a later paragraph. The first term of $c_{kk'}$ contains only two powers of V; since the reactions must involve both v_β^* and v_α, we can clearly write this first term as

$$v_{\alpha k'}(K_a+i\eta-K)^{-1}v_{\beta k}^*+v_{\beta k'}^*(K_a+i\eta-K)^{-1}v_{\alpha k}. \tag{8}$$

It is convenient to rewrite the energy denominator of the first term in Eq. (8):

$$(K_a+i\eta-K)^{-1}=(K_b+i\eta-K)^{-1}+(K_a+i\eta-K)^{-1}(K_b-K_a)(K_b+i\eta-K)^{-1}. \tag{9}$$

Employing Eq. (9) and the relations $E_a=E_b$ and $(E_a-K_l)(\chi_l,\Phi_a)=(\chi_l,U\Phi_a)$ we can write the matrix

element of the first term of (8) as

$$\sum_{\nu'}(\Phi_b,\chi_{\nu'})(\chi_{\nu'},v_{\alpha k'}(K_{\nu'}+i\eta-K)^{-1}v_{\beta k}{}^*\Phi_a)$$
$$+\sum_{l,\nu'}\{(\Phi_b,\chi_{\nu'})(\chi_{\nu'},v_{\alpha k'}(K_l+i\eta-K)^{-1}$$
$$\text{times }(K_{\nu'}+i\eta-K)^{-1}v_{\beta k}{}^*\chi_l)(\chi_l,U\Phi_a)$$
$$-(U\Phi_b,\chi_{\nu'})(\chi_{\nu'},v_{\alpha k'}(K_l+i\eta-K)^{-1}$$
$$\text{times }(K_{\nu'}+i\eta-K)^{-1}v_{\beta k}{}^*\chi_l)(\chi_l,\Phi_a)\},\quad(10)$$

which is more compactly expressed with commutator notation:

$$v_{\alpha k'}(K_b+i\eta-K)^{-1}v_{\beta k}{}^*$$
$$-[U,v_{\alpha k'}(K_a+i\eta-K)^{-1}(K_b+i\eta-K)^{-1}v_{\beta k}{}^*].\quad(10')$$

It is evident that the second term of (10) is similar to b_k; it then seems natural to group the sum of these terms with B. The sum over k and k' of the second term in (10) plus B will be denoted B' and represents the error associated with the impulse assumption. To the first nonvanishing orders in V and U, B' can be written

$$B'\cong\sum_{k,k'}v\beta_{k'}{}^*(K_a+i\eta-K)^{-1}[U,(K_a+i\eta-K)^{-1}v_{\alpha k}]$$
$$+\sum_k v_{\alpha k}(K_a+i\eta-K)^{-1}[U,(K_a+i\eta-K)^{-1}v_{\beta k}{}^*]$$
$$+\sum_{k\neq k'}[v_{\alpha k'}(K_a+i\eta-K)^{-1},U]$$
$$\times(K_a+i\eta-K)^{-1}v_{\beta k}{}^*.\quad(11)$$

B' is estimated in Part II for weak coupling meson-deuteron scattering. By inspection of (11) it is already clear, in the approximation second order in V, that B' is of the order (U/ω) or less of the corresponding impulse term. If the approximation, second order in V, is inadequate to describe the free nucleon collision, (as is probably the case for meson-nucleon scattering), it still seems plausible that B' is of the order (U/ω) of the impulse term; in a perturbation theory giving finite results, similar higher order corrections will be present in both B' and the impulse term and the two terms will again differ qualitatively by the factor $(U/\text{energy denominator})$.

Returning now to $c_{kk'}$, we see that it will not hurt to exchange the indices of the second term of (8) since we later sum over both k and k'; then

$$c_{kk'}=v_{\alpha k'}(K_b+i\eta-K)^{-1}v_{\beta k}{}^*+v_{\beta k}{}^*(K_a+i\eta-K)^{-1}v_{\alpha k'}$$
$$+\text{the terms just added to } D \text{ and } B;\quad(12)$$

the first two terms of (12) (i.e., $c_{kk'}$ minus the terms added to D and B) are hereafter labeled $e_{kk'}$. Some further manipulation is necessary. We can write

$$v_{\alpha k'}(K_b+i\eta-K)^{-1}v_{\beta k}{}^*$$
$$=v_{\alpha k'}(-\omega_0+\kappa_b+i\eta-\kappa)^{-1}v_{\beta k}{}^*,\quad(13a)$$

$$v_{\beta k}{}^*(K_a+i\eta-K)^{-1}v_{\alpha k'}$$
$$=v_{\beta k}{}^*(\omega_0+\kappa_a+i\eta-\kappa)^{-1}v_{\alpha k'},\quad(13b)$$

where ω_0 is the energy of the incident particle while κ is the kinetic energy operator of the nucleons. Further,

$$\text{Eq. (13a)}=v_{\alpha k'}(-\omega_0+\kappa_b(k')+i\eta-\kappa(k'))^{-1}v_{\beta k}{}^*,\quad(14a)$$

and

$$\text{Eq. (13b)}=v_{\beta k}{}^*(\omega_0+\kappa_a(k')+i\eta-\kappa(k'))^{-1}v_{\alpha k'},\quad(14b)$$

where $\kappa(k')$ is the kinetic energy operator for the k'th nucleon; this follows because $v_{\alpha k'}$ was assumed to be a function only of coordinates of the k'th nucleon and thus commutes with $(\kappa-\kappa(k'))$. Similarly, $v_{\beta k}{}^*$ commutes with $\kappa(k')$ and also with $v_{\alpha k'}$; consequently,

$$\text{Eq. (13a)}=v_{\beta k}{}^*(-\omega_0+\kappa(k')+i\eta-\kappa_a(k'))^{-1}v_{\alpha k'},\quad(15)$$

and is just the negative of (14b) except for the sign of $i\eta$ in the denominator. To obtain exact cancellation, we use the previous operator relation (6) and a familiar expression for the delta-function[15] to expand the energy denominator:

$$(\omega_0+\kappa_a(k')-i\eta-\kappa(k'))^{-1}=(\omega_0+\kappa_a(k')+i\eta-\kappa(k'))^{-1}$$
$$+2\pi i\delta(\omega_0+\kappa_a(k')-\kappa(k')).\quad(16)$$

Then,

$$e_{kk'}=-2\pi i v_{\beta k}{}^*\delta(\omega_0+\kappa_a(k')-\kappa(k'))v_{\alpha k'}.\quad(17)$$

The meaning of (17) is clear when we recall[16] the connection between the imaginary part of the diagonal element of the collision matrix and the total transition probability $\sum_c w_{ca}$, which arises from the unitary condition of the S matrix:

$$\sum_c w_{ca}=-2\,\mathrm{Im}T_{aa}.\quad(18)$$

The term $e_{kk'}$ then reflects the depletion of the diagonal element of the unitary matrix, $S=1+T$, by absorption of the field particles in a process first order in V. Term $e_{kk'}$ is summed over $k\neq k'$ to obtain E (the terms diagonal in k are contained in the impulse term A). E is not expected to contribute greatly to T, with $b\neq a$, because of its phase; further, if α or β are mesons, the matrix elements connect to states of high nucleon momentum and are thus small. (The matrix elements in E differ from zero only because of the binding in the initial or final states.)

Let us return now to consider the sum of the second term in $c_{kk'}$, Eq. (7), and $d_{kk'}$. This sum, abbreviated $d'_{kk'}$, can be expanded to fourth order in V (and zeroth order in U). It is easily verified that the sum of $d'_{kk'}$ over $k\neq k'$, D', is then approximated by

$$D'\cong V(K_a+i\eta-K)^{-1}V(K_a+i\eta-K)^{-1}V$$
$$\times(K_a+i\eta-K)^{-1}V-\sum_k V_k(K_a+i\eta-K)^{-1}V_k$$
$$\times(K_a+i\eta-K)^{-1}V_k(K_a+i\eta-K)^{-1}V_k.\quad(19)$$

Thus D' contains all possible transitions between the nucleons, fourth order in V and zeroth order in U, except for the fourth-order contribution of the impulse term.

We have investigated Eq. (19) in the fixed nucleon approximation and find that considerable simplification

[15] B. A. Lippman and J. Schwinger, Phys. Rev. **79**, 469 (1950), Eq. (1.58).
[16] See reference 15, Eq. (1.75).

is possible. The details of this calculation are given in Part II and only the results are here discussed. Before presenting these, however, a few preliminary comments are necessary.

It is seen that the numerators of Eq. (19) consist of various permutations of the product $v_{\beta k'}{}^* V_{k'''} V_{k''}{}^* v_{\alpha k}$, where $V_{k'''}{}^*$ and $V_{k'''}$ represent, respectively, creation and absorption of virtual field particles at nucleons k'' and k'''. It is then convenient to group the terms of Eq. (19) into the classes: (1) four nucleons different ($k \neq k' \neq k'' \neq k'''$), (2) three nucleons different, and (3) two nucleons different. The important class (3) further divides into: (3a) $k=k' \neq k''=k'''$, (3b) $k \neq k'=k''=k'''$ and $k' \neq k=k''=k'''$, (3c) $k=k'=k'' \neq k'''$ and $k=k'=k'''\neq k''$, and (3d) $k=k'' \neq k'=k'''$ and $k=k''' \neq k'=k''$. The calculation is carried out with no specification of the interaction V beyond the assumption that it is a function of the coordinates of only one nucleon. The prescription of Corinaldesi and Field[17] is used to calculate the matrix elements for diagrams containing "external lines." No subtraction techniques are necessary.

We then find the plausible result that classes (1), (2), (3a), and (3b) give zero contribution to the fourth order, fixed nucleon approximation for D'. Of the two remaining classes, (3c) represents scattering by one nucleon modified by the exchange of a virtual meson with another nucleon while (3d) represents absorption by one nucleon, emission by another, but with virtual meson exchange between just these two nucleons. It is therefore not surprising to find that the contribution of class (3c) to D' is equivalent to the $k=k'$ part of B' [as given by Eq. (11)], if we replace the second-order approximation to the nuclear potential arising from meson theory by the phenomenological potential U.[18] Further, the contribution of class (3d) to D' comprises three terms: (1) True double scattering (including a radiative damping contribution) as given by Eq. (29a) of C.&G. with the approximation that the single nucleon collision operator t_k is replaced by its second order, fixed nucleon approximation. (2) A similar term, characteristic of a field theory but not present for potential scattering, where t_k is replaced by the second-order matrix element for pair creation or absorption of the field particles. (3) A term involving the nuclear potential between k and k' similar to those terms in Eq. (11) where $k \neq k'$.

The calculation of D' has not been carried to higher orders in V but it seems quite plausible that the results of the preceding paragraph can be extended, so that that part of D' not explicitly containing U can be represented in general by the sum of three terms: (1) The multiple scattering term in Eq. (21) of C.&G. containing the single nucleon collision operators t_k. Such multiple scattering will not necessarily be small. (2) A term similar to the multiple scattering term (1) but containing some matrix elements for meson pair creation and emission. (3) A term similar to B' and those parts of D' explicitly containing the phenomenological nuclear potentials. It would then seem reasonable to estimate term (1) on the basis of the observed single nucleon collisions, although term (2), since it involves virtual pair processes, would appear more difficult to estimate on this basis. However, there is good reason to expect (2) to be less important than (1) because of the energy violation of pair processes.

One intuitively expects the result that there is no matrix element for absorption of α by one nucleon and emission of β by another in the absence of a nuclear potential or a multiple scattering linking these two nucleons. The proof of this statement, in the above weak coupling calculation, depended upon the cancellation of several contributions to the collision matrix corresponding to different sequences of absorption and emission. As pointed out by Professor Chew, the situation is similar to the calculation of meson scattering in the neutral scalar theory with fixed sources where one intuitively expects no scattering since there is no possibility of changing the degrees of freedom of the scatterer; indeed the second-order perturbation calculation does predict zero scattering, but the proof again rests on the cancellation of two contributions to the matrix element corresponding to different Feynman diagrams. These cases then lead us to observe that perturbation theory does verify our "common sense" predictions but in a somewhat clumsy (and often disguised) fashion. Further these examples give us confidence that our intuitive notions will be substantiated as the order of the calculation is increased.

To summarize, we have succeeded in eliminating the lowest order contributions of C from the collision matrix, Eq. (5), so that $T^{(+)}$ could be written

$$T^{(+)}=A+B'+D'+E. \tag{20}$$

A is still the impulse approximation; B' is essentially an estimate of the impulse condition (C) and is approximated in second order in V by Eq. (11); D', the "multiple scattering" term, in the fourth-order, fixed nucleon approximation, consisted of a term easily identifiable as double scattering and also one already included as the lowest order approximation of B' if we wished to replace the second-order approximation to nuclear potentials by the phenomenological potential U (it seems likely that this pattern will be maintained as the exact expression for D' is calculated to higher orders in V); E is a small correction term representing the effect of lowest order absorption processes.

We wish to thank Professor G. F. Chew for his generous advice and for the opportunity to study a preprint of his paper with Professor Goldberger. We would also like to thank Dr. M. H. Friedman and Mrs. Freda Salzman for comments.

[17] E. Corinaldesi and G. Field, Phil. Mag. **40**, 1159 (1949).

[18] It is then clear that we can disregard the contribution of class (3c) to D' since the resulting commutator is already included in B'. This and subsequent duplication results from our simultaneous use of phenomenological nuclear potentials and meson theory.

Diffraction in Time*

MARCOS MOSHINSKY
Instituto Nacional de la Investigación Científica, e Institutos de Física y Geofísica, Universidad de México, México, D.F., México
(Received June 6, 1952)

In a previous note a dynamical description of resonance scattering was given, and transient terms appeared in the wave function describing the process. To understand the physical significance of these terms, the transient effects that appear when a shutter is opened are discussed in this paper. For a nonrelativistic beam of particles, the transient current has a close mathematical resemblance with the intensity of light in the Fresnel diffraction by a straight edge. This is the reason for calling the transient phenomena by the name of diffraction in time.

The shutter problem is discussed for particles whose wave functions satisfy the Schrödinger equation, the ordinary wave equation, and the Klein-Gordon equation. Only for the Schrödinger time-dependent equation do the transient wave functions resemble the solutions that appear in Sommerfeld's theory of diffraction. The connection of transient phenomena with the time-energy uncertainty relation, and the interpretation of the transient current in a scattering process, are briefly discussed. The relativistic wave functions for the shutter problem may play an important role in the dynamical description of a relativistic scattering process.

I. INTRODUCTION

IN a previous paper[1] we analyzed the dynamical behavior of a resonance scattering process, when the scatterer (represented by an appropriate boundary condition) was introduced into the beam of incident particles at a definite time. As a result of the introduction of the scatterer, transient terms appeared in the wave function representing the process, and with their help we could make the transition from the initial state (plane wave) to the final state (plane plus scattered waves).

Transient terms are to be expected in a dynamical description of resonance scattering, from the analogy that this description has with the theory of resonant electric circuits.[2] As is well known, in circuit theory the appearance of resonances in the stationary current is closely related with the transients of the circuit, as the same parameters (resonant frequencies and damping factors) appear in both.[3]

The transient terms in a scattering process contain, besides those that could be considered the analogous of electric circuit theory, terms that are related to the time-energy uncertainty relation,[4] as quantum mechanics is used in the description of the scattering.

To understand the physical meaning of the transient terms in the resonance scattering process, it seemed of interest to analyze first the transient effects that appear when the propagation of a beam of particles is interrupted. The more complicated phenomenon, where an actual scatterer (represented by a potential or by boundary conditions[5]) is introduced into the beam of incident particles, will be discussed briefly at the conclusion of this paper.

We deal here with the transient terms in the wave function that appear when a shutter is opened. It will be shown in the next section, that when the state of the beam of particles is represented by a wave function satisfying the time-dependent Schrödinger equation, the transient current has a remarkable mathematical similarity with the intensity of light in the Fresnel diffraction by a straight edge.[6] The transient phenomena have therefore been given the name of diffraction in time.

The form of the transient terms of ψ that appear when the shutter is opened, is strongly dependent on the type of wave equation satisfied by ψ. In the present paper we analyze the transient terms that appear when the ψ's satisfy the Schrödinger equation, the ordinary wave equation, and the Klein-Gordon equation. Only for the Schrödinger equation is there an analogy with the phenomena of optical diffraction, which has to do with the resemblance that the solutions have with those that appear in Sommerfeld's[7] theory of diffraction.

II. THE SHUTTER PROBLEM

The problem we shall discuss in this section is the following: a monochromatic beam of particles of mass m, energy $(\hbar^2k^2/2m)$, moving parallel to the x-axis, is interrupted at $x=0$ by a shutter perpendicular to the beam, as illustrated in Fig. 1. If at $t=0$ the shutter is opened, what will be the transient particle current observed at a distance x from the shutter?

To set the mathematical problem, we must first give the behavior of the shutter, i.e., if it acts as a perfect absorber (no reflected wave), or a perfect reflector (an infinite potential barrier), or something between the two. For simplicity we will assume that the shutter

* Paper presented at the Physics Symposium sponsored by the Academia Brasileira de Ciencias and the Centro de Cooperación Científica para la America Latina (UNESCO) at Rio de Janeiro, Brazil.

[1] M. Moshinsky, Phys. Rev. **84**, 525 (1951) to be referred to as (A).

[2] E. P. Wigner, Am. J. Phys. **17**, 99 (1949).

[3] J. C. Jaeger, *An Introduction to the Laplace Transformation* (Methuen and Company, London, 1949), p. 31.

[4] M. Moshinsky, Rev. Mex. Fis. **1**, 28 (1952).

[5] E. P. Wigner, Phys. Rev. **70**, 15 (1946); Feshbach, Peaslee, and Weisskopf, Phys. Rev. **71**, 145 (1947).

[6] M. Born, *Optik* (Julius Springer Berlin, 1933), pp. 192–5.

[7] A. Sommerfeld, *Theorie der Beugung*, Chap. XX of the Frank-v. Mises, *Differential- und Integralgleichungen der Mechanik und Physik* (Fried. Vieweg and Sohn, Braunschweig, 1935), Vol. II, pp. 808–871.

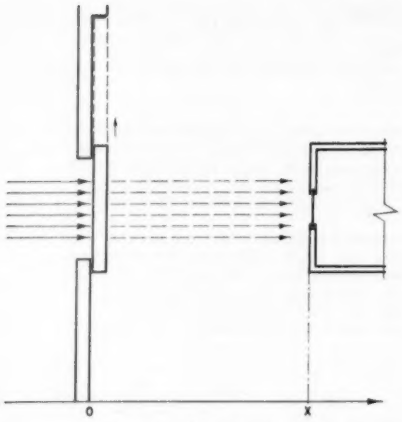

FIG. 1. The shutter problem.

acts as a perfect absorber, though it can be easily shown that for $x \gg \lambda$ (where λ is the wavelength $\lambda = (2\pi/k)$), the transient current obtained below holds for any type of shutter, so long as it acts as a device that, when closed, keeps the beam of particles on only one side of it.

For nonrelativistic particles, the wave function $\psi(x, t)$ that represents the state of the beam of particles for $t > 0$, satisfies the time dependent Schrödinger equation:

$$-i(\partial\psi/\partial t) = (\hbar/2m)(\partial^2\psi/\partial x^2), \tag{1}$$

and the initial conditions:

$$\psi(x, 0) = \begin{cases} \exp(ikx) & \text{if } x < 0 \\ 0 & \text{if } x > 0. \end{cases} \tag{2}$$

The solution of (1, 2) can be immediately given with the help of the functions $\chi(x, k, t)$, introduced in (A), and defined by:

$$\chi(x, k, t) = \exp(imx^2/2\hbar t)\, \exp(y^2)\, \operatorname{erfc}(y), \tag{3a}$$

where:

$$\operatorname{erfc}(y) = 2\pi^{-\frac{1}{2}} \int_y^\infty \exp(-y^2) dy, \tag{3b}$$

$$y = \exp(-i\pi/4)(2ht/m)^{-\frac{1}{2}}(x - vt), \quad v = (hk/m). \tag{3c}$$

The function $\chi(x, k, t)$ satisfies (1) as:

$$(\hbar/2m)(\partial^2\chi/\partial x^2) + i(\partial\chi/\partial t) \equiv (4it)^{-1} \exp(imx^2/2\hbar t)[d^2/dy^2 - 2y d/dy - 2] \exp(y^2) \operatorname{erfc}(y), \tag{4}$$

and from the definition (3b) of the error integral function, we see that the right-hand side of (4) vanishes. Furthermore, when $t \to 0$, $|y| \to \infty$ and argy is either $-(\pi/4)$ if $x > 0$ or $(3\pi/4)$ if $x < 0$. From the asymptotic properties of the error integral function when $|y| \to \infty$, summarized in appendix 2 of (A), we have:

$$\exp(y^2) \operatorname{erfc}(y) \to \begin{cases} 0 & \text{if } -(\pi/2) < \arg y < (\pi/2) \\ 2\exp(y^2) & \text{if } (\pi/2) < \arg y < (3\pi/2). \end{cases} \tag{5}$$

We conclude from the above that:

$$\psi(x, t) = \tfrac{1}{2}\chi(x, k, t), \tag{6}$$

satisfies Eq. (1) and the initial condition (2).

When $t \to \infty$, $|y| \to \infty$ and argy $= (3\pi/4)$, so using (5) again, we obtain:

$$\psi(x, t) \to \exp i[kx - (\hbar k^2/2m)t], \tag{7}$$

which would be the expected stationary form of the wave function.

The transient current $J(x, t)$ takes from (36) the form:

$$J(x, t) = (\hbar/2im)[\psi^*(\partial\psi/\partial x) - \psi(\partial\psi^*/\partial x)] = (v/4)\{|\chi(x, k, t)|^2 + (\tfrac{1}{2}\pi kvt)^{-\frac{1}{2}} \operatorname{Im}\{\exp i[(\pi/4) - (mx^2/2\hbar t)]\chi(x, k, t)\}\}, \tag{8}$$

where Im stands for the imaginary part of the curly bracket. The expression (8) simplifies considerably if we assume that $x \gg \lambda$. As we shall show below, $|\chi(x, k, t)|$ differs appreciably from zero only when t is of the order or larger than the time of flight $T = (x/v)$. For $t \gtrsim T$ we have that $(kvt)^{-\frac{1}{2}} \leqslant (kx)^{-\frac{1}{2}}$ is very small. Therefore, the second term in (8) is $\simeq 0$ for all $t > 0$ if $x \gg \lambda$, and in this case the current becomes:

$$J(x, t) = (v/4)\,|\operatorname{erfc}[-(\pi/2i)^{\frac{1}{2}}u]|^2, \tag{9}$$

where:

$$u = (kx)^{\frac{1}{2}}(\pi t/T)^{-\frac{1}{2}}[(t/T) - 1]. \tag{10}$$

From the asymptotic behavior (7) of ψ when $t \to \infty$, we see that the stationary current is $J_0 = v$. Using a simple relation[8] between the error integral function and

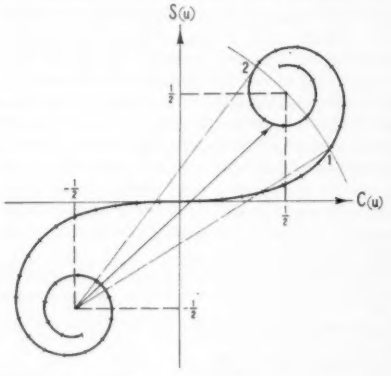

FIG. 2. Cornu spiral.

[8] E. Jahnke and F. Emde, *Tables of Functions* (Dover Publications, New York, 1945), fourth edition, p. 36.

the Fresnel integrals, the ratio of the transient to the stationary current becomes:

$$[J(x,t)/J_0]=\tfrac{1}{2}\{[\tfrac{1}{2}+C(u)]^2+[\tfrac{1}{2}+S(u)]^2\}, \quad (11)$$

where:

$$C(u)=\int_0^u \cos(\tfrac{1}{2}\pi u^2)du, \quad S(u)=\int_0^u \sin(\tfrac{1}{2}\pi u^2)du. \quad (12)$$

The right-hand side in (11) is identical to the expression[6] for the intensity of light in the Fresnel diffraction by a straight edge. The variable u has though a different meaning from the optical problem, as it is now the function of time given by (10).

In the Cornu spiral diagram of Fig. 2, the right-hand side of (11) is one-half of the square of the radius vector from the point $(-\frac{1}{2}, -\frac{1}{2})$ to the point on the spiral whose distance from the origin, along the curve, is u. From (10) we see that when $0<t\leqslant 0$, then $-\infty<u\leqslant 0$, while when $T\leqslant t<\infty$ then $0\leqslant u<\infty$. With the help of the Cornu spiral we see that when t goes from 0 to T, the ratio (J/J_0) increases monotonically from 0 to $\frac{1}{4}$, while when t is larger than T, then (J/J_0) behaves as a damped oscillation around the value $(J/J_0)=1$, tending to this value when $t\to\infty$. This behavior is illustrated in Fig. 3.

From the standpoint of classical mechanics, it is clear that $(J/J_0)=0$ if t is less that the time of flight T, while $(J/J_0)=1$ if $t\geqslant T$. This behavior is also illustrated in Fig. 3 by the straight line.

A good measure of the "width" of this diffraction effect in time, can be obtained from the difference τ between the first two times at which (J/J_0) takes the classical value, i.e., $\tau=t_2-t_1$, as shown in Fig. 3. The times at which the curve of Fig. 3 intersects with the straight line $(J/J_0)=1$, correspond to the values of u obtained from the intersection of the Cornu spiral with the circle of radius $\sqrt{2}$ and center $(-\frac{1}{2}, -\frac{1}{2})$. The values u_1, u_2 that correspond to t_1, t_2 are the lengths along the Cornu spiral from the origin to the points 1, 2 in Fig. 2, so that we have: $u_2-u_1=0.85$. As $x\gg\lambda$ we see from (10) that t_1, t_2 are very close to T, so we may write:

$$\tau\simeq(u_2-u_1)(\pi/kx)^{\frac{1}{2}}T=0.85(\pi x\hbar/mv^3)^{\frac{1}{2}}. \quad (13)$$

As an example (of possible interest in the operation of neutron velocity selectors), we have that for 300°K neutrons at a distance $x=1$ m, the diffraction width would be:

$$\tau=0.27\times10^{-3}\text{ sec.}$$

Borrowing from the terminology of optics, we could say that in classical mechanics a shutter casts a sharp shadow in time, i.e., the beam current jumps suddenly from zero to the stationary value at $t=T$, while in quantum mechanics there is a diffraction effect in time as illustrated in Fig. 3. When we make Planck's constant $\hbar$ tend to zero, we see from (13) that the diffraction width τ tends also to zero, and the quantum-mechanical current reduces to the classical current, as one should expect.

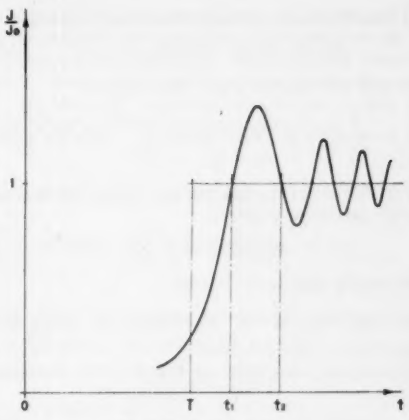

FIG. 3. Diffraction in time.

The analogy between the transient current (11) and the diffraction phenomena in optics, raises the question of whether the transient currents for other types of wave equations show this analogy. We shall see in the following sections that this is not the case, and that only when ψ obeys the Schrödinger equation, does it resemble the wave functions that appear in Sommerfeld's theory of diffraction.[7]

The transient current (11) increases monotonically from the very moment in which we open the shutter, and therefore, in principle, an observer at a distance x from the shutter could detect particles before a time (x/c), where c is the velocity of light. This would imply that some of the particles travel with velocities larger than c, and the error is due of course, to employing the nonrelativistic Schrödinger equation in the analysis.

We shall discuss in the following sections the transient wave functions associated with two relativistic equations, the ordinary wave equation and the Klein-Gordon equation. It will be shown in this case, that at a distance x from the shutter, the wave function $\psi(x,t)$ is zero for $t<(x/c)$, thus safeguarding the relativity principle. When in the solution for the Klein-Gordon equation we make $c\to\infty$, it will reduce essentially to (6), thus giving the transient current (11) in the nonrelativistic approximation.

III. THE ORDINARY WAVE EQUATION

We shall now deal with the same problem of the last section, but assume that ψ satisfies the ordinary wave equation

$$c^2(\partial^2\psi/\partial x^2)=(\partial^2\psi/\partial t^2). \quad (14)$$

If initially ψ and its time derivative are given by:

$$\psi(x,0)=F(x), \quad (\partial\psi/\partial t)_{t=0}=G(x), \tag{15}$$

then as is well known,[9] $\psi(x,t)$ has the form:

$$\psi(x,t)=\tfrac{1}{2}\left[F(x+ct)+F(x-ct)+c^{-1}\int_{x-ct}^{x+ct}G(x')dx'\right]. \tag{16}$$

For $t<0$ when the shutter was closed, we had on the left side of the shutter:

$$\psi(x,t)=\exp[ik(x-ct)], \quad \text{for} \quad x<0.$$

This implies that at $t=0$ we have:

$$F(x)=\exp(ikx), \quad G(x)=-ikc\exp(ikx), \quad \text{if} \quad x<0, \tag{17}$$

while $F(x)=G(x)=0$ if $x>0$.

Introducing these initial conditions in (16) we obtain:

$$\psi(x,t)=\begin{cases} 0 & \text{if} \quad t<(x/c) \\ \exp[ik(x-ct)]-\tfrac{1}{2} & \text{if} \quad t>(x/c). \end{cases} \tag{18}$$

The absolute value of the wave function jumps suddenly to the value $\frac{1}{2}$ at $t=(x/c)$, and it oscillates periodically thereafter. This behavior has certainly no resemblance to the diffraction in time effect obtained in the previous section.

IV. THE RELATIVISTIC SHUTTER PROBLEM

If we wish to extend the discussion of the transient effects of Sec. II, to a beam of electrons at relativistic energies, we would have, of course, to replace Eq. (1) by Dirac's equation. A fundamental change creeps in though by the fact that the wave function will involve the negative, as well as the positive energy eigenfunctions. A complete description of the phenomenon would necessitate then the introduction of hole theory, and the single particle picture would have to be abandoned.

As our main interest concerns the transients associated with the different wave equations, we shall not attempt to discuss here the problem when hole theory is involved, but rather will restrict ourselves to the single particle picture in which states of both positive and negative energy are available. Furthermore, the features of spin and statistics are irrelevant to our analysis, so that for simplicity, instead of Dirac's equation we shall use the Klein-Gordon equation. We shall briefly indicate though, at the end of this section, the relation of the solution for the Dirac equation with the solution to be obtained for the Klein-Gordon equation.

The wave function $\psi(x,t)$ satisfies now the equation:

$$(\partial^2\psi/\partial x^2)=c^{-2}(\partial^2\psi/\partial t^2)+\mu^2\psi, \tag{19}$$

where $\mu=(mc/\hbar)$.

[9] A. G. Webster, *Partial Differential Equations of Mathematical Physics* (G. E. Stechert and Company, New York, 1933), second edition, p. 78.

If initially ψ and its time derivative are given by:

$$\psi(x,0)=F(x), \quad (\partial\psi/\partial t)_{t=0}=G(x), \tag{20}$$

then using the Fourier integral theorem, we obtain:

$$\psi(x,t)=(2\pi)^{-\frac{1}{2}}\int_{-\infty}^{\infty}[f(\kappa)\cos(\epsilon ct) + (\epsilon c)^{-1}g(\kappa)\sin(\epsilon ct)]\exp(i\kappa x)d\kappa, \tag{21}$$

where $f(\kappa)$, $g(\kappa)$ are the ordinary Fourier transforms of $F(x)$, $G(x)$, and $\epsilon=(\kappa^2+\mu^2)^{\frac{1}{2}}$.

For $t<0$, when the shutter was closed, we assume as in the previous section, that:

$$\psi(x,t)=\exp[i(kx-Ect)], \quad \text{for} \quad x<0,$$

where E is the energy in units of reciprocal length, i.e., $E=(k^2+\mu^2)^{\frac{1}{2}}$. This implies that at $t=0$ we have:

$$F(x)=\exp(ikx), \quad G(x)=-iEc\exp(ikx), \quad \text{for} \quad x<0, \tag{22}$$

while $F(x)=G(x)=0$ for $x>0$.

The Fourier transforms $f(\kappa)$, $g(\kappa)$ become then:[10]

$$f(\kappa)=(2\pi)^{-\frac{1}{2}}\int_{-\infty}^{0}\exp[i(k-\kappa)x]dx=(2\pi)^{\frac{1}{2}}\delta_+(\kappa-k)$$

$$=(\pi/2)^{\frac{1}{2}}\{\delta(\kappa-k)+i[\pi(\kappa-k)]^{-1}\}, \tag{23}$$

$$g(\kappa)=-iEcf(\kappa). \tag{24}$$

Introducing (23), (24) in (21) we obtain:

$$\psi(x,t)=\tfrac{1}{2}\exp[i(kx-Ect)] - (4\pi i)^{-1}\mathrm{P}\int_{-\infty}^{\infty}(\kappa-k)^{-1}(\epsilon+E) \times\exp[i(\kappa x-\epsilon ct)]\epsilon^{-1}d\kappa - (4\pi i)^{-1}\mathrm{P}\int_{-\infty}^{\infty}(\kappa-k)^{-1}(\epsilon-E) \times\exp[i(\kappa x+\epsilon ct)]\epsilon^{-1}d\kappa. \tag{25}$$

As usual, when δ_+ functions are employed, the integrals must be interpreted in the sense of Cauchy's principal value[11] as indicated by the P. The initial conditions at $t=0$, can be obtained from (25) by closing the contour in the κ-plane, from above if $x>0$ and from below if $x<0$. The first and second integrals in (25) give the contribution from the positive and negative energies, respectively.

To eliminate the branch points at $\kappa=\pm i\mu$ in (25), we introduce in the first integral the change of variable:

$$\zeta=\mu^{-1}(\kappa+\epsilon), \tag{26}$$

[10] W. Heisenberg, Z. Physik **120**, 519 (1943).

[11] E. T. Whittaker and G. N. Watson, *Modern Analysis* (Cambridge University Press, New York, 1943), American edition, p. 117.

from which we have: $\kappa=\frac{1}{2}\mu(\zeta-\zeta^{-1})$, $\epsilon=\frac{1}{2}\mu(\zeta+\zeta^{-1})$. The limits of integration $[-\infty, \infty]$ for the κ transform into $[0, \infty]$ for the ζ.

In the second integral we introduce a ζ corresponding to negative energies, i.e., $\zeta=\mu^{-1}(\kappa-\epsilon)$. It is clear that with this ζ, the integrand in the second integral becomes the same function of ζ that we have in the first integrand. Furthermore, for this ζ the limits of integration are $[-\infty, 0]$.

Combining the two integrals we obtain:

$$\psi(x,t)=\tfrac{1}{2}\exp[i(kx-Ect)]$$
$$-(2\pi i)^{-1}\mathrm{P}\int_{-\infty}^{\infty}(\zeta+z)(\zeta-z)^{-1}(2\zeta)^{-1}$$
$$\times\exp\{\tfrac{1}{2}i\mu[(x-ct)\zeta-(x+ct)\zeta^{-1}]\}d\zeta, \quad (27)$$

where $z=\mu^{-1}(k+E)$.

The integrand of (27) has a pole at $\zeta=z$ and an essential singularity at $\zeta=0$, but the integral is convergent, and in the appendix it is evaluated by a suitable deformation of the contour.

From the analysis given in the appendix, it follows that:

$$\psi(x,t)=0 \quad \text{if} \quad t<(x/c), \quad (28a)$$
$$\psi(x,t)=\exp[i(kx-Ect)]+\tfrac{1}{2}J_0(\eta)$$
$$-\sum_{n=0}^{\infty}(\xi/iz)^n J_n(\eta), \quad \text{if} \quad t>(x/c), \quad (28b)$$

where:

$$\xi=[(ct+x)/(ct-x)]^{\frac{1}{2}}, \quad \eta=\mu(c^2t^2-x^2)^{\frac{1}{2}}, \quad (29)$$

and the J_n are the Bessel functions of order n.

The wave function $\psi(x,t)$ of (28) satisfies the Klein-Gordon equation, as can be easily seen when we express this equation in terms of the variables ξ, η of (29), so that (19) takes the form:

$$\left(\frac{\partial^2}{\partial\eta^2}+\frac{1}{\eta}\frac{\partial}{\partial\eta}-\frac{\xi^2}{\eta^2}\frac{\partial^2}{\partial\xi^2}-\frac{\xi}{\eta^2}\frac{\partial}{\partial\xi}+1\right)\psi(\xi,\eta)=0. \quad (30)$$

As $\xi^\alpha J_\alpha(\eta)$ is a solution of (30) for any α, we see that each term of the series in (28b) satisfies the Klein-Gordon equation.

For $n=0$ the solution $J_0[\mu(c^2t^2-x^2)^{\frac{1}{2}}]$ of the Klein-Gordon equation is well known in quantum electrodynamics.[12] For $n\neq 0$ the solutions $\xi^n J_n(\eta)$ do not seem to have had a wide use in quantum field theory, possibly because they are not in themselves Lorentz-invariant, but become so only after multiplication by z^{-n}.

When the rest mass of the particle vanishes, then $\eta\to 0$ and $z\to\infty$, so that all the terms in the series of (28b) vanish except $J_0(\eta)$ which becomes 1. The solution (28) reduces in this case, to the solution (18) of the ordinary wave equation, as we should expect.

We are now interested in the asymptotic values of $\psi(x,t)$ when $t\to(x/c)$ and when $t\to\infty$. In the first case, we see from (29) that $\eta\to 0$ and we can replace the Bessel functions by their asymptotic values:

$$J_n(\eta)\to(2^n n!)^{-1}\eta^n. \quad (31a)$$

The series in (28b) becomes then:

$$\sum_{n=0}^{\infty}(\xi/iz)^n J_n(\eta)\to\sum_{n=0}^{\infty}(n!)^{-1}(\xi\eta/2iz)^n$$
$$=\exp(\xi\eta/2iz). \quad (31b)$$

For $t=(x/c)$ the series takes the value $\exp[i(k-E)x]$ and the asymptotic form of $\psi(x,t)$ is:[13]

$$\lim_{t\to(x/c)}[\psi(x,t)]=\tfrac{1}{2}. \quad (32)$$

The wave function $\psi(x,t)$ jumps suddenly from zero to the value $\frac{1}{2}$ at $t=(x/c)$, just as in the case of the ordinary wave equation, and it does not build up continuously from $t=0$ as in the case of the Schrödinger equation.

To obtain the asymptotic form of $\psi(x,t)$ when $t\to\infty$, we notice first that in this case, $\xi\to 1$ and $\eta\to\infty$. Replacing in the series of (28b) the $J_n(\eta)$ by their asymptotic values:

$$J_n(\eta)\to(\tfrac{1}{2}\pi\eta)^{-\frac{1}{2}}\cos[\eta-\tfrac{1}{4}(2n+1)\pi], \quad (33a)$$

we get:

$$\left|\sum_{n=0}^{\infty}(\xi/iz)^n J_n(\eta)\right|\to\left|(\tfrac{1}{2}\pi\eta)^{-\frac{1}{2}}\sum_{n=0}^{\infty}(iz)^{-n}\right.$$
$$\left.\times\cos[\eta-\tfrac{1}{4}(2n+1)\pi]\right|\leqslant(\tfrac{1}{2}\pi\eta)^{-\frac{1}{2}}\sum_{n=0}^{\infty}z^{-n}. \quad (33b)$$

From its definition $z=\mu^{-1}(k+E)>1$ for any $k>0$, so that the series in (33b) converges, and therefore, when $\eta\to\infty$ the series in (28b) tends to zero. The asymptotic value of $\psi(x,t)$ when $t\to\infty$, becomes then:

$$\psi(x,t)\to\exp[i(kx-Ect)], \quad (34)$$

which is the stationary form of the wave function that we expect.

To pass from the relativistic wave function (28b) to the nonrelativistic wave function (6), we have to take $c\to\infty$. A simple way to make this transition is through the expression (25) for $\psi(x,t)$. When $c\to\infty$ we see that $ect=(\kappa^2+\mu^2)^{\frac{1}{2}}ct$, tends to:

$$ect\to\mu ct+(\hbar\kappa^2/2m)t+\cdots, \quad (35)$$

where all the other terms of the development vanish for $c\to\infty$. A similar result holds for Ect. Furthermore,

[12] P. A. M. Dirac, Proc. Cambridge Phil. Soc. **30**, 150 (1934); J. Schwinger, Phys. Rev. **75**, 678 (1949).

[13] The asymptotic behavior of $\psi(x,t)$ can also be derived, in a simple and rigorous fashion, from the integral representation of the wave function that is given in the appendix.

when $c\to\infty$ we see that $(E/\epsilon)\to 1$, and therefore, the negative energy part of (25) vanishes, while the rest takes the form:

$$\psi(x,t)\to\exp(-i\mu ct)\Big\{\tfrac{1}{2}\exp i[kx-(\hbar k^2/2m)t]$$

$$-(2\pi i)^{-1}\mathrm{P}\int_{-\infty}^{\infty}(\kappa-k)^{-1}\exp i[\kappa x-(\hbar\kappa^2/2m)t]d\kappa\Big\}$$

$$=\exp(-i\mu ct)\tfrac{1}{2}\chi(x,k,t). \quad (36)$$

The last result follows from the evaluation of the integral in (36), that was carried in appendix 1 of (A).

It follows from (36) that when $c\to\infty$, the transient current obtained with the relativistic wave function reduces precisely to (11).

Finally, we would like to remark that an analysis similar to the one carried above, can be given for the Dirac wave equation. Choosing a definite direction of spin, the Dirac wave function reduces to two components, each of which can be expressed, for $t>(x/c)$, in terms of linear combinations of the wave function (28b) and $J_0(\eta)$.

V. ANALOGIES WITH SOMMERFELD'S DIFFRACTION THEORY

In the previous sections, the shutter problem for different types of wave equations was analyzed, and we obtained the corresponding wave functions. Rather than to compare the related transient currents with the intensity of light in optical diffraction [as suggested by the form of the nonrelativistic current (11)], we shall look into the analogies between the wave functions themselves, and a family of solutions in Sommerfeld's theory of diffraction.

For electromagnetic diffraction problems in the plane, we need appropriate solutions of the two-dimensional Kirchhoff equation, which in polar coordinates has the form:

$$(\nabla^2+k^2)\phi\equiv(\partial^2\phi/\partial r^2)+r^{-1}(\partial\phi/\partial r)$$
$$+r^{-2}(\partial^2\phi/\partial\theta^2)+k^2\phi=0, \quad (37)$$

where $k=(2\pi/\lambda)$ and λ is the wavelength of the radiation.

The well-known family of solutions of (37) that is obtained with the help of the Riemann surface[14] analysis of Sommerfeld, can be written in the form:

$$\chi'(r,\theta,\theta_0)=\exp(ikr)\exp(y'^2)\,\mathrm{erfc}(y'), \quad (38a)$$

where:

$$y'=-\exp(-i\pi/4)(2kr)^{\frac{1}{2}}\sin[\tfrac{1}{2}(\theta-\theta_0)], \quad (38b)$$

and θ_0 is a parameter.

The χ' satisfy (37) as can be seen from the fact that:

$$[\nabla^2+k^2]\phi\equiv k^2(2ikr)^{-1}\exp(ikr)\times[d^2/dy'^2$$
$$-2y'd/dy'-2]\exp(y'^2)\,\mathrm{erfc}(y'), \quad (39)$$

and as shown in (4), the right-hand side of (39) vanishes.

Despite the fact that the time dependent Schrödinger equation is of the parabolic type, while the Kirchhoff equation is of the elliptic type, they have solutions of the form (3) and (38) which are remarkably similar. No such similarity exists between the wave functions (18) and (28) of the hyperbolic relativistic wave equations, and the family of solutions (38), so that we do not expect in this case, a resemblance between the transient current and optical diffraction effects.

When a semi-infinite perfectly reflecting plane is introduced at $\theta=-(\pi/2)$, in the path of an electromagnetic wave polarized in the plane and propagating in the direction $\theta=0$, the wave function $\phi(r,\theta)$ that satisfies[14] the boundary conditions at $\theta=-(\pi/2),(3\pi/2)$ and the asymptotic behavior at $r\to\infty$, becomes:

$$\phi(r,\theta)=\tfrac{1}{2}[\chi'(r,\theta,0)-\chi'(r,\theta,\pi)]. \quad (40)$$

A corresponding problem for the transient current appears when the shutter is represented as a perfect reflector, i.e., an infinite potential barrier. In this case, we must replace in the initial condition (2), $\exp(ikx)$ by $\exp(ikx)-\exp(-ikx)$, and with the help of (5) we immediately obtain that:

$$\psi(x,t)=\tfrac{1}{2}[\chi(x,k,t)-\chi(x,-k,t)]. \quad (41)$$

From (40), and assuming that $r\gg\lambda$, we obtain the characteristic Fresnel diffraction effect[6] for the intensity of the electromagnetic wave in the vicinity of $\theta=0$. From (41), and assuming $x\gg\lambda$, we obtain the transient current (11), which also shows a Fresnel diffraction effect in the vicinity of $t=T$, where T is the time of flight $T=(x/v)$.

IV. CONCLUSION

It is well known that ordinary diffraction phenomena for beams of particles are closely associated with the position-momentum uncertainty relations.[15] The appearance of diffraction in time effects for the transient current, when an obstacle is introduced or removed from the incident beam, suggests that these effects are closely connected with the time-energy uncertainty relation. This is shown to be the case by analyzing the transient wave function when an impenetrable spherical potential is introduced into the beam.[4] The ratio of the transient to the stationary scattered current has in this case, also the form (11). If the wave function is transformed to the energy-angular momentum representation,[4] it shows that when a scattered particle is detected at a time Δt after the introduction of the

[14] B. B. Baker and E. T. Copson, *The Mathematical Theory of Huygens' Principle* (Clarendon Press, Oxford, 1939), Chapter IV, pp. 130, 132, 142.

[15] W. Heisenberg, *The Physical Principles of Quantum Theory* (Chicago University Press, Chicago, 1930), Chapter II.

scatterer, there is an indetermination ΔE in its energy, such that:

$$\Delta t \Delta E \simeq h. \tag{42}$$

The χ-functions that are used in the nonrelativistic shutter problem, appear also (in the form $\chi(r, \pm k'', t)$, where r is the distance from the scatterer and k'' the momentum of the incident particles) in the dynamical description of the scattering by an impenetrable spherical potential,[4] and in the resonance scattering processes.[1] These functions account then for the transient effects due to the time-energy uncertainty relation. When a scatterer has a structure, such as in the single level scattering process,[1] there are other terms in the transient wave functions that depend on the poles of the scattering matrix. The transient effects that these terms give rise to in the current, are then no longer general quantum-mechanical effects, but are related to the specific nature of the scatterer.

The important role that the χ-functions play in the dynamical description of nonrelativistic scattering processes, suggests that their relativistic generalization, given by the wave function $\psi(x, t)$ of (28), may play a similar role in any dynamical description of relativistic scattering processes.

The author is indebted to Professors M. S. Vallarta and J. Lifshitz for helpful discussions.

APPENDIX

In this appendix, we shall evaluate the integral in (27), so as to determine the explicit form of the relativistic wave function.

Instead of taking the principal value of the integral in (27), we shall make the integration along the contour C of Fig. 4, where the singular points $\xi=0, z$ of the integrand, are by-passed from above by means of the semicircles C', C''. From Fig. 4 we obtain:

$$\mathrm{P}\int_{-\infty}^{\infty} - \int_C = \int_{-\delta}^{\delta} - \int_{C'} - \int_{C''}. \tag{43}$$

The integral around C'' must be interpreted as the limiting value when the radius of the semicircle tends to zero. As the integrand has a simple pole at $\xi=z$, we obtain:

$$-\int_{C''} = \pi i \operatorname{Res}(\xi=z) = \pi i \exp[i(kx - Ect)]. \tag{44}$$

From the form of the integrand in (27), we see that the first two integrals on the right-hand side of (43) vanish when $\delta \to 0$, assuming that $x, t > 0$. As the integrand has an essential singularity at $\xi=0$, but is regular outside this point (except for the pole at $\xi=z$), we conclude that the first two integrals of (43) add to zero for any $\delta < z$.

From (27) and (43) we obtain then:

$$\psi(x,t) = -(2\pi i)^{-1}\int_C (\xi+z)(\xi-z)^{-1}(2\xi)^{-1} \times \exp\{i(\mu/2)[(x-ct)\xi - (x+ct)\xi^{-1}]\}d\xi. \tag{45}$$

When $x > ct$ we can close the contour from above, and as the contribution from the dotted semicircle is clearly zero, and the integrand is analytic in that part of the ξ plane above C, we conclude that:

$$\psi(x,t) = 0, \quad \text{if} \quad x > ct. \tag{46}$$

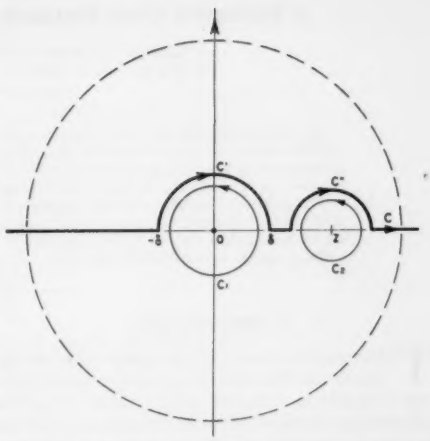

FIG. 4. Integration contour for the relativistic wave function.

When $x < ct$ we close the contour from below. Again the contribution of the dotted semicircle is zero, but now we have the singular points $\xi=0, z$ inside the contour. As the singular points are not branch points, we obtain that:

$$\psi(x,t) = (2\pi i)^{-1}\left[\int_{C_1} + \int_{C_2}\right], \quad \text{for} \quad x < ct, \tag{47}$$

where the contours C_1, C_2 are now the closed circles surrounding the points 0 and z, respectively.

The second integral in (47) is given by twice the value of (44). For the first integral we introduce the variables ξ, η defined by (29), and changing to the variable of integration given by

$$\zeta' = -i\xi^{-1}\xi, \tag{48a}$$

we obtain:

$$(2\pi i)^{-1}\int_{C_1} = (2\pi i)^{-1}\int_{C_1'}[(\zeta'-z')^{-1} - (2\zeta')^{-1}] \times \exp[\tfrac{1}{2}\eta(\zeta' - \zeta'^{-1})]d\zeta', \tag{48b}$$

where $z' = -i\xi^{-1}z$ and the radius of C_1' is less than $|z'| = \xi^{-1}z$.

Using the well-known formula:[16]

$$\exp[\tfrac{1}{2}\eta(\zeta' - \zeta'^{-1})] = \sum_{n=0}^{\infty}{}' \zeta'^n J_n(\eta) + \sum_{n=1}^{\infty}(-1)^n \zeta'^{-n} J_n(\eta), \tag{49a}$$

as well as the fact that for $|\zeta'| < |z'|$ we have:

$$(z'-\zeta')^{-1} = z'^{-1}\sum_{n=0}^{\infty}(\zeta'/z')^n, \tag{49b}$$

we obtain straightforwardly that:

$$(2\pi i)^{-1}\int_{C_1} = \operatorname{Res}(\zeta'=0) = -\sum_{n=1}^{\infty}(\xi/iz)^n J_n(\eta) - \tfrac{1}{2}J_0(\eta). \tag{50}$$

Introducing this result into (47), we obtain finally the explicit form of $\psi(x, t)$ for $x < ct$ as given by (28b).

[16] See reference 11, p. 101.

π^0 Production Cross Section for 430-Mev Protons on H and Be*

J. MARSHALL, L. MARSHALL, V. A. NEDZEL, AND S. D. WARSHAW
Institute for Nuclear Studies, University of Chicago, Chicago, Illinois
(Received June 23, 1952)

The differential cross section for the production of photons in the forward direction by the reaction (430-Mev $p+H\rightarrow p+p+\pi^0$; $\pi^0\rightarrow 2\gamma$) is measured as 0.20×10^{-27} cm²/sterad. The ratio of total to differential gamma cross section does not depend strongly on the symmetry of pion emission. Using an average calculated ratio, we find the pion-production cross section from hydrogen to be 0.45×10^{-27} cm².

The differential gamma-production cross section in the forward direction on Be is measured to be 4.35×10^{-27} cm²/sterad. We assume that in analogy with the case of H the ratio of total to differential photon cross section will not depend on symmetry of pion emission. Using the ratio calculated for isotropic emission we find $\sigma_{\pi^0}=8.7\times10^{-27}$ cm².

I. INTRODUCTION

THE absolute cross section for neutral pion production by 340-Mev protons has been measured in the case of carbon by Crandall[1] to be 1.4×10^{-27} cm². The relative cross sections for light nuclei at the same energy have been measured by Hales, Hildebrand, Knable, and Moyer.[2] They have interpreted the yield for nuclei from hydrogen to oxygen as due only to the interaction of the incident protons with the neutrons in the nuclei. In the case of hydrogen they observed zero yield within the experimental error.

Near the threshold of pion production, one expects the neutral pion yield from the collision of two protons or two neutrons to be smaller than that from a proton-neutron collision provided that the neutral pion is pseudoscalar.[3] This difference should tend to disappear with increasing energy as the higher angular momentum states of the final nucleons begin to contribute to the reaction.

Accordingly, we have used the 450-Mev maximum energy protons accelerated by the 170-inch synchrocyclotron of the University of Chicago to examine the neutral pion yields from hydrogen and from beryllium. At the higher energy one might expect to find a yield from hydrogen large enough to measure and to obtain additional information on the nature of the neutral pion.

The absolute cross section has been measured both for beryllium and for hydrogen.[4] These elements were bombarded with protons in the cyclotron; the gamma-rays from decay of neutral pions formed in the target were observed in the forward direction. The resulting differential gamma-ray cross section was multiplied by the calculated ratio of total to differential cross section. For hydrogen, this ratio was found to have approximately the same value whether one assumed the pions to emerge isotropically or according to a $\cos^2\theta$ distribution in the barycentric system of the colliding nucleons. For beryllium, whose nucleons have an internal momentum distribution which complicates the calculation, this ratio was calculated only for the isotropic model. It was then assumed in analogy with the calculations on hydrogen that the ratio was little affected by the type of angular distribution.

In the case of beryllium, the absolute cross section was measured in two independent ways. In the first method, the energy spectrum of the gamma-ray beam was measured using a pair spectrometer and was integrated to obtain the differential cross section. In the second method, the collimated gamma-ray beam was passed through lead and the conversion electrons measured in a water Čerenkov telescope.[5] The two values so obtained for the cross section agree within the estimated errors.

For the measurement of the absolute cross section in hydrogen, only the second method was used. This was necessitated by the much lower intensity of gamma-rays from the hydrogen target. The first method is believed to be less reliable because of possible error in the extremely energy dependent efficiency calculated for the round pole pair spectrometer used here.

II. METHOD OF THE WATER ČERENKOV COUNTER

A. Hydrogen Cross Section

There is no sizeable external proton beam from the Chicago synchrocyclotron. On this account, it was convenient to bombard our targets with the internal beam of the cyclotron. To eliminate the large background which would accompany the bombardment of a hydrogenous compound, liquid hydrogen was used as the target material.

The cyclotron beam, during acceleration, gains radius only at a rate of about 0.001 inch per revolution. In order to get the protons of the beam into the liquid hydrogen past the container walls, it was necessary to deflect the beam by a much larger amount in one revolution around the cyclotron. This is done very conveniently by vertical scattering.

A platinum scattering target 0.020 inch thick was

* Research supported by the joint program of the ONR and AEC.

[1] W. E. Crandall, University of California Report UCRL-1637 (unpublished).

[2] Hales, Hildebrand, Knable, and Moyer, Phys. Rev. **85**, 373 (1952).

[3] K. Watson and K. Brueckner, Phys. Rev. **83**, 1 (1951).

[4] L. Marshall *et al.*, Phys. Rev. **87**, 220 (1952); J. Marshall *et al.*, Phys. Rev. **87**, 220 (1952).

[5] John Marshall, Phys. Rev. **86**, 685 (1952).

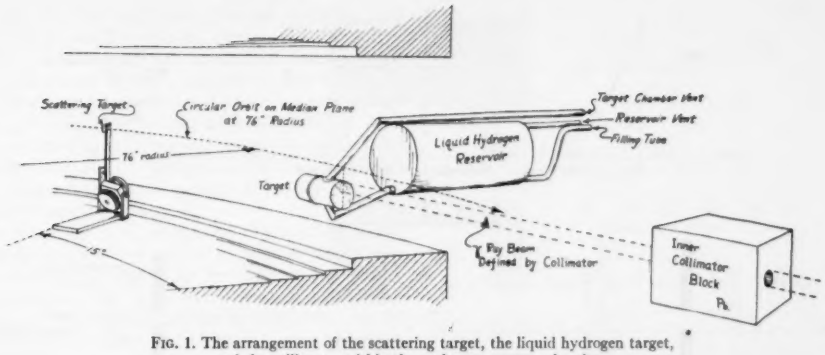

FIG. 1. The arrangement of the scattering target, the liquid hydrogen target, and the collimator within the cyclotron vacuum chamber.

placed at a 76-inch radius in the median plane of the cyclotron. It could be inserted or removed by a flip coil controlled externally, Fig. 1. The vertical oscillations of the beam have a frequency at this radius which is approximately one-quarter of the cyclotron frequency. One effect of the scatterer is to make the amplitude of the vertical oscillations much larger. The beam that passes through the scatterer has larger vertical oscillations than before, and has a phase of vertical oscillation such that there is a node at the scatterer, and consequently a loop one revolution later. In other words, the beam is blown up vertically with a maximum displacement about one revolution after hitting the scatterer.

The radial oscillations at this radius have a frequency that is only slightly smaller than the cyclotron frequency. Protons striking the scatterer are refocused radially about 375 degrees later. It was shown by an exploratory experiment that about 6 percent of the beam was deflected into an area of one cm^2 placed about three cm below the median plane.

The hydrogen target, constructed of copper, was a cylinder four inches long and two inches in diameter with 0.020-inch wall thickness except for the ends which were etched to make them 0.007 inch thick. It was mounted with its axis two inches below the median plane and parallel to the direction of the beam. It was placed fifteen degrees after the scattering target so that the scattered beam was focused into a vertical line through the target 375 degrees after scattering. Liquid hydrogen was admitted to the target from a reservoir (Fig. 1) by gravity feed whenever the target vent tube was open to the atmosphere. When the vent tube was closed the liquid hydrogen was pushed out of the target by its own vapor pressure. Tubes from the reservoir to the outside of the cyclotron allowed it to be refilled. The target was designed and its construction was supervised for the most part by Professors E. Long and E. Fermi who originally had intended to do experiments of this type.

Most of the cyclotron beam has vertical oscillation amplitude smaller than $\frac{3}{4}$ inch. A significant fraction, however, has larger amplitude and might strike the walls of the hydrogen target and cause an unpleasant background if it were not removed. For this purpose a clipper was provided above the median plane to remove protons of vertical amplitude more than $\frac{3}{4}$ inch.

Gamma-radiation from neutral pion decay in the target emerging in the forward direction passed through a hole in the cyclotron shield into the experimental area where it was detected. The gamma-rays were collimated by a two-element collimator. The first element was a $\frac{5}{8}$-inch round hole in a lead block eight inches long placed just outside the 76-inch orbit in the cyclotron chamber. The second element was a $\frac{3}{4}$-inch hole in another eight-inch lead block placed in the experimental area about 40 feet from the target (Fig. 2).

The second element of the collimator determined the solid angle subtended at the target by the detecting apparatus. The first element determined the effective area of the target. This area was chosen to be as close as possible to the top wall of the hydrogen target without allowing gamma-radiation from the wall to pass through the collimator.

The first lead block was mounted on a track so that the $\frac{5}{8}$-inch hole could be moved horizontally across the face of the target from outside the cyclotron. This motion was effected by means of a screw so that the position of the block was quite accurately reproducible.

Directly beyond the second lead block, a magnet was placed to sweep out of the beam any charged particles formed in the collimator. The final beam defined by this system was circular in shape and about $\frac{3}{4}$ inch in diameter. It consisted of high energy gamma-rays with a considerable contamination of neutrons from the end windows of the target.

The gamma-rays in the beam were converted partially to electron pairs by lead converters of various thicknesses. The electrons produced in the converter passed through a diphenyl acetylene scintillation crystal

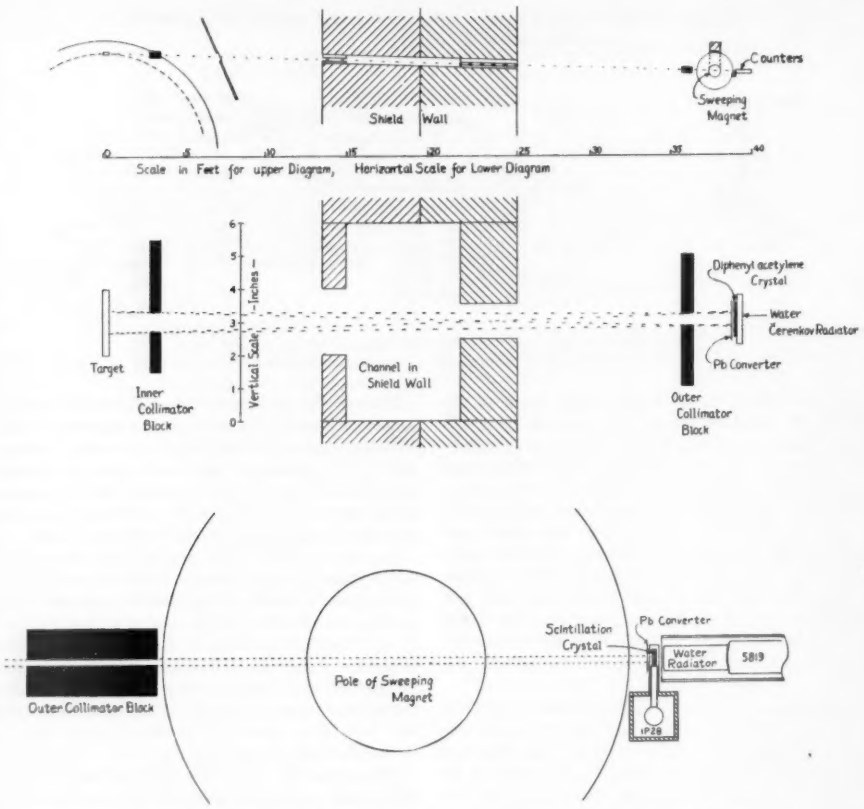

FIG. 2. Horizontal and vertical sections of the experimental layout and detail of the detector.

one inch square and $\frac{1}{4}$ inch thick, and then into a water Čerenkov radiator 1.5 inch in diameter and four inches long. The water of the Čerenkov radiator was contained in a glass tube the rear end of which was shaped so as to fit the cathode of a 5819 photomultiplier, and optical contact was provided by a thin layer of silicone vacuum grease (see Fig. 3). The photomultipliers which looked at the crystal and the Čerenkov radiator were connected through a 6BN6 fast coincidence circuit[6] to a scaling circuit.

The water Čerenkov counter was used in the detector telescope for a very important reason. Whereas a scintillator crystal produces light whenever it is traversed by ionizing particles, light is produced in water only by ionizing particles having velocity greater than 0.76 times the velocity of light. The telescope had to operate in a beam consisting of photons and neutrons up to 450 Mev, and had to observe only electrons from the photons. The knock-on protons from these neutrons have too small a velocity to produce Čerenkov radiation in water. The water Čerenkov counter then has the important characteristic of being sensitive only to electrons in this beam. It is true that mesons could be made having great enough velocity to be recorded; however, the number of these is insignificant.

The intensity of the cyclotron beam striking the scattering target was monitored through a separate collimator. Radiation passing through this collimator from the scattering target struck a paraffin converter. A scintillation crystal coincidence telescope counted particles from the converter.

The ratio of the counting rate of the detecting apparatus to that of the monitor was measured many times over, with and without liquid hydrogen in the target for two thicknesses of the lead converter with

[6] J. Fischer and J. Marshall, Rev. Sci. Instr. 23, 417 (1952).

and without the converter. The net counting rate {(H, Pb−H, no Pb)−(no H, Pb−no H, no Pb)} per monitor count and per unit thickness of lead converter was extrapolated to zero converter thickness (Fig. 4). This procedure was necessary to take account of electrons lost from the detecting apparatus through multiple scattering in the converter. From the extrapolated counting rate and the pair production cross section in lead, the total number of gamma-rays in the beam per monitor count was computed.

To obtain the pion production cross section, it was necessary to know the number of protons per monitor count striking the area of the hydrogen target seen by the collimator. This number was measured by the production of 15-hour radioactivity in aluminum foils by the reaction $Al^{27}(p,n3p)Na^{24}$. Two aluminum foils, each of 0.00025-inch thickness, were mounted on separate flip coils in such a way as to cover the exit window of the hydrogen target when they were raised. One of the foils was raised when and only when there was liquid hydrogen in the target. The other foil was raised when and only when the target was empty. Both foils were protected from stray protons by lead bricks when they were lowered. Also, a third foil was placed behind the lead to measure the background activity.

The time necessary to get data for one cross-sectional measurement was about three days. On the first day the vacuum chamber of the cyclotron was opened to allow the mounted foils and their flip coils to be put in place just behind the exit window of the liquid hydrogen target. The elements of the collimation system were carefully aligned. The area of the target seen by the detecting apparatus was determined as the area illuminated when a light was put in place of the detecting apparatus in the experimental area. The foils were raised into position covering the target window and the illuminated region was marked on them. This was the area passed through and activated by the same part of the proton beam which produced the pions whose decay was observed with the detecting apparatus. The N^{24} activity in this area of the foil therefore gave a measure of the integrated proton flux.

The tank was closed and evacuated. The second day was spent in measuring the water Čerenkov telescope counting rates for two thicknesses of lead converter, with and without liquid hydrogen in the target and with and without converter. At the same time the appropriate foil was raised so that one or the other foil always covered the end of the target when the detecting apparatus and the monitor were in operation. It was considered necessary to have one foil to measure the integrated flux through the empty target and a second foil for the flux through the target filled with liquid hydrogen, because the target filling might have affected the monitor, and the number of proton traversals of the target might also have been different with and without hydrogen. It turned out, however, that the ratio of foil activity to number of monitor counts was the same with and without hydrogen.

It was convenient to let the radioactivity in the cyclotron (and also incidentally the short-lived activities in the aluminum foils) decay overnight. On the third day the tank was opened for the removal of the foils. The activity distribution in the foils was mapped with a Geiger counter, and the critical areas of the two foils were cut out and measured under known conditions of solid angle and efficiency with an end window counter. The activity distribution is shown in Fig. 5. In this case it happened that the collimator was slightly displaced from the optimum radius relative to the radius of the scattering target.

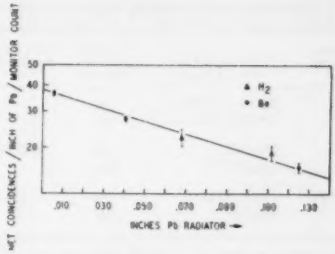

FIG. 4. Correction for thickness of lead converter.

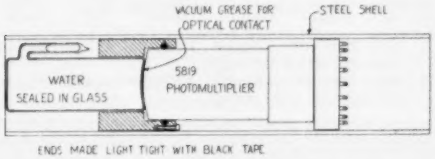
VACUUM GREASE FOR OPTICAL CONTACT
STEEL SHELL
WATER SEALED IN GLASS
5819 PHOTOMULTIPLIER
ENDS MADE LIGHT TIGHT WITH BLACK TAPE

FIG. 3. The water Čerenkov counter used to detect fast electrons.

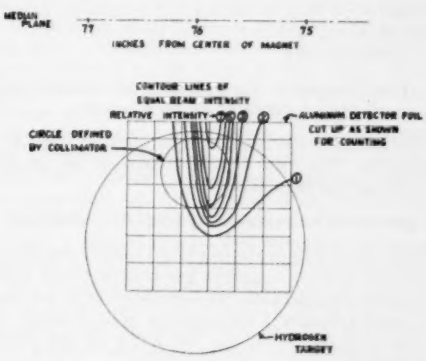

FIG. 5. The scattered-proton beam intensity distribution in the hydrogen target.

TABLE I. Total counts of the detecting apparatus for a 3-day run.

Thickness Pb converter inches	Coincidences per monitor count	Liquid hydrogen in target	Net coincidences per monitor count inch lead
0	16 coinc/6000 M	yes	
	11 coinc/6035 M	no	
0.068	805/26124	yes	0.223±0.024
	354/24079	no	
0.112 Pb	1159/28111	yes	0.188±0.015
	483/25122	no	

Net coincidences/monitor count/inch Pb extrapolated to zero thickness of lead = 0.38 ±0.07.

The total counts of the detecting apparatus for the three-day run are given in Table I. From the determination of the cross section for beryllium where there was considerably more intensity, similar data proved to extrapolate to zero radiator thickness with the same slope as the hydrogen data, and with smaller statistical error. Therefore, we extrapolated the hydrogen data to zero thickness with more confidence than the hydrogen data alone would appear to allow. The resulting value is:

Net coincidences/monitor count/inch Pb, extrapolated to zero thickness of Pb = 0.38±0.07.

This number is equal to the product:

Total photons at the converter per monitor count ×atoms/cm² for 1 in. Pb×σ (pair).

The value of σ (pair) was determined to be 32.7 $\times 10^{-24}$ cm² by averaging the experimental pair production cross section in Pb over the theoretical pion-decay gamma-ray spectrum for the forward direction. The spectrum was calculated assuming isotropic emission of the pions in the barycentric system. The pair production cross sections were read from a plot of cross section *vs* log energy obtained by extending a straight line drawn through the values of the cross section determined at 80 Mev by Lawson,[7] at 30 Mev by Lundby and Marshall,[8] and at 17.5 Mev by Walker.[9]

It follows that:

Total photons at the converter per monitor count $= 0.38/[8.5\times10^{22}\times32.7\times10^{-24}] = 0.13$.

The radiation subtended a solid angle of 5.60×10^{-7} steradian. The total number of photons per monitor count and per steradian is

$$\text{photons}/M\times\text{sterad} = 0.137/5.60\times10^{-7} = 2.45\times10^{5}.$$

From the activity of the foils (see Table II) one obtains the total number of protons per monitor count. These numbers are practically the same whether or not there is liquid hydrogen in the target, or in other words, the monitor is unaffected by the filling of the target. Therefore, we take an average value of 2.95×10^{9} protons per monitor count.

The differential gamma-production cross section is obtained from the relation:

$$\frac{\text{protons}}{M}\times\frac{\text{atoms H}}{\text{cm}^2}\times\frac{d\sigma_\gamma}{d\Omega}=\frac{\text{photons}}{M\times\text{sterad}}.$$

For the forward direction one finds:

$$\frac{d\sigma_\gamma}{d\Omega}=\frac{2.45\times10^{5}}{(2.95\times10^{9})(4.25\times10^{23})}$$

$$=0.20\times10^{-27}\ \text{cm}^2/\text{sterad}.$$

An upward correction of 1 percent should be made in this value to allow for pion production in the cold gaseous hydrogen present in the nominally empty target chamber. This correction may be neglected.

The total cross section for pion production is obviously equal to one-half the total cross section for gamma-production. The latter quantity may be estimated as the product:

$$\left\{\left(\frac{d\sigma_\gamma}{d\Omega}\right)_{0^\circ}\right\}_{\text{experimental}}\times\left\{\sigma_\gamma\Big/\left(\frac{d\sigma_\gamma}{d\Omega}\right)_{0^\circ}\right\}_{\text{calculated}}.$$

The latter quantity, the ratio of total to differential cross section in the lab system has been calculated for 450-Mev proton-proton collisions for two different distributions in the barycentric system of the two protons. For isotropic emission of the pions we find 4.7 for this ratio; for $\cos^2\theta$ emission of the pions we find 4.2. We conclude that for the purpose of calculating the total cross section it apparently makes little difference with what symmetry the pions are emitted.

Using a quantity midway between these numbers we obtain:

$$\sigma_{\pi^0}=\tfrac{1}{2}\sigma_\gamma=4.5\times\tfrac{1}{2}\times0.20\times10^{-27}=0.45\times10^{-27}\ \text{cm}^2.$$

There still remains to be discussed the question of whether or not the neutral pions, whose production cross section has been measured, were produced directly

TABLE II. Foil activity and number of protons per monitor count.

Monitor foils: The data given here relate to the area of the foils which measured the proton beam passing through the area of the target seen by the detector.

Foil No.	Weight mg	Number of Al atoms	Initial[a] number of Na^{24} atoms	Total number[b] of protons	Total number monitor counts (M)	Number protons per monitor count
1	8.95	2.00×10^{20}	5.35×10^{3}	2.47×10^{14}	82,416	2.99×10^{9}
	(with hydrogen in the target)					
2	8.45	1.89×10^{20}	4.84×10^{3}	2.37×10^{14}	81,410	2.92×10^{9}
	(no hydrogen in the target)					

[a] Corrected for solid angle of beta-counter, gamma-content, and absorption in foil, air, and window.

[b] No. of protons = No. of Na^{24} atoms/No. of Al atoms $\times\sigma(Al^{27}p,3pn)Na^{24}$. $\sigma(Al^{27}p,3pn\ Na^{24})$ at 450 Mev = 10.8×10^{-27} cm² [Luis Marquez, Phys. Rev. 86, 405 (1952)].

[7] J. L. Lawson, Phys. Rev. **75**, 433 (1949).
[8] A. Lundby and L. Marshall, Phys. Rev. (to be published).
[9] R. L. Walker, Phys. Rev. **76**, 1440 (1949).

in proton-proton collisions. Instead, it might be argued that the neutral pions are formed by charge exchange when negative pions collide with hydrogen atoms in the target. This background we call the "Panofsky effect."[10] Such negative pions are not produced in the hydrogen itself because of charge conservation, but they could conceivably come from the copper walls of the target container or from a more distant source such as the scattering target, the dee, or the poles of the cyclotron. In the case of negative pion production from a local source, the intensity of the gamma-radiation should be increased by increasing the amount of material in the target walls. To test this hypothesis, a sheet of copper $\frac{3}{32}$-inch thick was laid on top of the target itself. In the middle of a run, in which the usual measurements were made with and without liquid hydrogen, this sheet was pulled off the target from outside the cyclotron, and the measurement was continued with no other change in conditions. On the one hand the copper sheet occupied a position of considerably greater proton intensity; on the other hand the copper sheet was thicker than the copper wall of the target. If the observed photons resulted from Panofsky effect, their intensity should have been increased several times over in presence of the copper sheet. No difference in gamma-intensity was observed. This was taken as evidence against Panofsky effect from a local source of negative pions.

For the second hypothesis, namely that the observed effect could be due to negative pions arriving at the target from some relatively distant point, the intensity of gamma-rays should be almost constant over the width of the target. A test was made by observing the variation of gamma-intensity at the detector while the first element of the collimator was moved across the face of the target.

The observed intensities (hydrogen minus no hydrogen, with and without lead) are plotted against collimator position in Fig. 6. Over half the width of the target, the data suffered from a large background caused by our having forgotten to turn on the sweep magnet field. Nevertheless when the observed radial distribution (Fig. 5) of proton current in the target is combined with the width of the collimator slit, which was made especially narrow for this measurement, a dependence of intensity on radial position of the slit is computed which agrees quite well with the observed variation. This is taken to indicate that the neutral pions originate in proton-proton collisions.

B. Beryllium Cross Section

Since the Čerenkov telescope method accepts the entire gamma-spectrum simultaneously, and since it can make use of a rather thick converter, it is applicable to low intensity phenomena. In fact, the method was worked out after it became apparent that the gamma-rays from hydrogen were too few to be readily measurable with the pair spectrometer. The cross section of beryllium had already been measured with the pair spectrometer, but it was decided to measure it also with the Čerenkov telescope as a check on the validity of the method as applied to hydrogen.

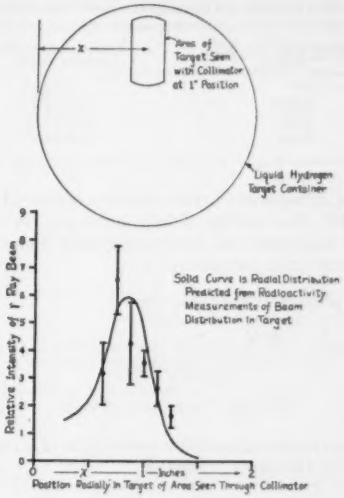

FIG. 6. This survey of the target showed that the gamma-rays observed in this experiment came from within the target.

The target was a cylinder of beryllium 1.73 cm long, 2.22 cm in diameter, and weighing 12.7 g. It was put in the median plane of the cyclotron with its inner face at 76 inches radius. It was mounted on a probe with its axis along a radius of the cyclotron. A copper rod $\frac{3}{16}$ inch in diameter was silver soldered to the beryllium both to support the target in the beam and to provide a measured heat leak to an Aquadag-coated sheet copper thermal radiator. The two junctions of a thermocouple were connected to the target and to the radiator. Hence, the temperature difference of the junctions measured the power delivered to the target by the proton beam. From this power it is possible to compute the total distance per second traveled by protons in the target.

The collimation in this case was similar to that for the hydrogen except that the inner lead collimator block was removed. The detecting apparatus and its geometry were the same. The counting monitor was arranged as before so that it counted radiation coming through a separate channel with the difference that in this case the radiation came from the beryllium target.

The counting data obtained at a power level of 2.22 watts in the target is given in Table III in the form of detector counts for 10^4 monitor counts. The background rate obtained with the beryllium target removed from the beam was negligible. The value of the net counting rate (Pb−no Pb) for 10^4 monitor counts and per inch

[10] Panofsky, Aamodt, and Hadley, Phys. Rev. 81, 565 (1951).

TABLE III. Counting data obtained at a power level of 2.22 watts.

Thickness of Pb converter, inches	Coincidences per 10^4 monitor counts
0	1315±25
0.0055	3325±41
0.041	12,575±65
0.125	21,410±84

of lead, extrapolated to zero thickness of converter, was 3.8×10^5. The number of lead atoms per cm² is 3.35×10^{22}. One finds from these numbers and from the lead pair production used above:

$$\frac{\text{Total photons at the converter}}{10^4M}$$

$$=\frac{3.8\times10^5/10^4M}{32.7\times10^{-24}\times2.54\times3.35\times10^{22}}=1.37\times10^5.$$

The converter subtended a solid angle of 5.60×10^{-7} sterad at the target. Therefore

$$\left\{\frac{\text{Total photons}/10^4M}{\text{sterad}}\right\}=\frac{1.37\times10^5}{5.60\times10^{-7}}=2.45\times10^{11}.$$

The time for 10^4 monitor counts was 2.9 minutes at this intensity, 2.22 watts. It is estimated that 18 percent of the heat in the target is produced from stars; then 82 percent is ionization energy lost in proton traversals of the target. We obtain for the total ionization energy dissipated in the target in the time taken for 10^4 monitor counts

$$10^4M=\frac{2.22\times10^7\times2.9}{1.6\times10^{-6}}\times0.82\times60\text{ Mev}$$

$$=1.98\times10^{15}\text{ Mev}.$$

Assuming the energy loss of a 430-Mev proton in beryllium to be 4.44 Mev per cm, one finds for the proton path length in the target corresponding to 10^4 monitor counts

$$1.98\times10^{15}/4.44=4.57\times10^{14}\text{ proton cm}.$$

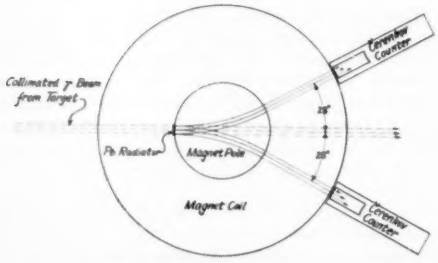

FIG. 7. The pair spectrometer.

Now the differential cross section follows directly from the relationship

$$\left(\frac{d\sigma_\gamma}{d\Omega}\right)_{\text{Be}}=\frac{\text{photons/sterad}}{\text{proton cm}}\times\frac{1}{(\text{atom Be/cm}^2)}$$

$$=\frac{2.45\times10^{11}}{4.57\times10^{14}}\times\frac{1}{1.23\times10^{23}}$$

$$=4.35\times10^{-27}\text{ cm}^2/\text{sterad}.$$

To convert the differential gamma-ray cross section to the total pion production cross section one needs to know the factor $\sigma_\gamma/(d\sigma_\gamma/d\Omega)_{0°}$ for a Teller-McMillan nucleus. For the case of isotropic emission of the pion from the barycentric system of the colliding nucleons

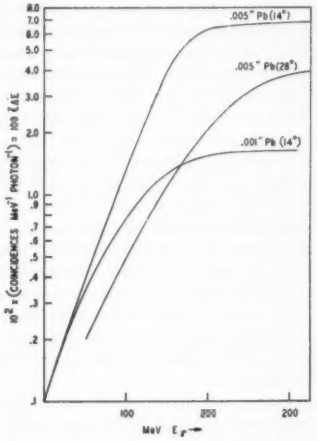

FIG. 8. The calculated variation of counting efficiency with gamma-ray energy.

we find a factor 4.0. We have not made the similar calculation for the case of the $\cos^2\theta$ pion emission from a Fermi gas nucleus. Instead, the argument may be proposed that as in the case of hydrogen this factor will not be changed much by the assumption of $\cos^2\theta$ pion emission, because the effect of a momentum distribution of the nucleons in the nucleus is to smooth out any directional features.

With the assumption then that the total cross section is 4 times the differential cross section in the forward direction for the case of beryllium regardless of the symmetry with which the pions are emitted, we find

$$\sigma_{\pi^0}\text{ for Be}=\tfrac{1}{2}\times4\times4.35\times10^{-27}\text{ cm}^2=8.7\times10^{-27}\text{ cm}^2.$$

III. METHOD OF THE PAIR SPECTROMETER

The pair spectrometer (Fig. 7), a round pole magnet of 11 inches diameter with a 2-in. gap, was placed in

the experimental area about 40 feet from the beryllium target already discussed in the previous section. The gamma-ray beam in the forward direction from the target came into the experimental area through a hole in the cyclotron shield. Electron contamination was removed with two magnetron magnets.

The beam was collimated with two diaphragms of lead bricks, a horizontal collimation $\frac{1}{2}$-inch high at the port of the cyclotron, and the other a $\frac{5}{8}$-inch diameter round collimation in the experimental area. A photograph of the beam made about 10 feet past the pair spectrometer during a measurement showed the beam cross section to be approximately a circle one inch in diameter.

The collimated beam went between the poles and along a diameter of the pair spectrometer magnet after passing through a lead converter on the circumference of the magnet. The detecting counters were placed symmetrically at an angle θ with respect to the beam so that only electron-positron pairs whose components had approximately equal energy came to them.

Because of the fact that the beam in the forward direction contained a great many high energy neutrons as well as the gamma-rays to be measured, we again used water Čerenkov counters, especially suitable for their sensitivity to electrons and not to protons from this beam. The two counters were connected through a 6BN6 coincidence circuit.

A measure of the photon spectrum was obtained by observing the coincidence rate at various magnet fields while the geometry of counters and spectrometer was kept fixed. This was done for the gamma-spectrum from beryllium using two thicknesses of lead converter 5 mil and 1.75 mil, at two values of θ, 14° and 28°.

A round pole spectrometer has the unpleasant feature that its efficiency is a rapidly varying function of magnetic field and is a different function for each thickness of converter and for each counter position. The finite size of the converter and the Coulomb scattering in it must be taken into account. A second point is that because of the finite size of the counters, the efficiency depends on the shape of the gamma-spectrum itself. Consequently, the shape of the pion-decay gamma-spectrum[11] for beyllium was calculated for the forward directed and was used to weight the probability of detection of a gamma-ray of given energy.

The calculated efficiency curves are shown in Fig. 8. The ordinate $\bar{\epsilon}\Delta E$ is essentially an average efficiency of detection times an effective energy width over which gamma-rays are detected for the given geometry and magnetic field. The conversion from observed counting rate to gamma-ray spectrum is accomplished by the

[11] The differential pion production cross section used here was calculated by Orear, Rosenfeld, Schluter, and Teng assuming isotropic emission of the pions in the barycentric system of the colliding nucleons for a Fermi gas momentum distribution.

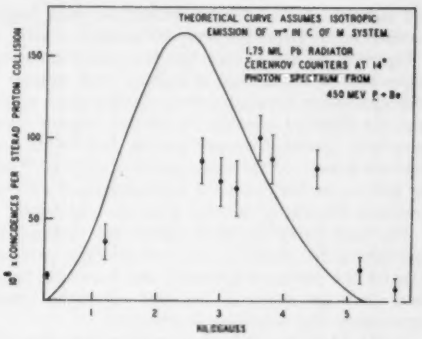

FIG. 9. The calculated and observed pair spectra from a 1.75-mil lead converter and with counters at 14°.

relation

$$\frac{1}{\bar{\epsilon}\Delta E} \times \frac{\text{coincidences}}{\text{sterad collision}} = \frac{\text{photons}}{\text{Mev sterad collision}}.$$

The solid angle subtended at the target by the collimated beam at the converter was 3.7×10^{-6} steradian. The number of coincidence counts for 10^4 monitor counts was recorded as a function of magnetic field during the measurement. The beam intensity was calculated from the recorded voltage of the target thermocouple for each period of 10^4 monitor counts. The average value for the energy equivalent of 10^4 monitor counts was 11.9 watt minutes.

In the manner previously described, one corrects this number to remove the energy contribution of stars

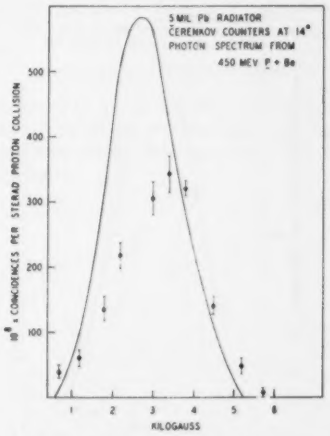

FIG. 10. The calculated and observed pair spectra from a 5-mil lead converter and with counters at 14°.

and converts it to 0.83×10^{15} proton cm path length traveled in the target for every 10^4 monitor counts.

Figures 9, 10, and 11 show the data observed for two angles and two thicknesses of radiator. The ordinate is coincidences per steradian proton collision which means that the observed coincidences per 10^4 monitor count have been corrected to unit proton path length and that also a total collision cross section of 220×10^{-24} cm^2 for protons on beryllium has been introduced for convenience. This factor cancels out in the final result.

The solid curves in these figures are obtained by multiplying the calculated spectrum described above by $\bar{\epsilon}\Delta E$ for the particular geometry and converter thickness. Only the shape of the solid curves has much significance. The amplitude is arbitrary.

In Fig. 12 the data have been converted to photons/steradian per collision by dividing it by $\bar{\epsilon}\Delta E$. One sees some tendency in all these figures for the experimental spectrum to contain somewhat more of the high energy component than the calculated spectrum. In the case of p–p collisions, the shape of the spectrum was calculated both for isotropic and for $\cos^2\theta$ production of the pions, and the latter curve was bulged more at high energies than the former. Although the $\cos^2\theta$ type of calculation has not been made for beryllium, one expected that similarly here there will be more of the high energy component. A possible explanation therefore of the excess of photons at high energy may be some $\cos^2\theta$ production of pions. An alternative factor which will have a similar effect is the p–p force acting on the final protons formed in the reaction

$$p+p\rightarrow\pi^0+p+p.$$

This effect has not been considered by us. The high points at low energies have large errors as a result of the very low spectrometer efficiency in this region and may or may not be significant.

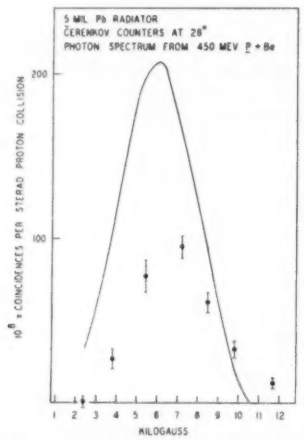
5 MIL Pb RADIATOR
ČERENKOV COUNTERS AT 28°
PHOTON SPECTRUM FROM 450 MEV p + Be
10⁸ x COINCIDENCES PER STERAD PROTON COLLISION
200
100
1 2 3 4 5 6 7 8 9 10 11 12
KILOGAUSS

FIG. 11. The calculated and observed pair spectra from a 5-mil lead converter and with counters at 28°.

The area within the dashed boundary in Fig. 12 which has been taken as a measure of the differential neutral pion production cross section is 1.38×10^{-2}. Therefore the differential cross section is 0.0138×220 mb$=3.0$ mb, except, however, that this figure must be increased by 12 percent to correct for the fact that the Born approximation pair production cross sections were used instead of the experimental cross sections for lead in the efficiency calculations. One obtains a value which within the probable errors of this measurement agrees with the Čerenkov telescope measurement previously described.

$$\left(\frac{d\sigma_\gamma}{d\Omega}\right)_{0^\circ} \text{ in Be}=3.36\times10^{-27}\text{ cm}^2.$$

Using now the previously discussed factor of 4.0 to obtain the total gamma cross section we find

$$\sigma_{\pi^0}=\tfrac{1}{2}\times4.0\times3.36\times10^{-27}\text{ cm}^2=6.72\times10^{-27}\text{ cm}^2.$$

IV. ERRORS

Errors that are quite difficult to evaluate enter into a large fraction of the measurements described in this paper. One major possible source of error is for instance the measurement of the proton beam intensity. In the case of the hydrogen cross section measurement we use the cross section for production of Na^{24}. Marquez[13] estimates the error in this cross section to be about 10 percent. Some of the sources of error in Marquez' measurement are eliminated because we used the same counter that he used. In the case of beryllium we use the rather well known rate of energy loss by ionization and apply an 18 percent correction for energy introduced into the target by nuclear reactions caused by the protons. This correction may be wrong by a considerable amount. The thermocouple measurement of the power in the beryllium target depends on a knowledge of the heat conductance of the target stem. We have determined this by measuring the thermal relaxation time of the target assuming a value for the heat capacity of beryllium. Some error is certainly introduced here.

Then there are minor errors in collimator geometry which may contribute to the general inaccuracy of the final result. We have assumed the Čerenkov counter to be 100 percent efficient to high energy electrons passing through the water radiator. This assumption is born out by the existence of a reasonably good counting rate plateau when the photomultiplier voltage is varied. On the other hand, we have assumed that the crystal scintillator placed in front of the radiator and other necessary materials do not absorb any appreciable fraction of the electron pairs found in the converter. In order to calculate the efficiency function of the pair spectrometer,

[13] See Table II, reference b.

it was necessary first to assume a shape for the distribution of gamma-rays with energy. Some error is easily possible here.

Because of all these sources of error, we have assigned uncertainties to the final results which are considerably larger than the statistical errors.

V. SUMMARY OF RESULTS

We have measured the cross section for the production of neutral pions by the bombardment of hydrogen with protons of about 430-Mev kinetic energy to be

$$\sigma_{\pi^0}(p,p)=(0.45\pm0.15)\times10^{-27}\ \text{cm}^2.$$

We have measured the cross section for the production of neutral pions by the bombardment of beryllium with 430-Mev protons to be

$$\sigma_{\pi^0}(p,\text{Be})=(8.7\pm2)\times10^{-27}\ \text{cm}^2$$

by the use of the Čerenkov counter telescope method. With the pair spectrometer the cross section of beryllium was measured to be $(6.7\pm3)\times10^{-27}$ cm^2. These results depend on the measurement of the differential cross section for gamma-ray production in the forward direction alone. The total cross sections were arrived at by multiplying the differential cross sections by computed angular distribution factors as described elsewhere in this paper.

Let us assume that the yield of neutral pions is the same whether the incoming proton hits a free or a bound proton. Then the cross section of hydrogen is σ_p and the cross section of beryllium is $4\sigma_p+5\sigma_N$. At 430 Mev we find

$$(4\sigma_p+5\sigma_N)/\sigma_p=(8.7\pm2)/(0.45\pm0.15).$$

$$\sigma_N/\sigma_p=3 \text{ with limits}\begin{cases}6.4\\1\end{cases}.$$

Similar treatment of the Berkeley measurements at 340 Mev gives the relation

$$\sigma_N/\sigma_p=13 \text{ with limits}\begin{cases}102\\6.8\end{cases}.$$

A decrease in this ratio is expected to occur with increasing energy. In the case of the p–p collisions, as long as the energy available to the final protons is small so that they are created in an S state, conservation of total angular momentum and parity require that the meson can be emitted only in an S state. When higher angular momentum states are available to the two final protons, the meson can be created in a P state. The P state yield is expected to be greater than the S state yield in analogy with the creation of charged mesons.[8]

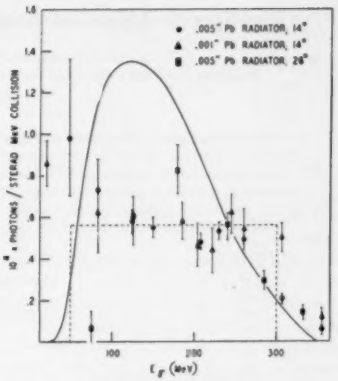

FIG. 12. The calculated and observed photon spectrum.

In the case of the beryllium nucleus, both p–p and p–n collisions occur. For p–n collisions the pion can be created in a P state even though both nucleons involved are constrained to an S state. Therefore at first the yield from p–p collisions, i.e., from hydrogen, should increase much faster with energy than the yield from p–n collisions, i.e., beryllium.

Assume now that at 430 Mev the cross section for pion production from a p–p collision in a nucleus is 0.45 mb, and that for a p–n collision is 3×0.45 mb$=1.3$ mb. We estimate the cross section for carbon at this energy as

$$6\times1.3+6\times0.45=10.5\ \text{mb},$$

which agrees with an extrapolation of the curve for σ_{π^0}(carbon) from 180 to 340 Mev given by Crandall.[1]

We are indebted to Professor Earl Long for the liquid hydrogen.

The Specific Alpha-Activities and Half-Lives of U^{234}, U^{235}, and U^{236}†

E. H. Fleming, Jr.,* A. Ghiorso, and B. B. Cunningham
Radiation Laboratory and Department of Chemistry, University of California, Berkeley, California
(Received June 24, 1952)

The specific alpha-activities and half-lives of U^{234}, U^{235}, and U^{236} have been determined. The material used for each determination was uranium very highly enriched in the isotope under investigation.

Accurate volume aliquots of U^{235} were electrodeposited quantitatively onto platinum disks and were counted in a medium geometry chamber. Accurate weight aliquots of U^{234} and of U^{236} were pipetted onto platinum disks, evaporated to dryness in an induction furnace, and counted in a medium geometry chamber.

The specific activities and half-lives found are as follows:

Isotope	Specific activity (disint/min mg)	Half-life (years)
U^{234}	$(1.370\pm0.009)\times10^{7}$	$(2.475\pm0.016)\times10^{5}$
U^{235}	$(4.74\ \pm0.10\ )\times10^{3}$	$(7.13\ \pm0.16)\times10^{8}$
U^{236}	$(1.406\pm0.011)\times10^{5}$	$(2.391\pm0.018)\times10^{7}$

I. INTRODUCTION

In 1939, Nier[1] determined the half-life of U^{235} by establishing the activity ratio of the AcU series to the U_I series in natural uranium from mass spectrographic analyses of radiogenic lead samples. About five years later, Clark and co-workers[2] determined the half-life of this nuclide by counting and pulse analyzing uranium slightly enriched in U^{235}. The two values were in disagreement by about 25 percent.

After Nier had published his work, Holmes[3] devised a method for calculating the age of the earth, using Nier's mass spectrographic data, including his value for the half-life of U^{235}. Holmes derived a value for the age of the earth of about 3.3 billion years. With the appearance of Clark's value, this figure became somewhat suspect, especially since the decay constant of U^{235} appeared in the calculations as an exponential.

Because of the widespread interest in an accurate value for the age of the earth, it was hoped that an accurate redetermination of the half-life of U^{235} could be made. Rapid development of electromagnetic separation equipment has made it possible to obtain elements very highly enriched in isotopes which occur in nature only in low abundance. Consequently, uranium has become obtainable as 99.94 percent isotopically pure U^{235}. The use of such highly enriched materials has made it possible to eliminate or minimize several uncertainties associated with previous half-life determinations.

In 1949 this laboratory was privileged to procure samples of uranium oxide highly enriched not only in U^{235}, but also in U^{234} and U^{236}, from Dr. C. E. Larson, Y-12 Plant, Carbide and Carbon Chemicals Division, Oak Ridge, Tennessee. Thus, the opportunity for making more accurate determinations of the specific activities and half-lives of each of the isotopes was presented.

In the report of this work which follows, an effort has been made to present in a realistic fashion the difficulties encountered, particularly where the precise determination of alpha-disintegration rates is involved.

II. CHEMICAL PURIFICATION OF THE MATERIALS

The oxides of two of the three isotopes, namely, $U_3^{236}O_8$ and $U_3^{234}O_8$, were found to be contaminated with chemical impurities, chiefly iron, calcium, aluminum, and magnesium, to the order of 2–4 percent.

It was necessary to reduce the amount of contamination in each of these samples to the order of 0.1 percent, since corrections based on spectrographic analysis by the copper spark method ordinarily are uncertain by about a factor of 2.

The following method of purification was employed:

(1) The oxide was dissolved in a minimum of hot, concentrated HNO_3, and the solution was brought to a pH of about 5 by neutralization with NH_4OH.

(2) The solution was chilled in an ice bath, and upon the addition of 30 percent hydrogen peroxide, uranium peroxide precipitated upon standing.

(3) The mixture was centrifuged, and the supernatant liquid was poured off to be treated once again as in step (2). About 95 percent of the uranium was precipitated with the first addition of peroxide.

(4) The precipitate was then washed with about three times its volume of 10 percent H_2O_2 by stirring, and the mixture was centrifuged. The supernatant liquid was removed with a transfer pipet. The precipitate was washed four more times in this same manner.

(5) After the fifth washing, enough 10 percent H_2O_2 was added to permit efficient slurrying, and the precipitate was transferred to a clean platinum crucible. The crucible was then placed under a heat lamp, and the contents were taken slowly to dryness. Baking in air, at a temperature of 850–975°C, caused the peroxide salt to be converted to the oxide, U_3O_8, with an over-all

† This work was performed under the auspices of the AEC.
* Present address: California Corporation, La Habra Laboratory, La Habra, California.
[1] A. O. Nier, Phys. Rev. **55**, 150, 153 (1939).
[2] Clark, Spencer-Palmer, and Woodward, Imperial Chemical Industries Limited, Research Department Declassified Report BR-522, unpublished (October, 1944).
[3] A. Holmes, Nature **157**, 680 (1946).

yield of 85–90 percent. A sample of the oxide was then analyzed spectrographically. Results of the several spectrographic analyses of the purified oxides are given in Table I.

The oxide composition, U_3O_8, was verified as follows: A sample of natural uranium purified as described above and a sample of the $(U^{235})_3O_8$ from Oak Ridge were subjected to an x-ray analysis. The compounds were found to be isostructural with identical lattice constants, which deviated very slightly from those reported in the literature for $UO_{2.667}$. It is not possible to make an accurate calculation of composition from the x-ray data alone, since the lattice constants are not sensitive to slight changes in composition over the solid solution range. However, by plotting composition *versus* partial pressure of oxygen at various temperatures, according to data compiled by Biltz and Müller,[4] a simple interpolation shows that the composition lies between $UO_{2.655}$ and $UO_{2.665}$, when the oxide is prepared under our conditions. The corresponding uncertainty in the uranium content of the oxides is ± 0.06 percent, and the deviation from the composition U_3O_8 was considered to be negligible.

III. URANIUM 235

A. Mass and Pulse Analysis

The Y-12 Mass Spectrometer Laboratory at Oak Ridge analyzed all the isotopically enriched uranium samples used in this work. The mass percentages of the isotopes in the uranium sample whose principal isotope is U^{235} are given in Table II.

Since the specific activity of U^{234} is about 3000 times that of U^{235}, the activity contribution of U^{234} is very significant in the above sample; therefore, it was necessary to determine the percentage of activity contributed by U^{234}. The 48-channel linear differential pulse-height analyzer was used for this purpose.[5] Pulse analysis showed that (65.3 ± 1.3) percent of the disintegrations were emitted from U^{235} and 34.7 percent from U^{234}.

B. Preparation of the Standard Solution

The balance used for weighing the oxide was an American Balance Corporation chainomatic semimicro analytical balance, with a load capacity of 200 g and a sensibility of about 25 μg. The weights, chain, and rider were calibrated against National Bureau of Standards calibrated weights. About 63 mg of the oxide were weighed in a clean porcelain crucible, which previously had been tare weighed. The uncertainty in weighing was conservatively estimated as $<\pm 0.1$ percent.

TABLE I. Spectrographic analyses of uranium oxide samples.

Oxide	% Fe_2O_3	% CaO	% Al_2O_3	% MgO	% others	% purity	Method
$(U^{235})_3O_8$	<0.01	<0.01	0.01	<0.01	<0.01	>99.95	Cu spark
$(U^{238})_3O_8$[a]	<0.04	<0.01	<0.01	<0.01	<0.1	>99.90	gallium oxide
$(U^{238})_3O_8$	0.14	<0.01	0.04	0.02	<0.01	>99.8	Cu spark

[a] $(U^{238})_3O_8$ was found to contain the amounts of impurities as shown when received, and no effort was made to purify it further.

TABLE II. Isotopic analysis of enriched uranium sample.

Percentage of isotope	Limits of error
235–99.94	± 0.010
238– 0.038	± 0.009
234– 0.022	± 0.005

The oxide was dissolved in 2 ml of warm concentrated HNO_3. The solution was cooled, 2 ml of concentrated H_2SO_4 added, and the solution heated to drive off the HNO_3. After recooling, the solution was quantitatively transferred from the crucible to a calibrated 10-ml volumetric flask, and distilled water was added until the solution was up to the mark. After thorough mixing, the standard solution was transferred to a 30-ml bottle, the glass stopper of which fitted over the outside of the neck. The resulting concentration of the standard solution was 5.312 ± 0.010 mg of pure uranium per ml of solution. All volume aliquots were taken from this bottle, and each time care was taken to avoid touching the inside of the neck with the wet tip of the micropipet.

Calibration, dilution to the standard volume, and subsequent removals of volume aliquots were all carried out at 24 ± 1°C.

A check on the concentration of the standard solution after one year indicated that any change in concentration due to evaporation was less than 0.1 percent during the short period when the electrodepositions were made.

C. Electrodepositon of the Material

Each uranium sample was prepared for counting by an electrodeposition technique described in detail by Hufford and Scott.[6] Figure 1 shows the component parts of the electrolysis cell used for most of the electrodepositions. Each platinum plate was cleaned, prior to assembling the cell, by boiling in hot concentrated HNO_3, rinsing with distilled water, and drying and annealing over a small Bunsen flame.

The stirring anode used was a platinum disk 10 mils thick and $\frac{5}{8}$ inch in diameter, riveted to a tantalum shaft $\frac{1}{8}$ inch in diameter. The shaft was placed securely in the chuck of a variable speed stirring motor, which was set to run at 500 rpm. Further control on the stirring speed was afforded by a variac interposed between the house line and the stirring motor.

After the cell was assembled, an accurate volume aliquot was removed from the standard solution with a

[4] W. Biltz and H. Müller, Z. anorg. u. allgem. Chem. **163**, 257 (1927).

[5] Ghiorso, Jaffey, Robinson, and Weissbourd, *The Transuranium Elements: Research Papers* (McGraw-Hill Book Company, Inc., New York, 1949), Paper No. 16.8, National Nuclear Energy Series, Plutonium Project Record, Vol. 14B, Div. IV.

[6] D. L. Hufford and B. F. Scott, *The Transuranium Elements: Research Papers* (McGraw-Hill Book Company, Inc., New York, 1949), Paper No. 16.1.

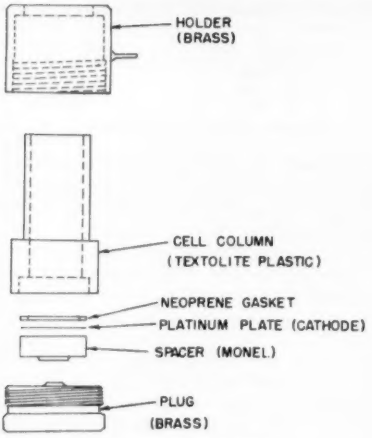

FIG. 1. Electrolysis cell.

calibrated[7] micropipet and transferred to the cell. The pipet was rinsed five times to ensure complete transfer. Then the deposition was carried out as described in reference 6.

After the deposition was complete, the cell was filled with distilled water at about 80°C, and half the solution pipetted out. This procedure was repeated twice. The current was broken, the anode was removed from the cell, and the remaining solution was poured out. Three rapid rinses with cold water sufficed to rid the cell of any oxalate, and the deposit was allowed to dry in the cell. After drying, the plate was removed from the cell and flamed. The resulting film was adherent and uniformly distributed.

The time for essentially complete deposition was shown to be about 30 minutes by experiment, but each deposition of U^{235} was run for about 90 minutes to ensure that 99.9+ percent of the uranium was deposited. That such was the case was proven by the following experiment. A quantity of uranium in solution was electrodeposited and the electrolytic solution was assayed for activity. Less than 0.1 percent of the original activity was found. The deposited sample was placed in a 2π alpha-counting chamber and the counting rate determined accurately. Then about 98 percent of the uranium was removed from the plate and redeposited on another plate. Both the first and second plates were then counted, and the sum of their counting rates was exactly equivalent to the counting rate of the first deposition.

[7] Each micropipet was calibrated for content with mercury. The calibration error, including the uncertainty in the correction for the meniscus effect, was less than ±0.1 percent.

IV. URANIUM 234 AND URANIUM 236

The experimental procedures used in preparing samples of U^{234} and U^{236} for counting were essentially the same and therefore will be discussed in the same section.

A. Mass and Pulse Analyses

The mass analyses reported by the Y-12 Mass Spectrometer Laboratory are summarized in Table III.

The sample whose principal isotope is U^{234} was not pulse analyzed, since the activity contributions of U^{235} and U^{238} were entirely negligible.

Pulse analysis of the U^{236} sample showed that 97.7 ±0.5 percent of the activity was contributed by U^{236} and 2.2 percent by U^{234}. The remaining 0.1 percent contributed by U^{235} was calculated from the mass percentage and the approximate specific activities of U^{234} and U^{235}.

B. Weight Measurements

The uranium oxide used to prepare each plate was weighed on a quartz fiber torsion balance of the type described by Cunningham.[8] The balance used was manufactured by the Ryerson Instrument Shop, University of Chicago, and is a modification of the Kirk, Craig, Gullberg, Boyer design. It has a load capacity of about 20 mg, a weighing range of about 3.4 mg, and a sensibility of 0.02 μg.

The balance was calibrated directly by weighing separately two 2 mg weights standardized to ±0.03 percent by the National Bureau of Standards. The factors obtained in the two calibrations were 0.3424 and 0.3425 μg per division of the torsion wheel scale. Weighings were reproducible to ±0.05 division read from the vernier scale of the torsion wheel. All samples weighed exceeded a mass of 100 μg, and thus were weighed with a precision of better than ±0.02 percent and an over-all uncertainty of less than 0.05 percent.

For each sample of oxide to be weighed, a weighing container was prepared from thin-walled quartz tubing of about 1-mm i.d., by sealing one end of the tubing in the flame of a microtorch, cutting the tubing about 4 mm from the sealed end, and fusing a quartz fiber of about 100-microns diameter to the side of the tube

TABLE III. Mass analyses of the U^{234} and U^{236} samples.

Principal isotope	Mass % of isotopes	Limits of error
U^{234}	234–95.99	±0.07
	235– 3.02	±0.03
	238– 0.98	±0.05
U^{236}	236–96.65	±0.07
	235– 3.09	±0.03
	234– 0.05	±0.01
	238– 0.21	±0.02

[8] B. B. Cunningham, Nucleonics **5**, 62 (1949).

near the opening. The fiber was bent to form a hook so that it could be suspended on the hang-down fiber of the torsion balance. The tube was cleaned in boiling nitric acid, distilled water, and dried in a clean covered beaker in an oven. Tubes of this size weighed approximately 6 mg.

After tare weighing on the torsion balance, a tube was mounted in a pair of screw-controlled cork-tipped forceps held in a micromanipulator. A small microfunnel drawn from $\frac{1}{4}$-inch Pyrex tubing was held by a clamp above the weighing tube. The weighing tube was carefully positioned directly under the stem of the funnel and brought upward until the stem of the funnel was inserted about $\frac{1}{3}$ of the way into the tube. The required amount of oxide was poured into the funnel, and it dropped neatly to the bottom of the weighing tube. The tube and sample were then weighed on the torsion balance.

C. Dissolution and Plating of the Materials

After weighing as described, the weighing tube with sample was placed in a clean 10-ml glass stoppered volumetric flask. Flask and contents were then weighed on the semimicro balance described in Sec. III. The flask was then tipped causing most of the oxide powder to fall out of the weighing tube into the bottom of the flask, and 350 μl of concentrated HNO_3 were added. After standing for about 6 hours in the cold, all the oxide was dissolved. Then 2.6 ml of 5.6M H_2SO_4 was added, and the flask was heated gently and shaken for about 20 minutes to ensure homogeneity of the solution.

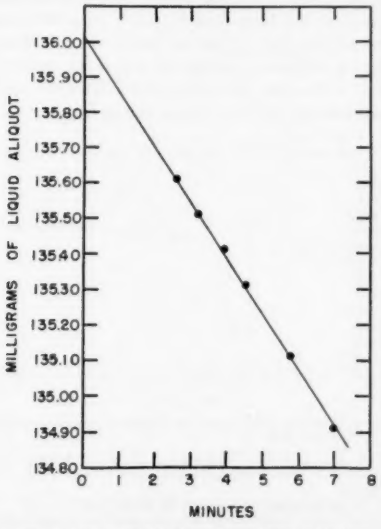

FIG. 2. Loss in weight of uranium aliquot with time.

The flask was reweighed and the concentration of uranium in μg/g of liquid was calculated.

A clean 2-mil platinum disk one inch in diameter was tare weighed on the same analytical balance. The disk rested on the bottom of a small porcelain titration disk inverted in a porcelain crystallizing dish $1\frac{1}{2}$ inches in diameter. About 100 μl of liquid of known uranium concentration was transferred with a micropipet to the platinum plate, and the liquid and plate weighed. Loss of liquid by evaporation was corrected for by taking successive weighings using a stop watch and extrapolating to the time when the 2–3 drops were placed on the plate as shown in Fig. 2. A typical set of weighings is given below.

Torsion Balance Weighing

1779.55 div.—sample+tube
−939.75 div.—tare
839.80 div.—sample

839.80×0.34245 = 287.59 μg oxide
287.59×0.8458 = 243.24 μg uranium
243.24×0.9599 = 233.49 μg U^{234}

Analytical Balance Weighing

12.89913 g flask+tube+oxide
−0.00029 oxide
12.89884 g flask+tube

16.85258 g flask+tube+liquid
−12.89884 flask+tube
3.95374 g liquid

$$\frac{233.49}{3.95374} = 59.055 \ \mu g \ U^{234}/g \text{ liquid}$$

Plate 24–21

15.29680 g plate+support+liquid (zero time extrapolation—see Fig. 2)
15.16079 plate+support
0.13601 g liquid

0.13601×59.055 = 8.032 μg U^{234} plated

Flask Reweighed: 16.71343 g

16.71343 − 12.89884 = 3.81459 g liquid remain

16.85258 − 16.71343 = 0.13915 g liquid removed

0.13915×59.055 = 8.218 μg U^{234} removed

233.49 − 8.22 = 225.27 μg U^{234} remain

$$\frac{225.27}{3.81459} = 59.055 \ \mu g \ U^{234}/g \text{ liquid (concentration check)}$$

After weighing the liquid on the platinum plate, the crystallizing dish and contents were placed in an induction furnace. As the temperature of the plate rose, the drop of liquid began to evaporate slowly, with no bubbling or spattering. When only H_2SO_4 remained as

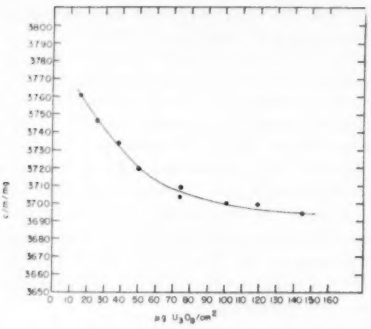

FIG. 3. Specific counting rate *vs* film thickness for samples in 2π-alpha-counting chamber.

solvent, careful control of the furnace resulted in the formation of a series of fairly concentric rings as the droplet was reduced in size. After complete evaporation, the plate was brought to a dull red heat over a microburner, and the plate was ready for counting.

V. COUNTING OF THE SAMPLES

Precise determinations of alpha-disintegration rates are subject to a number of errors, some of which are quite difficult to control. Many of these factors are discussed by Jaffey, Kohman, and Crawford in their *Manual on the Measurement of Radioactivity*.[9] However, a detailed discussion of all the problems is not to be found in any one place in the literature. The major considerations will be discussed below.

A thin sample of an alpha-radioactive substance mounted on a flat polished backing material emits 50 percent of its alpha-particles with a direction component toward the backing plate. In a conventional 50-percent geometry (2π) ionization chamber a significant fraction of these particles suffer multiple scattering by the atoms of the backing plate in such a way that they emerge from the plate in the direction of the sensitive volume of the counter. Cunningham, Ghiorso, and Hindman[10] found experimentally that the apparent specific activity of Pu^{239} was 4-percent higher when counted in a 50-percent geometry chamber than when counted in a 0.04-percent geometry chamber, and Cunningham, Ghiorso, and Jaffey[11] observed that 3.1 percent of the alpha-particles emitted from natural uranium were effectively backscattered from platinum, neglecting self-absorption.

Theoretical calculations by Crawford[12] indicate that alpha-particles with a range of 3.68 cm in air are backscattered from platinum to the extent of 3–3.5 percent, in good agreement with experiment. Moreover, they show that the amount of backscattering should depend on the atomic number of the backing material and the range (energy) of the alpha-particle. The dependency on atomic number has been partially verified by experiment.[11,13]

For "weightless" samples, a correction for the geometry factor of a 2π-chamber can be derived from Crawford's formulas, but if a sample is not "weightless," an appreciable number of the backscattered particles are self-absorbed by the radioactive substance, so that the specific counting rate decreases with increasing film thickness.[14] This fact is demonstrated by Fig. 3. By extrapolating to zero film thickness, at which no self-absorption takes place, the theoretical calculation can still be made.

When the counting rate of a weightless sample in a 2π-chamber is measured as a function of the gain setting of the scaling circuit, the plateau is usually found to have a linear slope of from 2–4 percent over the range of the plateau, as is shown in Fig. 4. Undoubtedly such slopes are caused principally by an increase in the number of backscattered particles detected with increased gain. Then the counting rate for a sample in such a chamber is arbitrary, since knowledge of the gain setting is insufficient for accurate evaluation of the counting yield.

This variation of counting rate with gain makes the absolute evaluation of a precise disintegration rate measured in a conventional 2π-chamber very unreliable. No method has been devised which permits accurate correction for this deviation, other than calibration against a counting chamber of accurately known geometry. Even then, the calibration is accurate only for a particular system at a unique gain setting.

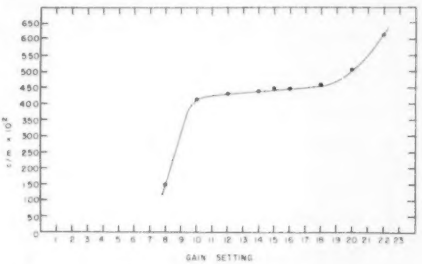

FIG. 4. Counting rate *vs* gain for sample in 2π-alpha-counter.

[9] Jaffey, Kohman, and Crawford, Metallurgical Laboratory Declassified Report M-CC-1602, unpublished (January, 1944).

[10] Cunningham, Ghiorso, and Hindman, *The Transuranium Elements: Research Papers* (McGraw-Hill Book Company, Inc., New York, 1949), Paper No. 16.3.

[11] Cunningham, Ghiroso, and Jaffey, *The Transuranium Elements: Research Papers* (McGraw-Hill Book Company, Inc., New York, 1949), Paper No. 16.6

[12] J. A. Crawford, *The Transuranium Elements: Research Papers* (McGraw-Hill Book Company, Inc., New York, 1949), Paper No. 16.55.

[13] C. A. Kienberger, Phys. Rev. **76**, 1561 (1949).

[14] B. F. Scott, reported in Metallurgical Laboratory Report CN-1764, unpublished (July, 1944).

However, such chambers do afford convenient means for determining precise relative data, provided the samples are reasonable uniform in thickness and have the same backing material and alpha-decay energy. They also are adequate for the determination of absolute disintegration rates with an uncertainty of the order of ± 3 percent.

Fortunately, precise determinations of alpha-disintegration rates are feasible. Jaffey[15] has demonstrated experimentally that the backscattered particles detected in a 2π-chamber are those caused by low angle scattering and are emitted at an angle less than about 35° with reference to the backing plate. Hence, low geometry chambers effectively eliminate the detection of all backscattered particles, by detecting only those particles which are emitted from the backing plate with an angle of about 85° or more. When the samples used in the preparation of Fig. 3 were counted in a low geometry chamber, the slope of the plateau decreased to zero.

Figure 5 shows a schematic diagram of a typical low geometry chamber used in this laboratory. The aperture at the top (often called a "collimator") is covered with a mica window $1\frac{1}{2}$–2 mg/cm² in thickness, with a very thin film of aluminum evaporated on the top side of the mica to make the window surface conducting. During operation, the chamber is evacuated so that the alpha-particles emitted in the proper direction from the sample travel freely up to the window, pass through it and are detected in the argon-filled region above the window in the conventional manner.

Figure 6 illustrates a plateau measured for such a chamber. It is seen that no ambiguity in counting rate is involved.

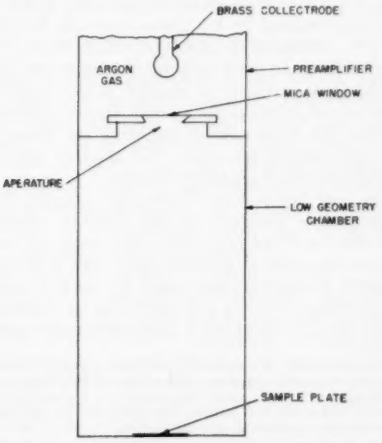

FIG. 5. Schematic diagram of low geometry chamber.

[15] A. H. Jaffey, unpublished work.

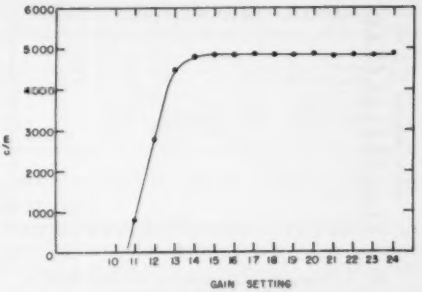

FIG. 6. Counting rate vs gain for sample in low geometry counter.

If we let c = radius of the aperture, h = distance from the sample to the plane of the aperture, and s = radius of a uniformly distributed sample coaxial with and parallel to the plane of the aperture, then for the case where $s=0$,

$$G_P=\frac{1}{2}\left[1-\frac{h}{(h^2+c^2)^{\frac{1}{2}}}\right]=\frac{c^2}{2\left[h^2+c^2+h(h^2+c^2)^{\frac{1}{2}}\right]},$$

where G_P = the "point source" geometry factor.

When c/h and $s/h \ll 1$, the following equation holds approximately:

$$1/G_s \cong 4h^2/c^2+3+3s^2/c^2-s^4/4c^2h^2+(9s^2-c^2)/4h^2,$$

where G_s is the geometry factor for samples of significant radius. G_s is defined accurately by the integral

$$\frac{1}{A}\int_A \Omega(G_P)dA,$$

where A is the area of the sample and $\Omega(G_P)$ is the solid angle subtended by the aperture and any point on the sample surface.

The approximate equation was developed by H. P. Robinson in this laboratory, by considering corrections involving the inverse square law and the cosine of the angle at the aperture subtended by the vertical axis of the chamber and an element of sample surface away from the center of the sample. It is accurate to ± 0.1 percent for such values as $s/h<0.15$, 0.2, 0.5, when $c/h<0.19$, 0.14, 0.07, respectively. It is entirely adequate for low geometry chambers of conventional dimensions.

When s/h and c/h are greater than values such as those given, accurate calculations of the geometry factors are very laborious. Tables have been prepared in the computer laboratory at the University of California which list values of G_s as a function of s/h from 0 to 2 and c/h from 0.01 to 4. The computations were based on the integral shown above, which is similar to the one described by Kovarik and Adams.[16] The inter-

[16] A. F. Kovarik and N. I. Adams, Phys. Rev. **40**, 718 (1932).

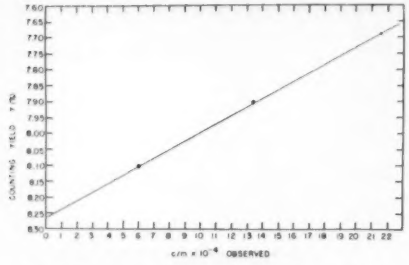

FIG. 7. Counting yield *vs* counting rate for samples in medium geometry counter.

vals of s/h and c/h are such that, for most cases, G_s can be determined with an error $<\pm 0.05$ percent by a first order interpolation. In extreme cases, a second order interpolation is necessary.

A distinction must now be made between the geometry factor, G_s, and the counting yield, Y. G_s was defined accurately above, and is, in one sense, the probability that the alpha-particles at a distance h from the aperture will emerge through the aperture, on purely geometrical grounds.

The counting yield is the ratio of the number of particles registered by the scaling circuit to the number emitted in all directions from the sample. Seldom does $Y=G_s$, for the following reasons:

(1) The evaluation of G_s requires experimental measurements of chamber and aperture dimensions and is subject to error. In the case of the low geometry chamber used for calibration work mentioned later, evaluation of G_s to ± 0.1 percent required that $d=2c$ be measured to ± 0.2 mil and h to ± 1.5 mils since d and h were 0.75 and 5.4 inches, respectively.

(2) Alpha-particles have a finite range through the material from which the aperture ring is constructed. Hence, the diameter used for calculating the geometry factor must be somewhat larger than that actually measured. For example, if 6-Mev alpha-particles were defined by an aperture ring made of aluminum having an edge beveled at an angle of 30° and an aperture of 0.2000-inch diameter, the effective diameter would be 0.2036 inch, and the error in the geometry factor calculated from the measured diameter would be about 3.5 percent.[17]

(3) Two or more alpha-particles entering the ionization chamber within an interval shorter than the resolving time of the scaling circuit register as a single event. Figure 7 gives the coincidence correction curve for the chamber used for counting all the samples prepared for this work. The uncertainty in the coincidence correction read from this curve is of the order of 3 percent. Since the coincidence correction itself is about 3 percent per 10^5 counts/min, the uncertainty contributed by the coincidence correction to counting rates in the region of 10^5 counts/min is about ± 0.1 percent, and is lower for lower counting rates.

(4) The calculation of G_s assumes that the sample is distributed as a perfectly uniform film, that no self-absorption occurs and that the sample is perfectly coaxial with the aperture and parallel to the plane of the aperture. Errors due to the last two requirements can easily be made insignificant, and errors due to the first can be made insignificant if the sample is prepared with care.[18]

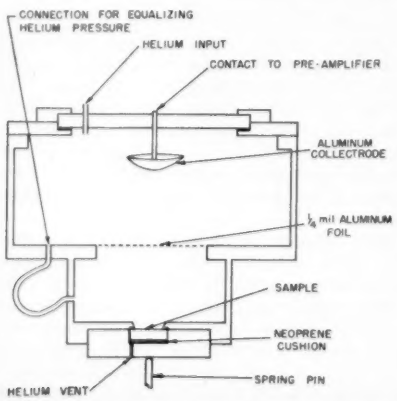

FIG. 8. Schematic diagram of medium geometry chamber.

The low geometry chamber of the type described previously was not suitable for counting the alpha-particles emitted by U^{235}, since the specific counting rate amounted to only 9 counts/min per mg of the isotope. A chamber of intermediate geometry ($G_s \cong 8$ percent) was designed by A. Ghiorso, especially for counting U^{235}. A diagram of the chamber is shown in Fig. 8 ($c \simeq 2$ inches and $h \simeq 3$ inches). Aluminum leaf about 0.1-mil thick, or about 0.7 mg/cm², is fixed across the aperture and serves as the window. The entire chamber is filled with helium gas during operation. Because of the high relative geometry, this chamber has been named a "medium geometry chamber."

The bold line in Fig. 9 shows the geometry factor *versus* sample diameter for this chamber calculated with the use of the geometry tables mentioned previously in this section. The four points seen in the figure represent calibration points taken by counting samples of the diameter shown and correcting for coincidence losses, and the dotted line is the experimental counting

[17] For this work, the aperture ring of the low geometry chamber was made of stainless steel and had a bevel of 60°. The aperture was about ¾ inch in diameter. The error due to a greater effective diameter was about 0.06 percent. The same error for the medium geometry chamber was about 0.006 percent.

[18] An experimental check was made with a sample of 40-mm diameter which had a visually bad distribution compared to those used for specific activity measurements. Error due to nonuniformity was shown to be <0.05 percent for this sample.

yield. The absolute disintegration rates of each of these samples were measured previously by counting in the low geometry chamber of $G_s \simeq 1/800$. The point at diameter 36.9 mm represents the value of the counting yield for three samples of this diameter given by the extrapolation to zero counting rate shown in Fig. 7.

It is seen from Fig. 9 that the calibration points differ from the calculated curve by about 0.5 percent. A complete explanation for this systematic difference has not been found.

The medium geometry chamber was used to count all samples of U^{234}, U^{235}, and U^{236}. The background of the chamber remained at (14.9 ± 0.1) counts/min throughout the work. The counting rates of the samples in this chamber ranged from 7000 to 12,000 counts/min for the various U^{234} samples, from 400 to 800 counts/min for U^{235} samples, and from 200 to 400 counts/min for those of U^{236}.

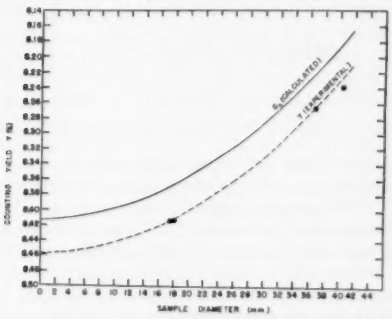

FIG. 9. G_s and Y vs sample diameter for medium geometry chamber.

VI. RESULTS AND DISCUSSION

Table IV summarized all the known sources of error involved in the determinations of the specific activities by the procedures used. The uncertainties in the pulse analysis values are standard (two-thirds) errors. The values for geometry factors were those determined by the dotted line of Fig. 9, which is based on the experimentally measured geometry of the medium geometry chamber. The uncertainties of the other values have been discussed in previous sections.

The results of this work are given in Table V.

Jaffey and co-workers[19] have measured the half-life of U^{236} by counting mass and pulse analyzed samples of uranium enriched in U^{236}. The weight of each sample was determined indirectly by counting neutron-induced fissions produced in the U^{235} present. The value found for the half-life of U^{236} was 2.457×10^7 yr. No limits of error were given for this figure, but in a private communication the principal author has set limits of ± 2 percent. The value is thus in agreement with that found by us.

[19] Jaffey, Diamond, Hirsch, and Mech, Phys. Rev. **84**, 785 (1951).

TABLE IV. Summary of limits of errors (in percent).

Uranium isotope	No. of samples counted	Std. dev. for all samples	Pulse analysis	Mass analysis	Sol'n conc.	Geom. factors	Chem. purity	Over-all standard error
234	9	±0.38	···	±0.07	±0.1	±0.50	±0.10	±0.65
235	9	±0.84	±2.0	±0.01	±0.2	±0.50	±0.10	±2.2
236	3	±0.14	±0.50	±0.07	±0.1	±0.50	±0.20	±0.79

Because of the wide interest in the three isotopes comprising natural uranium, Table VI is presented which summarizes the various specific activities, half-lives, mass ratios, and activity ratios reported in the literature of the past fifteen years. Unfortunately, many of the published papers are written with so few details that a critical analysis for sources of error is impossible. Nevertheless, an attempt has been made to evaluate the data so that "best" values may be stated which are themselves internally consistent. It has not been feasible to present all the reasons for each selection, but the principal reasons have been stated briefly. Conservative limits of error have been set for these "best" values.

The mass ratio U^{238}/U^{235} in natural uranium has been measured with mass spectrographs by at least three different groups. In 1932, Nier[1] reported a value of 139 ± 1.4. He showed further that the ratio was the same, within limits of error, for minerals varying in age from 10^9 to 10^9 years.

In 1946, Chamberlain and co-workers[20] found the same value, and in the same year Fox and Rustad[21] obtained a ratio of 137.0 ± 0.7 from a weighted average of 14 sets of readings, using an electron bombardment source. With a thermal source they found a value of 138.0 ± 0.3 from a weighted average of nine sets. The resolution corrections were much smaller with the latter source, mainly because metal ions, rather than UF_5^+ ions, were detected.

A "best value" for the mass ratio U^{238}/U^{235} in natural uranium of 138 ± 1.4 is estimated from these data.

The values quoted for the half-life of U^{234} vary from 2.29 to 2.7×10^5 yr. The values 2.7×10^5 yr ± 10 percent (Nier),[1] and 2.29×10^5 yr ± 6 percent (Chamberlain, *et al.*),[20] were derived by measuring the mass ratio of U^{238} to U^{234} in natural uranium and assuming radioactive equilibrium between the isotopes. Using 4.5×10^9

TABLE V. Specific activities and half-lives of U^{234}, U^{235}, and U^{236}.

Uranium isotope	Specific activity (disint/min mg)	Half-life (years)
234	$(1.370 \pm 0.009) \times 10^7$	$(2.475 \pm 0.016) \times 10^5$
235	$(4.74 \pm 0.10) \times 10^3$	$(7.13 \pm 0.16) \times 10^8$
236	$(1.406 \pm 0.011) \times 10^6$	$(2.391 \pm 0.018) \times 10^7$

[20] Chamberlain, Williams, and Yuster, Phys. Rev. **70**, 580 (1946).

[21] M. Fox and B. Rustad, Carbide and Carbon Chemicals Corporation Report BD-R-88, unpublished (January, 1946).

TABLE VI. Recent values of natural constants for the common uranium isotopes.

t_{234} (yr) $\times 10^{-5}$	Sp. Act.$_{234}$(disint/min mg) $\times 10^{-7}$	t_{238} (yr) $\times 10^{-9}$	Sp. Act.$_{238}$(disint/min mg) $\times 10^{-3}$	Ref.
2.7 ±0.27	1.3 ±0.13	7.06±0.21 (recalc.)	4.78±0.14	1
2.29 ±0.14	1.48 ±0.09			17
2.35 ±0.14	1.44 ±0.09			17
2.522±0.008	1.345±0.004	8.8 ±1.1	3.82±0.49	12
2.67 ±0.04	1.27 ±0.02			19
2.475±0.016	1.370±0.009	7.13±0.16	4.74±0.10	(This work)
		8.91		2
		7.53±0.23	4.48±0.14	22
2.48 ±0.02	1.37 ±0.01	7.13±0.14	4.74±0.09	"Best" values

t_{235} (yr) $\times 10^{-9}$	Sp. Act.$_{235}$ (disint/min mg)	t_{natural} (yr) $\times 10^{-9}$	Sp. Act.$_{\text{natural}}$ (disint/min mg)	Ref.
		2.221±0.008	1501±6	20
		2.221±0.004	1501±3	23
4.49±0.01	742.7±1.6	2.220±0.002	1502±1.5	12
4.51±0.01	738.8±1.6	2.221±0.004	1501±3	"Best" values

N_{238}/N_{235}	N_{238}/N_{234}	N_{234}/N_n (%)	$R=A_{238}/A_{235}$ (%)	$A_{234}/N_n=A_{235}/N_n$	A_{235}/N_n	Ref.
138.9±1.4	16,800±10%	0.00591 ±0.00059	4.6 ±0.1			1
139	19,700±6%					17
137.0±0.7						18
138.0±0.3						18
		0.005481 ±0.000012		737.4±1.6	27.2±3.5	12
			3.63±0.03			2
138.0±1.0	18,400±1%	0.00539 ±0.00004	4.6 ±0.1	733.5±1.6	34.1±0.8	"Best" values

yr for the half-life of U^{238},

$$T_{234}=4.5\times 10^9(N_{234}/N_{238})\text{ yr.}$$

Chamberlain's mass spectrograph gave better resolution than that used by Nier.

The value 2.35×10^5 yr±6 percent (Chamberlain, *et al.*)[20] was computed from measurements of the specific activity of uranium enriched in U^{234} and U^{235}, using a 2π-chamber, determining the mass abundances of each isotope in the enriched samples, and subtracting the activity contributions of U^{235} and U^{238} calculated from specific activities for these isotopes determined elsewhere. The counting yield of the 2π-chamber was determined by counting "thin samples" of known weight of natural uranium and dividing the specific counting rates by the specific activity of natural uranium as determined by Kienberger.[13]

The value 2.522×10^5 yr±0.3 percent (Kienberger)[13] was determined in a similar manner, again counting each sample in a 2π-chamber. From a single material, samples of varying thickness were prepared and counted, and a specific counting rate at zero film thickness was found by extrapolation. A value for backscattering from the nickel backing material was calculated from Crawford's[10] work. The specific activity of the material was computed from these data. The values of Kienberger and Chamberlain based on the same principle of measurement agree nearly within quoted limits of error.

The value 2.67×10^5 yr±1.3 percent (Goldin *et al.*)[22] was determined by genetic relationships. U^{234} was allowed to grow in by two beta-particle emissions from UX^1 (Th^{234}), which originally decayed from U^{238} by alpha-emission. The weight of U^{234} was calculated from the weight of the parent U^{238} (determined by counting), the several decay periods involved, and the decay constants of U^{238} and the intermediate isotopes. The method required many operations subject to error, including a chemical yield and separation of Th^{234} from natural uranium, which was assumed to be quantitative. The description of the work was insufficiently detailed to permit independent evaluation of these errors. However, one is forced to conclude that such a method is extremely unlikely to yield results in error less than a few percent. The limits of error of ±1.3 percent quoted seems unrealistic. Furthermore, the value determined is outside of agreement with the weighted mean of the other values by some 7.5 percent.

The value 2.475×10^5 yr±0.7 percent found by us was discussed in detail in previous sections. It is the only value determined by direct means with very highly enriched uranium and is independent of any constants of other isotopes or isotope ratios.

By weighting each value reported, considering the directness of each method of counting, and the limits of error quoted by each author, a best value for the half-life of U^{234} is computed as 2.48×10^5 yr±1 percent, with a concomitant specific activity of 1.37×10^7 disint/min mg. Considering limits of error, all values quoted in the table are in agreement with this value except Chamberlain's first value of 2.29×10^5 yr and Goldin's value of 2.67×10^5 yr.

[22] Goldin, Knight, Macklin, and Macklin, Phys. Rev. **76**, 336 (1949).

Nier[1] was among the first to determine a value for the half-life of U^{235}, *viz.*, 7.06×10^8 yr (recalculated in accordance with the work of Kovarik and Adams[22]). The half-life was calculated from the relation

$$R=\frac{\lambda_{235}N_{235}}{\lambda_{238}N_{238}}=\frac{\text{Activity of } U^{235}}{\text{Activity of } U^{238}}.$$

For the ratio N_{238}/N_{235}, he used the value 139. λ_{238} was computed from the specific activity of natural uranium[20] and $N_{238}/N_{\text{natural}}=0.9928$. R was determined by measuring the Pb^{207}/Pb^{206} ratio with a mass spectrometer for several radiogenic lead ores of known age, and utilizing the equation

$$\frac{N_{207}}{N_{206}}=\frac{1}{139}\,\frac{\exp(139R\lambda_{238}t)-1}{\exp(\lambda_{238}t)-1},$$

where t is the age of the ore.

R was found by graphical means to be 0.046 ± 2 percent. A 1-percent error in the ratio N_{238}/N_{235} has practically no effect on the value of R. Therefore, Nier's value of the half-life of U^{235} should be in error by less than about 3 percent. This assumption is strengthened by the beautiful consistency of his data.

Kienberger[13] reports a value of 8.8×10^8 yr$\pm$12.5 percent for the half-life of U^{235}, calculated by difference. He measured the specific activity of natural uranium and of U^{238} and computed the activity contribution of U^{238} in the former. By subtracting twice this contribution (U^{234} assumed to be in radioactive equilibrium with U^{238}) from the specific activity of natural uranium, the activity contribution of U^{235} is computed. Dividing this value by the mass abundance of U^{235} in natural uranium gives the specific activity of U^{235}. The figure is subject to great error because it is determined by a small difference between two large numbers. For example, if the value for the specific activity of natural uranium is in error by 0.1 percent, that for U^{235} would be in error by 4.5 percent.

Clark and co-workers[2] reported a figure for the half-life of U^{235} of 8.91×10^8 yr, based on a value of 0.0363 for R, computed from pulse analyses of natural uranium. It is now known[24] that their value for R is about 15-percent low, since they were unable to resolve high and low energy alpha-groups comprising about 15 percent of the alpha-spectrum of U^{235}. Correcting for this error gives $R=0.0425$, and a half-life of 7.64×10^8 yr. A further discrepancy of 7 percent compared to Nier's values remains unexplained.

A value of 7.53×10^8 yr$\pm$3 percent was obtained by Knight,[25] who measured the specific activity of a portion of the same highly enriched U^{235} used for our work, and found a specific disintegration rate of 7279 ± 23 disint/min mg, in good agreement with our value of 7257 ± 70 disint/min mg. Knight's pulse analysis, made with a one-channel pulse-height analyzer, indicated that about 61.6 percent of the disintegrations were those of U^{235}, giving 4484 disint/min mg of U^{235}.

Careful pulse analysis of this material made with the 48-channel differential pulse analyzer in this laboratory gave 65.3 ± 1.3 percent for the U^{235} contribution. Knight's gross specific activity multiplied by 0.653 gives a half-life of 7.10×10^8 yr.

From the values discussed above, a weighted average gives a best value of 7.13×10^8 yr$\pm$2 percent for the half-life of U^{235}, with a corresponding specific activity of 4.74×10^3 disint/min mg.

Kovarik and Adams[22] were the first workers to make a precise determination of the specific activity of natural uranium. They eliminated backscattering and self-absorption as sources of error by counting only those alpha-particles which passed through the holes of a metal grid. They obtained 1501 disint/min mg for the specific activity of natural uranium.

Curtiss and co-workers[26] counted samples of natural uranium of known weights and various thicknesses in a 2π-chamber. The samples were thick enough to absorb essentially all of the particles backscattered from the backing material. Therefore, a plot of specific counting rate *versus* film thickness yielded a straight line, and an extrapolated value of 750.6 disint/min mg at zero film thickness. The counting yield was considered to be 0.5 and the specific activity equal to 1501 disint/min mg$\pm$0.2 percent.

Kienberger[13] counted electrodeposited samples of natural uranium in a 2π-chamber and computed the counting yield of the chamber in the same manner as was done for his U^{234} work. He reports a value of 1502 disint/min mg$\pm$0.1 percent.

The excellent agreement among these three values probably is somewhat fortuitous. A best value is 1501 disint/min mg$\pm$0.2 percent for the specific activity of natural uranium, estimated from the data.

Kienberger,[13] using isotopically pure U^{238}, has determined a value of (742.7 ± 1.6) disint/min mg for the specific activity of this isotope, by the same method used for his natural uranium work. It is the only value reported in recent years that has been determined by direct means.

This may be compared with the specific activity of U^{238} calculated from the best values quoted thus far.

Thus, $N_{235}/N_{238}=1/138=0.725$ percent, and $N_{234}/N_{238}=ca$ 0.0054 percent (see below). Therefore, $N_{238}/N_n=0.719$ percent and $N_{235}/N_n=99.28$ percent.

Specific activity of U^n:	1501 ± 3.0 disint/min mg
Specific activity of U^{235} $\times0.00719$:	-34 ± 0.8
Activity contribution of U^{234} and U^{238} in U^n:	1467 ± 3.1 disint/min mg

[22] A. F. Kovarik and N. I. Adams, J. Appl. Phys. **12**, 296 (1941).
[24] A. Ghiorso, Phys. Rev. **82**, 979 (1951).
[25] G. B. Knight, Oak Ridge National Laboratory Report K-663, unpublished (August, 1950).
[26] Curtiss, Stockman, and Brown, National Bureau of Standards Report A-80, unpublished (December, 1941).

Activity contribution of U^{238} in U^n:

$$\tfrac{1}{2}\times 1467 = 733.5 \pm 1.6 \text{ disint/min mg}$$

$$\frac{733.5}{0.9928} = 738.8 \pm 1.6 \text{ disint/min mg},$$

the specific activity of U^{238}.

A relatively large error in the specific activity of U^{235} has but little effect on that of U^{238} calculated in this way. If the value for the specific activity of natural uranium is accurate to ± 0.2 percent, then the value 742.7 disint/min mg for U^{238} must be in error by at least 0.5 percent. Actually, the agreement seems surprisingly good.

The half-life corresponding to 738.8 disint/min mg is 4.51×10^9 yr. Although Nier[1] used the value 4.56×10^9 yr indirectly for the calculation of R, the difference has a negligible effect on R, and on the recalculated value of 7.06×10^8 yr for the half-life of U^{235}.

From the best values quoted thus far, $R = 0.046 \pm 0.001$. U^{234}/U^n in natural uranium may be calculated as follows: Since U^{238} and U^{234} are in radioactive equilibrium, activity of U^{234} equals the activity of $U^{238} = 733.5 \pm 1.6$ disint/min mg of U^n. Dividing by the specific activity of U^{234}, 1.37×10^7 disint/min mg ± 0.7 percent, the mass ratio U^{234}/U^n equals (0.00535 ± 0.00004) percent.

From mass spectrographic analysis, Nier[1] found the mass ratio U^{238}/U^{234} in natural uranium to be $16{,}800 \pm 10$ percent. From this figure the mass ratio U^{234}/U^n is calculated to be (0.00591 ± 0.00059) percent.

Chamberlain and co-workers[20] found $19{,}700 \pm 6$ percent for U^{238}/U^{234}, from which (0.00504 ± 0.00030) percent is calculated for U^{234}/U^n.

Kienberger determined the mass ratio U^{234}/U^n by analyzing samples of uranium highly enriched in U^{234}, and determining the specific activities of these samples. Using his values for the specific activities of U^{235} and U^n, he calculated the value (0.005481 ± 0.000012) percent.

The values of Nier and of Chamberlain and co-workers and the value calculated in this paper are in agreement, within quoted limits of errors, as is nearly the case with Kienberger's value if one considers his statement in the text of his paper that his value is good to at least 1 percent. From the relevant data discussed above, a "best value" for the mass ratio U^{234}/U^n is found to be (0.00539 ± 0.00005) percent.

In conclusion it seems worth while to point out that, with but few exceptions, the papers to which we have referred do not give the slightest information concerning a question of fundamental importance in much of the work, *viz.*, the chemical purity of the materials used. It would seem that this problem has been ignored by many workers in the past. Thus, the values reviewed above, where no mention of chemical purity is made, will stand in doubt merely because of this oversight.

Since Holmes[3] used the value 7.13×10^8 yr for the half-life of U^{235} in his calculations of geological time, which has been found to be the best value to date, no correction can be claimed necessary for his value of the age of the earth on this basis alone.

It is hoped that sometime within the near future, values which have been discussed at length here will be redetermined, particularly those associated with natural uranium and with U^{238}. The availability of uranium highly enriched in particular isotopes makes the task less formidable, and increases the possibility for accurate results. It is hoped further that especial attention be granted to the problems of determining precise alpha-disintegration rates, since within this realm undoubtedly lie the most bases for disagreement among the values reported in the literature.

The authors wish to thank Mrs. Winifred Heppler for her assistance in the experimental work and Mr. H. P. Robinson and his department for many helpful suggestions and aid in servicing the electronic instruments. Mr. John Conway and his department are due credit for the several spectrographic analyses performed on the purified samples.

The Absorption of High Energy X-Rays in Various Materials

H. JANZEN
Synchrotron Laboratory, Queen's University, Kingston, Ontario
(Received July 16, 1952)

Effective absorption cross sections of the x-rays exciting the well-known $Cu^{63}(\gamma,n)Cu^{62}$ reaction have been measured in a number of elements. In agreement with other workers, the experimental cross sections have been found to be lower than those predicted by theory by a fraction roughly proportional to Z^2, which amounts to about 10 percent for Pb. By using the results of these measurements as a standard, the effective energies, with Pb absorbers, of the x-rays exciting the $C^{12}(\gamma,n)C^{11}$, $Mo^{92}(\gamma,n)Mo^{91}$, and $Ag^{107}(\gamma,n)Ag^{106}$ reactions have been found to be 26.0±1.4, 17.0±1.0, and 16.1±0.9 Mev, respectively, in good agreement with resonance peak energies obtained by more elaborate methods.

EFFECTIVE absorption coefficients in nine different absorbers ranging in atomic number from 4 to 92, have been measured for the x-rays exciting the $Cu^{63}(\gamma,n)Cu^{62}$ reaction. By comparison with the results of these measurements, the effective energies of the x-rays exciting the $C^{12}(\gamma,n)C^{11}$, $Mo^{92}(\gamma,n)Mo^{91}$ and $Ag^{107}(\gamma,n)Ag^{106}$ reactions have been determined from their effective absorption coefficients in lead (Pb).

For these measurements a highly collimated beam from a 70-Mev synchrotron was used to excite the reactions in two similar foils, between which absorption sheets could be placed as shown in Fig. 1. The system was irradiated for three times the half-life of the product isotope of the reaction being studied with the synchrotron running at its maximum energy of 70 Mev and with no filtering of the beam other than the small amount due to the donut wall and the beam monitor ionization chamber. After the irradiation the initial activity of the desired product isotope was determined for each foil using a GM tube in a lead castle. From the ratio of the activity on the detecting foil B to that on the monitoring foil A (Fig. 1), divided by the system reduction constant as measured with no absorber in place, the percent transmission for each absorber thickness was obtained. Ten independent determinations of the system reduction constant, made during the course of the experiments, gave for this a value of 0.722±0.002.

The experimental log percent transmission curves were found to be straight lines within the limits of experimental error, and those obtained for the x-rays exciting the $Cu^{63}(\gamma,n)Cu^{62}$ reaction are shown in Fig. 2. From the slopes of the best fit straight lines effective electronic absorption cross sections were calculated, and these are shown plotted against absorber atomic number in Fig. 3. An analysis of the results gave values of the order of 2 percent for the probable error in the experimental points. Also shown in Fig. 3 is the variation of effective absorption cross section with atomic number calculated using theoretical absorption coefficients as given by the Klein-Nishina[1,2] and Bethe-Heitler[3] formulas, with the latter corrected for screening of the nucleus and for pair production in the fields of the atomic electrons by a method similar to that used by Walker.[4]

Effective absorption coefficients will depend also on the shape and energy of the (γ,n) resonance peak of Cu^{63}, as well as on the x-ray spectrum of the synchrotron. Johns *et al.*[5] investigated the $Cu^{63}(\gamma,n)$ cross-section curve and found a resonance peak at 17.5 Mev with a half-width of 6 Mev and threshold at 11 Mev. Our straight line log percent transmission curves (Fig. 2) indicate that there are no other prominent resonance peaks for this reaction in the energy interval from 0 to 70 Mev, and hence Johns' curve has been used in the calculations. The x-ray spectrum assumed was that determined experimentally in this laboratory by McDiarmid,[6] which is practically flat over the energy region of the Cu^{63} resonance peak. As limits of uncertainty, effective absorption cross sections were also calculated as above for a theoretical Schiff[7] spectrum and for monochromatic 17.5 Mev x-rays. The values so obtained were only about 1 percent lower and higher, respectively, than those indicated by the calculated line of Fig. 3.

The calculated line of Fig. 3 corresponds to an effective x-ray energy of 17.0±0.5 Mev, and from the figure it is seen that our experimental results are in excellent agreement with this calculated line for ab-

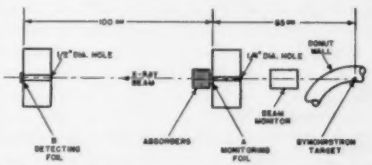

FIG. 1. Schematic diagram of the collimating system, showing the locations of the various components (not to scale).

[1] See W. Heitler, *Quantum Theory of Radiation* (Oxford University Press, London, 1936).
[2] O. Klein and Y. Nishina, Z. Physik **52**, 853 (1929).
[3] H. A. Bethe and W. Heitler, Proc. Roy. Soc. (London) **146**, 83 (1934).
[4] R. L. Walker, Phys. Rev. **76**, 527 (1949).
[5] Johns, Katz, Douglas, and Haslam, Phys. Rev. **80**, 1062 (1950).
[6] I. B. McDiarmid, Master's thesis (to be published).
[7] L. I. Schiff, Phys. Rev. **83**, 252 (1951).

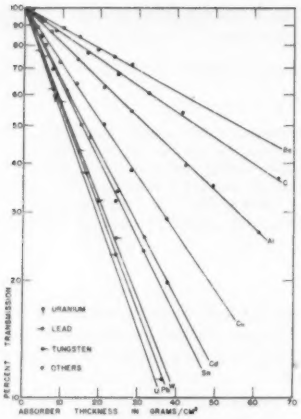

FIG. 2. Percent transmission curves for the x-rays exciting the $Cu^{63}(\gamma,n)Cu^{62}$ reaction in nine different absorbers as marked. Note that only one thickness of uranium absorber was available and the point shown is the average of five separate determinations. Some of the other points also are averages of two or more determinations.

sorbers of atomic number less than about 50. For absorbers of higher atomic number the discrepancy between calculated and experimental cross sections is greater than the experimental error and the uncertainty in the calculated values. Within the limits of error and uncertainty, however, the results agree throughout with those of Walker,[4] and in agreement with Walker[4,8] and Lawson[9] they indicate that the correction to the Born approximation varies as the square of the absorber atomic number. Up to an atomic number of 50 the results are also in fair agreement with those of Marshall.[10]

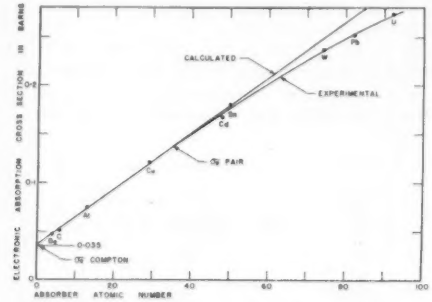

FIG. 3. Calculated and experimental effective electronic absorption cross sections of the x-rays exciting the $Cu^{63}(\gamma,n)Cu^{62}$ reaction, shown plotted against absorber atomic number.

[8] R. L. Walker, Phys. Rev. **76**, 1440 (1949).
[9] J. L. Lawson, Phys. Rev. **75**, 433 (1949).

Effective energies of the x-rays exciting the other reactions mentioned were determined by comparing their effective absorption coefficients in lead (Pb) with that of the x-rays exciting the $Cu^{63}(\gamma,n)$ reaction. The effective energies determined in this way are listed in Table I along with some resonance peak energies obtained by other workers.[11–17] The value of 17.0±0.5 Mev listed for the $Cu^{63}(\gamma,n)Cu^{62}$ reaction and used as the standard for comparison was calculated as described previously. In the energy region of the resonance peaks of these reactions (i.e., from about 10 to 40 Mev) x-ray absorption coefficients for lead increase quite markedly with energy. Calculations have shown that due to this the effective energies obtained will be about 0.5 Mev lower than the resonance peak energy, for a resonance curve shape similar to that of Cu^{63}. Referring to Table I this is seen to be the case for all except the carbon reaction, where the effective energy is considerably higher than the most reliable values for the peak energy. This is to be expected, however, for unlike the other reactions, the C^{12} resonance curve has been found to have a prominent high energy tail.[16,17]

TABLE I. Here experimental effective energies for the various reactions are listed along with some resonance peak energies obtained by other workers.

Reaction	Effective energy Mev	Resonance peak energy Mev	References
$Cu^{63}(\gamma,n)Cu^{62}$	17.0±0.5 (calculated as described in text)	17.5 18.0±1 18.1 22	5, 11 15 12 17
$C^{12}(\gamma,n)C^{11}$	26.0±1.4	22.4 22.9 30 30±4	13 12, 16 17 15
$Mo^{92}(\gamma,n)Mo^{91}$	17.0±1.0	17.5±1.5 18.7	15 14
$Ag^{107}(\gamma,n)Ag^{106}$	16.1±0.9	16.5	11

This work was carried out at the suggestion of Professor J. A. Gray, and grateful acknowledgment is made for his interest and advice throughout. Thanks are also due the National Cancer Institute of Canada, which supported the work.

[10] L. Marshall, Phys. Rev. **83**, 345 (1951).
[11] B. C. Diven and G. M. Almy, Phys. Rev. **80**, 407 (1950).
[12] L. Katz and A. G. W. Cameron, Can. J. Phys. **29**, 518 (1951).
[13] Haslam, Johns, Horsley, Phys. Rev. **82**, 270 (1951).
[14] R. Montalbetti and L. Katz, Phys. Rev. **83**, 892 (1951).
[15] R. Sagane, Phys. Rev. **83**, 174 (1951).
[16] R. Sagane, Phys. Rev. **84**, 587 (1951).
[17] G. C. Baldwin and G. S. Klaiber, Phys. Rev. **73**, 1156 (1948).

A Direct Comparison of the Kelvin and Electron Beam Methods of Contact Potential Measurement*

PAUL A. ANDERSON
State College of Washington, Pullman, Washington
(Received June 25, 1952)

Comparison of contact potential values determined for a given pair of surfaces by (1) the Kelvin method, which is insensitive to patch fields, and (2) the electron beam method which is, according to patch theory, sensitive to these fields, offers a means of testing the validity of the theory and of determining the extent to which patch effects influence electron beam measurements. A technique for carrying out such comparative measurements in a single sealed-off tube is described. Barium and silver are selected for the study because of the known reproducibility and long-period constancy of their work functions. The measured surfaces are prepared by fractional distillation following intensive outgassing and the technique allows repetitive checking through renewal of these surfaces. Special attention is given to the conditions required for satisfactory Kelvin measurements in all-glass, sealed-off systems.

The contact differences of potential found for silver films deposited on a tantalum substrate and barium films laid down on the silver were 1.79 ± 0.03 v by the electron beam method and 1.78 ± 0.01 v by the Kelvin method. This result is discussed from the standpoint of theoretical expressions for the Kelvin and e-beam values, the latter generalized to the case of an arbitrary number of patch types and arbitrary coverage factors. It is concluded (1) that crystal growth mechanisms are capable of reducing patch effects to insignificance under favorable conditions, but that (2) the most likely explanation of the present results is failure of the normal energy assumption and hence of the patch theory based on it to hold for the retarding field, slow electron case. It is suggested that an electron optical treatment of the patch field region may supply a more satisfactory theory.

THE dependence of the observed work function of a metal specimen on the condition of its surface is determined by (1) foreign surface contaminants which change the surface double layer to a value which is not characteristic of the metal itself, (2) the arrangement of the atoms of the metal in the outermost layers of the specimen, and (3) the method of measurement, if peculiarities in the response of the measuring arrangement to factors (1) or (2) are involved. It is well known that minute surface contaminations may render work function measurements valueless, and this fact has made the development of techniques for the preparation of clean surfaces the central objective in photoelectric and contact potential investigations. Factor (2), the primary structure factor, can be studied profitably only after definite evidence has been secured that surface contaminants are absent or inoperative. Such evidence is hard to get and after several decades of experimental work is available in reasonably convincing form for only a few metals. The study of monocrystalline surfaces of known indices, the only surfaces for which the work function has the full status of a material constant, is just beginning.

Factor (3), the main point of interest in the present work, has to be considered whenever surfaces containing "patches," that is, micro- or macroscopic areas of different work function, are involved. The question then arises as to how the observed work function is related to the average work function of the surface. The average work function is defined, in the symbols of Herring and Nichols,[1] as $\bar{\phi}=\sum f_i\phi_i$, where ϕ_i is the work function of patches of the ith type and f_i is the fraction of the surface occupied by patches of that type. This question has received little explicit attention in contact potential and photoelectric studies but is considered at length in Herring and Nichols' valuable review of thermionic emission phenomena.[1] Examination of this most recent treatment shows, however, that patch theory, in so far as its application to contact potential methods involving the collection of slow electrons in retarding fields is concerned, is useful mainly as an aid to formulating, rather than answering, the question of the relationship of observed to average work functions. In its present form, patch theory is based on the assumption ("normal energy approximation") that the motion of electrons close to a patchy surface is unaffected by the tangential components of the patch fields. This assumption appears to be reasonable for the case of strong accelerating fields but to be invalid for the slow electron, retarding field case.

A practicable line of attack on the problem of observed and average work functions, and means of determining the extent to which patch fields influence retarding-field contact potential measurements, would appear to be that of comparing such measurements with observations taken by a method which involves no interaction between electrons and patch fields. The Kelvin method of contact potential measurement has the characteristics needed for the yardstick method. Subject only to the easily verifiable condition that patch dimensions are small with respect to interplate spacing, conventional field theory shows that the observed contact potential difference is precisely equal to the difference between the average work functions of the surfaces.[1] For the comparison to be valid, it is evident that the contamination and primary structure factors must be eliminated, and this condition can be satisfied beyond question only if the two methods are applied to the same surfaces in a single tube. The

* Assisted by the ONR.
[1] C. Herring and M. H. Nichols, Revs. Modern Phys. **21**, 185 (1949).

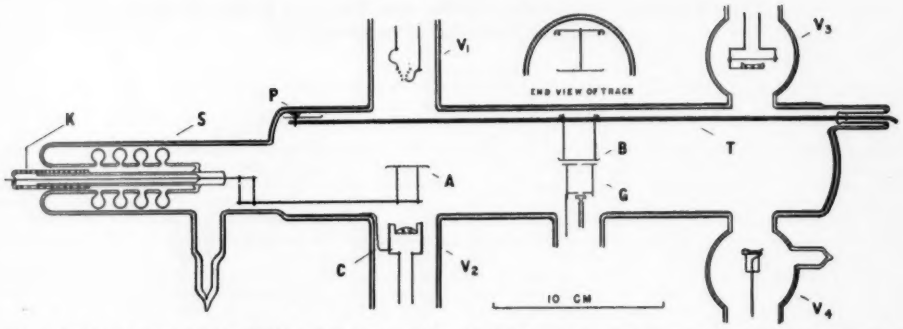

FIG. 1. Scale diagram of the tube. Rocking electrode A, a 10-mil Ta disk riveted to 60-mil Ta posts, is operated by the waxed-on metal tube K through all-glass sylphon S. Sliding electrode B, similarly constructed, is moved on track T (two 80-mil W wires) by tipping tube. Ag is vaporized by 25-mil W wire cone V_1 and 0.025×6 mm Ta foil trough V_2; Ba by Ta foil trough V_4 and 0.025×10 mm Ta foil radiator V_3. C is Pt contact partially embedded in wall. P is Ta foil shield to maintain insulation of T.

objective of the present work was a comparison of this kind between measurements taken by the Kelvin and electron beam methods of contact potential determination. Silver and barium were selected for the study because previous work in this laboratory has shown that each of these metals, when prepared by evaporation in an outgassed, sealed-off tube, consistently yields work function values which are highly reproducible and constant over long periods of time.

METHODS

The theory of the Kelvin method of contact potential measurement is well known. The experimental conditions necessary for satisfactory Kelvin measurements in confined spaces require some comment and are discussed below. The electron beam method, developed primarily for the purpose of minimizing the time interval between the deposition and measurement of a metal surface, has been described previously.[2] The measured surfaces of silver and barium are prepared by the distillation technique which has formed the basis of all of our contact potential studies.[2] This technique involves, in brief, condensation of the metal vapor on a glass or metal substrate after an exhaustive outgassing which includes repetitive fusion, fractional distillation and, when necessary, redistillation of the middle fractions in the measuring tube itself. Reproducibility of the work function is established, or inadequate outgassing revealed, by measurement of a series of different surfaces formed in successive vaporizations. For the purposes of the present problem, redistillation of the middle fractions was unnecessary and was omitted.

CONDITIONS FOR SATISFACTORY KELVIN MEASUREMENTS

In the conventional theoretical treatment of the Kelvin method, complete isolation of the metal pair is assumed implicitly. In practice, the pair is part of an array which must include an electrostatic shield and may include other metal or dielectric components. A set of contact potential differences rather than a single potential difference is involved, and no single applied potential can bring the field at the plates to zero. It is customary to minimize the effects of extraneous fields by making the spacing between the measured surfaces and the shield large with respect to the interplate spacing. The sharpness of the balance point, and precision of measurement, is then determined by the dimensions, spacings, and contact potential differences of the components of the array. Unpublished work in this laboratory has shown that with the customary foreign metal shielding sharp and reproducible balance points are obtained consistently only for plate-to-shield spacings which are too large to be practicable in glass systems which have to be intensively outgassed.[3] An alternative procedure which has been developed as particularly suitable for use with the distillation method of surface preparation and which is capable of eliminating extraneous fields entirely, is as follows. (1) The pair of surfaces under measurement is surrounded with a shield which is composed of one or the other of the metals of the pair, and (2) the supports of each plate are coated with the metal of which the plate itself is composed. Since large contact potential differences may exist between surfaces of the same metal if contamination is allowed, it is necessary that the shield and auxiliary coatings be prepared with the same care as are the measured surfaces themselves. This condition is met in the present work by coating the walls and accessory components of the measuring section of the tube with the vapor of high purity, outgassed silver simultaneously with the deposition of the silver surface which is to be measured. The barium electrode and its

[2] Paul A. Anderson, Phys. Rev. **76**, 388 (1949); **75**, 1205 (1949), and earlier reports cited therein.

[3] Similar conclusions have been reached independently by Dr. R. Bourion at Bristol (Doctoral thesis; University of Bristol, 1949, unpublished).

supports are treated similarly in an isolated section of the tube. The sharpness of the Kelvin balance obtainable with this technique appears to be limited only by the sensitivity of the detecting circuit.

TUBE DESIGN AND EXPERIMENTAL PROCEDURE

The tube, Fig. 1, is so designed that one of the two plates which form the substrates for deposition of the measured surfaces can be coated completely with silver while the other can be coated completely with either silver or barium. Two vaporizers are provided for each of the metals and are so disposed that practically complete coverage of the plates, front and back, and a continuous silver film on the walls of the measuring section are secured. This arrangement provides the following contact potential measurements: (1) Ag-Ag by the Kelvin method. This measurement checks the condition that the balance point for plates of the same metal must be sharp at an applied potential of zero if uniformity of average work function has been established by the deposition and if extraneous fields are in fact negligible. (2) Ba-Ag by the Kelvin method for an extensive series of pairs; the surfaces may be renewed simultaneously or independently for determining reproducibility and constancy and minimizing the possibility of accidental error. (3) Ba-Ag by the electron beam method for the same silver and barium surfaces measured in (2).

The outgassing procedure, involving baking of the tube, inductive heating of metal components, and repetitive fusion of the silver and barium charges before and after seal-off, was similar to that described in detail in previous reports.[2] The circuit and procedures for the electron beam measurements have been described.[2] The balance point detector for the Kelvin measurements was an FP-54 electrometer tube in an uncompensated circuit of conventional type with bucking voltage and galvanometer in the plate circuit. The rocking electrode A was connected to the shield and to ground through the low resistance potentiometer circuit which supplied the balancing voltage. The sliding electrode B was connected to the control grid of the FP-54 and to a 10^{10} ohm leak to ground. The extension tube which operated the glass sylphon passed through a slot in the wall of a large shielding cabinet and into an external frame in which the rest position of A and the amplitude of its motion were adjusted with set-screws and spring loading. The plate A could be displaced through a centimeter or more without danger of breakage.

The measuring schedule, started after the tube was sealed from the pumps, was as follows: (1) With plate B near the middle of the tube where it received no vapor, repetitive fusion of the silver and barium charges was continued until fusion produced no evolution of gas as indicated by a change in the anode current of the gun.[2] During this treatment, plate A and the Kelvin section of the tube received a heavy coat of silver while the barium deposit was localized at the other end of the tube. (2) Plate B was moved close to but not overlapping plate A and coated with silver during the simultaneous operation of both silver vaporizers. Plate A simultaneously received a fresh deposit of silver. (3) Plate B was moved into register with A and the Kelvin balance point for Ag-Ag determined by finding the applied potential which eliminated the current pulse produced when A was moved away from B. (4) Plate B was moved over the electron gun and the current-voltage characteristic of the silver surface determined. (5) Steps 2–4 were repeated to establish reproducibility. (6) Plate B was moved between the barium vaporizers and coated. Steps 3–5 were then carried through, with the simultaneous and separate renewal of surfaces mentioned above, to obtain the Ba-Ag contact potentials.

RESULTS

The electron beam measurements, taken by our standardized procedure,[2] gave the value 1.79 ± 0.03 volts for the contact potential difference Ag-Ba. Potential settings for the individual surfaces of silver and barium were constant to ±0.01 volt during aging periods extending from two minutes to an hour or more, in agreement with our earlier observations.[4] The observed contact potential was 0.16 volts lower than our earlier value and makes the work function of the silver films on tantalum equal to 4.31 ± 0.03 ev, as computed for a barium work function of 2.52 ev. Our 1941 measurements were made on mirror-like silver surfaces formed by deposition on glass. The silver films studied in the present work showed the coarsely crystalline (matte) structure characteristic of deposition on outgassed tantalum, and the difference in observed values is probably attributable to this difference in structure. It is interesting to note that Mitchell and Mitchell,[5] using the electron beam method of measurement and well-aged tungsten as a reference, have recently obtained 4.33 ev for the work function of silver films deposited on the tungsten. The difference between our present and earlier values is, of course, not significant for the present comparative measurements. The use of tantalum, however, introduces the possibility of preferential orientation of the deposited metal by the relatively large fibrous crystallites of the substrate and, perhaps, of a more complex surface structure than is obtained in deposition on glass. In our current work, designed to extend the method described here to other metals, glass substrates are being favored over the more convenient tantalum plates.

In the Kelvin measurements the contact potential difference Ag-Ag was zero to ±0.01 v in every case. The first pair of Ag-Ba surfaces to be measured gave the value 1.77 ± 0.01 v, and thereafter all pairs of Ag-Ba

[4] P. A. Anderson, Phys. Rev. **59**, 1034 (1941).
[5] E. W. J. Mitchell and J. W. Mitchell, Proc. Roy. Soc. (London) **A210**, 70 (1951).

films gave the value 1.78±0.01 v. The reproducibility and constancy of this value were such that potentiometer settings of 1.77 and 1.79 v bracketed the balance point in all of the thirty-five measurements taken after renewal of one or both of the surfaces and during aging. From the standpoint of reproducibility and constancy, this series of measurements was the most satisfactory obtained in our contact potential work to date. The stability was such as to suggest the possibility of carrying measurement to the millivolt level if the need for such precision should arise and if other factors can be controlled sufficiently to make a precision of this order significant. It should be emphasized, however, that the Kelvin technique as used in the present work does not provide the short time interval between deposition and measurement of a film which is obtainable with the electron beam method and which is necessary for establishing the fact that contaminants are absent or inoperative. It is possible that determination of a contact potential difference with the greatest practicable reliability should involve an initial study of the contamination factor by a short-interval method and subsequent measurement by the Kelvin method.

DISCUSSION

The measurements described above show that, for the particular conditions obtaining in these experiments, no difference between Kelvin and electron beam values larger than the uncertainty of measurement was detectable. The contact difference of potential between barium (B) and silver (A) given by the Kelvin technique is

$$eV_{BA}=\bar{\phi}_A-\bar{\phi}_B, \tag{1}$$

where each $\bar{\phi}$ is an average work function as defined above. It will be shown in a subsequent paper that if each of two patchy surfaces contains an arbitrary number n of patch types, of which j have work functions greater than $\bar{\phi}$, and if the normal energy assumption is accepted, then the contact difference of potential given by the electron beam method is

$$eV_{BA}'=\phi_A-\phi_B+(f_1\delta\phi_1+f_2\delta\phi_2\cdots+f_j\delta\phi_j)_A \\ -(f_1\delta\phi_1\cdots+f_j\delta\phi_j)_B. \tag{2}$$

Here each of the $\delta\phi$ terms is the work function of the designated patch type less the average work function of the surface concerned. All of the f values (fractions of the surface area occupied by the patch types) are arbitrary in this development.

In terms of Eqs. (1) and (2), our experimental results might be interpreted as indicating either (a) that the bracketed terms of Eq. 2 are individually large enough to be significant but are nearly equal in magnitude, or (b) that these terms are individually so small that their sum is negligible. It is conceivable that condition (a) might be satisfied fortuitously but this explanation is otherwise improbable. In general, (b) deserves careful scrutiny whenever the measured surfaces are formed by vapor condensation under conditions which favor an approach to thermodynamic equilibrium. When the deposition rate is low and the substrate temperature is high enough to allow free migration of the impinging atoms, crystal growth theory[6] predicts that crystal faces of low energy will predominate on the crystallites and that the energy spread between the dominant orientations will be small. The atomic arrangement which determines the surface energy must also determine the double-layer contribution to the work function. Large f values will, then, be associated only with small $\delta\phi$ values and each of the bracketed terms of Eq. (2) will be small. In principle, this trend toward minimization of the bracketed terms will always be operative in vapor deposition but it will, of course, be determinative only under the most favorable conditions. Evidence that barium migrates slowly even at room temperature is accumulating and the reproducibility of its work function may be due, in part at least, to this mechanism. It is unlikely that the silver films prepared in the present work satisfied the near-equilibrium conditions but this question is to be investigated.

The most likely conclusion to be drawn from the results is that Eq. (2) is invalid through failure of the normal energy assumption on which its derivation, like that of patch theory analyses in general, is based. The possibility of substituting for present patch theory a theory based on an electron-optical treatment of the patch field region suggests itself as worthy of investigation. In such a treatment, the tangential components of the patch fields will have little effect on the motion of electrons emitted into a strong accelerating field but will become important when the absorption of slow electrons is involved. Each of the bracketed terms of Eq. (2), as interpreted physically, is the increment in potential which must be applied to the collector to compensate for electron reflection at the high ϕ patches. In the electron-optical treatment, an important fraction of these "lost" electrons will be refracted toward the low ϕ patches and there collected. The application of conventional electron-optical techniques to the study of electron trajectories in patch fields appears to be feasible and is being investigated.

[6] H. E. Buckley, *Crystal Growth* (John Wiley and Sons, Inc., New York, 1951); P. A. Anderson, Phys. Rev. **40**, 596 (1932), and references cited therein.

Convergence of Intermolecular Force Series

GLENN M. ROE
Knolls Atomic Power Laboratory, Schenectady, New York*
(Received July 11, 1952)

The second-order perturbation energy of the hydrogen molecule ion is recalculated without resorting to the mathematical approximations used by Brooks or by Unsöld. The disagreement between the corrected perturbation calculations and the exact results of Hylleraas is presumably due to the neglect of exchange forces in the initial perturbation formula and cannot be removed by Brooks' proposed scheme of arbitrarily limiting the range of integration in the matrix elements.

IN a paper with the above title,[1] Brooks proposes to modify the dipole-dipole and dipole-quadrupole contributions to the van der Waals forces between helium atoms, as calculated by second-order perturbation methods, by arbitrarily limiting the range of integration in the matrix elements to that region of space where the spherical harmonic expansion of the perturbing potential converges. He justifies this procedure by examining the mathematically similar problem of the electronic energy of the hydrogen molecule ion, where comparison can be made with exact calculations. For H_2^+, Unsöld's[2] expression for the second-order perturbation energy is

$$\Delta E_2 = -(9/4)\{(0|V^2|0)-(0|V|0)^2\}, \quad (1)$$

where the ground-state wave function is $e^{-r}/\sqrt{\pi}$, and

$$V=(1/R)\{1-(1+r^2/R^2-2(r/R)\cos\theta)^{-\frac{1}{2}}\}, \quad (2)$$

R being in Bohr radii. Brooks expands (2) in powers of r, neglects the second matrix element in (1), and obtains the asymptotic series

$$\Delta E_2 \cong -9\sum_{n=1}(2n+2)!/2^{2n+3}(2n+1)R^{2n+2}. \quad (3)$$

By using his scheme of limiting the range of integration in (1) to $r<R$, he gets a revised expression

$$\Delta E_{2,B} = -9\sum_{n=1}\int_0^{2R} e^{-x}x^{2n+2}dx/2^{2n+3}(2n+1)R^{2n+2}, \quad (4)$$

which is convergent. Brooks then finds that the first term only of (4) gives better agreement with the known values of ΔE_2 than do the first two terms of (3)!

Actually, (2) can be inserted in (1) and the integrations carried out without resort to expansion in spherical harmonics. The exact result can be written in terms of the exponential-integral functions

$$\Delta E_2 = -(9/8R)\{(2R+1)e^{-2R}\,\overline{\mathrm{Ei}}(2R) + (2R-1)e^{2R}\,\mathrm{Ei}(-2R)-2/R\} - (9/2R)(1+1/R)e^{-2R}+(9/4)(1+1/R)^2e^{-4R}. \quad (5)$$

The sum of the series (4) may be written

$$\Delta E_{2,B} = \Delta E_2 - (9/4)(1+1/R)^2e^{-4R} - (9/8R)\{(4R-2/R)e^{-2R}+(1-2R)e^{2R}\,\mathrm{Ei}(-4R) - (2R+1)e^{-2R}\log 4\gamma R\}. \quad (6)$$

Numerical values for ΔE_2 and $\Delta E_{2,B}$, based on (5) and (6) rather than on an arbitrary choice of terms in (3) and (4), are given in Table I. The second column of the table gives an estimate of ΔE_2 (plus higher order perturbation energies) obtained by subtracting the first-order perturbation ΔE_1 calculated by Pauling,[3] from the exact value of the electronic energy of H_2^+ computed by Hylleraas.[4] The last column gives the values of $(\Delta E_2)_U$ computed by Unsöld,[2] who included only the first two spherical harmonics in the expansion of (2). While $\Delta E_{2,B}$ appears to be a somewhat better approximation than ΔE_2, the agreement with column 2 is still very poor.

TABLE I. Various estimates of the second-order perturbation energy of H_2^+.

R	$H_2^+-\Delta E_1$	ΔE_2	$\Delta E_{2,B}$	$(\Delta E_2)_U$
0.5	−0.314	−1.330	−0.312	−0.925
1.0	−0.164	−0.660	−0.263	−0.371
1.5	−0.087	−0.324	−0.171	−0.164
2.0	−0.049	−0.161	−0.101	−0.080
2.5	−0.029	−0.081	−0.058	−0.042
3.0	−0.018	−0.042	−0.033	−0.023

As pointed out by Pauling,[3] the failure of these second-order perturbation calculations to give agreement with the exact curves of Hylleraas is presumably due to the fact that Unsöld's original expression (1) is based on a hydrogen-like ground-state wave function and therefore neglects the possible effect of exchange forces. It is difficult to see how the artificial limitation of the range of integration, as proposed by Brooks, can correct for the fundamental inadequacy of (1). Thus, the improved agreement with Hylleraas which Brooks gets by his recipe appears to be a coincidence and cannot be used to justify the use of the same procedure for helium.

* Operated by the General Electric Company for the AEC.
[1] F. C. Brooks, Phys. Rev. **86**, 92 (1952).
[2] A. Unsöld, Z. Physik **43**, 563 (1927).
[3] L. Pauling, Chem. Revs. **5**, 173 (1928).
[4] E. A. Hylleraas, Z. Physik **71**, 739 (1931).

Diffusion, De-Excitation, and Ionization Cross Sections for Metastable Atoms. I

MANFRED A. BIONDI
Westinghouse Research Laboratories, East Pittsburgh, Pennsylvania
(Received July 7, 1952)

The lifetimes of metastable atoms in gases are determined from studies of the ionization which they produce in the afterglow following a pulsed discharge. Two distinct types of ionizing reactions are studied, the first in which the collision of a pair of metastable atoms results in ionization of one of them and de-excitation of the other, the second in which a metastable atom of one type loses its excitation energy in ionizing a normal atom of another type. From studies of this ionization as a function of various experimental parameters such as gas pressure, we obtain values of the diffusion, de-excitation, and ionization cross sections of metastable helium and neon atoms. The various measured cross sections agree reasonably well with values obtained from modern optical absorption studies.

THE lifetime of metastable atoms in gases is determined by their diffusion to container walls and by various inelastic collision processes in the gas. Previously, metastable lifetimes have been measured by optical absorption techniques[1,2] and by studies of the current pulse shape in a Townsend discharge,[3] or estimated from studies of the Townsend ionization coefficient at breakdown of a gas.[4] In the present experiment, metastable lifetimes are measured by studies of the ionization which the metastable atoms produce in the afterglow following a pulsed discharge.[5]

I. IONIZING REACTIONS INVOLVING METASTABLE ATOMS

A number of ionizing reactions involving metastable atoms have been suggested; of these two have been studied experimentally. The first reaction, proposed by Schade and Büttner,[6] involves the collision of two metastable atoms, resulting in the ionization of one of them and the de-excitation of the other. For example,

$$\mathrm{He}^*+\mathrm{He}^*\rightarrow\mathrm{He}+\mathrm{He}^++e, \tag{1}$$

where * indicates an atom excited to a metastable state and + indicates an ion. This reaction is energetically possible if the sum of the excitation energies of the metastables is equal to the ionization potential of the atom.[7]

The reaction illustrated by Eq. (1) was proposed in order to explain ionization in excess of that produced by avalanche electrons in the Townsend discharge.[8] Schade and Büttner's measurements in neon revealed a magnitude and a pressure dependence of this excess ionization which fitted the proposed reaction. However, they were unsuccessful in their attempts to demonstrate the metastable origin of this ionization by irradiation experiments;[9] therefore, their explanation was regarded as unsatisfactory. In the present experiment, we have been able to demonstrate the dependence of the observed ionization on the metastable concentration, and our data are consistent with the proposed metastable-metastable ionizing reaction.

A second ionizing reaction involving metastable atoms was studied by Penning's group at Eindhoven.[4] If a metastable atom of type 1 collides with a normal atom of type 2 and

$$V_1^*\geqslant V_2^+, \tag{2}$$

where V_1^* is the metastable excitation potential and V_2^+ is the ionization potential, then the metastable may yield its energy in ionizing the normal atom of type 2. Using neon and argon as an example, we have

$$\mathrm{Ne}^*+\mathrm{A}\rightarrow\mathrm{Ne}+A^++e. \tag{3}$$

Penning's group studied the effect of small admixtures of argon on the breakdown potential of neon. They were able to estimate a cross section for the Ne-A reaction which we shall compare with our results.

II. DIFFUSION AND DE-EXCITATION OF METASTABLE ATOMS

The ionizing processes described in the previous section are often of secondary importance in determining metastable lifetimes. Under many experimental conditions, metastable atoms are lost chiefly by diffusion to the enclosure walls (where they may lose their energy in an inelastic impact with the wall) and by de-exciting collisions with normal gas atoms.[10] The diffusion follows the usual description given in standard texts. The de-excitation collisions are of two types: those resulting in actual transfer of the metastable to a radiating state, and those which perturb the metastable atom suffici-

[1] K. W. Meissner and W. Graffunder, Ann. Physik **84**, 1009 (1927).
[2] J. P. Molnar and A. V. Phelps, Phys. Rev. (to be published).
[3] J. P. Molnar, Phys. Rev. **83**, 933 (1951).
[4] A. A. Kruithof and F. M. Penning, Physica **4**, 430 (1937); A. A. Kruithof and M. J. Druyvestyn, Physica **4**, 450 (1937).
[5] M. A. Biondi, Phys. Rev. **82**, 453 (1951); **83**, 653 (1951).
[6] R. Schade, Z. Physik **105**, 595 (1937); **108**, 353 (1938); H. Büttner, Z. Physik **111**, 750 (1939).
[7] An alternate reaction, in which two metastable atoms collide to produce a molecular ion, is also possible. We found no evidence of such formation of molecular ions in our experiments and hence shall neglect such a process in this paper.
[8] See, for example, M. J. Druyvestyn and F. M. Penning, Revs. Modern Phys. **12**, 87 (1940).
[9] See Sec. V.
[10] A. C. Mitchell and M. W. Zemansky, *Resonance Radiation and Excited Atoms* (Cambridge University Press, Cambridge, 1934), p. 245 ff.

ently to break the optical selection rule (collision-induced radiation).[11] The probability for these de-exciting collisions depends on the energy of the colliding particles and the separation between the metastable level and nearby radiating states of the atom. Quantitative calculations of the cross sections are not possible since detailed information concerning the potential energy curves for these reactions is not available at present.

III. EQUATIONS GOVERNING THE METASTABLE ATOM CONCENTRATION AND THE ELECTRON DENSITY

In the following sections, we shall consider only those processes discussed in Secs. I and II as significant in determining the metastable decay; that is, we shall neglect processes such as inelastic collisions between metastable atoms and electrons. Consequently, the differential equation governing the rate of change of metastable concentration is

$$\partial M/\partial t = D_m \nabla^2 M - \nu_d M - \nu_i M - \alpha_I M^2, \tag{4}$$

where M is the metastable atom concentration, D_m the metastable diffusion coefficient, ν_d the frequency of de-excitation, ν_i the frequency of ionization for reactions of the type illustrated by Eq. (3), and α_I is the ionization frequency per unit metastable concentration for the reaction given by Eq. (1). The de-excitation and ionizing rates are related to the appropriate cross sections σ by

$$\nu_d = n_g \bar{v}_1 \sigma_d, \tag{5}$$

$$\nu_i = n_a \bar{v}_2 \sigma_i, \tag{6}$$

$$\alpha_I = \bar{v}_3 \sigma_I, \tag{7}$$

where n_g is the parent gas concentration, n_a the admixed gas concentration, and the $\bar{v}$'s are the appropriate average velocities of relative motion between the colliding particles. If the last term of Eq. (4) is small compared to the sum of the others, the differential equation is approximately linear in M and may be solved by the usual separation techniques. The fundamental solution of Eq. (4) is

$$M \simeq M_0 \exp(-t/T_m), \tag{8}$$

where M_0 is the initial metastable concentration and contains the spatial dependence,

$$1/T_m = (D_m/\Lambda^2) + \nu_d + \nu_i, \tag{9}$$

and Λ is the characteristic diffusion length of the container.[12]

In low pressure noble gas afterglows, electrons and ions are lost chiefly by ambipolar diffusion to the walls of the container.[13] The production of electrons and ions during the afterglow is the result either of metastable-metastable collisions [Eq. (1)] or of metastable-admixed atom collisions [Eq. (3)]. In order to obtain data which are interpretable in simple fashion, the experiments are arranged so that either the reaction of Eq. (1) or of Eq. (3) dominates. As a result, the electron density during the afterglow obeys one of the two following equations:

$$\partial n/\partial t = D_a \nabla^2 n + \alpha_I M^2, \quad \text{metastable-metastable;} \tag{10a}$$

$$\partial n/\partial t = D_a' \nabla^2 n + \nu_i M, \quad \text{metastable-admixed;} \tag{10b}$$

where n is the electron (or positive ion) density, D_a is the ambipolar diffusion coefficient of the ions produced by metastable-metastable collisions, and D_a' is the ambipolar diffusion coefficient of the ionized admixed atoms.

If we substitute the time dependence for M given by Eq. (8) into Eqs. (10a) and (10b), we find for the lowest mode solutions

$$n = A \exp(-t/T_D) - B \exp(-2/T_m) \tag{11a}$$

and

$$n = A' \exp(-t/T_D') - B' \exp(-t/T_m), \tag{11b}$$

where

$$T_D = \Lambda^2/D_a, \quad B = \alpha_I M_0^2/(2/T_m - 1/T_D),$$

and

$$A = n(t=0) + B; \quad B' = \nu_i M_0/(1/T_m - 1/T_D'),$$

and

$$A' = n(t=0) + B'.$$

Equation (11a) is an approximate solution for the electron density since the spatial distribution of the ionization produced by the metastable-metastable reaction does not correspond exactly to the lowest mode of electron density distribution. However, analysis shows that the higher order terms will affect our measurements of the metastable time constant by less than five percent.[14]

Equations (11a) and (11b) indicate that a study of the build-up and decay of electron density following a pulsed discharge affords a direct measurement of the metastable ionizing rates and yields values of the metastable lifetimes. From studies of the variation of T_m, B, and B' as a function of parent gas density, admixed gas density, and metastable atom concentration, we can determine diffusion coefficients, de-excitation cross sections, ionizing cross sections, and initial metastable atom densities.

Before discussing the experimental measurements, it might be well to dispose of the question of why the metastable ionization, which contributes only a fraction of the total ionization *during* the discharge, results in an initial *increase* in electron density after the ionizing

[11] A third type of de-excitation collision involves formation of an excited molecule at the collision of the metastable atom and two normal atoms (see reference 2). This process was not of importance under the conditions of the present experiment.

[12] For a cylinder of radius R and height H,

$$\Lambda = [(\pi/H)^2 + (2.4/R)^2]^{-\frac{1}{2}}.$$

[13] Ambipolar diffusion, which is the simultaneous diffusion of electrons and ions in the presence of their space charge field, is discussed in M. A. Biondi and S. C. Brown, Phys. Rev. **75**, 1700 (1949).

[14] T. Holstein, private communication.

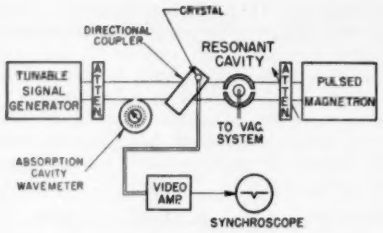

FIG. 1. Simplified block diagram of apparatus.

electric field is removed. During the discharge period, a stationary state is attained in which ionization by electron impact (~90 percent of the total ionization) and by metastable atoms balances the diffusion loss of electrons and ions.[15] During the afterglow, when the primary ionization (electron impact) ceases, the metastable atoms become the only source of ionization. If there were no change in the diffusion loss rate, one would expect the electron density to decrease monotonically during the afterglow. However, the electrons, which had an average energy of ~3 ev during the discharge, quickly lose their initial energy by recoil impacts with normal atoms and come to thermal equilibrium with the gas during the first 100 microseconds of the afterglow. This decrease in energy of the electrons causes a hundredfold decrease in the diffusion loss rate. Since the ionization rate has decreased only by a factor of ten, ionization by metastable atoms initially outweighs diffusion loss, and hence the electron density increases.

The mathematical formulation of this argument is contained in Eqs. (11a) and (11b). If the diffusion frequency, $1/T_D$, during the afterglow remained at the discharge value, then $1/T_D > 2/T_m$ and $1/T_D' > 1/T_m$, respectively. As a result, B and B' would be negative quantities; Eqs. (11a) and (11b) then indicate a monotonic decrease in electron density. Actually, the rapid "cooling" of the electrons by recoil collisions quickly reduces the diffusion rate $1/T_D$ to the point where it is less than the metastable ionization rate with the result that B and B' are positive, and an increase in electron density is indicated.

IV. EXPERIMENTAL METHOD

Microwave techniques are used to study the variation in electron density following a pulsed discharge. A detailed description of the method is given in an earlier paper.[16] The apparatus is shown in a simplified block diagram in Fig. 1. The gas to be studied is contained in a cylindrical quartz bottle (0.88-in. radius, 1.5-in. height) which is surrounded by a cavity resonant at roughly 3000 mc/sec. The gas is ionized by a pulse of power from the magnetron lasting ~300 μsec. Following the magnetron pulse, the variation in the electron density is determined by measuring the changing resonant frequency of the cavity. Under suitable experimental conditions, the change in resonant frequency is linearly proportional to the average electron density; the proportionality constant is calculable if the electric field distribution and the electron density distribution within the cavity are known. In this way, absolute values of the average electron density are obtained from measured frequency shifts.

In order to determine at what time during the afterglow the cavity has a particular resonant frequency, we observe the reflection of a *CW* signal of that frequency by the cavity. At the instant when the cavity's changing resonant frequency is equal to the signal frequency, the cavity absorbs the incident energy with the result that the reflected signal becomes a minimum. The signal's frequency is determined by the absorption cavity wave meter, and its reflection from the cavity is observed with the directional coupler, crystal, and video amplifier. The reflected signal is displayed on a synchroscope with a time-calibrated sweep. By noting the time at which minimum reflection occurs (resonance indication) for a number of different signal frequencies, we determine the resonant frequency of the cavity as a function of time, and from this the electron density during the afterglow.

To assure meaningful results, special care was used with regard to the purity of the gas samples studied. The vacuum system used in gas handling was of glass and metal throughout.[17] Metal valves[18] capable of high temperature bakeout were used for gas metering. The complete system (excluding the pumps) was baked at 420°C for 12 hours or more before each run. The residual pressure attained was $\sim 10^{-9}$ mm Hg, and the rate of rise of pressure in the system when isolated from the pumps and the pumping action of the ion gauge was $\sim 10^{-9}$ mm Hg/min. The gas samples used were either flasks of reagent grade gas from Air Reduction Company[19] or special flasks of very pure helium prepared by superleak techniques.[20]

V. MEASUREMENTS

An example of experimental measurements is given in Fig. 2 for the case of metastable-metastable ionization in low pressure helium and neon afterglows. In order to test the hypothesis that this initial increase in electron density is the result of ionization by metastable atoms, an experiment was performed in which the metastable atom concentration was reduced and the corresponding effect on the electron density noted. It

[15] See Sec. VI.
[16] M. A. Biondi, Rev. Sci. Instr. **22**, 500 (1951).
[17] The vacuum system is of a standard design evolved by the Atomic Physics Group at Westinghouse. The general features of such systems are described in an article by D. Alpert, Rev. Sci. Instr. (to be published).
[18] D. Alpert, Rev. Sci. Instr. **22**, 536 (1951).
[19] In most cases the significant impurities were present to $\lesssim 1:10^6$.
[20] M. A. Biondi, Rev. Sci. Instr. **22**, 535 (1951).

was found that irradiation of the helium afterglow with the 20,580A line (corresponding to the singlet $2P-2S$ transition) diminished the initial rise of electron density. Absorption of this line by a singlet metastable helium atom causes transfer to the $2P$ radiating state which may then return to ground state by emission of the resonance line. In this way, it was shown that reduction of the singlet metastable density resulted in decreased ionization during the afterglow. Irradiation by the 10,830A (triplet $2P-2S$) line, which can be absorbed by the triplet metastable atom, produced no effect on the electron density rise. Since an atom raised to the $2P$ triplet state can only radiate to the $2S$ triplet metastable state, irradiation with this line did not affect the metastable concentration and, hence, could not affect the electron density curves.

The data in Fig. 2 are analyzed in the following manner: The final slope of the measured density curve, n, is extrapolated back to early times. The difference between this extrapolated curve and the measured curve corresponds to the second term of Eq. (11a). This difference curve is shown plotted as Δn in Fig. 2. The slope of this curve is equal to $T_m/2$. Measurements of T_m were made in pure helium and in pure neon as a function of gas density. According to Eq. (9), in the absence of an ionizable admixed atom the decay constant, $1/T_m$, depends upon a diffusion term which is inversely proportional to the gas pressure and a de-excitation term which is linearly proportional to pressure. If Eq. (9) is multiplied by pressure, the first term on the right becomes constant and the second term proportional to pressure squared, that is,

$$p/T_m = \frac{D_m p}{\Lambda^2} + Cp^2. \tag{12}$$

Plots of p/T_m *vs* p^2 for helium and for neon are shown in Fig. 3.[21] From the intercept we calculate the metastable diffusion coefficient, while the slope yields the de-excitation rate. The results of these measurements are summarized in the first two columns of Table I.

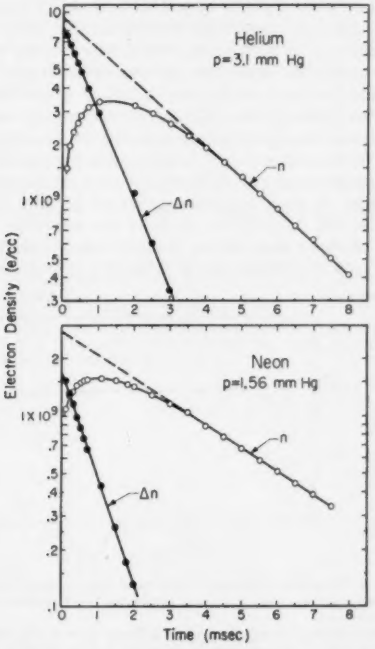

FIG. 2. Measured electron density, n, and derived difference density, Δn, in helium and neon afterglows.

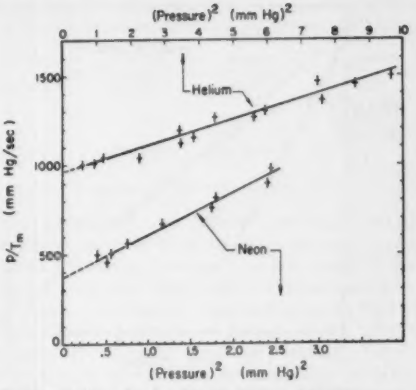

FIG. 3. Variation of metastable decay rate with gas pressure.

In order to study the ionization of admixed atoms, small amounts of argon were added to helium and to neon, and in a third experiment mercury was added to helium. In these experiments, conditions were arranged so that the ionization of admixed atoms greatly outweighed ionization by metastable-metastable collisions. For this case Eq. (10b) describes the production and loss of electrons, and hence the electron density follows the law given in Eq. (11b). In the He-A and Ne-A experiments, 0.115 percent A was added to helium and to neon. The He-A studies were carried out over the range 1.6 to 3.2 mm Hg of helium; the Ne-A studies between 1.4 and 4.7 mm Hg of neon.

In the He-Hg experiments 1.8 mm of helium were added to a sealed-off bottle containing a drop of mercury. The vapor pressure of the mercury was then controlled by varying the temperature of a cold tip on

[21] The maximum gas pressure used in these studies is limited by the increasing importance of conversion of the atomic ions to molecular ions which then recombine with electrons. In a region in which recombination loss is comparable to diffusion loss, Eqs. (10) and (11) no longer apply and analysis of the problem becomes extremely difficult.

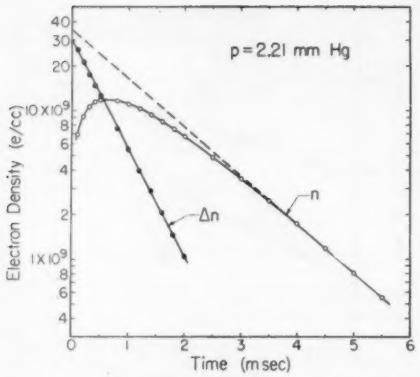

FIG. 4. Measured electron density, n, and derived difference density, Δn, in the afterglow of helium+0.115 percent argon.

the bottle. The He-Hg studies involved variation of the Hg vapor pressure from 2×10^{-7} to 1×10^{-5} mm Hg.

Typical data obtained in studies of ionization of argon atoms by helium metastable atoms are shown in Fig. 4. Here the difference curve, Δn, corresponds to the second term of Eq. (11b) so that its slope gives us T_m. Measurements of T_m permit us to calculate ν_i from Eq. (9) since the other two terms, D_m/Λ^2 and ν_d, were determined in the studies on pure helium. We calculate the cross section for ionization of argon atoms, σ_i, from our values of ν_i by use of Eq. (6). The results of the measurements are shown in Fig. 5. Similar results were obtained for the Ne-A and He-Hg experiments.

VI. RESULTS

The results of various measurements are summarized in Table I. The cross sections σ_d and σ_i are believed to be accurate to ±10 percent, except for σ_i of mercury which involves an uncertainty of ±20 percent. In addition to these coefficients and cross sections, we are able to determine initial metastable concentrations from the intercepts of the difference density curves. According to Eqs. (11a) and (11b), the intercepts give values of B and B', respectively, which in turn involve the initial metastable concentrations, M_0. We have calculated values of M_0 for two typical runs. For the case of metastable-metastable ionization in pure helium, we find an initial concentration of 5×10^{10} metastables/cc at 2.5 mm Hg.[22] For the case of ionization of argon by helium, we find an initial density of 2.5×10^{10} metastables/cc at 2.2 mm Hg pressure. These values permit us to estimate the fraction of ionization during the microwave discharge which is supplied by metastable ionization reactions.

During the discharge, a stationary state is attained in which the production of electrons and ions is balanced by their diffusion loss to the walls. The diffusion rate is simply $\nu_D n$, where $\nu_D=1/T_D$ is the diffusion rate per electron[23] and n is the electron density during the discharge. This loss rate is equal to the total production rate. The production during the discharge due to metastable atoms is either $\alpha_I M_0^2$ or $\nu_i M_0$, depending on which ionizing reaction is dominant. The ratios $\alpha_I M_0^2/\nu_D n$ and $\nu_i M_0/\nu_D n$ then yield the fraction of ionization due to metastables for the two types of reaction.

It is found that during the discharge in pure helium ~10 percent of the ionization is contributed by metastable-metastable collisions while in helium containing 0.1 percent argon ~25 percent of the ionization is the result of metastable atoms. These appreciable percentages emphasize the importance of this indirect ionization. Since conditions in the microwave discharge are very similar to those found in the positive column of dc or low frequency ac discharges, it is clear that proper account should be taken of metastable ionization in calculations on these types of discharges.

We have compared our measured diffusion, de-excitation, and ionization cross sections, as summarized in Table I, with measurements made by Molnar and Phelps[2] using modern optical absorption techniques. The diffusion coefficients for metastable atoms in helium and in neon agree within experimental error with the optical absorption measurements. Molnar and Phelps find no de-excitation for helium which follows the law given in Eq. (12), in contrast to our results. It should be noted that their measurements apply to the triplet metastable of helium, while our irradiation experiments (see Sec. V) indicate that we are measuring, at least in part, ionization produced by the singlet metastable. In order to eliminate the possibility that our observed de-excitation resulted from a small impurity in the helium, special flasks of very pure helium

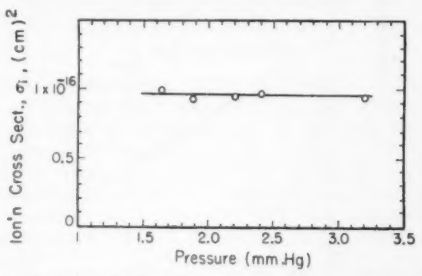

FIG. 5. Cross section for the ionization of argon atoms by helium metastables measured in helium containing 0.115 percent argon.

[22] For this estimate the value of the metastable-metastable ionizing cross section in helium was taken as 10^{-14} cm². The author is indebted to A. V. Phelps for making available this preliminary value from absorption experiments.

[23] Calculation of the ambipolar diffusion rate during the discharge follows the procedure given in A. von Engel and M. Steenbeck, *Elektrische Gasentladungen* (J. Springer, Berlin, 1932), Vol. 1, p. 183 ff.

were prepared using superleak techniques.[20] This helium was conservatively estimated to contain less than one part in 10^9 of impurity. The results given in Figs. 2 and 3 are for this special helium. From these measurements, we conclude that the de-excitation collisions were not the result of impurities.

De-excitation of a helium singlet metastable atom will result if it is sufficiently perturbed on collision with a normal atom to cause radiation to the ground state. A qualitative estimate for the probability of this process[24] indicates that it could account for our observed de-excitation rate. Quantitative calculations are not possible since they require detailed knowledge of the potential energy curves of the various excited states during the collision.

The de-excitation cross section for neon is in order of magnitude agreement with the optical absorption results. Here the de-excitation of the metastables is thought to involve the actual transfer of the metastable to a nearby radiating state on collision with normal atoms. In the absence of any quantitative theory for the probability of this process,[10] we can only conclude that our measured cross section is reasonable in magnitude.

The cross sections for ionization of argon by helium and neon metastables are in reasonable agreement with the results of Molnar and Phelps. The Ne-A result modifies the previous value obtained by Penning's group at Eindhoven.[4] Our value for the ionizing cross section is an order of magnitude smaller than their value. In view of the greater certainty of the present method and of the modern optical absorption studies,[2] we feel that the Eindhoven value is in error.[25]

The cross section for ionization of mercury by helium metastables is two orders of magnitude larger than for argon. MacDonald and Brown[26] have computed the breakdown potential of helium gas containing a small amount of mercury. An underlying assumption of their theory is that each helium atom which is excited to a metastable state ionizes a mercury atom, so that the first excitation potential of helium is the effective ionization potential for the He-Hg mixture. For this assumption to be valid, it is necessary that the He-Hg ionizing cross section be rather large. Our measured value of 10^{-14} cm^2 may be sufficiently large to justify their assumption.

TABLE I. Measured values for helium and neon metastable atoms.

Parent gas	$D_m p$(cm^2/sec) $-$(mm Hg)	σ_d(cm^2)	σ_i(cm^2)
Helium	520±20	9.6×10^{-21}	Argon 9.7×10^{-17} Mercury 1.4×10^{-14}
Neon	200±20	8.9×10^{-20}	Argon 2.6×10^{-16}

VII. DISCUSSION

The present measurements of ionization occurring in the afterglow of a microwave discharge confirm the hypothesis of Schade and Büttner[6] that collisions between pairs of metastable atoms produce significant ionization. The measurements on gas mixtures have extended the work of Penning's group[4] and have yielded more precise measurements of the ionizing cross sections. In addition, these studies have yielded values of the metastable diffusion and de-excitation cross sections which agree reasonably well with the results of modern absorption studies, indicating the value of microwave afterglow studies for measuring metastable lifetimes.

The author wishes to thank the members of the Atomic Physics group at Westinghouse for interesting discussions of this work. The author is particularly indebted to T. Holstein, who pointed out the metastable-metastable hypothesis and its consequences and contributed many valuable suggestions.

[24] One estimates the time of collision during which the metastable 2^1S_0 state is sufficiently perturbed by the colliding atom to cause a strong admixture of 2^1P_1 state. The ratio of this time to the natural radiative lifetime of the 2^1P_1 state gives the probability of de-excitation by collision-induced radiation.

[25] G. Schut and J. A. Smit, Physica **10**, 440 (1943), obtain a preliminary value, $\sigma_i = 6.7\times10^{-15}$ cm^2 for Ne-A, in order of magnitude agreement with our value.

[26] A. D. MacDonald and S. C. Brown, Phys. Rev. **75**, 411 (1949).

Atomic Masses from Palladium through Xenon*

RICHARD E. HALSTED†
Department of Physics, University of Minnesota, Minneapolis, Minnesota
(Received July 22, 1952)

The atomic masses of 42 stable nuclides in the region from palladium through xenon have been measured with a double focusing mass spectrometer. Combined with nuclear reaction mass differences the data provide a table of 74 mass values between mass numbers 102 and 136. A fit of the Wigner semi-empirical mass formula to these values reveals an irregularity at the magic number of 50 protons similar in nature to those previously reported from this laboratory at 20 and 28 protons. Also evident is an inability of the formula to account for the binding energy variations between isobaric nuclei. An empirical modification of the formula is observed to correct largely for this latter effect.

THIS paper presents the results of a portion of an extensive program of mass measurement undertaken with the double focusing mass spectrometer developed at the University of Minnesota. Atomic masses for 47 nuclides have been previously reported.[1–3] 42 additional atomic mass values of stable isotopes containing approximately 50 protons are given here. The treatment of data in the most recent report[1] has been paralleled to facilitate a consideration of all data from this laboratory. A brief description of the apparatus and measurement procedure has been previously given.[2,3]

EXPERIMENTAL RESULTS

Table I summarizes the mass doublets measured and the mass differences obtained. The atomic masses derived from these data for the heavy nuclide of each doublet are also presented in the last column of Table I in the form of mass defects (atomic mass minus mass number). It is possible to obtain mass values for many of these isotopes by combining previously reported nuclear reaction and mass spectrographic measurements. Due to the uncertainty of the source of possible error in values from combined data, only mass defects previously determined in terms of the mass standards O^{16}, H^1, and C^{12} by the work of any single laboratory are given for comparison purposes. In the computation of these mass defects, the masses of H^1 and C^{12} determined in this laboratory have been arbitrarily employed except in the case of the time-of-flight measurements. There the method of adjusting the reported results for comparison purposes was not obvious and was believed of no concern in view of the magnitude of the errors quoted.

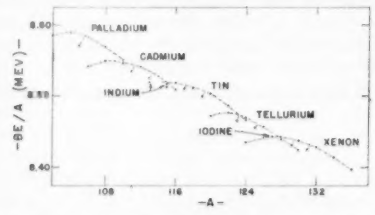

FIG. 1. Mass spectrometric values for average binding energy per nucleon.

Much of this work was done concurrently with that last reported.[1] As in the previous work, a "run" consists of 10 or more consecutive tracings of the mass doublet. Different runs were in most cases scattered over a period of several months. Recorded hydrocarbon ion currents have been corrected for the inherent presence of an unresolved component containing a C^{13} atom instead of one C^{12} and one H^1 atom. An upper limit was placed on the possibility of a systematic error proportional to mass by measuring with every day's set of data a known mass difference, i.e., the difference between two hydrocarbon fragments differing in mass by one hydrogen atom. Seventy-one such measurements over a period of nine months gave an average value of 1.0078. The deviation of this value from the assumed correct value of 1.008146 is approximately 1/3000. No correlation was observed, however, between such hydrogen mass measurements and the deviations of associated mass doublets from their average values. Therefore, no correction was made to the data for this error. The errors quoted for the doublets in Table I are a combination of the statistical probable error and a possible error of 1/3000.

In Table II, mass differences from the results of this paper are compared with mass differences determined from the energy balance of nuclear reactions. The agreement is considered good in most cases. Further evidence of data consistency can be seen in the plot of average binding energy per nucleon presented in Fig. 1. Probable errors are of the size of the plotted points. Connecting lines have been drawn for the isotopes of even Z elements to aid in identification and emphasize regularity. The systematic pattern evident in this figure encourages confidence in the reliability of these results.

* This paper summarizes a Ph.D. thesis accepted by the Graduate School of the University of Minnesota. The research was supported by joint programs of the ONR and AEC. Some preliminary results were reported at the Chicago Meeting (October, 1951) of the American Physical Society.

† Present address: General Electric Research Laboratory, Schenectady, New York.

[1] Collins, Nier, and Johnson, Phys. Rev. **86**, 408 (1952).
[2] Collins, Nier, and Johnson, Phys. Rev. **84**, 717 (1951).
[3] A. Nier and T. Roberts, Phys. Rev. **81**, 507, 624 (1951).

TABLE I. Experimental mass doublets and derived[a] atomic masses expressed as mass defects ($M-A$).

Doublet	No. of runs	ΔM (10^{-4} aMU)	Mass defect of heavy nuclide (10^{-4} aMU, all negative)
1. $C_4H_8 - \frac{1}{2}Pd^{108}$	4	710.6±0.4	625.0±0.9
2. $C_4H_4 - \frac{1}{2}Pd^{104}$	5	796.8±0.5	634.5±1.1
			636.3±4.2[b]
3. $C_8H_9 - Pd^{105}$	4	1656.5±1.4	616.0±1.5
4. $C_7H_5 - \frac{1}{2}Pd^{105}$	4	878.3±0.9	634.7±1.8
5. $C_8H_{12} - Pd^{104}$	4	1751.1±1.8	629.1±1.8
Weighted average of 4 and 5			632.0±1.9
6. $C_4H_6 - \frac{1}{2}Pd^{106}$	4	952.4±0.5	619.9±1.1
			631.0±3.3[b]
7. $C_4H_7 - \frac{1}{2}Pd^{110}$	4	1025.6±0.6	603.5±1.3
8. $C_4H_8 - \frac{1}{2}Cd^{106}$	5	861.8±0.7	601.6±1.4
9. $C_4H_6 - \frac{1}{2}Cd^{106}$	5	949.4±0.5	614.0±1.1
10. $C_4H_7 - \frac{1}{2}Cd^{110}$	5	1031.0±0.6	614.3±1.3
11. $C_9H_{15} - Cd^{111}$	5	2131.5±0.8	602.2±1.0
12. $C_4H_8 - \frac{1}{2}Cd^{112}$	5	1109.8±0.5	608.9±1.2
13. $C_8H_{16} - Cd^{112}$	4	2224.3±0.9	613.6±1.0
Weighted average of 12 and 13			611.5±1.7
			601.4±4.0[c]
14. $C_9H_{17} - Cd^{113}$	5	2286.1±0.9	593.9±1.1
15. $C_4H_9 - \frac{1}{2}Cd^{114}$	4	1186.6±0.7	599.5±1.5
16. $C_3H_5O - \frac{1}{2}Cd^{114}$	4	823.0±0.6	600.9±1.2
Weighted average of 15 and 16			600.3±0.9
17. $C_3H_6O - \frac{1}{2}Cd^{116}$	4	893.9±0.6	579.8±1.2
			578.5±4.2[c]
18. $C_9H_{17} - In^{113}$	5	2287.7±1.0	595.5±1.2
19. $C_9H_7 - In^{115}$	5	1512.0±1.0	596.0±1.1
20. $C_9H_7 - Sn^{115}$	5	1514.6±2.5	598.6±2.5
21. $C_3H_6O - \frac{1}{2}Sn^{116}$	4	907.8±0.9	607.5±1.8
22. $C_8H_8 - Sn^{116}$	3	1604.7±1.4	607.2±1.5
Weighted average of 21 and 22			607.3±1.1
			620.5±5.2[d]
23. $C_9H_9 - Sn^{117}$	5	1673.7±0.9	594.8±1.0
24. $C_3H_7O - \frac{1}{2}Sn^{118}$	4	986.3±1.3	601.6±2.6
25. $C_9H_{10} - Sn^{118}$	4	1762.9±1.9	602.5±1.9
Weighted average of 24 and 25			602.2±1.6
26. $C_9H_{11} - Sn^{119}$	6	1829.7±1.1	587.8±1.2
27. C_3 $- \frac{1}{2}Sn^{120}$	4	489.2±0.7	594.1±1.4
			612.5±4.2[d]
28. C_8H $- \frac{1}{2}Sn^{122}$	4	561.1±0.7	575.1±1.5
29. $C_8H_2 - \frac{1}{2}Sn^{124}$	5	630.5±0.5	551.0±1.1
30. $C_9H_{12} - Te^{120}$	4	1894.5±1.5	571.2±1.6
31. C_3H $- \frac{1}{2}Te^{120}$	5	563.9±0.4	580.7±0.8
32. $\frac{1}{2}Te^{120} - C_3H$	4	4444.9±2.0	563.2±3.9
33. $C_8H_2 - \frac{1}{2}Te^{124}$	6	641.1±0.5	572.2±1.1
34. $\frac{1}{2}Te^{120} - C_3H_2$	4	4368.0±1.6	554.0±3.1
35. $C_3H_3 - \frac{1}{2}Te^{126}$	6	715.6±0.3	558.0±0.7
36. $C_{16}H_8 - Te^{126}$	4	1570.9±1.2	535.1±1.3
37. $C_3H_5 - \frac{1}{2}Te^{128}$	6	856.7±0.4	514.7±1.0
			532 ±8[e]
38. $C_{10}H_7 - I^{127}$	6	1501.6±1.2	547.2± 1.3
			540 ±10[f]
39. $C_3H_2 - \frac{1}{2}Xe^{124}$	4	626.1±0.3	542.2± 0.7
40. $C_3H_3 - \frac{1}{2}Xe^{126}$	5	712.7±0.7	552.4± 1.4
41. $C_{16}H_8 - Xe^{126}$	5	1591.3±0.7	555.4± 0.9
42. $C_3H_7 - \frac{1}{2}Xe^{128}$	5	865.4±0.4	539.9± 1.5
			544 ±13[g]
			543.0± 2.6[h]
			545 ±15[f]
43. $C_3H_3 - \frac{1}{2}Xe^{130}$	7	874.3±0.4	549.9± 1.0
			550 ±20[f]
44. $CO_2 - \frac{1}{2}Xe^{131}$	5	3549.3±1.4	532.7± 4.2
			560 ±20[f]
45. $C_3H_4 - \frac{1}{2}Xe^{132}$	5	950.0±0.6	538.2± 1.3
46. $CO_2 - \frac{1}{2}Xe^{132}$	7	218.0±0.5	538.8± 1.4
Weighted average of 45 and 46			538.5± 1.0
			526.0± 6.5[h]
			550 ±20[f]
47. $C_3H_7 - \frac{1}{2}Xe^{134}$	6	1022.2±0.5	519.7± 1.2
			530 ±20[f]
48. $C_3H_8 - \frac{1}{2}Xe^{136}$	5	1091.5±0.4	495.4± 1.1

[a] Derived mass defects assume $H^1 = 1.008146$, $C^{12} = 12.003842$.
[b] Duckworth, Woodcock, and Preston, Phys. Rev. **78**, 479 (1950).
[c] H. Duckworth and R. Preston, Phys. Rev. **79**, 402 (1950).
[d] H. Duckworth (private communication, October, 1951).
[e] Duckworth, Kegley, Olson, and Stanford, Phys. Rev. **83**, 1114 (1951).
[f] Hays, Richards, and Goudsmit, Phys. Rev. **84**, 824 (1951); **85**, 1065 (1952).
[g] F. W. Aston, *Mass Spectra and Isotopes* (Edward Arnold and Company, London, 1942).
[h] C. Kegley and H. Duckworth, Nature **167**, 1025 (1951).

It is also of interest to note that the isotopes of tin have a greater average binding energy per nucleon than might have been expected by extrapolation from the other data of the figure.

There are several cases where the mass difference between naturally occurring isobars is of particular interest. Cd^{113} and In^{113}, In^{115} and Sn^{115}, and Sb^{123} and Te^{123} are three of the few known examples of adjacent "stable" isobars. In^{115} has been recently reported to emit natural β-radiation of 0.63±0.03 Mev energy with a half-life of $6\pm2\times10^{14}$ yr.[4] The same experimenters detected no radiations from the pair at mass 113 but established minimum half-lives ranging from 1×10^{13} to 2×10^{15} yr for several possible modes of decay. The mass spectrometric results of $In^{115}-Sn^{115}=0.24\pm0.25$ Mev and $Cd^{113}-In^{113}=0.15\pm0.15$ Mev agree that In^{115} is heavier than Sn^{115} and that more energy is available for decay at 115 than at 113. They suggest that Cd^{113} is the possible radioactive member of the $Cd^{113}-In^{113}$ pair. Combined with reaction data, the results reported here indicate that Te^{123} is the possible radioactive member of the pair at $A=123$.

The possibility of double β-decay of the isotopes Sn^{124}, Te^{123}, Te^{130}, Pd^{108}, and Pd^{110} has also received experimental attention in the literature.[5–8] The conclusions of these experiments are not significantly altered by the specific values for the transition energies determined from the masses of this paper. In the one case where a mass spectrographic value for the available transition energy has been previously reported,[9] the value of 1.5±0.4 Mev obtained for the $Sn^{124}-Te^{124}$ energy difference compares favorably with the 1.97 ±0.13 Mev result of this paper.

[4] E. Martell and W. Libby, Phys. Rev. **80**, 977 (1950).
[5] M. Kalkstein and W. Libby, Phys. Rev. **85**, 368 (1952).
[6] M. Inghram and J. Reynolds, Phys. Rev. **76**, 1265 (1949).
[7] R. G. Winter, Phys. Rev. **85**, 687 (1952).
[8] E. Fireman and D. Schwarzer, Phys. Rev. **86**, 451 (1952).
[9] B. Hogg and H. Duckworth, Phys. Rev. **86**, 567 (1952).

TABLE II. Comparison of mass spectrometric and nuclear reaction mass differences.

	From Table I	From nuclear reactions	Reactions used	Ref.
$Xe^{128}-I^{127}$	1-0.00083 ±16	1-0.00070 ±44	$I^{128}(\beta)Xe^{128}$	a
			$I^{127}(n,\gamma)I^{128}$	b
$Te^{128}-I^{127}$	1.00121 ±18	1.00061	$Te^{128}(n,2n)Te^{127}$	c
			$Te^{127}(\beta)I^{127}$	d
$I^{127}-Xe^{126}$	1.00052 ±19	1.00029 ±15	$I^{127}(\gamma,n)I^{126}$	e,f
			$I^{126}(\beta)Xe^{126}$	a
$Te^{125}-Te^{124}$	1.00183 ±33	1.00169 ±32	$Te^{125}(\gamma,n)Te^{124}$	g
$Te^{122}-Sn^{120}$	2.00134 ±16	2.00167 ±40	$Sb^{122}(\beta)Te^{122}$	a
			$Sb^{121}(d,p)Sb^{122}$	h
		[2.00126] r	$[Sb^{121}(n,\gamma)Sb^{122}]$	i
			$Sn^{121}(\beta)Sb^{121}$	j
			$Sn^{120}(d,p)Sn^{121}$	h
$Sn^{119}-Sn^{118}$	1.00143 ±20	1.00199 ±16	$Sn^{119}(\gamma,n)Sn^{118}$	k
$Sn^{118}-Sn^{117}$	1-0.00074 ±18	1-0.00107 ±22	$Sn^{117}(d,p)Sn^{118}$	h
		[0.00103] r	$[Sn^{117}(n,\gamma)Sn^{118}]$	i
$Sn^{116}-In^{115}$	1-0.00113 ±16	1-0.00126 ±25	$In^{115}(\beta)Sn^{115}$	j
			$In^{115}(d,p)In^{116}$	h
$In^{115}-Sn^{115}$	0.00026 ±27	0.00068 ±3	$In^{115}(\beta)Sn^{115}$	m
		[0.00053 ±2] r	$[In^{115m}(\beta\gamma)Sn^{115}]$	n
$Cd^{114}-Cd^{113}$	1-0.00064 ±14	1-0.00035 ±65	$Cd^{113}(n,\gamma)Cd^{114}$	o
		[1.00147 ±22] r	$[Cd^{113}(n,\gamma)Cd^{114}]$	b
$Cd^{112}-Cd^{111}$	1.00176 ±20	1.00207 ±16	$Cd^{112}(\gamma,n)Cd^{111}$	k
$Cd^{110}-Cd^{108}$	2-0.00003 ±16	2-0.00048 ±94	$Ag^{110}(\beta)Cd^{110}$	a
			$Ag^{109}(n,\gamma)Ag^{110}$	b
			$Ag^{109}(\gamma,n)Ag^{108}$	p
			$Ag^{108}(\beta)Cd^{108}$	q
$Pd^{105}-Pd^{104}$	1.00185 ±19	1.00126 ±32	$Pd^{105}(\gamma,n)Pd^{104}$	g

[a] A. C. G. Mitchell, Revs. Modern Phys. **22**, 36 (1950).
[b] H. Kubitshek and S. Dancoff, Phys. Rev. **76**, 531 (1949).
[c] H. Wäffler, Helv. Phys. Acta **23**, 239 (1950).
[d] *Nuclear Data*, National Bureau of Standards Circular 499 (1950).
[e] McElhinney, Hanson, Becker, Duffield, and Diven, Phys. Rev. **75**, 542 (1949).
[f] Ogle, Brown, and Carson, Phys. Rev. **78**, 63 (1950).
[g] Sher, Halpern, and Stephens, Phys. Rev. **81**, 154 (1951).
[h] J. A. Harvey, Phys. Rev. **81**, 353 (1951).
[i] B. Kinsey, cited by Harvey, reference h.
[j] C. M. Nelson *et al.*, Oak Ridge National Laboratory Report (ORNL 828) (cited in reference d, Supplement No. 2).
[k] Hanson, Duffield, Knight, Diven, and Pavlevski, Phys. Rev. **76**, 578 (1949).
[l] E. Bleuler and W. Zunti, Helv. Phys. Acta **19**, 375 (1945).
[m] E. Martell and W. Libby, Phys. Rev. **80**, 977 (1950).
[n] Bell, Ketelle, and Cassidy, Phys. Rev. **76**, 574 (1949).
[o] C. D. Moak and J. W. T. Dabbs, Phys. Rev. **75**, 1776 (1949).
[p] G. C. Baldwin and H. W. Koch, Phys. Rev. **67**, 1 (1945).
[q] M. Goodrich and E. Campbell, Phys. Rev. **85**, 742 (1951).
[r] Mass difference obtained using bracketed alternative reaction.

COMPARISON WITH THE WIGNER FORMULA

Comparisons of experimentally determined masses with those predicted by existing semi-empirical mass formulas can reveal inadequacies in the hypotheses upon which the formulas are based. Of particular interest is the possibility of finding irregularities associated with nuclear shell structure. The Bohr-Wheeler and Wigner mass formulas have both been used in investigations of this nature.[1,2,10,11] In the interest of correlating results in this mass region with those at lower masses previously reported from this laboratory, the Wigner formula will be considered in the following development.

Wigner[12] has derived expressions for the Coulomb energy (CE), kinetic energy (KE), and potential energy (PE) components of the binding energy of a nucleus. With the insertion of a nuclear radius constant of 1.45×10^{-13} cm derived from mirror nuclei, these quantities become

$$\mathrm{CE}=0.635Z(Z-1)/A^{\frac{1}{3}}\ \text{milli-mass units}, \quad (1)$$

$$\mathrm{KE}=14.640A+32.53(T^2+\delta/2)/A\ \text{mMU}, \quad (2)$$

$$\mathrm{PE}=-\tfrac{1}{2}A(A-1)L'-\Xi L\ \text{mMU}. \quad (3)$$

For a given nucleus of mass number A, Z=number of protons, N=number of neutrons, $T=(N-Z)/2$="isotopic spin," and

$$\delta=\begin{cases}0 \text{ for even } N, \text{ even } Z;\\ 1 \text{ for odd } N, \text{ even } Z;\\ 1 \text{ for even } N, \text{ odd } Z;\\ 2 \text{ for odd } N, \text{ odd } Z.\end{cases}$$

L' is the average potential energy per pair of nucleons from forces independent of coupling symmetry. The magnitude of L is the average potential energy per pair of nucleons from forces dependent on symmetry of coupling. The sign of L changes with symmetry, so the contribution of these forces to the total potential energy is L times the difference, Ξ, in number of symmetrically and antisymmetrically coupled pairs of particles. In the mass region of interest here, Ξ is a negative number and can be computed from the formula

$$\Xi=2A-A^2/8-T(T+4)/2-3\delta/4. \quad (4)$$

The total binding energy of a nucleus is given by

$$\mathrm{BE}=\mathrm{CE}+\mathrm{KE}+\mathrm{PE}, \quad (5)$$

where BE and PE are both negative quantities.

The binding energy is determined experimentally by a knowledge of the atomic mass M,

$$\mathrm{BE}=M-(ZM_{\mathrm{H}}+NM_n), \quad (6)$$

where M_{H} is the mass of the hydrogen atom and M_n is the mass of the neutron. The present status of the

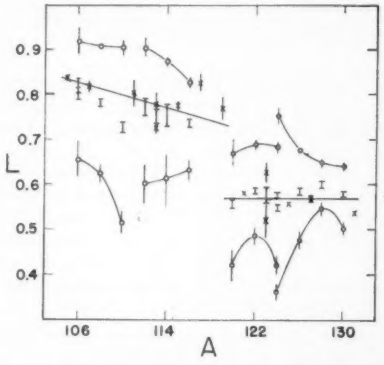

FIG. 2. L-values from unmodified Wigner formula. Lines have been drawn to emphasize pattern in the data. The isobaric pairs entering into given L-value determinations are classified by the symbols: O = adjacent even A isobars; × = adjacent odd A isobars; I = isobars differing by $Z=2$. For the points on the curves above the straight lines, the odd-odd nucleus has one less proton than the even-even nucleus. For points on the curves below the straight lines, the odd-odd nucleus has one more proton than the even-even nucleus.

[10] C. Townes and W. Low, Phys. Rev. **80**, 608 (1950).
[11] A. H. Wapstra, Phys. Rev. **84**, 837, 838 (1951).
[12] E. Wigner, *University of Pennsylvania Bicentennial Conference* (University of Pennsylvania Press, Philadelphia, 1941). Also see G. Gamow and C. L. Critchfield, *Atomic Nucleus and Nuclear Energy Sources* (Oxford Press, London, 1949).

TABLE III. Data used in comparing experimental mass values with Wigner formula.

Nuclide	Reaction	Mev	−Mass defect (mMU)	−PE (mMU)	−Ξ
Pd^{102}			62.5±0.1	2723.1	1119
Pd^{104}			63.4±0.1	2772.7	1174
Rh^{105}	β^-	0.570[a]	61.0±0.2	2788.1	1212
Pd^{105}			61.6±0.2	2795.6	1203
Rh^{106}	β^-	3.55[b]	59.4±0.3	2811.6	1242
Pd^{106}			63.2±0.2	2821.8	1231
Ag^{106}	(p,n)	−3.8[c]	60.0±0.2	2826.3	1224
Cd^{106}			60.2±0.1	2834.6	1215
Ag^{107}	(d,p)	4.78[d]	61.3±0.2	2852.0	1252
Cd^{107}	β^+	0.32[e]	59.7±0.2	2858.6	1244
Pd^{108}			62.0±0.1	2870.3	1290
Ag^{109}	β^-	1.49[f]	59.8±0.1	2875.3	1282
Cd^{108}			61.4±0.1	2884.4	1272
Ag^{109}	(γ,n)	9.3[g]	60.6±0.5	2900.7	1311
Pd^{110}			60.4±0.1	2918.9	1351
Ag^{110}	β^-	2.86[b]	58.4±0.2	2923.6	1342
Cd^{110}			61.4±0.1	2933.5	1331
Ag^{111}	β^-	1.06[h]	59.1±0.1	2949.1	1372
Cd^{111}			60.2±0.1	2957.2	1362
Cd^{112}			61.2±0.2	2982.8	1392
In^{112}	β^+	1.7[i]	58.2±0.4	2987.6	1384
Sn^{112}	β^-	1.0[i]	59.3±0.5	2996.7	1374
Ag^{112}	β^-	2.1[j]	57.1±0.2	2997.6	1435
Cd^{112}			59.4±0.1	3006.1	1424
In^{113}			59.6±0.1	3013.4	1414
Cd^{114}			60.0±0.1	3031.7	1455
In^{114}	(γ,n)	−9.5[d]	58.4±0.6	3037.2	1446
Sn^{114}	β^-	2.05[k]	60.6±0.6	3046.8	1435
Cd^{115}	β^-	1.80[l]	57.7±0.2	3054.7	1488
In^{115}			59.6±0.1	3063.2	1477
Sn^{115}			59.9±0.2	3070.9	1467
Cd^{116}			58.0±0.1	3080.1	1520
In^{116}	β^-	2.95[m]	57.7±0.2	3086.4	1510
Sn^{116}			60.7±0.1	3096.4	1498
In^{117}	β^-	1.73[n]	57.6±0.1	3111.4	1542
Sn^{117}			59.5±0.1	3120.5	1531
Sn^{118}			60.2±0.2	3145.7	1563
In^{119}	β^-	2.7[o]	55.9±0.3	3160.2	1609
Sn^{119}			58.8±0.1	3169.4	1597
Sn^{120}			59.4±0.1	3195.1	1630
Sb^{120}	(γ,n)	−9.25[p]	56.5±0.3	3199.4	1620
Te^{120}			57.1±0.2	3207.4	1608
Sn^{121}	(d,p)	4.0[d]	57.1±0.4	3218.2	1665
Sb^{121}	(n,γ)	7.02[q]	57.4±0.2	3225.2	1653
Sn^{122}			57.5±0.2	3243.9	1699
Sb^{122}	β^-	1.94[b]	56.0±0.1	3249.0	1688
Te^{122}			58.1±0.1	3258.0	1675
Sn^{123}	(γ,n)	−8.50[r]	55.0±0.2	3267.0	1735
Sb^{123}	(γ,n)	−9.3[s]	57.0±0.3	3275.1	1722
Te^{123}			56.3±0.4	3281.3	1710
Sn^{124}			55.1±0.1	3292.6	1770
Sb^{124}	β^-	2.973[b]	54.0±0.2	3297.6	1758
Te^{124}			57.2±0.1	3307.2	1744
I^{124}	β^+	3.83[b]	53.1±0.2	3310.8	1734
Xe^{124}			54.2±0.1	3319.8	1722
Sb^{125}	β^-	0.768[b]	54.6±0.3	3323.5	1793
Te^{125}			55.4±0.3	3330.7	1780
Te^{126}			55.8±0.1	3356.2	1815
I^{126}	β^-	1.268[b]	53.9±0.2	3361.5	1804
Xe^{126}			55.2±0.1	3370.2	1791
Te^{127}	β^-	0.70[t]	54.0±0.2	3379.9	1852
I^{127}			54.7±0.1	3387.3	1839
Te^{128}			53.5±0.1	3404.8	1888
I^{128}	β^-	2.02[b]	53.4±0.1	3411.3	1876
Xe^{128}			55.5±0.1	3420.4	1862
Xe^{129}			54.0±0.2	3444.1	1899
Te^{130}			51.5±0.1	3454.0	1963
I^{130}	β^-	2.975[b]	51.8±0.2	3460.5	1950
Xe^{130}			55.0±0.1	3470.1	1935
I^{131}	β^-	0.968[b]	52.2±0.4	3486.3	1987
Xe^{131}			53.3±0.4	3493.8	1973
Xe^{132}			53.8±0.1	3519.6	2010
Xe^{134}			52.0±0.1	3568.8	2087
Xe^{136}			49.5±0.1	3617.7	2166

[a] R. Duffield and L. Langer, Phys. Rev. **81**, 203 (1951).
[b] A. C. G. Mitchell, Revs. Modern Phys. **22**, 36 (1950).
[c] T. Enns, Phys. Rev. **56**, 872 (1939).
[d] J. A. Harvey, Phys. Rev. **81**, 353 (1951).
[e] Bradt, Gugelot, Huber, Medicus, Preiswerk, and Scherrer, Phys. Rev. **68**, 57 (1945).
[f] M. Goodrich and E. Campbell, Phys. Rev. **85**, 742 (1951).
[g] G. Baldwin and H. Koch, Phys. Rev. **67**, 1 (1945).
[h] Helmholz, Hayward, and McGinnis, Phys Rev. **75**, 1469 (1949).
[i] D. Tendam and H. Bradt, Phys. Rev. **72**, 1118 (1947).
[j] R. Duffield and J. Knight, Phys. Rev. **75**, 1613 (1949).
[k] F. Maienschein and J. Meem, Phys. Rev. **76**, 899 (1949).
[l] Cork, Kutledge, Stoddard, Branyan, and LeBlanc, Phys. Rev. **79**, 938 (1950).
[m] E. Bleuler and W. Zunti, Helv. Phys. Acta **19**, 375 (1945).
[n] J. Cork and J. Lawson, Phys. Rev. **56**, 291 (1939).
[o] R. Duffield and J. Knight, Phys. Rev. **75**, 1967 (1949).
[p] McElhinney, Hanson, Becker, Duffield, and Diven, Phys. Rev. **75**, 542 (1949).
[q] B. B. Kinsey, cited by Harvey, reference d.
[r] Hanson, Duffield, Knight, Diven, and Pavlevski, Phys. Rev. **76**, 578 (1949).
[s] Johns, Katz, Douglas, and Haslam, Phys. Rev. **80**, 1062 (1950).
[t] *Nuclear Data*, National Bureau of Standards Circular 499 (1950).

theory of nuclear forces does not permit a computation of binding energy from Eq. (5) to compare with Eq. (6). It is of interest, however, to combine the experimental binding energy with the computed Coulomb and kinetic energies and examine the behavior of the functions L and L' in the resulting value for the potential energy.

For this purpose, Table III has been prepared containing the masses of 74 stable and radioactive isotopes between mass numbers 102 and 136. Nuclear reaction mass differences have been combined with the masses reported in this paper. The type of reaction and reaction energy used in computing the mass defects are also given for the nuclei concerned. The Bureau of Standards Circular *Nuclear Data* provided an invaluable aid in locating this information. Although the question might legitimately be raised as to whether or not certain individual values are the "best" values from existing data, the table as a whole presents a much more extensive and accurate compilation of masses than previously possible in this mass region. With 1.008146 and 1.008987 for the hydrogen atom and neutron masses, respectively, Eqs. (5) and (6) combine to give

$$-\text{PE}=\text{mass defect}+8.146Z+8.987N+\text{CE}+\text{KE mMU}. \quad (7)$$

The potential energy values obtained from this formula are listed in Table III. The value of Ξ, which is an integer from its definition as a count of couplings, is given in the final column.

From Eq. (3) one can see that potential energy difference between two isobars (nuclei of same A) designated a and b, is independent of L', and that one can obtain a value for the function L from the relation

$$L=-(\text{PE}_a-\text{PE}_b)/(\Xi_a-\Xi_b). \quad (8)$$

Values for L' can then be obtained by returning to Eq. (3). Figure 2 is a plot of experimental points for the function L determined by applying Eq. (8) to the isobars

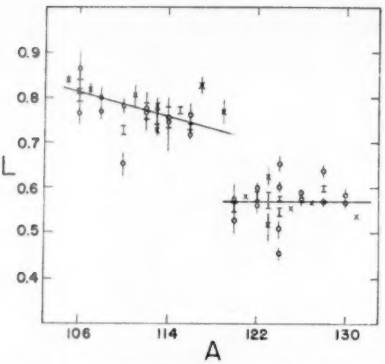

FIG. 3. L values from modified Wigner formula. The notation is identical to that of Fig. 2.

of Table III. As previously observed by Frisch,[13] there is evidence of systematic eccentricities in the data. Lines have been drawn to make this fact more evident. Straight lines have been drawn through two central groups of points. These L values were obtained from adjacent odd A isobaric nuclei and from isobaric pairs differing by $Z=2$. The upper series of curves contains adjacent even A isobars where the odd-odd nucleus has one less proton than the even-even member of the pair. These are even A isobars between the elements I−Xe, Sb−Te, In−Sn, and Ag−Cd. The remaining adjacent even A L values, those where the odd-odd nucleus contains one more proton than the even-even nucleus, fall in the lower curves. These points come from Te−I, Sn−Sb, Cd−In, and Pd−Ag.

The conclusion of interest evident in Fig. 2 is the fact that a simple line function for L will not fit the data. More specifically, there is a definite discontinuity in the L values between mass numbers 119 and 120

TABLE IV. An example of nuclear wave function modification which will contribute towards an improved fit of the Wigner formula to mass data.

Assumed by Wigner			Empirical change
n			n
$n\,\bar{n}$			$n\,\bar{n}$
$n\,\bar{n}$			$n\,\bar{n}$
$n\,\bar{n}\,p$			$n\,\bar{n}\,p$
$n\,\bar{n}\,p$			$n\,\bar{n}\,p$
$n\,\bar{n}\,p\,\bar{p}$			$n\,\bar{n}\,p$
$n\,\bar{n}\,p\,\bar{p}$			$n\,\bar{n}\,p\,\bar{p}$
	$\frac{1}{2}(Z-1)$	$\frac{1}{2}(N-1)$	
$n\,\bar{n}\,p\,\bar{p}$			$n\,\bar{n}\,p\,\bar{p}$

[13] D. H. Frisch, Phys. Rev. **84**, 1169 (1951).

associated with the magic number of 50 protons. Also, the Wigner formula does not correctly predict the potential energy difference between adjacent even A isobars. Concerning the magic number discontinuity, all L values below $A=119$ in Fig. 2 are determined from isobars involving isotopes with $Z=50$ (tin) or less. All L values above $A=120$ are determined from isobars involving isotopes with $Z=50$ or more. Unfortunately, the masses of the antimony isotopes below Sb^{120} are not accurately known. Hence it is not at present possible to observe an overlap of these two regions, e.g., the difference in L determined from $Sn^{119}-In^{119}$ and $Sb^{119}-Sn^{119}$. However, one might infer from the absence of a discontinuity in the curve for tin in Fig. 1 that the observed break in Fig. 2 is associated with 50 protons. It should also be noted that this discontinuity in L is in the same direction as those observed at 20 and 28 protons in previous results from this laboratory.

The two extreme L values at a given even A contain the same odd-odd nucleus. Hence if the mass formula correctly accounted for the potential energy associated

TABLE V. A summary of the effect of breaking up one possible pair of particles on Wigner formula components for heavy nuclei.

Type of nucleus N	Z	Change	$\Xi'-\Xi$	$f(P)'$
even	even	$n\to n$	-2	$(T^2)+2$
		$p\to p$		
odd	odd	$n\to n$	-3	$(T^2+1)+4$
		$p\to p$		
odd	even	$n\to n$	-3	$(T^2+\frac{1}{4})+4$
		$p\to p$	-2	$(T^2+\frac{1}{4})+2$
even	odd	$n\to n$	-2	$(T^2+\frac{1}{4})+2$
		$p\to p$	-3	$(T^2+\frac{1}{4})+4$

with an odd-odd configuration, the effect in Fig. 2 would be to collapse the extreme L values into the central group. The discontinuity at 50 protons would still remain. A simple empirical alteration of the Wigner formula will appreciably improve its account of the potential energy differences between isobaric nuclei. The revision occurs in formulas (2) and (4) which become

$$\mathrm{KE}'=14.640A+32.53(T^2+2+3\delta/2)/A\ \mathrm{mMU}, \quad (9)$$

$$\Xi'=2A-A^2/8-T(T+4)/2-2-5\delta/4. \quad (10)$$

A revised plot for L is given in Fig. 3. The method of arriving at this revision is presented below.

Wigner's assumptions lead to the conclusion that the greatest nuclear binding occurs when as many states as possible are occupied by four nucleons and the remaining nucleons are paired off, two to a state. It was observed, however, that the type of correction necessary to account for the observed potential energy differences between isobaric nuclei was in the nature of an increased

TABLE VI. Difference in 10^{-4} aMU between a fitted Wigner formula and experimental masses. The Wigner functions L and L' are obtained in each case by a least squares fit of the nuclides indicated by heavy type. (a) Unmodified Wigner formula fitted to nuclides containing 50 or less protons; (b) unmodified Wigner formula fitted to nuclides containing 50 or more protons; (c) empirically modified Wigner formula fitted to nuclides containing 50 or less protons; (d) empirically modified Wigner formula fitted to nuclides containing 50 or more protons.

(a)

Neutrons	Rh	Pd	Ag	Cd	In	Sn	Sb	Te	I	Xe
82										−58
80										−57
78								−28	−44	−56
									−51	−62
76								−34		−56
								−33	−50	−63
74						10	−16	−29	−48	−55
						1	−25	−34	−54	
72						7	−10	−28		−56
						−2	−21	−34	−62	
70					−5	6	−19	−25		−57
						−1	−25			
68				4	−5	1		−32		
				−3	−6	1				
66			−3	3	−2	1				
				−3	−10	−1				
64		14	−5	2	−7	2				
			−12	−3	−12					
62		9	−2	1		1				
	−2		−6							
60	−3	8	1	4						
		−3	−3	1						
58		8		5						
56		5								
	45	46	47	48	49	50	51	52	53	54
					Protons					

(b)

Neutrons	Rh	Pd	Ag	Cd	In	Sn	Sb	Te	I	Xe
82										35
80										22
78								5	9	13
									−3	4
76								−1		7
								−7	−8	−3
74						−1	−8	−1	−7	4
						−10	−18	−10	−14	
72						−2	−2	−2		0
						−9	−13	−8	−23	
70					−28	1	−8	2		−1
						−4	−14			
68				−26	−24	2		−2		
				−31	−21	5				
66			−42	−16	−8	10				
				−18	−13	11				
64		−27	−30	−7	−2	21				
			−32	−7	−4					
62		−14	−12	5		30				
	−35		−9							
60	−24	4	7	25						
		0	10	27						
58		22		41						
56		39								
	45	46	47	48	49	50	51	52	53	54
					Protons					

(c)

Neutrons	Rh	Pd	Ag	Cd	In	Sn	Sb	Te	I	Xe
82										−54
80										−53
78								−28	−36	−52
									−38	−53
76								−33		−54
								−27	−37	−54
74						5	−11	−30	−42	−53
						3	−14	−29	−41	
72						4	−6	−28		−54
						−2	−10	−29	−50	
70					−3	2	−14	−25		−56
						2	−14			
68				−1	−6	−3		−33		
				−1	1	4				
66			−3	−1	1	−2				
				−1	−1	3				
64		7	−4	−3	−4	−2				
			−4	−2	−3					
62		2	−1	−4		−3				
	6		2							
60	−3	3	2	−1						
		−2	6	3						
58		2		1						
56		−1								
	45	46	47	48	49	50	51	52	53	54
					Protons					

(d)

Neutrons	Rh	Pd	Ag	Cd	In	Sn	Sb	Te	I	Xe
82										31
80										19
78								2	10	10
									4	5
76								−8		3
								−5	−1	−1
74						−4	−6	−8	−6	−1
						−9	−10	−8	−8	
72						−6	−1	−6		−4
						−7	−6	−7	−17	
70					−25	−2	−6	−2		−6
						−2	−6			
68				−30	−21	−2		−5		
				−28	−13	7				
66			−40	−20	−6	6				
				−17	−4	14				
64		−29	−27	−9	−1	18				
			−22	−4	4					
62		−17	−10	3		27				
	−25		−1							
60	−20	1	10	21						
		4	19	30						
58		20		38						
56		36								
	45	46	47	48	49	50	51	52	53	54
					Protons					

dependence on δ in Eqs. (2) and (4). This effect can be produced by breaking up one possible pair of nucleons. For example, with the following notation:

n = neutron with spin up, $\bar{n}$ = neutron with spin down,
p = proton with spin up, $\bar{p}$ = proton with spin down,

the suggested change in nuclear wave function for the case of breaking up a proton pair in an odd-odd nucleus may be symbolized as in Table IV. The result of breaking up one pair of particles in all the various configurations of interest in this mass region is summarized in Table V. Ξ' denotes the revised value of Ξ. $f(P)'$ denotes the revised value of the sum of the squares of the partition quantum numbers entering into the deriva-

tion of the kinetic energy term of the binding energy of a nucleus. The original value of this quantity is enclosed in parenthesis.

The values for $\Xi'-\Xi$ and $f(P)'$ in the case of odd-even and even-odd nuclei are observed in Table V to depend upon whether a neutron pair or a proton pair is broken up. The best account of experimental data was given by assuming an average of these two possibilities for each case, i.e., $\Xi'-\Xi=-2\frac{1}{2}$, $f(P)'-f(P)=3$. Equations (9) and (10) show how the kinetic and potential energy terms are affected by these changes.

The effect of the empirical modification can best be demonstrated by fitting both forms of the Wigner formula to observed binding energies. For this purpose, the function L has been approximated by a straight line on either side of the magic number discontinuity. Following the procedure of reference 1, it has been assumed that AL is constant for L values determined by isotopes of $Z=50$ or less. For L values determined by isotopes of $Z=50$ or more, L has been assumed constant. Since a large discontinuity is not observed in the binding energies, L' must change in a manner which largely compensates for the observed change in L. The values for L' obtained by substituting the average L values in the expression for potential energy, Eq. (3), can also be approximated closely in these limited mass regions by straight line functions. The empirical functions obtained for the cases of interest by a least square fit of straight lines to data are given by

1. $L=87.42/A$, $AL'=68.692+0.04129A$,
2. $L=0.56992$, $AL'=50.398+0.15760A$,
3. $L=86.48/A$, $AL'=68.709+0.03968A$,
4. $L=0.57162$, $AL'=50.457+0.15779A$,

where the cases referred to are 1. unmodified Wigner formula fitted to nuclides with $Z\leqq 50$; 2. unmodified Wigner formula fitted to $Z\geqq 50$; 3. modified Wigner formula fitted to $Z\leqq 50$; 4. modified Wigner formula fitted to $Z\geqq 50$.

Tables VI (a), (b), (c), and (d) give the differences between observed and computed binding energies in 10^{-4} aMU for these four cases. The entries in heavy type are the residuals for the fitted region. A positive value indicates that the nucleus has greater stability than predicted by the empirical formula. In each case the differences have been tabulated beyond the region of fit. In Table VI (a) the average deviation within the region of fit is 0.45 Mev. This is due primarily to a pattern of alternate high and low values evident along either rows or columns. Empirical formula revision reduces this average deviation to 0.27 Mev as observed in Table VI (c). The observed increase in error beyond the region of fit suggests that a change of slope in the binding energy surface is associated with the breaks in the functions L and L'. In Table VI (b) the pattern of alternate high and low values within the region of fit is again evident. However, it is superimposed upon a strong trend in the residuals which points out the inadequacy of the approximations introduced in fitting the Wigner formula to the data of this region. In Table VI (d) empirical formula revision has again reduced the local irregularities. The average deviation in this case is reduced only from 0.87 to 0.75 Mev due to the previously noted larger source of error in the fit.

The instances of deviation of individual points from the general pattern of results in Figs. 2 and 3, and Tables VI also merit examination. Deviations in excess of 10 percent of the average L values drawn in Fig. 3 occur at mass numbers 110, 117, 123, 124, and 128. The L value at $A=117$ is derived from a 1939 magnetic spectrometer measurement for $In^{117}(\beta)Sn^{117}$. At $A=110$ the upper point is derived from the well established $Ag^{110}(\beta)Cd^{110}$ decay. The lower L value at $A=128$ is also derived from a well-established β-decay. Errors in either or both of the stable isotopes at each of these mass numbers could result in the observed deviations. In these two cases the mass spectrometric measurements might well be checked in the interest of confirming the systematic pattern of results or establishing deviations from it. At $A=124$, the deviation appears well established since the extreme lower point is derived from $I^{124}(\beta^+)Te^{124}$. The tabulated mass of Sb^{123} involves (γ,n), β, and mass spectrometric measurements. An error in this value could cause the spread in L values at $A=123$.

In conclusion, the type of discontinuities previously observed between mass data and fitted Wigner formula at the magic numbers of 20 and 28 protons is equally evident at 50 protons. An empirical alteration of the formula was found to appreciably improve its agreement on either side of the discontinuity. The residuals in the least square fits still exceed the probable error in measurement. Prediction of mass values within a limited mass range by means of a locally fitted Wigner formula is rendered uncertain by some apparently well-established deviations. It should be noted again that this development has, in effect, assumed that the expressions for kinetic and Coulomb energy are correct and blamed the potential energy term for observed irregularities. This may have resulted in a distorted picture of the nature of the discrepancies. Nevertheless, systematic deviations from the formula are sufficiently well established to suggest that a profitable re-examination of its basic assumptions might be made.

The author gratefully acknowledges the guidance of Dr. A. O. Nier in this investigation.

The construction of the apparatus used in this study was aided materially by grants from the Graduate School and the Minnesota Technical Research Fund subscribed to by General Mills, Inc., *Minneapolis Star* and *Tribune*, Minnesota Mining and Manufacturing Company, Northern States Power Company, and Minneapolis Honeywell Regulator Company.

Energy Levels in Si^{28} Excited by Alpha-Particles on Mg^{24}†

S. G. KAUFMANN,* E. GOLDBERG,‡ L. J. KOESTER,§ AND F. P. MOORING*
University of Wisconsin, Madison, Wisconsin

(Received April 14, 1952)

Alpha-particles produced by the Wisconsin electrostatic generator were used to bombard thin $Mg^{24}F_2$ targets evaporated onto pure graphite backings. The reaction products separated by a 90° magnetic analyzer were observed at a laboratory angle of 164±5°. Excitation curves for the reactions $Mg^{24}(\alpha, \alpha)Mg^{24}$ and $Mg^{24}(\alpha, p)Al^{27}$ were obtained and compared to the excitation curves of the $Al^{27}(p, p)Al^{27}$ and the $Al^{27}(p, \alpha)Mg^{24}$ reactions that had been obtained earlier. Cross sections for the reaction $Mg^{24}(\alpha, p)Al^{27}$ were found to bear a simple qualitative relationship to those of the inverse reaction $Al^{27}(p, \alpha)Mg^{24}$, as suggested by the principle of detailed balance. These two excitation curves could be brought into good correspondence by assuming a Q-value of -1.613 Mev for the reaction $Mg^{24}(\alpha, p)Al^{27}$. Some J-values have been assigned to the levels formed in the compound nucleus Si^{28}.

INTRODUCTION

THE energy levels of Si^{28} excited by protons of energies between 1 and 4 Mev impinging upon Al^{27} have been surveyed recently by Shoemaker, Faulkner, Bouricius, Kaufmann, and Mooring.[1] Their curve giving scattering cross section as a function of proton energy shows a number of resonances, of which only those excited by protons in the low energy region (Fig. 2A) are well enough separated to permit a description in terms of the single level scattering formula. Higher energy regions show increasing density of levels with a consequent loss of definition of each individual level. An interpretation of the high energy data is therefore not possible.

The well-separated resonances in the low energy region of the experimental results of Shoemaker and his associates are superimposed upon a potential scattering background which follows closely the energy dependence of pure Coulomb scattering. A comparison of these resonances with theoretical predictions is possible and has been attempted. The single level resonance formula, taking into account only one partial wave in each resonance, has led to the conclusion that it is likely that most of the resonances analyzed were due to a resonating S-wave in the proton beam. Because of the high spins of the colliding particles, a unique and satisfactory conclusion concerning the J-value of the compound state associated with each resonance analyzed could not be reached. Additional information concerning the J-values was judged to be necessary before J-values could be assigned and the individual resonances be described with more assurance and in greater detail.

On the basis of the energies available from the Wisconsin electrostatic generator, from mass values and the Q-value of the $Al^{27}(p, \alpha)Mg^{24}$ reaction, it was expected that the levels of Si^{28} corresponding to the proton resonances lying in the low energy region of the $Al(p, p)Al$ data could be reached through the bombardment of Mg^{24} by alpha-particles. Such a scattering experiment appeared particularly desirable because neither the alpha-particle nor the Mg^{24} nucleus in its ground state has a spin. Only one partial wave could possibly partake in a resonance, and its orbital momentum L would be equal to the spin J of the compound state of the Si^{28}. For this reason, if the orbital momentum of the partial alpha-particle wave could be inferred from the properties of the resonances observed in the $Mg^{24}(\alpha, \alpha)Mg^{24}$ scattering, the J-value of the Si^{28} nucleus could be definitely assigned, and additional valuable information might be obtained concerning the mechanism of the scattering of protons by Al^{27}.

EXPERIMENTAL ARRANGEMENT

The accelerator used was the Wisconsin electrostatic generator, whose output was separated according to particle momentum by a variable magnetic field. A cylindrical electrostatic analyzer separated the beam according to particle energy and was adjustable to permit beams of predetermined energy and energy spread to pass on to the target assembly. Ions which were not scattered from the target were collected in a Faraday cup and integrated[2] so as to measure the total number of charged particles which had fallen upon the target. Ions that were scattered into a given solid angle, between 159° and 169° in the backward direction, were separated by a magnetic analyzer which is described in reference 1. Those ions that the magnet deflected by 90° were recorded by a proportional counter at the end of their path.

Targets used in the experiment were prepared from $Mg^{24}O$ which was obtained from the Y-12 plant of Oak Ridge National Laboratory. Since the preparation of thin targets is most conveniently done by an evaporation of the target material, and since the evaporation of MgO requires temperatures too high to be practicable, the oxide was converted into the fluoride through mix-

† Work supported by the AEC and the Wisconsin Alumni Research Foundation.
* Now at Argonne National Laboratory, Chicago, Illinois.
‡ AEC Predoctoral Fellow.
§ Now at the University of Illinois, Urbana, Illinois.
[1] Shoemaker, Faulkner, Bouricius, Kaufmann, and Mooring, Phys. Rev. 83, 1011 (1951).
[2] G. M. B. Bouricius and F. C. Shoemaker, Rev. Sci. Instr. 22, 183 (1951).

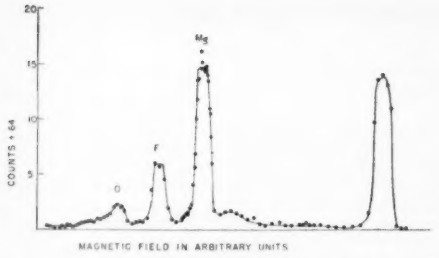

FIG. 1. Momentum analysis of the target. Mg^{24}, F, and O peaks are clearly defined. The peak on the high side of the magnetic field is due to a heavy impurity.

ing it with HF and retaining the precipitate of the reaction. The MgF_2 was evaporated onto polished backings of spectroscopically pure graphite to a thickness equivalent to an energy absorption of 13 kev for 1-Mev alpha-particles. A sample of the momentum distributions of alpha-particles recoiling from the various constituents of this target is shown in Fig. 1. The data have been obtained through a method quite similar to that employed for the corresponding momentum analyses in the paper of Shoemaker *et al.*

Particles were detected in a proportional counter filled with a mixture of 98 percent argon and 2 percent CO_2, sealed from the main vacuum system by a 1/20-mil nickel window. An examination of this window, carried out by permitting alpha-particles of various energies to strike it, showed that the window would not permit alpha-particles of energy below 1.2 Mev to penetrate into the counter with energies sufficient to give usable and well-defined signals.

The $Mg^{24}(\alpha, p)Al^{27}$ reaction was surveyed with a 1/10-mil nickel window in front of the proportional counter. As computations had predicted, this window was thick enough to suppress the alpha-particle background but did permit protons of the reaction to penetrate and to register with large, uniformly sized signals.

EXPERIMENTAL RESULTS

Figure 2 shows the experimental data. A portion of the yield curves of the $Al^{27}(p, p)Al^{27}$ and $Al^{27}(p, \alpha)Mg^{24}$ reactions that are given in the paper of Shoemaker *et al.* is reproduced in Figs. 2A and 2B. The proton scattering curve of Fig. 2A was taken with a target thickness of 1.4 kev,[2] and the proton beam was resolved energetically to have an energy spread at half-maximum intensity of 0.07 percent of its mean energy. The survey of the $Al^{27}(p, \alpha)Mg^{24}$ reaction below 1.3 Mev was made five months after the survey of the region above this energy. The target thicknesses were 13 kev in both surveys, and the energy spread of the beam in the earlier work was 0.07 percent. Because energy calibrations were not made with sufficient frequency over this extended period of time, discrepancies in the energy scales as high as 10 kev were found in some cases. Later difficulties with shifts in the generator energy scale were traced to poor contacts in the Rubicon potentiometer which determines the energy of the generator. It is likely that this was the major cause of the shifts in this experiment. The accuracy of the Q-value given in the next section is directly affected by these discrepancies. The results of the alpha-particle bombardment of Mg^{24} are shown in Figs. 2C and 2D. The $Mg^{24}(\alpha, p)Al^{27}$ curve of Fig. 2C was taken with 13-kev targets and an energy spread of 0.1 percent. The same target and energy spread were used for the curve showing elastic scattering of alpha-particles from Mg^{24} (Fig. 2D). The curves of Figs. 2C and 2D were taken in September 1950.

Q-VALUE AND INVERSE REACTION CROSS SECTIONS

The match of the energy scales in the center-of-mass system of the different experimental curves, as it is shown in Fig. 2, defines a difference in the origin of the energy axes of the $Mg^{24}(\alpha, p)Al^{27}$ and the $Al^{27}(p, \alpha)Mg^{24}$ reaction to be 1.613 Mev. The good correspondence in the curves of the two inverse reactions has been considered sufficient evidence that the difference in the origin of the energy scales as shown in the figure represents the Q-value of the reaction. Corrections have been made for the shift in the peak of each resonance due to target thickness. By bringing each pair of sufficiently defined resonance peaks (those corresponding to alpha-particle energies of 2.755, 2.931, 2.955, 3.002, 3.137, 3.203, 3.280 Mev on the $Mg^{24}(\alpha, p)Al^{27}$ yield curve) of the inverse reaction curves into coincidence in turn, seven values for the Q-value of the reaction were obtained which did not differ by more than 3 kev from their average value of 1.613 Mev. Referring to the shift in energy scales discussed in the previous section, it is assumed that our Q-value may be in error by about 10 kev.

Not only is the level structure reproduced in the two inverse curves, but the intensities of corresponding peaks appear to be in good agreement. Small deviations can be discovered in the detailed structure: a small (α, p) peak at 2.84-Mev alpha-particle energy is not matched by a perceptible rise on the (p, α) curve; the doublets in the neighborhood of 1.51 and 1.6 Mev on the (p, α) curve are opposite to single peaks on the alpha-scale, whose asymmetry suggests that the resolution of the alpha-run was not sufficient to separate the two levels. If such discrepancies find their explanation in terms of resolution differences in the two runs, then the over-all aspect of the two curves may be said to verify qualitatively the principle of detailed balance. The theoretical ratio of the reaction cross sections is

$$\sigma_{\alpha p}/\sigma_{p\alpha}=(2s+1)(2i+1)(mv_p)^2/(mv_\alpha)^2$$
$$=12(mv_p)^2/(mv_\alpha)^2,$$

[2] All target thicknesses are expressed in terms of absorption thickness of incoming particles at 1 Mev.

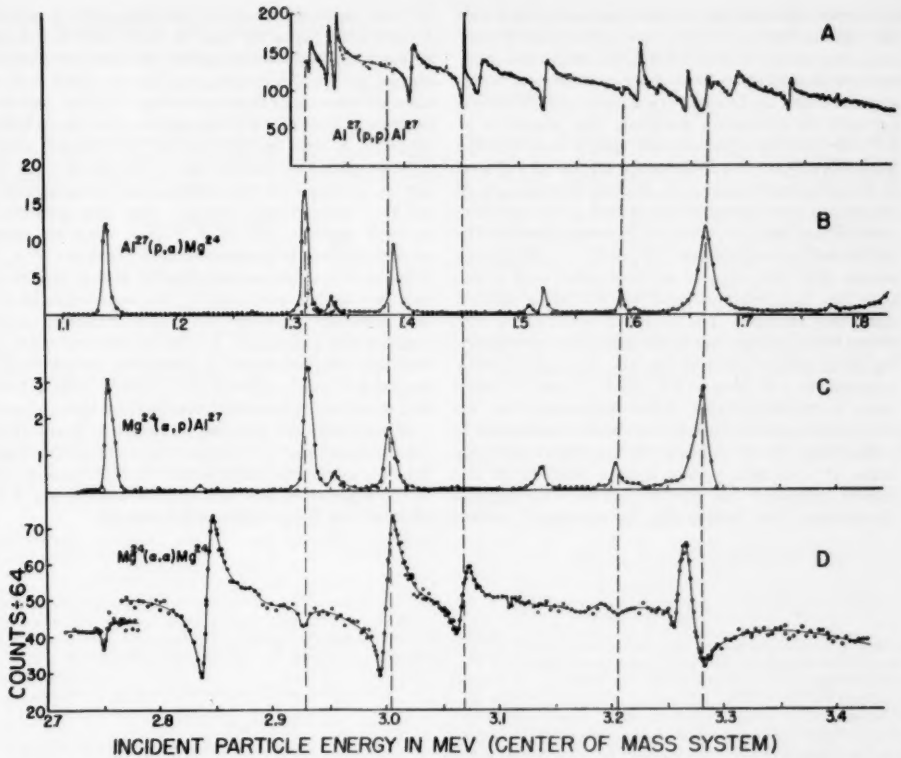

FIG. 2. A. $Al^{27}(p, p)Al^{27}$ curve taken with 1.4-kev targets, beam energy spread 0.07 percent; B. $Al^{27}(p, \alpha)Mg^{24}$ curve taken with 13-kev targets (region below 1.3 Mev), and with 13-kev targets and beam energy spread of 0.07 percent (region above 1.3 Mev). Data shown in curves 2A and 2B are reproduced from reference 1; C. $Mg^{24}(\alpha, p)Al^{27}$ curve taken with 13-kev targets, beam energy spread 0.1 percent; D. $Mg^{24}(\alpha, \alpha)Mg^{24}$ curve taken with 13-kev targets, beam energy spread 0.1 percent.

where mv_p is the momentum of the emitted proton, mv_α is the momentum of the emitted alpha particle, s is the spin of the Al^{27} nucleus in the ground state, and i is the spin of the proton. An attempt has been made to compare this with the experimental value. The computations were handicapped by the uncertainty in target thickness, particularly for the (p, α) curve, which was known only roughly from the geometry used in the preparation of the target. Assuming that the theoretical ratio of cross sections, as given in the principle of detailed balance, is correct, it was computed that the absorption thickness of the magnesium target for alpha-particles must be approximately three times as much as the absorption thickness of the aluminum target for protons. However, in the preparation of the targets, the geometry used had been such that both targets should have had equal absorption thickness for the respective ions with which they were to be bombarded. A discrepancy of a factor of approximately three, therefore, remains between the experimental results and the theoretical prediction, and this discrepancy is probably due to errors in the determination of target thickness.

ESTIMATES OF ORBITAL ANGULAR MOMENTA

A detailed analysis of the data, comparing accurately the energy dependence of the theoretical and observed scattering cross sections in the resonance regions, has not yet been made. A more qualitative interpretation of the resonances, using only the ratio of minimum to maximum scattering cross section belonging to any one resonance, has been attempted through the aid of a diagram reproducing the essentials of the scattering formula in the complex plane. Through some simple, graphical steps, the angle $(\alpha_L - \alpha)$ has been determined,[4] from which the L-value of the resonating partial wave can be determined. This analysis has given the follow-

[4] L. I. Schiff, *Quantum Mechanics* (McGraw-Hill Book Company, Inc., New York, 1949), p. 120, Eq. (20.24).

ing results: The scattering resonances at 2.83 and 3.00 Mev on the $Mg^{24}(\alpha, \alpha)Mg^{24}$ curve have ratios of minimum cross section to Rutherford cross section and maximum cross section to Rutherford cross section, which agree well with the theoretical values for pure S-scattering with no competing reactions. The resonance at 2.93 Mev on the alpha-particle energy scale has the qualitative aspect of a D-resonance suggesting a D-level in the compound nucleus. S-, P-, and F-resonances at this energy are expected to show a peak in the scattering cross section which, in our data, is not perceptible. The corresponding resonance on the proton scattering cross section (Fig. 2A) suggests an S-resonance with amplitude less than that predicted for scattering without competing reactions. The proton S-resonance is consistent with the D-resonance observed in the corresponding alpha-particle curve of Fig. 2D. The alpha-particle resonance at 3.07 Mev on Fig. 2D has a ratio of maximum to minimum cross section suggesting that the S-wave resonates here. It is correlated energetically to a sharp and strong resonance in the proton scattering curve at 1.45 Mev proton energy. Analysis of this proton resonance has shown that it, too, suggests S-scattering. No J-value for the compound nucleus Si^{28} can be found which is consistent with a proton S-wave falling upon Al^{27} and an alpha-particle S-wave falling upon Mg^{24}. It is assumed that the Si^{28} nucleus formed by 3.07-Mev alpha-particles on Mg^{24} is in a state different from that formed by 1.45-Mev protons impinging upon Al^{27}. The assumption that the angular momenta of these two states in Si^{28} are different seems to be supported by the fact that at this energy no (α, p) nor (p, α) transitions are observed. In the region above 3.1-Mev alpha-particle energy, only one prominent anomaly appears, that at 3.25 Mev. Since the cross section dips to a minimum on both sides of the peak, it is assumed that the anomaly at 3.25 Mev is caused by two overlapping levels in Si^{28}. The appearance of the corresponding region in the proton scattering curve confirms this assumption. A more detailed analysis than that just described might be profitable, but the experimental data, both with regard to absolute cross sections and resolution is somewhat marginal for that purpose.

The authors are indebted to Professor R. G. Herb for the supervision of this experiment and to Dr. Virgil Johnson for help in taking data. The Mg^{24} isotope used in this experiment has been obtained through the Y-12 plant of Oak Ridge National Laboratory.

Letters to the Editor

PUBLICATION of brief reports of important discoveries in physics may be secured by addressing them to this department. The closing date for this department is five weeks prior to the date of issue. No proof will be sent to the authors. The Board of Editors does not hold itself responsible for the opinions expressed by the correspondents. Communications should not exceed 600 words in length and should be submitted in duplicate.

The Current Density in Quantum Electrodynamics

H. C. CORBEN*
Institute of Physics, University of Genoa, Genoa, Italy
(Received September 5, 1952)

IF e_0, m_0 denote the charge and rest mass of the positron, the equation for a particle of chage e,

$$\{\gamma_i D_i + i(e/e_0)\kappa\gamma_4\}\psi = 0, \tag{1}$$

where $D_i = \partial_i - (ie/\hbar c)A_i$ and $\kappa = m_0 c/\hbar$, yields the Dirac Hamiltonians

$$H = -e_0\varphi - c\boldsymbol{\alpha}\cdot(\mathbf{p}+e_0\mathbf{A}/c) - \rho_3 m_0 c^2,$$
$$H = \quad e_0\varphi - c\boldsymbol{\alpha}\cdot(\mathbf{p}-e_0\mathbf{A}/c) + \rho_3 m_0 c^2,$$
$$H = -c\boldsymbol{\alpha}\cdot\mathbf{p}, \quad (\boldsymbol{\alpha} = \rho_1\boldsymbol{\sigma}),$$

for electrons, positrons, and neutrinos, respectively, provided that we take

$$\gamma_k = \rho_3\sigma_k (k = 1, 2, 3), \quad \gamma_4 = \rho_3, \quad \gamma_5 = \rho_1, \tag{2}$$

rather than the usual expressions of the γ_μ in terms of the Dirac operators. The latter are in fact obtained from (2) under the transformation $\rho_1 \to \rho_3$, $\rho_3 \to \rho_1$, $\rho_2 \to -\rho_2$. Equation (1) requires that the charge e be a pseudoscalar and that the potentials A_i form a pseudovector.

In addition to the usual current-density pseudovector,

$$j_i = ec\psi^\dagger\gamma_i\psi, \quad (\psi^\dagger = i\psi^*\rho_2),$$

there exists the pseudovector density,

$$j_i^* = -\tfrac{1}{2}i(e_0\hbar/m_0)(\psi^\dagger\gamma_5 D_i\psi - D_i^*\psi^\dagger\gamma_5\psi),$$

which is also conserved in virtue of Eq. (1). Since j_i^* is also gauge-invariant, one could use it instead of j_i to specify the current density.

In the absence of an electromagnetic field, j_i^* reduces to j_i; and in general, it follows from Eq. (1) that j_i^* may be alternatively written as follows:

$$j_i^* = j_i + (c/4\pi)\partial_j h_{ji}, \tag{3}$$

where

$$h_{ij} = -h_{ji} = -(ie_0\hbar/m_0 c)\psi^\dagger\gamma_5(\gamma_i\gamma_j - \delta_{ij})\psi. \tag{4}$$

If j_k generates the field f_{ik},

$$\partial_i f_{ik} = -(4\pi/c)j_k, \tag{5}$$

the new current density j_k^* generates a new field f_{ik}^*:

$$\partial_i f_{ik}^* = -(4\pi/c)j_k^*, \tag{6}$$

where

$$f_{ik}^* = f_{ik} - h_{ik}. \tag{7}$$

In the same way that the new current density reduces to the old in the absence of an electromagnetic field, the new electromagnetic field reduces to the old in the absence of a particle field.

With this field f_{ik}^* may be associated an energy density,

$$u^* = (E^{*2}+H^{*2})/8\pi = (E^2+H^2)/8\pi + Y + Z,$$

where

$$Y = -(e_0\hbar/2m_0 c)[\psi^*\rho_3(\boldsymbol{\sigma}\cdot\mathbf{H} - i\boldsymbol{\alpha}\cdot\mathbf{E})\psi],$$
$$Z = \tfrac{1}{2}\pi(e_0\hbar/m_0 c)^2[(\psi^*\rho_3\boldsymbol{\sigma}\psi)^2 + (\psi^*\rho_2\boldsymbol{\sigma}\psi)^2].$$

Free-particle solutions of Eq. (1) may be characterized by the sign of the charge,

$$e = \pm(e_0/m_0 c^2)(w^2 - p^2c^2)^{\frac{1}{2}},$$

and for the positive energy solutions corresponding to zero momentum,

$$\rho_3\psi = (e/e_0)\psi.$$

The term Y therefore contains the interaction energy of the field f_{ij} with the magnetic and electric moments of the electron-positron field. For atomic electrons the term Z yields on integration an energy of fine structure order, although if an electron were to be confined to distances of the order of nuclear dimensions, integration of Z would yield an energy of several hundred Mev.

If we use f_{ik}^* and j_i^* instead of f_{ik} and j_i in the Lagrangian that leads to (1) and (5), i.e.,

$$L = \tfrac{1}{2}i\hbar c(\psi^\dagger\gamma_i\partial_i\psi - \partial_i\psi^\dagger\gamma_i\psi) - (e/e_0)m_0 c^2\psi^\dagger\gamma_5\psi + j_i^* A_i/c - f_{ij}^* f_{ij}^*/16\pi,$$

where f_{ij}^*, j_i^* defined by (3), (4), and (7), the Lagrangian equations which result with A_i, $\psi^\dagger$, ψ as independent variables are Eq. (6) and the nonlinear equation,

$$\gamma_i D_i\psi + (ie/e_0)\kappa\gamma_5\psi = -(e_0/4m_0 c^2)h_{ij}\gamma_5\gamma_i\gamma_j\psi.$$

This modification does not destroy the conservation property of j_i, j_i^*. Some applications of this equation will be published in *Il Nuovo Cimento*.

* On leave of absence from Carnegie Institute of Technology, Pittsburgh, Pennsylvania.

Atomic Oxygen *g*-Factors*

E. B. RAWSON† AND R. BERINGER
Sloane Physics Laboratory, Yale University, New Haven, Connecticut
(Received September 15, 1952)

WE have recently studied the Zeeman splittings of the ground $^3P_2$ and metastable $^3P_1$ states of atomic oxygen in an attempt to determine the effects of the electron spin-moment anomaly in a complex atomic state. The microwave resonance apparatus is similar to that used for hydrogen[1] and paramagnetic gases.[2] Transitions between adjacent M levels of a given atomic term are observed in a stream of vapor which originates in a discharge tube and passes through a microwave cavity. The cavity is in a proton-controlled magnetic field, and a second proton-resonance coil, whose mineral-oil sample volume simulates the atomic vapor stream, is later fitted into the cavity and its proton-resonance frequency measured. The six microwave transitions in oxygen are labeled $a(M=1\to0$ in $^3P_1)$, $b(M=0\to-1$ in $^3P_1)$, $c(M=2\to1$ in $^3P_2)$, $d(M=1\to0$ in $^3P_2)$, $e(M=0\to-1$ in $^3P_2)$, and $f(M=-1\to-2$ in $^3P_2)$. The six transition energies are slightly different due to Paschen-Back terms. On LS coupling they are symmetrical about $g_J\mu_0 H$ in pairs (a, b), (c, f), (d, e). Provided only that this symmetry exists, g_J can be calculated from frequencies alone. For the pair (a, b),

$$g_J = g_p\nu(1+f_a^2/f_b^2)/[f_a(1+f_a/f_b)],$$

with[3] $g_p = g_a/(g_s/g_p) = 2(1.0011454)/658.2271$ for our cylindrical sample of mineral oil. The f's are simulator proton-resonance frequencies, and ν is the fixed microwave frequency.

If the coupling in the ^3P term is pure LS, one expects a simple contribution[4] to g_s from the electron-spin anomaly with $g_J = 3/2 + 0.0011454$. Unfortunately, the ground $(2p)^4$ configuration in oxygen departs considerably from LS coupling, and the electrostatic and LS splittings cannot be fitted without configuration mixing. We have not calculated configuration-interaction contributions to the Paschen-Back effect.

Tentative results based on two runs agreeing to 4 parts in 10^4 are $g_J(a, b) = 1.500971$, $g_J(c, f) = 1.500905$, and $g_J(d, e) = 1.500904$. The two values for the $^3P_2$ levels are sensibly identical, some 44 parts in 10^4 less than $g_J(a, b)$ and 161 parts in 10^4 less than the LS

coupling value. The Paschen-Back splittings of the four $^3P_2$ transitions are in good (±0.06 percent) agreement with *LS* theory, but those for the $^3P_1$ transitions are not: 10.18 gauss between a and b as compared with 17.22 gauss for *LS* theory. The Paschen-Back difficulties may lie in an anomalous perturbation of the $(M=0, {}^3P_1)$ level by the $^3P_0$ term.

In all of the experiments another spectrum was found which consisted of three very narrow lines interleaved with the four $^3P_2$ transitions. The interval between these lines was the same as for the four $^3P_2$ lines, and their mean g value was lower than for the $^3P_2$ lines by 2 to 5 parts in 10^6. The origin of this spectrum is not established. It apparently cannot arise from any known oxygen term, but may be the result of argon contamination of the discharge tube. Further study of this spectrum is in progress.

* Assisted by the ONR.
† AEC Predoctoral Fellow. Part of a dissertation submitted to Yale University for the Ph.D. degree.
[1] R. Beringer and E. B. Rawson, Phys. Rev. **87**, 228 (1952).
[2] R. Beringer and J. G. Castle, Phys. Rev. **78**, 581 (1950); **81**, 82 (1951).
[3] Koenig, Prodell, and Kusch, Phys. Rev. **83**, 687 (1951).
[4] P. Kusch and H. M. Foley, Phys. Rev. **74**, 250 (1948).

X-Rays from the π-Mesic Atom*

A. M. L. Messiah and R. E. Marshak
University of Rochester, Rochester, New York
(Received September 15, 1952)

It is well known that the nuclear absorption of slow μ^- mesons takes place primarily from the K shell of the appropriate μ-mesic atom and leads to the $Z_{eff}{}^4$ law[1] (Z_{eff} is the effective nuclear charge). The $Z_{eff}{}^4$ law is the result of a competition between the Z-independent μ^- meson decay and the $Z_{eff}{}^4$-dependent nuclear absorption for a bound $1s$ μ^- meson, the two becoming equally probable for $Z_{eff}\approx 10$. Since the probability for nuclear absorption is greatly reduced when the μ^- meson finds itself in a $2p$ state and since the $2p\rightarrow 1s$ optical transition probability is $1.3\times 10^{12}Z^4$ sec^{-1}, it follows that even for the heaviest elements all μ^- mesons reaching the $2p$ state (and this means the vast majority[2]) will emit K_α x-ray lines.

On the other hand, the strong interaction of π-mesons with nuclei alters the entire picture for π-mesons. The interaction is so strong that the majority of π-mesons will not reach the K shells for any but the two lightest elements, namely, hydrogen and helium. This can be seen as follows: For deuterium several authors[3] have shown that the probability for nuclear absorption from the $2p$ state, w_{abs}, is 20–30 times smaller than the $2p\rightarrow 1s$ optical transition probability, $w_{2p\rightarrow 1s}$. Now $w_{abs}\approx Z^4$ (restricting ourselves to light nuclei where $Z_{eff}\approx Z$) and $w_{2p\rightarrow 1s}\approx Z^4$, so that $w_{abs}\approx w_{2p\rightarrow 1s}$ when $Z^4\approx$ 20–30 or $Z\approx$ 4–5 provided that the nuclear absorption per deuteron stays the same in heavier nuclei. This, however, is not the case since the deuteron is such a loosely bound structure. An estimate of the effect of nuclear binding can be deduced from the relative cross sections for nuclear absorption at low positive kinetic energies of the π^- meson; this leads to the use of $5Z$ as the effective number of deuterons[4] and therefore to $5Z^4\approx$ 20–30 or $Z\approx 2$ as the value above which nuclear absorption from the $2p$ state prevails over the emission of π^-K_α x-rays.

Actually, the pseudoscalar character of the π-meson field and the apparent importance of gradient coupling for determining the salient features of the π-meson-nucleon interaction[5] enable one to establish a close connection between w_{abs} and the cross section σ for nuclear absorption from the continuum. Thus, if we write for the interaction Hamiltonian[6]

$$H=(f/\mu)\Sigma_i\tau^i(\sigma^i\cdot\nabla)\phi, \tag{1}$$

then[7]

$$w_{abs}=(\hbar^3/q\mu)\sigma\,|\nabla\phi(0)|^2\mathfrak{R}, \tag{2}$$

where σ^i, τ^i are the spin and isotopic spin operators of the ith nucleon, $\phi(0)$ is the Coulomb wave function of the π^- meson evaluated at the nucleus, q the π^- momentum in the continuum, and $\mathfrak{R}$ the ratio of the square of the nuclear matrix elements from the bound state and the continuum. It would certainly seem like a good approximation to set $\mathfrak{R}=1$ when the kinetic energy of the π^- meson is small compared to its rest mass. If we use Eq. (2), insert 3 mb[8] for the cross section for the reaction $\pi^++D\rightarrow P+P$ at 25 Mev and assume charge symmetry, we obtain $w_{abs}=0.06w_{2p\rightarrow 1s}$. For carbon, the lowest energy at which the absorption cross section has been measured is 62 Mev[9] with the result $\sigma=150$ mb; inserting this value into Eq. (2) yields $w_{abs}\approx 11w_{2p\rightarrow 1s}$, which prediction is much less reliable than the deuteron prediction. For nuclei other than deuterium and carbon, nuclear absorption cross sections are not available for π-meson energies below 85 Mev.[10]

One would expect a monotonic increase in the ratio $w_{abs}/w_{2p\rightarrow 1s}$, roughly as Z^2 beyond deuterium, unless special selection rules associated with Eq. (1) operate for a given nucleus. Such selection rules could lead to strong fluctuations in the ratio $w_{abs}/w_{2p\rightarrow 1s}$ and have already been shown to exist[11] for H^2, He^3, and He^4. It can also be shown that if Wigner's supermultiplet theory (based on the spin and charge independence of nuclear forces) were rigorously true, the $\tau^i(\sigma^i\cdot\nabla)$ operator would give a strictly zero contribution for all nuclei belonging to the supermultiplet (0, 0, 0). This follows because the $\tau^i(\sigma^i\cdot\nabla)$ operator does not act on the space coordinates of the nucleons and therefore only allows transitions to final states whose space part belongs to the same irreducible representation of the group of permutations, namely, to final states belonging to the same supermultiplet (0, 0, 0); however, the conservation laws of spin and isotopic spin are violated. The case of O^{16} is especially interesting since the same selection rule obtains on the basis of the shell model assuming charge-independent and central (but not necessarily spin-independent) nuclear forces; the resulting $(1s)^4(1p)^{12}$ configuration yields an O^{16} wave function which accidently belongs to the supermultiplet (0, 0, 0). It is, of course, very unlikely that any of these selection rules will hold absolutely, both because the π-meson-nucleon interaction must possess an s component (in addition to the p component, see reference 6) and because "shell structure" effects ought to lose their potency for processes involving such high energy transfers as π^- absorption.[12] Nevertheless, it is conceivable that fluctuations in the ratio $w_{abs}/w_{2p\rightarrow 1s}$ can be observed, and it would be interesting to study π-mesic x-ray yields for "magic number" nuclei and their near neighbors. Since He^4 raises difficult experimental problems and since, for $Z\gtrsim 10$, nuclear absorption from the $3d$ level should rapidly dominate over the $3d\rightarrow 2p$ optical transition, O^{16} is the only suitable candidate for this type of experiment. Preliminary measurements of the π-mesic x-ray yields from C and O performed at this laboratory[13] support the theoretical interpretation presented in this note and indicate that "shell structure" does indeed play a role in the absorption of slow π^- mesons.

We are indebted to Camac *et al.*[11] for informing us of their results prior to publication.

* This work was assisted by the AEC and the French Direction of Mines.
[1] Harrison, Keuffel, and Reynolds, Phys. Rev. **83**, 680 (1951).
[2] J. A. Wheeler, private communication to Dr. J. B. Platt.
[3] S. Tamor and R. Marshak, Phys. Rev. **80**, 766 (1951); Brueckner, Serber, and Watson, Phys. Rev. **81**, 575 (1951) and **84**, 258 (1951).
[4] Comment of H. A. Bethe, Proceedings of the Rochester Conference on Meson Physics, January 11–12, 1952, unpublished.
[5] Durbin, Loar, and Steinberger, Phys. Rev. **84**, 581 (1951).
[6] Equation (1) represents the dominant term (there is an s-coupling term of order μ/M where μ and M are the π-meson and nucleon masses, respectively) in the *PS*(*PV*) theory; however, it is not excluded that some higher order treatment of the *PS*(*PS*) theory will similarly lead to the dominance of the p-coupling type interaction.
[7] Brueckner, Serber and Watson, reference 3.
[8] Clark, Roberts, and Wilson, Phys. Rev. **83**, 649 (1951); also reference 5.
[9] Byfield, Kessler, and Lederman, Phys. Rev. **84**, 17 (1952); A. M. Shapiro's measurement at 48 Mev [Phys. Rev. **84**, 1063 (1951)] does not distinguish between star production and inelastic scattering.
[10] Chedester, Isaacs, Sachs, and Steinberger, Phys. Rev. **82**, 958 (1951); Bernardini, Booth, and Lederman [Phys. Rev. **83**, 1075 (1951)] have results at energies as low as 30 Mev but for photographic emulsion.
[11] Messiah, Caianiello, and Basri (H^3), Phys. Rev. **83**, 652 (1951); A. M. L. Messiah (He^3), Phys. Rev. **87**, 639 (1952); A. G. Petschek (He^4), private communication.
[12] "Shell structure" effects have been considered for μ^- absorption by Ca and Pb [J. M. Kennedy, Phys. Rev. **86**, 616 (1952)].
[13] Camac, McGuire, Platt, and Schulte, Phys. Rev. **88**, 134 (1952); the K_α lines from C and O should be 100, 175 kev, respectively, with widths of the order of 2 to 5 (due to nuclear absorption from the K shell).

Photon Absorption Cross Sections in Bismuth and Tantalum*

J. HALPERN, R. NATHANS, AND A. K. MANN
University of Pennsylvania, Philadelphia, Pennsylvania
(Received September 12, 1952)

MEASUREMENT of the energy dependence of the photoneutron cross section of heavy elements, for which charged particle emission is strongly inhibited by the Coulomb barrier, gives to a good approximation the total probability of photon capture on those elements. The observed integrated cross section, i.e., the area under the excitation function, can be compared with that predicted by application of the sum rules for dipole absorption to nuclei,[1] and the shape of the excitation function provides information on nuclear structure.[1–3]

Previously, measurements have been made of the neutron yields from elements bombarded with 18- and 22-Mev bremsstrahlung[4] and with monochromatic photons of energy 17.6 Mev;[5] and excitation functions have been constructed from radioactivity data obtained from nuclei resulting from (γ, n) reactions.[6] The neutron yield measurements do not directly give integrated cross-section information because they do not distinguish between reactions of various neutron multiplicities.[7–9] The radioactivity measurements lead to integrated cross sections of (γ, n) reactions only.

Using a method of delayed neutron detection,[10] we have measured the excitation function for neutron yield from bismuth and tantalum and have separated the (γ, n) and $(\gamma, 2n)$ components. The apparatus of reference 10 has been modified so that the detection efficiency is independent of neutron energy.[11] Figure 1 shows the yields of neutrons from the targets at various maximum bremsstrahlung energies produced by the University of Pennsylvania betatron. Thin targets of 434 mg/cm² and 468 mg/cm² of bismuth and tantalum, respectively, were used. Figure 2 shows the excitation function constructed from the tantalum yield data of Fig. 1. The points shown in the figure are obtained from the photon-difference method[6] and the calculated bremsstrahlung distributions at 1-Mev intervals. Using the radioactivity data of Johns *et al.*[6] for the (γ, n) excitation function, the (γ, n) and $(\gamma, 2n)$ components can be separated and the total cross section plotted in Fig. 3. A similar curve for bismuth is also given in the same figure.

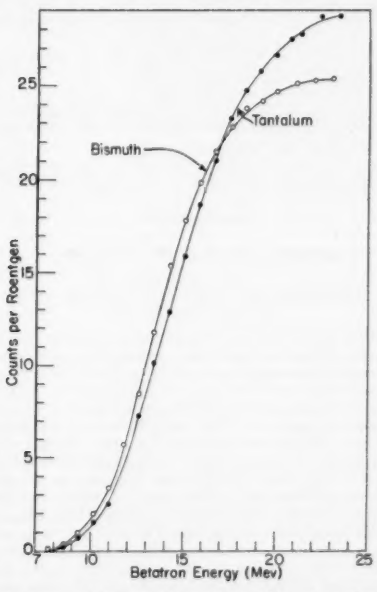

FIG. 1. Neutron yield curves for tantalum and bismuth. Statistical accuracy of the points is better than 2 percent everywhere except at 7.75 and 8.55 Mev, where the error does not exceed 4 percent.

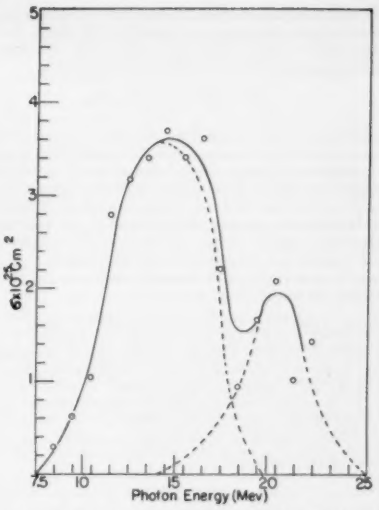

FIG. 2. Excitation function for neutron yield in tantalum. The dotted lines show contributions due to the (γ, n) and $(\gamma, 2n)$ reactions.

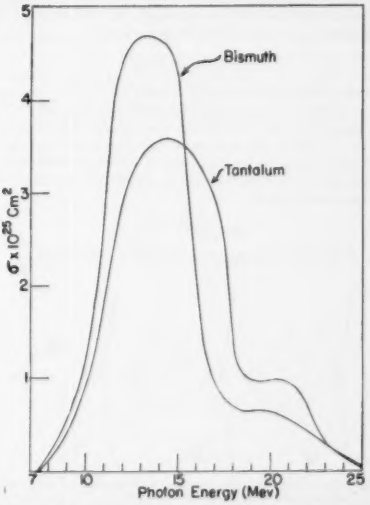

FIG. 3. Total cross section curves for tantalum and bismuth.

The total integrated cross sections are 2.8 Mev-barns for tantalum and 3.0 Mev-barns for bismuth, with the $(\gamma, 2n)$ contributing approximately 15 percent in each case. The sum rule prediction that the integrated cross section be given by

$$\int_0^\infty \sigma dE = 0.060(NZ/A)(1+0.8x),$$

where x is the fraction of exchange force in the proton-neutron interaction, is in excellent accord with the results. The calculation of the fraction of exchange force, however, would require better techniques than the photon-difference method of obtaining cross sections from the yield data, especially as to any tail on the curves above 23 Mev, and also some determination of the importance of (γ, γ) processes. As can be seen, the shapes of the excitation functions of bismuth and tantalum are markedly different.

Work is continuing on other elements as well as on the detection of coincidences in the $(\gamma, 2n)$ process.

* Support in part by the joint program of the ONR and AEC.
[1] J. S. Levinger and H. A. Bethe, Phys. Rev. **78**, 115 (1950).
[2] M. Goldhaber and E. Teller, Phys. Rev. **74**, 1046 (1948).
[3] H. Steinwedel and J. H. D. Jensen, Z. Naturforsch. **5a**, 413 (1950).
[4] G. A. Price and D. W. Kerst, Phys. Rev. **77**, 806 (1950).
[5] McDaniel, Walker, and Stearns, Phys. Rev. **80**, 807 (1950).
[6] H. E. Johns *et al.*, Phys. Rev. **80**, 1062 (1950).
[7] J. S. Levinger and H. A. Bethe, Phys. Rev. **85**, 577 (1952).
[8] J. Heidmann and H. A. Bethe, Phys. Rev. **84**, 274 (1952).
[9] L. Eyges, Phys. Rev. **86**, 325 (1952).
[10] Siber, Halpern, and Mann, Phys. Rev. **84**, 387 (1951).
[11] Details of the apparatus have been submitted for publication to the *Review of Scientific Instruments*.

Fourth-Order Vacuum Polarization

M. Baranger, F. J. Dyson, and E. E. Salpeter
Laboratory of Nuclear Studies, Cornell University, Ithaca, New York
(Received September 10, 1952)

We have calculated the contribution from vacuum polarization to the fourth-order radiative correction to the motion of a slow electron in an external field.

Consider a single scattering of an electron in an electrodynamic potential varying in time and space as $\exp(iq_\mu x_\mu)$; we write q^2 for $(q^2-q_t^2)$, and m for the electron mass. If $q^2 \ll m^2$, the radiative corrections to scattering can be expanded in powers of (q^2/m^2) and of the fine structure constant α. The lowest term, which is due to vacuum polarization, in this expansion is the well-known Uehling[1] term whose ratio to the zero-order scattering is

$$(1/15)(\alpha/\pi)(q^2/m^2). \tag{1}$$

The terms of order α^2 are the fourth-order radiative corrections. Various authors[2] have already discussed and evaluated all these terms, except for the contribution from vacuum polarization. The term in α^2 due to vacuum polarization comes from the three fourth-order diagrams shown in Fig. 1. To lowest order in q^2 these diagrams give a correction potential, whose ratio to the zero-order potential is of the form

$$K(\alpha/\pi)^2(q^2/m^2), \tag{2}$$

where K is a dimensionless constant to be determined.

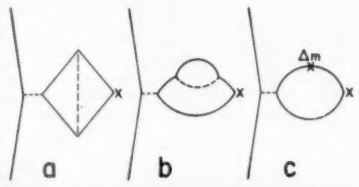

FIG. 1. The three Feynman diagrams contributing to the fourth-order vacuum polarization. Solid lines denote electrons, broken lines photons. Crosses denote the external potential, and the cross plus Δm denotes the mass renormalization operator.

The evaluation of the constant K was carried out along the lines of the Feynman formalism.[3-6] To carry out the mass-renormalization in an unambiguous way a regulation procedure[3,6] was used, involving "photons" of very large mass Λ. The calculations were arranged, making use of the principle of gauge invariance, so that charge renormalization and photon self-energy divergences were automatically excluded. The contributions to K from the three diagrams in Fig. 1 were evaluated separately. The calculations were tedious but very much simpler than those of other fourth-order terms,[2] because in this case the final expressions to be integrated were always rational functions with a single simple denominator. The underlying reason for this simplification is not clear to us. No transcendentals appear in the final results, which are

$$K_a = (1231/8100) + (1/30)\log(\Lambda^2/m^2), \tag{3a}$$
$$K_b = (23/450) - (2/15)\log(\Lambda^2/m^2), \tag{3b}$$
$$K_c = -(1/20) - (1/10)\log(\Lambda^2/m^2), \tag{3c}$$
$$K = K_a + K_b - K_c = 41/162. \tag{4}$$

The constant K is independent of the cutoff Λ.

The vacuum polarization terms have a nonzero expectation value for the $2S$-state of hydrogenic atoms, zero expectation value for the $2P$-state (to this order). They therefore contribute to the Lamb shift, the contribution of the fourth-order terms, Eq. (2), being -0.239 Mc/sec for hydrogen and deuterium, compared with -27.13 Mc/sec from the Uehling term, Eq. (1). All other fourth-order contributions to the Lamb shift have been calculated previously,[2] and also the corrections[7] to the second-order terms produced by the failure of the approximation $q^2 \ll m^2$. Including these contributions, and corrections due to nuclear mass, radius, and structure,[8] the theoretical values[9] for the Lamb shift are (1057.19 ± 0.16) Mc/sec for hydrogen and (1058.49 ± 0.16) Mc/sec for deuterium. These values are about half a megacycle smaller than the corresponding experimental values.[10]

We are indebted to Professor N. M. Kroll and Dr. J. Minkowski and Dr. S. Triebwasser for unpublished communications.

[1] E. A. Uehling, Phys. Rev. **48**, 55 (1935).
[2] R. Karplus and N. M. Kroll, Phys. Rev. **77**, 536 (1950); Bersohn, Weneser, and Kroll, Phys. Rev. **86**, 596 (1952).
[3] R. P. Feynman, Phys. Rev. **76**, 769 (1949).
[4] F. J. Dyson, Phys. Rev. **75**, 1736 (1949).
[5] R. Jost and J. M. Luttinger, Helv. Phys. Acta **23**, 201 (1950).
[6] W. Pauli and F. Villars, Revs. Modern Phys. **21**, 434 (1949).
[7] M. Baranger, Phys. Rev. **84**, 866 (1951); Karplus, Klein, and Schwinger, Phys. Rev. **86**, 288 (1952).
[8] E. E. Salpeter, Phys. Rev. (to be published).
[9] These values do not include any allowance for sixth- and higher order corrections, which might add terms larger than the quoted probable error.
[10] Triebwasser, Dayhoff, and Lamb (to be published).

Isomeric Levels in Pb^{201} and Pb^{202}

N. J. Hopkins*
Radiation Laboratory, McGill University, Montreal, Canada
(Received August 26, 1952)

Short period gamma-activities following proton bombardment of thallium targets have been studied using a sodium iodide scintillation spectrometer. Decay periods of 50 seconds and 5.6 seconds have been observed, and assignments have been made to isomeric levels of Pb^{201} and Pb^{202}, respectively. The γ-ray energies measured were 0.67, 0.42, and 0.25 Mev for the 50-second decay and 0.89 Mev for the 5.6-second decay. Channel analysis of the spectra was accomplished by brightening individual pulses with a circuit due to Watkins[1] and displaying on a triggered oscilloscope. Photographing the screen on moving film yielded permanent records which were later projected and analyzed to give the pulse-height distributions. The 0.510-Mev γ-ray of Sr^{85} was used as a convenient calibration line together with Co^{60} lines.

The 5.6-second period was measured using a method due to Breckon and Martin.[2] For the 50-second activity it was possible to carry out chemical separation of the active lead from the thallium target. This showed conclusively that the activity was in

the lead of the precipitate and not in the thallium of the filtrate. Neither of the activities was observed following bombardments of mercury targets. Thresholds for production were compared with the threshold for production of 8-hour Pb^{201}, and this comparison supported the proposed assignments. Comparison of the energy of the 5.6-second γ-ray with the energy of a γ-ray found in polonium extracted from a bismuth target indicated that the α-decay of Po^{206} probably goes to the 5.6-second excited level of Pb^{202}.

Intensity of the 0.67-Mev line of the 50-second activity appeared to be about four times that of the two lower energy lines on the basis of comparisons of the areas under the photoelectric capture peaks. Although definite transition types cannot be specified, it is interesting to note that the energies 0.42 and 0.25 Mev are in line with the energy spacings of $i_{13/2}$ to $f_{5/2}$ and $f_{5/2}$ to $p_{1/2}$ levels for adjacent isomers of odd neutron number as plotted by Hill.[3] The type of transition giving rise to the intense 0.67-Mev line is particularly puzzling since a crossover transition $i_{13/2}$ to $p_{1/2}$ is ruled out as being of type $M6$. Further data are required before this point can be clarified.

In the course of this investigation the period of the known Pb^{207} metastable state was redetermined as 0.80 ± 0.02 second.

Indebtedness is expressed to Dr. J. S. Foster, Director of the Radiation Laboratory, to Dr. S. W. Breckon and Dr. A. L. Thompson, and to the National Research Council of Canada for two studentships.

* Now at Atomic Energy of Canada, Limited, Commercial Products Division, Ottawa, Canada.

[1] D. A. Watkins, Rev. Sci. Instr. **20**, 495 (1949).
[2] S. W. Breckon and W. M. Martin, McGill University, theses, 1951 (unpublished); Can. J. Phys. (to be published).
[3] R. D. Hill, Brookhaven Quarterly Progress Report S-11, p. 18 (1951) (unpublished).

Heat Pulses in He II Below 1°K

C. J. Gorter
Kamerlingh Onnes Laboratory, Leiden, The Netherlands
(Received September 16, 1952)

THE fact that below 1°K the speed by which heat pulses travel in He II increases enormously[1] has generally been regarded as a confirmation of the Landau version of the two-fluid model.[2] According to that version the so-called normal fluid would essentially consist of rotons, the role of which would be taken over by phonons below 1°K.

In different laboratories it has been observed, however, that the width of the heat pulses increases greatly, and this might suggest that at the lowest temperatures one does not have to do with second sound proper but with the normal transmission of heat pulses in a medium of a certain specific heat and thermal conductivity. The formulas of Kronig and Thellung[3] might be appropriate to describe the transition to the phenomenon of second sound above 1°K. The magnitude of the speeds observed suggests that the mean free path of the phonons responsible for the thermal conductivity is determined by the width of the vessel.[4] The difference with Landau's picture would consist of his emphasis on the momentum of the phonons and of their large effective diameter for collisions.

Mr. H. C. Kramers in Leiden is preparing to investigate the expected influence of the length and the width of the vessel. The publication of the present letter was stimulated by a discussion with Dr. Pellam and Dr. De Klerk, who kindly showed me the recent results obtained at the Bureau of Standards.

Finally, it might be suggested that the increase of the second sound velocity[5] above 1°K upon dissolving He^3 also could be accompanied by an increase of damping and dispersion and so indicate an earlier transition to the very low temperature case.

[1] K. R. Atkins and D. V. Osborne, Phil. Mag. **41**, 1078 (1950).
[2] L. D. Landau, J. Phys. (U.S.S.R.) **5**, 495 (1941).
[3] R. Kronig and A. Thellung, Physica **16**, 678 (1950).
[4] H. B. G. Casimir, Physica **6**, 156 (1939); **5**, 495 (1938).
[5] E. A. Lynton and H. A. Fairbank, Phys. Rev. **80**, 1043 (1950).

Mass Assignment and Gamma-Radiations of the Seven-Hour Molybdenum Isomer

G. E. Boyd and R. A. Charpie
Oak Ridge National Laboratory, Oak Ridge, Tennessee
(Received September 12, 1952)

THE 7-hr isomer activity in molybdenum produced by proton[1–3] and by deuteron irradiation of niobium,[2,4] by alpha-particle bombardment of zirconium,[2,5,6] and in very low yield by fast neutron irradiation[6] of enriched Mo^{94} is of interest in that its assignment to mass 93 cannot be easily reconciled with predictions from shell theory.

Some doubt concerning this mass assignment has persisted, for, unexpectedly, it has not been possible to prepare 7-hr Mo^{93} by deuteron bombardment[6] of enriched Mo^{92}, or by a (γ, n) reaction when enriched Mo^{94} was irradiated with 23-Mev γ-rays.[7] In addition, despite numerous attempts, we have been unable to produce any detectable amounts by irradiating molybdenum enriched to 92.1 percent in mass 92 with slow neutrons in the Oak Ridge graphite pile, nor has this period been observed as a daughter from intense sources of 2.75-hr Tc^{93} produced by a (d, n) reaction on Mo^{92}. Again, in recent bombardments of molybdenum with 20-Mev protons no 7-hr molybdenum whatever from the energetically possible (p, pn) reaction could be detected, although easily measurable quantities of the well-known 67-hr Mo^{99} were formed.

To make quite certain that the 7-hr activity was correctly assigned chemically, a molybdenum fraction was separated from niobium irradiated with 20-Mev protons and exhaustively purified. The decay of gamma-radiations from this purified source was accurately exponential for more than 60 hours and gave a half-life value of 6.95 ± 0.05 hours. Measurements of the γ-ray spectrum were also made using a (Tl+Na)I crystal scintillation counter spectrometer. Energies of 290, 690, and 1464 kev for the photoelectric peaks (Fig. 1) which decayed with a 7-hr half-life were estimated to within 3 percent by comparison with the 141-kev Ce^{144}, the 661-kev Cs^{137}, and the 1175-kev and 1332-kev Co^{60} γ-rays, respectively. These values appear to be in good agreement with recent magnetic lens spectrometer measurements of conversion and photoelectron energies,[8] except for the lowest energy transition. The observed relative intensities of the (unconverted) γ-rays were as 11.2:4:1, which, when compared with the detection efficiency ratios of 18.3:4.1:1 for 290-, 690-, and 1464-kev quanta, respectively, indicate the latter two γ-rays to be equally abundant, and the lowest energy gamma to have a total conversion coefficient of 0.6 ± 0.2. Measurements on a portion of the original proton-

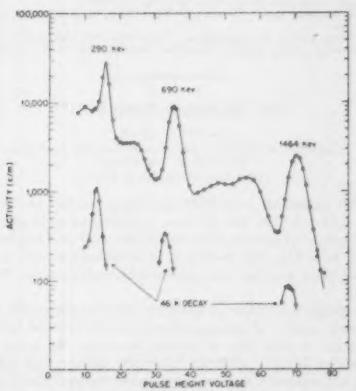

FIG. 1. Gamma-ray spectrum of 6.95-hr Mo^{93} (Tl+NaI scintillation counter spectrometer).

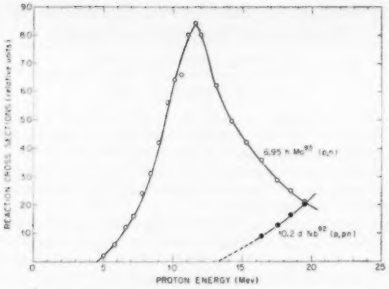

FIG. 2. Relative yields of Mo^{93} and Nb^{92} from Nb^{93}+20-Mev protons.

irradiated Nb showed the same 290-, 690-, and 1465-kev gammas from Mo as well as the 905-kev ray from 10.2-day Nb^{92} formed by a (p, pn) reaction.

The 7-hr Mo may be formed by either a (p, γ), a (p, n), or a $(p, 2n)$ reaction. The first of these alternatives seemed unlikely in view of the 3.7±0.2 Mev reaction threshold observed by Blaser *et al.*[3] However, the possibility of a $(p, 2n)$ reaction remained to be considered. Accordingly, an excitation curve was determined using a stacked foil technique in which one-mil Nb foils were bombarded for 90 minutes with a *ca* 10 μa beam of 20.1-Mev protons. The decay of the beta-activity produced in the Nb foils was resolvable into two periods only—the 6.95-hr Mo and the 10.2-day Nb^{92}. The yield of 6.95-hr Mo when plotted against the incident proton energy (Fig. 2) is seen to reach a maximum at about 11.5 Mev, after which it diminishes with increasing energy. The curve for the formation of 10.2-day Nb^{92} by a (p, pn) reaction shows a threshold at 13.3 Mev and has not reached a maximum at 19.5 Mev. The excitation curve for a $(p, 2n)$ reaction on Nb^{93} should resemble that for the (p, pn) reaction except that its threshold should be approximately 0.6 Mev lower. It seems necessary to conclude that the 6.95-hr Mo isomer is formed by a (p, n) reaction with Nb^{93} and hence must be assigned to mass 93.

[1] L. Dubridge, private communication to G. T. Seaborg; Revs. Modern Phys. **16**, 1 (1944).
[2] D. N. Kundu and M. L. Pool, Phys. Rev. **70**, 111 (1946).
[3] Blaser, Boehm, Marmier, and Sherrer, Helv. Phys. Acta **24**, 441 (1951). These authors find the 7-hr Mo to be formed with an abnormally small cross section.
[4] M. L. Wiedenbeck, Phys. Rev. **70**, 435 (1946).
[5] P. R. Stout and W. R. Meagher, Science **108**, 471 (1948).
[6] Kundu, Hult, and Pool, Phys. Rev. **77**, 71 (1950).
[7] R. B. Duffield and J. D. Knight, Phys. Rev. **76**, 573 (1949); see reference 3 also.
[8] L. Ruby and J. R. Richardson, Phys. Rev. **83**, 698 (1951); see also M. Goldhaber and A. W. Sunyar, Phys. Rev. **83**, 906 (1951), Table I.

Soft Radiation from Pu^{239}†

HARVEY I. ISRAEL
University of California, Los Alamos Scientific Laboratory, Los Alamos, New Mexico
(Received September 5, 1952)

THE radiations from Pu^{239} have been studied in the region 5–25 kev. For this purpose, a proportional counter, filled with argon to a pressure of 53-cm Hg and with methane to a pressure of 6-cm Hg, was employed in combination with a single-channel pulse analyzer and associated amplifying and counting circuits.

Advantage was taken of the fact that the plutonium sources used were capable of causing detectable quantities of fluorescent x-radiation in thin foils of various materials. By using a thin absorber of suitable material, there was obtained the spectrum from plutonium on which was superposed the peak resulting from the characteristic K x-radiation of the absorber material. Such a peak could then be used for purposes of calibration.

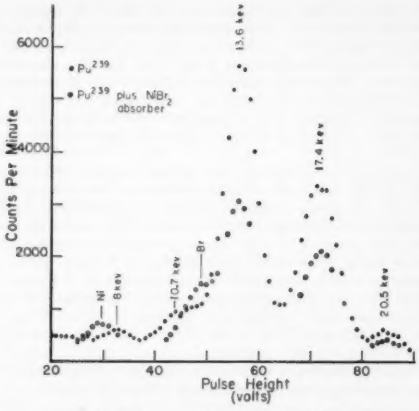

FIG. 1. Spectrum of soft radiation from Pu^{239}.

A typical result is shown in Fig. 1. The source, covered with sufficient Scotch tape to absorb all alpha-radiation, consisted of 0.164 mg PuO_2 on 2-mil Be and was approximately 2 cm^2 in area. The absorber used was a thin layer of $NiBr_2$ crystals put down on Scotch tape. The contribution of the absorber material to the spectrum can easily be noted.

The spectra obtained show peaks at 20.5±0.4, 17.4±0.3, and 13.6±0.3 kev. These values agree with the observed values for the L x-rays of uranium. The peak at 10.7 kev is assumed to be the escape peak for the 13.6-kev radiation, and the peak at 8 kev is considered to be the result of fluorescent radiation from a brass case in which the glass proportional counter was placed.

Using a collimated source, a determination of the L-photon yield was made. Calculations carried out in the usual way[1] gave the results shown in Table I. The total yield, 2.9×10^{-2} photons per alpha-particle, is in error by not more than 50 percent and is in agreement with that reported by Dawson and West.[2]

TABLE I. L-photon yield in Pu^{239} disintegration.

Photon energy (kev)	13.6	17.4	20.5
Photons/alpha-particle	1.2×10^{-2}	1.4×10^{-2}	0.3×10^{-2}

In all phases of the work, much valuable assistance was given by Simon Shlaer. The sources were supplied and prepared by John G. Povelites.

† Work done under the auspices of the AEC.
[1] W. Rubinson and W. Bernstein, Phys. Rev. **86**, 545 (1952).
[2] D. West and J. K. Dawson, Proc. Phys. Soc. (London) **A84**, 586 (1951).

Spherical Model of a Ferromagnet

H. W. LEWIS AND G. H. WANNIER
Bell Telephone Laboratories, Murray Hill, New Jersey
(Received September 12, 1952)

IN a paper having the above title[1] Berlin and Kac have presented a model for cooperative action in crystals to which statistical mechanics can be applied rigorously. We wish to point out that the mathematical manipulations of that paper can be reduced to almost nothing by the use of a grand rather than a canonical ensemble. We feel that this observation is of some consequence in a domain of research in which progress is largely impeded by mathematical difficulties.

The simplification consists in replacing the partition function (11) by the corresponding grand partition function in which the quantities ϵ_i are not restrained by a side condition:

$$Q_N=(2\pi)^{-N/2}\int_{-\infty}^{+\infty}\cdots\int_{-\infty}^{+\infty}\times d\epsilon_1 d\epsilon_2\cdots d\epsilon_N \exp[K\Sigma_{i,j}{}'\epsilon_i\epsilon_j-s\Sigma_i\epsilon_i{}^2]. \quad (1)$$

Here s is the conjugate variable to $\Sigma_i\epsilon_i{}^2$; after evaluation of Q_N it is to be adjusted at each temperature so that the Berlin-Kac condition holds:

$$\partial \ln Q_N/\partial s=-N. \quad (2)$$

This means that we satisfy the restraint of their model in the mean; this is sufficient by the principles of fluctuation theory, provided each member of the assembly is itself a macroscopic system. The evaluation of an expression of the form (1) also occurs in BK (C3). It is, however, followed by an integration in the complex plane which appears to play an essential role in the determination of the temperature singularity of the three-dimensional model.

In the present mode of computation we proceed entirely from (1) and (2). In evaluating (1) we follow BK [Eqs. (5) to (8)] with the one reservation that the lowest mode must be excepted from the smoothing-out process (this is familiar from the theory of Einstein condensation). Thus, we find

$$\ln Q_N=-\tfrac{1}{2}\ln(2s-12K)-\tfrac{1}{2}\frac{N}{(2\pi)^3}\int_0^{2\pi}\int\int\times d\omega_1 d\omega_2 d\omega_3 \ln[2s-4K(\cos\omega_1+\cos\omega_2+\cos\omega_3)]. \quad (3)$$

Equations (1), (2), and (3) are sufficient to yield

$$U=-\tfrac{1}{2}J\partial \ln Q_N/\partial K=(JN/4K)(1-2s). \quad (4)$$

This is BK Eq. (18), the key equation to most of the derived results. To complete our derivation, we must only show that we can also derive the correct dependence of s upon temperature. Applying condition (2) to (3), we get

$$1=\frac{1}{2N(s-6K)}+\frac{1}{2(2\pi)^3}\int_0^{2\pi}\int\int\frac{d\omega_1 d\omega_2 d\omega_3}{s-2K(\cos\omega_1+\cos\omega_2+\cos\omega_3)}. \quad (5)$$

For K sufficiently small, this equation yields for s a value substantially larger than $6K$; the first term is then negligible and Eq. (C23) of BK is obtained. As K increases, the boundedness of the integral comes into play, and s must approach $6K$ sufficiently closely so that the first term in (5) can make up the deficit. This feature leads to the "sticking" of s at the value $6K$ and yields the entire low temperature behavior of the model. All results of the BK paper are thus derived.

[1] T. H. Berlin and M. Kac, Phys. Rev. **86**, 821 (1952). In this letter it is referred to as BK.

Three New Neutron Deficient Xenon Isotopes*

BRUCE DROPESKY† AND EDWIN O. WIIG
Department of Chemistry, University of Rochester, Rochester, New York
(Received September 17, 1952)

WHILE investigating the spallation reactions which occurred when iodine was bombarded with 240-Mev protons in the Rochester cyclotron, three previously unreported xenon isotopes were found.

About 200 mg of anhydrous lithium iodide (~99 percent pure, A. D. Mackay, Inc.), wrapped in a small envelope of 1-mil aluminum foil and clamped to the cyclotron probe, was exposed to the internal beam for one hour. Within 20 minutes of the end of the bombardment, collection of the xenon was completed and counting begun. The all-glass gas-collecting system consisted of a reaction tube containing a cold finger and an inlet for helium gas, a trap of potassium hydroxide-coated glass wool kept at dry ice temperature, and one or more charcoal traps held at liquid air temperature. The reaction tube contained about 10 drops each of frozen concentrated nitric and sulfuric acids, to which the target iodine was added, and was connected to the line by a ground glass joint. With helium slowly flowing through the system, the reaction mixture was heated until most of the iodine was collected on the cold finger (−78°C) and the xenon, carried by the helium, was adsorbed on the cold charcoal. All water and acid vapors were presumably removed by the potassium hydroxide trap. The charcoal trap, in the form of a small U-tube, was sealed, cut from the line, and cemented to a Lucite disk for counting.

Decay of the xenon activity, as counted through the glass wall (0.5–1.0 mm thick) of the U-tubes, was followed with a scintillation counter having a NaI(Tl) phosphor and also with a halogen filled GM tube. Resolution of a gross decay curve obtained with the latter yielded the following half-lives: ~35 minutes, 1.7 hours, 20.1 hours, and >20 days.

A xenon sample placed in our low resolution beta-ray survey spectrometer showed positrons of >2.8 Mev with ~1.8-hour half-life, and 3.1-Mev positrons of 20-hour half-life. The agreement between the latter positron energy and that of the reported[1] 3.6-minute I^{128} suggested that Xe^{128} with a 20-hour half-life had been produced, while the other activities indicated Xe^{121} and/or Xe^{123} were made.

Parent-daughter isolation experiments were performed to determine whether the 20-hour activity was the parent of I^{128} and to determine the half-lives of Xe^{125} and/or Xe^{127}. The separation was based on complete desorption of xenon from charcoal at elevated temperatures[2] and the retention of iodine daughters as solid iodide if silvered charcoal is used. A glass line consisting of a series of small U-tube traps, each filled with ~0.3 g silvered, activated charcoal held in place with glass wool, was used for making rapid periodic separations of the iodine daughters from the parent xenon. A large charcoal trap at −196°C, containing all the xenon collected from one target, was attached to the line by a ground glass joint and the system pumped down with a Cenco Hyvac pump. The xenon was transferred to the first trap of the series by cooling that trap with liquid nitrogen and warming the original large trap with an electric heater, after which the large trap was sealed from the line. This procedure was repeated at regular in-

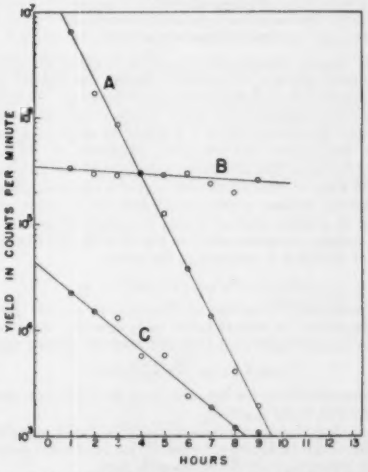

FIG. 1. Yields of iodine daughters at successive one-hour separations from xenon parent. Curve *A* (shelf 1, 2 mm from crystal), yields of I^{125}, shows the half-life of Xe^{125} to be 40(±2) minutes, and curve *C* (shelf 1), yields of I^{128}, gives 1.7(±0.2) hours for the half-life of Xe^{128}. Curve *B* (shelf 6, 80 mm from crystal) shows the yields of I^{128} to be compatible with 20(±1) hours for the Xe^{128} half-life, observed directly.

tervals of one hour for the first 9 traps. The activity of each sample of iodine grown in from the xenon was determined. The last trap was sealed and mounted for counting immediately upon transferring the xenon to it. From 3 to 5 minutes elapsed from the starting of a parent-daughter separation and the placing of the iodine sample under the scintillation counter.

All iodine daughter samples showed the presence of 3.4(±0.1)-minute and 1.45(±0.1)-hour activities, presumably I^{129} and I^{131}, respectively, 13-hour I^{135}, and 17-day Te^{131}. Several determinations of the I^{131} half-life on radiochemically pure iodine separated from the target gave a value of 1.5(±0.1) hours rather than the reported 1.8 hours, and the tellurium activity isolated from these samples confirmed the observation[3] that I^{131} decays to the lower 17-day isomeric state of Te^{131}. From the yields of I^{131} and I^{133} *versus* the time of parent-daughter separations the half-lives of Xe^{131} and Xe^{133} were determined to be 40(±2) minutes and 1.7(±0.2) hours, respectively (curves *A* and *C*, Fig. 1). The yields of I^{132} (curve *B*) proved to be completely compatible with the half-life of 20(±1) hours found with a GM tube for the xenon in the last trap of the series. Scintillation counter data on this sample proved that 32-day Xe^{127} had also been produced and indicated that 18-hour Xe^{135} was likewise present. All limits of error placed on numerical values are based on an estimate of the apparent reliability of the data.

Other workers, Tilley[4] at McGill University and Mathur and Hyde[5] at the University of California, Berkeley, have independently obtained information in substantial agreement with ours.

* Research carried out under contract with the AEC.
† du Pont Fellow in chemistry, 1951–52.
[1] Young, Pool, and Kundu, Phys. Rev. **83**, 1060 (1951).
[2] J. A. Ayres and I. B. Johns, *Radiochemical Studies: The Fission Products* (McGraw-Hill Book Company, Inc., New York, 1950), Paper No. 311, National Nuclear Energy Series, Plutonium Project Record, Vol. 9, Div. IV.
[3] L. Marquez and I. Perlman, Phys. Rev. **78**, 189 (1950).
[4] D. E. Tilley, Abstract 77, Royal Society of Canada meeting (June, 1952).
[5] H. B. Mathur and E. K. Hyde, private communication.

Angular Correlations in $(d,p\gamma)$ Reactions*

L. J. GALLAHER AND W. B. CHESTON
Washington University, St. Louis, Missouri
(Received September 8, 1952)

THE angular distribution of protons produced in (d, p) reactions has been calculated by Butler[1] and others[2,3] under the assumption that a stripping process is the primary mechanism operative. Comparison of this theory with experimental results for the proton distribution makes it possible, in many cases, to determine the angular momentum l_N transferred to the target nucleus by the capture of a neutron. In general, the information obtained about l_N does not provide a unique spin assignment for the resultant nucleus; a parity determination is always unambiguous. If a target nucleus of spin $\mathbf{j}_0$ captures a neutron with orbital angular momentum l_N from the deuteron, the spin of the resultant nucleus $\mathbf{j}_1$ is restricted to the values

$$|j_0+l_N+\tfrac{1}{2}|_{\min}\leqq j_1\leqq j_0+l_N+\tfrac{1}{2}. \quad (1)$$

The production of a nucleus (j_1) from a target nucleus (j_0) may be characterized by several values of l_N provided these values differ by an even number of units and obey the limiting relation

$$|j_0+j_1+\tfrac{1}{2}|_{\min}\leqq l_N\leqq j_0+j_1+\tfrac{1}{2}. \quad (2)$$

It is to be noted that if either j_0 or j_1 are zero, only one value of l_N contributes to the reaction.

The methods and approximations applied in the (d, p) stripping calculations can be extended to the $(d, p\gamma)$ correlation function. The correlation function $f(\theta, \vartheta)$ takes the form

$$f(\theta,\vartheta)=\text{const}\sum_{l_N}\frac{\Lambda_{l_N}(\vartheta)}{(2l_N+1)}|g_{l_N}(\theta)|^2. \quad (3)$$

$|g_{l_N}(\theta)|^2$ is the angular distribution with respect to the incoming deuteron of the protons produced in the absorption of a neutron (l_N) from the deuteron by the target nucleus (j_0) leading to the nuclear state (j_1). $\Lambda_{l_N}(\vartheta)$ is the angular correlation function for the (n, γ) reaction in which a free neutron of angular momentum l_N is absorbed by a target nucleus (j_0) leading to a new nucleus (j_1) in the excited state which subsequently decays by 2^L multipole emission to the nuclear state (j_2). ϑ is the angle between the directions of propagation of the absorbed neutron and the emitted γ-ray. $\Lambda_{l_N}(\vartheta)$ is explicitly[4]

$$\Lambda_{l_N}=\sum_{\sigma}\sum_{m_1m_2}|A_{\sigma}{}^{l_N}|^2 \times\langle\sigma l_N m_1 0|j_1m_1\rangle^2\langle j_1Lm_1(m_2-m_1)|j_2m_2\rangle^2F_L{}^{m_2-m_1}(\vartheta). \quad (4)$$

σ is the vector sum of $\mathbf{j}_0$ and $\mathbf{S}_N$ (neutron spin); $A_{\sigma}{}^{l_N}$ is that part of the matrix element for the neutron capture process exclusive of the Clebsch-Gordan coefficients representing the dependence on the magnetic quantum numbers; $F_L{}^{m_2-m_1}(\vartheta)$ is the classical distribution for the (m_2-m_1) contribution to the 2^L multipole radiation; m_1, m_2 are the sets of magnetic quantum numbers belonging to the states (j_1) and (j_2), respectively. It immediately follows that if the (d, p) process is characterized by only one value of l_N, the emitted γ-ray is correlated to the direction of the absorbed neutron—or what is equivalent, the direction of the recoiling nucleus (j_1)—just as if the neutron had been captured from an unbound state.[5] This obtains when $j_0=0$ and Eq. (3) becomes

$$f(\theta,\vartheta)=\text{const}\,|g_{l_N}(\theta)|^2 \times\sum_{m_1m_2}\langle j_1Lm_1(m_2-m_1)|j_2m_2\rangle^2F_L{}^{m_2-m_1}(\vartheta)\delta(m_1\pm\tfrac{1}{2}). \quad (5)$$

Equation (5) exhibits no unknown parameters except those contained in the internal wave function of the deuteron implicit in $g_{l_N}(\theta)$. For the general reaction in which $j_0\neq0$, no statements can be made concerning $f(\theta, \vartheta)$ which are independent of a specific nuclear model needed to calculate the functions $A_{\sigma}{}^{l_N}$.

Equation (5) can be applied directly to the $A^{40}(d, p)A^{41*}(\gamma)A^{41}$ reaction, which has been studied experimentally by Gibson and Thomas.[6] These authors have demonstrated that the 1.34-Mev state of A^{41} has either odd parity and spin $\frac{1}{2}$ or $\frac{3}{2}$, or possibly even parity and spin $\frac{1}{2}$, whereas the ground state has spin 7/2 or 5/2 and odd parity. Table I gives the dependence on $\cos\vartheta$ of the angular correlation function $f(\theta, \vartheta)$ for each possible assignment of spin and parity to the 1.34-Mev and ground states of A^{41}. It is to be noted that if the measured angular correlation function is isotropic, the 1.34-Mev state has spin $\frac{1}{2}$, but no definite statements can be made of its parity or the spin of the ground state. On the other hand, a measured angular correlation which is nonisotropic will determine the spins and parities of both states of A^{41}.

TABLE I. Predicted angular distribution of γ-rays from the 1.34-Mev level of A^{41*} formed in a (d, p) reaction on A^{40}. ϑ is the angle between the recoiling A^{41*} and the 1.34-Mev γ-ray; L is the pole of the emitted γ-ray.

A^{41*} spin	A^{41*} parity	A^{41} spin	A^{41} parity	L	$f(\theta,\vartheta)/\lvert g_{l_N}(\theta)\rvert^2$
1/2	odd	7/2	odd	arbitrary	1
		5/2	odd		
1/2	even	7/2	odd		
		5/2	odd		
3/2	even	7/2	odd	2	$1+(3/13)\cos^2\vartheta$
		5/2	odd	1	$1-(1/7)\cos^2\vartheta$
				2	$1-(5/11)\cos^2\vartheta$

The authors wish to acknowledge several illuminating discussions on this problem with Dr. H. Primakoff.

* Assisted by the joint program of the ONR and AEC.
[1] S. T. Butler, Proc. Roy. Soc. (London) **208A**, 559 (1951).
[2] Bhatia, Huang, Huby, and Newns, Phil. Mag. **43**, 485 (1952).
[3] F. Friedman and W. Tobocman, private communication.
[4] Biedenharn, Arfken, and Rose, Phys. Rev. **83**, 586 (1951).
[5] This has been independently demonstrated by Biedenharn, Boyer, and Charpie, Phys. Rev. **88**, 517 (1952).
[6] W. Gibson and E. Thomas, Proc. Roy. Soc. (London) **A210**, 543 (1952).

Stripping and the Nuclear Shell Model

S. T. Butler
Laboratory of Nuclear Studies, Cornell University, Ithaca, New York
(Received September 2, 1952)

It has previously been pointed out[1] that the angular distributions from certain (d, p) and (d, n) nuclear reactions should give a sensitive measure of the accuracy of the nuclear shell model in ascribing definite orbital angular momentum states to nucleons in a nucleus. The possibility of this is due to the fact that these reactions proceed via the stripping process,[2] and that their angular distributions are characterized by the orbital angular momenta l with which the captured particle can be accepted into the final state. Each allowed value of l produces a peak in the angular distribution, the peaks resulting from different l values being quite separate. In cases when the selection rules allow more than one value of l, therefore, the purity of the final nuclear states involved can be investigated by a measurement of the relative heights of the peaks resulting from the different l values. For this it is possible to choose examples[1] which are very sensitive to deviations from pure independent particle nuclear states.

Some of the experiments suggested in reference 1 have now been performed,[3,4] and in order to make quite clear their interpretation, we will discuss in this note precisely what nuclear property is being measured in these experiments, i.e., what nuclear property determines the relative heights of the maxima resulting from different l values.

The most convenient starting point for this is to write the stripping differential cross section (for a (d, p) reaction, for example), as obtained by the method of reference 2, in the form

$$\sigma(\theta_p)=\frac{\pi^2 C^2 m_p^* m_d^* k_p(2J+1)}{qK_d m_n^{*2}(2j_0+1)} \times \sum_{M m_0 \mu_n} \Big| \sum_{l_n m_n} a_0(Jj_0 l_n, M m_0 m_n \mu_n) F_{l_n}(\theta_p) \Big|^2, \quad (1)$$

where

$$F_{l_n}(\theta_p)=\left[\frac{1}{K^2+a^2}-\frac{1}{K^2+(a+b)^2}\right]\left\{\sum_{r=0}^{l_n}\frac{(l_n+r)!}{r!(l_n-r)!(2\kappa r_0)^r} \times\left[\left(\kappa+\frac{r}{r_0}\right)+\frac{\partial}{\partial r_0}\right]\left(\frac{r_0}{Z}\right)^{\frac{1}{2}} J_{l_n+\frac{1}{2}}(Zr_0).\right.$$

Here m_d^*, m_p^*, and m_n^* are the appropriate reduced masses of the deuteron, proton, and captured neutron, respectively, q is a number close to unity,[5] and all other factors are as defined in reference 2 except that the spin of the initial nucleus has been written j_0 (with orientation m_0).

The factor in (1) depending on the wave functions of the initial and final nuclei is the $a_0(Jj_0 l_n, M m_0 m_n \mu_n)$, which is defined as follows: Let the wave function $\psi(J, M; \xi, \tau_n)$ of the final nucleus be expanded in terms of states i of the initial nucleus, i.e.,

$$\psi(J, M; \xi, \tau_n)=\sum_{i m_i \mu_n l_n m_n} u_i(j_i, m_i; \xi)\psi_n(\mu_n) Y_{l_n m_n}(\theta_n \varphi_n) \times \frac{f_i(Jj_0 l_n, M m_i m_n \mu_n; r_n)}{r_n}. \quad (2)$$

Here the $u_i(j_i, m_i; \xi)$ are the wave functions for the states i of the initial nucleus (with spins j_i and orientations m_i) and $\psi_n(\mu_n)$ is the neutron spin function. Then $a_0(Jj_0 l_n, M m_0 m_n \mu_n)$ is directly proportional to the wave function $f_0(Jj_0 l_n, M m_0 m_n \mu_n; r_n)$ taken at the nuclear surface; we have in fact

$$a_0(Jj_0 l_n, M m_0 m_n \mu_n)=f_0(Jj_0 l_n, M m_0 m_n \mu_n; r_0)/g_{l_n}(r_0),$$

where

$$g_{l_n}(r_0)=\left\{\sum_{r=0}^{l_n}\frac{(l_n+r)!}{r!(l_n-r)!(2\kappa r_0)^r}\right\}.$$

It may be mentioned that the above simple form for the nuclear dependence is obtained from Eq. (29) of reference 2 by expressing the factor db/dk_p appearing there in terms of the factor $a(k_p)$, using the method outlined in Sec. 2 of reference 2.

By making use of the symmetry properties of the wave functions $f_0(Jj_0 l_n, M m_0 m_n \mu_n \gamma_n)$, the summation over spin orientations in (1) can now readily be performed, and the cross section becomes

$$\sigma(\theta_p)=\frac{\pi^2 C^2 m_p^* m_d^* k_p(2J+1)}{qK_d m_n^{*2}(2j_0+1)} \sum_{l_n} \frac{|f_0(Jj_0 l_n; r_0)|^2}{g_{l_n}^2(r_0)} |F_{l_n}(\theta_p)|^2. \quad (3)$$

Here $|f_0(Jj_0 l_n; r_0)|^2$ is the probability density for finding a neutron with orbital angular momentum l_n at the surface of the final nucleus, when the nucleus it leaves behind (core) is in the ground state.

Thus the experiments suggested in reference 1 measure deviations in the shell model, expressed in terms of the relative sizes of the various $|f_0(Jj_0 l_n; r_0)|^2$ factors for allowed values of l_n. This gives directly, therefore, an idea of the relative admixtures of orbital angular momentum states for the captured neutron when the core is in the ground state. It should be noted though that these experiments in no way measure admixtures of states in the final nucleus which are due to excitation of the core.

I am indebted to Dr. N. Austern for discussions in connection with this work.

[1] H. A. Bethe and S. T. Butler, Phys. Rev. **85**, 1045 (1952).
[2] S. T. Butler, Proc. Roy. Soc. (London) **A208**, 559 (1951).
[3] Parkinson, Beach, and King, Phys. Rev. **87**, 387 (1952).
[4] J. S. King and W. C. Parkinson, Phys. Rev. **88**, 141 (1952).
[5] The number q is given, to a very good approximation, by $\int |\psi(J, M; \xi, \tau_0)|^2 d\xi d\tau_n$.

Energy Levels Associated with the Radioactive Decay of Gd^{153} and Tb^{161}†

J. M. Cork, J. M. LeBlanc, W. H. Nester, and F. B. Stumpf
Department of Physics, University of Michigan, Ann Arbor, Michigan
(Received August 18, 1952)

The irradiation of gadolinium with slow neutrons in the pile yields two long-lived radioactive emitters. One activity, first observed[1] by Fajans and Voigt, has a half-life reported as from 150 to 236 days and is believed[2] to be due to Gd^{153}, being formed by neutron capture from Gd^{152}, whose normal abundance is only 0.2 percent. Another activity of about 7-day half-life is really in Tb^{161}, being formed[3] by beta-gamma decay from a short-lived Gd^{161}. From the conversion electrons observed in high resolution magnetic spectrometers, a single gamma-ray appears to be associated with each activity.

The 103.7-kev gamma-ray in the Eu^{153} nucleus, following K capture in Gd^{153}, is found to have a K/L ratio of 5.2 ± 1. From the empirical relations[4] of Goldhaber and Sunyar this indicates either an $M2$ or a mixture of $E2$ and $M1$ transitions. However, from the long radiation lifetime (0.001 sec) required for the $M2$ radiation, which has not been observed, it appears preferable to assume the existence of the mixture. This same gamma-ray together with

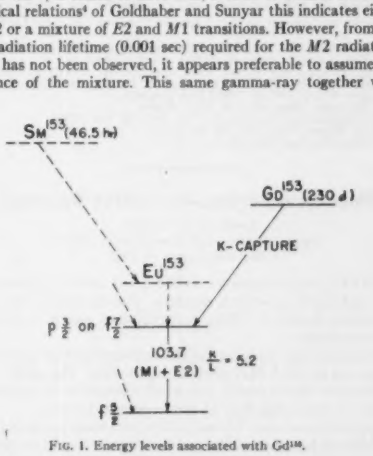

FIG. 1. Energy levels associated with Gd^{153}.

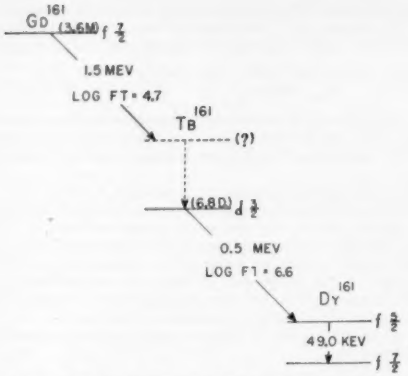

FIG. 2. Energy levels associated with Gd^{161} (from shell theory).

others has been observed in the beta-decay of Sm^{153}. It must follow in the ordering of the levels of Eu^{153} that the 103.7-kev transition leads directly to the ground state of the nucleus. It has been noted[5] that the measured parity of this ground state ($f_{5/2}$) is not in agreement with the value expected from shell theory ($d_{5/2}$).

In the Dy^{161} nucleus a single gamma-ray of energy 49.0 kev is found. At the low energy no K conversion electron line could occur. The L/M conversion ratio is found to be 3.7 ± 0.8. Since conversion occurred mainly in the L_1 level, the radiation[6] is quite probably $M1$. The half-life of the Tb^{161} activity was followed through six octaves and was found to be 6.8 ± 0.1 days. The beta-energies and the gamma-energy in Gd^{161} have not been re-evaluated in this investigation.

From shell theory for odd-even nuclei it is possible to assign spin and parity values to the observed levels of the isobar 161, with one exception. The log ft value for the beta-decay in Gd^{161} is 4.8. This indicates an allowed transition with no parity change. Shell theory indicates the ground state of Gd^{161} to be $f_{7/2}$ and the only low-lying excited state of Tb^{161} of the same parity is an $h_{11/2}$ state, which would require a spin change of two. It may be that the data leading to the β value are inaccurate. Otherwise, this particular transition cannot be regarded as in satisfactory agreement with the extreme single particle theory. The complete data are shown graphically in Fig. 1 for Gd^{153} and in Fig. 2 for Gd^{161}.

† This investigation received the joint support of the ONR and AEC.
[1] K. Fajans and A. Voigt, Phys. Rev. **60**, 533 (1941).
[2] Cork, Shreffler, and Fowler, Phys. Rev. **74**, 240 (1948); R. Hein and A. Voigt, Phys. Rev. **79**, 783 (1949); and B. Ketelle, Oak Ridge National Laboratory Report-299, 35 (1949) (unpublished).
[3] F. Butement, Phys. Rev. **75**, 1276 (1949).
[4] M. Goldhaber and A. Sunyar, Phys. Rev. **83**, 906 (1951).
[5] M. G. Mayer, Phys. Rev. **78**, 16 (1950).
[6] J. Mihelich, Phys. Rev. **87**, 646 (1952).

Total Cross Sections for 14-Mev Neutrons*

LEONARD S. GOODMAN
Argonne National Laboratory, Chicago, Illinois
(Received August 18, 1952)

TOTAL cross sections for 14-Mev, T(d, n)He neutrons were measured for several elements. The deuterium ions were accelerated through a 130-kv potential drop against a tritiated zirconium target.

Detection of the neutrons was accomplished with an anthracene crystal and an RCA 5819 photomultiplier tube. The signal, after amplification, was biased so that recoil protons (in the anthracene crystal) of energy less than 12 Mev were not detected.

The usual corrections for background and room scattering were made. In-scattering corrections were made according to the method of McMillan and Sewell.[1] The results listed in Table I are, within statistical counting errors, in reasonable agreement with more accurate data by Coon, Graves, and Barschall.[2]

TABLE I. Total cross sections for 14-Mev neutrons (in units of 10^{-24} cm^2).

H	0.69 ±0.06	Ti	2.2 ±0.2	Zr	3.6 ±0.2
D	0.82 ±0.08	V	2.4 ±0.1	Mo	3.6 ±0.3
Be	1.4 ±0.1	Cr	2.3 ±0.2	Sn	4.0 ±0.4
C	1.20 ±0.04	Fe	2.4 ±0.2	Sb	4.6 ±0.3
O	1.5 ±0.1	Ni	2.5 ±0.1	W	4.8 ±0.3
Mg	1.8 ±0.2	Cu	2.5 ±0.1	Pb	5.1 ±0.4
Al	1.8 ±0.1	Zn	3.0 ±0.2	Bi	5.2 ±0.5

The author wishes to express his gratitude to Professor Samuel K. Allison, representing the University of Chicago Physics Department, for his considerate interest and assistance throughout the progress of the experiment.

We would like to thank Dr. J. H. Coon for the privilege of seeing his report before it appeared in print.

* These data are part of a paper which was written to fulfill a partial requirement for a Ph.D. degree at the University of Chicago.
[1] E. M. McMillan and D. C. Sewell, AEC report MDDC-1558 (unpublished).
[2] Coon, Graves, and Barschall, Phys. Rev. **88**, 562 (1952).

Spin-Spin Relaxation in Ferromagnetic Resonance*

FREDERIC KEFFER†
Department of Physics, University of California, Berkeley, California
(Received September 15, 1952)

WE demonstrate here the theoretical possibility of a non-vanishing line width in ferromagnetic resonance at 0°K arising from zero-point fluctuations of spin-spin magnetic dipole fields.

The Hamiltonian of the spin system is

$$\mathcal{H}=\mathcal{H}^0+\mathcal{H}^{++}+\mathcal{H}^{--}+\mathcal{H}^{+}+\mathcal{H}^{-}, \tag{1}$$

with

$$\mathcal{H}^0=-Hg\beta\Sigma_j S_j^z+\Sigma_{k>j}(A_{jk}\mathbf{S}_j\cdot\mathbf{S}_k+B_{jk}S_j^zS_k^z),$$
$$\mathcal{H}^{++}=\Sigma_{k>j}E_{jk}S_j^+S_k^+;\quad \mathcal{H}^{--}=\Sigma_{k>j}E_{jk}{}^*S_j^-S_k^-,$$
$$\mathcal{H}^{+}=\Sigma_{k\neq j}F_{jk}S_j^+S_k^z;\quad \mathcal{H}^{-}=\Sigma_{k\neq j}F_{jk}{}^*S_j^-S_k^z,$$

where

$$A_{jk}=-2J_{jk}+\tfrac{1}{2}D_{jk}(3\gamma_{jk}{}^2-1),$$
$$B_{jk}=-\tfrac{3}{2}D_{jk}(3\gamma_{jk}{}^2-1),$$
$$E_{jk}=\tfrac{3}{2}D_{jk}[\beta_{jk}{}^2-\alpha_{jk}{}^2+2i\alpha_{jk}\beta_{jk}],$$
$$F_{jk}=-\tfrac{3}{2}D_{jk}\gamma_{jk}(\alpha_{jk}-i\beta_{jk}).$$

In the above J_{jk} is the exchange integral between spins j and k; $D_{jk}=g^2\beta^2/r_{jk}{}^3$ if purely magnetic dipole forces are operative; and α_{jk}, β_{jk}, γ_{jk} are direction cosines of r_{jk} taken with respect to the crystal axes. We shall assume for simplicity that the applied field H lies along a crystal axis.

The only part of $\mathcal{H}$ commuting with S^z is $\mathcal{H}^0$. The remainder of $\mathcal{H}$ breaks down the selection rules $\Delta M=\pm1$ in a resonance experiment, causing weak satellite lines to appear at $\Delta M=0,\pm2,\pm3$. In evaluating the second and fourth moments of the principal ($\Delta M=\pm1$) resonance line for a paramagnetic sample, therefore, Van Vleck[1] used the ingenious trick of limiting the Hamiltonian to $\mathcal{H}^0$.

If, however, $J>Hg\beta$, the energies of the many states of a given S^z are spread over a spin-wave spectrum larger than the Zeeman splitting of states of different S^z. States of different S^z are then nearly degenerate and are strongly mixed by the dipole terms. Thus M ceases to be even approximately a good quantum number, and the satellite picture breaks down. In paramagnetic resonance in a sample with large exchange forces, therefore, the moments should be evaluated by use of the entire Hamiltonian. This has the effect of multiplying Van Vleck's second moment by 10/3; and from general considerations it can be seen that the line width,

as estimated by Van Vleck from "exchange narrowing," should also be multiplied by 10/3.

In the case of ferromagnetic resonance, as Van Vleck has shown,[2] use of the truncated $\mathcal{H}^0$ leads to a second moment which goes rapidly to zero below the Curie point. Here in order to justify use of the entire Hamiltonian we must show a strong mixing of the ground (saturated) state with the next highest state. This can be produced by pseudodipole forces of magnitude sufficient to account for anisotropy and magnetostriction, i.e., of the order of 10^4 to 10^6 oersteds.

Using the entire Hamiltonian, we find[3] at 0°K for a spherical face-centered cubic crystal with individual spin quantum number S:

$$\begin{aligned}
\hbar\langle\omega\rangle_{Av} &= g\beta H,\\
\hbar^2\langle\omega^2\rangle_{Av} &= g^2\beta^2H^2+4S\Sigma_j|F_{jk}|^2,\\
\hbar^3\langle\omega^3\rangle_{Av} &\cong 8JS(24S-1)\Sigma_j|F_{jk}|^2,\\
\hbar^4\langle\omega^4\rangle_{Av} &\cong 16J^2S(24S-1)^2\Sigma_j|F_{jk}|^2. \qquad (2)
\end{aligned}$$

Here we have given only the leading exchange terms of the third and fourth moments and have limited the exchange integral J to nearest neighbors. From magnetic dipole forces alone we obtain for a f.c.c. crystal and lattice constant a:

$$\Sigma_j|J_{jk}|^2 \cong 36g^4\beta^4a^{-6} = (3g\beta M_s/2S)^2, \qquad (3)$$

where M_s is the saturation magnetization.

If the resonance curve were Gaussian, the half-width would be[1]

$$(\Delta H)_{\frac{1}{2}} = 2.35(\hbar/g\beta)[\langle\Delta\omega^2\rangle_{Av}]^{\frac{1}{2}} \cong 7M_s/S^{\frac{1}{2}}. \qquad (4)$$

This is increased by $\sim$50 times when pseudodipole forces are introduced. However, since the third and fourth moments involve J, the line must be much more sharply peaked than a Gaussian. Van Vleck[1] suggests that this "exchange narrowing" might reduce the line width by a factor $\sim D/J$. Again introducing pseudodipole forces to determine D, we are left with a line width of the reasonable order of hundreds of oersteds.

From Eq. (4) we note that if $S\to\infty$ with M_s held constant (classical limit), the width disappears. We are thus dealing with a zero-point quantum effect.

As can be seen from Eq. (2), the only part of the Hamiltonian contributing to the moments, apart from the Zeeman and exchange terms, is $\mathcal{H}^{++}+\mathcal{H}^{--}$. This is in agreement with the results of spin-wave theory. In the approximation used by Holstein and Primakoff[4] $\mathcal{H}^{++}+\mathcal{H}^{--}$ is effectively dropped, whereas $\mathcal{H}^0+\mathcal{H}^{++}+\mathcal{H}^{--}$ is retained; this introduces demagnetizing fields but leads to no mixing of spin waves of different wave number k. On using the $\mathcal{H}^{++}+\mathcal{H}^{--}$ term, Akhieser[5] finds a mixing of spin waves and hence a spin-spin relaxation. Further progress on the spin-spin relaxation problem might well come from using pseudodipole forces and otherwise improving Akhieser's calculation.

I wish to thank Professor C. Kittel, Professor J. H. Van Vleck, and Dr. M. H. Cohen for many enlightening discussions of this problem.

* This work was supported in part by the ONR.

† Now at the Department of Physics, University of Pittsburgh, Pittsburgh, Pennsylvania.

[1] J. H. Van Vleck, Phys. Rev. **74**, 1168 (1948).
[2] J. H. Van Vleck, Phys. Rev. **78**, 266 (1950).
[3] In evaluating moments at 0°K we take only the ground-state matrix element rather than the customary spur, and assume complete alignment of spins in the ground state. This is only approximately correct due to the strong pseudodipole forces.
[4] T. Holstein and H. Primakoff, Phys. Rev. **58**, 1098 (1940).
[5] A. Akhieser, J. Phys. (U.S.S.R.) **10**, 217 (1946).